THE PHYSICAL REVIEW

VOLUME 96 Second Series NUMBER 5

DECEMBER 1, 1954

Published for the

AMERICAN PHYSICAL SOCIETY

by the

AMERICAN INSTITUTE OF PHYSICS

Lancaster, Pa. and New York, N. Y.

THE
PHYSICAL REVIEW

A journal of experimental and theoretical physics established by E. L. Nichols in 1893

SECOND SERIES, VOL. 96, NO. 5 DECEMBER 1, 1954

Theory of the Thermoelectric Power of Semiconductors

CONYERS HERRING *
Institute for Advanced Study, Princeton, New Jersey and Bell Telephone Laboratories, Murray Hill, New Jersey
(Received June 29, 1954)

The usual theory of thermoelectric power fails to account for the marked rise in this quantity which has been found recently for some semiconductors as the temperature is lowered below room temperature. This paper develops the recently suggested explanation that the thermoelectric power Q is the sum of the usual electronic term Q_e, resulting from the spontaneous tendency of the charge carriers to diffuse from hot to cold, and a phonon term Q_p, resulting from the drag on the charge carriers exerted by the phonons streaming from hot to cold in thermal conduction. An equivalent description of the term Q_p can be given in terms of the contribution to the Peltier heat flux in an isothermal specimen, due to phonons dragged along by the electric current. As a prelude to the discussion of Q_p, the existing theory of Q_e is first subjected to some refinements required by recent developments in semiconductor theory. The theory of Q_p is then formulated in a simple but general way by making use of an approximate proportionality between heat current and crystal momentum in the phonon system. Using recently-derived results on the probability that a very low-frequency phonon will be scattered by other phonons, an explicit expression for $Q_p(T)$ is derived, which should be valid in the range of moderately low temperatures and low carrier concentrations. At lower temperatures, but still far above the range where the thermal conductivity is appreciably size-dependent, Q_p is dominated by the scattering of phonons from the boundaries of the specimen; the theory of this effect is worked out in detail. Although Q_p is independent of carrier concentration when the latter is low, a considerable decrease is predicted at high carrier concentrations, or at very low temperatures, because of a saturation effect. The effect of Fermi degeneracy on all these phenomena is discussed. Available data on p germanium show all these effects and can be fitted by the theory. The comparison indicates that a large proportion of the low-temperature lattice scattering of holes in p germanium is by shear modes. Although n germanium seems less suited for quantitative comparison, it, also, shows all the predicted effects.

I. INTRODUCTION

THE thermoelectric powers of a number of single crystal specimens of germanium have recently been measured by Frederikse[1] and by Geballe and Hull[2] over the range from room temperature to that of liquid hydrogen. Both workers find, for specimens of high to moderate resistivity, a marked rise in the numerical value of the thermoelectric power at low temperatures, a rise quite incomprehensible in the framework of the usual theory[3–7] of thermoelectric power. A similar effect has been observed by Mansfield and Salam[8] for single crystals of molybdenite. The explanation, suggested independently by Frederikse[1] and the author,[9] seems to lie in the role played by the thermal vibrations of the lattice. In the presence of a temperature gadient these are not isotropic; in fact, the phenomenon of thermal conduction implies that the waves travel preferentially from hot to cold. The scattering of charge carriers by the phonons is therefore not random, but such as to push the carriers more often toward the cold end than the reverse. Zero current results only when the cold end acquires enough of an excess of carriers so that their electrostatic field counterbalances the combined effect of this phonon drag and the normal tendency of carriers to diffuse from hot to cold.[10] Thus the observed thermo-

* Present address: Bell Telephone Laboratories, Murray Hill, New Jersey.

[1] H. P. R. Frederikse, Phys. Rev. **91**, 491 (1953); **92**, 248 (1953).

[2] T. H. Geballe, Phys. Rev. **92**, 857 (1953); T. H. Geballe and G. W. Hull, Phys. Rev. **94**, 1134 (1954).

[3] C. Wagner, Z. physik. Chem. **B22**, 195 (1933).

[4] R. H. Fowler, Proc. Roy. Soc. (London) **A140**, 505 (1933).

[5] V. A. Johnson and K. Lark-Horovitz, Phys. Rev. **69**, 259 (1946); **92**, 226 (1953).

[6] J. Yamashita, J. Phys. Soc. Japan **4**, 310 (1949); G. Lautz, Z. Naturforsch. **8a**, 361 (1952); O. Madelung and H. Welker, Z. angew. Physik **5**, 12 (1953).

[7] R. W. Wright, Proc. Phys. Soc. (London) **A64**, 984 (1951).

[8] R. Mansfield and S. A. Salam, Proc. Phys. Soc. (London) **B66**, 377 (1953).

[9] C. Herring, Phys. Rev. **92**, 857 (1953).

[10] While this manuscript was being prepared, Dr. H. P. R. Frederikse and Dr. R. H. Parmenter independently called to my attention two papers of L. Gurevich, J. Phys. (U.S.S.R.) **9**, 477 (1945); **10**, 67 (1946), which develop the theory of this phonon drag effect in a metal. Gurevich does not discuss the effect for semiconductors, although he mentions that it should be present.

electric power Q can be expressed as the sum of an electronic part Q_e, given by previous theories, and a phonon part Q_p.

The explanation just given has been formulated in terms of the differential Seebeck voltage Q; it may therefore be called the Q approach. A different, though necessarily equivalent, approach is through the Peltier heat Π, which is related thermodynamically to Q. The high Q values at low temperatures mean that the energy flux accompanying a given electric current in an isothermal semiconductor is much greater than that which the electronic charge carriers of the usual theory would transport. The proposed explanation is that in the presence of a current the scattering of the charge carriers by the lattice vibrations tends to increase the amplitudes of lattice waves traveling in the same direction as the carriers and to decrease the amplitudes of waves moving in the opposite direction. This results in a net transport of energy by the waves in the direction of motion of the carriers. This approach to the phenomenon may be called the Π approach. Since the Kelvin relation, Eq. (1) below, must apply in all cases, these two approaches must give equivalent results, and this can be confirmed in detail using specific models such as the one of Secs. III to V below. However, in this paper we shall use only the Π approach. Frederikse[1] has treated the subject from the standpoint of the Q approach.

A few qualitative features of the suggested interpretation are obvious at once, and their agreement with observation gives one confidence to explore the proposed effect in detail. The mutual drag of charge carriers and phonons should obviously increase the magnitude of Q, or Π, regardless of sign, i.e., for either n- or p-type material. Moreover, as long as one sign of carrier predominates over the other the effect on Q or Π should clearly be independent of the concentration n of carriers, at least if n is sufficiently low. Finally, the effect should be more pronounced at low than at high temperatures since at high temperatures the lattice vibrations are more rapidly restored to randomness by the effects of anharmonicity of the interatomic forces, i.e., by phonon-phonon collisions. All these predictions agree with observation.

The object of the present paper is to develop the theory of the phonon effect quantitatively, and to see what basic information on semiconductors can be derived from a comparison of the results with experiment. Since the attack on this problem has to be based on the theoretical concepts available in the present-day theory of semiconductors, it is pertinent to begin by examining the reliability of these concepts. A general survey of the relation of theory and experiment in regard to electronic transport shows that for impurity semiconductors one needs to distinguish three or four regions in the range of possible impurity concentrations. When the impurity (and dislocation) concentration is very low, nearly all the charge carriers move as isolated entities in regions of perfect crystalline material, and their motion can be rigorously described in terms of the concepts of band theory, at least if the mobility is high enough to justify treating the interaction with the lattice vibrations as a small perturabation on the motion of the carriers. As the impurity concentration is increased it becomes necessary to take account of impurity scattering and related effects. While this can be done with present-day theory, the available treatment is not altogether satisfactory. At still higher impurity concentrations, available theory becomes completely unreliable for quantitative predictions. This is because of what can be crudely described as a jumping of charge carriers from one impurity atom to the next, an "impurity band" conduction which mingles and competes with normal conduction.[11] The onset of Fermi degeneracy normally occurs in this range. When the impurity and carrier concentrations get very high, available theoretical concepts start to work a little better again, as one can treat the carriers as a degenerate Fermi gas and treat the impurities as merely sources of scattering. However, in this region present theory uses many unjustified simplifications. Moreover, it is by no means clear that one should use here the same effective mass parameters, etc., as in the region of very low impurity concentration.

The exposition given in the following sections reflects the different positions of theory in the several regions just described, and the success achieved by the present theory in these various regions turns out, as expected, to be in proportion to the reliability just estimated for present concepts in these same regions. No attempt is made to give a detailed discussion of thermoelectric power in the region of impurity band conduction, although it will be clear that both the electronic and phonon contributions will usually have the same order of magnitude in this range as in the neighboring regions of lower and higher impurity concentration. Section II reviews and modernizes the theory of the electronic contribution Q_e for low to moderate impurity concentrations. Section III is devoted to a formulation of the phonon effect problem in terms of relaxation times and rates of transfer of lattice momentum, a formulation applicable in principle to all ranges of impurity concentration. Sections IV and V give the detailed solution for small concentrations, neglecting the effects of scattering of phonons from the boundaries of the specimen. The latter effects, which make Q_p size-dependent at low temperatures, are taken up in Sec. VI. Section VII discusses, for concentrations below the impurity band range, a saturation effect which decreases the phonon contribution when the carrier concentration becomes sufficiently high or the

[11] K. Shifrin, J. Phys. (U.S.S.R.) **8**, 242 (1944); H. M. James and A. S. Ginzbarg, Phys. Rev. **77**, 749 (1950); J. Phys. Chem. **57**, 840 (1953); C. Erginsoy, Phys. Rev. **80**, 1104 (1950); **88**, 893 (1952); C. S. Hung and J. R. Gliessman, Phys. Rev. **79**, 726 (1950) C. S. Hung, Phys. Rev. **79**, 727 (1950); G. W. Castellan and F. Seitz, *Semiconducting Materials*, H. K. Henisch, Editor, (Butterworths Scientific Publications, London, 1951), p. 8; W. Baltensperger, Phil. Mag. **44**, 1355 (1953).

temperature sufficiently low. The region of Fermi degeneracy is treated briefly in Sec. VIII, where both the electronic and phonon contributions are discussed. All detailed comparisons of the various parts of the theory with experiment are relegated to Sec. IX, as many of the significant conclusions of this paper come from a comparison of different regions of temperature and concentration.

II. ELECTRONIC THEORY *VERSUS* EXPERIMENT

Let Q be the absolute thermoelectric power of any substance and let Π be its absolute Peltier coefficient, defined as the energy flux per unit current when the energy zero is taken at the Fermi level, or more properly, the electrochemical potential of the electrons. At any absolute temperature T these quantities are known to obey the relation

$$Q=\Pi/T, \tag{1}$$

first obtained (in difference form) by Lord Kelvin[12] in 1854. The relation in Eq. (1) is now known to be a consequence of Onsager's principle of microscopic reversibility.[13] For the sake of later applications it is worth emphasizing that the derivation of (1) remains valid for the apparent Q and Π of a rod-shaped specimen, even when the rod is of such small diameter that boundary effects cause this apparent Q and Π to differ from the values which would be measured on a very large specimen of identical material.

As Wagner[3] and others have pointed out, Eq. (1) provides an easy way of calculating the thermoelectric power of any model of a metal or semiconductor for which the solution of the Boltzmann equation for isothermal electrical conduction is known: one need merely calculate Π from this solution. The familiar theory of thermoelectric power, derived from the Lorentz-Sommerfeld theory of conduction in metals, considers only transport by electronic carriers. For a nondegenerate semiconductor with a single sign of carrier predominating this gives the electronic contribution

$$e\Pi_e=\epsilon_F-\epsilon_b-\Delta\epsilon_T, \tag{2}$$

where ϵ_F is the Fermi level, ϵ_b is the energy of the edge of the band (valence or conduction) in which the carriers move, and $\Delta\epsilon_T$, the average energy of the transported electrons relative to the band edge, is a quantity of the order of kT and therefore usually rather smaller than $\epsilon_F-\epsilon_b$. From this alone it is fairly obvious that no reasonable assumptions regarding band structure and scattering processes will suffice to bring (2) into agreement with the sharp rise of Q at low temperatures which has been found experimentally for germanium. Nevertheless, we shall discuss the terms of (2) in some detail, partly to reinforce this point, and partly because it will be necessary later on to have as accurate an expression as possible for the electronic contribution to Q.

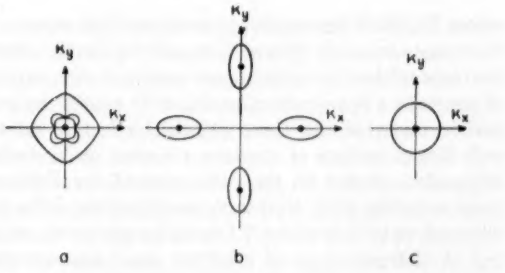

FIG. 1. Schematic forms of the locus in **K** space of states with a given value of energy, near the band edge value, for three possible cases: *a*, single-valley, many-sheeted case; *b*, many-valley, single-sheeted case; *c*, single-valley, single-sheeted case, the model most often assumed in the literature. The band edge points $\mathbf{K}_i$, at which the energy is an extremum, are identified by heavy dots.

Consider first the term $\epsilon_F-\epsilon_b$ in Eq. (2). In order to evaluate this from measurements of Hall coefficient or density of carriers one must make some assumption about the effective mass of the carriers. Now it is known[14] that the electronic energy band structures of silicon and germanium are more complicated than has usually been assumed in semiconductor theory, although the exact structures have not yet been established conclusively. Some of the models which are likely to occur for germanium, silicon, and similar semiconductors are illustrated in Fig. 1. One possibility is that the band edge is a triply degenerate state with wave vector $\mathbf{K}=0$, slightly split by spin-orbit coupling. For this case the locus in **K**-space of states of a single energy near the band edge consists of three concentric surfaces of (in general) complicated shapes [Fig. 1(a)]. Another possibility, illustrated in Fig. 1(b) is that the band edge consists of a number of states with different wave vectors $\mathbf{K}_\nu\neq 0$, symmetrically related to one another; the locus of a given energy consists of a number of identical ellipsoids centered around the points $\mathbf{K}_\nu$. A third possibility, not shown in the picture, is that there are a number of such band edge points with a twofold degeneracy at each $\mathbf{K}_\nu$, slightly lifted by spin-orbit coupling; the energy locus is a family of identical pairs of complex surfaces. If one attempts to use, for these substances, formulas of the conventional model [Fig. 1(c)] which contain effective mass as a parameter, it turns out that different formuals require different effective masses, since they involve different types of averages over the parameters describing the multivalued nonspherical energy surfaces. For example, we may define a "density-of-states mass" $m^{(N)}$ by

$$N(\epsilon)=(4\pi/h^3)(2m^{(N)})^{\frac{3}{2}}|\epsilon-\epsilon_b|^{\frac{1}{2}},$$

[12] W. Thomson, *Mathematical and Physical Papers* (Cambridge University Press, London, 1882), Vol. I, p. 232.

[13] L. Onsager, Phys. Rev. **37**, 405 (1931); **38**, 2265 (1931); H. B. Callen, Phys. Rev. **73**, 1349 (1948). For a detailed discussion of the Kelvin relations and full bibliography see S. R. de Groot, *Thermodynamics of Irreversible Processes* (Interscience Publishers, Inc., New York, 1951), Chap. VIII.

[14] W. Shockley, Phys. Rev. **78**, 173 (1950); F. Herman and J. Callaway, Phys. Rev. **89**, 518 (1953).

where $N(\epsilon)d\epsilon$ is the number of levels per unit volume in the range ϵ to $\epsilon+d\epsilon$. This $m^{(N)}$ equals the inertial effective mass m^* for the conventional model; if each surface of constant ϵ is a single ellipsoid, $m^{(N)}$ equals the geometric mean of the three principal effective masses m_i^*; if each surface of constant ϵ is a set of N_v similar ellipsoids centered on the cubic axes of the Brillouin zone, as in Fig. 1(b), $N(\epsilon)$ is N_v times as great as for one ellipsoid, so $m^{(N)}$ must be $N_v^{\frac{1}{3}}$ times the geometric mean, etc. A different type of effective mass measurement comes from the inertial effect on the high frequency dielectric constant, measured by Benedict and Shockley.[15] The inertial mass $m^{(I)}$ which this effect measures may be defined as the average, over all the carriers, of the ratio of force applied to rate of change of crystal momentum. For ellipsoidal energy surfaces, whether single or multiple, $m^{(I)-1}$ is the arithmetic mean of the curvatures m_i^{*-1} of the plots of ϵ_K against wave number K in the principal directions. We therefore have $m^{(N)} > m^{(I)}$ for any multiellipsoid model, both because of the relation of arithmetic and geometric means and because of the multiplicity of the ellipsoids. In fact, it can be proved that $m^{(N)} > m^{(I)}$ whatever the shape or multiplicity of the constant energy surfaces near the band edge, e.g., the nonellipsoidal shapes suggested by Shockley.[14] However, Eq. (3), and with it the concept of $m^{(N)}$, is only useful for a many-sheeted model like Fig. 1(a) if the spin-orbit splitting is $\gg kT$ or $\ll kT$. If spin-orbit splittings of the order of kT are present, $m^{(N)}$ as we have defined it may vary considerably with energy over the thermal range.

In terms of $m^{(N)}$ the usual formula[16] gives

$$|\epsilon_F-\epsilon_b|/kT=\ln[2(2\pi m^{(N)}kT)^{\frac{3}{2}}/h^3n], \tag{3}$$

where n is the density of carriers. Combining this with (1) and (2), we have for the electronic contribution Q_e to the thermoelectric power, in microvolts per degree,

$$Q_e=\mp 86.2\left[\ln\frac{4.70\times 10^{15}}{n}+\tfrac{3}{2}\ln\frac{m^{(N)}}{m}+\frac{|\Delta\epsilon_T|}{kT}+\tfrac{3}{2}\ln T\right], \tag{4}$$

where n is in cm^{-3} and where the upper sign is for n type, the lower for p. This is the familiar formula;[5,6] we have merely elucidated its applicability to complex band structures. Specifically, Eq. (4) applies to all such except many-sheeted cases where the spin-orbit splitting is of the order of kT, and even for these Eq. (4) may be used, though less conveniently, by letting $m^{(N)}$ be a temperature-dependent quantity defined by Eq. (3) and measuring $\Delta\epsilon_T$ from the lowest band-edge state.

[15] T. S. Benedict and W. Shockley, Phys. Rev. **89**, 1152 (1953); T. S. Benedict, Phys. Rev. **91**, 1565 (1953).

[16] See, for example, W. Shockley, *Electrons and Holes in Semiconductors* (D. Van Nostrand Company, Inc., New York, 1950), p. 464.

Consider now how $\Delta\epsilon_T/kT$ is determined. We shall make the common assumption, briefly discussed at the start of Appendix A, that the processes responsible for scattering the charge carriers can be described by a relaxation time $\tau_e(\mathbf{K})$; we allow τ_e to depend on position $\mathbf{K}$ in wave-number space. Then the first-order perturbation $f^{(1)}$ of the electron distribution function $f(\mathbf{K})$ by and electric field $\mathbf{E}$ obeys

$$f^{(1)}\propto\tau_e\mathbf{E}\cdot\nabla_K f^{(0)}\propto\tau_e\mathbf{E}\cdot\mathbf{v}_K f^{(0)}, \tag{5}$$

where $f^{(0)}$ is the unperturbed distribution function for the electrons or holes and $\mathbf{v}_K$ is the group velocity of a carrier in the $\mathbf{K}$th state. From (5) it follows that, for a cubic crystal

$$\Delta\epsilon_T=\langle v^2(\epsilon-\epsilon_b)\tau_e\rangle/\langle v^2\tau_e\rangle, \tag{6}$$

where the angular brackets mean averages over $f^{(0)}$. Note that Eqs. (5) and (6) involve no assumption regarding the dependence of ϵ on $\mathbf{K}$, except that of cubic symmetry; they are therefore valid for all the types of degenerate or "many-valley" bands, even in the presence of spin-orbit splitting.

An important class of cases for which Eq. (6) can be evaluated is that for which $\tau_e\propto|\epsilon-\epsilon_b|^r$ for any given direction of motion of the carrier within any one of the sub-bands or valleys; r is supposed independent of direction, but the constant of proportionality need not be. For many-sheeted models this can of course only be a good approximation if the spin-orbit splitting is $\gg kT$ or $\ll kT$. Lattice scattering by phonons of long wavelength corresponds to $r=-\frac{1}{2}$, while the extreme case of Conwell-Weisskopf scattering[17] by ionized impurities corresponds to $r=\frac{3}{2}$. For this class of cases Eq. (6) gives

$$|\Delta\epsilon_T/kT|=(5/2)+r. \tag{7}$$

A good estimate of the effective value of r which approximates conditions in any given specimen can be obtained from the ratio of Hall mobility μ_H to drift mobility μ, since for the conventional model of Fig. 1(c)[18]

$$\frac{\mu_H}{\mu}=\frac{\langle v^2\tau_e^2\rangle\langle v^2\rangle}{\langle v^2\tau_e\rangle^2}=\frac{\Gamma(5/2)\Gamma(5/2+2r)}{[\Gamma(5/2+r)]^2}. \tag{8}$$

In addition, the sign of r must be known, since a given μ_H/μ occurs for two values of r, one <0 and one >0. Although the relation (8) requires modification[19] for band structures of the types shown in Figs. 1(a) and 1(b), the modification for Fig. 1(b) can be shown to be slight unless the anisotropy of the ellipsoids is extreme. Although the variation of τ_e with ϵ may sometimes depart considerably from power-law form, a number of calculations which have been made for different τ_e's have given values of $\Delta\epsilon_T/kT$ which, for given μ_H/μ,

[17] E. Conwell and V. F. Weisskopf, Phys. Rev. **77**, 388 (1950); H. Brooks, Phys. Rev. **83**, 879 (1951).

[18] Reference 16, p. 280.

[19] C. Herring (to be published).

have usually been within about 0.2 unit of the values obtained by eliminating r between the right-hand expressions (7) and (8). The table recently published by Johnson and Lark-Horovitz,[5] based on the usual combination of lattice with Conwell-Weisskopf scattering, also gives values within this limit.

The actual range of values of $\Delta\epsilon_T/kT$ is a little different from the range 2.0 to 4.0 which one can get by combining ordinary lattice scattering ($r=-\frac{1}{2}$) with various amounts of Conwell-Weisskopf scattering. The ratio μ_H/μ for high-purity p-type germanium is close to 1.8 at 300°K,[20,21] and it is likely[22] that this is due to τ_ϵ decreasing more sharply with $|\epsilon-\epsilon_b|$ than corresponds to $r=-\frac{1}{2}$. A value $r=-0.8$ would fit this μ_H/μ, and for this value, $\Delta\epsilon_T/kT=1.7$. By about 100°K, μ_H/μ has decreased to a value close to the 1.18 which corresponds to $r=-\frac{1}{2}$. At the other extreme, Spitzer and Härm[23] have shown that the limiting value of $\Delta\epsilon_T/kT$ for pure ionized impurity scattering is 3.20, not 4.0, provided the number of ions equals the number of electrons. The difference between this result and that obtained from the Conwell-Weisskopf formula is due to the fact that Spitzer and Härm take electron–electron interactions into account. The value 4.0 is only to be expected if the ions greatly exceed the electrons in number, i.e., for a highly compensated specimen.

At high carrier and impurity concentrations, we may well question the legitimacy of computing the position of the Fermi level as was done for Eq. (4), and of treating the impurities merely as a source of scattering. To get an idea of the size of the error in Eq. (4) due to fuzzing of the band edge, etc., we may try to modify the relation of n to ϵ_F by the Debye-Hückel correction.[24] However, to be consistent we must also correct $\Delta\epsilon_T$ for the potential energy which the carriers transport. For the simplest case $r=0$ the effect on Π_e due to the change in ϵ_F turns out just to compensate that due to the change in $\Delta\epsilon_T$; this suggests that the correction to Eq. (4) is small under all nondegenerate conditions. When impurity band conduction becomes appreciable, however, the theory leading to Eq. (4) is of course very questionable.

The dashed line in Fig. 2 shows values of Q_e computed from Eq. (4) for a typical high-purity specimen of p-type germanium, for reasonable guesses at $m^{(N)}$ and $\Delta\epsilon_T$. For this sample n was obtained from Hall measurements with correction for the roughly known[20,21] ratio of Hall to drift mobility. The observed Q values, shown for comparison in the full curve, show a marked rise at low temperature, which occurs very much sooner than the rise in the theoretical Q_e due to depletion of the concentration of free carriers. It is clear that the observed values could be fitted to Eq. (4) only by assuming fantastic—and highly temperature-dependent—values of $m^{(N)}$ or the exponent r in Eq. (7). Provided the impurity content is not too high, all specimens both of p- and n-type germanium studied in references 1 and 2 show the same marked deviation from Eq. (4) at low temperatures. Inhomogeneity of the samples can hardly be blamed for the high Q values; not only would inhomogeneity be hard to reconcile with the consistency and reproducibility of the data but, as a consideration of simple series and parallel circuits shows, it would be likely to act in the wrong direction. We are therefore forced to consider the only other mechanism of energy transport which can contribute to Π, namely, transport by traveling elastic waves in the lattice.

III. ELEMENTARY CONSIDERATIONS ON ENERGY TRANSPORT BY PHONONS

We shall show first that there is an approximate proportionality between energy flux and crystal momentum in the phonon system. Let $N_{\mathbf{q}\alpha}$ be the mean number of quanta of excitation present in the traveling wave normal mode of wave vector $\mathbf{q}$ and polarization α. In thermal equilibrium, with no current, this of course takes the Planck value

$$N^{(0)}(\mathbf{q},\alpha)=[\exp(\hbar\omega(\mathbf{q},\alpha)/kT)-1]^{-1}, \qquad (9)$$

where $\omega(\mathbf{q},\alpha)$ is the frequency of the mode. In the presence of a current, $N(\mathbf{q},\alpha)$ will differ from Eq. (9), but we suppose it to be still a smoothly varying function

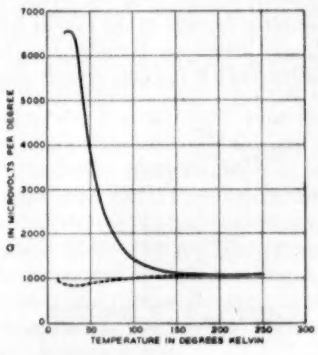

FIG. 2. Comparison of observed thermoelectric power Q with the theoretical electronic contribution. Full curve: values observed by Geballe and Hull, reference 2, for their specimen No. 7 (p-type Ge, 1.5×10^{14} excess acceptors/cc). Dashed curve: electronic contribution calculated from (4), with $m^{(N)}/m=0.6$ and with $\Delta\epsilon_T/kT$ assumed (see text) to increase from 1.7 at 250° to 2.0 an and below 100°.

[20] F. J. Morin, Phys. Rev. **93**, 62 (1954).
[21] M. B. Prince, Phys. Rev. **92**, 681 (1953).
[22] A different interpretation is indicated by recent work of Harman, Willardson, and Beer, Phys. Rev. **94**, 1065 (1954) and a forthcoming publication. According to these authors, the primary cause of the large room-temperature Hall coefficient is the parallel participation of high- and low-mass holes, as required by the two-band model of reference 32. I am indebted to Dr. Beer for supplying me with details of this work in advance of their publication.
[23] L. Spitzer, Jr., and R. Härm, Phys. Rev. **89**, 977 (1953).
[24] See for example R. H. Fowler and E. A. Guggenheim, *Statistical Thermodynamics* (Cambridge University Press, London, 1939).

of $\mathbf{q}$. The flux density of energy flow is

$$\mathbf{j}=\sum_{\mathbf{q},\alpha}N(\mathbf{q},\alpha)\hbar\omega(\mathbf{q},\alpha)\mathbf{v}(\mathbf{q},\alpha)$$

$$=(2\pi)^{-3}\sum_{\alpha}\int N(\mathbf{q},\alpha)\hbar\omega(\mathbf{q},\alpha)\mathbf{v}(\mathbf{q},\alpha)d\mathbf{q}, \quad (10)$$

where $\mathbf{v}(\mathbf{q},\alpha)=\nabla_{\mathbf{q}}\omega(\mathbf{q},\alpha)$ is the group velocity, and where the summation is over a density of $\mathbf{q}$ values corresponding to unit volume of material. If we have to deal only with modes of long wavelength, we can set $\omega(\mathbf{q},\alpha)=c(\mathbf{q},\alpha)\mathbf{q}$, where $c(\mathbf{q},\alpha)$, the phase velocity of the mode, depends on the direction of $\mathbf{q}$ but not on its magnitude. This will certainly be the case at low temperatures, and it will in fact turn out to be the case for our problem at all temperatures. If the crystal is taken to be elastically isotropic we can make the further simplification $\mathbf{v}(\mathbf{q},\alpha)=c_\alpha\mathbf{q}/q$, and even for an anisotropic crystal this may be a fair approximation to use in Eq. (10), if suitable average sound velocities are used. To this approximation

$$\mathbf{j}\approx\sum_{\mathbf{q},\alpha}N(\mathbf{q},\alpha)(\hbar\mathbf{q})c_\alpha^2=\mathbf{P}_l\bar{c}_l^2+\mathbf{P}_t\bar{c}_t^2=(\mathbf{P}_l+\mathbf{P}_t)\bar{c}^2, \quad (11)$$

where the subscripts l and t refer to longitudinal and transverse waves, respectively, $\bar{c}$ is a suitable average of the two sound velocities, and

$$P_\alpha=\sum_{\mathbf{q}}N(\mathbf{q},\alpha)\hbar\mathbf{q}=(2\pi)^{-3}\int N(\mathbf{q},\alpha)\hbar\mathbf{q}d\mathbf{q} \quad (12)$$

is the total crystal momentum per unit volume of all modes of polarization type α, the summation being, as before, over a density of $\mathbf{q}$ values appropriate to unit volume of material.

The interest of the relation in Eq. (11) is, of course, that crystal momentum is conserved in collisions of phonons with the charge carriers, and also in phonon-phonon collisions, unless these are of the Umklapp type. We may therefore calculate $\mathbf{j}$ by equating the rate at which the phonon system receives crystal momentum from the electronic carriers to the rate at which it loses it via Umklapp collisions, boundary scattering, etc. Since an electric field $\mathbf{E}$ imparts crystal momentum to the carriers at a rate $\mp ne\mathbf{E}$ per unit volume, where n is the density of carriers, the former rate may be written

$$[d(\mathbf{P}_l+\mathbf{P}_t)/dt]_e=\mp fne\mathbf{E}, \quad (13)$$

where the upper sign is for electrons, the lower for holes, and where f is the fraction of the crystal momentum lost by the electrons which is delivered to the lattice vibrations ($f=1$ in the absence of impurity scattering). For the other term, let us define an effective relaxation time $\bar{\tau}$ for the phonon system by setting for the rate of loss of crystal momentum via the various types of collisions which do not conserve this quantity,

$$[d(\mathbf{P}_l+\mathbf{P}_t)/dt]_c=-(\mathbf{P}_l+\mathbf{P}_t)/\bar{\tau}. \quad (14)$$

We may now calculate $\mathbf{j}$ from Eqs. (11), (13), and (14), eliminating $\mathbf{E}$ in favor of the current density $\mathbf{J}=ne\mathbf{E}\mu$, where μ is the mobility. The result is

$$\mathbf{j}\approx\mp(\bar{c}^2f\bar{\tau}/\mu)\mathbf{J}. \quad (15)$$

The coefficient of $\mathbf{J}$ in this expression is the phonon contribution Π_p to the Peltier heat. It may be placed in a form more suitable for comparison with the electronic contribution in Eq. (2) by writing $\mu=(e/m^*)\bar{\tau}_e$, where m^* and $\bar{\tau}_e$ are suitably defined averages of the effective mass and relaxation time of the carriers, respectively. Thus,

$$e\Pi_p\approx\mp\bar{c}^2ef\bar{\tau}/\mu=\mp m^*\bar{c}^2(f\bar{\tau}/\bar{\tau}_e). \quad (16)$$

The factor $m^*\bar{c}^2$ is much smaller than the right of Eq. (2) for a nondegenerate semiconductor, being only of the order of 10^{-4} ev for germanium. Thus for the phonon contribution to exceed the electronic, the weighted ratio of phonon to electron or hole relaxation times must be of the order of hundreds of thousands.

A few words are in order at this point regarding the meaning of the $\bar{\tau}$ occurring in Eq. (16). We note, to begin with, that most of the crystal momentum fed in from the charge carriers to the phonon system, or at least a major part of it, is fed in to a very small fraction of the normal modes, namely, those with very small wave vectors $\mathbf{q}$, of the order of the wave vector of a thermal electron. The course of the crystal momentum given to the phonon system by the charge carriers is therefore roughly describable by the hydraulic analogy shown in Fig. 3. Crystal momentum, represented by water, is fed into an upper container, representing the modes of low q. From this it can either escape to the modes of higher q (water passing through the orifice on the right of the upper container) or be lost forever by, for example, scattering of the low-q phonons from the boundaries of the specimen (water passing through the orifice on the left). That part of the crystal momentum which reaches the modes of high q, represented by the lower container, is eventually lost by Umklapp, impurity, or boundary scattering (water passing through the orifice on the extreme right). Now because of their long wavelength the modes of small q are less susceptible to all kinds of scattering than are the rest of the modes, except

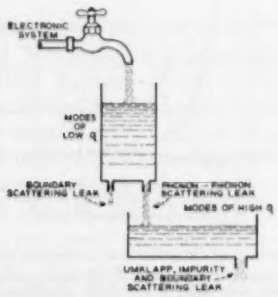
ELECTRONIC SYSTEM
MODES OF LOW q
BOUNDARY SCATTERING LEAK
PHONON — PHONON SCATTERING LEAK
MODES OF HIGH q
UMKLAPP, IMPURITY AND BOUNDARY SCATTERING LEAK

FIG. 3. Hydraulic analogue of the transfer of crystal momentum $\mathbf{P}$ from the electronic system to lattice modes of low and high wave number q, and the ultimate destruction of $\mathbf{P}$.

at very low temperatures where boundary scattering affects all modes alike. This means that both orifices leading from the inner container are narrow. It is therefore quite possible that in a steady state there will be more crystal momentum in the modes of low q than in those of high (more water in the inner container than the outer). In fact, if the scattering of low-q phonons by high-q phonons (middle leak) is sufficiently slow, the rate of annihilation of the crystal momentum of the high-q phonons (leak on extreme right) may be quite inconsequential in determining the total amount of crystal momentum (water) in the system, i.e., $\bar{\tau}$ may be determined almost entirely by the rates of the two leaks out of the low-q system.

To orient ourselves regarding the relative rates of the various leaks in Fig. 3 for the germanium experiments we are trying to intepret, we shall consider two limiting cases. In a thermal conduction experiment, with no charge carriers, the thermal gradient feeds in crystal momentum to each mode $\mathbf{q}$, α at a rate which depends only on the direction of $\mathbf{q}$ and not on its magnitude, as long as $\hbar\omega(\mathbf{q},\alpha) \lesssim kT$.[25] This corresponds to placing the containers of Fig. 3 out in the rain, instead of feeding only the inner one from a faucet. If, as we have been speculating, the leaks from the inner container are slower than that from the outer, a given rate of feeding in water will yield a steady state with less water in the containers for feeding by rain than for feeding by faucet. In other words, the effective phonon mean free time for thermal conduction, τ_c, will be less than the effective $\bar{\tau}$ to be used in Eq. (16). To see whether this is in fact the case, we may try calculating Eq. (16) using for $\bar{\tau}$ the τ_c determined from Debye's formula,[26]

$$\kappa = \tfrac{1}{3}Cc^2\tau_c, \tag{17}$$

for the thermal conductivity κ, in which C is the specific heat per unit volume, and c an average sound velocity. With the values of κ measured by Geballe[27] for fairly pure germanium, values of $Q_p = \Pi_p/T$ were computed from Eqs. (17) and (16), and are shown in the lower curve of Fig. 4, together with values of $Q-Q_e$ from Fig. 2. We have taken $f=1$, its maximum possible value, for this comparison. The suspicions outlined in the preceding paragraph are confirmed: Use of τ_c for $\bar{\tau}$ gives values of Q_p which are vastly too small.

Having thus verified that $\bar{\tau} \gg \tau_c$, we now explore the other extreme. If nothing else puts a lower limit on the loss of crystal momentum by the low-q phonons, boundary scattering will. For the specimens used in most of the work of Geballe and Hull it is reasonable to assume diffuse reflection of phonons at the boundaries of the specimen, and to take a mean free path L of the order of 0.15 cm between such reflections. With $\bar{c} \approx 5\times10^5$ cm/sec., we obtain $\tau_b = L/\bar{c} \approx 3\times10^{-7}$ sec. Using this for $\bar{\tau}$,

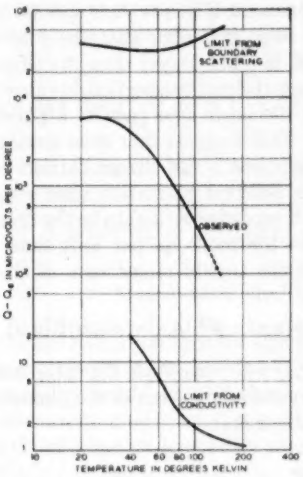

FIG. 4. Middle curve: Empirical phonon contribution Q_p to the thermoelectric power of the Ge specimen of Fig. 2, obtained by subtracting the Q_e curves from the observed Q curves. Upper curve: Approximate upper limit to Q_p, obtained from (16) with $f=1$ and a phonon mean free path of 0.15 cm, the limit set by boundary scattering. Lower curve: Lower limit to Q_p, obtained by inserting the mean free path for thermal conduction into (16). The curvature of the upper plot, which differs from the behavior of the more refined expression (42) derived below, is due to the use of the assumption $f=1$, which allows the irregular variation of the mobility to be felt.

and again taking $f=1$ for simplicity, we get the upper curve of Fig. 4. We see that at the lowest temperatures $\bar{\tau}$ does indeed seem to be starting to approach the boundary scattering value, but that over the range from say 50° to 200°K, $\bar{\tau} \ll \tau_b$.

We have thus arrived at the following picture, which we must develop quantitatively in the next two sections: In an isothermal specimen carrying a current, most of the crystal momentum of the phonon system—and therefore most of its heat current—resides in the normal modes of long wavelength. Except at very low temperatures, crystal momentum is lost from these modes principally by interactions with modes of shorter wavelength, and the relaxation time for these interactions may be used as the $\bar{\tau}$ in Eq. (16), even though these interactions do not themselves destroy any crystal momentum. At the lowest temperatures, $\bar{\tau}$ is compounded out of the relaxation time for these interactions and that for boundary scattering. At no temperature is $\bar{\tau}$ likely to be appreciably affected by scattering processes which involve only phonons of shorter wavelength than those with which the charge carriers interact; in other words, the rate of the right-hand leak in Fig. 3 is never likely to be important.

IV. RATE OF TRANSFER OF CRYSTAL MOMENTUM TO PHONONS

The picture developed in the preceding section, though valid as an over-all description, needs con-

[25] P. G. Klemens, Proc. Roy. Soc. (London) **A208**, 108 (1951).
[26] P. Debye, *Vorträge über die kinetische Theorie der Materie und der Elektrizität* (Teubner, Berlin, 1914), pp. 19–60.
[27] T. Geballe (private comminication).

siderable refinement if it is to yield specific quantitative results. We have just seen that the $\bar{\tau}$ to be used in (15) and (16) is much longer than the effective relaxation time τ_e for thermal conduction, because of the great variation of the mean free path of a phonon with its wavelength. This suggests that even among the modes of low q, with which the charge carriers interact, we should use a different relaxation time $\tau(\mathbf{q},\alpha)$ for each mode. Thus if we define $\mathbf{R}(\mathbf{q},\alpha)$ to be the crystal momentum fed into the mode $\mathbf{q}\alpha$ per unit time, and define $\mathbf{p}(\mathbf{q},\alpha)$ to be the crystal momentum of this mode, we write

$$\mathbf{p}(\mathbf{q},\alpha)-\mathbf{p}^{(0)}(\mathbf{q},\alpha)=\tau(\mathbf{q},\alpha)\mathbf{R}(\mathbf{q},\alpha), \tag{18}$$

where $\mathbf{p}^{(0)}(\mathbf{q},\alpha)=N^{(0)}(\mathbf{q},\alpha)\hbar\mathbf{q}$ is the value in equilibrium. The total crystal momentum of the phonons of branch α in unit volume is

$$\mathbf{P}_\alpha=(2\pi)^{-3}\int\mathbf{p}(\mathbf{q},\alpha)d\mathbf{q}=(2\pi)^{-3}\int\tau(\mathbf{q},\alpha)\mathbf{R}(\mathbf{q},\alpha)d\mathbf{q}. \tag{19}$$

In this section we shall calculate $\mathbf{R}(\mathbf{q},\alpha)$, and in the next one we shall combine it with $\tau(\mathbf{q},\alpha)$ and evaluate the integral in Eq. (19), which we can then substitute into Eq. (11) to get the phonon contribution to the Peltier heat flow. The next section will also include a discussion of the legitimacy of using the mean free time concept in Eq. (18).

To avoid excessive mathematical complication in the initial development of the theory, we shall make several simplifications in this section. Specifically, we shall assume Maxwellian statistics and the conventional model of Fig. 1(c). For this model only the longitudinal modes are important. A more general treatment is given in Appendix A, which assumes the many-valley model of Fig. 1(b), a model for which transverse as well as longitudinal phonons can scatter the charge carriers. This treatment leads to expressions for $\mathbf{R}(\mathbf{q},\alpha)$ and Q_p which are similar to those derived for the simpler model in this section and the next, provided the effective mass in the simple model is taken to be a suitable average of the effective masses in the three principal directions of a valley, an average which may be different for longitudinal and transverse modes. The many-sheeted model of Fig. 1(a), unfortunately, seems too complicated to treat quantitatively; however, it, too, should have properties similar to those of the simple model. In this section where we use the simple model, we shall drop the index α, since only the longitudinal branch is important. In the following section, however, where we shall derive formulas for practical application, we shall resume the distinction between longitudinal and transverse branches, in order to have equations which may be placed in correspondence with those of Appendix A.

The quantity $\mathbf{R}(\mathbf{q})$ is compounded out of the distribution function of the carriers and the scattering probability for emission or absorption of a phonon. The former is easily obtained if we assume that the combined effect of all the scattering processes acting on the charge carriers can be described by a relaxation time $\tau_e(K)$, dependent on the magnitude but not on the direction of the wave vector $\mathbf{K}$. Then an electric field in the x direction produces a first-order perturbation $f^{(1)}$ of the distribution function of the charge carriers which, by (5), is

$$f^{(1)}(\mathbf{K})\propto\tau_e(K)K_x\exp(-\hbar^2K^2/2m^*kT). \tag{20}$$

In this and the following equations all factors independent of $\mathbf{K}$ and $\mathbf{q}$ are absorbed into the proportionality sign.

For a crystal free from flaws and impurities the transition probability from state $\mathbf{K}$ to state $\mathbf{K}+\mathbf{q}$ with absorption of a longitudinal phonon $\mathbf{q}$, or to $\mathbf{K}-\mathbf{q}$ with emission, is

$$\begin{aligned}W_{a,e}(\mathbf{K}\rightarrow\mathbf{K}\pm\mathbf{q})&\propto|M|^2\delta[\epsilon(\mathbf{K})-\epsilon(\mathbf{K}\pm\mathbf{q})\pm\hbar\omega(\mathbf{q})]\\&\propto\begin{pmatrix}N(\mathbf{q})\\N(\mathbf{q})+1\end{pmatrix}q\delta[\epsilon(\mathbf{K})-\epsilon(\mathbf{K}\pm q)\pm\hbar\omega(\mathbf{q})],\end{aligned} \tag{21}$$

since the squared matrix element for the transition, $|M|^2$ is independent of $\mathbf{K}$ and depends on $\mathbf{q}$ only through a factor very nearly proportional to q and to the occupation numbers $N(\mathbf{q})$ (absorption) and $N(\mathbf{q})+1$ (emission).[28] For the purpose of this section and the next two, the occupation numbers $N(\mathbf{q})$ can be set equal to their thermal equilibrium values in Eq. (9); this means that for the present we are considering only semiconductors with such low concentrations of carriers that the unbalance of the phonon system in the presence of a current is much less than the unbalance in the distribution of the carriers. In Sec. VII we shall consider the case of such high carrier concentrations that the unbalance of the phonons is of the same order as that of the carriers.

It is generally assumed that (21) continues to hold even when there are enough impurities present to cause appreciable impurity scattering. In other words, it is generally assumed that when two or more scattering mechanisms operate, the probability for a given electron to suffer any one type of scattering is the same as it would be if all the other types were absent, so that the reciprocal relaxation times for the different mechanisms add. We shall use this assumption here, although its validity at moderately high-impurity concentrations may be questioned.

Returning to (20) and (21), we now combine these equations to get the rate $\mathbf{R}(\mathbf{q})$ of crystal momentum transfer to the mode $\mathbf{q}$. Remembering that the equilibrium carrier distribution $f^{(0)}$ contributes nothing, that $f^{(1)}$ is an odd function of $\mathbf{K}$, and that the W_a, W_e of (21) are unchanged if we reverse the directions

[28] See for example reference 16, pp. 520–531. This proportionality involves the assumption of elastic isotropy of the crystal, but deviations from isotropy are not likely to modify it greatly.

of both $\mathbf{K}$ and $\mathbf{q}$, we can write

$$\mathbf{R}(\mathbf{q})=\hbar\mathbf{q}[dN(\mathbf{q})/dt]_e\propto\mathbf{q}\int f^{(1)}\times[W_e(\mathbf{K}\to\mathbf{K}-\mathbf{q})-W_a(\mathbf{K}\to\mathbf{K}+\mathbf{q})]d\mathbf{K}$$

$$=\mathbf{q}\int f^{(1)}[W_e(\mathbf{K}\to\mathbf{K}-\mathbf{q})+W_a(\mathbf{K}\to\mathbf{K}-\mathbf{q})]d\mathbf{K}$$

$$\propto\mathbf{q}\int\tau_e(\mathbf{K})K_z\exp(-\hbar^2K^2/2m^*kT)\times\{q[N(\mathbf{q})+1]\delta(2\mathbf{K}\cdot\mathbf{q}-q^2-2K_cq)+qN(\mathbf{q})\delta(2\mathbf{K}\cdot\mathbf{q}-q^2+2K_cq)\}d\mathbf{K}, \quad (22)$$

where $K_c=m^*c/\hbar$. An approximation commonly made in the theory of semiconductors[29] is to neglect the energy change suffered by an electron when it is scattered by a phonon. In this section we shall adopt this approximation, which is equivalent to neglecting the terms $\pm 2K_cq$ in the arguments of the δ functions in (22). Although the legitimacy of this must certainly fail at sufficiently low temperatures, it can be shown from a treatment using the full (22) that the results obtained with the present approximation are adequate throughout the liquid hydrogen range.[30] When K_c is neglected the two δ functions in (22) become the same. Choosing a polar coordinate system for $\mathbf{K}$ with axis in the direction of $\mathbf{q}$, we have

$$d\mathbf{K}=K^2d\varphi d(\cos\theta)dK=Kd\varphi d(\mathbf{K}\cdot\mathbf{q}/q)dK, \quad (23)$$

$$\text{Average of } K_z \text{ on } \varphi=\mathbf{K}\cdot\mathbf{q}q_z/q^2. \quad (24)$$

Thus with the equipartition value of $N(q)(\gg 1)$, (22) reduces to

$$\mathbf{R}(\mathbf{q})=BJ(\mathbf{q}q_z/q)\int_{q/2}^{\infty}\tau_e(K)\times\exp(-\hbar^2K^2/2m^*kT)KdK, \quad (25)$$

where B is a constant and J is the current density; the lower limit $q/2$ represents the minimum value of K for which a θ value can be found to make the argument of the δ function vanish. The dependence of $R_z(\mathbf{q})$ on q is shown in Fig. 5 for different assumptions regarding τ_e, and also for a typical case of degenerate statistics, worked out in Appendix A.

The constant of proportionality B in Eq. (25) is independent of $\mathbf{q}$ and for given electric field $\mathbf{E}$ it is independent of the amount of impurity scattering, etc., contained in $\tau_e(K)$. We can evaluate it by equating the sum of $\mathbf{R}(\mathbf{q})$, over all $\mathbf{q}$ in the longitudinal branch in unit volume, to its known value Jf/μ, where μ is the mobility and f is the fraction of the crystal momentum lost by the charge carriers which is delivered to low-energy acoustic modes of the lattice. The sum can be simplified by interchanging the order of integration on $\mathbf{K}$ and $\mathbf{q}$; it is

$$(2\pi)^{-3}\int R_z(\mathbf{q})d\mathbf{q}=(6\pi^2)^{-1}BJ\int_0^{\infty}q^3\int_{q/2}^{\infty}\tau_e(K)\times\exp(-\hbar^2K^2/2m^*kT)KdKdq$$

$$=(2/3\pi^2)BJ\int_0^{\infty}K^5\tau_e(K)\times\exp(-\hbar^2K^2/2m^*kT)dK. \quad (26)$$

Let $\tau_{eL}(K)$ be the relaxation time for scattering by low-energy acoustic modes only, and let μ_L be the value which the mobility would have if this were the only scattering mechanism operating. Let averages over the Maxwellian distribution be denoted by angular brackets Then[31]

$$\mu=(e/m^*)\langle K^2\tau_e\rangle/\langle K^2\rangle, \quad (27)$$

$$\mu_L=(e/m^*)\langle K^2\tau_{eL}\rangle/\langle K^2\rangle, \quad (28)$$

$$f=\langle K^2\tau_e/\tau_{eL}\rangle/\langle K^2\rangle. \quad (29)$$

Since $\tau_{eL}\propto K^{-1}$ we have

$$f\mu_L=(e/m^*)\langle K\rangle\langle K^3\tau_e\rangle/\langle K^2\rangle^2, \quad (30)$$

$$f/\mu=\langle K\rangle\langle K^3\tau_e\rangle/\mu_L\langle K^2\rangle\langle K^2\tau_e\rangle. \quad (31)$$

Note that $\langle K^3\tau_e\rangle/\langle K^2\tau_e\rangle$ equals the integral in Eq. (26) divided by a similar integral with K^5 replaced by K^4. Equating Eq. (26) to J times Eq. (31) we have finally

$$B=\frac{3\pi^2}{2}\frac{\langle K\rangle}{\mu_L\langle K^2\rangle\int_0^{\infty}K^4\tau_e(K)\exp(-\hbar^2K^2/2m^*kT)dK}. \quad (32)$$

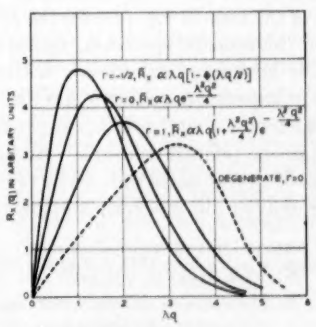
$R_z(q)$ IN ARBITRARY UNITS
λq
$r=-1/2, \bar{R}_z \propto \lambda q[1-\Phi(\lambda q/2)]$
$r=0, \bar{R}_z \propto \lambda q e^{-\frac{\lambda^2 q^2}{4}}$
$r=1, \bar{R}_z \propto \lambda q\left(1+\frac{\lambda^2 q^2}{4}\right)e^{-\frac{\lambda^2 q^2}{4}}$
DEGENERATE, $r=0$

FIG. 5. Dependence of $\bar{R}_z(q)$, the spherical average of (25) or (A4), on λq, where λ is the thermal electron wavelength defined by (40). Full curves: Classical statistics, Eq. (25), for various values of the exponent r in $\tau_e\propto|\epsilon-\epsilon_b|^r$. Dashed curve: Typical case of Fermi degeneracy, Eq. (A4), with $|\epsilon_F-\epsilon_b|=4kT$, $r=0$, isotropic effective masses assumed. Areas under different portions of any curve represent relative contributions to the integral (19), hence to Q_p, if $s=0$ is assumed in (36). All curves have been arbitrarily normalized to the same area.

[29] See for example reference 16, p. 252.

[30] C. Herring (to be published).

[31] See, for example, reference 16, p. 276.

Regarding the applicability of these results to the many-valley model, the conclusions reached in Appendix A are the following: When a relaxation time dependent only on energy exists, an integral expression for the $R(\mathbf{q},\alpha)$ of each branch can be written down which is a superposition of expressions of the form in Eq. (25) with different m^*'s ranging from the highest to the lowest of the principal m^* of a single valley. Here K is to be defined by setting the $\hbar^2K^2/2m^*$ equal to the energy. We may note that if the energy surfaces in a single valley happen to be nearly spherical, Eq. (25) will be quite good as it stands, for either branch. The constant B_α going with branch α is to be evaluated by setting the right of Eq. (26) equal to Jf_α/μ, where f_α is the fraction of the crystal momentum of the carriers which is lost to branch α. The variation of f_α/μ with temperature, amount of impurity scattering, etc., is similar to that given by Eq. (31) if μ_L is replaced by the corresponding partial mobility μ_α and a constant factor of the order of unity is inserted.

In Sec. VI we shall consider temperatures so low that only boundary scattering is important for the phonons. For this case the $\tau(\mathbf{q},\alpha)$ in Eq. (19) becomes independent of the magnitude of q, and it is unnecessary to evaluate the $R(\mathbf{q},\alpha)$'s; we shall merely use Eqs. (16) and (31) with a $\bar{\tau}$ determined by the dimensions of the specimen. We shall then need to know the ratio of the quantities in angular brackets in Eq. (31); values of this ratio for several limiting cases are given in Table I.

V. PHONON CONTRIBUTION TO Q FOR SMALL CARRIER CONCENTRATIONS, WITH NEGLECT OF BOUNDARY SCATTERING

We have now to evaluate the integral in Eq. (19) for the total crystal momentum of the phonons in a current-carrying specimen. In accordance with the remarks made near the end of the preceding section, we shall use an expression of the form in Eq. (25) for the $R(\mathbf{q},\alpha)$ of each branch α of the acoustic spectrum. In the temperature range where boundary and mosaic scattering of the phonons is unimportant, we should use the law of variation of $\tau(\mathbf{q},\alpha)$ with T and q which is predicted by the theory of phonon-phonon collisions.[32] According to this theory most of the collisions suffered by phonons of very small wave number q at moderate and low temperatures are with phonons of energy $\sim kT$, and very few are with each other. It is therefore legitimate for our purposes to regard each such mode $\mathbf{q},\alpha$ as having a relaxation time $\tau(\mathbf{q},\alpha)$ equal to the time required for this mode to share its lattice momentum with other modes—i.e., the time constant of the middle leak of Fig. 3.

TABLE I. Values of $\mu_L f/\mu$ from (31), and of the coefficient of λ^{2+} in (39), for $\tau_\alpha \propto K^{2r}$.

r	$f'=\mu_L f/\mu$	Coeff. λ^2/μ_α, $s=0$	Coeff. λ^2/μ_α $s=1$
−1.00	0.85	0.85	1.50
−0.75	0.93	0.74	1.00
−0.50	1.00	0.67	0.75
0	1.13	0.57	0.50
1.00	1.36	0.45	0.30
1.50	1.46	0.42	0.25

[32] C. Herring, Phys. Rev. **95**, 954 (1954).

At temperatures well below the Debye temperature the theory for an elastically anisotropic cubic crystal such as germanium predicts that as $q\to 0$,

$$1/\tau_l(\mathbf{q})\sim A_l T^3 q^2, \tag{33}$$

where $\tau_l(\mathbf{q})$ is the value of $\tau(\mathbf{q},\alpha)$ when α is the highest-frequency (longitudinal) acoustic branch, and

$$1/\tau_t(\mathbf{q})\sim A_t T^4 q \tag{34}$$

for the other two (transverse) branches. The coefficients A_l, A_t may depend slightly on the direction of $\mathbf{q}$. For an elastically isotropic crystal (34) is still valid, but (33) is replaced by

$$[1/\tau_l(\mathbf{q})]_i\sim A_{li} T q^4. \tag{35}$$

A rough estimate made for germanium[31] suggests that (33) should be applicable when $\hbar\omega_q \lesssim 0.15kT$; (34) should apply over a wider range, while for a typical elastically isotropic crystal the validity of (35) would be restricted to a rather narrower range. Whether or not q is small enough for any of these asymptotic expressions to apply, it is always true that $1/\tau(\mathbf{q},\alpha)\propto T^5$ if $\mathbf{q}$ and T are scaled proportionately, provided T and $\hbar\omega(\mathbf{q})/k$ are $\ll$ the Debye temperature. A crystal with a very small elastic anisotropy should have a longitudinal relaxation time following (35) down to quite small q, and then changing over to (33).

Although we are only concerned with temperatures rather smaller than the Debye temperature, we may get some insight into the probable direction of departures from (33) and (34) in the upper part of this range by considering the extreme of very high temperatures. For this case, $1/\tau(\mathbf{q})$ for any given mode is proportional to T, the q dependence being similar to that at lower temperatures.[31]

Since we expect the longitudinal and transverse relaxation times to be of the same order when $\hbar\omega(\mathbf{q})\sim kT$, (33), (34), and (35) suggest that $\tau_l(\mathbf{q})\gg\tau_t(\mathbf{q})$ if $\hbar\omega(\mathbf{q})\ll kT$, as is the case for the phonons active in scattering the charge carriers. Thus we expect the longitudinal modes to contribute much more than the transverse ones to the thermoelectric power, over most of the temperature range. At low temperatures, however, boundary scattering reduces the longitudinal contribution much more than the transverse, so the two contributions may become comparable. We shall therefore carry through the analysis of this section in a form applicable to either branch. We shall use the adjustable assumption,

$$1/\tau(\mathbf{q},\alpha)=A_\alpha T^{3-s-r} q^{2+s}. \tag{36}$$

For simplicity A_α is assumed independent of the direction of $\mathbf{q}$. To a first approximation we may set $s=\gamma=0$, as this corresponds to the ideal case of longitudinal modes, small q, and low T. In a more refined calculation we may add to this contribution Q_{pl} of the longitudinal modes a smaller contribution Q_{pt}, obtained from the formulas of this section with $s=-1$. Departure of s from the ideal value 0 for longitudinal modes may occur if the important range of q's is not sufficiently small; we expect $|s|$ to be rather smaller than unity. For a temperature range covering sizable fractions of the Debye temperature a positive γ may need to be used. Mosaic scattering may be taken into account crudely by adjusting γ and s, or in a more refined way by a theory like that of the next section.

With $\tau(\mathbf{q})$ from Eq. (36) and $\mathbf{R}(\mathbf{q})$ from Eq. (25), the integral in Eq. (19) for P_α becomes a double integral over $\mathbf{K}$ and $\mathbf{q}$. As in Eq. (26), we can interchange the order of integration and carry out the integration on $\mathbf{q}$. The result is

$$P_\alpha=\frac{2^{2-s}}{6\pi^2(2-s)}\frac{B_\alpha J}{A_\alpha T^{3-s-\gamma}}\int_0^\infty K^{3-s}\tau_e(K)\times\exp(-\hbar^2K^2/2m^*kT)dK. \quad (37)$$

We may eliminate B_α by using Eq. (32), if the simple model applies, or more generally, by using Eq. (26) equated to Jf_α/μ, where as before f_α is the fraction of the crystal momentum of the charge carriers which is delivered to phonons of branch α. The phonon contribution to the thermoelectric power is related to P_l and P_t by Eq. (11), and is of the form $Q_{pl}+Q_{pt}$; we find

$$Q_{p\alpha}=\Pi_{p\alpha}/T=\frac{\delta_\alpha^2 f_\alpha}{2^s(2-s)A_\alpha T^{4-s-\gamma}\mu}\frac{\langle K^{1-s}\tau_e\rangle}{\langle K^3\tau_e\rangle}, \quad (38)$$

where as before the angular brackets denote Maxwellian averages. This applies, of course, only at temperatures high enough for boundary scattering to be unimportant. As is shown in Appendix A, Eq. (38) applies to the many-valley model if a suitable average of the effective masses in the different directions is used in relating K to the energy, i.e., in Eqs. (39) and (40) below.

If for the moment τ_e is assumed to follow the same law of variation with K at all temperatures, the ratio of angular brackets in Eq. (38) is proportional to $T^{-1-\frac{1}{2}s}$ and f_α/μ goes as $T^{\frac{1}{2}}$, so $Q_{p\alpha}$ varies as $T^{-\eta}$ with $\eta=(7/2)-\frac{1}{2}s-\gamma$. Though our derivation has assumed the simple model of Fig. 1(c), or, in Appendix A, the many-valley model of Fig. 1(b), it is not hard to see that this law of temperature variation has a general validity. In particular, it applies to the many-sheeted model of Fig. 1(a), provided the splitting introduced into this model by spin-orbit coupling is either $\gg kT$ or $\ll kT$. For if the scattering probability for transition of a carrier from state $\mathbf{K}$ to state $\mathbf{K}'$ depends only on $\mathbf{K}/T^{\frac{1}{2}}$, $\mathbf{K}'/T^{\frac{1}{2}}$, the function $\mathbf{R}(\mathbf{q},\alpha)$ for one temperature will be derivable from $\mathbf{R}(\mathbf{q},\alpha)$ for any other temperature by a simple scale change, the q scale going as $T^{\frac{1}{2}}$. Thus the $\bar{\tau}$ of Eq. (16), which is an average of the $\tau(\mathbf{q},\alpha)$ of Eq. (36) with weights proportional to $\mathbf{R}(\mathbf{q},\alpha)$ will be given by Eq. (36) with an effective q proportional to $T^{\frac{1}{2}}$. This leads to the same exponent η as Eq. (38).

Since ideally $s=\gamma=0$, the ideal value of η is 7/2. This accords fairly well with the observation of Geballe and Hull[2] that for p germanium Q_p goes nearly as $T^{-3.2}$. However, there are a number of refinements which need to be made in an accurate comparison of theory and experiment, of which we shall consider one here and others in the following sections, and it is therefore best to defer a detailed comparison until Sec. IX. The refinement we shall consider here arises from variations in the way τ_e depends on K. These variations, which affect both f_α/μ and the last fraction in Eq. (38), may arise from impurity scattering, or, for the many-valley model of Fig. 5(b), because the importance of intervalley scattering decreases with decreasing T. If we approximate the behavior of $\tau_e(K)$ at any temperature by K^{2r}, both these effects cause the effective exponent $2r$ to increase with decreasing T. For such a law we have, when Eq. (31) is valid,

$$\frac{f_\alpha}{\mu}\frac{\langle K^{1-s}\tau_e\rangle}{\langle K^3\tau_e\rangle}=\frac{\Gamma(2+r-\frac{1}{2}s)}{\Gamma(5/2)\Gamma(5/2+r)}\frac{\lambda^{2+s}}{\mu_\alpha}, \quad (39)$$

where

$$\lambda=(\hbar^2/2m^*kT)^{\frac{1}{2}} \quad (40)$$

is a thermal electron wavelength, and $\mu_\alpha\propto T^{-\frac{1}{2}}$ is the mobility which would occur if the only scattering of the carriers were that by phonons of branch α. The principal correction required for the general many-valley model is, according to Appendix A, the insertion of a constant factor independent of T and of the behavior of $\tau_e(K)$; this might be absorbed into the definition of μ_α, and does not affect the temperature dependence of Eq. (39).

If $s>-1$, the value of Eq. (39) decreases as r increases, as is shown in Table I. Thus the effect of intervalley scattering, or of impurity scattering if the assumption of Eq. (21) is valid, is to make the exponent η in $Q_pT^{-\eta}$ smaller than $(7/2)-\frac{1}{2}s-\gamma$. This is what one expects physically. The greater the amount of impurity scattering, or the less the amount of intervalley scattering, the larger will be the effective average K of the carriers which contribute most to the current, hence the larger will be the effective average q of the modes to which most of the crystal momentum is delivered. Although for given current this means that more crystal momentum will be delivered to the low-energy longitudinal phonons, as shown by the $\mu_l f/\mu$ values of Table I, it also means that the average $\tau(\mathbf{q})$ of the modes to which it is delivered will be less, and the latter effect outweighs the former because of the rapidity of the variation of $\tau(\mathbf{q})$ with q. Use of a more realistic law than K^{2r} for the dependence of τ_e on K turns out not to change this conclusion qualitatively. However, it is

conceivable that when impurity scattering is important the increase in the delivery of crystal momentum to the phonons may be greater than one would compute by the present procedure of merely using an altered distribution of electron velocities with the same expression in (21) for the lattice scattering probability. If this occurs the increase in delivery may compensate or outweigh the decrease in the average $\tau(\mathbf{q})$.

We shall try to make some rough quantitative estimates of the effect of temperature variation of the carrier scattering law on the temperature variation of Q_p. Consider first the effect, in pure p-type germanium, of intervalley scattering, if the model of Fig. 1(b) applies, or of optical mode scattering, if Fig. 1(a) is applicable[32] with spin-orbit splitting $\gg kT$. We have seen in Sec. II that this can be described roughly by letting r vary from -0.8 at 300°K to -0.5 at 100°K. For such a variation we find from (39) and Table I that the effective temperature exponent η for Q_p over this range should fall below 7/2 by 0.1 or 0.15 if $s=0$, or that it should fall below 3 by 0.3 or more if $s=1$. Similar crude estimates of r and the lowering of η can be made from mobility data on samples with impurity scattering.[21,34] According to the existing theory of impurity scattering,[34,35] an amount of impurity scattering sufficient to reduce the mobility to half that in pure material should reduce the ratio of Hall to drift mobility to a minimum value only slightly above unity. If we therefore assume that this amount of impurity scattering raises the effective r from $-\frac{1}{2}$ to 0, we can deduce from the observed temperature change required to increase the role of impurity scattering by this amount that for $s=0$ the temperature exponent η should fall below 7/2 by an amount of the order of 0.1 or 0.2 when the mobility has been reduced to half or so of the lattice mobility. At this stage, as Table I shows, Q_p should be about 15 percent below the value in pure material. If $s=1$ the reduction of η below 3 is 0.3 or so, and Q_p is about $\frac{2}{3}$ the value for pure material when the mobility has been reduced to half.

VI. EFFECT OF FINITE SIZE OF THE SPECIMEN

The analysis of the preceding section, giving a variation of Q_p as an inverse power of T, was based on the assumption in Eq. (36) for the variation of phonon relaxation time with temperature and wave number. This assumed law will break down at very low temperatures because of scattering of the phonons by the boundaries of the specimen. Such boundary scattering is the obvious explanation for the fact[2] that at the lowest temperatures Q_p falls below the power law extrapolation (see for example Fig. 4). It was therefore predicted while the experiments were in progress that in this temperature range the effective thermoelectric power could be appreciably changed by changing the diameter of the specimen. This prediction was confirmed.[2] The interest of this boundary effect lies in the opportunity which it provides not only to check the general theoretical picture we have presented, but also to extract from the experimental data some new information on the properties of the semiconductor. We shall therefore devote this section to analyzing the effect of boundary scattering in some detail. We shall consider here only the case of low carrier concentrations, so that Fermi degeneracy and the saturation effect discussed in the next section do not occur.

We can get a little orientation on the problem of boundary scattering by recalling, and slightly amplifying, the simple calculation which was made in Sec. II to establish an upper limit to Q_p. This calculation, after suitable refinement, gives the asymptote which Q_p must approach at very low temperatures. The necessary refinement is easy to make. We replace the expression in Eq. (16) by a sum of two terms, one for longitudinal and one for transverse phonons. We neglect anisotropy of sound velocity within each branch. The values $\bar{\tau}_{bl}$, $\bar{\tau}_{bt}$ to be used for the mean phonon relaxation time $\bar{\tau}$ are of course averages over the boundary scattering times of phonons with different directions of motion. Fortunately, however, these averages are to be made with a weighting factor q_x^2/q^2, as Eqs. (19) and (25) show; since this is the same weighting factor as occurs in the theory of thermal conduction,[25] we can use the relation between $\bar{\tau}_b$ and the dimensions of the specimen which has been derived by Casimir[36] for the latter case. This type of analysis gives

$$c_l\bar{\tau}_{bl}=c_t\bar{\tau}_{bt}=L, \tag{41}$$

where c_l and c_t are mean longitudinal and transverse sound velocities respectively, and where for a specimen of square cross section with completely diffuse scattering at the boundaries L is 1.1 times the square side. Noting that both for the simple model and for the many-valley model of Appendix A the variation of f_l/μ and f_t/μ with temperature and composition is proportional to that of Eq. (31), we have from Eqs. (16) and (1):

$$\text{asymptotic } Q_p=\mp(L/\mu T)(f_lc_l+f_tc_t)\propto f'T^{\frac{1}{2}}, \tag{42}$$

where as before f_l, f_t are the fractions of the crystal momentum of the carriers lost to longitudinal and transverse acoustic modes, respectively, and where f' is the ratio of angular brackets in Eq. (31). This quantity f', tabulated in Table I, depends on the amount and kind of impurity scattering. The absolute value of Q_p for a given lattice mobility μ_L depends slightly on the ratio of f_l to f_t; it would be independent of this ratio if c_l were the same as c_t.

Since, as Fig. 4 shows, Q_p is still far below the asymptote in Eq. (42) at the lowest temperatures used by

[32] Suggested by C. Kittel, Phys. Rev. **94**, 768 (1954).
[34] P. P. Debye and E. M. Conwell, Phys. Rev. **93**, 693 (1954).
[35] H. Jones, Phys. Rev. **81**, 149 (1951); V. A. Johnson and K. Lark-Horovitz, Phys. Rev. **82**, 977 (1951); E. Conwell, Proc. Inst. Radio Engrs. **40**, 1331 (1952).
[36] H. B. G. Casimir, Physica **5**, 495 (1938).

Geballe and Hull, it is clear that to get a theoretical Q_p for these temperatures we shall have to consider the case where boundary scattering and phonon-phonon scattering are of comparable importance. However, there are two points worth noting in the simpler theory. One is that at the lowest temperatures the contribution of transverse phonons to Q_p may well be comparable with that of longitudinal ones, and so it may be that even at temperatures where Q_p is well below its asymptote the transverse contribution is perceptible. The other is that, as Table I shows, a semiconductor with ionized impurity scattering predominant should have a higher asymptotic Q_p than one with lattice scattering only, while one with neutral impurity scattering predominant should be intermediate. This effect of impurity scattering is opposite to that obtained from the theory of Sec. IV for temperatures above the boundary scattering range. This is to be expected: for the higher range of temperatures the decrease of the mean $\tau(\mathbf{q})$ with increasing impurity scattering outweighs the increase in the total crystal momentum delivered to the phonons by a given current, at least if (21) is valid; when boundary scattering is dominant, however, $\tau(\mathbf{q})$ is constant and the latter effect predominates. We shall see that this reversal in the effect of impurity scattering occurs at temperatures where Q_p is well below its asymptote.

Let us now try to calculate Q_p when boundary scattering and phonon-phonon scattering are of comparable importance. The usual procedure in cases of this sort is to assume that the reciprocal relaxation time for each mode is the sum of the contributions which the two types of scattering would yield separately. However, as we shall show, this assumption is not accurate enough for our present purpose. A better procedure is to consider how the crystal momentum in a volume element $\Delta_\mathbf{q}$ of q space is distributed spatially over the cross section of the specimen. In the presence of a current $\mathbf{J}$, crystal momentum is fed into this range of modes at a rate which is independent of position and proportional to the quantity $\mathbf{R}(\mathbf{q})$ defined in Section IV. Phonon-phonon scattering removes crystal momentum from these modes in every element of the volume, at a rate proportional to the local density $\Delta\mathbf{P}(\mathbf{q};\mathbf{r})$ of crystal momentum. Boundary scattering also removes crystal momentum but only from regions adjoining the boundaries; the rate is proportional to the value of $\Delta\mathbf{P}$ at the boundary and to the component of phonon velocity toward the boundary, if the latter is positive, while the rate is zero if the normal velocity is negative. For the simplest geometry, that of a plane-parallel slab with faces normal to the y axis, current in the x direction, we have in a steady state:

$$(2\pi)^{-3}\mathbf{R}(\mathbf{q})\,\Delta_\mathbf{q}-c(q_y/q)\partial\Delta\mathbf{P}/\partial y-\Delta\mathbf{P}/\tau(\mathbf{q})=0, \quad (43)$$

where $\tau(\mathbf{q})$ is the phonon-phonon relaxation time and where we assume for simplicity that the group velocity

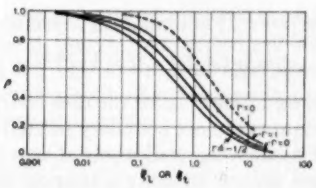

FIG. 6. Full curves: ratio ρ_l of the longitudinal phonon contribution to Q_p for a specimen of finite diameter to the value for an infinite specimen, as a function of the quantity ξ_l defined by (46), for different values of the exponent r in $\tau_e\propto|\epsilon-\epsilon_b|^r$. Dashed curve: corresponding ratio ρ_t for the transverse phonon contribution, abscissa ξ_t given by Eq. (47).

is $c\mathbf{q}/q$. If $q_y>0$ the boundary condition is that $\Delta\mathbf{P}$ must vanish on the back surface, which we take for simplicity to be the plane $y=0$. The solution of Eq. (43) is then

$$\Delta\mathbf{P}=\Delta\mathbf{P}_0[1-\exp(-yq/q_yc\tau)], \quad (44)$$

where

$$\Delta\mathbf{P}_0=(2\pi)^{-3}\mathbf{R}\tau\Delta_\mathbf{q}. \quad (45)$$

Thus for large $y/c\tau$, $\Delta\mathbf{P}$ is distributed uniformly over the specimen except for a small region near the back face (i.e., the face $\mathbf{q}$ points away from), while when $y/c\tau$ is very small $\Delta\mathbf{P}$ increases nearly linearly from back to front. Consequently, for a given total crystal momentum in a specimen of given size, the rate of removal by boundary scattering is twice as great for large τ as for small.

The ratio ρ of the Q_p of a finite specimen to that of an infinite specimen is simply the ratio of the integral of $\Delta\mathbf{P}$ over the cross section and over $\mathbf{q}$ to the integral of $\Delta\mathbf{P}_0$. An approximate evaluation of this ratio is given in Appendix B, the evaluation being exact as $T\to0$ and in error as $T\to\infty$ by only 10 percent or 20 percent of the deviation of the ratio from unity. For longitudinal modes—$s=0$ in Eq. (36)—ρ_l is a function of the dimensionless variable,

$$\xi_l=3\pi\mathcal{E}_l\lambda^3/32A_lT^5L\propto1/T^4L, \quad (46)$$

where λ is the thermal electron wavelength in Eq. (40). Physically ξ_l is the ratio of the phonon-phonon scattering time to $L/\mathcal{E}_l$ for phonons of wave number $(32/3\pi)^{\frac{1}{4}}/\lambda$. Graphs of ρ_l against ξ_l are given in Fig. 6 for three values of the exponent r in $\tau_e\propto|\epsilon-\epsilon_b|^r$, and some of the values are given in Table II. The calculation for trans-

TABLE II. Values of ρ_l plotted in Fig. 6.

ξ_l	ρ_l $r=-\frac{1}{2}$	$r=0$
0.003	0.981	0.989
0.01	0.953	0.969
0.03	0.898	0.928
0.1	0.778	0.835
0.3	0.604	0.676
1.	0.371	0.440
3.	0.195	0.238
10.	0.085	0.10[c]

verse modes ($s=-1$) is similar: ρ_t depends on

$$\xi_t=3\pi\hbar_t\lambda/8A_tT^4L\propto 1/T^{9/2}L. \quad (47)$$

Figure 6 shows a plot of ρ_t for the case $r=0$; this is the most important case since boundary scattering becomes important for transverse modes only at very low temperatures, where neutral impurity scattering often dominates τ_e.

In future comparisons of theory and experiment along the lines of that given in Sec. IX below, it may turn out that important inferences can be drawn from the abruptness or gradualness of the onset of boundary scattering. It is only in regard to this feature that the various assumptions used in the theory can be tested, since any theoretical expression for $Q_p(L,T)$ which is asymptotic to $Q_P(\infty,T)$ at high T and to Eq. (42) at low T will give roughly the right sort of bending over of the plot of Q_p against T. The variation of abruptness of onset with different choices of L, A_l, A_t is of course covered by Eqs. (46) and (47) and Fig. 6. We may also ask, however, how the abruptness varies with the value of the exponent s in Eq. (36), or with variation of the nature of the boundary scattering, e.g., if the boundary scattering takes place at grain or mosaic boundaries, or at finely distributed foreign inclusions. The answer to the latter question is supplied, at least in some cases, by the remarks made after Eq. (45). For under conditions where one should assume additivity of phonon-phonon and boundary scattering probabilities, boundary scattering is twice as effective at high T, for a given effectiveness at low T, as when Eq. (44) applies. Thus making the boundary scattering take place uniformly throughout the volume makes the onset as T is lowered more gradual. The effect of varying the exponents can be surmised from a comparison of Eq. (46) with Eq. (47) and of the full with the dashed curve in Fig. 6. The onset of boundary scattering is more abrupt for $s=-1$ (transverse) than for $s=0$ (longitudinal), both because Eq. (47) has a higher exponent of T than Eq. (46) and because the initial downard bend of the dashed curve is more abrupt than that of the full curve. One can easily see, after a little reflection on the form of the curve of $\tau(\mathbf{q})$ against q and its shift with temperature, that this trend to a more gradual onset with increasing s must hold over the entire range of possible values of s. Explicit quantitative calculations, not reproduced here, have given additional confirmation of this fact.

The theory of this section contains only one constant not previously introduced, namely, the boundary scattering length L. This constant is determined by the size and shape of the specimen if it can be assumed that the scattering of elastic waves impinging on the surface of the specimen is completely diffuse; in any case, a calculation on this assumption gives a lower limit to L. Three facts make the assumption of diffuse scattering plausible for specimens like those of reference 2. The first is the approximate agreement of the theory of Casimir,[36] based on this assumption, with thermal conduction experiments[37] on rods of quartz, potassium chloride, sapphire, and diamond, at temperatures low enough to be in the boundary scattering range. The second is that the surfaces of the specimens of reference 2 were sandblasted. The third is that when a longitudinal wave impinges on the surface, a good part of the reflected energy will reside in transverse nodes, and if the temperature is not too low this part of the energy flux will quickly be randomized by phonon-phonon scattering.

VII. THE SATURATION EFFECT IN THE NONDEGENERATE RANGE

In the caluclations of the two preceding sections it has been assumed that the probability of emission or absorption of a phonon by a charge carrier is the same as it would be if the phonon system were in thermal equilibrium. In Sec. IV, where this assumption was introduced, it was mentioned that it is asymptotically valid for small densities of charge carriers, but must fail for sufficiently high densities. It is easy to see that when this assumption breaks down, Q_p will be less than the value given by the theory of the preceding sections. Consider first the II picture. Suppose the charge carriers are drifting in the positive x direction under the action of an applied field. If there are more phonons moving in the positive than in the negative x direction, then scattering processes in which the x component of velocity of a carrier is increased will be more frequent than if the phonons were in thermal equilibrium, while those in which the x component of velocity is decreased will be less frequent. For a given velocity distribution of the carriers, therefore, the resistance offered by the lattice vibrations to the motion of the carriers will be less than if the phonons were in equilibrium, and concomitantly the carriers will deliver less crystal momentum to the phonons. Thus the phonon contribution Π_p to the Peltier flux will be less than one would calculate on the assumption of phonon equilibrium. One can reach the same conclusion using the Q picture: if the density of charge carriers is sufficiently high the thermal conduction current carried by the low-energy phonons in a temperature gradient will be decreased by the interaction of these phonons with the charge carriers, and the phonons will therefore exert less drag on the carriers than they would if the perturbation of the phonon distribution by the carriers were neglected. In this section we shall try to discuss this effect quantitatively.[38]

As was mentioned in Sec. III, the effect we wish to discuss occurs when, for an isothermal current-carrying

[37] W. J. de Haas and Th. Biermasz, Physica **5**, 47, 320, 619 (1938); R. Berman, Proc. Roy. Soc. (London) **A208**, 90 (1951); Advances in Physics **2**, 103 (1953); Berman, Simon, and Ziman, Proc. Roy. Soc. (London) **A220**, 171 (1953). The latter authors have estimated the reflection for diamond to be roughly midway between diffuse and specular.

[38] A study of the influence of this effect on the electrical conductivity and its frequency dependence has been carried out by B. Goodman (unpublished). I am indebted to Dr. Goodman for information about this work.

specimen, "the unbalance of the phonons is of the same order as that of the carriers." This suggests that we begin by formulating a quantitative definition of "unbalance." This is easily done when, as in the present problem, the most important interactions between the various parts of a statistical assembly conserve a vector quantity such as crystal momentum. In the usual formulation of statistical mechanics for a complicated assembly, it is shown that if energy is the only extensive quantity which is conserved in the motion of the assembly and in its interaction with external systems, such as thermal reservoirs, there is a one-parameter family of equilibrium distributions, the single parameter being temperature, an indirect measure of energy content. But if several extensive quantities are conserved, the possible equilibrium distributions contain a corresponding number of parameters.[39] Thus if all the interactions of electrons and phonons with each other conserved crystal momentum as well as energy, the possible equilibrium distributions would be described by parameters T, $\boldsymbol{\beta}$, such that in a given distribution the probability of any quantum state of total energy E and total crystal momentum $\mathbf{p}$ would be proportional to $\exp[(-E+\boldsymbol{\beta}\cdot\mathbf{p}/kT]$. Note that $\boldsymbol{\beta}$ has the dimensions of velocity. In particular, a charge carrier distribution of this sort, with a given value of $\boldsymbol{\beta}$, could be in equilibrium with a phonon distribution having the same $\boldsymbol{\beta}$. A repetition of the usual Fermi-Dirac and Einstein-Bose derivations gives for the single-particle distribution functions of electrons and phonons,[24] respectively,

$$f(\mathbf{K};\boldsymbol{\beta},T)=\left[\exp\left(\frac{\epsilon(\mathbf{K})-\epsilon_F-\boldsymbol{\beta}\cdot\hbar\mathbf{K}}{kT}\right)+1\right]^{-1}, \quad (48)$$

$$N(\mathbf{q};\boldsymbol{\beta},T)=\left[\exp\left(\frac{\hbar\omega(\mathbf{q})-\boldsymbol{\beta}\cdot\hbar\mathbf{q}}{kT}\right)-1\right]^{-1}, \quad (49)$$

where as previously ϵ_F is the Fermi level, $\epsilon(\mathbf{K})$ is the energy of an electronic state of wave number $\mathbf{K}$, etc. Although these equations represent an equilibrium distribution only when all interactions conserve crystal momentum, they form a useful reference point even in the presence of other types of motivations and interactions (impurity scattering, electric field, Umklapp collisions, etc.), because they show the relation between the electron and phonon distribution functions which the electron-phonon intereaction is attempting to establish. Thus if we take all $\boldsymbol{\beta}$'s to be in the field direction x, we may define an unbalance velocity β_{ex} for each electronic state $\mathbf{K}$ by Eq. (48), and similarly a β_{px} for each phonon mode $\mathbf{q}$ by Eq. (49), and may describe the electron-phonon interaction as one which attempts to equalize the β_{ex} and β_{px} of each carrier-mode pair which interact.

[39] J. W. Gibbs, *Elementary Principles in Statistical Mechanics*, in *Collected Works* (Longmans, Green, and Company, New York, 1928), Vol. 2, pp. 37–40.

When an infinitesimal current flows in an isothermal conductor the $\boldsymbol{\beta}_e$ and $\boldsymbol{\beta}_p$ just defined are infinitesimal. On equating Eq. (48) to the usual expression $f^{(0)}+f^{(1)}$ for the electronic distribution function in the presence of a field $\mathbf{E}$ one finds easily

$$\beta_{ex}(\mathbf{K})=\pm(eE/m^*)\tau_e(\mathbf{K})=v_{Dx}(\mathbf{K}), \quad (50)$$

where the upper sign is for electrons, the lower for holes, and where $\mathbf{v}_D$ is an effective drift velocity of the carriers in states $\mathbf{K}$ and $-\mathbf{K}$. Here we have for simplicity assumed the conventional semiconductor model of Fig. 5(c), with effective mass m^*, and have assumed a relaxation time $\tau_e(\mathbf{K})$ to exist. Similarly we find from Eq. (49)

$$\beta_{px}(\mathbf{q})=\frac{[\omega(\mathbf{q})]^2\Delta p_x(\mathbf{q})}{kTq_x^2}\approx\left[\frac{q}{q_x}\right]^2\left[\frac{c\tau(\mathbf{q})R_x(\mathbf{q})}{kT}\right]c, \quad (51)$$

where $\Delta\mathbf{p}(\mathbf{q})$ is the excess crystal momentum in the $\mathbf{q}$th mode, given by Eq. (18), $\tau(\mathbf{q})$ is its relaxation time, c is a mean sound velocity, and $\mathbf{R}(\mathbf{q})$ is as before the rate at which the electronic system feeds lattice momentum into the $\mathbf{q}$th mode. Note that in our problem $\Delta p_x \propto q_x^2/q^2$, so β_{px} is roughly independent of the direction of $\mathbf{q}$.

In the approximation we have been using in the preceding sections, $\mathbf{R}(\mathbf{q})$ is given by Eq. (25) or (A4) and $\beta_{px}(\mathbf{q})$ is thus an integral over the various $\beta_{ex}(\mathbf{K})$. When the various β_{px} become comparable with the β_{ex}, however, the $\mathbf{R}(\mathbf{q})$ of Eq. (25) or (A4) must be replaced by an expression which vanishes when $\boldsymbol{\beta}_p=\boldsymbol{\beta}_e$. Since the $\boldsymbol{\beta}$'s are infinitesimal, the correct expression must have the form,

$$\beta_{px}(\mathbf{q})=\int\Phi(\mathbf{q},\mathbf{K})[\beta_{ex}(\mathbf{K})-\beta_{px}(\mathbf{q})]d\mathbf{K}, \quad (52)$$

where Φ can be taken from Eq. (25) or (A4). Since the approximation of the preceding sections consisted in neglecting the β_{px} in the integrand of Eq. (52), we have for the ratio of the Q_p derived from Eq. (52) to the $Q_p^{(0)}$ derived previously

$$\frac{Q_p}{Q_p^{(0)}}=\int\left(\frac{\int\Phi\beta_{ex}d\mathbf{K}}{1+\int\Phi d\mathbf{K}}\right)d\mathbf{q}\Big/\int\int\Phi\beta_{ex}^{(0)}d\mathbf{K}d\mathbf{q}. \quad (53)$$

Here we distinguish $\beta_{ex}^{(0)}$, the value calculated neglecting saturation, from β_{ex}, the true value. Although we shall not attempt such a refinement, the latter should strictly be calculated from an integral expression analogous to Eq. (52) but with the roles of $\mathbf{K}$ and $\mathbf{q}$ interchanged.

We shall not try to evaluate Eq. (53) to as high a degree of refinement or for such a variety of conditions as we have employed in the preceding sections; this is partly because of the greater computational difficulty of Eq. (53) and partly because for conditions where Eq. (53) is significantly below unity some of our basic assumptions are probably not very accurate, e.g., the

neglect of the influence of impurities on the band structure. We shall content ourselves with assuming $\beta_{ez}=\beta_{ez}^{(0)}$ and treating only longitudinal modes for the case $\tau_e=$ constant, a case which is probably not too far from the truth throughout a good part of the concentration range of interest. For this case, by Eq. (50), β_{ez} is independent of $\mathbf{K}$, and it can be factored out of Eq. (53). On comparing Eqs. (25) and (32) with (51) and (52), with the β_{pz} in the integrand of the latter omitted, we find, for longitudinal modes $\mathbf{q}$,

$$\int \Phi d\mathbf{K}=\frac{8\pi}{3}\left(\frac{\mathcal{E}_l^2 ne\lambda^4 f_l'}{kT\mu_L}\right)q\tau(\mathbf{q})\exp(-\tfrac{1}{4}\lambda^2q^2), \quad (54)$$

where as before n is the density of carriers, λ is the thermal electron wavelength in Eq. (40), μ_L is the value the mobility would have if only low-energy phonons scattered, and f_l' is the fraction of the crystal momentum which would be delivered to longitudinal modes under these conditions. Since the most interesting saturation effects occur at low temperatures where boundary scattering may be appreciable, it is desirable to use an expression for $\tau(\mathbf{q})$ which at least approximates those of the preceding section. We shall therefore assume

$$1/\tau(\mathbf{q})=A_lT^5q^2+(\mathcal{E}_l/L). \quad (55)$$

This is a crude version of the additive probability assumption which in the preceding section we rejected as inadequate. However, it is good enough for the present purpose, and it is easy to see that an approach paralleling that of Eq. (43) would lead to great mathematical complications. Insertion of Eqs. (55) and (54) into Eq. (53) and changing of the variation of integration to $\exp(-\frac{1}{4}\lambda^2q^2)$ give, for the case $\tau_e=$ constant,

$$\frac{Q_{pl}}{Q_{pl}^{(0)}}=\frac{\int_0^1[1+(\lambda^3\mathcal{E}_l/4LA_lT^5)(-\ln x)^{-1}+(4\pi/3)(\mathcal{E}_l^2ne\lambda^5/A_lkT^4\mu_l)x(-\ln x)^{-\frac{1}{2}}]^{-1}dx}{\int_0^1[1+(\lambda^3\mathcal{E}_l/4LA_lT^5)(-\ln x)^{-1}]^{-1}dx}. \quad (56)$$

The denominator of Eq. (56) represents the value of ρ_l, the ratio of Q_{pl} (without saturation) for a finite specimen to that for an infinite specimen, as given by the present approximation in Eq. (55). The ratio in Eq. (56) can therefore be described as a function of the two parameters ρ_l and n/n_1, where

$$n_1=(3/4\pi)(kT^4\mu_LA_l/f'\mathcal{E}_l^2e\lambda^5)$$
$$=\frac{1}{4\pi}\left(\frac{T}{T_0}\right)^5\frac{(k/e)}{Q_{pl}^{(0)}(T_0)}\cdot\frac{1}{[\lambda(T_0)]^3} \quad (57)$$

by Eq. (38), where T_0 is any convenient reference temperature at which it is legitimate to take $\mu=\mu_L$ (so $r=-\frac{1}{2}$), and where $Q_{pl}^{(0)}(T_0)$ is to be evaluated for $L=\infty$.

Figure 7 shows some plots of $Q_{pl}/Q_{pl}^{(0)}$ against n/n_1 for various values of ρ_l, as obtained by numerical evaluation of Eq. (56). The behavior of these is qualitatively understandable. Increasing the amount of boundary scattering decreases each $\tau(\mathbf{q})$, hence decreases Eq. (54). Since the decrease in this quantity is always by a greater ratio than the decrease in this quantity divided by one plus itself, the denominator of Eq. (53) decreases more than the numerator. Thus for a given A_l, the greater the boundary scattering, the larger Eq. (53).

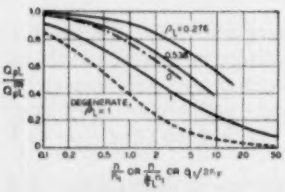

FIG. 7. Full curves: saturation ratio $Q_{pl}(T,L,n)/Q_{pl}^{(0)}$, for nondegenerate statistics, as a function of carrier density n, measured in units of the n_1 of Eq. (57). Here $Q_{pl}^{(0)}$ is $Q_{pl}(T,L,0)$, and the three curves are for different values fo $\rho_l=Q_{pl}(T,L,0)/Q_{pl}(T,\infty,0)$. Dot-dash curve: same for case of pure boundary scattering ($\rho_l\to 0$), abscissa n/ξ_ln_1, where ξ_l is given by Eq. (46). Dashed curve: saturation ratio for degenerate statistics, $L=\infty$, as a function of $q_1/2K_F$, q_1 given by Eq. (61).

The same sort of reasoning gives us some insight into the extent of the errors introduced by the assumption $\beta_{ez}=$ constant. The quantity $\int\Phi d\mathbf{K}$ is given by Eq. (54) independently of the law of variation of β_{ez}, which enters only as shown in Eq. (53). Since $\int\Phi d\mathbf{K}$ decreases with increasing q except when $\tau(\mathbf{q})$ is close to the boundary scattering value, we may expect that at not too low temperatures any increase in the $|\beta_{ez}|$ of states of large K relative to those of small K will increase $Q_p/Q_p^{(0)}$. Now there are two things which may cause β_{ez} to depart from constancy. One is that the combination of lattice and impurity scattering may cause the effective exponent r in $\tau_e(K)\propto K^{2r}$ to differ from the value zero which we have assumed in this section. From what has just been said we may describe this effect by saying that the more impurity scattering, the less saturation. The other effect is the difference between β_{ez} and $\beta_{ez}^{(0)}$ in Eq. (53). It is clear that β_{ez} is larger than the $\beta_{ez}^{(0)}$ given by Eq. (50) with the unsaturated τ_e, since the phonons do not slow down the charge carriers as effectively as previously assumed. Therefore the ratio $Q_p/Q_p^{(0)}$ will be greater than it would be for $\beta_{ez}=\beta_{ez}^{(0)}$, i.e., the calculation leading to Eq. (56) slightly overestimates the amount of saturation.

It can be verified that if, for given $Q_p^{(0)}$, we make the

decrease of $\tau(\mathbf{q})$ with q more gradual by using an $s<0$ in Eq. (36), the value of Eq. (53) will be increased.

Finally, we note that if transverse modes contribute appreciably to Q_p, $Q_p/Q_p^{(0)}$ will be less than the $Q_{pl}/Q_{pl}^{(0)}$ computed here, because the transverse modes saturate less readily than the longitudinal.

VIII. EFFECTS OF FERMI DEGENERACY

All the calculations of Sec. II and Secs. IV through VII have assumed the charge carriers to obey Maxwell-Boltzmann statistics. We wish now to examine briefly the way in which the electronic and phonon contributions to the thermoelectric power are modified when the carrier density is so high that degenerate Fermi statistics must be used. Our treatment of this case will be very rough, for two reasons: in the first place, as was pointed out in the introduction, we do not yet know how to treat degenerate semiconductors accurately; secondiy, the phonon contribution, which is the principal concern of this paper, is much less important at high carrier densities than at low, partly because of the saturation effect discussed in the preceding section.

Wright[7] has given an expression for the thermoelectric power of the conventional semiconductor model [Fig. 1(c)], for arbitrary degree of degeneracy. Just as in Sec. II, if the charge carriers have a relaxation time τ_e dependent only on energy the conventional model may be expected to give the same Q_e as the models of Figs. 1(a) and 1(b), provided that any spin-orbit splitting of the former model is either very large or very small. If $\tau_e \propto |\epsilon-\epsilon_b|^r$, Wright's expression for eTQ_e is the same as Eq. (2) with

$$\Delta\epsilon_T = \pm\left(\frac{5+2r}{3+2r}\right)\frac{F_{r+\frac{1}{2}}}{F_{r+\frac{3}{2}}}, \tag{58}$$

where

$$F_\nu(\zeta^*) = \int_0^\infty \frac{\zeta^\nu d\zeta}{1+e^{\zeta-\zeta^*}}, \quad \zeta^* = \pm\frac{(\epsilon_F-\epsilon_b)}{kT},$$

and where the upper sign is for n type, the lower for p. As in Sec. II, ϵ_F is the Fermi level, ϵ_b the band edge energy. The F_ν for half-integral ν values can be obtained from the tables of McDougall and Stoner.[40] Figure 8 shows the Q_e values calculated in this way from Eqs. (2) and (58), for $r=0$ and 1, as functions of ζ^*. Curves of Q_e *vs* T can be calculated from these, for any desired case, by using the relation of ζ^* to T given by the dashed curve. The mobilities of typical specimens just starting to become degenerate, analyzed in terms of the Conwell-Weisskopf-Brooks formula,[17] suggest values of r in the range 0.8 to 1.2. As extreme degeneracy is approached, however, it is not likely that r gets any closer to the Conwell-Weisskopf limit 1.5, because the scattering by the impurity ions becomes more nearly isotropic and less dependent on energy as their screening radius be-

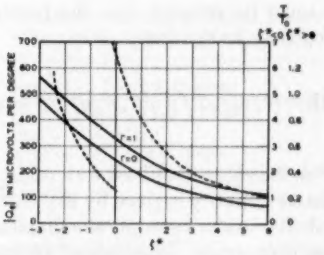

FIG. 8. Full curves: Q_e for the simple model with degenerate statistics, as a function of $\zeta^*=\pm(\epsilon_F-\epsilon_b)/kT$, for two values of the exponent r in $\tau_e \propto |\epsilon-\epsilon_b|^r$. Dashed curve (two scales on right): relation of ζ^* to T/T_0, where $T_0=(n/5.30\times10^{14})^{\frac{2}{3}}m/m^{(N)}$.

comes shorter. Moreover, as we have already noted for the non-degenerate case, electron-electron scattering makes r closer to zero than in the one-electron theory.

We turn now to the phonon contribution Q_p under conditions of Fermi degeneracy. If the saturation effect of the preceding section were absent, the principal effect of degeneracy ought to be to increase the effective average q of the modes to which the carriers deliver their crystal momentum, hence to decrease the effective $\tau(\mathbf{q})$ and so decrease Q_p below the value given by Eq. (38). If we make the assumption, now definitely risky, that lattice and impurity scattering act independently, so that (21) holds, the effect can be evaluated quantitatively. Although saturation is usually quite advanced before strong degeneracy sets in, a calculation neglecting saturation is still of some value, as it sets an upper limit to Q_p. The calculation is easy if $|\epsilon_F-\epsilon_b| \gg kT \gg \hbar\omega(\mathbf{q})$, where the $\omega(\mathbf{q})$ are the frequencies of the phonons which do most of the scattering. The calculation for this case is given in Appendix A, and leads to Eq. (A10). The relation of this equation to Eq. (38) or (A8) is simple: the ratio of averages in the last factor of Eq. (38) has been replaced by the ratio of the same quantities evaluated at the Fermi surface; this takes account of the shorter phonon lifetime due to the larger q's with which the degenerate electrons interact. This excitation of larger q values is shown in more detail by the sample plot ln Fig. 5 of $\bar{R}_x(q)$ for a degenerate specimen, a plot derived from Eq. (A4). However, it must be remembered that Eq. (A8), and hence Eq. (A10), cease to be valid when the degeneracy is so advanced that the phonon energies are not $\ll kT$. For such high degeneracy the average q of the phonons effective in lattice scattering will be smaller than we have assumed, and the last factor in Eq. (A10) should be replaced by something larger, probably of the order of $(m^*c^2/kT)^{1+\frac{1}{2}r}$. However, Q_p continues to decrease, since under these conditions τ_{el}^{-1} decreases with increasing degeneracy, at least when (21) is assumed to hold.

In actual cases the phonon part of the thermoelectric power will of course be reduced by the saturation effect. The expression in Eq. (53) of the preceding section gives the factor by which the calculation of the preceding

[40] J. McDougall and E. C. Stoner, Trans. Roy. Soc. (London) A237, 67 (1938).

paragraph must be reduced. For the present case we have, analogously to Eq. (54),

$$\int \Phi d\mathbf{K} = (\mathcal{E}_l^2 ne/kTJ)[q^2 R_x^{(0)}(\mathbf{q})/q_x^2]\tau(\mathbf{q}), \qquad (59)$$

where $R_x^{(0)}$ is the value computed with neglect of saturation. The latter quantity is given by Eq. (A4) of Appendix A. We shall consider here only the simplest case, that of complete degeneracy, longitudinal phonons ($s=0$), and single-valley spherical energy surfaces. For this case $q^2R_x^{(0)}/q_x^2$ is proportional to q up to a value of q equal to twice the radius K_F of the Fermi surface, and is zero for $q>2K_F$. In other words, the dashed curve of Fig. 5 would be simply a triangle if degeneracy were complete. The factor of proportionality in $R_x^{(0)}$ can be evaluated by the condition,

$$(2\pi)^{-3}\int R_x(\mathbf{q})d\mathbf{q} = (\tau_e/\tau_{eL})_{\epsilon_F} enE,$$

where as in Sec. IV τ_{eL} is the relaxation time for scattering by the low-energy longitudinal modes. With $s=0$ in Eq. (36) for $\tau(\mathbf{q})$ the expression in Eq. (59) reduces to

$$\int \Phi d\mathbf{K} = q_1/q, \quad (q<2K_F)$$
$$= 0, \quad (q>2K_F), \qquad (60)$$

where

$$q_1 = \tfrac{1}{2}\pi^2(\tau_e/\tau_{eL})_{\epsilon_F}\lambda^4 k\mathcal{E}_l^2 ne/\mu\epsilon_F^2 A_l T^2. \qquad (61)$$

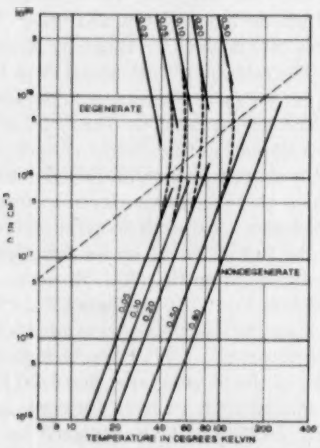

FIG. 9. Contours of constant saturation ratio $Q_{pl}/Q_{pl}^{(0)}$ in the $n-T$ plane, for the case $m^{(N)}=m$, $m^*=0.3m$, $Q_{pl}^{(0)}(80°)=1000$ μv/deg. The dashed curve is the boundary between degenerate and nondegenerate conditions, arbitrarily defined as the locus of values for which the Fermi level coincides with the band edge. The full lines are taken from Eq. (57) and Fig. 7 (nondegenerate) and from Eqs. (61) and (62) (degenerate). The dotted lines indicate qualitatively the connection of the regions of validity of the degenerate and nondegenerate formulas. Boundary scattering has been neglected.

Inserting Eq. (60) into (Eq. (53) we find, after an elementary integration

$$Q_{pl}/Q_{pl}^{(0)} = 1-(q_1/K_F) + \tfrac{1}{2}(q_1/K_F)^2 \ln[1+(2K_F/q_1)]. \qquad (62)$$

As n increases, q_1/K_F decreases, since it goes as n/ϵ_F^2 if τ_{eL} is proportional to K_F^{-1}. Thus Eq. (62) predicts less saturation the larger n. This is clearly because increasing K_F increases the mean q of the participating phonons, and so, by decreasing the mean $\tau(\mathbf{q})$, makes the phonons harder to saturate. The effect would be even more pronounced if we assumed an exponent $s>0$ in Eq. (36). However, as is shown by the sample contours of constant saturation ratio in Fig. 9, saturation is always marked at degenerate densities.

It must be borne in mind that the calculations of this section, including in particular Fig. 9, have many limitations. We have assumed the conventional model of a semiconductor, and so have negelcted such things as perturbation of the band structure by the impurity ions, electron interactions, and nonadditivity of scattering probabilities. Moreover, our calculations of $Q_{pl}^{(0)}$ and $Q_{pl}/Q_{pl}^{(0)}$ are crude in that they assume $|\epsilon_F-\epsilon_b| \gg kT$ but $hcK_F \ll kT$. Finally, both Eq. (56) and Eq. (62) must become untrustworthy when they predict extremely small saturation ratios, since they are based on the assumption that the crystal momentum of a low-energy phonon disappears when it suffers a collision; actually, it is merely delivered to higher-frequency modes with rather short relaxation times. Very roughly, we may say that the saturation effect should not decrease Q_{pl} below the value of Fig. 4 corresponding to the use in Eq. (16) of the conductivity relaxation time τ_c given by Eq. (17). However, this limit is not likely to be reached when the contribution of transverse modes to Q_p is appreciable, since these saturate much more slowly than the longitudinal ones we have treated.

IX. COMPARISON WITH EXPERIMENT

The theoretical notions which have been presented in the preceding sections account qualitatively for most of the features of the thermoelectric power data of Geballe and Hull[2]. Specifically, they account for the rise of the thermoelectric power Q as T is lowered (Sec. IV) the bending over at the lowest temperatures (Sec. V), the decrease of the low temperature Q when the diameter of the specimen is reduced (Sec. V), the approximate lack dependence of Q on carrier concentration n at low n (Sec. IV), and the decrease of Q at high n (Secs. VI and VII). Table III summarizes the way in which the principal adjustable constants of the theory enter into these various phenomena. Only those constants are listed which are not usually well known from other types of measurement and which have a major, rather than just a minor, effect on the phenomenon under consideration. In each entry an effort has been made to arrange the constants in order of decreasing importance. In the

middle two rows the value of Q_p at moderate temperature and low n is assumed known. In the last two rows (degenerate) the effective masses have been primed to emphasize the fact that they need not be the same as for nondegenerate material.

Because of the probable availability in the near future of more accurate and detailed experimental data, it seems best to give merely an illustrative discussion of the data of reference 2, without attempting to extract accurate values of the constants or to discuss the uniqueness of the fit critically. We shall try to show only (i) that approximate quantitative agreement of theory and experiment is possible with entirely reasonable values of the constants; (ii) that even the gross features of the data lead to some significant new conclusions about germanium; and (iii), that the study of thermoelectric power at low temperatures is a promising tool for getting a great deal of useful information on semiconductors.

Most of the comparisons to be made below will be for p-type rather than n-type germanium. This is because it is more likely for p- than for n-germanium that the band structure is one to which most of the analysis of this paper is applicable in the medium- and high-temperature range. Specifically, the band structure of p germanium is very probably either of the many-valley type of Fig. 1(b), or of the single-valley degenerate type with a fairly large spin-orbit splitting and energy surfaces which near the band edge are nearly concentric spheres.[33] In the former case all the analysis of this paper applies at any temperature, and in the latter case it should apply when kT is small compared to the spin-orbit splitting, a condition which should be fulfilled below 100°K, though perhaps not at room temperature. For n-germanium, on the other hand, the disparity between the effective masses measured in the cyclotron resonance experiment[41] and the inertial average measured by Benedict and Shockley[15] suggests that the model for this case may be of the degenerate many-valley type, with a spin-orbit splitting small enough so that departures from constant curvature in the $\epsilon-K$ relation may be appreciable at 100°K. If this is the case, the mathematics of this paper is inapplicable except at very low temperatures. Even if the structure is of the simple many-valley type, Fig. 1(b), the extremely high anisotropy[41,42] of the effective mass will make the value of the m^* of Appendix A very uncertain.

1. *P*-Type Germanium, Low *n*

In the range around room temperature the phonon contribution Q_p is negligible compared with the electronic term Q_e. As Geballe and Hull[2] have shown, the data in this region can be fitted by using Eqs. (4) and (7) for the Q_e of the holes, and combining this, when intrinsic conduction is appreciable, with a similar formula for the Q_e of the electrons, according to the rule for emf's in parallel. They found $m^{(N)}/m=0.75\pm0.15$, assuming the effective exponent r in $\tau_e\propto|\epsilon-\epsilon_b|^r$ to vary from -0.5 to -0.8 in the way proposed in Sec. II above. The result is not especially sensitive to this assumption. This is roughly consistent with an inertial mass $m^{(I)}=0.3m$ and a six-valley model. If on the other hand one assumes a similar inertial mass but a band edge at $K=0$ with spin-orbit splitting, as cyclotron resonance experiments[41,43] suggest,[33] the only possibility for fitting the thermoelectric data is to have the spin-orbit splitting small enough to cause appreciable departures from Eqs. (3) and (6).

TABLE III. Constants determining various features of the thermoelectric power $Q(n,T,L)$.

Feature or region	Principal constants	Eqs.
High T, low n, Q_e	$m^{(N)}$, $(\Delta\epsilon_T/kT)$ or r	(4)
Medium T, low n, Q_p	$A_l m^{*\frac{1}{2}}/f_l$	(38)
Low T, low n, effect of size on Q_p	Lf_l, and perhaps $A_l m^{*\frac{1}{2}}L$, $(1-f_l)L$	(46) (47), (38)
Saturation of Q_{pl}, nondegenerate	m^*	(57)
High T, degenerate, Q_e	$m^{(N)'}$, r	(58)
Medium T, degenerate, Q_p	$A_l m^{*\frac{1}{2}}/m^{(N)'\frac{1}{2}}f_l$, $m^{(N)'}/m^{*\prime}$ $A_l m^{*\frac{1}{2}}/m^{(N)\frac{1}{2}}f_l$, etc.	(A10), (61), (62),

In the range around liquid air temperature Q_p can be determined fairly accurately as $Q-Q_e$, with Q_e from Eq. (8) with the previously determined $m^{(N)}$ and r. Geballe and Hull[2] have plotted, in their Fig. 6, values obtained in this way, and we have already remarked, in Sec. V, the approximate agreement of the predicted and observed values of the exponent η in $Q_p\propto T^{-\eta}$. Although we shall see below that boundary scattering and possibly even the contribution of the transverse phonons can affect η appreciably, the absolute value of Q_p at say 80°K is only slightly different from the contribution of Eq. (38) of the longitudinal phonons in an infinite medium. By Eqs. (38), (39), and (40) this value therefore determines the quantity $A_l(m^*)^{1+\frac{1}{2}s}/f_l$, if r and s are known or assumed. For the purest specimens we may take $r=-\frac{1}{2}$ at 80°. For the ideal case $s=0$, the last factor of Eq. (38) reduces to $\frac{2}{3}\lambda^2$, and with $\gamma=0$ we have

$$A_l m^*/f_l m=\hbar^2 c_l^2/6kT^5\mu m Q_{pl}. \tag{63}$$

Numerical values are

$$c_l=5.33\times10^5 \text{ cm/sec},$$
$$\mu=3.8\times10^4 \text{ cm}^2/\text{volt sec},$$
$$Q_p=9.4\times10^{-4} \text{ volt/deg},$$

for specimen 8 of the Geballe-Hull paper at 80°. These give the value 3.6×10^{-12} cm^2/deg^2 sec for the right of Eq. (63). This value needs to be corrected for boundary scattering and possibly for the contribution of transverse phonons; as we shall see, the corrections are

[41] Lax, Zieger, Dexter, and Rosenblum, Phys. Rev. **93**, 1418 (1954).
[42] S. Meiboom and B. Abeles, Phys. Rev. **93**, 1121 (1954).
[43] Dresselhaus, Kip, and Kittel, Phys. Rev. **92**, 827 (1953).

probably such as to increase the value given by something like 20 percent.

Comparisons of theory and experiment in the boundary scattering range have been made for a number of different choices of the amount of participation of transverse modes and various values of the ratio $f_l L/L_0$, i.e., the product of the fraction of the scattering of the carriers due to longitudinal modes by the ratio of the true boundary scattering length to that for diffusely scattering boundaries. Figure 10 shows an example for which almost no participation of transverse phonons is required, i.e., for which Q_{pl} is negligible over the termperature range covered, even though $f_t=1-f_l$ is sizable. The theoretical curve for $r=-\frac{1}{2}$ was constructed by choosing arbitrarily a value for the ξ_l of Eq. (46) at 80°, hence of ρ_l (80°), determining the Q_{pl} of an infinite specimen at 80° so that $\rho_l Q_{pl}$ (80°,∞) equalled the observed Q_p, determining $\rho_l(T)$ from Eq. (46) and Fig. 6, and finally multiplying ρ_l by $(80/T)^{3.5}Q_{pl}(80°,\infty)$. The value shown for $f_l L/L_0$ is, of course, merely the value required to give the chosen $\xi_l(80°)$ and $Q_{pl}(80°,\infty)$, when Eqs. (46) and (38) are combined. The curve for $r=0$, constructed to correspond to the same atomic constants, is shown to illustrate the order of magnitude of the effect which might be produced by the increasing importance of impurity scattering at the lower temperatures.

Several conclusions can be drawn from the comparisons of theory and experiment which have been made to date, and they can all be illustrated by reference to Fig. 10. The most noteworthy and striking of these is that

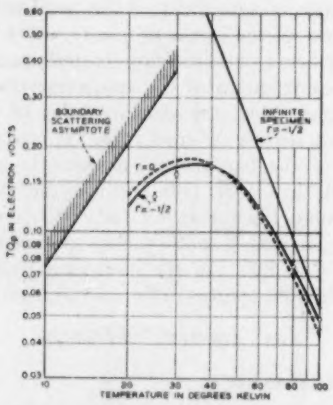

FIG. 10. Sample comparision of theory and experiment on Q_p for p type germanium with $n=1.9\times10^{14}$ cm^{-3}, $L_0=0.153$ cm. Points: observed Q (Geballe and Hull, specimen 8) minus Q_e obtained from (8) with $n^{(N)}=0.75n$, $\Delta\epsilon_T=2kT$. The vertical lines give the order of magnitude of the uncertainty due to scatter in the observed Q's; no estimate of systematic errors has been included. Full curve: Q_{pl} for $r=-\frac{1}{2}$, computed as described in the text from the theory of Sec. VI, with fit to the observed value at 80°, and with the parameter choice $f_l(80°)\ L/L_0=0.46$. Dashed curve: Q_{pl} for $r=0$. The line at the right represents the values Q_{pl} would attain if there were no boundary scattering; that at the left gives the lower limit to $Q_{pl}+Q_{pt}$ when phonon-phonon scattering becomes negligible compared with boundary scattering, as calculated from Eq. (42) with $L=L_0$, $(f_l+f_t)/\mu=(Q/80)^{\frac{1}{2}}/\mu(80°)$.

an f_l value at 80° of the order $\frac{1}{2}$ or less is required to fit the data, i.e., that about half or more of the lattice scattering at 80° must be due to shear modes. This is qualitatively obvious from the fact that the observed points bend away from the "infinite specimen" line so far below where this line intersects the lower limit of the "boundary scattering asymptote" derived from Eq. (42). If this early bendover is not due entirely to the saturation effect, a possibility which seems ruled out by Fig. 4 of reference 2, it must mean that the contribution Q_{pl} of the longitudinal modes is dominant and is approaching an asymptote considerably lower than that of the total $Q_{pl}+Q_{pt}$. Further calculations which have been made show that no fit is possible with $f_l>0.6$. and if the boundary scattering is not completely diffuse the limit will be even lower. However, values of $f_l L/L_0$ smaller than the 0.46 used for Fig. 10 are possible if the contribution Q_{pt} from transverse modes is assumed to come in at a high enough temperature to partially compensate the early bendover of Q_{pl}.

The high- and low-temperature extremes of Fig. 10 are worth noting. Even at 100° the theoretical curve of Q_{pl} is appreciably below the "infinite specimen" line, the difference corresponding to $\rho_l=0.89$. This illustrates the fact, implicit in (B5) of Appendix B, that at high T, where only a negligible proportion of the modes are dominated by boundary scattering, the effect of boundary scattering on the remaining (higher q) modes, though small, is far from negligible. The exponent η in $Q_p \propto T^{-\eta}$ over the range 80°–100° is reduced by boundary scattering from 3.50 to 3.03. Note that the reduction of η would have been twice as great if we had assumed simple additivity of $1/\tau(\mathbf{q})$ and $1/\tau_b$, instead of using the treatment of Eqs. (43) and (44).

At low T the observed points fall below the theoretical curves, whereas ideally they should pass above as the contribution Q_{pt} of the transverse modes starts to be appreciable. This may be at least partly due to experimental errors, which become larger in this range, or to inhomogenity of the sample. If the effect turns out to be real it will dictate choice of a smaller value of $f_l L/L_0$; however, too small a value would worsen the fit at higher T. According to the calculations presented below in Fig. 11, the saturation effect of Sec. VII should not have made a major reduction in the Q_p of this specimen by 25°.

Figure 7 of reference 2 shows the effect on Q of a moderate reduction in the dimensions of specimen 7. As the diameter reduction was not absolutely uniform, it is hard to estimate its effect precisely; however, the data given suggest that the cut down specimen had an effective L about 0.78 times the original value. Figure 11 gives a comparison of the observed change in Q produced by cutting down with the change in Q_{pl} computed from (46) and Fig. 6. At 40° and 30° the agreement is all that could be desired, and favors the belief that the numerical assumptions of Figures 10 and 11 are not far from the truth. However, the uncertainties in the

experimental data are considerable, and as data covering a much wider range of sizes will probably be available soon, it is hardly worthwhile to speculate about such things as the departures of the points from the curve at high and low T.

2. Nondegenerate p-Type Germanium, Larger n

Figure 4 of the paper of Geballe and Hull[2] shows that as the carrier concentration n increases, Q_p changes little at first, but eventually decreases markedly. This is undoubtedly the saturation effect of Sec. VII, and we shall discuss it in detail presently. The slight rise in the plotted Q_p occurring just before the fall may or may not be real. It is of the same order of magnitude as the correction which would be produced in Q_p by taking impurity scattering into account in the calculation of $\Delta\epsilon_T$ (see Sec. II). If any part of the rise is real, it may conceivably be due to breakdown of the assumption that impurity scattering and lattice scattering act independently, an assumption involved in our use of Eq.

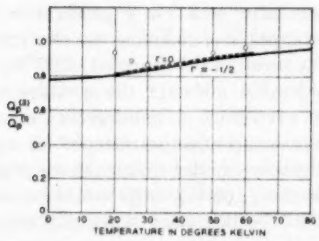

FIG. 11. Sample comparison of observed and calculated values of the change in Q_p due to reducing diameter of sample. Curves: calculated from Fig. 6 with numerical assumptions of Fig. 10. Points, Geballe and Hull, specimen 7, $L_0^{(2)}/L_0^{(1)}\approx 0.78$.

(21). At sufficiently large impurity density this speculation may be broadened into the statement that impurity band conduction is affecting both Q_e and Q_p.

The saturation effect can be predicted quantitatively from the theory of Sec. VII, provided we can adopt a value for the critical density n_1 defined by Eq. (57) and for the boundary scattering reduction factor ρ_l in Fig. 7. If T_0 is taken in the liquid air range, so that $Q_{pl}(T_0)$ is known, the only unknown quantity in Eq. (57) is the effective mass m^* entering into λ. For p germanium this cannot be far from the value $0.3m$, which is close to the inertial average mass[15] or to the larger of the two cyclotron-resonance masses.[43,44] As for ρ_l, which in Fig. 10 is

[44] It is clear that for the two-band model (see reference 33) the larger mass determines the effective average wave number q of the phonons which scatter the holes. The reason is that only transitions in which both initial and final hole states are of the small-mass type can give q's significantly smaller than those going with large-mass states of the same energy. But such transitions are rare, because only a small fraction of the holes are in small-mass states, and these are scattered predominantly into large-mass states, because the latter states are so much more plentiful than the former.

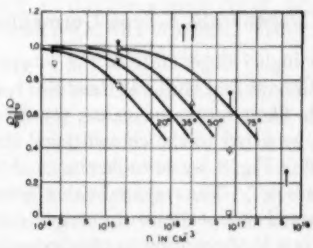

FIG. 12. Comparison of observed saturation ratios for p type germanium with the theory of Sec. VII. Curves: theoretical values obtained from Fig. 7 as described in the text. Points: observed values, from Fig. 4 of reference 2. The vertical line on each point gives a roughly estimated upper limit to the amount by which the "observed" ratios should be reduced to take account of the effect of impurity scattering in increasing the theoretical Q_e and thus reducing the "observed" Q_p. Ratios have been fitted to unity for $n=1.9\times10^{14}$ cm^{-3} except for the 20° curve, where theory and experiment were made to coincide at 1.5×10^{15}.

the ratio of the value given by the curve to that on the "infinite specimen" line, Fig. 10 gives the values 0.24–0.27 at 35°, 0.49–0.56 at 50°, and 0.77–0.82 at 75°, the first figure of each pair referring to $r=-\frac{1}{2}$, the second to $r=0$. Calculations similar to those of Fig. 10 but with other reasonable choices of the adjustable parameters have usually given values within a few hundredths of a unit of these, so it will be reasonable, for a rough analysis, to take the ρ_l values at 35° and 50° to be the same respectively as those used in Fig. 7, *viz.*, 0.28 and 0.54, and to interpolate Fig. 7 to $\rho_l=0.8$ for 75°. The theoretical curves so obtained are compared with experiment in Fig. 12, assuming $Q_p\approx Q_{pl}$.

Except for the 75° data, the agreement is very good indeed—a little too good, in fact, since practically all the minor effects which have not been incorporated into the theory ought to cause the present theoretical curves to be too far to the left. These effects include the contribution of transverse modes; the effect of saturation on the mobility of the electrons, i.e., $\beta_{ex}\neq\beta_{ex}^{(0)}$ in Eq. (53); departures from the assumption $r=0$; possible failure of the phonon scattering law to assume its asymptotic form in (33), resulting in an effective $s<0$ in Eq. (36); and the previously mentioned possible increase in the electron-lattice interaction in the presence of strong impurity scattering. The low ratio shown by the 20° point at the extreme left is probably due to some systematic error in the data for this specimen, as the points for this specimen at other temperatures (not shown) are out of line with the general trend of the other specimens.

While the present calculation with $m^*=0.3m$ gives reasonable agreement for the saturation effect, an m^* say twice as large would, by Eq. (57), require a shift of the calculated curves to the right by a factor $2^{\frac{1}{2}}$, and so would not fit. In view of the one-sided nature of most of the corrections which the theory is likely to need, it is probably safe to say that an $m^*\gtrsim 0.6m$ would be hard to reconcile with the data.

3. Degenerate *p*-Type Germanium

The most highly degenerate of the *p*-type specimens studied by Geballe and Hull was their No. 1, with $n=7.1\times10^{18}$ cm^{-3}. Their measured value, $Q=296$ μv/deg at 300°K, can be fitted to the conventional theory of Q_e, as presented in Fig. 8, by suitable choice of the density-of-states mass $m^{(N)}$. The required value is roughly $0.8m$ if τ_e is assumed independent of energy ($r=0$), $0.4m$ if $\tau_e\propto|\epsilon-\epsilon_b|$ ($r=1$). According to the discussion given in Sec. VIII, an effective r near 1 would be reasonable, but a value nearer to 0 is not excluded. It is interesting to see that the range of $m^{(N)}$ values suggested by the thermoelectric data includes the value found for high-resistivity material; however, the band structure for the degenerate material has been formed by the growth and coalescence of impurity bands, and might easily have a higher or lower $m^{(N)}$.

If we take this result as evidence that the conventional theory of Q_e is a fair approximation to the truth, we may compute Q_p by comparing Q with theoretical Q_e values at lower temperatures, fitting Q_e to Q at room temperature. This procedure gives, for the specimen mentioned, values from 160 to 220 μv/deg for $Q_p(60°)$, assuming the effective r to be between 0 and 1 and to increase or remain constant as the temperature is lowered. Such values accord with the predictions of Sec. VIII in being far below the value for high-resistivity material (1900–2000 μv/deg), but they are rather larger than expected. If at 60° we take $m^{(N)}=0.8m$, the more favorable of the possible room temperature values, we find from (A10) that in the absence of saturation the ratio of Q_p for specimen No. 1 to that for a nondegenerate specimen should be about 0.3 at 60°. The ratio of the Q_p values just quoted is at least a quarter of this, so the saturation ratio should be at least $\frac{1}{4}$. The curves of Fig. 9, though rough, suggest that the saturation ratio for the contribution of the longitudinal phonons alone should be a little less, of the order of 0.1 to 0.2. More complete data will be needed to decide whether this discrepancy is trivial or whether it arises from the transverse phonon contribution, from inadequacy of the conventional theory of Q_e, from incorrectness of the assumed band structure, or from inappropriateness of any band model for the calculation of Q_p. Concerning the underlying band structure, it is to be noted that for a given m^* a change in the number of valleys, e.g., from 6 to 1, has no effect on the predicted saturation effect in the nondegenerate range, but affects the saturation considerably in the degenerate range.

4. *N*-Type Germanium

The data of reference 2 on *n*-type germanium show the same qualitative features as for *p*-type, the only appreciable differences being a more gradual bending over at low temperatures and a smaller exponent η in the high-temperature law $Q_p\propto T^{-\eta}$. There are several conceivable causes for the small value 2.4 found for the apparent η:

(i) As was suggested above, the band structure may be of the degenerate many-valley type, with a fairly small spin-orbit splitting. This would be in line with the fact that Geballe and Hull[2] had to take $m^{(N)}\approx0.75m$ to fit their *n*-type Q_e around room temperature, whereas with a nondegenerate four-valley model one would expect $m^{(N)}/m=4^{\frac{1}{3}}(0.08^2\times1.3)^{\frac{1}{3}}=0.51$, with the cyclotron masses,[40] or $m^{(N)}/m>4^{\frac{1}{3}}\times0.6=1.5$, with the Benedict-Shockley mass.[15] If the suggested spin-orbit splitting were present, the theory of all these effects above liquid air temperature would require revision. In particular, the extrapolation of Q_e to the liquid air region would become uncertain, since both the position of the Fermi level and the term $\Delta\epsilon_T$ in Eq. (2) might depend on T in a way different from that assumed in Eqs. (4) and (7). In such a case, the resulting modification of Q_e might be in part responsible for the small exponent η. In addition, the temperature variation of Q_p might well be altered, since both the effective m^* and the effective f_l in our formulas could be changing with temperature.

(ii) As we have seen for *p* germanium, boundary scattering is capable of reducing the effective exponent η appreciably, even in the range 80°–100°K. This effect could considerably alleviate the η discrepancy for *n* germanium, even with a nondegenerate many-valley model, if the average effective mass m^* for *n* germanium were considerably smaller than that for *p* germanium. In such case the ξ_l of Eq. (46) would be considerably larger, and so the boundary scattering ratio ρ_l would depart more from unity at any given temperature. A value $\Delta\eta=d\ln\rho_l/d\ln T$ close to unity would not be inconceivable.

(iii) It is possible, of course, that the exponents s and γ in Eq. (36) depart appreciably from their ideal zero values, i.e., that the limiting form of the phonon-phonon scattering law for small T and $q\to0$ is not realized. In such case the larger η for *p* germanium would probably have to be attributed to something like spin-orbit complications.

Particularly interesting are the data on the reduction of Q_p due to cutting down the thickness of the specimen. From Fig. 7 of reference 2 it appears that when a specimen initially 0.16×0.148 cm was reduced to 0.16×0.025 cm over most of its length, Q_p was reduced in the ratio 0.83 at 60°K, 0.65 at 25°K. At first sight it seems surprising that the reduction in Q_p is not more pronounced: we might intuitively suppose that at 25° it should be comparable with the ratio of thicknesses. However, a study of the formulas of Casimir,[35] which determine the boundary scattering length L, shows that for a slab-shaped specimen L is much larger than the thickness, and in fact increases logarithmically without limit as the width increases, for fixed thickness. Although no exact expression for L is available, it seems reasonable that L for the cut-down specimen may have been large enough (0.3 to 0.4 of the original value) to

make possible a fit of the 60° result to the theory of Sec. VI, with $Lf_l/L_0 \lesssim 1$. The 25° result could be accounted for by such an L if the contribution Q_{pt} of the transverse phonons to Q_p is an appreciable fraction of the total at this temperature. However, there are other factors which should be looked into, among them the effect of the highly anisotropic effective mass, which will cause the function $R_z(\mathbf{q})$ to have a much broader peak that the function used in Sec. VI, hence to differ in its boundary scattering properties.

The data on the saturation effect for n germanium, Fig. 5 of reference 2, are less detailed than the data for p type, but are sufficiently similar in their behavior to justify the belief that they too can be roughly accounted for by the theory of Sec. VII.

X. PREDICTED BEHAVIOR OF OTHER SEMICONDUCTORS

The comparison of theory and experiment just given for germanium indicates that many interesting things can be learned about a semiconductor from a study of its thermoelectric power in the range where Q_p is appreciable. The planning of future experiments in this field may be facilitated by a rough prediction of the order of magnitude of the Q_p to be expected for a new material. For cubic materials, to which Eq. (38) applies, Q_p at any given T should be proportional to $c^2 f_l/\mu A_l m^*$, where c is the velocity of sound, μ the mobility, m^* the effective inertial mass defined in Appendix A, A_l the phonon-phonon scattering coefficient defined by (33), and f_l the fraction of the scattering of the carriers which is due to low-energy longitudinal phonons. The variation of A_l with the material can be estimated by dimensional means, if we are willing to assume the different materials to have the same ratio of anharmonic to harmonic elastic constants. Under this assumption A_l must depend only on $\hbar$, k, c, and the density ρ. Dimensional analysis gives

$$A_l \propto k^3/\hbar^2 c^3 \rho, \tag{64}$$

whence

$$Q_p \propto \rho c^5 f_l/\mu m^*. \tag{65}$$

Semiconductors belonging to the trigonal system, if suitable ones can be found, would be of especial interest, since according to reference 32 these should have an asymptotic phonon-phonon scattering law of the type in Eq. (36) with $s=1$, $\gamma=0$, and correspondingly should have rather large phonon-phonon relaxation times, hence large Q_p.

ACKNOWLEDGMENTS

I am much indebted to T. H. Geballe for frequent discussions of the experimental material. T. S. Benedict, B. Goodman, C. Kittel, and F. J. Morin have also provided useful material and suggestions.

I am grateful to the staff of the Institute for Advanced Study for their hospitality during the year 1952–1953.

APPENDIX A: CALCULATION OF Q_p FOR THE MANY-VALLEY MODEL, WITH FERMI STATISTICS

We wish to calculate the quantity $\mathbf{R}(\mathbf{q})$, defined at the start of Sec. IV, for the many-valley model of Fig. 1(b), and for Fermi statistics. To make the calculation tractable we assume that the combined effect of all scattering processes acting on the charge carriers can be described by a relaxation time $\tau_\epsilon(\epsilon)$ which is a function of energy only. This can be shown to be justified for any intervalley scattering and for intra-valley lattice scattering provided the phonon energy can be neglected and provided only the volume dilatation contributes to the deformation potential.[45] However, use of a $\tau_\epsilon(\epsilon)$ is only roughly correct if shearing distortions contribute, as they usually will.

The total $\mathbf{R}(\mathbf{q})$ which we wish to calculate is a sum of contributions from the different valleys surrounding the different band edge points $\mathbf{K}_b$. For a cubic crystal, however, the average of $\mathbf{E}\cdot\mathbf{R}(\mathbf{q})$ over the different valleys and over directions of $\mathbf{q}$ is the same as the average, for a single valley, over all directions of $\mathbf{q}$ and the electric field $\mathbf{E}$. Let us therefore fix attention on one of the valleys, say that around $\mathbf{K}_1$. Let the coordinate axes be chosen parallel to the principal axes of the ellipsoidal energy surfaces in this valley. The variation of energy with $\mathbf{K}$ in this valley is given by

$$|\epsilon_K - \epsilon_b| = (\hbar^2/2m)(\alpha_x \Delta K_x^2 + \alpha_y \Delta K_y^2 + \alpha_z \Delta K_z^2), \tag{A1}$$

where ϵ_b is the band edge energy, $\alpha_i = m/m_i^*$ are effective mass ratios for different directions, and $\Delta\mathbf{K} = \mathbf{K} - \mathbf{K}_1$. With this notation, the first-order distribution function in this one valley is given by the analog of Eq. (20),

$$f^{(1)}(\mathbf{K}) \propto \tau_\epsilon(\epsilon_K)(\sum E_i \alpha_i \Delta K_i) df^{(0)}(\epsilon_K)/d\epsilon_K, \tag{A2}$$

where $f^{(0)}$ is the Fermi function.

We shall consider only the case in which the phonon energies are negligible compared with the electron energies and with kT. For this case one gets the same result by neglecting the exclusion principle in the transition probabilities as by including it through factors $(1-f)$. Therefore the first two lines of Eq. (22) remain valid for the contribution of each valley in the present problem. When we come to insert Eq. (21) in Eq. (22), however, we meet the complication that the matrix element M is in general dependent on the direction of $\mathbf{q}$, since the deformation potential for the valley at $\mathbf{K}_1$ in general depends on a particular component of the shearing strain as well as on the volume dilatation. While it is not quite consistent to take this anisotropy of M into account while assuming a relaxation time dependent only on energy, we shall do this here, partly because the analysis for this case is fairly easy, and

[45] These arguments will be given in a forthcoming publication (reference 19). It can also be shown that for a many-valley model the shortcomings of the assumption of existence of a $\tau(\epsilon)$ can be corrected, to a fair approximation, by use of three relaxation times, a procedure roughly equivalent to letting τ depend on position over an energy surface, as we did in (5) and (6) of the text.

partly because anisotropy of M is likely to be more important than failure of the relaxation time assumption.

It is convenient to associate with any vector $\mathbf{V}$ a primed vector $\mathbf{V}'$, defined by $V_i'=\alpha_i^{\frac{1}{2}}V_i$. Then (A2) can be written

$$f^{(1)}\propto\tau_s(\Delta K')(\mathbf{E}'\cdot\Delta\mathbf{K}')[df^{(0)}/d\epsilon]_{\epsilon=\hbar^2\Delta K'^2/2m}. \quad \text{(A3)}$$

By steps like those used in (22) to (25) of the text we find

$$\mathbf{E}\cdot\mathbf{R}_1(\mathbf{q})=\frac{G(\mathbf{E}\cdot\mathbf{q})(\mathbf{E}'\cdot\mathbf{q}')}{q'}\times\int_{q'/2}^{\infty}\tau_s(\Delta K')\frac{df^{(0)}}{d\epsilon}\Delta K'd\Delta K', \quad \text{(A4)}$$

where G is a function of the direction of $\mathbf{q}$, proportional to $|M|^2$. Averaging of (A4) over directions of $\mathbf{E}$ replaces the factor in front of the integral by $Gq'E^2/3$.

The averaging over directions of $\mathbf{q}$ is not easy to carry out explicitly on Eq. (A4). However, if we assume $\tau(\mathbf{q})$ to obey Eq. (36), we may evaluate the left sides of Eqs. (26) and (19), as in the text, by interchanging the order of integration on $\mathbf{K}$ and $\mathbf{q}$. With

$$d\mathbf{q}=(\alpha_x\alpha_y\alpha_z)^{-\frac{1}{2}}q'^2dq'd\Omega, \quad \text{(A5)}$$

we find

$$(2\pi)^{-3}\int\mathbf{E}\cdot\mathbf{R}(\mathbf{q})d\mathbf{q}=\frac{2}{3\pi^2}\frac{N_VE^2\langle G\rangle'}{(\alpha_x\alpha_y\alpha_z)^{\frac{1}{2}}}\times\int_0^{\infty}\Delta K'^{\frac{1}{2}}\langle\tau_s(\Delta K')\frac{df^{(0)}}{d\epsilon}d\Delta K' \quad \text{(A6)}$$

$$(2\pi)^{-3}\int\tau(\mathbf{q})\mathbf{E}\cdot\mathbf{R}(\mathbf{q})d\mathbf{q}=\frac{2^{2-s}}{6\pi^2(2-s)}\frac{N_VE^2\langle G(q'/q)^{2+s}\rangle'}{AT^{3-s-\gamma}(\alpha_x\alpha_y\alpha_z)^{\frac{1}{2}}}\times\int_0^{\infty}\Delta K'^{\frac{1}{2}-s}\tau_s(\Delta K')\frac{df^{(0)}}{d\epsilon}d\Delta K', \quad \text{(A7)}$$

where N_V is the number of band edge points $\mathbf{K}_v$, and $\langle\ \rangle'$ denotes an average over directions of $\mathbf{q}'$. For phonons of branch α ($\alpha=l$ or t), Eq. (A6) may be set equal to $\mathbf{E}\cdot\mathbf{J}f_\alpha/\mu$, where f_α is the fraction of the crystal momentum given up by the carriers which is delivered to low energy modes of this branch. Combining this with Eqs. (A7), (19), and (11) we find for the contribution of phonons of this branch to the thermoelectric power

$$Q_{p\alpha}=\frac{P_\alpha\mathcal{E}_\alpha^2}{JT}=\frac{f_\alpha\mathcal{E}_\alpha^2\langle G_\alpha(q'/q)^{2+s}\rangle'}{2^s(2-s)\mu AT^{4-s-\gamma}\langle G_\alpha\rangle'}\times\frac{\int_0^{\infty}\Delta K'^{\frac{1}{2}-s}\tau_s(\Delta K')(df^{(0)}/d\epsilon)d\Delta K'}{\int_0^{\infty}\Delta K'^{\frac{1}{2}}\tau_s(\Delta K')(df^{(0)}/d\epsilon)d\Delta K'}. \quad \text{(A8)}$$

Let us specialize first to Maxwellian statistics. For each direction of $\mathbf{q}$ the expression (A4) is of the same form as Eq. (25), so the present $R_x(\mathbf{q})$ will be an average of curves like the full ones in Fig. 5, the average being taken over a family of curves of the same shape but different horizontal scales. Thus the peak of the final $R_x(\mathbf{q})$ curve will be broader and flatter than in Fig. 5; this difference in shape will disappear as α_x, α_y, α_z approach equality. Now in applications like those of Secs. V and VI, we wish to approximate $\mathbf{R}(\mathbf{q})$ by the equations of the text, which involve m^* or λ. A good choice for this parameter is the one which makes E times Eq. (37) equal Eq. (A7). With this choice the approximating $\mathbf{R}(\mathbf{q})$ has the same integral and the same $(-2-s)$th moment as the correct one. Equating the ratio of Eq. (37) to Eq. (26) to the ratio of Eq. (A7) to Eq. (A6), we find

$$m^*=m\left[\frac{\langle G'\rangle}{\langle G(q'/q)^{2+s}\rangle'}\right]^{2/(2+s)}. \quad \text{(A9)}$$

This m^* always lies between the minimum and the maximum of the effective masses $m_i^*=m/\alpha_i$ in the three principal directions. Numerical evaluation of Eq. (A9) has shown that if G is isotropic m^* is usually quite close to the geometric mean of the m_i^*, i.e., to $m^{(N)}/N_P^{\frac{1}{3}}$. For the maximum possible anisotropy of G, on the other hand, m^* may be closer to one of the extremes m_i^* than to the geometrical mean. With the identification in Eq. (A9), Eq. (A8) coincides with Eq. (38). For the general many-valley model, f_α/μ is not rigorously given by an expression like Eq. (31), but a study of the analogs to Eqs. (27) and (29) shows that the variation of f_α/μ with the scattering exponent r must be very similar to that used in Eq. (39).

In the limit of extreme degeneracy $df^{(0)}/d\epsilon$ becomes a delta function and Eq. (A8) becomes, with Eqs. (A9) and (40),

$$Q_{p\alpha}=\frac{f_\alpha\mathcal{E}_\alpha^2\lambda^{2+s}}{2^s(2-s)\mu A_\alpha T^{4-s-\gamma}}\left(\frac{kT}{\epsilon_F}\right)^{1+\frac{1}{2}s}. \quad \text{(A10)}$$

The significance and limitations of this equation are discussed in Sec. VIII. Note that for the present case f_α/μ exceeds the value in nondegenerate material in the ratio $(16\epsilon_F/9\pi kT)^{\frac{1}{2}}$.

APPENDIX B: EVALUATION OF THE BOUNDARY SCATTERING RATIO ρ

We would like to evaluate

$$\rho=\int\int\int\Delta P_x dydzd\mathbf{q}\Big/\int\int\int\Delta P_{0x}dydzd\mathbf{q}, \quad \text{(B1)}$$

where y and z run over the cross section of a cylindrical specimen of any specified shape with its axis in the x direction and where $\Delta\mathbf{P}$ is the density of crystal mo-

mentum in $\mathbf{q}$ and coordinate space, as defined in Sec. VI, and ΔP_0 is the same in the absence of boundary scattering.

We shall assume for the present that the boundary scattering is completely diffuse. Then the argument of the text, leading to Eq. (44), can be applied to any shape of cross section provided y is defined as the distance from the back surface, measured in a direction normal to the specimen axis and coplanar with this axis and $\mathbf{q}$, so that $q_z=0$. Let us define $1/\tau_b(\mathbf{q},T)$ to be the ratio of the rate of destruction of $\Delta\mathbf{P}$ by boundary scattering to the integral of $\Delta\mathbf{P}$ over the cross section. If $y_1(z)$ is the maximum value of y, i.e., the thickness of the specimen at z,

$$1/\tau_b(\mathbf{q},T)=(cq_y/q)\times\int\Delta P_x(\mathbf{q};y_1,z)dz\Big/\int\Delta P_x(\mathbf{q};y,z)dydz, \quad \text{(B2)}$$

where $\Delta\mathbf{P}$ is given by Eq. (44). This τ_b is, of course, the τ_b which has to be combined with $\tau(\mathbf{q})$ by the method of adding reciprocals, in order to get the effective relaxation time for mode $\mathbf{q}$. The difference between the present theory and the usual one lies in the fact that Eq. (B2) depends on temperature, i.e., on $\tau(\mathbf{q})$. At low temperatures $\tau(\mathbf{q})\to\infty$ and the integrals in Eq. (B2) simplify; at high temperatures $\tau(\mathbf{q})\to 0$ and they simplify again. One finds easily

$$\tau_b(\tau\to 0)/\tau_b(\tau\to\infty)=2\Big(\int y_1dz\Big)^2\Big/\int dz\int y_1^2dz. \quad \text{(B3)}$$

For the slab this has the value 2 mentioned in the text; for a circular cylinder it is $3\pi^2/16=1.85$; for a square it varies from 1.5 to 2, depending on the direction of $\mathbf{q}$. Thus for all these cases the mean value of Eq. (B3) over directions is within 10 percent or so of 2. This suggests the following approximation for the evaluation of Eq. (B1): Let us choose an average $\bar{y}_1$ of $y_1(z)$ as the limit on y in Eq. (B1), in such way that at low T ($\tau\to\infty$) we get the right ρ. Then use of this same $\bar{y}_1$ should give $1-\rho$ correct to 10 percent or so at high T ($\tau\to 0$). It is reasonable to expect the behavior at intermediate T to be nearly correct also.

To determine $\bar{y}_1$, we note that the correct ρ for $\tau\to\infty$ corresponds to a weighted average $\bar{\tau}_b$, with weight q_x^2/q^2, equal to L/c, where L is the Casimir length introduced in the text. For a circular cylinder we have $q_x/q=\cos\theta$, $q_y/q=\sin\theta$, and if $y_1=\bar{y}_1$ is taken independent of z in Eq. (B2), then for $\tau\to\infty$,

$$\tau_b^{-1}=2c\sin\theta/\bar{y}_1, \qquad \bar{\tau}_b=3\pi\bar{y}_1/8c=L/c. \quad \text{(B4)}$$

In the present approximation the value of Eq. (B1) for longitudinal modes becomes, by (44), (45), and (33),

$$\rho\approx\frac{\Big\langle 3\cos^2\theta\int_0^\infty\Big\{1-\frac{q_l^2\sin\theta}{q^2}\Big[1-\exp\Big(\frac{-q^2}{q_l^2\sin\theta}\Big)\Big]\Big\}F(q)dq\Big\rangle}{\int_0^\infty F(q)dq}, \quad \text{(B5)}$$

where the angular brackets denote an average over directions of $\mathbf{q}$,

$$q_l^2=3\pi c/8LA_lT^3, \quad \text{(B6)}$$

and

$$F(q)\propto\bar{R}_x(q)=\lambda q[1-\Phi(\lambda q/2)] \quad (r=\tfrac{1}{2}) \quad \text{(B7)}$$

$$=\lambda q\exp(-\lambda^2q^2/4), \quad (r=0) \quad \text{(B8)}$$

etc. (see Fig. 5), Φ being the error function and λ being defined by Eq. (40). For $r=-\frac{1}{2}$ and 0 the integral on q in (B5) can be evaluated analytically:

$$r=-\tfrac{1}{2}:\rho\approx 1-\langle 3\cos^2\theta\cdot 4\xi_l\sin\theta\ln(\tfrac{1}{2}+\tfrac{1}{2}[1+(\xi_l\sin\theta)^{-1}]^{\frac{1}{2}})\rangle, \quad \text{(B9)}$$

$$r=0:\rho\approx 1-\langle 3\cos^2\theta\cdot\xi_l\sin\theta\ln[1+(\xi_l\sin\theta)^{-1}]\rangle, \quad \text{(B10)}$$

where

$$\xi_l=\lambda^2q_l^2/4 \quad \text{(B11)}$$

has the value given by Eq. (46). The full curves for $r=-\frac{1}{2}$ and 0 in Fig. 6 were constructed by evaluating the angular averages in (B9) and (B10) numerically. The curve for $r=1$ was estimated from these two and the rigorously known limiting behavior at large and small ξ_l.

For transverse modes we may evaluate Eq. (B1) similarly, using (34) instead of (33) for $\tau(\mathbf{q})$ in Eqs. (44) and (45). The result is, for $r=0$

$$\rho\approx 1-\langle 3\cos^2\theta\{1-\Phi[(\xi_l\sin\theta)^{-1}]\}\times\exp[(\xi_l\sin\theta)^{-2}]\rangle, \quad \text{(B12)}$$

where ξ_l is given by Eq. (47). The dashed curve in Fig. 6 was again obtained by numerical evaluation of the angular average.

Optical Studies of Injected Carriers. III. Infrared Absorption in Germanium at Low Temperatures

ROGER NEWMAN
General Electric Research Laboratory, Schenectady, New York
(Received August 5, 1954)

The absorption spectra of carriers injected into germanium at 302°K, 201°K, and 82°K are given. For clean material these spectra are qualitatively identical with the absorption spectra of free holes at the same temperatures. In some samples studied anomalous spectra were observed. Anomalous spectra were in general observed in samples containing Fe. The anomalies are tentatively identified with trapping effects.

THE infrared absorption produced by carriers injected into germanium at room temperature has been observed by several authors.[1–3] The important conclusion of these papers was that the absorption spectrum of the injected carriers was essentially identical with the spectrum of holes as observed in germanium made p type by impurity doping.[4,5] In particular the structure found in the absorption of p-type germanium was also found in the spectrum of injected carriers. The contribution of the injected electrons to the total absorption was presumably negligible compared to that of the injected holes.

It has been found by several authors[2,5] that very profound changes occur in the hole absorption as the temperature of the sample is changed. In particular the modifications from 300°K to say 77°K are most striking. These changes have been ascribed to changes in the distribution of hole population among overlapping branches of the valence band. Although it seemed evident from the room temperature measurements that carriers produced by injection and by impurity doping produce the same absorption effect, it was nevertheless felt worthwhile to check this conclusion by measurement of the injection spectra at low temperatures. In addition it was thought that for samples in which trapping effects are present, these effects might show up in the absorption spectra of the injected carriers.

The modulation scheme used here to detect the absorption of the injected carriers was that described in Part I (reference 1) of this series. Thirteen cps current modulation was employed and a thermocouple was used as a detector. Fused junction diodes were used. The diodes were prepared as follows: a sample was cut into a block $\sim\frac{1}{4}$ in.$\times\frac{1}{4}$ in.$\times\frac{1}{2}$ in., a junction was prepared on a large face by fusing on a large indium dot (for n type) or an indium-arsenic dot (for p type). Tinned ($\frac{1}{32}$ in.) "Fernico" was soldered onto the face opposite the junction. The operations were performed under hydrogen. Using a Wood's metal solder, the assembly was then soldered by means of the "Fernico" to a copper sample holder. The latter was inserted into a cryostat which could be used for transmission measurements.

The intermediate layer of Fernico greatly minimized the problem of the germanium cracking when cooled. No success was had when the germanium was soldered either directly to the copper or through a 10-mil thick "Fernico" strip. However, using the method described there was only one failure in the thirteen units prepared. Good heat dissipation was achieved. Operating at power levels of $\sim$50 w resulted in less than a 10°C temperature rise for the diode at about liquid nitrogen temperature. Probably the main thermal resistance was between the sample holder and the cryostat proper.

The cryostat was placed in the sample section of a Perkin Elmer spectrometer. The radiation passed through the large faces of the diode perpendicular to the direction of current flow.

RESULTS AND DISCUSSION

In Part I of this series it was shown that at the limit where the modulation in the transmission of the sample is small then a quantity M/C is proportional to the absorption coefficient of the injected carriers. Here M is the signal obtained at a given wavelength by on-off modulation of the injection current and C is the signal obtained by complete modulation of the light beam at that wavelength, for example, by mechanical chopping of the light. In Figs. 1–3, are shown some representative plots of the quantity M/C as a function of wavelength at several temperatures. The data are quoted in arbitrary units. However, a direct measure of M/C for regions 1 mm wide adjacent to the junction on a few representative samples indicated that, for the currents used, $M/C<0.1$ at all wavelengths employed and the linear approximation is valid.

If we are correct in assuming that the spectrum of free injected carriers should be essentially identical with that of free holes, then of the spectra shown in the figures only that of Fig. 1 may be regarded as normal. Plots of the absorption spectrum of p-type germanium at the various temperatures can be superposed on the curves shown in this figure with excellent agreement.

The remaining figures show increasing departures from this norm. The data shown were taken in a manner

[1] R. Newman, Phys. Rev. **91**, 1311 (1953).
[2] H. B. Briggs and R. C. Fletcher, Phys. Rev. **91**, 1342 (1953).
[3] A. F. Gibson, Proc. Phys. Soc. (London) **B66**, 588 (1953).
[4] H. B. Briggs and R. C. Fletcher, Phys. Rev. **87**, 1130 (1952).
[5] Kaiser, Collins, and Fan, Phys. Rev. **91**, 1380 (1953).

identical with that used in obtaining that of Fig. 1. Caution was used to avoid sources of spurious effect. It is our belief, therefore, that the spectra shown in these curves are genuine and mainfest a new type of phenomenon.

Table I lists the different samples which have been studied, some of their room temperature properties and the characterization of their spectra at liquid nitrogen temperature as normal or anomalous. For the moment let us restrict our attention to *n*-type samples. Although the sampling is not exhaustive, one can probably state that equilibrium carrier density and lifetime do not, as such, determine whether a sample will show

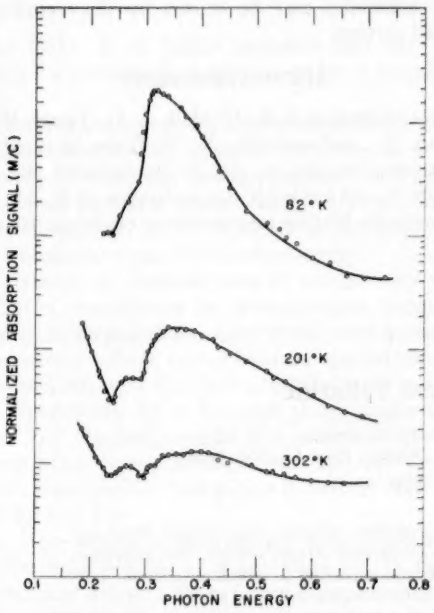

FIG. 1. Absorption spectra (arbitrary log scale) of injected carriers at several temperatures for sample M104. *M* is the signal obtained at a given wavelength by on-off modulation of the injection current and *C* is the signal obtained by complete modulation of the light beam at that wavelength, e.g., by mechanical chopping of the light (see reference 1).

anomalous behavior. For example, compare samples PC201 and DP277.

On the other hand, doping with iron seems, in general, to give samples with an anomalous spectrum. It is known that iron produces traps (probably hole traps) which are stable at low temperatures.[6] These traps are presumably responsible for the long time photoeffects and breakdown effects[7] observed in these

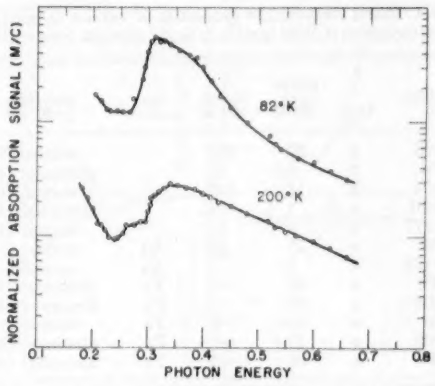

FIG. 2. Absorption spectra (arbitrary log scale) of injected carriers at several temperatures for sample P104.

samples. It is also reasonable to hypothesize that some such trapping effects are likewise producing the anomalous spectra observed here. It is worth noting that the iron-doped sample M56, the only one of this group that did not show an anomalous spectrum, likewise did not show any long time photoeffects either. *N*-type Au-doped samples sometimes show trapping effects too.[8] Measurements were made on two gold-doped samples. However, no anomalies were observed.

The appearance of the anomalous spectra is such as to suggest a superposition of a normal absorption curve and a more or less flat background. One is tempted to identify the latter with the effects of trapped carriers (e.g., holes in the *n*-type or electrons in *p*-type material). As a consequence of this point of view, the ratio of the intensities of the flat background to the normal (0.32 ev) peak might be expected to remain constant over a certain range of injection current, while above a certain injection level, corresponding to trap saturation, the

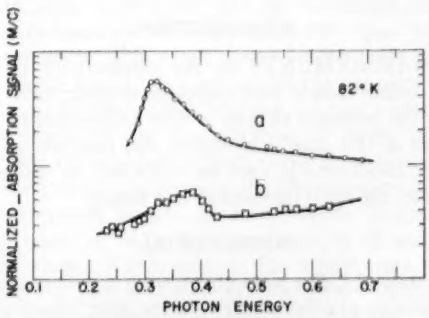

FIG. 3. Absorption spectra (arbitrary log scale) of injected carriers at 82°K for samples M108(a) and M95(b).

[6] Tyler, Woodbury, and Newman, Phys. Rev. **94**, 1419 (1954), details to be published.

[7] The breakdown effect will be described in more detail elsewhere. [W. W. Tyler, Phys. Rev. **96**, 226 (1954)]. However, briefly the phenomenon is this: An injecting electrode (e.g., In dot) is put on a piece of *n*-type Fe-doped germanium which goes to high resistance ($\sim 10^{12}$ ohm cm) at 77°K. The diode is cooled to liquid nitrogen temperature. If a high voltage ($\sim 10^2$ to 10^3 volts/cm) is applied to the diode, it breaks down and the germanium subsequently behaves as if it were *n*-type material with an equivalent resistivity of the order of a few ohm cm. The sample remains broken down even when the field is reduced to about 1 volt/cm. The breakdown effect can also be initiated at low voltages by illuminating the sample.

[8] R. Newman, Phys. Rev. **94**, 278 (1954).

TABLE I. Room temperature properties of various samples, and characterization of their spectra at liquid nitrogen temperature.

Sample No.	Type	ρ(ohm cm) 300°K	τ(μsec) 300°K	Impurity[a]	Spectrum (~80°K)[b]
M103	p	30	200		normal (1)
P104	p	0.5	55		abnormal (2)
M104	n	15	400		normal (1)
PC201	n	7	39		abnormal (3b)
DP277	n	5	55		normal (1)
E-30	n	25	10	Au	normal (1)
DP177	n	2	7	Au	normal (1)
M95[c]	n	45	~3	Fe	abnormal (3b)
M108[c]	n	40	~3	Fe	abnormal (3a)
M56	n	30	~3	Fe	normal (1)
M105	n	35	~3	Fe	abnormal (3a)
P11	n	30	~3	Fe	abnormal (3a)

[a] Other than conventional donors or acceptors.
[b] The numbers in brackets refer to the figure which best represents the observed spectrum at liquid nitrogen temperatures.
[c] Breakdown diodes.

peak should increase faster than the background. Unfortunately, when one goes to very high signal levels appreciable distortion in the observed spectrum will result because of the saturation of the M/C ratio. It might then be impossible to observe the effects of trap saturation even if these existed. Over the range of injection curves where our data are meaningful, we have not seen the saturation effect. Increasing the ambient light level in an attempt to saturate the traps dc-wise, likewise produced no observable effect.

CONCLUSIONS

The spectrum of injected carriers in clean germanium is shown to be qualitatively identical with the spectrum of holes in p-type germanium in its wavelength and temperature dependence. In some germanium samples, anomalous spectra are observed at low temperature. These anomalies may be caused by the trapping of injected carriers.

ACKNOWLEDGMENT

The cooperation of R. N. Hall, A. G. Tweet, W. C. Dunlap, Jr., and especially W. W. Tyler in supplying germanium samples is greatly appreciated. It is a pleasure to acknowledge the assistance of E. M. Pell who made the lifetime measurements on the diode units.

PHYSICAL REVIEW VOLUME 96, NUMBER 5 DECEMBER 1, 1954

Semiconducting Cadmium Telluride

DIETRICH A. JENNY AND RICHARD H. BUBE
Radio Corporation of America, RCA Laboratories Division, Princeton, New Jersey
(Received August 17, 1954)

Both n-type and p-type conductivity can be obtained in cadmium telluride. The intrinsic band gap of cadmium telluride is 1.45 ev. Electron and hole mobilities are at least 30 cm²/volt sec. The activation energies of p-type impurities are much larger than those of n-type impurities in cadmium telluride, indicating an explanation for the failure to find p-type conductivity in cadmium sulfide or selenide.

INTRODUCTION

MEASUREMENTS on the conductivity of cadmium sulfide and cadmium selenide have indicated the presence of only n-type conductivity.[1] The purpose of this note is to report that both n-type and p-type conductivity can be obtained in cadmium telluride, the third member of this family.

EXPERIMENTAL

Crystals of CdTe were grown from a slow cooling of the reaction product of New Jersey Zinc "super-pure" Cd, American Smelting and Refining "high-purity" Te, and the proportion of impurity desired.[2] Both Cd and Te were further purified by the zone-melting process[3] before being used in this preparation. For test, crystals were shaped into approximately rectangular samples, the ends of which were plated with nickel and copper, and then leads were soldered to the plated portions.

RESULTS

Figure 1 gives the transmission data[4] from which a band gap of about 1.45 ev can be determined for CdTe. This gap should be compared with the gap of CdSe, 1.74 ev, and the gap of CdS, 2.42 ev.

It is found in general that n-type conductivity is obtained in CdTe if impurities are chosen from groups III or VII of the Periodic Table, and p-type conductivity is obtained for impurities from groups I or V. Typical point-contact rectification curves are given in Fig. 2 for n-type CdTe:Ga and p-type CdTe:Sb.

Hall effect measurements give a value of 30 cm²/volt sec as a lower limit for the mobility in both n-type and

[1] R. W. Smith, RCA Rev. 12, 350 (1951).
[2] Much of the growth and treatment of these crystals was carried out by E. Blanche Lawton.
[3] W. G. Pfann, J. Metals 194, 747 (1952).
[4] Measurements by H. B. DeVore.

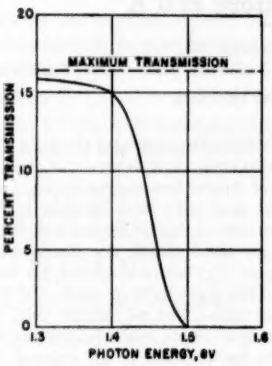

FIG. 1. Percent transmission of a CdTe crystal as a function of the incident photon energy.

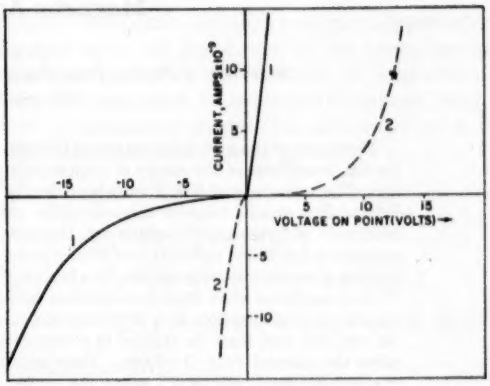

FIG. 2. Point-contact rectification curves for (1) *n*-type CdTe:Ga, and (2) *p*-type CdTe:Sb.

p-type CdTe. It is highly probable that the drift mobility for electrons is, at least, an order of magnitude larger.

The activation energy for *n*-type impurities is found to be much smaller than the activation energy for *p*-type impurities. Conductivity measurements to liquid helium temperature[6] give an activation energy of about 0.003 ev for iodine impurity in CdTe. Other *n*-type impurities have a comparably small activation energy.

The results of measurements of conductivity as a function of temperature for several *p*-type impurities are given in Table I. Only those crystals which showed ohmic current-voltage curves between applied voltages of 0.05 and 600 volts (for both polarities) were used for these experiments. All of the plots of log conductivity against $1/T$ obtained, consist of a single straight line between liquid nitrogen temperature and 100°C. The activation energies for these *p*-type impurities vary from about 0.3 to 0.5 ev.

The large activation energies for *p*-type impurities in CdTe make possible an explanation for the failure to detect any *p*-type CdS or CdSe; it is probable that the activation energies of *p*-type impurities are even larger in CdS or CdSe, for which the band gap is larger than in CdTe. (This is true of *n*-type impurities, e.g., the activation energy of iodine in CdS is found to be about 0.02 ev.)

TABLE I. Activation energies for *p*-type impurities in CdTe.

Impurity	Percent added[a]	Conductivity, 25°C, mho/cm	Activation energy, ev
Li	0.1	3×10^{-8}	0.27
Sb	0.01	3×10^{-5}	0.36
P	0.01	4×10^{-6}	0.38
Ag	0.1	5×10^{-7}	0.49
Pb	0.01	8×10^{-8}	0.51

[a] Weight percent added in the preparation; the proportion of impurity in the final crystals is not known.

[5] Measurements by M. L. Schultz.

A possible explanation of the large difference in activation energy between *n*-type and *p*-type impurities in these materials may be made along the following lines. An *n*-type impurity in CdTe consists of an ion which has its full share of valence electrons, but which has an additional electron bound about it in order to maintain charge neutrality of the crystal as a whole. Since the electronic requirements of the ion itself are satisfied, the binding energy for the additional electron is not very large. A *p*-type impurity in CdTe consists of an ion which needs an extra electron to complete its own electronic requirements, but it must acquire this electron from a neighboring host-crystal ion which also needs this electron for its electronic requirements. The energy required to remove an electron from a Te ion and give it to a *p*-type impurity would probably be considerably larger than the energy to remove an excess electron from an *n*-type impurity.

When the conductivity *vs* temperature curves of the *p*-type impurities of Table I are subjected to Fermi-level analysis,[6] it is found that the calculated Fermi-level is independent of temperature and equal to the measured slope. This result means on the basis of the usual simple model,[7] that either (1) the concentration of acceptor centers in each of these samples is approximately equal to the concentration of levels in the uppermost kT-wide part of the valence band (assuming no donor centers present); or (2) the concentration of acceptor centers in each of these samples is approximately equal to twice the concentration of unintentionally present donor centers. The latter more likely possibility is very similar to the apparent "balance of impurities" reported by Debye and Conwell[8] for a series of germanium samples with arsenic impurity.

[6] See, for example, A. Rose, RCA Rev. **12**, 362 (1951).
[7] R. H. Bube, J. Chem. Phys. (to be published).
[8] P. P. Debye and E. M. Conwell, Phys. Rev. **93**, 693 (1954).

Magnetic Anisotropy at 0°K*

JACK R. TESSMAN
Department of Physics, Pennsylvania State University, State College, Pennsylvania
(Received August 16, 1954)

The results of the spin-wave method of Holstein and Primakoff are extended to obtain approximate values for the dependence of the energy of magnetically saturated cubic crystals upon the direction of magnetization. The anisotropy at 0°K is calculated for the cases of dipolar ferromagnetism and exchange ferromagnetism. In a nearest neighbor approximation, the results agree with those obtained by Van Vleck from a treatment of ferromagnetic anisotropy. However, in the case of dipolar interaction, the nearest neighbor approximation is not sufficient and more distant neighbors are included. For dipolar ferromagnetism, the method gives the following results: In a face-centered cubic (fcc) lattice of spins S, the anisotropy constant K_1 is a maximum when there is no external field and is then given by $K_1=-0.11\ M_0^2/S$, where M_0 is the saturation magnetization. In a body-centered cubic (bcc) lattice, with no external field, $K_1=-0.15M_0^2/S$. An external field must be applied to obtain saturation in a simple cubic (sc) lattice; $K_1=+0.43M_0^2/S$ when the external field $H=0.6M_0$. More generally, in the presence of an external field H, then $K_1=\kappa(M_0^2/S)((4\pi/3)+H/M_0)^{-1}$, where $\kappa=-0.46$ for an fcc lattice, -0.63 for a bcc lattice, and $+2.06$ for an sc lattice. All values given are for specimens having zero demagnetizing field.

1. INTRODUCTION

CLASSICALLY, a saturated cubic lattice of dipoles has no anisotropy energy.[1] The dipole interaction energy of the lattice, when all the dipoles are aligned parallel, is independent of the direction of polarization. Nor does the quantum mechanical exchange interaction introduce any anisotropy. However, Kittel[2] has extended to magnetic dipole interactions an argument derived by Van Vleck[3] in treating ferromagnetic anisotropy, and finds that anisotropy arises quantum mechanically because the lowest energy state is not one of complete saturation. The dipoles cannot be aligned parallel as in a classical model, and it is therefore possible for the dipolar energy to depend upon the direction of polarization, or magnetization.

Holstein and Primakoff[4] have noted the applicability of spin-wave theory to the calculation of anisotropy. A spin wave may be thought of as a wave-like disturbance of the z components of spin of the atoms in a crystal, resulting in the deviation of the z components of spin from their maximum possible value S. The *spin deviation*, $S-S^z$, is not localized on any one atom but is distributed throughout the crystal in wavelike fashion. In the presence of dipole-dipole type interactions, the quantum mechanical energy of the spin waves in the lowest energy state is dependent upon the direction of magnetization. The treatment below extends the results of HP and obtains approximate values for the anisotropy energy of a cubic lattice of dipoles at 0°K, both in the absence and presence of an exchange interaction, that is, for the cases of dipolar ferromagnetism and exchange ferromagnetism.

2. THE HAMILTONIAN

Consider a system of identical atoms, each carrying a magnetic moment, and located at the lattice points of a cubic lattice. The Hamiltonian of the system, in the presence of an external field and including exchange interactions and magnetic dipole interactions, is

$$\mathcal{H}=-\tfrac{1}{2}\sum_{\substack{l,m=1\\ l\neq m}}^{N}2J(R_{lm})\mathbf{S}_l\cdot\mathbf{S}_m+\tfrac{1}{2}a^{-3}\sum_{\substack{l,m=1\\ l\neq m}}^{N}(g^2\mu_B{}^2/R_{lm}{}^5)\times[R_{lm}{}^2(\mathbf{S}_l\cdot\mathbf{S}_m)-3(\mathbf{S}_l\cdot\mathbf{R}_{lm})(\mathbf{S}_m\cdot\mathbf{R}_{lm})]-\sum_{l=1}^{N}g\mu_BS_l{}^zH. \quad (1)$$

The notation follows essentially that of HP. N is the total number of atoms; $\mathbf{R}_{lm}=\mathbf{R}_l-\mathbf{R}_m$, the vector from the mth atom to the lth atom, in units of the lattice constant a; $J(R_{lm})$ is the exchange integral between the lth and mth atoms; $g\mu_B\mathbf{S}_l$ is the magnetic moment operator for the atom at $\mathbf{R}_l$; H is the external magnetic field and is in the z direction.

Holstein and Primakoff have given the approximate solution for the eigenvalues of this Hamiltonian when the magnetization M of the sample is very close to its maximum possible value $M_0=ng\mu_BS/a^3$, that is $M_0-M\ll M_0$. Here n is the number of atoms per unit cell.

The approximate solution is

$$E\equiv E_{N\mathbf{k}}=C+\sum_{\mathbf{k}}[\tfrac{1}{2}(A_{\mathbf{k}}{}^2-|B_{\mathbf{k}}|^2)^{\frac{1}{2}}-\tfrac{1}{2}A_{\mathbf{k}}]+\sum_{\mathbf{k}}(A_{\mathbf{k}}{}^2-|B_{\mathbf{k}}|^2)^{\frac{1}{2}}N_{\mathbf{k}}. \quad (2)$$

The quantity C is the energy that would be obtained for the sample if it were considered as a classical assembly of magnetic dipoles and if all the dipoles were oriented in the same direction, that also being the direction of the magnetic field H. It includes, too, the exchange energy of such a model. In a cubic crystal, the energy C is independent of the direction of orientation

* This work was begun at the University of California, Berkeley, California. A preliminary report was presented to the meeting of the American Physical Society, Berkeley, California, December 1951. See J. R. Tessman, Phys. Rev. **85**, 752(A) (1952).
[1] R. Becker, Z. Physik **62**, 253 (1930).
[2] C. Kittel, Phys. Rev. **82**, 965 (1951).
[3] J. H. Van Vleck, Phys. Rev. **52**, 1178 (1937).
[4] T. Holstein and H. Primakoff, Phys. Rev. **58**, 1098 (1940). See their footnote 17c. This paper will be referred to as HP.

of the dipoles with respect to the crystal lattice[1] and therefore need not concern us further in calculating the anisotropy energy.

The $N_{\mathbf{k}}$'s take on the values 0, 1, 2, $\cdots$ and are the quantum numbers of the spin waves. The summation is over all the spin waves. $A_{\mathbf{k}}$ and $B_{\mathbf{k}}$ are given by:

$$\begin{aligned}A_{\mathbf{k}}=&-\tfrac{3}{2}g^2\mu_B{}^2Sa^{-3}\textstyle\sum_h R_h^{-3}(1-3z_h{}^2/R_h{}^2)\\&+\tfrac{1}{2}g^2\mu_B{}^2Sa^{-3}\textstyle\sum_h R_h^{-3}(1-3z_h{}^2/R_h{}^2)\\&\times[1-\exp(i\mathbf{k}\cdot\mathbf{R}_h)]+2S\textstyle\sum_h J(R_h)\\&\times[1-\exp(i\mathbf{k}\cdot\mathbf{R}_h)]+g\mu_BH,\\B_{\mathbf{k}}=&-\tfrac{3}{2}g^2\mu_B{}^2Sa^{-3}\textstyle\sum_h R_h^{-5}(x_h{}^2-y_h{}^2-2ix_hy_h)\\&+\tfrac{3}{2}g^2\mu_B{}^2Sa^{-3}\textstyle\sum_h R_h^{-5}(x_h{}^2-y_h{}^2-2ix_hy_h)\\&\times[1-\exp(i\mathbf{k}\cdot\mathbf{R}_h)].\end{aligned}\tag{3}$$

Here $\mathbf{R}_h=(x_h,y_h,z_h)$ is used in place of $\mathbf{R}_{lm}$. It is the vector from one atom to any other atom in the lattice and the summation is over all such other atoms; $\mathbf{k}$ is the wave vector of the spin waves in units of $1/a$. It takes on N discrete values, with its x, y, and z components uniformly spaced over a range $\sim-\pi$ to $\sim+\pi$ determined by the imposition of periodic boundary conditions.

3. DIRECTIONAL DEPENDENCE

At $T=0°$K, the sample will be in its lowest energy state, corresponding to all $N_{\mathbf{k}}=0$. The $A_{\mathbf{k}}$ and $B_{\mathbf{k}}$ are functions of the x, y, and z coordinates of the atoms situated at the lattice points and thus do depend upon the orientation of the lattice with respect to the z axis. The z direction is the direction of magnetization of the sample. We thus must evaluate

$$\textstyle\sum_{\mathbf{k}}[\frac{1}{2}(A_{\mathbf{k}}{}^2-|B_{\mathbf{k}}|^2)^{\frac{1}{2}}-\frac{1}{2}A_{\mathbf{k}}]\tag{4}$$

in order to obtain the anisotropy energy.

The summations in the expressions (3) for $A_{\mathbf{k}}$ and $B_{\mathbf{k}}$ are evaluated by HP as follows: The first summation, in each case, is broken up into two parts. One part is the sum over all atoms contained within a sphere described about $R_h=0$. This part vanishes for a cubic crystal. The second part is the sum over the remaining atoms outside the sphere. This is evaluated by replacing the sum by an integral, in accordance with the prescription

$$g\mu_BSa^{-3}\textstyle\sum_h f(\mathbf{R}_h)\rightarrow M_0\int f(\mathbf{R})d\mathbf{R}.$$

This prescription amounts to smearing out the atoms uniformly through the crystal instead of localizing them at the lattice points.

The second summation in Eqs. (3) for $A_{\mathbf{k}}$ and $B_{\mathbf{k}}$ is evaluated by HP by immediately replacing the sum by an integral throughout the entire crystal. As far as distant atoms are concerned, this has no significant effect. But with regard to near neighbors, this eliminates any effects due to the discrete localization of the atoms at the lattice points and any consequent dependence of the sum upon the orientation of the crystallographic axes with respect to the direction of magnetization. Thus the sums must be evaluated in greater detail to show the anisotropy energy. This is pointed out in HP.

We introduce the following symbols:

$$\begin{aligned}F&=g^2\mu_B{}^2S/a^3,\\T_1&=-F\textstyle\sum_h{}^{R_0}R_h^{-3}(1-3z_h{}^2/R_h{}^2),\\T_{2\mathbf{k}}&=-\tfrac{1}{2}F\textstyle\sum_h{}^{R_0}R_h^{-3}(1-3z_h{}^2/R_h{}^2)\exp(i\mathbf{k}\cdot\mathbf{R}_h),\\T_{3\mathbf{k}}&=-\tfrac{3}{2}F\textstyle\sum_h{}^{R_0}R_h^{-5}(x_h{}^2-y_h{}^2-2ix_hy_h)\exp(i\mathbf{k}\cdot\mathbf{R}_h),\\T_4&=2S\textstyle\sum_h J(R_h),\\T_{5\mathbf{k}}&=-2S\textstyle\sum_h J(R_h)\exp(i\mathbf{k}\cdot\mathbf{R}_h),\\I_1&=-g\mu_BM_0\int_{R_0}^{\text{o.b.}}R^{-3}(1-3z^2/R^2)d\mathbf{R},\\I_{2\mathbf{k}}&=-\tfrac{1}{2}g\mu_BM_0\int_{R_0}^{\text{o.b.}}R^{-3}(1-3z^2/R^2)\exp(i\mathbf{k}\cdot\mathbf{R})d\mathbf{R},\\I_{3\mathbf{k}}&=-\tfrac{3}{2}g\mu_BM_0\int_{R_0}^{\text{o.b.}}R^{-5}(x^2-y^2-2ixy)\exp(i\mathbf{k}\cdot\mathbf{R})d\mathbf{R}.\end{aligned}\tag{5}$$

The sums $A_{\mathbf{k}}$ and $B_{\mathbf{k}}$ can then be approximated as follows:

$$\begin{aligned}A_{\mathbf{k}}&=T_0+I_1+T_{2\mathbf{k}}+I_{2\mathbf{k}}+T_4+T_{5\mathbf{k}}+g\mu_BH,\\B_{\mathbf{k}}&=T_{3\mathbf{k}}+I_{3\mathbf{k}}.\end{aligned}\tag{6}$$

In this approximation, a sphere of radius R_0 is described about the atom at the origin and the summations in the expressions (3) for $A_{\mathbf{k}}$ and $B_{\mathbf{k}}$ are taken over all the atoms contained within the sphere. Beyond the sphere, the atoms are considered as uniformly smeared out and the summations are replaced by integrals. The symbol $\sum_h{}^{R_0}$ means summation over all atoms for which $R_h<R_0$ but excluding $R_h=0$; $\int_{R_0}^{\text{o.b.}}$ is an integration from the surface of the sphere to the outer boundary of the specimen. The specimen is taken as a needle-shaped ellipsoid with the major axis parallel to the direction of magnetization.

For a cubic crystal, T_1 vanishes. Also, for every atom at $\mathbf{R}_h$, there is another atom at $-\mathbf{R}_h$. Thus, in the various sums above, $\exp(i\mathbf{k}\cdot\mathbf{R}_h)$ can be replaced by $2\cos(\mathbf{k}\cdot\mathbf{R}_h)$ and the summation is then only over half the lattice space. Such a summation will be represented by the symbol $\sum_{\frac{1}{2}h}{}^{R_0}$.

The integrals I_1, $I_{2\mathbf{k}}$, and $I_{3\mathbf{k}}$ can be evaluated by integration by parts and by the evaluation procedure described in HP, Appendix II. For $kR_0\ll1$, the surface integrals over the surface of the sphere of radius R_0 can be evaluated by expanding $\exp(i\mathbf{k}\cdot\mathbf{R})$. For $kR_0\gtrsim1$, the integrals $I_{2\mathbf{k}}$ and $I_{3\mathbf{k}}$ approach zero because of the rapid variation of the integrand.

We obtain:

$$T_1=0,\quad T_{2\mathbf{k}}=-F\sum_{\frac{1}{2}h}{}^{R_0} R_h^{-3}(1-3z_h^2/R_h^2),$$

$$T_{3\mathbf{k}}=-3F\sum_{\frac{1}{2}h}{}^{R_0} R_h^{-5}(x_h-iy_h)^2\cos\mathbf{k}\cdot\mathbf{R}_h,$$

$$T_4=2S\sum_h J(R_h),\quad T_{5\mathbf{k}}=-4S\sum_{\frac{1}{2}h} J(R_h)\cos\mathbf{k}\cdot\mathbf{R}_h,$$

$$I_1=(4\pi/3)g\mu_B M_0,$$

$$I_{2\mathbf{k}}=\tfrac{2}{3}\pi g\mu_B M_0+2\pi g\mu_B M_0(-k_z^2/k^2+k^2R_0^2/30+k_z^2R_0^2/30),\quad \text{for } kR_0\ll 1, \tag{7}$$

and

$$I_{2\mathbf{k}}\to 0 \text{ for } kR_0\gtrsim 1,$$

$$I_{3\mathbf{k}}=2\pi g\mu_B M_0(k_x-ik_y)^2(1-k^2R_0^2/10)k^{-2},\quad \text{for } kR_0\ll 1,$$

and

$$I_{3\mathbf{k}}\to 0 \text{ for } kR_0\gtrsim 1.$$

Let us now gather terms in $A_\mathbf{k}$ and write it as

$$A_\mathbf{k}=Q+T_{2\mathbf{k}}+T_{3\mathbf{k}}, \tag{8}$$

where

$$Q=T_1+I_1+I_{2\mathbf{k}}+T_4+g\mu_B H. \tag{9}$$

Then,

$$\tfrac{1}{2}(A_\mathbf{k}{}^2-|B_\mathbf{k}|^2)^{\frac{1}{2}}-\tfrac{1}{2}A_\mathbf{k}\approx-|B_\mathbf{k}|^2/4Q, \tag{10}$$

where the square root has been expanded and terms of higher order by a factor of $T_{2\mathbf{k}}/Q$ and $T_{5\mathbf{k}}/Q$ have been dropped as have higher order terms in $B_\mathbf{k}/Q$. This expansion will be more accurate, then, if the terms T_4 or $g\mu_B H$, in Q, are large; that is, in the presence of a large exchange interaction or large external field.

If, in accordance with (7), we consider values of $\mathbf{k}$ such that $I_{3\mathbf{k}}=0$, then

$$|B_\mathbf{k}|^2=|T_{3\mathbf{k}}|^2=9F^2\sum_{\frac{1}{2}h}{}^{R_0}\sum_{\frac{1}{2}h'}{}^{R_0}\tau_h\tau_{h'}{}^*\times\cos(\mathbf{k}\cdot\mathbf{R}_h)\cos(\mathbf{k}\cdot\mathbf{R}_{h'}),$$

where

$$\tau_h=R_h^{-5}(x_h-iy_h)^2.$$

This expression for $|B_\mathbf{k}|^2$ can be broken up and written

$$|B_\mathbf{k}|^2=9F^2\sum_{\frac{1}{2}h}{}^{R_0}|\tau_h|^2\cos^2(\mathbf{k}\cdot\mathbf{R}_h)+9F^2\sum_{\frac{1}{2}h,h\neq h'}{}^{R_0}\sum_{\frac{1}{2}h'}{}^{R_0}\tau_h\tau_{h'}{}^*\cos(\mathbf{k}\cdot\mathbf{R}_h)\cos(\mathbf{k}\cdot\mathbf{R}_{h'}).$$

We are now ready to evaluate

$$\sum_\mathbf{k}[\tfrac{1}{2}(A_\mathbf{k}{}^2-|B_\mathbf{k}|^2)^{\frac{1}{2}}-\tfrac{1}{2}A_\mathbf{k}].$$

This summation is equal to $N\langle\tfrac{1}{2}(A_\mathbf{k}{}^2-|B_\mathbf{k}|^2)^{\frac{1}{2}}-\tfrac{1}{2}A_\mathbf{k}\rangle_{Av}$, where the average is over the values of $\mathbf{k}$.

If we pick R_0 sufficiently large, then the number of values of $\mathbf{k}$, for which $kR_0<1$, can be made as small as desired as compared with the total number of values of $\mathbf{k}$. Thus, the contribution of those spin waves, for which $kR_0<1$, to the calculation of the above average, can be made negligibly small and we can take $kR_0\gtrsim 1$ for all the values of $\mathbf{k}$.

We have, for $kR_0\gtrsim 1$,

$$\tfrac{1}{2}(A_\mathbf{k}{}^2-|B_\mathbf{k}|^2)^{\frac{1}{2}}-\tfrac{1}{2}A_\mathbf{k}\approx-|B_\mathbf{k}|^2/4Q=-(9F^2/4Q)\{\sum_{\frac{1}{2}h}{}^{R_0}|\tau_h|^2\cos^2(\mathbf{k}\cdot\mathbf{R}_h)+\sum_{\frac{1}{2}h,h\neq h'}{}^{R_0}\sum_{\frac{1}{2}h'}{}^{R_0}\tau_h\tau_{h'}{}^*\times\cos(\mathbf{k}\cdot\mathbf{R}_h)\cos(\mathbf{k}\cdot\mathbf{R}_{h'})\}. \tag{11}$$

When this expression is averaged over the range of $\mathbf{k}$ values, the second term in the curly brackets vanishes because of the orthogonality of the cosine factors. For the first term, $\langle\cos^2(\mathbf{k}\cdot\mathbf{R}_h)\rangle_{Av}=\tfrac{1}{2}$. Thus,

$$\sum_\mathbf{k}[\tfrac{1}{2}(A_\mathbf{k}{}^2-|B_\mathbf{k}|^2)^{\frac{1}{2}}-\tfrac{1}{2}A_\mathbf{k}]=-N(9F^2/8Q)\sum_{\frac{1}{2}h}{}^{R_0}R_h^{-10}(x_h^2+y_h^2)^2. \tag{12}$$

This expression represents that portion of the lowest energy value which depends upon the direction of magnetization. In the lowest energy state, the energy, *per unit volume*, which depends upon the direction of magnetization, is then

$$-\frac{9}{8}\frac{n}{a^3}\frac{F^2}{Q}\sum_{\frac{1}{2}h}{}^{R_0}\frac{1}{R_h^6}\left(1-\frac{z_h^2}{R_h^2}\right)^2. \tag{13}$$

4. ANISOTROPY CONSTANT, K_1

If the z axis, the direction of magnetization of the crystal, has direction cosines γ_1, γ_2, γ_3 with respect to the crystallographic cubic axes, x', y', and z', then $z_h=\gamma_1x_h'+\gamma_2y_h'+\gamma_3z_h'$. Now, $\gamma_1^2+\gamma_2^2+\gamma_3^2=1$, and $\gamma_1{}^4+\gamma_2{}^4+\gamma_3{}^4=1-2(\gamma_1^2\gamma_2^2+\gamma_2^2\gamma_3^2+\gamma_3^2\gamma_1^2)$. The summation, $\sum_{\frac{1}{2}h}{}^{R_0}R_h^{-6}(1-z_h^2/R_h^2)^2$, can be evaluated quite readily for each of the three cubic crystal types, the face-centered cubic (fcc), the body-centered cubic (bcc), and the simple cubic (sc). The summation is equal to an expression of the form $b_1+b_2\Gamma$, where b_1 and b_2 are constants and $\Gamma=\gamma_1^2\gamma_2^2+\gamma_2^2\gamma_3^2+\gamma_3^2\gamma_1^2$.

The term $b_2\Gamma$ gives the directional dependence. Its values for the three crystal types are

$$6.50\Gamma \text{ for fcc},\quad 2.20\Gamma \text{ for bcc},\quad -1.84\Gamma \text{ for sc}, \tag{14}$$

where the first 7 zones of neighbors were used for the fcc calculation, the first 6 zones for the bcc, and the first 4 zones for the sc. In each case, $R_0=2$, that is, $R_h=2$ for the last zone used, and the contribution of the last zone to the total is -0.03Γ.

Dipolar Ferromagnetism

The anisotropy constant K_1 is given by the coefficient of Γ in the expression (13). For the case of a cubic lattice of magnetic dipoles such that the exchange interaction is negligible, then

$$J=0,\quad \text{and}\quad Q=(4\pi/3)g\mu_B M_0+g\mu_B H.$$

If there is no external field, then $Q=(4\pi/3)g\mu_B M_0$. Remembering that $M_0=ng\mu_B S/a^3$ and that $n=4$ for an fcc lattice and $n=2$ for a bcc lattice, then K_1 can be

obtained from (13) and (14). We get

$$K_1(\text{fcc}) = -0.11 M_0^2/S,$$
$$K_1(\text{bcc}) = -0.15 M_0^2/S, \quad (15)$$

for pure magnetic dipoles with $H=0$.

In the sc case, it is necessary to apply an external field in order to obtain a parallel arrangement. Otherwise, an antiparallel arrangement has lower energy.[5] The smallest value which the external field may have and still maintain a parallel arrangement of the dipoles is $H=0.6M_0$. This gives

$$K_1(\text{sc}) = +0.43 M_0^2/S, \quad (16)$$

for pure magnetic dipoles with $H=0.6M_0$.

In the presence of an external field H, the expressions for K_1, in the three cases, become

$$K_1(\text{fcc}) = -0.46(M_0^2/S)(4\pi/3 + H/M_0)^{-1},$$
$$K_1(\text{bcc}) = -0.63(M_0^2/S)(4\pi/3 + H/M_0)^{-1}, \quad (17)$$
$$K_1(\text{sc}) = +2.06(M_0^2/S)(4\pi/3 + H/M_0)^{-1},$$

for pure magnetic dipoles.

Exchange Ferromagnetism

In the presence of a large short-range exchange interaction, such that $g\mu_B M_0$ and $g\mu_B H$ are negligible compared to J, then the anisotropy constant K_1, from (13), is

$$K_1 = -\frac{9}{8}\frac{n}{a^3}\frac{F^2}{2zJS} b_2, \quad (18)$$

where z is the number of nearest neighbors, and b_2 is gotten from (14). We obtain

$$K_1(\text{fcc}) = -0.08(M_0^2/S)(g^2\mu_B^2 a^{-3}/J),$$
$$K_1(\text{bcc}) = -0.08(M_0^2/S)(g^2\mu_B^2 a^{-3}/J), \quad (19)$$
$$K_1(\text{sc}) = +0.17(M_0^2/S)(g^2\mu_B^2 a^{-3}/J).$$

[5] J. A. Sauer, Phys. Rev. **57**, 142 (1940).

This gives the anisotropy constant of a ferromagnet *when the anisotropy energy is due to magnetic dipole interactions.*

Spin-orbit effects are partially represented, according to Van Vleck,[3] by an equivalent dipole-dipole interaction which may be much larger than the true magnetic dipole-dipole interaction. Van Vleck estimates the equivalent dipole-dipole interaction, C', for nearest neighbors to be $\sim J/100$, whereas $g^2\mu_B^2 a^{-3} \sim J/10^4$. The equivalent dipole-dipole interaction can be substituted for the true magnetic dipole-dipole interaction in the above calculation by substituting $C'(r_0^3/a^3)$ for $g^2\mu_B^2/a^3$ in (13); r_0 is the nearest neighbor distance. Inasmuch as C' is of short-range character, therefore the summation in (13) should only be carried out over nearest neighbors. In place of (14), the dependence of the summation on Γ is then, for nearest neighbors only,

$$8.00\Gamma \text{ for fcc}, \quad 4.21\Gamma \text{ for bcc}, \quad -2.00\Gamma \text{ for sc}. \quad (20)$$

We then obtain

$$K_1(\text{fcc}) = -1.13(n/a^3)(S^2C'^2/2zJS),$$
$$K_1(\text{bcc}) = -2.00(n/a^3)(S^2C'^2/2zJS), \quad (21)$$
$$K_1(sc) = +2.25(n/a^3)(S^2C'^2/2zJS).$$

This gives the anisotropy constant of a ferromagnet at $T=0°\text{K}$ *when the anisotropy energy is due to the spin-orbit interaction* considered as an equivalent short-range dipole-dipole interaction. The anisotropy values (21) are in exact agreement with the values of K_1 which may be obtained from Eq. (32) of Van Vleck's paper[3] on the anisotropy of cubic ferromagnetic crystals.

ACKNOWLEDGMENTS

I wish to thank Professor C. Kittel for suggesting the problem and for many discussions concerning it. I wish to thank Professor F. Keffer, particularly, for discussions concerning the method finally adopted in this paper.

Exciton Bands in Crystalline Benzene

DAVID FOX AND O. SCHNEPP
Department of Physics and Laboratory of Physical Chemistry, Isreal Institute of Technology, Haifa, Israel
(Received July 20, 1954)

The structures of the two lowest exciton bands of crystalline benzene have been investigated. The separations are given between those band levels to which optical transitions are allowed from the crystal ground state.

BY assuming that the lower excited electronic states of crystals of aromatic molecules are exciton states, Davidov[1] has shown that the sharp absorptions in the ultraviolet can be explained on the basis of strictly obeyed translational selection rules. Recently, Broude, Medvedev, and Prikhot'ko[2] have investigated the absorption spectrum of single crystals of benzene in polarized light and found two lines polarized at right angles to each other, separated by 25 cm^{-1}, and corresponding, in the molecule, to the pure electronic transition from the ground state to the lowest excited singlet state. This lowest molecular state has been interpreted as belonging to the irreducible representation B_{2u} of the symmetry group D_{6h} of the molecule, although it may possibly belong to B_{1u} instead.[3] Davidov[4] concluded that the observations of Broude *et al.* confirm the former assignment. However, he made an approximation with regard to the crystal structure; in the light of more recent x-ray data,[5] his conclusions must be reexamined. Winston[6] concluded that three transitions, with mutually perpendicular polarizations, are allowed in each of the exciton bands corresponding to the B_{1u} and B_{2u} molecular states.

We have investigated the intensities of allowed transitions and the band structure in the benzene crystal. In first-order perturbation theory, the energy can be separated into two groups of terms: "band-shift" terms, which are independent of the wave vector, **K**, of the exciton wave function, and "band-splitting" terms, which depend on **K**. The intermolecular interaction energy was expanded in a multipole-multipole series, and only the lowest-order nonvanishing terms were retained. For the band-splitting terms, it was found group-theoretically that the significant terms were matrix elements of octupole-octupole interactions between pairs of molecules and that the molecular matrix element of every octupole component could be expressed in terms of a single parameter, whose value depended on the choice of molecular wave functions. In this way, the structure of each band was determined to within a scale factor from crystal data alone; the scale factors were calculated by assuming the wave functions of Mayer and Sklar.[7] For the levels to which transitions are allowed by the translational selection rules (states with $\mathbf{K}=0$), the energies, referred to the center of the band, and the polarizations of the transitions are given in Table I. One state in each band is forbidden by factor group selection rules. It may be shown that, to within the accuracy of the present calculations (about 10 percent), translationally allowed levels lie at the extrema of each band. The band widths are thus 720 cm^{-1} and 58 cm^{-1}. By comparing the results in the table with the observations of Broude *et al.*,[2] we conclude that the lowest excited state of molecular benzene does indeed belong to the representation B_{2u}. To obtain level separations of the order of 25 cm^{-1} in the B_{1u} case would require much more radical modifications in the Mayer and Sklar wave functions than are reasonable.

TABLE I. Energies and transition polarizations of $\mathbf{K}=0$ exciton states corresponding to B_{1u} and B_{2u} molecular benzene states.

B_{1u}		B_{2u}	
Polarization	Energy (cm^{-1})	Polarization	Energy (cm^{-1})
a	−360	a	−29
c	−180	c	− 7
b	180	forbidden	7
forbidden	360	b	29

The results of the intensity calculations and the details of the energy calculations will be given elsewhere. The incompleteness of experimental data prevents full comparison with the theoretical predictions. An absorption experiment, using polarized light, in which the crystal directions are known from an independent determination, seems desirable. Agreement between such an experiment and the predictions would lend support to the assumption of the existence of exciton states in crystals of aromatic molecules.

[1] A. S. Davidov, J. Exptl. Theoret. Phys. (U.S.S.R.) **18**, 210 (1948).
[2] Broude, Medvedev, and Prikhot'ko, J. Exptl. Theoret. Phys. (U.S.S.R.) **21**, 665 (1951).
[3] Sponer, Nordheim, Sklar, and Teller, J. Chem. Phys. **7**, 207 (1939); Parr, Craig, and Ross, J. Chem. Phys. **18**, 1561 (1950).
[4] A. S. Davidov, J. Exptl. Theoret. Phys. (U.S.S.R.) **21**, 673 (1951).
[5] E. G. Cox and J. A. S. Smith, Nature **173**, 75 (1954).
[6] H. Winston, J. Chem. Phys. **19**, 156 (1951).
[7] M. Goeppert-Mayer and A. L. Sklar, J. Chem. Phys. **6**, 645 (1938).

High-Frequency Resistance of Tin and Indium in the Normal and Superconducting State

C. J. GREBENKEMPER
Naval Research Laboratory, Washington, D. C.

(Received August 20, 1954)

Additional measurements have been made on the surface resistance of tin and indium near 24 000 Mc/sec. The results are in general agreement with those reported previously. The high-frequency resistance appears to be varying with frequency in the superconducting region as the three-halves power rather than the predicted second power. This appears to be the case for both tin and indium.

The effect of evaporating a thin indium film over an electroplated film is discussed. Data for the normal state are in general agreement with the Reuter-Sondheimer theory of the anomalous skin effect.

ADDITIONAL measurements have been made on the surface resistance of tin and indium at frequencies near 24 000 Mc/sec. The results are in general agreement with those reported previously.[1] The method used is the same as that described in the earlier paper. The electric Q factor is measured as a function of temperature and the surface resistance calculated from the measurements.

TIN

The results in the normal state are in agreement with the earlier work. In the superconducting state the results are slightly different from the preliminary measurements reported previously.[1] The residual resistance at absolute zero is 0.2 percent of the resistance at the transition. The more recent measurements[2] are more precise than the earlier measurements. A higher-mode cavity was used which made it possible to measure the Q values more precisely. Table I gives the values of the normal conductivity, the residual resistance at absolute zero, and the values of $A(\omega)$. $A(\omega)$ is the slope of the linear plot of R/R_n *versus* $f(t)\equiv t^4(1-t^2)/(1-t^4)^2$, where R_n is the surface resistance in the normal state just above the transition temperature T_c, and t is the reduced temperature T/T_c. The value of $A(\omega)$ for tin at 24 000 Mc/sec is 0.24. This compares with our preliminary value of 0.265. Fawcett,[3] in some recent work on tin, has also determined $A(\omega)$ at 24 000 Mc/sec and obtained a value of 0.24. He used an electrolytic polished surface. If Pippard's results at 1200 Mc/sec are extrapolated to this higher frequency using the assumption that in the superconducting region the resistance is varying with frequency as the three-halves power, the value of $A(\omega)$ obtained is 0.238. The measured values appear near this extrapolated value. The results would also indicate there is little difference between an electropolished surface and a mechanically polished surface. Figure 1 is a linear plot of the low-temperature resistance *versus* $f(t)$; the slope $A(\omega)$ is determined from this figure. Figure 2 is a plot of the normalized surface resistance *vs* temperature. The curve is very similar to the one at the lower frequency except that at temperatures near 3.4°K the curve is more rounded than the curve for the lower frequency.

TABLE I. Experimental results.

Frequency Mc/sec	Metal	Normal surface conductivity ohm^{-1}	R/R_n extrapolated to absolute zero	$A(\omega)$	Remarks
9145	Tin	150	0	0.127	Polished, electroplate
9137	Indium	40	0.005	0.081	Electroplated
24 185	Indium	34	...	...	Polished, machined
24 050	Indium	31	0.007	0.21	Electroplated
24 080	Tin	79	0.002	0.24	Polished, machined

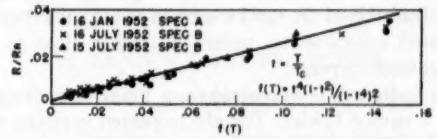

FIG. 1. Linear plot of low-temperature resistance of tin.

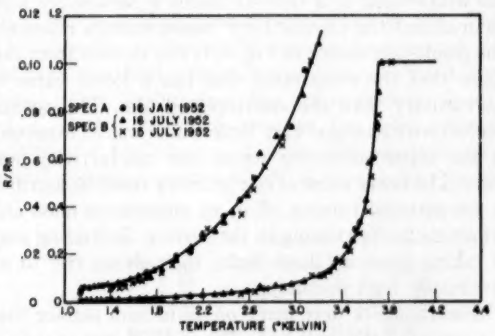

FIG. 2. Surface resistance of tin in superconducting state. The ordinate scale 0–1.2 applies to the lower curve. The upper curve represents the same data on an ordinate scale expanded 10×.

INDIUM

Indium acts very similarly to tin in its behavior in the superconducting region. The curve of the normal-

[1] C. J. Grebenkemper and J. P. Hagen, Phys. Rev. **86**, 673 (1952).

[2] A portion of this paper was presented at the Schenectady Cryogenics Conference, 1952. [*Note:* An error exists in the printed abstract of the meeting. $A(\omega)$ should be 0.24 rather than 0.25.]

[3] E. Fawcett (private communication).

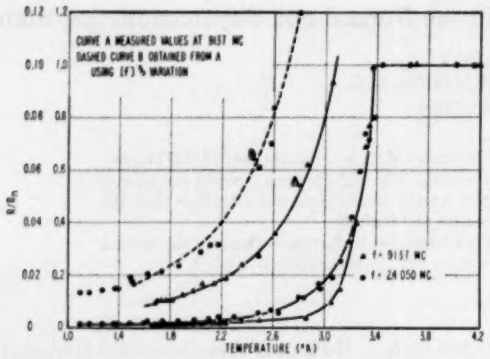

FIG. 3. Surface resistance of indium. The ordinate scale 0–1.0 applies to the lower curves. The upper curves represent the same data on an ordinate scale expanded 10×.

ized surface resistance *vs* temperature is shown in Fig. 3. If the "superconducting resistance" is assumed to vary with frequency as the three-halves power of frequency and the results obtained at the lower frequency are extrapolated to this frequency the dashed curve is obtained. It can be seen in this figure that the measured experimental points lie rather close to the extrapolated curve.

The indium was deposited on a brass base designed to fit a cavity holder. The electroplated surfaces were plated from the Indium Corporation of America patented bath Cy-An-In. No further treatment after plating was given the finished product. The appearance of the film was very good, being much superior to that surface used in the previous work.[1] After measurements were completed on one specimen, a thin film of indium was evaporated in a bell jar under a reasonably high vacuum and the conductivity measurements repeated. The results are shown in Fig. 4. It can be seen from this figure that the evaporated film has a lower value of conductivity than the electroplated film. The normal conductivity changed very little which was as expected. In the superconducting region the conductivity was lower. The lower value of conductivity could be ascribed to the material coming off in an amorphous mass and numerous faults existing in the surface. Scattering may be taking place at these faults thus giving rise to an abnormally high resistance.

Measurements were made on an indium surface that was mechanically polished. The indium was cast in a brass holder and the inner surface machined and polished in a similar manner to that of tin. The polishing process was rather difficult since indium is extremely soft. After the specimen was polished an attempt was made to clean the surface by using a dilute solution of HCl. The experimental results are shown in Figs. 3 and 4. The polished indium specimen did not yield as high a value of conductivity as the electroplated specimen in the superconducting region. This could be caused by the polishing techniques or to some etching taking place in the attempt to clean the specimen after polishing.

The values of the normal conductivity are given in Table I. The value at 9100 Mc/sec is lower than would be expected if indium behaved in a similar manner to tin. The values obtained at 24 000 Mc/sec are almost as large as the values at 9100 Mc/sec. This may be caused by the poor surface used at 9100 Mc/sec and the much better surface used at 24 000 Mc/sec.

CONCLUSIONS

It appears that the resistance in the superconducting region is varying with frequency as the three-halves power of the frequency rather than the predicted

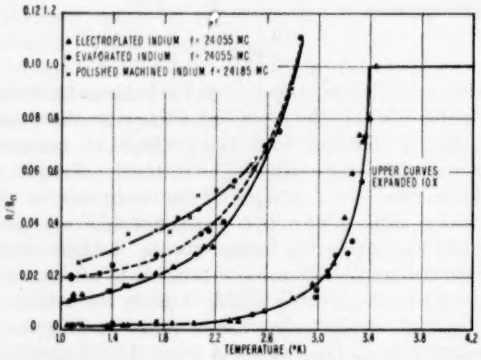
ELECTROPLATED INDIUM f = 24055 MC
EVAPORATED INDIUM f = 24055 MC
POLISHED MACHINED INDIUM f = 24185 MC
UPPER CURVES
EXPANDED 10X
TEMPERATURE (°K)

FIG. 4. Surface resistance of indium. The ordinate scale 0–1.0 applies to the lower curve. The upper curves represent the same data on an ordinate scale expanded 10×.

variation of the second power. This relationship appears to apply for both tin and indium. For tin the residual resistance at absolute zero is 0.2 percent of the resistance at the transition temperature. The value of $A(\omega)$ for tin is 0.24. For a good polished surface it is quite possible that the residual resistance would approach zero at absolute zero. For an electroplated indium surface the residual resistance is 0.7 percent and $A(\omega)=0.21$. These results are for an untouched electroplated film. For a good polished indium surface the indium results would probably be very similar to tin.

ACKNOWLEDGMENT

The author is indebted to Dr. John P. Hagen for his frequent advice and encouragement.

Emission of Energetic Secondary Electrons Produced by 1.3-Mev Electron Bombardment*

R. A. SHATAS, J. F. MARSHALL, AND M. A. POMERANTZ
Bartol Research Foundation of The Franklin Institute, Swarthmore, Pennsylvania

(Received May 6, 1954)

The emission of energetic secondary electrons (delta rays or knock-on electrons) produced by 1.3-Mev primaries which penetrate thin targets with negligible mean energy loss has been investigated. These have previously not been observable in the customary thick-target experiments because of the inherent impossibility of distinguishing between true secondaries and reflected primaries which have suffered large energy losses. The present arrangement does not record back-scattered primaries, but only emitted electrons. The delta ray yields from various targets (Al, Ni, Au, Ag, Cu, C) ranging in thickness from 5×10^{-6} to 10^{-2} in. have been measured. The determinations of I_δ/I_P vary between 0.3 percent and 2.1 percent independent of surface treatment, and there is only a small dependence of the yield upon target material for an equivalent thickness expressed in mg cm^{-2}. For 45.8 mg cm^{-2} Ni, the delta ray yield is 2.08 ± 0.15 percent. This may be compared with 1.48 ± 0.25 percent, the yield of low-energy secondaries as measured with the cleanest surface attainable in the demountable experimental tube.

I. INTRODUCTION

ALTHOUGH secondary emission from solids bombarded by electrons having energies below several thousand ev has been the subject of considerable investigation, the advantages of extending the observations to high primary energies have remained generally unrecognized. Sources of electrons in the Mev region have been available for many years, and numerous studies of electron scattering have been conducted. Nevertheless, the only previous secondary emission measurements have been those in the range from 30 kev to 340 kev obtained by Trump and Van de Graaff[1] with the electrostatic generator in the course of experiments directed primarily at investigating the mechanisms of voltage breakdown in high vacuum, and from 18 kev to 1.4 Mev by Miller and Porter[2] with the linear accelerator.

The conventional arrangement for measuring the yield of secondary electrons involves a thick target in which the primary is completely absorbed. When the bombarding energy is low, the description of the phenomenon of secondary emission comprises essentially four processes, some of which are not particularly amenable to theoretical analysis. These are: (1) the primary interaction, (2) the primary energy loss, (3) the escape of secondaries, and (4) integration of the first three steps over the range of the primary. By invoking a combination of very high primary energy and targets which are sufficiently thin to permit the bombarding electrons to pass through with negligible scattering and energy loss, a significant simplification of the theoretical treatment results. For this reason, and in order to study certain other aspects of secondary electron emission, a program of experiments was undertaken utilizing the multiple-cavity linear accelerator as the source of a 1.3-Mev electron beam. In contrast with the methods employed previously, the present techniques have permitted the direct observation of energetic secondary electrons, long familiar to cosmic ray investigators as *knock-on electrons* or *delta rays*.

II. EXPERIMENTAL PROCEDURE

A. Method

The electrons leaving a bombarded target can be ascribed to three different mechanisms. Some of the primary electrons are directly reflected, whereas others are scattered with some loss of energy. Finally, secondary electrons are emitted by the target as a consequence of interactions between the primary electrons and the electrons in the solid. In the usual experimental arrangement, which is illustrated schematically in Fig. 1(a), it is impossible to distinguish between true secondaries and back-scattered primaries which have suffered large energy losses. In this case, the target current, $I_P-I_\delta-I_{RP}$, is the difference between the total primary current and the current of secondary electrons plus back-scattered primaries which do not return to the

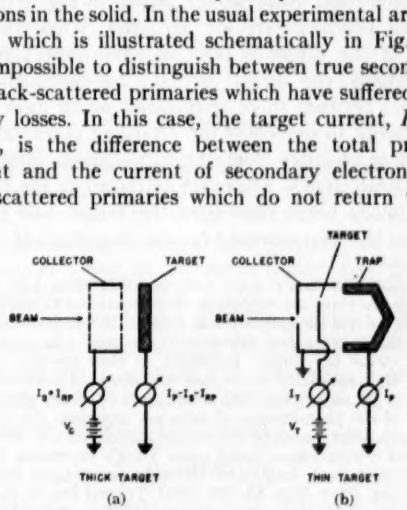

FIG. 1(a). Conventional arrangement for measuring secondary electron emission from thick targets. It is impossible to distinguish between energetic secondaries and back-scattered primaries in this case. (b). Arrangement for measuring secondary electron emission from thin targets through which the primaries pass with negligible energy loss. Primaries scattered from the target are not recorded.

* Assisted by the Office of Ordnance Research and the U. S. Office of Naval Research.

[1] J. G. Trump and R. J. Van de Graaff, J. Appl. Phys. **18**, 327 (1947); Phys. Rev. **75**, 44 (1949).

[2] B. L. Miller and W. C. Porter, Phys. Rev. **85**, 391 (1952).

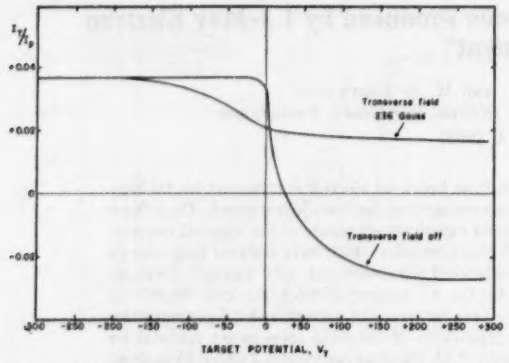

FIG. 2. Dependence of I_T/I_P upon V_T [see Fig. 1(b)] with and without a transverse magnetic field. The ratio is defined as positive when there is a net emission of electrons from the target.

target. The collector current is composed of both secondary electrons leaving the target, I_S, and primaries scattered from the target, I_{RP}. The classification in terms of secondaries and scattered or reflected primaries is made on the basis of the energy distribution of the collected electrons, obtained by applying retarding potentials, $-V_C$, to the collector with respect to the target. Collected electrons which can overcome some rather arbitrarily-assigned retarding potential are then regarded as scattered and reflected primaries, whereas the electrons of lower energies are designated as true secondaries. Thus, high-energy secondaries and scattered primaries are indistinguishable, and the contribution of the former to the total yield is, in fact, assumed to be negligible.

In the present arrangement, shown in Fig. 1(b), the scattered primaries are not recorded. When the potential of the target is positive with respect to the surroundings, the target current,[3] I_T, represents the difference between those secondaries which have sufficient energy to overcome the retarding potential, V_T, and the secondaries from the surroundings (trap and collector electrodes) which are attracted to the target. The primary beam penetrates the target, and is observed as the trap current,[4] I_P, the magnitude of which is essentially unaffected by the presence of the thin targets utilized in the present experiments. The secondaries from the surroundings can be prevented from reaching the target by the application of a transverse magnetic field of appropriate magnitude in the vicinity of the target, thereby permitting the determination of the delta ray yield.

The effect is revealed in Fig. 2, which shows the dependence of the ratio,[5] I_T/I_P, upon target potential, V_T, with a transverse magnetic field either on or off. With no magnetic field, all of the secondaries leave the target when V_T is negative. In this case, low-energy secondaries from the surroundings are repelled by the target, although high-energy secondaries may be collected. However, when the target potential is between -15 v and zero, all extraneous low-energy secondaries are not retarded, and those which strike the target cause the net target current to decrease. When V_T is sufficiently positive, a net collection of electrons by the target occurs, since the low-energy secondaries from the surroundings are now attracted, and the yield becomes negative. However, the application of a transverse magnetic field prevents the stray electrons from reaching the target, and a net emission is manifested by the positive yield.

This provides a lower limit for the delta-ray yield, since both imperfect protection of the target from extraneous electrons and the return of emitted delta rays to the target tend to reduce the net target current. In practice, the measured value probably coincides with the actual value within the experimental uncertainty.

B. Tube Design

The arrangement of the electrodes in the demountable experimental tube is shown in Fig. 3. The tube is

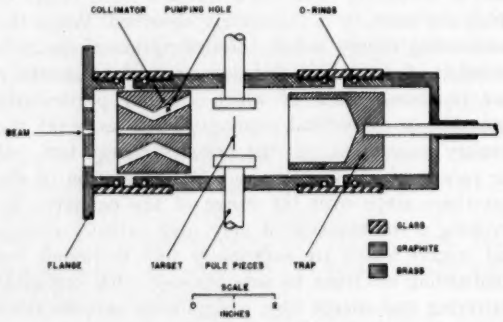

FIG. 3. Cross-sectional view of experimental tube utilized for determination of secondary electron yields.

[3] Contributions to I_T from sources other than low energy secondary electrons are negligible. Back-scattered primaries and delta rays leaving the graphite trap amount to less than 3 percent of the incident beam (see reference 1) and only a fraction ($\approx\frac{1}{4}$) of these strike the target. Inasmuch as their energies are, in general, high compared with that necessary to penetrate the thickest target employed, their effect upon I_T is not observable. Because of the phenomenon of delta-ray emission, the effect of stopped primaries cannot be determined experimentally. However, theoretical computations based upon Yang's expression for the distribution in path lengths of electrons penetrating thin foils [C. N. Yang, Phys. Rev. **84**, 599 (1951)] reveal that in the most extreme case from this point of view (45.8 mg cm^{-2} Ni) only 0.05 percent of the emergent primaries traverse paths exceeding 1.5 times the thickness of the foil. Since the range of the primaries is 15 times that of this particular target, obviously only a minute fraction of the primaries will stop.

[4] Although I_P actually represents the incident primary current minus back-scattered primaries and secondaries escaping from the trap electrode, the contributions of the latter are negligible. The error in the yields arising from neglect of back-scattered primaries and secondaries ($<0.03I_P$) is less than other experimental uncertainties.

[5] The ratio I_T/I_P is defined as positive when the sense of the current I_T corresponds to a net emission of electrons from the target, and negative when the number of electrons emitted is less than the number collected from other sources, per primary electron.

attached to a magnetic spectrum analyzer by means of a flange with an *O*-ring gasket at the output end of the linear accelerator.

The graphite collimator defines the size of the primary beam, which is approximately 6 mm in diameter at the target. The eccentric pumping holes provide adequate pumping speed without the introduction into the target region of the copious background of stray electrons from the analyzer.

The target is supported by a rod equipped with a sliding *O*-ring gasket arrangement (not illustrated) which permits positioning the 1-in.$\times 1\frac{1}{4}$-in. foil in or out of the path of the beam by remote control. The graphite trap which collects the primary electrons after they have penetrated the target can also be moved in vacuum to facilitate observations of any possible dependence of the results upon geometrical factors. In order to preclude the influence of ionization currents generated by the intense x-ray background, coaxial leads (not shown in Fig. 3) insulated from the brass envelope, are introduced through vacuum seals.

C. Linear Accelerator and Auxiliary Apparatus

The essential features of the four-cavity linear accelerator utilized in these experiments have been described previously.[6] Several modifications have produced a high degree of stability in operation, and the maximum attainable output current has been increased to peak values of 60 ma at 1.3–1.5 Mev by removal of the buncher cavity and improvements in the electron injection system. In the present measurements, the targets were generally bombarded by rectangular one microsecond pulses of primary electrons at a repetition rate of 20 pulses per second and pulse height 0.05–1.0 ma. The energy spectrum, determined by the geometry of the analyzer, is triangular with a half-width of 7 percent, corresponding to 94 kev at 1.35 Mev.

Trap and target currents are measured simultaneously by a pair of two-stage negative-feedback dc amplifiers[7] with integrating networks in the input. The maximum sensitivity is 10^{-12} amp per division, and the variation in the calibration of the electronic meters is less than 1 percent.

D. Determination of Delta Ray Yields

Figure 4 represents the series of observations comprising a typical delta ray yield determination. A potential as low as +18 v applied to the target with respect to its surroundings is sufficient to impede the escape of the low-energy secondaries produced in the target. However, in the absence of a transverse magnetic field, low-energy secondaries emitted by the auxilliary electrodes are collected by the target, as a result of which a small net negative I_T/I_P is measured. When the transverse field is applied, stray low-energy secondaries are deflected away from the target, and with the field strength of appropriate magnitude, the target current is comprised primarily of electrons emitted by the target. I_T/I_P then remains constant over a "plateau" region of magnetic field strength. This reveals that a negligible contribution is attributable to extraneous effects. As confirmed by direct observation with a fluorescent screen placed at the position normally occupied by the trap, the primary beam is deflected considerably, and hence suffers appreciable scattering while traversing the collimator, when the field intensity exceeds a maximum value, which with the present arrangement is 240 gauss.

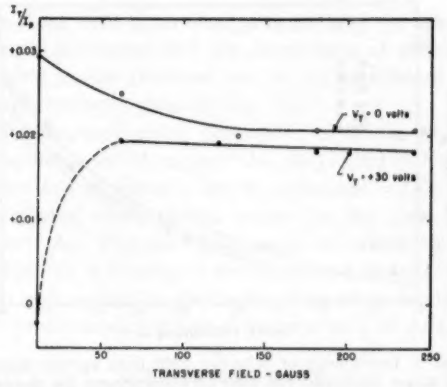

FIG. 4. Typical series of observations of delta-ray yield. With $V_T > 18$ v, I_T/I_P is measured as a function of the transverse magnetic field strength. Plateau values represent I_δ/I_P.

The delta ray yield of a particular target is determined from the average of at least eight individual measurements, with two different target voltages, spanning the magnetic field strength plateau. The dependence upon V_T, ($V_T > +18$ v) is negligible.

E. Targets

Various metals (Al, Ni, Au, Ag, Cu) commercially available in foil, leaf, or sheet form, ranging in thickness from 5×10^{-6} in. (Au) to 10^{-2} in. (Al) were employed as targets. Carbon targets were prepared by grinding the faces of a thin section sliced from a 1-in. diameter graphite rod.

In contrast with the conditions which prevail in measurements of low-energy secondary electrons, it is not necessary to exercise the customary precautions regarding surface cleanliness in view of the high energy with which the delta rays emerge.

III. RESULTS

All of the determinations of delta-ray yield are summarized in Fig. 5, where I_δ/I_P is plotted as a function of target thickness expressed in mg cm^{-2}. The standard deviation of each point is approximately ± 10 percent of the indicated value. The experimental uncertainty is governed by fluctuations of the primary

[6] B. L. Miller, Rev. Sci. Instr. **23**, 401 (1952).
[7] S. Roberts, Rev. Sci. Instr. **10**, 181 (1939).

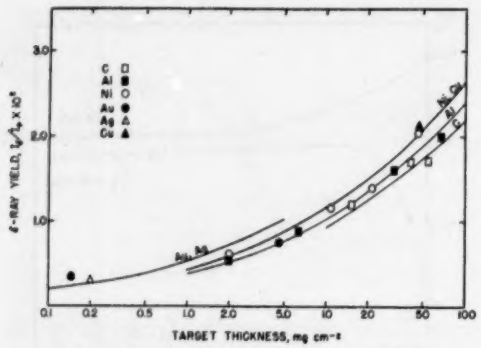

FIG. 5. Dependence of delta-ray yield from various materials upon target thickness. The solid curves represent the theoretical predictions discussed in Sec. IV.

beam. Data obtained with a preliminary experimental tube having different dimensions from those indicated in Fig. 3 were in satisfactory accord with these results. Detailed comparison of total yields, including low-energy secondaries, was not attempted because of the dependence of the latter upon surface conditions. However, it is of interest to note the relative magnitudes of the yields of low- and high-energy secondaries from a typical target.

Although the delta-ray yield was independent of surface treatment in all cases, the *total* yield invariably decreased when the target was degassed by electron bombardment from an adjacent filament in the experimental tube immediately prior to the measurement. The minimum low-energy yield from 45.8 mg cm^{-2} Ni subjected to the maximum practicable heating was 1.48±0.25 percent, a value which is presumably higher than that characteristic of an extremely clean specimen. The corresponding delta-ray yield is 2.08±0.15 percent. Measurements of the yield of low-energy secondaries are now under way with sealed-off tubes processed in accordance with the procedures requisite for insuring the cleanliness of the target surfaces.

IV. THEORETICAL DISCUSSION

On the basis of a model involving several simplifying approximations, the delta-ray yield expected theoretically from a target of specified atomic number and thickness may be computed. The assumptions are: (a) the electrons in the target can be treated as unbound; (b) the delta-ray energies are much lower than the energy of the primary; and (c) a secondary created at a distance x from the surface of the target will emerge if its residual range is greater than x.

Under these conditions, the delta-ray yield (δ) is given by

$$\delta=\int_0^l f(E)dx, \tag{1}$$

where $f(E)$ is the number of secondaries produced per unit path of the primary, with energy greater than E, the minimum energy necessary for escape from depth $(l-x)$, and l is the thickness of the target. Assuming the rate of energy loss of the secondaries to be given by

$$dE/dx=-\psi(E) \tag{2}$$

and changing the variable of integration in Eq. (1) from x to E, we obtain

$$\delta=\int_0^{E_l}\frac{f(E)}{\psi(E)}dE, \tag{3}$$

where E_l is the energy of an electron whose range is equal to l, and is obtained from

$$l=\int_0^{E_l}\frac{dE}{\psi(E)}. \tag{4}$$

The rate of production of internal secondaries may be obtained either from Møller's expression[8] for the production of knock-on electrons, or from a purely classical calculation. Both yield

$$f(E)=C\mu/E. \tag{5}$$

Here, $\mu=mc^2$, the rest energy of the electron, and

$$C=2\pi N_0 r_0^2 Z/A=0.3(Z/A)\ \text{g}^{-1}\ \text{cm}^2,$$

where N_0 is Avogadro's number, Z and A are the charge and mass numbers of the target material, and $r_0=e^2/\mu$ is the classical radius of the electron.

The rate of energy loss is given by the Bethe-Bloch expression,

$$\psi(E)=(C\mu^2/E)\ln(2E/I)\ \text{ev g}^{-1}\ \text{cm}^2. \tag{6}$$

(Relativistic effects are unimportant in the present case.) Here, as is customary, I is assumed to be proportional to the atomic number of the target material, $I=aZ$. The final results are found to be extremely insensitive to the choice of the constant of proportionality, and for purposes of calculation, a is taken to be 11.5 ev.[9]

Substituting Eqs. (5) and (6) in Eq. (3), one obtains

$$\delta=\frac{I}{2\mu}\bar{E}i\left(\ln\frac{2E_l}{I}\right), \tag{7}$$

where

$$\bar{E}i(x)=\int_{-\infty}^{x}\frac{e^{-t}}{t}dt$$

and Eq. (4) becomes

$$l=\frac{I^2}{4C\mu^2}\bar{E}i\left(2\ln\frac{2E_l}{I}\right). \tag{8}$$

Solving Eq. (8) for $\ln(2E_l/I)$ and substituting in Eq.

[8] C. Møller, Ann. Physik **14**, 531 (1932).
[9] R. R. Wilson, Phys. Rev. **60**, 749 (1941).

(7), one then obtains the delta-ray yield as a function of the thickness and atomic number of the target.

From an analysis similar to that already outlined, one can determine the energy distribution of the emergent secondaries, and it is found that almost all of them have energies between 10 and 100 kev.[10] Consequently, assumption (b) is valid, as is (a) for all but the most tightly-bound target electrons. Assumption (c) is not so well justified, since the path of an emerging secondary is in general longer than the distance from its point of origin to the surface, and the computed yields are consequently too high by about a factor of two. The ratio of the computed to the experimentally-determined yield is, however, substantially the same in all cases, indicating that the dependence of the delta ray yield on the thickness and atomic number of the target is correctly given by Eq. (7).

The computed yields normalized to fit the experimental value for 46 mg cm^{-2} Ni are plotted in Fig. 5. Theory and experiment are in agreement within the experimental uncertainties, except for the case of 5 mg cm^{-2} Au. This discrepancy may be caused by the fact that the scattering of the secondaries has not been taken into account in the theory. This effect would be more pronounced in a high-Z material such as gold.

[10] A lower limit to the delta-ray energies has been determined by an independent method of observing the energy distribution of the low-energy secondary electrons, and no current of delta rays with energies less than 2 kev has been detected [Shatas, Marshall, and Pomerantz, Phys. Rev. **94**, 757 (1954)].

ACKNOWLEDGMENT

The authors wish to acknowledge the assistance of Arthur E. Smith in the experimental program.

PHYSICAL REVIEW VOLUME 96, NUMBER 5 DECEMBER 1, 1954

Hall Effect in Bismuth at Low Temperatures*

J. M. Reynolds, H. W. Hemstreet, T. E. Leinhardt, and D. D. Triantos
Physics Department, Louisiana State University, Baton Rouge, Louisiana

(Received July 30, 1954)

The dc Hall effect in bismuth has been investigated over a range of fields from 0 to 8000 gauss and at temperatures in the liquid helium region. It is observed that the Hall effect oscillates in a manner which is periodic in H^{-1} and that this period is independent of temperature. The dependence of the amplitude of the oscillations on field and temperature is of the general form given by the theoretical work of Grimsal and Levinger.

At low temperatures the magnetic susceptibility of bismuth and many other metals shows oscillations which are periodic in the reciprocal of the magnetic field intensity.[1–3] At high fields such oscillations occur to a smaller extent in the magnetoresistance.[4] The Peierls,[5] Blackman,[6] and Landau[7] theory relates the oscillations of the de Hass-van Alphen effect to the Larmor precessions of the conduction electrons and to the quantization of this motion in the plane perpendicular to the magnetic field. As this precession gives rise to the Hall effect, it is not surprising that the Hall effect in bismuth is also periodic in $1/H$.[8] Grimsal and Levinger[9] have recently obtained a formula for the periodic part of the Hall effect in bismuth, based on Blackman's formulation[6] of the theory of the de Haas-van Alphen effect. The data reported here are interpreted in terms of Grimsal and Levinger's formulation.

* Supported by the National Science Foundation.

[1] W. J. de Haas and P. M. van Alphen, Leiden Comm. No. **212a** (1930) and No. **220d** (1932).
[2] D. Schoenberg, Proc. Roy. Soc. (London) **A170**, 341 (1939).
[3] D. Schoenberg, Trans. Roy. Soc. (London) **A245**, 1 (1952).
[4] P. B. Alers and R. T. Webber, Phys. Rev. **91**, 1060 (1953).
[5] R. Peierls, Z. Physik **80**, 763 (1933).
[6] M. Blackman, Proc. Roy. Soc. (London) **A166**, 1 (1938).
[7] L. D. Landau, see Appendix to reference 2.
[8] Reynolds, Leinhardt, and Hemstreet, Phys. Rev. **93**, 247 (1954).
[9] J. S. Levinger and E. G. Grimsal, Phys. Rev. **94**, 772(A) (1954); and E. G. Grimsal, Thesis, Louisiana State University (1954) (Unpublished—copies available from L. S. U. Phyics Department.)

EXPERIMENTAL

The single crystals were grown in vacuum by the Bridgman method, from Johnson, Matthey bismuth (Johnson, Matthey & Co., Ltd., London). Crystal Bi-1, reported on earlier,[8] was in the form of a right parallelopiped of dimensions 25.5 by 7.5 by 0.88 mm. The orientation of its crystallographic axes were such that when mounted in the flask the current passed parallel to a binary axis and the magnetic field was at an angle of 25° with the trigonal axis.

In order to allow measurements to be made on one crystal, both with the field parallel and with it perpendicular to the trigonal axis, a crystal (Bi-4) was prepared which was more nearly cubical in shape (6.7×5.2 ×5.2 mm), with one pair of faces perpendicular to the trigonal axis, another pair perpendicular to a binary axis, and the third pair of faces parallel to the plane of

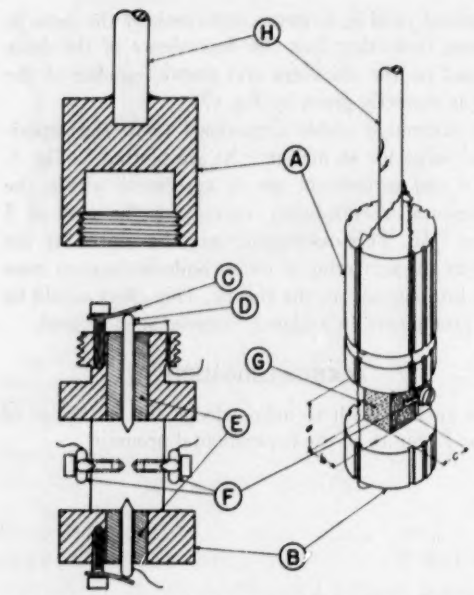

FIG. 1. Crystal holder. *A*, Lucite cap; *B*, Lucite holder; *C*, phosphor-bronze spring; *D*, current probes; *E*, brass bushings; *F*, Hall probes; *G*, Bi crystal; *H*, Lucite support.

the trigonal and the binary axis. The crystal was grown in the form of a cylinder and then cut to shape on a water-cooled carborundum saw.

The crystals were mounted in Lucite holders (Fig. 1) in direct contact with liquid helium. The Hall probes (*F*) and the current probes (*D*) were made of phosphor-bronze and were 0.84 mm in diameter. The current probes passed through brass bushings (*F*) for ease in alignment. To assure good contact, both the specimen and the probe tips were etched in nitric acid immediately before mounting.

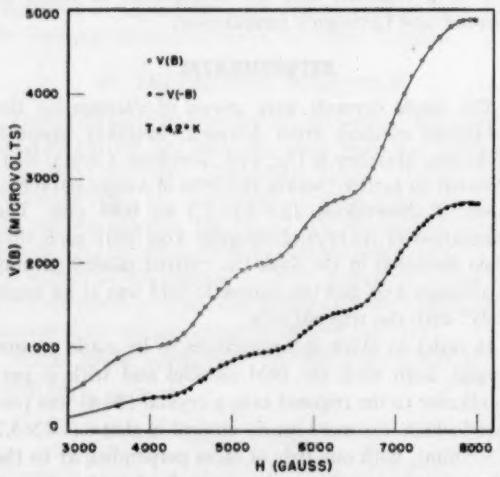

FIG. 2. The potential observed on the Hall probes at 4.2°K. Field perpendicular to the trigonal axis.

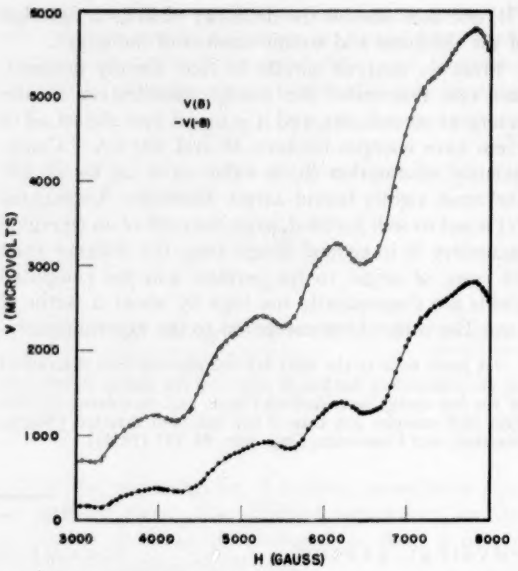

FIG. 3. The potentials observed on the Hall probes at 1.4°K. Field perpendicular to the trigonal axis.

The dc Hall voltage was measured by means of a White potentiometer, and an L and N Type K potentiometer was used to monitor the current through the sample. At each temperature the probe voltage was

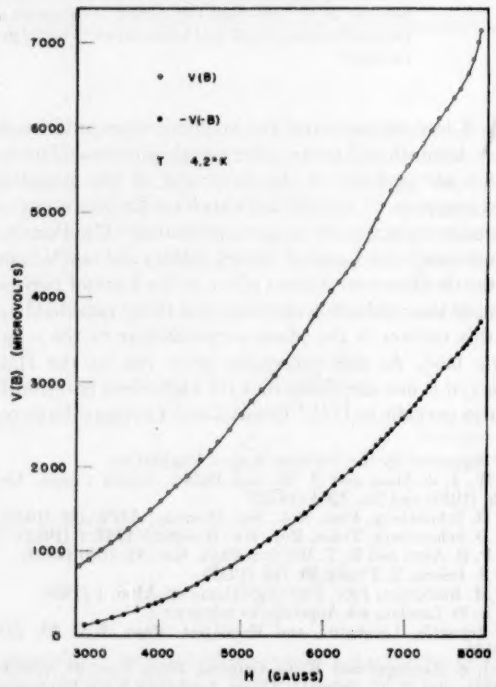

FIG. 4. The potentials observed on the Hall probes at 4.2°K. Field parallel to the trigonal axis.

measured at closely spaced intervals of the field value. After such a field sweep was complete, it was then repeated with the field reversed in direction. The Hall voltage is taken to be

$$V_H=\tfrac{1}{2}[V(B)-V(-B)]. \quad (1)$$

This is done to eliminate the effect of the large magnetoresistance of bismuth.

RESULTS

(A) Field Dependence

In Figs. 2–5 $V(B)$ and $-V(-B)$, for sample Bi-4, are plotted against the magnetic field. The data in

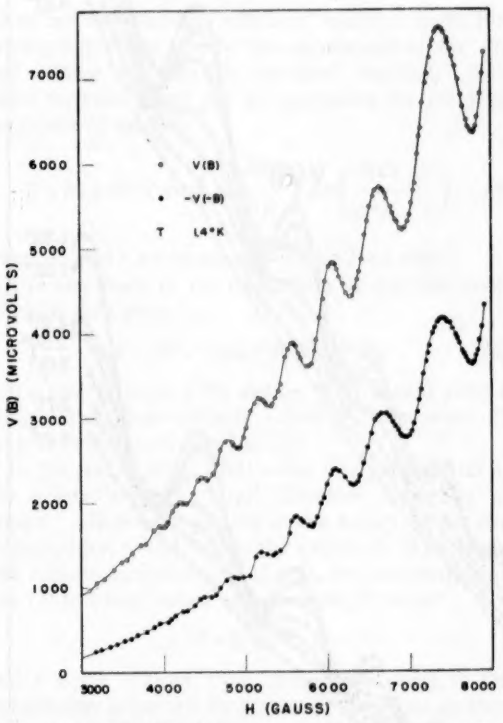

FIG. 5. The potentials observed on the Hall probes at 1.4°K. Field parallel to the trigonal axis.

Figs. 2 and 3 were taken with the field perpendicular to the trigonal axis, while those in Figs. 4 and 5 were taken with the field parallel to the trigonal axis. In all these measurements the current was parallel to a binary axis. The oscillations are appreciable only at the lower temperature, and simplest for the field parallel to the trigonal axis.

According to Eq. (1) the Hall voltage is given in each figure by the average of the two curves. These averages were obtained graphically and from them values of the Hall coefficient were obtained. The Hall coefficients were then plotted against H^{-1}, and these curves are seen in Fig. 6 for three orientations at 1.4°K.

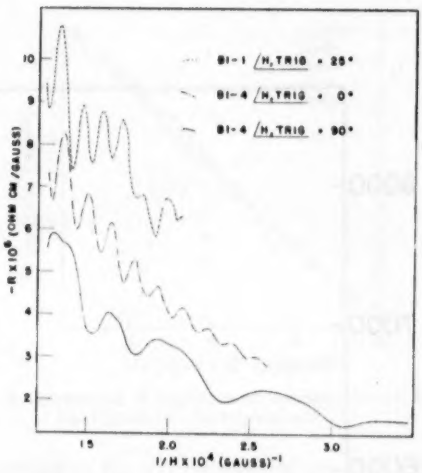

FIG. 6. The Hall coefficients. $T=1.4$°K.

The upper curve, for which the field is 25° from the trigonal axis, is taken from the data previously reported on sample Bi-1, while the lower and middle curves are taken from the data in Figs. 3 and 5, respectively. One can see that as the field approaches parallelism with the trigonal axis the oscillations simplify to a single period in H^{-1}. To illustrate the periodicity of the oscillations, the successive values of H^{-1} for which the Hall coefficient is a maximum or minimum are plotted against their corresponding integers (Fig. 7).

(B) Temperature Dependence

Some two months after the data shown in Figs. 4 and 5 were taken, sample Bi-4 was remounted in a flask and the Hall measurements were taken at seven different temperatures, ranging from 4.21°K down to 1.38°K. The field was chosen to be along the trigonal axis, because the oscillations have a simple period for this orientation. These data are shown in Fig. 8. One sees immediately from Fig. 8 that the period and phase of the oscillations are independent of temperature, while the amplitude decreases rapidly with increasing temperature.

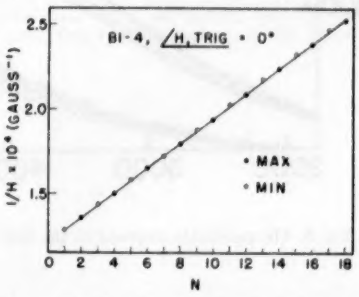

FIG. 7. Values of H^{-1} for which maxima and miulma in the Hall coefficients occur, plotted against their corresponding integers.

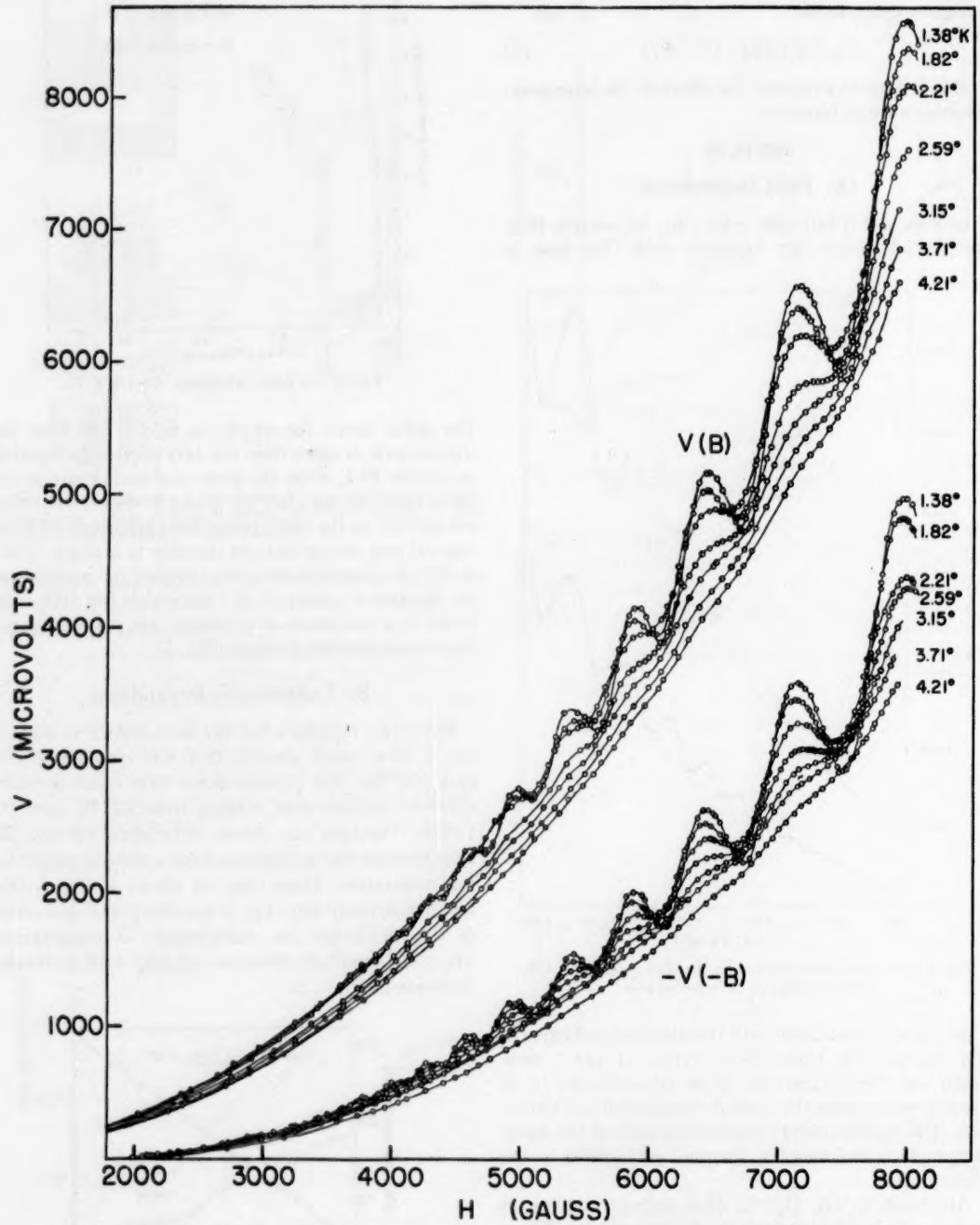

FIG. 8. The potentials observed on the Hall probes for various temperatures. Field parallel to the trigonal axis.

Analysis of Data

Dingle,[10] Grimsal, and Levinger[9] derive for the number of "de Haas-van Alphen electrons"

$$N=N_0+\sum_{P=1}^{\infty}\frac{(-1)^P}{P^{\frac{1}{2}}}\frac{m^{\frac{1}{2}}}{2\pi^2\hbar^3}\frac{P\chi}{\sinh P\chi}(\beta^*H)^{\frac{1}{2}}\times\sin\left(2\pi P\frac{E_0}{\beta^*H}-\frac{\pi}{4}\right), \quad (2)$$

where $\chi=2\pi^2kT/\beta^*H$. E_0 is the Fermi energy and β^* is the "effective" double Bohr magneton given by

$$\beta^*=e\hbar/m^*c,$$

where m^* is a suitable "effective" electron mass. Replacing hyperbolic sine by the exponential in Eq. (2) and putting this into the two-band "isotropic" Hall effect formula, they[9] get an expression for the Hall coefficient of the form

$$R=R_0+rH^{\frac{1}{2}}T\exp\left(-\frac{2\pi^2kT}{\beta^*H}\right)\sin\left(\frac{2\pi E_0}{\beta^*H}-\frac{\pi}{4}\right), \quad (3)$$

where R_0 and r are constants. (Using $P=1$ only.)

The amplitude of the oscillations in the Hall coefficient is then given by

$$A=rH^{\frac{1}{2}}T\exp(-2\pi^2kT/\beta^*H) \quad (4)$$

and a plot of $\ln(A/TH^{\frac{1}{2}})$ against T/H should yield a straight line whose slope is $-2\pi^2k/\beta^*$, from which β^* may be determined. (See Fig. 9.)

In the plot of $\ln(A/TH^{\frac{1}{2}})$ *versus* T/H, the scatter of the points is rather large. However, according to Dingle,[3] collision broadening of the energy levels, due to impurities, would reduce the amplitude of de Haas-van Alphen oscillations, as though the temperature in Eq. (2) had been raised by an amount Z, where

$$Z=h/2\pi^2k\tau$$

and τ is the collision time. Adding this term to the temperature improved the scatter of the points greatly. In plots of $\ln[A/(T+Z)H^{\frac{1}{2}}]$ *versus* $(T+Z)/H$ the points fell most nearly on a straight line for $Z=0.5$. This particular plot is seen in Fig. 9. The slope of the line drawn in Fig. 9 yields the value $\beta^*=3.0\times10^{-19}$ erg/gauss.

[10] R. B. Dingle, Proc. Roy. Soc. (London) **A211**, 500 (1952).

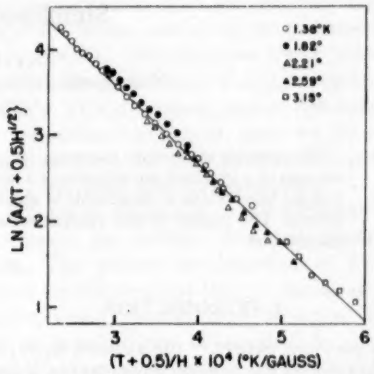

FIG. 9. Dependence of amplitude on temperature and field. Field parallel to the trigonal axis.

According to Eq. (2) the slope of the line in Fig. 6 should be $\frac{1}{2}(\beta^*/E_0)$. This gives $\beta^*/E_0=1.5\times10^{-5}$ gauss^{-1}. The above value of β^* then gives

$$E_0=2.0\times10^{-14}\text{ erg}.$$

From his susceptibility data, Shoenberg[3] gets a value

$$E_0=2.9\times10^{-14}\text{ erg},$$

using Landau's[7] formulation of the theory. We have found no satisfactory explanation for the discrepancy. However, the theory employed in the analysis of the Hall effect data is not as yet refined to the point that one could expect very exact agreement in calculations of such parameters. Another objection to the theory as it now stands is that it does not account for the field dependence of the nonoscillatory part of the Hall effect, i.e., R_0 in Eq. (3) is a constant. Equation (3) does, however, describe the essential features of the oscillatory part of the Hall effect. It is periodic in H^{-1} and this period is independent of temperature. The dependence of the amplitude of the oscillations on field and temperature seem to be of the right form from the fit of the points in Fig. 9.

The authors wish to express their appreciation to Dr. J. S. Levinger, Dr. E. G. Grimsal, and Dr. D. C. Ralph for their valuable discussions.

Note added in proof.—The authors have learned through private communication from T. G. Berlincourt that the periodic Hall effect has been observed in graphite at the Naval Research Laboratory.

Simplified Impurity Calculation*

G. F. KOSTER† AND J. C. SLATER
Massachusetts Institute of Technology, Cambridge, Massachusetts
(Received August 30, 1954)

The methods of previous papers by the authors are applied to a simplified impurity calculation. This is the case of a localized perturbation in a simple cubic lattice. We consider the effect of the perturbation on a single band which is describable in terms of a Wannier function which only has nearest neighbor interactions. The results of this calculation are compared with some approximate treatments of impurity calculations.

I. INTRODUCTION

IN two previous papers,[1,2] the authors have proposed a treatment of the impurity problem in solids. This method consisted of expanding the perturbed wave function in terms of a linear combination of the Wannier functions of the unperturbed crystal. The coefficients in this linear expansion were shown to satisfy a set of simultaneous linear equations which had the form of difference equations. The method used to solve these equations was a Green's function method for the difference equations. The procedure was applied to simple cases drawn almost exclusively from one-dimensional crystals. These are quite unrealistic and it is desirable to work through, by this method, a three-dimensional impurity problem.

Fortunately, there exists a three-dimensional impurity problem which can be carried through analytically in some detail. This does not correspond to any crystal found in nature but it will have features in common with more realistic computations. The problem concerns itself with the effect of an impurity on the wave functions of a single band in a simple cubic lattice. This band is assumed to be cosine-like in the x, y, and z directions of reciprocal space. This is to say that the dependence of energy on the propagation vector is a sum of cosines of k_x, k_y, and k_z. If this is the case, the evaluation of the Green's function for the difference equations can be carried out analytically and the solutions can be studied in detail.

We are able to study the manner in which the bound state appears below the band as we vary the perturbative potential. The wave function of the bound state can be found numerically. This enables us to compare the wave function found in this precise manner with the wave functions found by approximate procedures. In particular, we can compare it with the wave function that appears from replacing the exact difference equations by approximate differential equations. Another approximation can be studied. This approximation consists of cutting the crystal off after a finite number of lattice spacings. We shall be able to see how valid it is to replace the infinite crystal by a small finite crystal. In addition to the bound states, the scattering problem in this lattice can be carried through. It is hoped that this simple example will illustrate the use of the method of treating the impurity problem proposed in the previous papers and will also indicate features which we might expect to find in more precise impurity problems.

II. STATEMENT AND DIRECT SOLUTION OF THE PROBLEM

We shall assume that we have a simple cubic lattice whose primitive translations are given by

$$\mathbf{R}_{pqr}=pR\mathbf{i}+qR\mathbf{j}+rR\mathbf{k}. \tag{1}$$

Here R is the lattice spacing and $\mathbf{i}$, $\mathbf{j}$, and $\mathbf{k}$ are unit vectors in the x, y, and z directions respectively. Each lattice site will be further assumed to have full cubic symmetry. Let us imagine that associated with this solid there is a band of energies which has associated with it Wannier functions[3] which have full cubic symmetry with respect to the lattice site about which they are defined. These energies are the eigenstates of some one-electron Hamiltonian. We assume in addition that the Wannier functions only have interactions between each other when they are nearest neighbor or closer. If we denote the Wannier function associated with the lattice site $\mathbf{R}_{pqr}$ by $a(\mathbf{r}-\mathbf{R}_{pqr})$ and the one-electron Hamiltonian by H, this means that the only nonvanishing matrix elements of the Hamiltonian are given by

$$\begin{aligned}\mathcal{E}(0)&=\int a(\mathbf{r}-\mathbf{R}_{pqr})Ha(\mathbf{r}-\mathbf{R}_{pqr})dv,\\ \mathcal{E}(1)&=\int a(\mathbf{r}-\mathbf{R}_{pqr})Ha(\mathbf{r}-\mathbf{R}_{p+1,q,r})dv\\ &=\int a(\mathbf{r}-\mathbf{R}_{pqr})Ha(\mathbf{r}-\mathbf{R}_{p,q+1,r})dv, \text{ etc.}\end{aligned} \tag{2}$$

We wish to study the effects of a perturbation on this perfect periodic lattice. We restrict ourselves in this

* The research in this document was supported jointly by the U. S. Army, Navy, and Air Force under contract with the Massachusetts Institute of Technology.
† Staff member, Lincoln Laboratory, Massachusetts Institute of Technology, Cambridge, Massachusetts.
[1] G. F. Koster and J. C. Slater, Phys. Rev. **95**, 1167 (1954). This paper will be referred to as (I).
[2] G. F. Koster, Phys. Rev. **95**, 1436 (1954). This paper will be referred to as (II).
[3] G. H. Wannier, Phys. Rev. **52**, 191 (1937).

section to a perturbative potential which extends over only one lattice site. If we call the perturbative potential $V(\mathbf{r})$, this means that the only nonvanishing matrix component of the perturbative potential is

$$V(0)=\int a(\mathbf{r}-\mathbf{0})V(\mathbf{r})a(\mathbf{r}-\mathbf{0})dv. \quad (3)$$

The perturbative potential has, for convenience, been assumed to be centered at the central lattice site.

Following the procedure outlined in an earlier paper[1] by the authors, we expand our perturbed wave function in terms of the Wannier functions of the band which we have described:

$$\psi(\mathbf{r})=\sum(p,q,r)U_{p,q,r}a(\mathbf{r}-\mathbf{R}_{p,q,r}). \quad (4)$$

ψ is the perturbed wave function and the U's are unknown coefficients which are to be determined by minimizing the expectation value of the perturbed Hamiltonian. This minimization gives rise to a set of difference equations for the U's [Eqs. (8) of (I)] which in this case reduce to

$$[\mathcal{E}(0)-E]U_{p,q,r}+\mathcal{E}(1)[U_{p+1,q,r}+U_{p-1,q,r}+U_{p,q+1,r}+U_{p,q-1,r}+U_{p,q,r+1}+U_{p,q,r-1}]=0,$$
$$\text{unless } p=q=r=0, \quad (5)$$

$$[\mathcal{E}(0)+V(0)-E]U_{0,0,0}+\mathcal{E}(1)[U_{1,0,0}+U_{-1,0,0}+U_{0,1,0}+U_{0,-1,0}+U_{0,0,1}+U_{0,0,-1}]=0.$$

E is the energy of the perturbed state. If the perturbative term were set equal to zero, the solutions to this difference equation would just give rise to the Bloch solutions to the unperturbed lattice and the energies would be just the energies in the energy band which would be given by

$$E=\mathcal{E}(0)+2\mathcal{E}(1)[\cos k_1R+\cos k_2R+\cos k_3R]. \quad (6)$$

Here k_1, k_2, k_3 can take on arbitrary values. We must now look for the solutions to the difference equations for the states when the perturbation does not vanish. Instead of solving the problem of the perturbed lattice by the method proposed in (I), we solve it in this section by direct solution of the difference equations. We do this since we shall treat in a later section the case of the finite lattice and this method of solution easily gives us the proper results for this case. In a later section, we shall solve the same problem by the method proposed in (I) which will be much simpler for the case of an infinite lattice.

Our problem has the symmetry properties of the cube, and our solution to the problem must form a basis function for one of the irreducible representations of the cubic group. We know that we are looking for a function which forms a basis for the identity representation of the cubic group. We know this because any other representation of the cubic group would have a vanishing contribution from the Wannier function at the origin and hence would not be perturbed by our localized potential. We therefore know that we are looking for a function which is an even function of p, of q, and of r. This is the same type of symmetry shown by the s function; only here since we do not have spherical symmetry, we must not expect that the function $U_{p,q,r}$ will show spherical symmetry.

The difference equations (5) fortunately can be solved, though the solution does not appear in the literature. The writers are indebted to Dr. H. C. Schweinler for pointing out that an analogous problem has been solved by McCrae and Whipple.[4] The same method of solution can be applied to the present problem. What we shall do is find solutions of the difference equations with the energy E for those equations not involving the perturbation and then form a linear combination of them to satisfy the special equation which involves the perturbation $V(0)$. For boundary conditions, we shall assume that $U_{p,q,r}$ vanishes on the faces of a cube which extends N atoms in the plus x direction and in the minus x direction and the same distances in the plus and minus y and z directions.

The method of solution introduces an apparent lack of symmetry between the three directions in space: one axis, which we shall take to be the r axis, must be treated differently from the others. Though the solution appears unsymmetrical, this is only in the way of writing it, not in the solution itself. Let us take a function

$$U_{p,q,r}=\cos\left[\frac{(2m+1)\pi}{2N}p\right]\cos\left[\frac{(2n+1)\pi}{2N}q\right]\times\sinh[(r-N)\beta], \quad r\geq 0. \quad (7)$$

Here m and n are integers which take values up to $N-1$. This function satisfies the boundary conditions in the x and y directions and also in the positive z direction. If we substitute this into the first of Eqs. (5), we find that we have a solution provided

$$E=\mathcal{E}(0)+2\mathcal{E}(1)\left\{\cos\left[\frac{(2m+1)\pi}{2N}\right]+\cos\left[\frac{(2n+1)\pi}{2N}\right]+\cosh\beta\right\}. \quad (8)$$

For a given energy value, the quantity β is determined from Eq. (8) in terms of m, n, and E. Now let us make up a solution as a sum of $(N-1)^2$ such terms, all corresponding to the same E; it will clearly be a solution of the first of Eqs. (5), and we have merely to satisfy the second. However, before we go on we must look at the symmetry properties of the solution.

The solutions in Eq. (7) have even symmetry with respect to the p and q axes. In order to give the solution

[4] W. H. McCrea and F. J. W. Whipple, Proc. Roy. Soc. Edinburgh, **60**, 281 (1940).

the proper symmetry with respect to the r axis, we must for negative values of r replace $\sinh(r-N)\beta$ by $\sinh(-r-N)\beta$. We shall then have a condition of joining these two solutions along the plane $r=0$, as well as the condition which we must satisfy at $p=q=r=0$. We can now write our solution in the form

$$U_{p,q,r}=\sum(m,n)c(m,n)\cos\left[\frac{(2m+1)\pi}{2N}p\right]\times\cos\left[\frac{(2n+1)\pi}{2N}q\right]\sinh[(r-N)\beta],\quad r\geqslant 0. \quad (9)$$

In the summation, m and n are to run up to the values $N-1$, and the c's are coefficients to be determined. The solution above applies only when $r\geqslant 0$; for negative r we use $\sinh[(-r-N)\beta]$. The quantity β is to be determined in terms of m and n by the use of Eq. (8). We shall now apply the condition of continuity over the plane $r=0$, but for the case where p and q are not both equal to zero.

To do this we substitute Eq. (9) into the first equation of (5), for the special case where $r=0$, remembering the situation for negative r's. We find at once that the result, when we make use of Eq. (7), reduces to the statement that the expression in Eq. (9), computed for $r=-1$, must equal the same expression computed for $r=1$. In other words, though the expansion in Eq. (9) is correct only for positive r's, this shows that it must still converge for $r=-1$ (so long as we do not have $p=q=0$), and must give the correct value at such a point. We can then write this condition in the form

$$\sum(m,n)c(m,n)\cos\left[\frac{(2m+1)\pi}{2N}p\right]\cos\left[\frac{(2n+1)\pi}{2N}q\right]\times\cosh N\beta\sinh\beta=0. \quad (10)$$

We shall now show that all such equations, provided p and q are not both zero, can be satisfied by the assumption,

$$c(m,n)=1/(\cosh N\beta\sinh\beta), \quad (11)$$

where β is defined in rerms of m and n by Eq. (8).

To do this we note that in case Eq. (11) holds the summation in Eq. (10) becomes $\sum(m,n)\cos[(2m+1)\pi/2N]\cos[(2n+1)\pi/2N]$. Such a sum is immediately shown to be zero on account of the familiar theorems on the orthogonality of the cosine functions. We thus see that our expression (9), in which the c's are given by Eq. (11), forms an exact solution to our difference equations (5) everywhere, except that we have not yet considered the point $p=q=r=0$.

If we substitute our solution in the second of Eqs. (5) and make use of (8) we find that we must have

$$V(0)\sum(m,n)[\sinh N\beta]/[\cosh N\beta\sinh\beta]=2N^2\mathcal{E}(1). \quad (12)$$

The quantity being summed depends on m and n through the relation in Eq. (8). This is the eigenvalue condition which determines the energy as a function of the perturbative potential $V(0)$. We shall now go on and let our lattice become infinite to see how this modifies our expressions.

If we allow N to become infinite, Eq. (12) reduces to

$$V(0)\sum(m,n)1/\sinh\beta=2N^2\mathcal{E}(1). \quad (13)$$

We can now replace the summations over m and n by integrations over continuous variables α_1 and α_2. If we do this, and also express the sinh in (13) in terms of the cosh, and the cosh in terms of $\alpha_1=(2m+1)\pi/2N$ and $\alpha_2=(2n+1)\pi/2N$ through the use of (8), we obtain for the eigenvalue condition (13) the result that

$$\frac{V}{\pi^2}\int_0^\pi d\alpha_1\int_0^\pi d\alpha_2\left[\left(\frac{E-\mathcal{E}(0)}{2\mathcal{E}(1)}-\cos\alpha_1-\cos\alpha_2\right)^2-1\right]^{-\frac{1}{2}}=2\mathcal{E}(1). \quad (14)$$

The wave function can also be expressed in terms of an integral by substituting (11) into (9) and passing to the limit as N becomes infinite. In this case the wave function $U_{p,q,r}$ would be proportional to

$$\int_0^\pi d\alpha_1\int_0^\pi d\alpha_2\frac{\cos\alpha_1 p\,\cos\alpha_2 q e^{-r\beta}}{\sinh\beta}, \quad (15)$$

where once again β must be expressed in terms of α_1 and α_2 through the energy expression. We shall defer the study of the wave function and the energy until the next section where we shall formulate the same problem in terms of the method of solution proposed in (I).

III. SOLUTION OF THE PROBLEM BY MEANS OF THE GREEN'S FUNCTION FOR DIFFERENCE EQUATIONS

In this section, we shall solve the difference equations for the infinite perturbed lattice by means of the method proposed in (I). In that paper, we have discussed just the case of a perturbation localized on one lattice site. If we apply the results for the wave function summed up in Eq. (42) of (I) and for the eigenvalue condition summed up in Eq. (43) of (I), we get in our case for the wave function,

$$U_{p,q,r}=(1/N)V(0)\sum(\mathbf{k})[\exp(i\mathbf{k}\cdot\mathbf{R}_{p,q,r})]/[E-E(\mathbf{k})]U(0), \quad (16)$$

and for the condition determining the energy,

$$(V(0)/N)\sum(\mathbf{k})[E-E(\mathbf{k})]^{-1}=1. \quad (17)$$

In these expressions, the energies $E(\mathbf{k})$ are given by Eq. (6) of this paper. If we replace k_1R, k_2R and k_3R by α_1, α_2, and α_3, respectively, we can convert these

summations to integrations over the α's. If this is done, the solutions to the difference equations are given by

$$U_{p,q,r}=\frac{V(0)}{\pi^3}\int_0^\pi d\alpha_1\int_0^\pi d\alpha_2\int_0^\pi d\alpha_3 \times\frac{\cos p\alpha_1\cos q\alpha_2\cos r\alpha_3}{E-\mathcal{E}(0)-2\mathcal{E}(1)[\cos\alpha_1+\cos\alpha_2+\cos\alpha_3]}U(0), \quad (18)$$

and the eigenvalue conditions become

$$\frac{V(0)}{\pi^3}\int_0^\pi d\alpha_1\int_0^\pi d\alpha_2\int_0^\pi d\alpha_3\{E-\mathcal{E}(0) -2\mathcal{E}(1)[\cos\alpha_1+\cos\alpha_2+\cos\alpha_3]\}^{-1}=1. \quad (19)$$

The eigenvalue condition when written in this form looks different from the eigenvalue condition expressed in Eq. (14). It is easy to show, however, that by integration over α_3, Eq. (14) may be obtained from Eq. (18). The integration over α_3 is a simple integral.

The wave function and eigenvalue condition could be evaluated by numerical integration in the form indicated. This however is not a convenient form in which to do the integrals. In the Appendix, we show a method by which these conditions can be rewritten which will reduce both of these integrals to single integrals. Taking the results from the Appendix we find that the solution to the difference equations is given by

$$U_{p,q,r}=V'(0)U(0)\int_0^\infty e^{-E't}I_p(t)I_q(t)I_r(t)dt, \quad (20)$$

and the eigenvalue condition by

$$V'(0)\int_0^\infty e^{-E't}[I_0(t)]^3dt=1. \quad (21)$$

The I's are the Bessel functions of imaginary argument and we have let

$$V'(0)=V(0)/2\mathcal{E}(1) \quad \text{and} \quad E'=[E-\mathcal{E}(0)]/2\mathcal{E}(1).$$

This is a more convenient form in which to do the integrals and they can easily be done numerically.

We are now in a position to study the dependence of the energy E' on the perturbative potential $V'(0)$. We first notice that if the energy E' is greater than 3, the integral (21) diverges. This can most easily be seen by considering the asymptotic form of the function $I_0(t)$. For large values of t, the asymptotic form of $I_0(t)$ contains a factor e^t. This means that the integrand in (21) will go as $\exp[(3-E')t]$. Thus for $E'<3$ the integrand will become infinite as we approach the upper limit and the integral will diverge. This result can also be seen by consideration of the integral in the form (14). In this case for $E'<3$ the integrand will develop a singularity which makes the integral infinite.

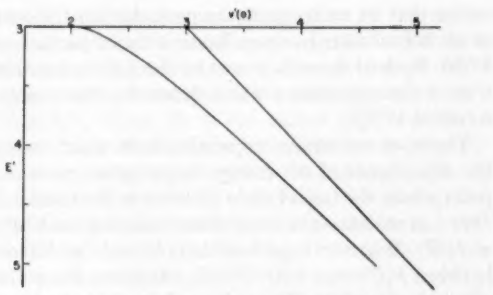

FIG. 1. Energy of bound state as a function of perturbative potential.

Thus for this case there is no solution to our problem. The case where $E'=3$ is easy to interpret. This corresponds to the case $E=\mathcal{E}(0)+6\mathcal{E}(1)$, which is the value of the energy at the center of the Brillouin zone, from (6). If $\mathcal{E}(1)$ is positive, this is the top of the energy band, and in this case we find a discrete state only when E is above the top of the band; when $\mathcal{E}(1)$ is negative, it is the bottom of the band, and we have a discrete state only below the bottom of the band. This of course is as it should be. Since the integral in Eq. (21) is positive by its definition, this means that from Eq. (21) we have a solution when $V(0)$ has the same sign as $\mathcal{E}(1)$ [$V'(0)$ positive]. We shall not take up the opposite case, where the discrete level appears at the value of energy corresponding to the corner of the Brillouin zone rather than the center, but it can easily be handled by putting in a change in the sign of the U's associated with adjacent lattice points.

The value of the integral in Eq. (21), when carried out numerically for the case $E'=3$, turns out to be 0.4990. As the value of E' increases above three the value of the integral decreases. Thus in order to satisfy Eq. (21) the perturbative potential $V'(0)$ must increase. In other words, in order to have a discrete state, $V(0)$ must be at least equal to $2\mathcal{E}(1)/0.4990$, which is approximately $4\mathcal{E}(1)$. That is, from the difference equations we have shown that there is no discrete state unless the perturbative potential is greater than a critical value. Furthermore, we have been able to evaluate this critical value, for the simple cubic lattice with nearest neighbor interaction. The total width of the band in this case is $12\mathcal{E}(1)$ [since each of the cosines in the energy expression (6) can go through the values from -1 to 1]. In other words, the quantity $V(0)$ must be equal to at least a third of the width of the band, in order that there be a discrete state.

In addition to the value $E'=3$, the integral in Eq. (21) has been carried out for a number of other values of E' greater than three in order to study the dependence of energy of the bound state on the perturbative potential. In Fig. 1 we plot the energy of the bound state E' in terms of the perturbative potential $V'(0)$. We notice that in the graph the bound state appears to leave the graph quadratically with the perturbation. We also

notice that as we increase the perturbation the energy of the bound state becomes linear with the perturbation $V'(0)$. Both of these facts can be checked by consideration of the expressions which determine the energy in terms of $V'(0)$.

The most convenient expression from which to study the dependence of the energy on perturbation near the point where the bound state first leaves the band is Eq. (19). Let us define the integral which multiplies $V'(0)/\pi^3$ as $I(E')$. What we must first do is to find the difference between $I(E')$ and $I(3)$. $I(3)$ is, of course, the value of the integral which determines the value of the perturbation which first gives rise to a bound state. By comparison with Eq. (21), we see that $I(3)=\pi^3(0.4990)$. From Eq. (19) we see that the aforementioned difference is given by

$$I(E')-I(3)=\int_0^\pi d\alpha_1\int_0^\pi d\alpha_2\int_0^\pi d\alpha_3 \times\{[E'-\cos\alpha_1-\cos\alpha_2-\cos\alpha_3]^{-1} -[3-\cos\alpha_1-\cos\alpha_2-\cos\alpha_3]^{-1}\}. \quad (22)$$

We are to study this difference for values of E' very close to 3. Because of this the principal contribution to this difference will come from values of α_1, α_2, and α_3 very close to zero. We shall expand the cosines in terms of the first two terms of their power series and introduce polar coordinates in the space of α_1, α_2, and α_3, defining $r^2=\alpha_1^2+\alpha_2^2+\alpha_3^2$. If this is done, Eq. (22) can be rewritten as

$$I(E')-I(3)=(4\pi/8)\int_0^\infty\{[E'-3+r^2/2]^{-1} -(\tfrac{1}{2}r^2)^{-1}\}r^2dr. \quad (23)$$

We have extended the upper limit to infinity since we know that the principal contribution to this integral comes from small values of the argument on account of the small size of $E'=3$. In Eq. (23), the fractions can be given a common denominator. When this is done, the integral reduces to an elementary integral which gives the result:

$$I'(E)-I(3)=(-\pi^2/\sqrt{2})(E'-3)^{\frac{1}{2}}. \quad (24)$$

Let us now substitute this result into the eigenvalue condition (19):

$$[V'(0)/\pi^3][-(\pi^2/\sqrt{2})(E'-3)^{\frac{1}{2}}+I(3)]=1. \quad (25)$$

We can now solve this relation for $E'-3$ in order to obtain the result:

$$E'-3=2\pi^2\{1/V'(0)-I(3)/\pi^3\}^2. \quad (26)$$

The second term in the curly brackets we recognize as the value $V'(0)$ of the perturbation potential which first produces a bound state. Since the value of $V'(0)$ for a value of energy near 3 will differ from this by a small quantity this expression can be rewritten (correct to terms of the second order)

$$E'-3=2\pi^2(I(3)/\pi^3)^4\{V'(0)-\pi^3/I(3)\}^2. \quad (27)$$

We have thus demonstrated our contention that the energy of the bound state behaves quadratically with the perturbative potential as the bound state leaves the bottom of the band. Of course, this quadratic dependence is with the difference between the potential and the value of the potential that first produces a bound state.

We are also interested in the dependence of the energy on perturbation for large values of E'. Returning to Eq. (19) the integrand is seen to become essentially independent of the α's for large values of E'. Thus, in this case, Eq. (19) reduces to

$$[V'(0)/\pi^3][\pi^3/E']=1, \quad V'(0)=E'. \quad (28)$$

We have plotted the straight line defined by Eq. (28) in Fig. 1 and it can be seen that the curve of energy *versus* perturbation approaches this straight line asymptotically for large values of $V'(0)$.

We have now completed the discussion of the dependence of the energy on the perturbing potential. In the next section, we shall study the dependence of the wave function on the perturbative potential and compare these results with those of the differential equation approach to the impurity problem.

IV. THE WAVE FUNCTION FOR THE IMPURITY LEVEL

In this section, we shall study the wave function of the bound state as expressed in terms of the coefficients of the Wannier functions. These coefficients are given by either Eq. (15), (18), or (20). Before we give the results of these computations it is instructive to do the problem by the differential equation approach in order to have an approximate solution with which we can compare our exact solution. This differential equation approach was briefly described in (I) and we shall make use of the equations as written there.

The coefficients of the Wannier functions $U_{p,q,r}$ when expressed as a function of the continuous variables p, q, and r can be shown to satisfy approximately the differential equation,

$$\frac{-h^2}{8\pi^2m}\nabla^2U+[E_0+V(\mathbf{r})]U=EU. \quad (29)$$

This is essentially Eq. (12) of (I). We have specialized that equation to the case at hand. For our case, near $\mathbf{k}=0$ there is only one effective mass since for small values of $\mathbf{k}$ the band is spherically symmetric. E_0 is the value of the energy at the bottom of the band and $V(\mathbf{r})$ is the perturbing potential. In the problem as solved by the difference equations, the only property of this potential that we have used is the fact that it only has matrix elements between two Wannier functions

located at the central lattice site. In order to carry out this differential equation approach, we must specify this potential in more detail. We shall assume that it is a three-dimensional square well.

If we look for a solution of Eq. (29) which is independent of angle, the radial Schrödinger function will satisfy the equation,

$$\frac{-h^2}{8\pi^2 m}\frac{d^2}{dr^2}(rU)+VrU=ErU. \tag{30}$$

We have adjusted our zero of energy to lie at the bottom of the band. Now if V is zero, as we have outside our potential well, the quantity rU satisfies the differential equation for a free particle, so that it can be written in the form $\exp(ikr)$, where $k=(2\pi/h)(2mE)^{\frac{1}{2}}$. Inside the potential well, in a similar way, where we shall assume the potential energy to be $-V_0$, we have a solution of the form $\exp(ik_0r)$, where $k_0=(2/h)(2m(E+V_0)^{\frac{1}{2}})$. For a bound state, we must assume that $E+V_0$ is positive, but that E, the kinetic energy outside the potential well, is negative. Inside, then, we must use the solution $rU=\sin k_0r$; for only by using such a solution will the actual wave function U be finite at the origin. We must use outside a solution $\exp(-\gamma r)$, where $\gamma=(2\pi/h)\times(-2mE)^{\frac{1}{2}}$, the energy being negative. These two functions must join smoothly at the boundary of the well. Now the exponential must be sloping down at the boundary of the well, or in the limit where γ is very small it will have a horizontal tangent. Thus we cannot join the functions smoothly unless the sine function has gone through at least a quarter wavelength within the well, so as to rise to its first maximum at the boundary of the well. In this limit, then, where E is zero, and the wavelength within the well is $h(2mV_0)^{-\frac{1}{2}}$, the condition for the existence of a bound state is that $4R_0$ should be at least a wavelength, or that V_0 must be at least $h^2/(32mR_0^2)$. (R_0 is the radius of the square well.) The fact that the differential equation approach gives a finite value of the perturbation necessary for the appearance of a bound state agrees with the result of the last section. Actually, closer examination of this approach would even show that for small increases of V_0 over the critical value, the energy will be proportional to $(V_0-V_{\text{crit}})^2$, but at sufficiently great V_0, the energy will be proportional to V_0. The wave function will become more and more concentrated in the potential well as V_0 increases, falling off more and more rapidly in the exponential region outside the well, where it has the form $\exp(-\gamma r)/r$. Finally, for an extremely deep well, the wave function will be negligible outside the well, and will become identical with that of a particle in a well with infinitely high barriers at the boundary.

Before going on to a detailed discussion of the wave function, it is interesting, though probably not very significant, to compare the condition for the critical value of $V(0)$ which we find from the difference equation approach with the corresponding value for the square potential well and Schrödinger's equation. We have seen that in that case we have a discrete state provided V_0, the depth of the potential well, is greater than $h^2/(32mR_0^2)$, where R_0 is the radius of the well. To compare these, we must first substitute for the effective mass: if the energy as a function of $\mathbf{k}$ is given by Eq. (6) then the effective mass is $-h^2/2\mathcal{S}(1)R^2$ (the negative sign because it is positive at the bottom of a band, which comes at $k=0$ is $\mathcal{S}(1)$ is negative). If we had a Schrödinger equation with this effective mass, then, we find that the critical value of V_0 is $(\pi^2/4)(R^2/R_0^2)\mathcal{S}(1)$. We may ask what value R_0, the radius of the square well, must be, in order that this critical value of V_0 should agree with $4\mathcal{S}(1)$, the approximate critical value of $V(0)$. Clearly $R_0=(\pi/4)R$, so that R_0 is of atomic dimensions, R being the interatomic distance in the simple cubic lattice. The volume of the sphere within which the potential is V_0 is $(4\pi/3)R_0^3$, which equals $(\pi^4/48)R^3$, or roughly $2R^3$, or twice the volume per atom in the simple cubic lattice. It seems likely, therefore, that the solution of Schrödinger's equation for such a potential well might give a fair approximation to the solution of the difference equations.

In order to calculate the coefficients of the Wannier functions ($U_{p,q,r}$), we shall use the form in Eq. (20). We shall not present here the normalized values of the coefficients $U_{p,q,r}$ but instead the values of the integral in Eq. (20), namely

$$\int_0^\infty e^{-E't}I_p(t)I_q(t)I_r(t)dt. \tag{31}$$

For any given value of E' this gives the proper dependence of the coefficients of the distance from the origin. It does not however (since the wave function is not normalized) give the proper dependence of a given coefficient on the energy. In Table I we give the results of the calculation of the quantity in Eq. (31) carried out numerically using Simpson's rule. The table gives the values of the quantity in Eq. (31) for points along the x direction where y and z are equal to zero, for a number of values of the energy. From Fig. 1 we can of course get the corresponding value of the perturbing potential. In Fig. 2, we plot the quantity $pU_{p,0,0}/U_{1,0,0}$ as a function of p for various values of E' on semilog paper. With this type of plot we can compare the results of our rigorous solution of the difference equations with the results of the differential equation approach.

TABLE I. $\int_0^\infty dt e^{-E't}[I_0(t)]^3 I_p(t)$ as a function of E' and p.

p \ E'	3.0	3.1	3.2	3.5	4.2	5.0
0	0.4990	0.4311	0.4001	0.3410	0.2646	0.2137
1	0.1658	0.1123	0.0935	0.0645	0.0371	0.0238
2	0.0778	0.0376	0.0270	0.0141	0.00564	0.00278
3	0.0501	0.0154	0.00929	0.00350	0.000924	0.000343
4	0.0411	0.00717	0.00365	0.000964	0.000162	0.0000439

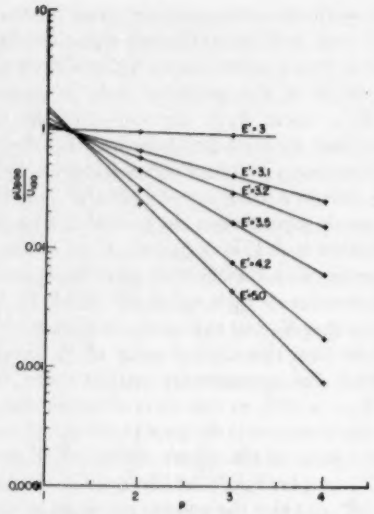

FIG. 2. Coefficients of the Wannier function in the (100) direction ($p(U_{p,0,0}/U_{1,0,0})$) as a function of p for various values of E'.

We have seen above that the differential equation approach would give as the wave function $\exp(-\gamma r)/r$. This would mean that if the exact solutions of the difference equations were well approximated by the solution of the differential equation when these results were plotted semilogarithmically, as they are in Fig. 2, the result would be a straight line. We have not plotted the points $U_{0,0,0}$ since the differential equation solution which falls off exponentially does not apply at this point. We notice that for $E'=3$ the graph is very nearly linear and horizontal. This is what would be predicted by the differential equation approach ($\gamma=0$). For $E'>3$ the linearity becomes quite good for points removed from the impurity atom (i.e., $p=2$, 3, 4 lie nearly on a straight line). We can actually compare these results with another approximation which we mentioned in (I).

In (I) we expanded the denominator in the expression for the Green's function in a power series in $\mathbf{k}$. This type of expansion would give an approximation to the solution of the difference equations for the values of the energy close to the point where the bound state appears beneath the band. This resulting approximate form of the Green's function is Eq. (46) of (I). If we specialize this expression to the case we consider in this paper, we get the result that

$$U_{p,q,r} \approx (p^2+q^2+r^2)^{-\frac{1}{2}} \times \exp\{-[2(E'-3)]^{\frac{1}{2}}[p^2+q^2+r^2]^{\frac{1}{2}}\}. \quad (32)$$

We notice that this result agrees in form with the result of the differential equation approach. It is based however on the difference equation approach since it involves an approximation to the Green's function. Furthermore, in order to derive this expression no assumption had to be made about the form of the potential besides those made in the original difference equations. This expression also gives the dependence of the falloff of the wave function with distance on the energy. We can actually compare the slopes on the semilog plot with those approximated by the expression (32). Equation (32) predicts a slope,

$$(\log_{10}e)/[2(E'-3)]^{\frac{1}{2}}. \quad (33)$$

For $E'=3.1$ this gives a value 0.193; for $E'=3.2$ the value is 0.275. The corresponding slopes calculated from the actual values of $U_{p,0,0}$ are 0.209 for $E'=3.1$ and 0.285 for $E'=3.2$. We can see therefore that the approximation to the slope gives a value to within 5 percent of the true value.

We also notice that both Eq. (32) and the differential equation approach make an additional prediction about the wave function. These expressions predict that the solutions of the difference equations should be spherically symmetric. In order to check this dependence on angle, for $E'=3.5$ we have computed the values of (31) for other directions than the 100 direction. The results are given in Table II. We have plotted in Fig. 3

$$(p^2+q^2+r^2)^{\frac{1}{2}}\int_0^\infty e^{-E't}I_p(t)I_q(t)I_r(t)dt,$$

which is proportional to the distance from the origin multiplied by $U_{p,q,r}$, *versus* the distance from the origin $[(p^2+q^2+r^2)^{\frac{1}{2}}]$. The plot is again on semilog paper. The straight line in the plot connects the points in the 100 direction. If the approximate expressions were valid and the coefficients of the Wannier function did display spherical symmetry, then all the points in the graph would be on a single straight line. It is clear from the graph that this is not the case. The approximate expression seems to give the proper dependence on

TABLE II. $I_{p,q,r}=\int_0^\infty dt e^{-E't}I_p(t)I_q(t)I_r(t)$ for $E'=3.5$ as a function of p, q, and r.

p	q	r	$I_{p,q,r}$
0	0	0	0.3410
0	0	1	0.0645
0	0	2	0.0141
0	0	3	0.00350
0	0	4	0.000964
0	1	1	0.0242
0	1	2	0.00765
0	1	3	0.00236
0	2	2	0.00318
0	2	3	0.00120
0	3	3	0.000527
1	1	1	0.0125
1	1	2	0.00486
1	1	3	0.00172
1	2	2	0.00228
1	2	3	0.000935
1	3	3	0.000435
2	2	2	0.00122
2	2	3	0.000553
2	3	3	0.000277
3	3	3	0.000150

distance in a given direction but fails to give the proper dependence on direction. We can, therefore, see from this simple example that the differential equation approach gives results that are qualitatively correct but faulty in some of the aspects of the wave function.

In all of the preceding we have assumed that the perturbative potential extends over only one lattice site. This is, of course, a rather unrealistic assumption. It has, in addition, the bad feature that the only bound state is a state which is completely symmetric under the operations of the point group. In order to have bound states with higher types of symmetry, we must have our perturbative potential extend over more lattice sites. In the next section we shall carry out the impurity problem for a more extended perturbation. We shall let it extend over the nearest neighbors of the central lattice site. Unfortunately, we shall have to assume a shape for the potential. This we shall do in a completely arbitrary manner, the object being to illustrate the use of the general procedure for solving for states of higher types of symmetry rather than to have a model which has any exact physical counterpart.

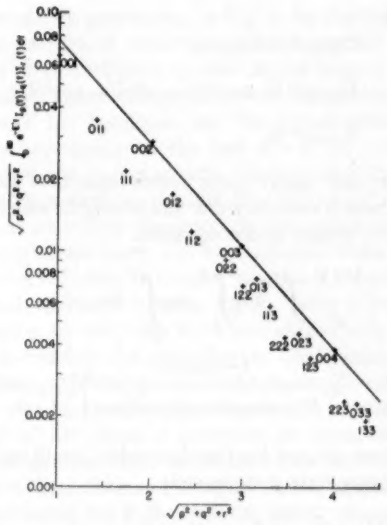

FIG. 3. The coefficients of the Wannier function times the distance from the origin as a function of the distance from the origin.

V. A MORE EXTENDED PERTURBATION

If our perturbative potential $V(\mathbf{r})$ extends over more than one lattice site, we must solve the general difference equations which are Eqs. (8) of (I). In (I) we showed that we could solve these equations in the form of Eq. (38) of that same paper. For the special case under consideration in this paper, these equations reduce to

$$U_{p,q,r}+\frac{1}{\pi^3}\sum(p',q',r',p'',q'',r'')\int_0^\pi d\alpha_1\int_0^\pi d\alpha_2\int_0^\pi d\alpha_3 \times\frac{\exp i[(p-p')\alpha_1+(q-q')\alpha_2+(r-r')\alpha_3]}{E'-\cos\alpha_1-\cos\alpha_2-\cos\alpha_3} \times V'(p',q',r';p'',q'',r'')U_{p'',q'',r''}=0. \quad (34)$$

In this equation,

$$V(p',q',r';p'',q'',r'')=\frac{1}{2\mathcal{E}(1)}\int a(\mathbf{r}-\mathbf{R}_{p',q',r'})V(\mathbf{r}) \times a(\mathbf{r}-\mathbf{R}_{p'',q'',r''})dv. \quad (35)$$

We shall now specialize this relation by assuming that the only nonvanishing matrix elements of the perturbation are

$$V'(0)=\frac{1}{2\mathcal{E}(1)}\int a(\mathbf{r}-\mathbf{0})V(\mathbf{r})a(\mathbf{r}-\mathbf{0})dv,$$

$$V'(1)=\frac{1}{2\mathcal{E}(1)}\int a(\mathbf{r}-\mathbf{R}_{1,0,0})V(\mathbf{r})a(\mathbf{r}-\mathbf{R}_{1,0,0})dv \quad (36)$$

$$=\frac{1}{2\mathcal{E}(1)}\int a(\mathbf{r}-\mathbf{R}_{0,1,0})V(\mathbf{r})a(\mathbf{r}-\mathbf{R}_{0,1,0})dv$$

$$=\text{etc.}$$

The "etc." in the last equation means that there are further nonvanishing matrix elements where both Wannier functions are located at the six nearest neighbors of the central atom and that the values of these matrix elements are the same as those which are indicated. We have assumed that our potential has full cubic symmetry and that there are only two distinct nonvanishing matrix elements of our perturbation; $V'(0)$ and $V'(1)$. From this we can conclude that the solutions of this perturbed periodic potential problem must form bases for the irreducible representations of the full cubic group.

In (I), we saw that the method of solving the set of simultaneous equations embodied in Eq. (34) of this paper was to cause the determinant of the coefficients of the U's to vanish for those U's which were associated with the lattice sites over which the perturbation extends. In the case of the perturbative potential of limited range which we set up in the last paragraph, this would mean that we would have to solve a set of simultaneous linear homogeneous equations of the seventh order. This is because $V(r)$ only has matrix elements for Wannier functions on the central lattice site and the six nearest neighbors. Symmetry further reduces the order of this set of equations since we know that the wave functions must form bases for irreducible representations of the full cubic group.

Let us first look for those solutions which have the symmetry of the p states with respect to the cubic group. This implies a certain relation between the U's. Let us set up the state which has the symmetry of the z-like p state. (The p states are of course triply degenerate, the y-like and the z-like being degenerate with the x-like.) The relations that this implies between our

U's are

$$U_{0,0,1}=-U_{0,0,-1},$$
$$U_{1,0,0}=U_{-1,0,0}=U_{0,1,0}=U_{0,-1,0}=0, \quad (37)$$
$$U_{0,0,0}=0.$$

We can now insert these restrictions into Eq. (34). Since there is now only one independent coefficient, the Eqs. (34) reduce to one equation.

$$U_{0,0,1}-\left\{\frac{V'(1)}{\pi^3}\int_0^\pi d\alpha_1\int_0^\pi d\alpha_2\int_0^\pi d\alpha_3 \times\frac{1-\cos2\alpha_3}{E'-\cos\alpha_1-\cos\alpha_2-\cos\alpha_3}\right\}U_{0,0,1}=0. \quad (38)$$

This gives at once for the eigenvalue condition for the triply degenerate p states that

$$1=\frac{V'(1)}{\pi^3}\int_0^\pi d\alpha_1\int_0^\pi d\alpha_2\int_0^\pi d\alpha_3 \times\frac{1-\cos2\alpha_3}{E'-\cos\alpha_1-\cos\alpha_2-\cos\alpha_3}. \quad (39)$$

We can of course carry out the same process which brought us from Eq. (18) to Eq. (20) and finally express the eigenvalue condition in the form,

$$V'(1)\int_0^\infty e^{-E't}\{[I_0(t)]^3-[I_0(t)]^2I_2(t)\}dt=1. \quad (40)$$

In (I) we also showed that the wave function for regions beyond the extent of the perturbation was expressible in terms of the coefficients of the Wannier functions within the region of the perturbation. In the case at hand, for the p states, this would mean that

$$U_{p,q,r}=V'(1)U_{0,0,1}\int_0^\infty e^{-E't}\{I_{r-1}(t)-I_{r+1}(t)\} \times I_q(t)I_p(t)dt. \quad (41)$$

Using the fact that $I_n(t)=I_{-n}(t)$, we can easily show that the solution to the difference equations (41) shows the symmetry of a p state with z-like symmetry. The states degenerate with this state can be obtained by permuting the indices p, q, and r.

We know that there are two d-like irreducible representations to the cubic group. We can look for bound states of these symmetries. The first are the d functions with symmetry properties like xy, xz, and yz. If we determine the relations between values of the coefficients of the Wannier functions for the seven lattice sites over which the perturbation extends for this type of symmetry, we find that all seven coefficients vanish. This means that there is no triply degenerate d-like bound state.

The other representation of the cubic group with d-like symmetry is doubly degenerate and has basis functions which transform as x^2-y^2 and $3z^2-r^2$. Let us consider the partner in this irreducible representation which has x^2-y^2-like symmetry. The relations between the seven coefficients of the Wannier functions which this symmetry induces are

$$U_{0,0,1}=U_{0,0,-1}=U_{0,0,0}=0,$$
$$U_{1,0,0}=U_{-1,0,0}=U_{0,1,0}=-U_{0,-1,0}. \quad (42)$$

If we use these relations in Eq. (34), we notice that we only have one independent coefficient of the seven under consideration. We can proceed as we did for the p-like states and obtain for the eigenvalue condition,

$$V'(1)\int_0^\infty e^{-E't}I_0(t)\{[I_0(t)]^2+I_2(t)I_0(t) -2[I_1(t)]^2\}dt=1. \quad (43)$$

We can also, once again, write the solutions of the difference equations in terms of the coefficients of the Wannier functions for those lattice sites over which the impurity extends. For the x^2-y^2 states this gives us

$$U_{p,q,r}=V'(1)U_{1,0,0}\int_0^\infty e^{-E't}\{I_{p-1}(t)I_q(t)I_r(t) +I_{p+1}(t)I_q(t)I_r(t)-I_p(t)I_{q+1}(t)I_r(t) -I_p(t)I_{q-1}(t)I_r(t)\}dt. \quad (44)$$

The other partner in this irreducible representation would of course have the same eigenvalue condition, but the solutions to the difference equations would be given by

$$U_{p,q,r}=V'(1)U_{1,0,0}\int_0^\infty e^{-E't}\{I_p(t)I_q(t)I_{r+1}(t) +I_p(t)I_q(t)I_{r-1}(t)-\tfrac{1}{2}I_{p+1}(t)I_q(t)I_r(t) -\tfrac{1}{2}I_{p-1}(t)I_q(t)I_r(t)-\tfrac{1}{2}I_p(t)I_{q+1}(t)I_r(t) -\tfrac{1}{2}I_r(t)I_{q-1}(t)I_r(t)\}dt. \quad (45)$$

This is the state with $3z^2-r^2$ symmetry.

We have now found the eigenvalue conditions for five bound states: three p-like states and two d-like states. We might expect that the solution of our simultaneous linear equations for the seven lattice sites over which the impurity extends would give rise to a total of seven states. This is indeed the case. The two solutions which we are lacking have s-like symmetry. For these solutions we can again find the relations that symmetry introduces between the coefficients of the Wannier functions. In this case they are as follows:

$$U_{1,0,0}=U_{-1,0,0}=U_{0,1,0}=U_{0,-1,0}=U_{0,0,1}=U_{0,0,-1}. \quad (46)$$

The remaining coefficient $U_{0,0,0}$ need not vanish because of symmetry. We see that for the case of s-like symmetry we have two independent coefficients instead of only one as we had for the p- and d-like states. If we now put these relations in Eq. (34), we obtain a pair of simultaneous linear equations for the two independent U's.

$$\begin{aligned}&\left\{1-V'(0)\int_0^\infty e^{-E't}[I_0(t)]^3dt\right\}U_{0,0,0}\\&-\left\{(\sqrt{6})V'(1)\int_0^\infty e^{-E't}[I_0(t)]^2I_1(t)dt\right\}U_{1,0,0}=0,\\&-\left\{(\sqrt{6})V'(0)\int_0^\infty e^{-E't}[I_0(t)]^2I_1(t)dt\right\}U_{0,0,0}\\&+\left\{1-V'(1)\left[\int_0^\infty e^{-E't}I_0(t)[I_0(t)I_0(t)\right.\right.\\&\qquad\left.\left.+I_2(t)I_0(t)+4I_1(t)I_1(t)]dt\right]\right\}U_{1,0,0}=0.\end{aligned}\tag{47}$$

In order to find the energies of the bound s-like states, we must make the determinant of the coefficients vanish. This would be done by the variation of E' giving rise to two s-like states of different energies. The solution of the difference equations for regions outside of the perturbation would take the form, in this case,

$$\begin{aligned}U_{p,q,r}=V'(0)U_{0,0,0}&\int_0^\infty e^{-E't}I_p(t)I_q(t)I_r(t)dt\\&+6V'(1)U_{1,0,0}\int_0^\infty e^{-E't}\{I_{p+1,q,r}\\&\qquad+I_{p-1,q,r}+\text{Per.}\}dt.\end{aligned}\tag{48}$$

In Eq. (48) the symbol "+Per." means that one is to add the terms with p, q, and r cyclically permuted. We can see from Eqs. (47) and (48) that if we let the perturbation extend over only one lattice site, as we did in the earlier section, we should obtain Eq. (20) for the solution of the difference equations and Eq. (21) for the eigenvalue condition. This means, of course, that we set $V'(1)$ equal to zero.

This is about as far as we can carry the discussion of the states arising from this perturbation without some further assumption. The additional assumption that we make is that there is a known ratio between $V'(0)$ and $V'(1)$. In order to calculate the energy levels of the bound states numerically, we assume that

$$V'(0)=2V'(1).\tag{49}$$

This is, of course, completely arbitrary but it will enable us to study the energies of the bound states as a function of $V'(0)$.

Using the expressions in Eqs. (40), (43), and (47) for the eigenvalue conditions we have calculated the energies of the bound states as a function of $V'(0)$. The results are shown graphically in Fig. 4. In this figure, we plot the energies of the bound states *versus* the matrix element of perturbation on the central atom $[V'(0)]$. The straight lines on the graph are the asymptotes of the energies of the bound states. The lowest s-like state becomes asymptotic to the line $E'=V'(0)$ while the energies of the higher s- and the p- and d-like states become asymptotic to the line $E'=V'(1)=\frac{1}{2}V'(0)$. We can see at once from the graph that for small values of the perturbation there will be no bound state. For a certain critical value of the perturbation a bound, s-like state will appear. For some higher value of the perturbation a second s-like state will appear as a bound state. Increasing the perturbation finally causes the appearance of bound p- and d-like states. The order in which these higher states become bound is probably a function of the shape of potential we have assumed, and is not general. Even in the model we have assumed we notice that, whereas the higher s state comes out of the band before the p-like state for higher values of the perturbative potential, it crosses over the p-like state and finally lies above this p state in energy. It always remains, however, below the d-like state.

The fact that an s state is the first one to become bound upon increasing the perturbation is not surprising, since this is the only type of symmetry which allows us to have a nonvanishing coefficient of the Wannier function at the central atom. It is this central atom which has the largest perturbation associated with it and consequently it is very favorable energetically to have the wave function with a nonvanishing value at the central lattice site. Changing the ratio of $V'(0)$ and $V'(1)$ would not have any effect on the qualitative appearance of this graph. Since the eigenvalue conditions for the bound p- and d-like states depends only on the value of $V'(1)$ increasing $V'(0)/V'(1)$ would have the effect of requiring a larger value of $V'(0)$ to cause the appearance of bound states of these symmetries. This means that the three high states s', p, and d would be shifted to the right on the graph if we increased the ratio in Eq. (49).

This completes the discussion of the bound states which appear under the assumption that our wave

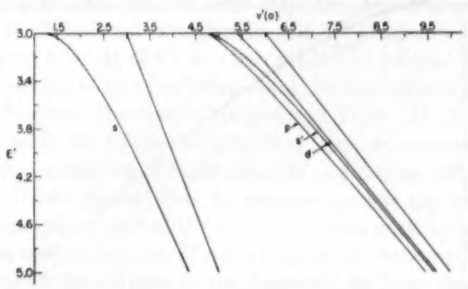

FIG. 4. Energy of the bound states of s, p, and d-like symmetry as a function of the perturbative potential.

function vanishes at infinity. In the next section, we discuss the case where we assume somewhat different boundary conditions. We shall assume that our wave function vanishes on the surface of a cube of finite size which surrounds the impurity.

VI. BOUNDARY CONDITIONS ON A FINITE CUBE

In the previous sections, we demanded that the solution for the bound state of our perturbed problem vanish at infinity. We might well ask how quickly the energies of the bound states would converge to the energy of the bound state of the infinite crystal, if we demand that our wave function vanish at the surface of a cube and then let the cube increase in size. In order to do this, we return to Eq. (5). These are the difference equations which are to be satisfied subject to the boundary condition that $U_{p,q,r}$ vanish when either p, q, or r are $\pm N$. This means we are solving the problem of an impurity which extends over only one lattice site within a box of dimensions $2N\times 2N\times 2N$. If we look back at Sec. II, we find that we have already accomplished this before we let our boundary conditions go to infinity. The eigenvalue condition for this case was given in Eq. (12). This equation can be rewritten in the form

$$V'(0)\sum_{0}^{N-1}(n)\sum_{0}^{N-1}(m)\frac{\tanh N\beta_{mn}}{\sinh\beta_{mn}}=N^2, \qquad (50)$$

where the dependence of β_{mn} on its indices is given by Eq. (8); that is,

$$\cosh\beta_{mn}=E'-\cos\frac{(2m+1)\pi}{2N}-\cos\frac{(2n+1)\pi}{2N}. \qquad (51)$$

In order to calculate the dependence of the energy on the perturbation for various values of N, all we need do is solve Eq. (51) for the various values of $\cosh\beta_{mn}$ corresponding to a given value of E' and then carry out the summation in Eq. (50) to find the value of the perturbation corresponding to this value of E'. This has been done for a number of values of N. In particular, the values of N used were 3, 6, and 10. The results are plotted in Fig. 5 where we have plotted the energy of the lowest state (bound state) as a function of the perturbative potential as well as a function of N for the values indicated. This diagram is, of course, completely analogous to Fig. 1 and we have included on this graph the case of $N=\infty$. We notice that as we increase the size of the crystal the curves approach the curve for $N=\infty$ very rapidly. The curve for $N=10$ is indistinguishable from the case of the infinite boundary conditions. We can also notice from these graphs that for larger values of the perturbation the difference between the curves for the various values of N becomes smaller and smaller.

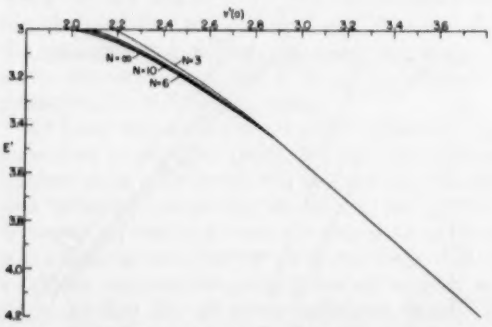

FIG. 5. Energy of the bound state as a function of perturbation for boundary conditions on a cube of half width N.

These results are not difficult to interpret. We are dealing with a bound state. This means that the wave function falls off as a function of the distance from the origin. Thus, in the case of the infinite crystal, by the time the distance from the origin is about ten lattice sites, the coefficients of the Wannier function have fallen off to essentially zero. Taking as our boundary conditions the vanishing of the wave function at any point beyond this should give the same results as the infinite case, since the wave function is essentially zero anyway. We also know that, as we increase the value of the perturbative potential, the coefficients fall off more and more rapidly as a function of distance. For the case of an infinite perturbation, the wave function of the bound state would be completely localized at the central lattice site, regardless of the size of the cube which we used for the boundary conditions. This means that, as we increase the size of the perturbation, we should expect that the value of N would make less and less difference in determining the energy of the lowest state.

These results are actually of some interest since they illustrate the validity of an approximation method. The energies which we obtained from Eq. (50) are, of course, the same as we should have obtained by solving the secular equation in Eq. (5) where we cut off the secular equation after some finite size. In this case, we let the size be $(N-2)^3$. (Symmetry would reduce this order considerably.) This is, of course, quite different from solving the determinant of the Green's function method, since this is equivalent to solving the secular equation like Eq. (5) only of infinite size. This finite secular equation forms the basis of an approximation, therefore, and we can see that this approximation will be quite good, provided the coefficients of the Wannier functions for the atoms most distant from the perturbation have dropped off to a very small value. This method of approximation is used quite often in the discussion of F-centers in alkali halides. In particular, Inui and Uemura[5] have calculated the energy levels of F-centers using just the approximation which we mentioned. They calculated these energy levels by solving the secular equation, cutting it off after some finite number of neighbors. In the case mentioned, they cut the secular equation off in one case after nearest neighbors and in

[5] T. Inui and Y. Uemura, Progr. Theoret. Phys. (Japan) **5**, 252 (1950).

another case after second nearest neighbors. From their results it appears that they are getting reasonably good results by cutting off the wave function after second nearest neighbors judging by the improvement of the second nearest neighbor results over the nearest neighbor results. This would lead one to suspect that the effect of the perturbation is sufficiently strong to make the approximation they have used quite valid.

VII. EFFECT OF THE PERTURBATION OF THE WAVE FUNCTIONS IN THE BAND

In this section, we shall discuss the case where the energy of the perturbed state lies in the allowed band of energies. This is the case where $-3 \leqslant E' \leqslant 3$. In order to do this, we shall apply the method developed in (II). If we follow the method of that paper, we assume that our solution to the difference equations consists of two parts. The first is the incident Bloch wave and the second is the wave scattered by the impurity. For the problem at hand the solution of the difference equations is given by

$$U_{p,q,r}=\exp(i\mathbf{k}\cdot\mathbf{R}_{p,q,r})+\sum(p',q',r)c_{p',q',r'} \times K_{E'}(\mathbf{R}_{p,q,r}-\mathbf{R}_{p',q',r'}). \quad (52)$$

This is Eq. (25) of (II). The c's are unknown coefficients to be determined and represent the strength of the scattered wave. The quantity $K_{E'}(\mathbf{R}_{p,q,r}-\mathbf{R}_{p',q',r'})$ is the Green's function which is useful for the case of energies lying in the band. For our simplified impurity calculation, we can see from the Appendix and (II) that this Green's function will be given by

$$K_{E'}(\mathbf{R}_{p,q,r})=(1/i)\sum(\mathbf{k})\int_0^\infty \{\exp[iEt-iE(\mathbf{k})t]\} \times\{\exp(i\mathbf{k}\cdot\mathbf{R}_{p,q,r})\}dt \quad (53)$$

$$=(N/i)\int_0^\infty dtJ_p(t)J_q(t)J_r(t)\exp[iE't].$$

In deriving this form of the Green's function we have converted the summation over $\mathbf{k}$ to an integration and have then made use of the explicit form of $E(\mathbf{k})$ given by Eq. (6) to carry out this integration in order to arrive at the Bessel functions in the right-hand side of (53).

In order to solve the scattering problem, we must find the c's. In (II) they were shown to satisfy a set of simultaneous linear inhomogeneous equations [Eq. (19) of (II)]. In this section, we shall specialize to the case of the impurity extending over only one lattice site. If this is done, the only quantity which appears of all the c's is $c_{0,0,0}=c(0)$ and this is given by the condition,

$$\left\{-N+V'(0)(N/i)\int_0^\infty dt[J_0(t)]^3\exp(iE't)\right\}c(0) =-V'(0). \quad (54)$$

TABLE III. $I_c=\int_0^\infty dt[J_0(t)]^3\cos E't$; $I_s=\int_0^\infty dt[J_0(t)]^3\sin E't$ as a function of E'.

E'	I_c	I_s
0.0	0.8963	0.0000
0.2	0.8970	0.0740
0.4	0.8967	0.1530
0.6	0.8999	0.2416
0.8	0.9071	0.3557
1.0	0.8691	0.6027
1.2	0.6171	0.6268
1.4	0.5063	0.6057
1.5	0.4631	0.5988
1.6	0.4259	0.5909
1.8	0.3602	0.5762
2.0	0.3038	0.5621
2.2	0.2537	0.5496
2.4	0.2055	0.5378
2.5	0.1826	0.5321
2.6	0.1585	0.5260
2.8	0.1062	0.5167
3.0	0.0134	0.4926

In terms of $c(0)$, the solution to the difference equations is given by

$$U_{p,q,r}=\exp(i\mathbf{k}\cdot\mathbf{R}_{p,q,r}) +c(0)(N/i)\int_0^\infty dtJ_p(t)J_q(t)J_r(t)\exp[iE't]. \quad (55)$$

We can see from this that the quantity $c(0)$ is the amplitude of the scattered wave. The square of its absolute value, which is the intensity of the scattered wave, is then given by

$$|c(0)|^2=\{[1/V'(0)-I_s]^2+I_c^2\}^{-1}. \quad (56)$$

Equation (56) was obtained from Eq. (55) and I_c and I_s are given by

$$\frac{i}{N}K_{E'}(0)=\int_0^\infty dt[J_0(t)]^3\exp(iE't)$$

$$=\int_0^\infty dt[J_0(t)]^3[\cos E't+i\sin E't]=I_c+iI_s. \quad (57)$$

The quantities I_c and I_s were approximately evaluated by the Whirlwind computer at M.I.T.[6] Simpson's rule and an interval of 0.2 in t was used. The integral was carried out to $t=48$ at which point the convergence was fairly good. The results are given in Table III. From the table, we can see at once that there is some error in the calculation of these integrals as a function of E'. In (II) we showed that for energies outside the band the imaginary part of the Green's function must vanish. This means that for $E'=3$, I_c should be zero instead of 0.013. In addition in the Appendix we have shown

[6] Availability of Digital Computer Laboratory time for this problem was made possible by the U. S. Office of Naval Research.

that for $E' \geqslant 3$ we should have the equality

$$\int_0^\infty dt e^{-E't}[J_0(t)]^3 = \frac{1}{i}\int_0^\infty dt e^{iE't}[J_0(t)]^3 = \int_0^\infty dt[J_0(t)]^3 \sin Et. \quad (58)$$

Comparison of Tables II and III shows that for $E'=3$ the integral involving the Bessel function of imaginary argument gives the value 0.4990 whereas the integral involving the Bessel function of real argument gives the value 0.4926. We see therefore that the numerical evaluation of the integrals in this section is probably accurate to within about 2 percent, but this is sufficient for our purposes. In Fig. 6 we have plotted the values of $|c(0)|^2$ as a function of the perturbation for a number of values of the energy using Eq. (56).

Let us see what we can learn about the nature of scattering in a solid from this simple example. We notice that the intensity of the scattered wave is independent of the **k** vector of the incident wave. The scattered intensity depends only on the energy of the incident wave. This result arises from the fact that our impurity extends over only one lattice site and is not peculiar to the particular form of the energy band which we have assumed in this paper. In any problem of scattering in a solid in which the impurity is localized to one lattice site, the scattered intensity will be independent of the **k** vector of the incident wave. Another feature of the intensity of the scattered wave can be seen from Fig. 6. We notice that for $E'=3$ (when the energy is at the top or bottom of the band) there is a singularity of the scattered intensity for a certain value of the perturbative potential. For $E'=3$ we notice that this singularity arises when $I_0=1/V'(0)$. This however is nothing more than the condition that a bound state appear. Thus we see that for that strength of perturbation for which a bound state can first appear at the bottom of the band the scattered intensity for energies at the bottom of the band becomes infinite.

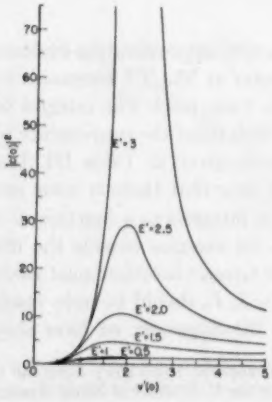

FIG. 6. Intensity of the scattered waves as a function of the perturbative potential for various values of the energy of the incident wave.

This same effect is familiar in scattering in free space. If we scatter a plane wave from a square well potential in three dimensions a similar thing happens. The scattering cross section for zero energy becomes infinite for that value of the well depth for which a bound state is first allowed.[7] We can see how this will arise even for the general case of scattering in solids.

In (II), we saw that the c's were given by the solution of the set of simultaneous equations [Eq. (19) of that paper]. The condition for the solution of this set of simultaneous inhomogeneous equations is that the determinant of the coefficients of the c's must not vanish. It has already been pointed out in that paper that for energies lying outside the bands the vanishing of this determinant is just the eivenvalue condition for the appearance of bound states. If we choose an energy at the bottom or top of a band and then vary the perturbative potential, there will be a value of this potential for which the bound state can first appear, and this value of the perturbative potential will cause the determinant of the coefficients of the c's to vanish. This will mean that the c's will become infinite as the perturbative potential approaches this value. This can most easily be seen from the well known method of expressing the solution of a set of simultaneous linear inhomogeneous equations as the ratio of two determinants. The denominator is the determinant of the coefficients of the unknowns, and the numerator is the determinant of the coefficients of the unknowns where one column has been replaced by the inhomogeneous terms. As the coefficients of the unknowns approach values which make their determinant vanish, in general the unknowns will develop singularities.

We have seen in this section that the method of treating scattering in a solid can be applied to the simplified impurity calculation presented in this paper. This example shows us that the scattering is strongest for those energies in the band which lie near the energies of the bound states which appear as a result of the perturbation. There appears to be reason to believe that this result can be generalized to more realistic impurity calculations.

VIII. DISCUSSION

From the preceding discussion, we get a fairly complete understanding of the problem of a single perturbing atom in a simple cubic lattice, and a general idea of the effect of a perturbation extending over a number of lattice sites. The results of the single perturbed atom when compared with the differential equation approach turned out to be at least qualitatively close to this approximate approach. We may assume that the same thing will hold without qualitative change in other types of lattices. We may expect, therefore, that if a perturbation extends over a number of lattice sites for

[7] N. F. Mott and H. S. Massey, *The Theory of Atomic Collisions* (Oxford University Press, London, 1949), pp. 28–38.

sufficiently large perturbations, a number of bound states will appear. As a general rule, the discussion which we have given makes it fairly plain that as the perturbative potential increases, these discrete levels may split off from the continuum successively, rather than all at once. The various wave functions will have different types of symmetry. These functions must belong to the various irreducible representations of the point symmetry group of the crystal with respect to the center of perturbation, provided the perturbation also has the symmetry of the point group of the crystal. Thus, as we have seen, if the perturbative potential and the crystal both have cubic symmetry, we shall have the various possible symmetry types of the cubic group, one being s-like, a threefold degenerate p-like type and so on. We might try to apply what we learned in our simple case to give a qualitative discussion of more physical cases. In doing so we shall repeat many things already known and discussed by other authors, but it may be useful to review their discussions in the light of what we have learned about difference equations.

The particularly interesting problem in three dimensions is the Coulomb potential. The reason for this comes from its occurrence in semiconductors. We are not going to examine the nature of the perturbing field to be expected in the various types of problems; this is a problem in self-consistent fields, rather than of solving the periodic potential problem, and we wish to separate these two parts of the question, first understanding the nature of the solutions of the one-electron Schrödinger equation before we build up determinantal many-electron wave functions and apply a condition of self-consistency. However, we may anticipate enough to state the general situation encountered when an impurity atom is introduced substitutionally into a crystal. The result is quite different, depending on whether we are dealing with a good conductor like a metal, or a poor conductor like a semiconductor. Let us assume that the impurity atom has a nuclear charge greater or less than that of the crystal by a few units. If there were no shielding, this would introduce a perturbation of the Coulomb type, which outside the impurity atom itself would be proportional to the difference between the nuclear charges of the impurity atom and the atoms of the crystal. In an actual case, most of this field will be shielded by a rearrangement of the electronic charge. There will usually be enough discrete levels with wave functions concentrated close to the impurity atom so that these levels can be occupied by electrons, or emptied, as the case may be, to make the impurity atom approximately uncharged. In a good conductor, the conduction electrons will rearrange their charge distributions so as to shield this Coulomb potential almost completely, just as any electric field in a metal is almost completely neutralized by the conduction electrons. Ordinarily in a metal, then, the perturbative potential arising from the self-consistent problem is confined almost entirely to the perturbing atom. In other words, we have almost precisely the case which we have been taking up in this paper, leading to discrete levels if the perturbative term $V(0)$ is great enough, but to no new energy levels if it is below a critical value.

An impurity atom in a metal, as we have just stated, has its field almost completely neutralized even at the position of its nearest neighbors by the conductivity, just as we should conclude from looking at the electrical properties of a metal from the macroscopic point of view. In a semiconductor, on the contrary, the conductivity is not great enough for this to happen, and the problem is much more like the electrostatic one of a charge in a dielectric. The dielectric constants of some of the important semiconductors are very high, that of germanium being of the order of magnitude of 16. The electric field of a point charge in such a dielectric will be less than in empty space, being inversely proportional to the dielectric constant. This dielectric constant is itself a manifestation of the self-consistent field. If we look at it microscopically, we see that the charge polarizes all the surrounding atoms, displacing their electrons with respect to their nuclei so as to produce dipoles on them; and it is well known that it is the superposition of the fields of these dipoles which cancels most of the field of the polarizing charge. We should get at this effect, in a completely logical treatment of our problem, by solving for the wave functions of the polarized atoms in the external polarizing field, which would be part of the self-consistent field, and by making the problem self-consistent, which would imply that each atom had just such a dipole moment that the sums of these dipole fields produce the dielectric effect by simple electrostatics. Ordinarily, however, we are willing not to look into the problem in such a fundamental way, but to accept the value of the macroscopic dielectric constant as being given, and to assume that it correctly describes the self-consistent effect of the polarizing charge in the dielectric.

We conclude, then, that if a dielectric contains an impurity atom which normally has an excess or deficiency of charge, the potential produced by this atom at a distance will be that produced by its net charge, computed for the actual dielectric constant. That is, we shall have a Coulomb potential, but one ordinarily a good deal less in magnitude than in free space, on account of the large dielectric constant. We might thus assume that it is a fairly good approximation to replace our difference equations by the approximate differential equation. We shall then have Schrödinger's equation for a hydrogen-like problem, but with a potential decreased in proportion to the dielectric constant, and an effective mass instead of the real mass. The solutions will then be the ordinary hydrogenic solutions, but the wave functions will be much more spread out, and the energies will be less. In this case we have an infinite number of stationary states, instead of a finite number as with the perturbation located only on a finite number of lattice

sites. Furthermore, we do not have any critical lower limit for the magnitude of the perturbation potential, below which we do not find discrete states; that is a characteristic of the problem where the perturbations are confined to a finite number of atoms.

We also find something in the Coulomb case which we do not in the case of a single perturbing atom: The differential equation forms a good approximation to the solution of the difference equations. The reason is that in this case the solution really varies slowly from atom to atom, and we have seen in (I) that this is the condition for the applicability of the differential equation method. Thus, for the ground state of hydrogen, the wave function is $\exp(-\gamma r)$, which remains finite at $r=0$, and varies slowly from atom to atom, if γR is small compared to unity, where R is the interatomic distance. We have this situation in the cases we are interested in. This is in striking contrast to the case of a single perturbing atom, where we have seen that the wave function is of the form $[\exp(-\gamma r)]/r$. We can thus feel that the conventional derivation of the impurity levels in a semiconductor, on the basis of the hydrogenic wave function, is generally legitimate.

There is, however, a feature of the situation which has generally been overlooked, and which can be very important. The dielectric effect shields the field of the perturbing atom at the positions of all of the neighbors, but does not affect the perturbative potential on the perturbing atom itself. In other words, the perturbation $V(0)$, the average of the perturbative potential over the Wannier function located on the impurity atom, can be just as great in a semiconductor as in a metal. This is larger than the value which would be consistent with the hydrogenic problem, roughly in the ratio of the dielectric constant. In other words, the Schrödinger problem which is really appropriate in this case is one with a Coulomb potential at all neighboring atoms, with a dielectric term to make it small, but in addition a potential well at the central atom. We may now legitimately combine the types of arguments which we have used in discussing the potential well problem, and the Coulomb problem. We may assume that unless the potential well becomes too deep, exceeding a critical value, the wave function and energy level will not be appreciably affected by it. In other words, it is likely that the hydrogenic wave function and energy level corresponding to the Coulomb potential can, so to speak, resist the effect of a perturbation on the central atom, provided this perturbation is not too large. The wave function will be modified in the immediate neighborhood of the central atom, but it extends over so many atoms that this modification is not very important, and will not change the energy very much. If the perturbation of the central atom becomes too great, however, the problem will change completely. The energy level will fall far below the hydrogenic value (we are assuming that the perturbing potential is negative, as it would be if the perturbing ion were positively charged, or as in the case of a donor atom below the bottom of the conduction band). At the same time, the wave function will become much more concentrated around the perturbing atom, as in the discrete level, in the problem of the single perturbing atom.

This situation can very likely occur in practice. We understand, in the first place, on the basis of this argument, why in so many cases we seem to get good agreement, quantitative as well as qualitative, between the simple hydrogenic theory and the observed impurity levels in semiconductors. These are the cases in which the perturbative energy on the perturbing atom is less than the critical value. Different perturbative atoms, under these circumstances, would have almost, though not quite, the same wave function and energy levels, the discrepancies coming only in the immediate neighborhood of the perturbing atom. On the other hand, we should also expect cases of greater perturbations, in which the whole character of the wave functions and energy level changes, and the energy level is much further below the conduction bands (or much further above the valence bands, if we are dealing with acceptor impurities). This may well be the explanation of the deep traps, which seem to occur particularly in silicon. Such trapping levels seem to explain the long time constants observed in some experiments with silicon,[8] and similar levels have been postulated in silicon after neutron bombardment;[9] these, of course, may well come from interstitial rather than substitutional impurity atoms, and this is a problem slightly different from those we have discussed, but the principle is not different.

Finally, we should mention that if the dielectric constant of a semiconductor is not very great, the Coulomb type of problem will lead to a wave function which is no longer extended over many atoms, but is more concentrated. In such a case it will no longer be justified to replace the difference equations by the differential equation, and we must anticipate quantitative errors in the use of the hydrogenic solution. We hardly expect, however, any very striking qualitative change in the situation.

The authors wish to express their gratitude to the Project Lincoln and the Research Laboratory of Electronics computing groups for their help with the numerical calculations involved in this paper.

APPENDIX

We recall that in (I) the quantity which formed the Green's function for the difference equations and played a central role in the solution of the perturbed periodic lattice was the quantity,

$$\int (d\mathbf{k}) \frac{e^{i\mathbf{k}\cdot\mathbf{R}_p}}{E-E(\mathbf{k})}. \tag{A1}$$

[8] J. R. Haynes and J. A. Hornbeck, Phys. Rev. **90**, 152 (1953).
[9] W. E. Johnson and K. Lark-Horovitz, Phys. Rev. **76**, 442 (1949).

$\mathbf{R}_p$ was a lattice vector of the crystal and $E(\mathbf{k})$ was the energy in one of the energy bands as a function of position in reciprocal space. The integration was to be carried out over the first Brillouin zone. (The crystal is assumed to be infinite.) Let us consider the case where the energy E, the energy of the state we are considering, does not lie in the band. We shall assume that it lies above the band. (The case where it lies below the band can easily be worked out by similar methods.) In this case $E>E(\mathbf{k})$, for all values of $\mathbf{k}$. Since this is the case we can replace Eq. (A1) by

$$\int_0^\infty dt \int (d\mathbf{k}) e^{-[E-E(\mathbf{k})]t} e^{i\mathbf{k}\cdot\mathbf{R}_p}. \tag{A2}$$

The integration over t can be carried out at once to give the previous form of the Green's function.

We notice, at once, that this expression in Eq. (A2) has a striking resemblance to the Green's function which we proposed in (II) for the solution of the perturbed periodic potential problem,

$$\frac{1}{i}\int_0^\infty dt \int (d\mathbf{k}) e^{+i[E-E(\mathbf{k})]t} e^{i\mathbf{k}\cdot\mathbf{R}_p}. \tag{A3}$$

In (II), we mentioned that the Green's function when taken in this form could be used for the case where E lies outside of the band even though it was originally proposed for the case where E lies in the band. We can show that the form of the Green's function in Eq. (A3) is actually the same as the form in Eq. (A2) and therefore also Eq. (A1). Let us imagine that we replace the variable t, in Eq. (A2), by the complex variable $z=x+iy$. We may now do a contour integral along a contour which extends along the real axis from plus infinity to the origin, from thence up the imaginary axis to plus infinity, and finally we close the contour along a quarter of a circle at infinity which connects the real to the imaginary axis. Since $E>E(\mathbf{k})$ for all $\mathbf{k}$, the real part of the exponent in Eq. (A2) will be negative for all values of $x\neq 0$ on the contour we have chosen, since the contour is contained in the first quadrant. This means that the quantity,

$$\int (d\mathbf{k}) e^{-[E-E(\mathbf{k})]z} e^{i\mathbf{k}\cdot\mathbf{R}_p}, \tag{A4}$$

will vanish at almost all points along the quarter of a circle at infinity since it has an infinite real negative part to the exponent. There is one point where it might not vanish. This is the point, which approaches infinity, which lies at the intersection of the quarter circle and the imaginary axis. There is no real part to the exponent at this point. We are saved by the fact that at this point the oscillating nature of the exponential function for large values of complex exponent will cause the integration over $\mathbf{k}$ to give a vanishing result in Eq. (A4). Thus we see that the contribution to the contour integral from the quarter circle will vanish. We are therefore left with the statement that

$$\int_\infty^0 dt \int (d\mathbf{k}) e^{-[E-E(\mathbf{k})]x} e^{i\mathbf{k}\cdot\mathbf{R}_p} + i\int_0^\infty dy \int (d\mathbf{k}) e^{-i[E-E(\mathbf{k})]y} e^{i\mathbf{k}\cdot\mathbf{R}_p} \tag{A5}$$

must be equal to $2\pi i$ times the sum of the residues within the contour. However, the quantity in Eq. (A4) has no poles within this contour. We integrate a finite quantity over the first Brillouin zone; therefore Eq. (A4) must be finite. This gives us the result that Eq. (A5) vanishes. From this fact, we conclude that Eq. (A2) is the same as Eq. (A3) by taking the complex conjugate of Eq. (A5) and replacing the variables of integration x and y by t.

We are now in a position to apply these results to the problem at hand. In the case of the simple cubic lattice with nearest neighbor interactions the integrations over reciprocal space can be carried out explicitly. In Sec. III of this paper the solution to the difference equations was given by Eq. (18). Applying the transition from Eq. (A1) to Eq. (A2) to this case we obtain the result,

$$U_{p,q,r}=\frac{V'(0)}{\pi^3}U(0)\int_0^\infty dt\int_0^\pi d\alpha_1\int_0^\pi d\alpha\int_0^\pi d\alpha_3 \times\cos p\alpha_1\cos q\alpha_2\cos r\alpha_3 \times e^{-[E'-\cos\alpha_1-\cos\alpha_2-\cos\alpha_3]t}. \tag{A6}$$

Using the definitions of the Bessel functions of imaginary argument[10] reduces this to

$$U_{p,q,r}=V'(0)U(0)\int_0^\infty e^{-E't}I_p(t)I_q(t)I_r(t)dt. \tag{A7}$$

Equation (A5), when applied to this case, would give the result:

$$\frac{1}{i}\int_0^\infty dt e^{-iE't}J_p(t)J_q(t)J_r(t). \tag{A8}$$

Here we have used the definition of the ordinary Bessel function to obtain the result. This form of the Greens' function is valid within as well as outside of the band. The form (A7) would, of course, be valid only outside of the band ($E'>3$).

[10] H. Jeffreys and B. E. Jeffreys, *Methods of Mathematical Physics* (Cambridge University Press, Cambridge, 1950), p. 579.

Self-Diffusion in Copper*

A. KUPER, H. LETAW, JR., L. SLIFKIN, E. SONDER, AND C. T. TOMIZUKA
Department of Physics and Electrical Engineering Research Laboratory, University of Illinois, Urbana, Illinois

(Received August 30, 1954)

The self-diffusion coefficient of copper has been determined by tracer techniques through the use of a precision grinder and a precision lathe. The temperature dependence over the range 685–1062°C is given by $D=0.468\exp(-47\,140/RT)$ cm²/sec.

INTRODUCTION

SELF-DIFFUSION of copper has been studied by a number of investigators.[1] The temperature range and accuracy of the measurements have been severely limited by the short half-life of the only available isotope, 12.88-hr Cu^{64}. The present determination was undertaken because of the availability of a precision grinding machine for diffusion studies.[2] The precision grinder permits the determination of diffusion coefficients when mean penetrations are of the order 1μ or greater. The high sensitivity of this method is of particular applicability in the case of a short-lived isotope.

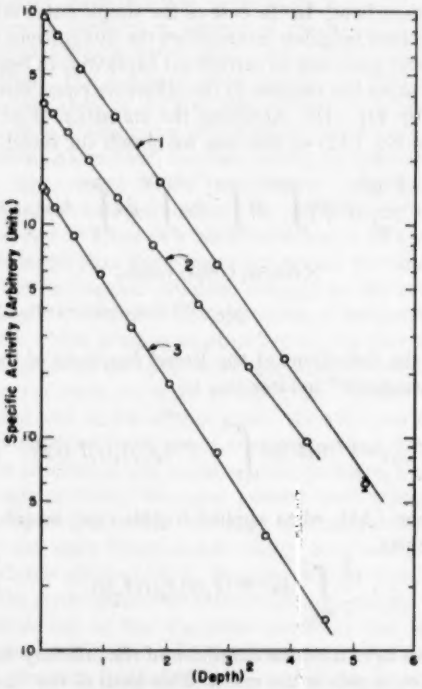

FIG. 1. Penetration curves for specimens sectioned on a lathe. See Table I for the scaling factors for the distance.

EXPERIMENTAL

Cylindrical single-crystal specimens were prepared in vacuum from American Smelting and Refining Company spectroscopically pure copper using procedures described earlier.[3] The specimens were electroplated with layers of Cu^{64} of the order of 50A thick from an acidic $CuNO_3$ solution. The radioactive Cu^{64}, obtained from the Oak Ridge National Laboratory, was found to be contaminated with small amounts of long-lived impurities. These, since they diffused into the samples more rapidly than copper, caused some of the penetration plots to deviate from linearity at the larger penetration depths (curves 4, 6, and 7 in Fig. 2). Diffusion coefficients were determined from penetration curves which were corrected for the residual specific activity of the impurities. This difficulty was subsequently eliminated by the use of spectroscopically pure copper irradiated at Oak Ridge.

The plated specimens were annealed for periods of 8 to 48 hours at temperatures held constant to within ±1°C. Specimens which were annealed at temperatures above 820°C (penetrations $>100\mu$) were sectioned on a lathe and analyzed by beta-counting techniques used previously.[4] The precision grinder was employed to section the other specimens (penetrations 10–100μ), beta counting being carried out as described.[2]

RESULTS

Eight successful measurements were performed over the temperature range 1062–660°C. The penetration

TABLE I. Self-diffusion in copper.

Curve	Unit of (depth)² (cm²)	Slicing method	Temperature (deg C)	Time (sec)	D (cm²/sec)
1	6.45×10^{-4}	lathe	1063	4.1×10^{4}	4.12×10^{-9}
2	2.58×10^{-4}	lathe	936.7	1.26×10^{5}	5.91×10^{-10}
3	6.45×10^{-5}	lathe	839.0	1.49×10^{5}	1.05×10^{-10}
4	7.37×10^{-6}	grinder	812.2	3.32×10^{4}	6.80×10^{-11}
5	5.16×10^{-6}	grinder	765.2	1.06×10^{5}	2.20×10^{-11}
6	2.34×10^{-6}	grinder	715.5	1.21×10^{5}	7.92×10^{-12}
7	1.11×10^{-6}	grinder	684.8	1.40×10^{5}	3.71×10^{-12}
8	7.37×10^{-7}	grinder	660.2	1.40×10^{5}	2.53×10^{-12}

* Supported in part by the U. S. Atomic Energy Commission and in part by the Office of Naval Research.

[1] For instance, B. V. Rollin, Phys. Rev. **55**, 231 (1939); Steigman, Shockley, and Nix, Phys. Rev. **56**, 13 (1939); and M. S. Maier and H. R. Nelson, Trans. Am. Inst. Mining Met. Engrs. **147**, 39 (1942).

[2] Letaw, Slifkin, and Portnoy, Phys. Rev. **93**, 892 (1954); Rev. Sci. Instr. (to be published).

[3] Sonder, Slifkin, and Tomizuka, Phys. Rev. **93**, 970 (1954).

[4] C. T. Tomizuka and L. Slifkin, Phys. Rev. **96**, 610 (1954).

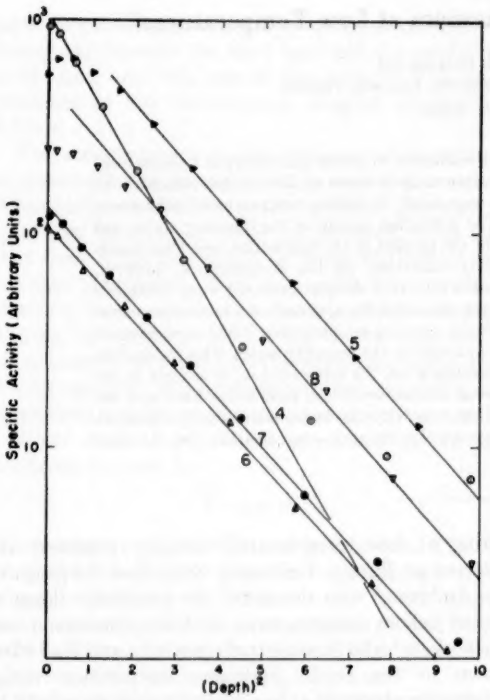

FIG. 2. Penetration curves for specimens sectioned by a grinding machine. See Table I for the scaling factors.

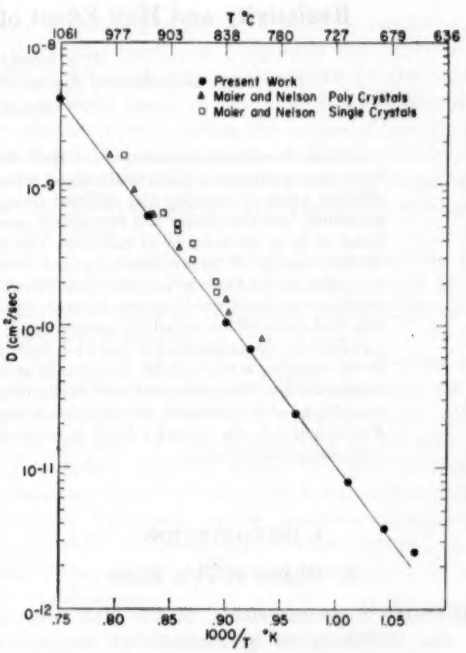

FIG. 3. Diffusion data plotted as log$D$ *versus* $1/T$.

curves for the three specimens sectioned on the lathe are shown in Fig. 1, while those obtained on the precision grinder are plotted in Fig. 2. The scaling factors for these curves as well as a summary of the data are shown in Table I. The logarithms of the diffusion coefficients are plotted against the reciprocal of the absolute temperature in Fig. 3. A least-squares calculation gives the temperature dependence over the range 1062−685°C as

$$D=0.468\exp(-47\,140/RT)\ \text{cm}^2/\text{sec}.$$

The number of measurements and the temperature range *statistically* determine the activation energy to 0.005 percent and the frequency factor to 6 percent. These figures seem too optimistic, since systematic errors of unknown origin probably can exceed the estimated range of errors.

The three upper points in Fig. 3 were double-weighted in the calculation since the maximum probable error in the lathe technique was 2 percent, while the grinding machine yielded data with an accuracy of about 5 percent. The lowest-temperature point in Fig. 3 was not included in this calculation since its deviation from the best least-squares straight line was much greater than could be accounted for by possible systematic errors. Further diffusion coefficients will be obtained in the neighborhood of this temperature in order to determine whether or not a real deviation exists.

The results of the present work are seen to agree rather well with the data of Maier and Nelson[1] which are shown in Fig. 3. Those authors suggest different values of the activation energy of self-diffusion in copper depending on the crystalline state of the sample. The present data agree better with their results for polycrystals even though only single crystals were used in this research.

It is of interest to compare data from previous calculations and experiments relating to diffusion processes in copper with those reported here. The frequency factor calculated by Zener's theory[5] is 0.28 cm²/sec as contrasted with the experimental value of 0.47. The present experiment does not alter the estimate by Overhauser[6] of the energy of formation of a vacancy because the activation energy obtained by Maier and Nelson[1] differs from our value by only 0.02 ev. Also, the conclusions of Huntington and Seitz[7] remain valid.

The authors wish to express their gratitude to Dr. R. J. Gnaedinger for his contribution in the initial preparation of the specimens. Sincere thanks are also due Mr. J. H. Gillete, Superintendent of the Radioisotope Control Department, Oak Ridge National Laboratory, for his cooperation in the preparation and delivery of the isotope.

[5] C. Zener, J. Appl. Phys. **22**, 372 (1951).
[6] A. W. Overhauser, Phys. Rev. **90**, 393 (1953).
[7] H. B. Huntington and F. Seitz, Phys. Rev. **61**, 315 (1942) and H. B. Huntington, Phys. Rev. **61**, 325 (1942).

Resistivity and Hall Effect of Germanium at Low Temperatures*

C. S. HUNG† AND J. R. GLIESSMAN‡
Department of Physics, Purdue University, Lafayette, Indiana
(Received July 21, 1954)

An experimental investigation of the Hall effect and the resistivity of germanium alloys at temperatures from room temperature down to the liquid helium temperature range is reported. Germanium samples with different kinds of impurity and different concentrations were used. At higher temperatures, satisfactory agreement between theory and experiment was found. The activation energy of the impurity states was found to be of the order of 10 millivolts. The scattering of the carriers in the conduction and filled bands consists mainly of lattice scattering and ionized impurity scattering. At low temperatures, however, anomalies in the Hall curves were observed. The Hall curve for every sample measured went through a maximum as the temperature was lowered. At the same time the resistivity approached a saturation value. The Hall curves of low resistivity samples finally became flat at very low temperatures. These anomalies are explained on the assumption of small but finite mobility of carriers in the impurity states. This conduction in the impurity states assumes importance at low temperatures when the concentration of carriers in the conduction band becomes very low. When this simultaneous conduction in the conduction band and the impurity band is considered, the behaviors in the Hall and the resistivity curves are satisfactorily explained. The mobility in the impurity band is found to increase with the impurity concentration, but is rather temperature-independent.

I. INTRODUCTION

A. Object of This Work

PREVIOUS measurements[1] of the Hall effect and the resistivity of germanium at temperatures between 80°K and 900°K have shown that germanium behaves as an impurity semiconductor. The concentration of electrons in the conduction band and of holes in the filled band follow the dissociation equation as predicted by theory.[2] The scattering of the electrons and the holes is due mainly to lattice vibrations and to Coulomb scattering by the ionized impurity centers.[3]

The flatness of the Hall coefficient *versus* temperature curves for temperatures between 300°K and 80°K indicates that the activation energies of the impurity states in germanium are very low. Furthermore, for some samples, the concentration of electrons in the conduction band (or the concentration of holes in the filled band) is so large that the assembly of electrons must be treated as a degenerate gas in this temperature range.[4]

It would be interesting, therefore, to investigate the behavior of germanium at lower temperatures in order to determine the activation energies of the impurity states, the behavior of the degenerate electron gas at very low temperatures, and to check the theory of scattering at low temperatures. Samples prepared and selected at Purdue University have been investigated by Ambrose,[5] who measured the resistivity down to liquid helium temperatures, and by Estermann and co-workers,[6] who investigated resistivity and Hall effect down to the liquid hydrogen temperature range. Anomalies observed at low temperatures, especially by the latter group, prompted the undertaking of the current program of low-temperature investigation at Purdue University.

This paper reports the measurements of resistivity and Hall effect from room temperature down to liquid helium temperatures, the extent of agreement with theory based on the usual model of impurity semiconductor, the anomalies observed at low temperatures, and the modification of the model proposed in order to explain the anomalies.

B. Germanium as an Impurity Semiconductor

Figure 1 illustrates the simple energy level diagram for germanium as an impurity semiconductor. N_D and N_A are the concentrations of donors and acceptors, respectively. ΔE_D and ΔE_A are the respective energy gaps from the conduction and filled bands. These energy

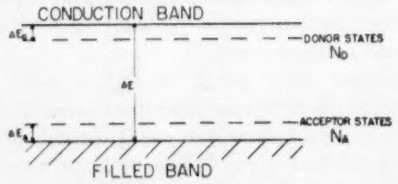

FIG. 1. Energy-level diagram for an impurity semiconductor.

* Work supported by the U. S. Army Signal Corps contracts with Purdue University.

† Last known address: University of Leiden, Leiden, The Netherlands.

‡ Now at Hughes Aircraft Company, Culver City, California.

[1] Lark-Horovitz, Middleton, Miller, and Walerstein, Phys. Rev. **69**, 258 (1946); A. E. Middleton and W. W. Scanlon, Phys. Rev. **92**, 219 (1953), especially Figs. 6, 7, and 9.

[2] R. H. Fowler, Proc. Roy. Soc. (London) **A140**, 505 (1933).

[3] K. Lark-Horovitz and V. A. Johnson, Phys. Rev. **69**, 258 (1946); K. Lark-Horovitz, Elec. Eng. **68**, 1047 (1949); H. C. Torrey and C. A. Whitmer, *Crystal Rectifiers* (McGraw-Hill Book Company, Inc., New York, 1948), pp. 58–61.

[4] V. A. Johnson and K. Lark-Horovitz, Phys. Rev. **71**, 374, 909 (1947); **72**, 531 (1947).

[5] J. R. Ambrose, Naval Research Laboratory (private communication).

[6] I. Estermann and A. Foner, Phys. Rev. **79**, 365 (1950); I. Estermann, Carnegie Institute of Technology ONR reports (unpublished).

gaps, for germanium, are usually small compared to the energy gap between the filled band and the conduction band. ΔE_D and ΔE_A are of the order of 0.01 ev as measured at low temperature, whereas ΔE is about 0.75 ev.

The measurements to be discussed were made at temperatures low enough for the contribution of intrinsic electrons and holes to be neglected. The impurity states are usually considered as localized states such that there is no conduction in them. Carriers of only one sign are present. If $N_D > N_A$, the carriers will be electrons in the conduction band, and the sample is N-type. Conversely, if $N_A > N_D$, the carriers will be holes in the filled band, and the sample is P-type. Only N-type samples will be discussed, but the same considerations may be readily extended to P-type samples.

When there is only one kind of carrier, the Hall coefficient is given by

$$R = \pm r/ne, \tag{1}$$

where n is the concentration of free carriers. The sign of the Hall coefficient coincides with the sign of the charge carriers; r is a numerical factor of the order of unity and is dependent on the statistics obeyed by the carriers and on the nature of the collisions between the carriers and the lattice and impurity ions.[7]

With a small but finite energy gap between the donor states and the conduction band, the concentration of electrons is expected to decrease rapidly with decreasing temperature, as soon as kT becomes smaller than ΔE_D. The Hall coefficient R is then expected to increase rapidly with decreasing temperature.

The resistivity is given by

$$\rho = (ne\mu)^{-1} \tag{2}$$

where

$$1/\mu = 1/\mu_L + 1/\mu_I; \tag{3}$$

μ is the mobility of the electrons in the conduction band. $1/\mu_L$ and $1/\mu_I$ correspond to the scattering of the electrons due to lattice vibrations and by the impurity ions, respectively. Furthermore,

$$\mu_L = A(T/300)^{-\frac{3}{2}}, \tag{4}$$

where A corresponds to the value of μ_L at room temperature and is of the order of 3600 cm²/volt-sec when T is expressed in °K. The scattering by the impurity ions is of the nature of Coulomb scattering, and the expression given by Conwell and Weisskopf,[8] is

$$\mu_I = \frac{8.25\times10^{17}T^{\frac{3}{2}}}{N_s \ln\{1+2.57\times10^{8}(N_s)^{-\frac{1}{3}}T^2\}} \text{ cm}^2/\text{volt-sec}, \tag{5}$$

where N_s is the concentration of Coulomb scattering centers. The above analysis has been found satisfactory above liquid air temperature when N_s is assumed equal to the carrier density n. Previously this analysis was found to be satisfactory when applied for the resistivities measured down to liquid air temperatures using the relation $N_s = n$. During the course of this work, it was found that, for samples of high resistivity, the above analysis is satisfactory[9] down to 10°K, provided that the concentration of scattering centers is taken as $N_s = n + 2N_A$.

Since μ_I is a slowly varying function of the temperatures, while n varies exponentially with T, the resistivity is expected to increase indefinitely as the temperature is lowered.

In Sec. III it will be shown that, at very low temperatures, the resistivity and Hall coefficient do not increase indefinitely with $1/T$ according to the picture above. Instead, as the temperature is lowered, the Hall coefficient is found to pass through a maximum. At the same time, the resistivity is found to approach saturation. This leads to the conclusion discussed in Sec. IV that the conduction in the impurity states must be taken into consideration, especially at very low temperatures.

II. EXPERIMENTAL PROCEDURE

A. Preparation of Samples

The samples used were obtained from W. E. Taylor, formerly of the Physics Department of Purdue University. The antimony-doped samples were obtained by adding antimony to high purity germanium so that there was only one predominant impurity in these samples. The neutron-bombarded samples were originally high-resistance N-type. Slow neutrons cause transmutations of the germanium atoms resulting in the introduction of both gallium and arsenic impurities.[10] The samples were annealed to heal the displacements caused by the fast neutrons. It was calculated that the ratio of gallium atoms to arsenic atoms was about 3 to 1. Gallium is a P-type and arsenic is an N-type impurity. In such a case, there would be four impurity scattering centers produced but only two P-type carriers due to the recombination of one electron with one hole.

The samples are cut from an ingot to a size of about 1 cm×2 mm×5 mm. The samples are then ground with No. 600 carborundum and etched to reduce surface effects. The etching solution contains hydrofluoric acid and cupric nitrate.[1] It could be seen after etching that the samples were mostly single crystals. Some samples were ground again and used without additional etching. Preliminary measurements of the room temperature resistivities along the length of the sample showed the samples to be homogeneous. It was found later, however, that, in some cases, inhomogeneities appeared at low temperatures.

The current and potential leads are 0.002-in. enamel-

[7] V. A. Johnson and K. Lark-Horovitz, Phys. Rev. **82**, 977 (1951); H. Jones, Phys. Rev. **81**, 149 (1951).

[8] E. Conwell and V. F. Weisskopf, Phys. Rev. **69**, 258 (1946); **77**, 388 (1950).

[9] C. S. Hung and V. A. Johnson, Phys. Rev. **79**, 535 (1950).

[10] Cleland, Lark-Horovitz, and Pigg, Phys. Rev. **78**, 814 (1950).

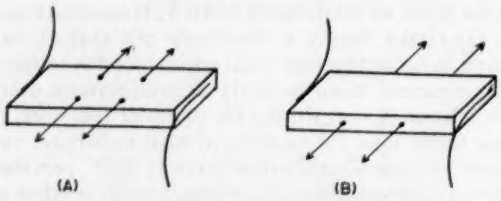

FIG. 2. Two types of current lead and probe arrangement which were used.

covered copper wires that are attached to the sample with Cerroseal 35 solder. This solder consists mostly of tin with a small quantity of indium. It is very malleable at room temperatures and assures good contact at low temperatures. The sample is first cleaned with alcohol and then the solder put on the ends and on four spots in the middle, using zinc chloride flux. The size of the solder spots for the potential leads are kept as small as possible to minimize shorting the sample with solder. The size of these spots is of the order of 0.2 to 0.4 mm in diameter. The four potential leads and the two current leads are arranged as shown in Fig. 2. This probe arrangement permits two Hall measurements and two resistivity measurements simultaneously. The advantage of this is that one can detect inhomogeneities that may become pronounced at low temperatures. Furthermore, the measurement can be continued even if a poor contact develops at one of the soldered probes.

There is some uncertainty about the two points between which the probe separation should be measured. If the probe distances are measured to be about 0.1 to 0.2 cm, there is the possibility of an error of about 20 percent to 30 percent. This error will appear in the absolute value of the Hall coefficient and the resistivity. It is possible to reduce this error in the case of the Hall probes by soldering the probes to the side of the sample as shown in Fig. 2(B). Then the width of the sample, which is rather easily measured, is equivalent to the distance between the Hall probes.

It is desirable to check the effect that soldered contacts might have on the measurements at low temperatures. For this reason measurements were repeated on one of the samples with pressure contacts. The four spots shown in Fig. 2 were plated with rhodium, and then the probes were pressed onto the plated spots.

All of the samples are placed on holders made of Bakelite or baked lavite and then put into the cryostat.

B. The Cryostat

The cryostat was constructed so that a continuous range of temperatures from 1.3°K to 300°K could be obtained. The cryostat proper and the devices for the control and calibration of temperature are shown in Fig. 3.

The sample is enclosed in the copper cylinder (A), which forms the bulb of a gas thermometer. This, in turn, is enclosed in a brass cylinder (B). The space

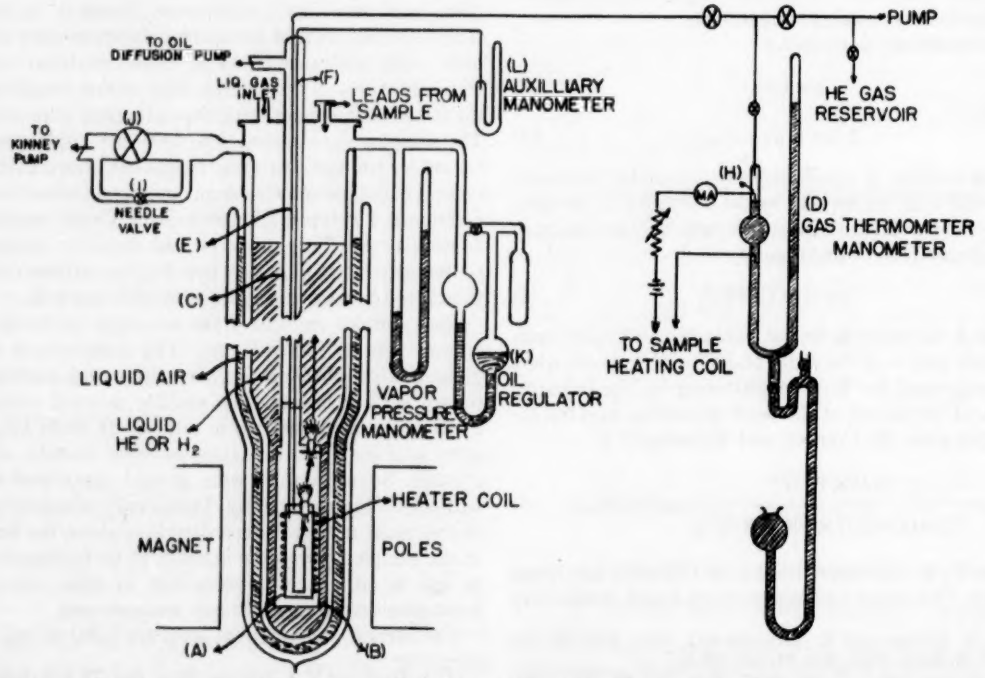

FIG. 3. The cryostat and devices for the control and calibration of temperature.

between the cylinders is part of a high vacuum system that is connected to an oil diffusion pump through the monel tubing (C). It can be pumped to a vacuum of better than 10^{-5} mm Hg pressure. The space between the two cylinders serves to insulate the gas thermometer bulb from the liquid bath. A heater wire is wound nonmagnetically around the gas thermometer bulb and is used to heat the sample to temperatures above that of the liquid bath.

The gas thermometer bulb is connected to a mercury manometer (D) outside through a capillary (E) with an inside diameter of 1 mm. An auxillary capillary (F) is placed alongside the gas thermometer capillary (E) and in thermal contact with it. The auxilliary capillary is used in conjunction with a small closed-end manometer (L) and serves as a method of correcting for the temperature gradient that exists along the capillary in the calculation of temperature. These two capillaries are then run up through the monel tubing (C). They are thermally insulated from the liquid bath except near the lower end so that the average temperature of the capillaries is in the order of 50°K, when a liquid helium bath is used. The capillary correction to the temperature calibration is, therefore, small. The temperature calibration is accurate to within 1 percent.

There is no direct heat leak to the inside of the gas thermometer bulb from room temperature. The bulb is entirely shielded by the brass cylinder (B) and the high-vacuum pumping line (C). The leads to the sample enter through two offset copper to glass seals. The monel tubing (C) is provided with a light shield (G). The heat leak from the gas thermometer bulb to the bath comes from the capillary tubings, and from the sample leads.

It is possible to control automatically the temperature above that of the liquid bath with a simple device which is built into the manometer (D). The level of the mercury, in conjunction with a tungsten wire (H), serves as a heater current switch. As the level of the mercury rises or falls with a change in temperature, contact is made or broken with the tungsten wire, turning the heater current on or off, as the case may be. The variation in pressure of the mercury is less than 0.4 percent.

Temperatures below those of the liquified gases are obtained by reducing the vapor pressure of the bath. Thermal contact between the sample and the bath is established by introducing exchange helium gas into the vacuum space. A needle valve (I) by-passing the 2-in. diameter packless valve (J) is used for controlling the pumping speed. The vapor pressure is maintained constant with the aid of an oil regulator (K).

The leads from the sample are placed around the monel tubing (C) and are relatively susceptible to stray electric fields. For this reason, it is desirable to provide shielding for the leads when high-resistance samples are to be measured. This has been done in a second cryostat by running the wires down to the sample through the monel tubing (C). They are separated by polystyrene spacers to minimize the capacity between the wires.

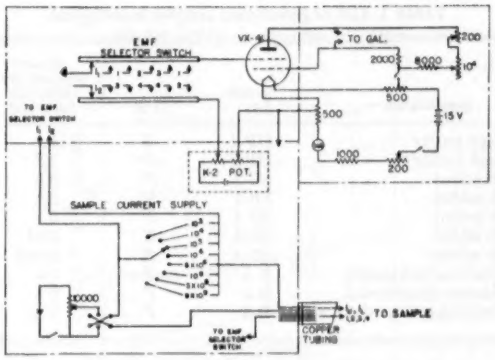

FIG. 4. Electrometer circuit used when sample resistance exceeds 10^8 ohms.

C. The Electrical Measuring Circuit

(a) *Potentiometer and Galvanometer Circuit for Use with Low Resistance Samples*

The potential developed across the sample probes is balanced against a Leeds and Northrup type K-2 potentiometer to obtain a null reading on a reflecting galvanometer. Heavy copper knife switches are used in the emf selector switches and the emf reversing switch to minimize contact potential. The sample current source is a 6-volt storage battery connected through a series of variable resistances. The current is measured by measuring the potential drop across a standard 10-ohm resistor with the potentiometer.

The galvanometer used is Leeds and Northrup type 2500B with a current sensitivity of 3×10^{-10} amp/mm and an external damping resistance of 10 000 ohms. The period of the galvanometer is 7 seconds. The voltage sensitivity of the circuit is 3 microvolts/mm. For very low-resistance samples, a low-resistance galvanometer is used to obtain better voltage sensitivity.

(b) *Electrometer Tube Circuit for Use with High-Resistance Samples*

When the resistance of the samples is higher than 10^4 ohms, the voltage sensitivity of the galvanometer decreases with increasing resistance. For high-resistance samples at low temperatures, an electrometer circuit (Fig. 4) is used. This circuit employs a VX-41 Victoreen electrometer tube with the Leeds and Northrup 2500B galvanometer in the output. The potential to be measured is applied to the control grid and balanced with the potentiometer. Upon measuring, a balance is indicated by a zero deflection of the galvanometer when the control grid ground switch is opened.

The emf selector switch has polystyrene insulation to minimize electrical leakage and gold contacts for low contact resistance. The electrometer is generally used

TABLE I. List of germanium samples investigated.

Specification	Sample No.	Type	Room temperature resistivity (ohm-cm)
High purity	HP-1	*N*	15
High purity	HP-2	*P*	7.5
Sb added	SB-2	*N*	0.4
Sb added	SB-1	*N*	0.3
Sb added	SB-3	*N*	0.1
Sb added	SB-4	*N*	0.04
Sb added	SB-5	*N*	0.004
Neutron-bombarded	B-1	*P*	0.6
Neutron-bombarded	B-2	*P*	0.2
Neutron-bombarded	B-3	*P*	0.05

when the sample resistance is greater than 10^5 ohms. The useful sensitivity of the electrometer circuit is 150 microvolts/mm. For sample resistance of less than 10^{10} ohms it is not necessary to take into account the control grid current for emf correction. This control grid current is about 10^{-14} amp.

The leads from the cryostat are brought to the electrometer circuit unit through copper tubing for shielding purposes and are spaced with polystyrene insulators to minimize capacitance to ground.

The sample current is again determined from the potential drop across a standard resistor. A selection of resistors varying from 10^3 to 9×10^9 ohms is available.

It is possible to switch the galvanometer from the plate circuit to the grid circuit of the electrometer tube. Then one can utilize the sample current source of the electrometer unit and the aforementioned shielding without using the electrometer tube itself.

D. The Magnet

The magnetic field from an electromagnet with pole faces four inches in diameter and a variable pole gap is used. The magnet is calibrated with a GE fluxmeter. With a pole gap of 5 cm, a field of 5000 gauss is obtained with a current of 15 amp.

The disturbances of the magnetic field by the glass Dewars, the liquified gas and the brass and copper cylinders, (a) and (b) of Fig. 3, are negligible at all temperatures. The tin solder is not superconducting at any temperature with a magnetic field above 300 gauss.[11] The Wood's metal solder is not expected to be superconducting at a magnetic field much above 1000 gauss.

III. EXPERIMENTAL RESULTS

Measurements were made on the samples listed in Table I. For each measurement of Hall emf or resistivity, four readings are taken with opposite directions of sample current and opposite directions of magnetic field to eliminate thermal emf and pickup in the circuit. Most of the measurements were made with soldered current and potential leads. For sample SB-1, measurements were made with both ground and etched surfaces, and the results were essentially the same, both on the Hall measurements and the resistivity measurements, at all temperatures. Measurements were also made on sample SB-2, both with soldered leads and with pressure contacts, and the results were the same.

It was found that measurements on the same sample in different runs may differ by a few percent, but the shapes of the Hall and the resistivity *vs* temperature curves were the same.

A sample homogeneous at room temperature may show very large inhomogeneity at very low temperatures. The values of resistivities from the two sets of probes may then differ by a factor of 2 or 3 even though the sample is quite uniform in the liquid hydrogen temperature range. Measurements on the same sample with the potential leads resoldered to apparently the same positions may therefore yield different values at very low temperatures. However, the shapes of the Hall and the resistivity curves again remain the same. No essential difference was found between measurements made with increasing temperature and with decreasing temperature.

The magnetic fields used in the Hall measurements were usually between 1 and 5 kilogauss. The larger field was used when the Hall emf is small. The magnetic field dependence of the Hall coefficient was checked for every sample for at least a few points spaced evenly on the $1/T$ curve. In some cases the Hall coefficient and the resistivity for a magnetic field of 5 kilogauss may be higher by 30 percent than the values at 1 kilogauss, but this effect of magnetic field dependence does not change the essential characteristics of the Hall coefficient and resistivity *versus* temperature curves.

The measurements were also made with different currents through the sample. The electric field in the sample was usually from 10 millivolt per cm to 1 volt per cm, except for the extremely low resistance samples for which the field might be below 1 millivolt per cm. The current was limited in the case of low-resistance samples by the consideration of heat input to the sample. The values of Hall coefficient and resistivity were essentially independent of the current for fields between a few millivolts/cm and a few hundred millivolts/cm.

A. The Hall Measurements

The High-Purity and the Antimony-Doped Samples

In Fig. 5 are shown the Hall coefficient *versus* $1/T$ curves for the high-purity and the antimony-doped samples. For the higher resistivity samples, including HP-1, HP-2, SB-1, SB-2, and SB-3, the curves can be conveniently divided into three sections: (a) the exhaustion range, where the Hall coefficient is almost constant, (b) the intermediate-temperature range where the Hall coefficient increases rapidly with decreasing temperature, and (c) the low-temperature

[11] J. G. Daunt and K. Mendelssohn, Proc. Roy. Soc. (London) **A160**, 127 (1937).

range where the Hall coefficient *vs* $1/T$ curve goes through a maximum and drops rapidly with decreasing temperature. For low-resistivity samples, this division is not easily made. For the first two temperature regions, the model presented in Sec. I serves as a satisfactory basis for discussion.

(a) *The exhaustion range.*—Within this range, all the electrons from the donor states are excited into the conduction band and so the concentration of carriers is constant with temperature. Equation (1) then indicates that the Hall coefficient would be constant except for the temperature dependence of r.[7] In Fig. 6 is shown an enlargement of the Hall coefficient graph in the exhaustion ranges of the various samples. The upper temperature limit of the exhaustion range for most samples extends to room temperature, except for the highest resistivity sample HP-1 for which the intrinsic contribution of carriers becomes appreciable above 200°K. The lower temperature limit of the exhaustion range extends to temperatures near 30° or 40°K for the higher resistivity samples. This is to be expected from their low activation energy. It is to be noticed in Fig. 6 that the slope of the Hall coefficient *vs* $1/T$ curve, as the temperature is lowered from room temperature, is lower for samples of higher purity. Finally, for the highest resistivity samples, the Hall coefficient actually goes down as T is lowered from room temperature, and reaches a minimum at about 80°K. This behavior of the Hall coefficient, especially the minimum in the curve, suggests that in this region the dependence[7] of r on T is predominant over the dependence of n on T, since one does not expect the concentration of carriers to increase as the temperature is lowered.

(b) *The intermediate-temperature range.*—In this range

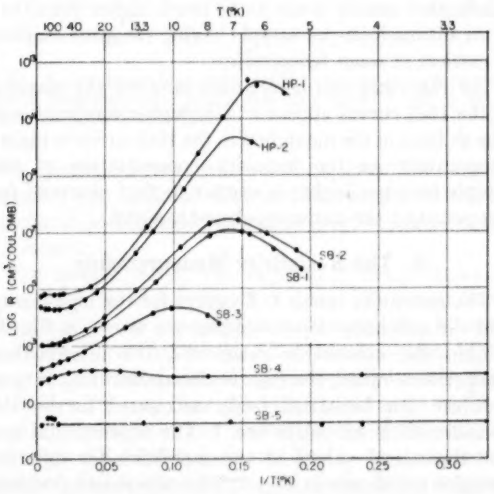

FIG. 5. Semilogarithmic plot of the Hall coefficient *vs* reciprocal of Kelvin temperature for high-purity undoped germanium samples HP-1 and HP-2 and antimony-doped germanium samples SB-1, SB-2, SB-3, SB-4, and SB-5. All these samples are *N*-type except HP-2.

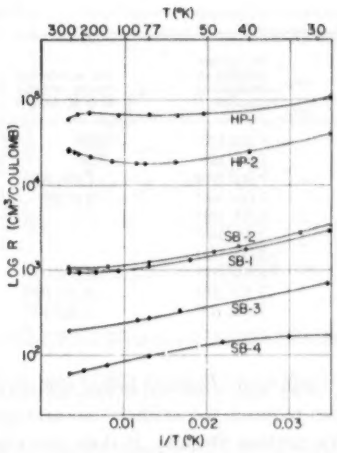

FIG. 6. Enlargement of a section of Fig. 5 to show details of Hall effect behavior in the exhaustion range.

the Hall coefficient rises rapidly with decreasing temperature. The dependence of n on T is now predominant. The linear logarithmic increase of R, or the linear logarithmic decrease of n with $1/T$, is expected from the simple model with a rather sharp impurity level. The activation energy obtained from the slope of the log$R$ *vs* $1/T$ curves by use of the dissociation equation[2] are shown in Table II.

(c) *The low-temperature range.*—For all samples measured, the Hall coefficients do not increase indefinitely as the temperature is lowered; instead the Hall coefficient goes through a maximum and then drops rapidly as T is lowered. The temperature at which this maximum occurs is higher for samples of higher impurity content. At temperatures below the maximum, the Hall coefficients of the higher-resistivity samples continue to drop as long as the Hall values remain measurable. On the basis of comparison with the neutron-bombarded samples (Fig. 7), one might expect all Hall curves to level out to constant values at temperatures well below the maximum.

It is important to note here that the values of the Hall coefficient in the neighborhood of the maximum of the Hall curve are practically independent of the magnetic field for fields between 1000 and 5000 gauss and also independent of the current through the sample for currents varying by a factor of ten.

It is improbable that the concentration of electrons in the conduction band should increase with decreasing temperature. Furthermore, r cannot be expected to change by more than a factor of 2, according to the free electron theory.

Nonuniformity in the impurity concentration of the sample, either macroscopic or microscopic, can cause a decrease in the Hall coefficient, even though the carrier density remains constant or decreases with decreasing temperature. However, accounting for the large drop

TABLE II. Sample properties.

Sample	n_0, carrier density in exhaustion range (cm^{-3})	N_s, scattering center density at 0°K (cm^{-3})	$N_D = n_0 + \frac{1}{4}N_s$ (or N_A for P-type) (cm^{-3})	Activation energy (ev)	Saturation resistivity at low temperatures (ohm-cm)	Donor (or acceptor) band mobility cm^2/volt-sec
HP-1 (N)	1.2×10^{14}	10^{14}	1.7×10^{14}	0.0135	4×10^{8}	1.5×10^{-4}
HP-2 (P)	2.5×10^{14}	10^{15}	7.5×10^{14}	0.0123	10^{7}	3×10^{-3}
SB-1 (N)	7.0×10^{15}	1.8×10^{15}	7.9×10^{15}	0.0093	2×10^{4}	0.05
SB-2 (N)	7.0×10^{15}	2×10^{16}	8.0×10^{15}	0.0083	10^{5}	0.01
SB-3 (N)	4.5×10^{16}		4.5×10^{16}	0.0055	3×10^{2}	0.5
SB-4 (N)	1.5×10^{17}		1.5×10^{17}		0.5	100
SB-5 (N)	4.0×10^{18}		4.0×10^{18}		0.0045	
B-1 (P)	8.5×10^{15}	8.5×10^{15}	1.3×10^{16}	0.0090	3×10^{2}	2.8
B-2 (P)	3.3×10^{16}	3.3×10^{16}	5×10^{16}		3	67
B-3 (P)	1.8×10^{17}	1.8×10^{17}	2.7×10^{17}		0.1	400

in the Hall coefficient observed below the maximum in some samples requires too artificial an arrangement of the impurity centers. Besides, it does not explain the systematic shifting of the Hall curve maxima to higher temperatures as the impurity content goes up. The sharp decrease of the Hall coefficient therefore must mean a breakdown of the simple model presented in Sec. I. Among the factors affecting this breakdown of Eq. (1) are the total concentration of impurity ions (N_D for N-type Ge) and the concentration of carriers at the temperature where this occurs.

For the lowest resistivity samples, SB-4 and SB-5, the division into these three regions seems rather artificial. It is hard to say from the Hall curves alone whether the intermediate-temperature range and the low-temperature range are absent or whether they have merged into one with the exhaustion range. Comparison with the resistivity curves, as discussed in the next section, however, gives more information about the nature of these Hall curves.

For the present, it will be noted that the activation energy for sample SB-4 is certainly not equal to zero, despite the flatness of the Hall curve. For sample SB-5, whether the activation energy is zero or not is immaterial to the conduction.

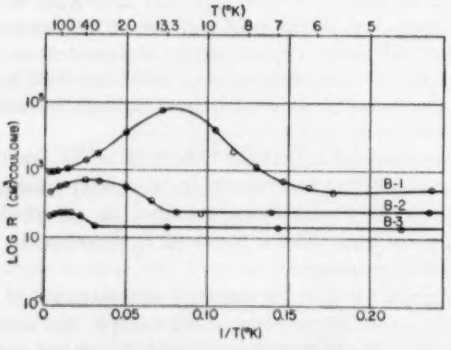

FIG. 7. Semilogarithmic plot of the Hall coefficient *vs* reciprocal of Kelvin temperature for germanium samples, initially N-type, but converted to P-type by neutron bombardment.

The Bombarded Samples

In Fig. 7 are shown the Hall curves for the neutron-bombarded samples. The same division into the three temperature regions applies. In the case of the highest-resistivity sample, B-1, this division is easily made, and the activation energy is found to be approximately 0.009 ev. For the two lower-resistivity samples, the intermediate-temperature regions are rather short, and the values of their activation energies cannot be readily ascertained.

The concentration of carriers in sample B-1 at its Hall maximum is less than the carrier concentrations in antimony-doped samples SB-1, SB-2, and SB-3 at the same temperature, and the Hall coefficients and resistivities of these latter samples are still rising rapidly at this temperature. This fact implies that the low-temperature behavior depends not only on the carrier concentration at a given temperature but also on the concentration of impurity centers (N_D for N-type). As mentioned in Sec. I, the impurity concentration of a bombarded sample is apt to be much higher than that of an antimony-doped sample having the same number of carriers at room temperature.

For the other two bombarded samples, the maxima in the Hall curves appear at still higher temperatures. The shifting of the maximum in the Hall curve to higher temperature as the impurity concentration of the sample becomes higher is similar to that observed for the pure and the antimony-doped samples.

B. The Resistivity Measurements

The resistivity *versus* $1/T$ curves for the high-purity and the antimony-doped samples are shown in Fig. 8. Within the exhaustion range and the intermediate temperature range, the resistivities as functions of temperature can be satisfactorily accounted for by the considerations set out in Sec. I. The experimental and the theoretical values of the mobilities for different samples are shown in Fig. 9. The experimental values of the mobilities are obtained from the relation

$$\mu = (1/r)(R/\rho), \tag{6}$$

where r is taken as $3\pi/8$.

The theoretical values of mobility are calculated from Eqs. (3), (4), and (5). Due to the simultaneous presence of donors and acceptors in a sample, the concentration of ionized impurity centers is not zero at zero absolute temperature, but is $N_0=2N_A$ in the case of N-type samples, or $N_0=2N_D$ in the case of P-type samples.[9] The concentration of ionized impurity centers at any temperature is then given by

$$N_s=n+N_0. \tag{7}$$

N_0 is determined by fitting the theoretical mobility curve to the experimental points. The values of N_0 are listed in Table II.

The importance of N_0 in the mobility consideration is as follows: Since n decreases rapidly with temperature, without N_0 the mobility would increase rapidly with decreasing temperature. Experimentally this is certainly not the case. The mobility passes through a maximum and then decreases slowly as the temperature is lowered.

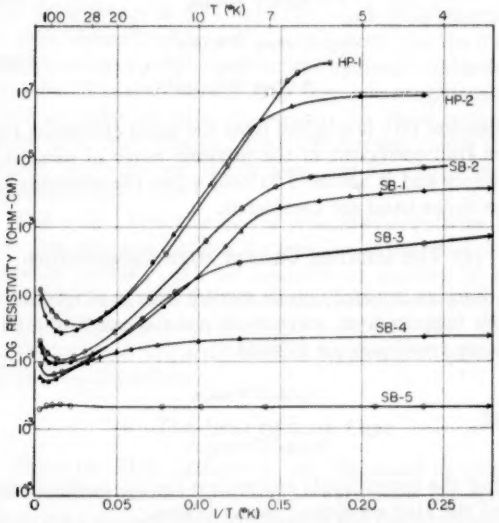

FIG. 8. Semilogarithmic plot of the resistivity *vs* reciprocal of Kelvin temperature for germanium samples HP-1, HP-2, SB-1, SB-2, SB-3, SB-4, and SB-5.

For sample SB-5, the degeneracy temperature is around 100°K, and the theoretical mobility is calculated according to the considerations discussed by Johnson and Lark-Horovitz.[4] Sample SB-2 is omitted from Fig. 8 to avoid confusion with the points of SB-1, since their mobilities are very close. The theoretical curve of SB-3 is absent because of the inhomogeneity of the sample.

Sample SB-4 has a high mobility in its donor band (see Sec. IV) so that only at relatively high temperatures could its mobility be analyzed in the above way. For sample SB-5 the concentration of impurity centers is so large that either the impurity band has completely overlapped with the conduction band or the mobilities

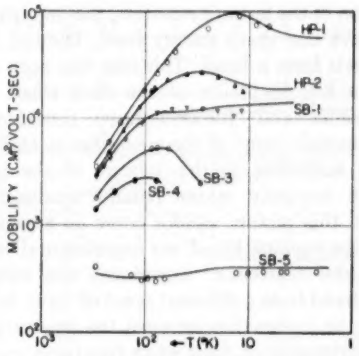

FIG. 9. Plot of log mobility *vs* log Kelvin temperature for germanium samples HP-1, HP-2, SB-1, SB-3, SB-4, and SB-5.

in the two bands are the same. The above analysis of the theoretical mobility applies in either case.

The resistivities of the neutron-bombarded samples are shown in Fig. 10. They have the same general shape as those of the high-purity and the antimony-doped samples. At liquid nitrogen temperature and above, the resistivity can be accounted for by lattice scattering plus impurity scattering, with $N_0=2N_D=n_0$, where n_0 is the number of holes in the exhaustion range.

In the low-temperature region the resistivities of all of the samples mentioned do not increase indefinitely as temperature is lowered but approach saturation values at temperatures corresponding to their respective Hall maxima.

IV. DISCUSSION

The results clearly indicate that the ordinary model, even if it is expanded to take into account the presence of both donor and acceptor levels, cannot explain the anomalous behavior of the Hall effect. This can only be understood if a mechanism is found which will introduce a combination of mobilities due to different types of scattering.

Schottky[12] has pointed out that, due to the random

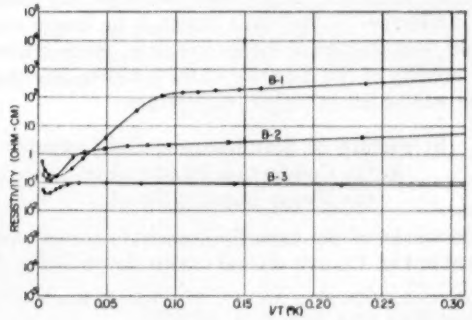

FIG. 10. Semilogarithmic plot of resistivity *vs* reciprocal of Kelvin temperature for neutron-bombarded germanium samples B-1, B-2, and B-3 (P-type).

[12] W. Schottky, Z. Elektrochem. 45, 33 (1939).

distribution of the impurity centers, the impurity states do not have one sharp energy level. Instead, the impurity levels form a band. This idea has been used by Busch[13] in his discussion of the Hall effect in SiC. Lark-Horovitz and Johnson have considered this model to explain some of the anomalies in Hall curves. However, according to this picture of the impurity band, the impurity states remain localized states. Therefore, this picture cannot serve as a satisfactory basis for the explanation of our experimental results.

James and Ginzbarg[14] introduced the idea of an impurity band from a different point of view. According to them, the interaction between the impurity states, or the overlapping of their wave functions, causes the formation of an impurity band. The broadening of the impurity level into a band therefore means the "delocalization" of the impurity states. James pointed[15] out the possibility of conduction in this impurity band.

The possibility of conduction in the impurity band as an explanation of the behavior of the Hall curves at low temperatures will now be presented:

(a) The Mobility of Electrons in the Donor States, or Holes in the Acceptor States

The impurity states are not strictly localized states as pictured in Fig. 1. Due to the finite distance between the impurity centers, an electron in one donor state has a finite probability of going over to another donor state in its spatial neighborhood provided that the latter is not occupied. When an electric field is applied, a small but finite conduction will take place in these impurity states.

It is assumed that the conductivity is proportional to the electric field applied; that is, a definite mobility may be assigned to these states. As the concentration of impurity centers is increased, the impurity states become less localized and the mobility increases accordingly. This mobility in the impurity states is usually small compared to the mobility of electrons in the conduction band or of holes in the filled band. At low temperatures, however, when the concentration of electrons in the conduction band becomes very small, the conduction in the donor states is no longer negligible. For samples of higher impurity concentration, the mobility of the impurity states is higher, and their effect will be felt at higher temperature.

(b) Picture of Simultaneous Conduction in the Conduction Band and in the Donor Impurity Band

The model of the impurity semiconductor as represented in Fig. 1 is now revised to that shown in Fig. 11. The impurity states are now represented as narrow bands. The acceptor band is filled by electrons from the donor band and is inactive in conduction; n_e and n_D denote the concentration of electrons in the conduction band and in the donor band respectively; μ_e and μ_D denote the respective mobilities. The total number of electrons is

$$n_0=n_e+n_D=N_D-N_A. \tag{8}$$

Since N_A is never zero, n_0 is necessarily smaller than N_D, the concentration of donor states. The donor band is, therefore, never filled, and conduction is assured at all temperatures.

The conductivity and the Hall coefficient for the semiconductor are now given by the following expressions:

$$\sigma=n_e e\mu_e+n_D e\mu_D, \tag{9}$$

$$R=-\frac{r}{e}\frac{n_e\mu_e^2+n_D\mu_D^2}{(n_e\mu_e+n_D\mu_D)^2}. \tag{10}$$

Equation (10) is adapted from the usual expression for the Hall coefficient in the intrinsic range of semiconductors and is assumed to hold when the electrons in the donor band are considered.

(c) The Limiting Case of High Temperature

Since μ_D is usually much smaller than μ_e at relatively high temperatures, when n_e is not too small, the following conditions are fulfilled:

$$n_e e\mu_e \gg n_D e\mu_D,$$

and

$$n_e e\mu_e^2 \gg n_D e\mu_D^2.$$

Thus the approximate expressions for the conductivity and the Hall coefficient are as follows:

$$\sigma=n_e e\mu_e, \tag{11}$$

$$R=r/n_e e. \tag{12}$$

Equations (11) and (12) are just the same as Eqs. (1) and (2). They are valid in the exhaustion range and in the intermediate-temperature range. The analysis of σ and R given in Sec. III, therefore, remains valid.

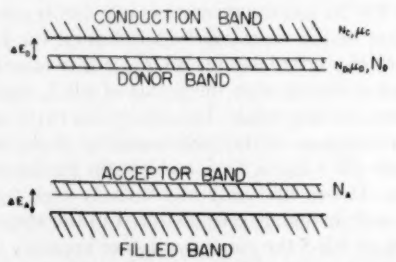

FIG. 11. Energy level diagram for an impurity semiconductor, modified to show finite width of donor and acceptor bands.

[13] G. Busch, Helv. Phys. Acta **19**, 189 (1946); G. Busch and H. Labhart, Helv. Phys. Acta **19**, 463 (1946).

[14] A. S. Ginzbarg, Ph.D. Thesis, Purdue University, 1949 (unpublished); Hubert M. James and Arthur S. Ginzbarg, J. Phys. Chem. **57**, 840 (1953).

[15] H. M. James (private communication); H. M. James and A. S. Ginzbarg (reference 14).

(d) The Limiting Case of Low Temperature

Because of the finite activation energy, ΔE_D, the electron concentration in the conduction band continues to drop as the temperature is lowered. Finally a temperature is reached at which

$$n_c e\mu_c^2 \ll n_D e\mu_D^2, \quad n_c e\mu_c \ll n_D e\mu_D.$$

Then the σ and R expressions become

$$\sigma = n_D e\mu_D, \tag{13}$$

$$R = r/n_D e. \tag{14}$$

At low temperatures nearly all the electrons have fallen back to the donor states. Equation (14) then shows that the Hall coefficient is practically constant at very low temperatures, and that its value is just the same as the Hall coefficient in the exhaustion range when all the electrons are in the conduction band. This behavior is experimentally observed, approximately, for the low-resistance sample SB-4 and for the neutron-bombarded samples. The deviation of R at very low temperatures from its value at room temperature for these samples may come from the fact that the carriers in the impurity bands are not free carriers, and Eq. (10) is only approximately valid.

The ohmic behavior of the measured resistivity at low temperatures justified the previous assumption that definite mobility can be assigned to carriers in an impurity band. The flatness of the resistivity curves at very low temperatures indicates further that this mobility in an impurity band is approximately temperature-independent.

(e) The Intermediate Case

Since the Hall coefficients are the same at room (exhaustion) temperature and at extremely low temperature and since, also, the value of the Hall coefficient increases as the temperature is lowered below the exhaustion range, the Hall coefficient must pass through

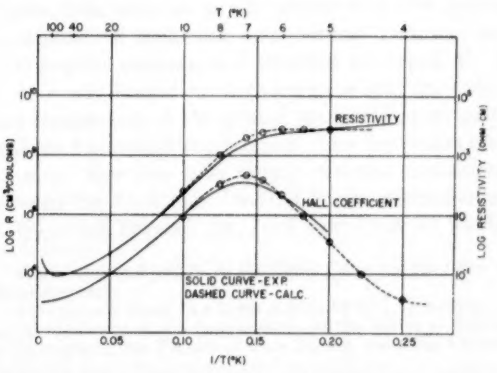

FIG. 12. Comparison of measured Hall and resistivity curves of antimony-doped germanium sample SB-1 (N-type) with the corresponding curves calculated on the basis of impurity band conduction.

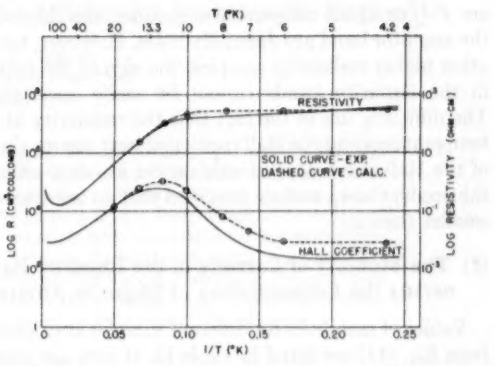

FIG. 13. Comparison of measured Hall and resistivity curves of neutron-bombarded germanium sample B-1 (P-type) with the corresponding curves calculated on the basis of impurity band conduction.

a maximum; this maximum in R explains the observed anomaly described in Sec. III.

The theoretical values of the Hall coefficient and the conductivity in the intermediate case can be obtained from Eqs. (9) and (10), provided that all the four quantities, n_c, n_D, μ_e, and μ_D, are known as functions of temperature.

In the case of a rather well defined energy gap ΔE_D, n_c is expected to decrease almost exponentially with $1/T$; then n_c, at low temperatures, can be obtained from a straight line extrapolation of the experimental $\ln(1/Re)$ *vs* $1/T$ curve.

n_D can be obtained from Eq. (8) and the information on n_c. It is practically a constant for temperatures corresponding to the intermediate case, except for the case of very low resistivity samples.

μ_e can be obtained by extending the mobility curves shown in Fig. 9 and with the help of Eqs. (3), (4), (5), and (7). As a first approximation, it can be considered as a constant.

μ_D is also practically constant with temperature as evidenced by the flatness of the resistivity curves shown in Figs. 8 and 10. Its value can be obtained from Eq. (13), in which σ is the measured value of conductivity at very low temperatures, and $n_D = n_0$.

The maximum in the Hall coefficient is found to occur when

$$n_c\mu_c = n_D\mu_D. \tag{15}$$

The calculated Hall coefficient and resistivity curves for samples SB-1 and B-1, together with the experimental points, are shown in Figs. 12 and 13. The agreement is seen to be satisfactory, considering the crude approximation in applying Eq. (10) to carriers in the impurity bands. The Hall coefficient and resistivity have also been calculated for the other samples and found to agree with experiment.

For the low-resistivity sample SB-5, which is N-type at all temperatures, the carriers in the donor band are definitely electrons. For the bombarded samples, which

are P-type at all temperatures studied, the carriers in the acceptor band are definitely holes. However, for the other higher resistivity samples, the sign of the carriers in the impurity bands cannot be easily ascertained. The difficulty lies in the fact that the resistivity at low temperatures and the Hall coefficient near the maximum of the Hall curve depend only on the absolute value of the product of n_D and μ_D, provided that μ_D is sufficiently smaller than μ_e.

(f) The Mobility of Carriers in the Impurity Bands *versus* the Concentration of Impurity Atoms

Values of mobilities for different samples as calculated from Eq. (13) are listed in Table II. If they are plotted as functions of the impurity concentration, there is considerable scattering in the points. Roughly, the curve can be represented by the relation

$$\mu_D = B(N_D)^{\beta}, \tag{16}$$

where β is close to 1.5. B seems to be somewhat different for the antimony-doped samples and for the neutron-bombarded samples.

The relation expressed by Eq. (16) is certainly very crude, since one would expect μ_D to depend not only on the concentration of impurity centers, but also on the type of impurity atoms introduced, and on how the impurity bands are filled. A definite picture of the mechanism of impurity bands has to be formed before one can predict the mobility and the sign of the carriers in these bands.

V. CONCLUSION

From the above discussion, it is seen that the behavior of the Hall and the resistivity curves over the entire temperature range can be satisfactorily accounted for on the basis of simultaneous conduction by two kinds of carriers in different energy bands and with different mobilities. These two bands have been taken, in this discussion, as the conduction band and the donor band (or the filled and the acceptor band). It is important, however, to notice the difference between the impurity bands and the conduction and filled bands. First, the conduction and filled bands arise from the regular lattice structure, whereas the impurity bands arise from the randomly distributed impurity centers. The latter bands are therefore not homogeneous throughout the crystal. And, secondly, the impurity centers are usually so far apart that, although the impurity states are not strictly localized, the carriers in these states are far from being free. A theoretical investigation of the behavior of carriers in the impurity bands is very desirable. An experimental investigation of the mobility of carriers in the impurity bands as functions of the concentration of impurity centers and of the concentration of carriers, and also for different kinds of impurity centers, would be helpful to the theoretical study.

The authors wish to express their sincere gratitude to Dr. K. Lark-Horovitz for the suggestion of this work and his encouragement on which its success has depended. They are indebted to Dr. W. E. Taylor for the supply of the germanium samples, and to Professors H. Y. Fan, H. M. James, and V. A. Johnson for stimulating discussions. Lastly, their deepest gratitude is due Professor P. H. Keesom, whose advice, given throughout the course of this work, including the design of the cryostat, has been both generous and indispensible.

Absorption of Microwaves by Oxygen in the Millimeter Wavelength Region*†

J. O. ARTMAN‡ AND J. P. GORDON
Columbia University, New York, New York

(Received December 29, 1953)

Pressure broadening of the absorption lines near 60 000 Mc/sec because of the oxygen molecule has been examined in pure oxygen, and in oxygen-nitrogen mixtures. The apparatus consisted of a large nonresonant cavity spectrometer, with bolometer detectors. At pressures of a few millimeters, a fairly constant $(\Delta\nu/P)$ value of 1.94±5 percent (Mc/sec) per mm Hg has been found for pure oxygen, independent of the rotational state of the molecule. To explain absorption in dry air at pressures from one-quarter to one atmosphere, a value of 0.75 for the broadening ratio of $(\Delta\nu/P)$ for O_2-N_2 to $(\Delta\nu/P)$ for O_2-O_2 accounts satisfactorily for the broadening effect of nitrogen. A theoretical analysis has been applied assuming the important molecular interactions are the London dispersion (polarizability) and exchange forces. Dipole-dipole forces are absent, and quadrupole- and magnetic-dipole effects are found to be too weak to be effective.

INTRODUCTION

ALTHOUGH many high-precision measurements have been made on the resonant frequencies of molecules in the microwave region, there are relatively few and far less exact measurements on the line shapes and intensities of microwave absorption lines. Detailed and extensive knowledge of line shapes would be valuable, however, in determining the nature of intermolecular forces. The particular case of O_2 which has been examined here is unusual in that electric dipole and certain other long-range forces which ordinarily broaden microwave transitions are absent. Furthermore, much of the absorption of millimeter waves in the atmosphere comes from transitions in O_2, and hence measurements of this spectrum are of help in understanding and calculating microwave transmission in the atmosphere.

Historically the O_2 spectrum was one of the first to be observed in the microwave region. In the electronic ground state of the oxygen molecule $(^3\Sigma_g^-)$ the electron spins pair to give a net spin of unity. The magnetic moment associated with this electronic spin can interact with the magnetic field of microwave radiation, resulting in absorption of energy.[1] The electron spin S may take on three orientations with respect to K, the angular momentum of molecular end-over-end rotation; the total angular momentum J therefore can equal $K-1$, K, or $K+1$. Transitions between these spin fine structure components of the ground state rotational levels lie in the 5 mm wavelength region. (One line occurs near 2.5 mm.) Selection rules permit resonant transitions between the $J=K$ and $J=K+1$ levels, referred to as + lines; and between the $J=K$ and $J=K-1$ levels, referred to as − lines. For $(O^{16})_2$, symmetry considerations restrict K to odd integers.

The Van Vleck-Weisskopf, collision-broadening, line-shape theory[2] is believed to be the most appropriate in the microwave spectral region. (For this theory to be applicable the line breadth must be caused primarily by pressure broadening.) Using this theory Van Vleck has prepared formulas for O_2 absorption[1] in which the line breadth $\Delta\nu$ appears as an undetermined parameter. This line-breadth parameter $\Delta\nu$ represents the effect of collision damping in broadening the spectral line. $\Delta\nu$, which corresponds to the molecular collision rate, usually is directly proportional to the molecular density, i.e., to the pressure P; hence the pressure normalized impact parameter $\Delta\nu/P$ is the more meaningful quantity. The theory of Anderson[3] is currently believed to be the most suitable for calculating microwave line-breadth parameters.

In the past the microwave O_2 spectrum has been examined at various pressures. At low pressures the widths of the resolved O_2 lines have been observed. At high pressures, where the wings of the individual resonances overlap greatly, the intensity caused by the envelope of the unresolved lines has been measured. Precision and accuracy generally were poor. The data often could not be easily interpreted; proposed theories and line-breadth mechanisms could not be seriously tested.

In order to obtain independent reliable information on line widths and intensities we have carefully investigated the microwave O_2 spectrum at both high and low pressures. In general, the high-pressure measurements were in accord with the low-pressure results. Mechanisms proposed as responsible for line breadth have been critically examined. Theoretical line-breadth calculations have been revised and extended: a line-width computation that corresponds closely to the experimental results is presented.

* Work supported jointly by the Signal Corps and the Office of Naval Research.

† This paper is based on a thesis submitted by J. O. Artman in partial fulfillment of the requirements for the degree of Doctor of Philosophy in the Faculty of Pure Science, Columbia University.

‡ Now at Lincoln Laboratory, Massachusetts Institute of Technology, Cambridge, Massachusetts.

[1] J. H. Van Vleck, Phys. Rev. **71**, 413 (1947). A summary of previous theoretical and experimental work is also given here.

[2] J. H. Van Vleck and V. F. Weisskopf, Revs. Modern Phys. **17**, 227 (1945).

[3] P. W. Anderson, dissertation, Harvard University, 1948; Phys. Rev. **76**, 647 (1949).

EXPERIMENTAL TECHNIQUE

The untuned cavity spectrometer was used in these experiments. This type of spectrometer is particularly suitable for line breadth and absolute intensity measurements. The microwave nonresonant cavity spectrometer was first described by Lamb,[4] and has been employed previously in the investigations of Becker and Autler[5] and Weingarten.[6]

A simplified diagram of the spectrometer is shown in Fig. 1. Microwave radiation is introduced by a suitable horn; since the wavelength is small in comparison to cavity dimensions, a large number of normal modes of oscillation can exist. The moving blades of a fan-like "mode-mixer" periodically vary the boundary conditions, insuring the presence of a large number of modes all with essentially the same degree of excitation and absorption. Under these conditions the response of randomly disposed square-law detecting elements, averaged in time and over the cavity volume, is proportional to the Q of the cavity and contents. This Q is then determined absolutely by comparison with the Q after addition of a known loss; the known loss is provided by a microwave reference window which, when opened, permits radiation egress from the cavity.[7] For each absorption determination three or four measurements are required: detector response when the cavity is evacuated, response after addition of gas, and response under at least one of these two previous conditions when, in addition, the microwave window is opened. (See Appendix A.)

In the arrangement for the O_2 measurements, 5-mm radiation is obtained from a crystal frequency doubler powdered by a 1-cm klystron. The 5-mm radiation is modulated at 20 cps by a motor-driven variable waveguide attenuator before being introduced to the cavity.

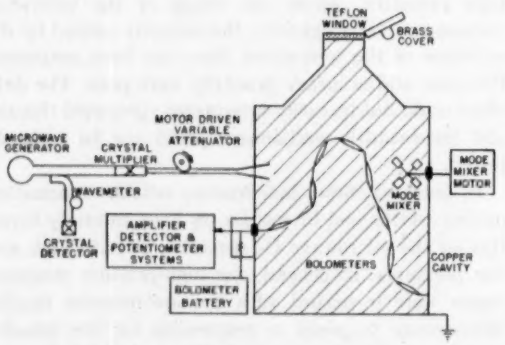

FIG. 1. Nonresonant cavity spectrometer.

[4] W. E. Lamb, Jr., Phys. Rev. **70**, 308 (1946).
[5] G. E. Becker and S. H. Autler, Phys. Rev. **70**, 300 (1946).
[6] I. R. Weingarten, dissertation, Columbia University, 1948 (unpublished).
[7] The energy loss caused by passage of radiation through the window was derived by Lamb (see reference 4). The behavior of cavity and window predicted by Lamb has been verified by Becker and Autler (see reference 5) and by Weingarten (see reference 6).

TABLE I. O_2 line breadth parameter as function of rotational quantum number K ($T=300°K$).

K	Series	Experimental value	Theoretical fit
			(Mc/sec) per mm Hg
1	+	2.20±10%	2.075
1	−		2.064
3	+	2.23±10%	1.944
3	−		1.943
5	+	1.96± 5%	1.940
5	−	1.99± 5%	1.937
7	+	1.92± 5%	1.937
7	−	1.82± 5%	1.935
9	+	1.93± 5%	1.938
9	−	2.00± 5%	1.937
11	+		1.939
11	−	1.97±10%	1.938
13	+		1.940
13	−	1.86± 5%	1.940
15	+		1.941
15	−	1.99± 5%	1.941
17	+		1.942
17	−	1.82±10%	1.942
19	+		1.942
19	−	1.92±10%	1.942
21	+		1.943
21	−		1.943
23	+		1.943
23	−		1.943
25	+		1.943
25	−		1.943
27	+		1.944
27	−		1.944
29	+		1.944
29	−		1.944

The response of a chain of vacuum bolometers is fed into a high-gain, narrow-band, 20-cps amplifier, rectified, and finally measured with a conventional potentiometer arrangement or alternatively displayed on a recording potentiometer.

The microwave window is made from a Teflon disk which can be covered by a brass lid. The effective area of this window was determined by comparison with a "standard" reference window opening on the conical surface of the cavity. This window comparison was made at a wavelength of 1.35 cm, necessarily before the outer (pressure) lid of the cavity was made vacuum tight. The window calibration is presumed to be the same at the higher frequencies at which the O_2 absorption occurs and, as explained below, was corroborated by integrated intensity measurements of individual O_2 lines.

EXPERIMENTAL RESULTS

Low Pressure Observations: Resolved O_2 Lines

Observations were made on resolved O_2 lines at pressures of 2 to 10 mm Hg. (The positions of most of these resonances have been accurately determined by Burkhalter *et al.*[8]) Traces were made over the contours of several lines while the source frequency was swept mechanically. From these traces peak intensity and half-width were determined independently at various

[8] Burkhalter, Anderson, Smith, and Gordy, Phys. Rev. **79**, 651 (1950).

O_2 pressures. Since the product of peak intensity and half-width (this quantity has been called integrated intensity) is calculable in terms of known constants these results furnish a check on the window calibration. The window calibration at 5 mm, as inferred from integrated intensity measurements, was equal to that at 1.35 cm within 5 percent experimental error.

The normalized impact parameter $\Delta\nu/P$ and peak intensity γ_p were found to be independent of pressure[9] over the range investigated (2–10 mm Hg). In determining line shapes over extended frequency ranges, corresponding points on four separate recorder traces had to be correlated. The assumptions had then to be made that the klystron-power level did not change between pairs of window-open, window-closed traces (see Appendix A), and that the klystron frequency sweep rate was linear between the 30-Mc/sec frequency standard marker pips. These assumptions were not always good, but numerous traces were taken to minimize the error involved. Figure 2 shows a typical resulting curve. Agreement with the Van Vleck-Weisskopf line shape is made to within experimental error.

Subsequently the window calibration was assumed valid and line breadths were inferred from measured peak intensities by using the integrated intensity relationships. Intensity contributions from the wings of adjoining lines were subtracted when necessary. The values of $\Delta\nu/P$, measured at ambient temperature, were referred to 300°K. (For this, a hard sphere model of O_2 was assumed, giving $\Delta\nu/P$ a temperature variation of $T^{-\frac{1}{2}}$.) Because of experimental difficulties, the uncertainties assigned to the $\Delta\nu/P$ values are larger than the probable errors derived on a purely statistical basis. The data are shown in Fig. 3; the recent results of Anderson,

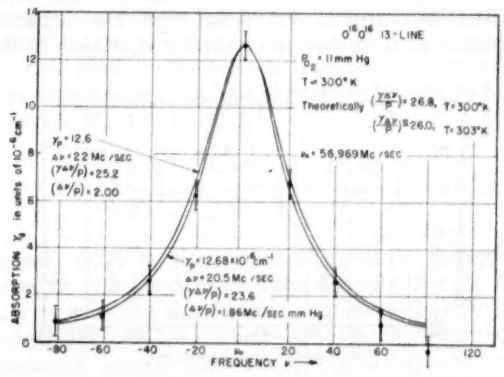
$O^{16}O^{16}$ 13⁻ LINE
p_{O_2} = 11 mm Hg
T = 300° K
Theoretically $(\frac{\gamma\Delta\nu}{p})$ = 26.8, T = 300°K
$(\frac{\gamma\Delta\nu}{p})$ = 26.0, T = 303°K
ν_0 = 56,969 Mc/sec
γ_p = 12.6
$\Delta\nu$ = 2.2 Mc/sec
$(\gamma\Delta\nu/p)$ = 25.2
$(\Delta\nu/p)$ = 2.00
γ_p = 12.68 × 10⁻⁶ cm⁻¹
$\Delta\nu$ = 20.5 Mc/sec
$(\gamma\Delta\nu/p)$ = 23.6
$(\Delta\nu/p)$ = 1.86 Mc/sec mm Hg
ABSORPTION γ_p in units of 10⁻⁶ cm⁻¹
FREQUENCY ν ⟶

FIG. 2. Plot of the shape of the 13⁻ line in the absorption spectrum of $(O^{16})_2$.

[9] Pressure independence of $\Delta\nu/P$ and peak intensity indicate that only pressure broadening is contributing to line breadth. Other effects such as natural line breadth, Doppler breadth, and saturation breadth can be shown to be negligible. Zeeman splitting because of the earth's magnetic field which could conceivably be significant was not observed—the iron tank enclosing the copper microwave cavity had been degaussed.

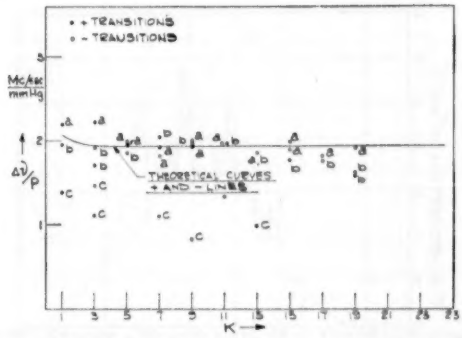

FIG. 3. Results of recent line-width measurements in the $(O^{16})_2$ spectrum. Our results are labeled "a", those of Anderson *et al.* (see reference 10) are "b", and those of Gokhale and Strandberg (see reference 11) are "c". Errors are assigned to points marked "a" as follows: ±10 percent for 1^+, 3^+, 11^-, 17^-, and 19^-; ±5 percent for the others.

Smith, and Gordy,[10] and of Gokhale and Strandberg,[11] are also shown. In Table I as well as in Fig. 3 our data are compared with the results of a theoretical calculation (discussed later). Experimental values for the 1^- and 3^+ lines are slightly larger than the theoretical expectations; the experimental values for large K may be lower than theoretical expectations.

The ratio of O_2-N_2 broadening to O_2 self-broadening was determined by the reduction in peak intensity of an O_2 line on addition of N_2. The broadening ratio is given by

$$\beta=\left[\frac{\gamma(O_2-O_2)}{\gamma(O_2-N_2)}-1\right]f(O_2)\Big/[1-f(O_2)],$$

where $\gamma(O_2-O_2)$ refers to the peak line intensity in pure O_2, and $\gamma(O_2-N_2)$ refers to the peak line intensity upon addition of N_2. The fraction of O_2 is denoted by $f(O_2)$. For the observed lines, β was found to be 0.90±15 percent. Anderson, Smith, and Gordy[10] report a β value of 0.79 for the 9− O_2 line. As indicated below, β can also be obtained from the high-pressure observations.

High-Pressure Observations: Envelope of O_2 Lines

O_2 absorption in dry air at ambient temperature was measured at pressures of $\frac{1}{4}$, $\frac{1}{2}$, and 1 atmosphere to determine whether high-pressure absorption could be calculated from low-pressure half-width parameters. The results are shown in Figs. 4–6. As in the case of the low-pressure data, experimental uncertainties are believed to be greater than the statistical probable errors. Two theoretical absorption curves were computed at all three pressures: one with an oxygen self-broadening impact parameter of about 1.97 Mc/sec per mm Hg and an N_2-O_2 broadening ratio β of 0.92; the other with the O_2 impact parameters listed in Table I, and β

[10] Anderson, Smith, and Gordy, Phys. Rev. **87**, 561 (1952).
[11] B. V. Gokhale and M. W. P. Strandberg, Phys. Rev. **84**, 844 (1941).

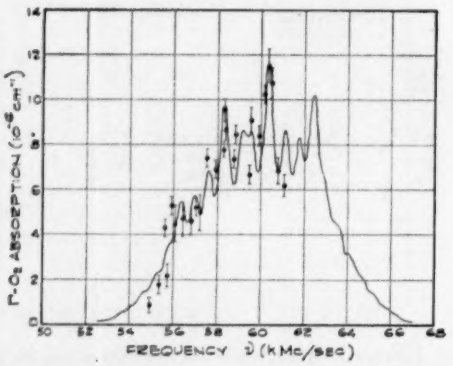

FIG. 4. Microwave absorption in dry air at ¼ atmosphere pressure and 300° Kelvin by oxygen. A theoretical plot is shown using $\beta=0.75$.

equal to 0.75. Only for the 1-atmosphere data was it really evident that the second set of parameters furnished the better fit to the experimental points. Both theoretical absorption curves are shown, together with the 1-atmosphere data, in Fig. 6. In Figs. 4 and 5, the theoretical curves are based on the second set of parameters.

The one-atmosphere data correspond to an oxygen-nitrogen broadening ratio perhaps slightly smaller than the 0.75 shown in Fig. 6. The total line width at one atmosphere pressure thus appears to be less than one would expect from the low-pressure values of $(\Delta\nu/P)$ for O_2 and the ratio β. The value 0.75 for β is just about at the 15 percent error limit ascribed to the low-pressure measurements. More accurate measurements are thus needed to determine whether this discrepancy is real. Perhaps the assumption of linear dependence of the half-widths on the pressure does not hold exactly up to one atmosphere, or perhaps the Van Vleck-Weisskopf line-shape formula is not applicable over as wide a range about the center of a line as was previously supposed.

Previous investigation of O_2 absorption at high pressures has been limited. (Early work is summarized by Van Vleck.[1]) Beringer[12] in 1944 used wave-guide techniques to measure O_2 attenuation in O_2-N_2 mixtures. His data were not sufficiently accurate to decide between the line breadth values of 0.02 and 0.05 cm^{-1}/atmos. (The conversion factor from cm^{-1}/atmos to (Mc/sec) per mm Hg is 39.5.) Beringer also found the nitrogen-oxygen broadening ratio to be about unity. Mueller's observations of microwave transmission in the atmosphere and in a wave guide (see Van Vleck, reference 1) suggested a value of 0.02 cm^{-1}/atmos. The microwave radiometer was used by Dicke *et al.*[13] to determine absorption of radiation in the 1-cm wavelength region. Dicke's data correspond to a breadth of 0.02 cm^{-1}/atmos. Lamont[14] also proposed a $\Delta\nu/P$ value of about 0.02 cm^{-1}/atmos from field attenuation measurements at 5-mm wavelengths. Later Strandberg *et al.*[15] employed a wave-guide bridge to observe O_2 absorption at millimeter wavelengths in oxygen-nitrogen mixtures at atmospheric pressures. Although the absorption found corresponded to a line breadth of 0.04 cm^{-1}/atmos, fluctuations in absorption indicated a value $\leqslant 0.02$ cm^{-1}/atmos. Strandberg also reported unusual behavior of O_2 absorption in O_2-N_2 mixtures. Nicoll and Warner[16] have examined solar absorption with a microwave radiometer at 8 mm wavelength. They have not attempted however to determine experimentally the separate contribution of O_2 and H_2O to observed attenuation.

When experimental uncertainties are considered, these previous results for the center of the atmospheric O_2 absorption are not inconsistent with our $\Delta\nu/P$ value of 1.94 (Mc/sec) per mm Hg (0.049 cm^{-1}/atmos) and our nitrogen-oxygen broadening ratio value of 0.75.

THEORY

In the microwave spectral region the impact type of pressure-broadening theory is generally applicable.[17] The impacts may be described semiclassically as follows: The molecules are essentially isolated from each other; occasional molecular encounters cause perturbations in the energy levels of a radiating molecule; hence, during the encounter or "collision" the frequency of the radiator is modified. If subsequently radiation continues without loss of energy a phase change,

$$2\pi \sum_{\text{collision}} \Delta\nu\Delta t \quad \text{or equivalently} \quad \sum_{\text{collision}} \Delta E\Delta t/\hbar,$$

has been introduced, ΔE is the change in energy level separation caused by the perturbation. The change of phase in such *adiabatic* encounters is equivalent to the

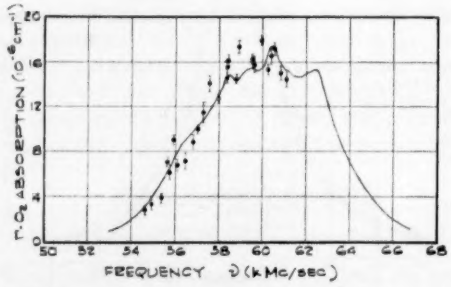

FIG. 5. Microwave absorption in dry air at ¼ atmosphere pressure and 300° Kelvin by oxygen. A theoretical plot is shown $\beta=0.75$.

[12] R. Beringer, Phys. Rev. **70**, 53 (1946).
[13] Dicke, Beringer, Kyhl, and Vane, Phys. Rev. **70**, 340 (1946).
[14] H. R. Lamont, Phys. Rev. **74**, 353 (1948); Proc. Phys. Soc. (London) **61**, 562 (1948).
[15] Strandberg, Meng, and Ingersoll, Phys. Rev. **75**, 1524 (1949).
[16] G. R. Nicoll and F. L. Warner, Telecommunications Research Establishment Memorandum 471, July 1951 (unpublished).
[17] C. H. Townes and A. L. Schawlow, *Microwave Spectroscopy* (McGraw-Hill Book Company, Inc., New York, to be published). A general discussion of microwave line breadth is included.

introduction of new frequencies, and therefore contributes to line broadening.

Collisions in which the radiator makes a transition are called by Townes[17] *diabatic* collisions; here the behavior of the radiator after collision is unrelated to its prior condition. By definition, a collision can be said to occur when the change in phase in a molecular encounter is at least one radian. But in the microwave spectral region the interaction energy necessary to produce such a phase change can be shown to be more than sufficient to cause a transition, i.e., in the microwave spectral region almost all molecular encounters result in diabatic collisions. Any microwave pressure-broadening theory must take into account these diabatic collisions. In the particular case of O_2 the collision diameter is so small that they are especially important.

The impact pressure-broadening theory of Anderson[3] appears to be the most appropriate for use in the microwave spectral region. This formulation differs from most others in that the effects of diabatic as well as adiabatic collisions are taken into account. Anderson derives line-shape formulas similar to those of Van Vleck-Weisskopf and in addition obtains general expressions for line breadth.

Various interactions have been proposed to account for O_2 and O_2-N_2 broadening.[3,8,10,18,19] In principle the change in phase including the sum of *all* the interactions should be evaluated. (This point often has not been clearly stated in the literature.) A more feasible procedure is first to estimate the quantitative importance of these interactions by comparing the phase changes caused by each interaction acting alone, and then to perform a line breadth calculation considering only the important effects. Fortunately in the case of O_2 only two types of interactions are significant; a fairly rigorous calculation can then be made on the basis of just these two effects.

Analogously to the gas-kinetic collision rate formula, the pressure-normalized microwave line breadth parameter $(\Delta\nu/P)_{ij}$ can be written

$$\left(\frac{\Delta\nu}{P}\right)_{ij}=\frac{n_j}{P}\frac{v_i}{\sqrt{2}}b_{ij}^2\left[\frac{1+M_i/M_j}{2}\right]^{\frac{1}{2}},$$

where n_j/P is the pressure-normalized molecular density, v_i is the average molecular velocity, M_i, M_j are the molecular masses, and b_{ij} represents the effective microwave collision diameter. The experimental data presented indicate that both O_2-O_2 and O_2-N_2 collision diameters are fairly independent of the rotational quantum number K of the radiating molecule and that O_2-N_2 broadening is less than O_2-O_2 broadening. The O_2-O_2 line breadth [$\sim$1.95 (Mc/sec) per mm Hg] corresponds to a $b(O_2-O_2)$ value of 4.40A, while for

[18] M. Mizushima, Phys. Rev. **83**, 94 (1941); **84**, 363 (1951).
[19] Anderson, Smith, and Gordy, Phys. Rev. **82**, 264 (1951).

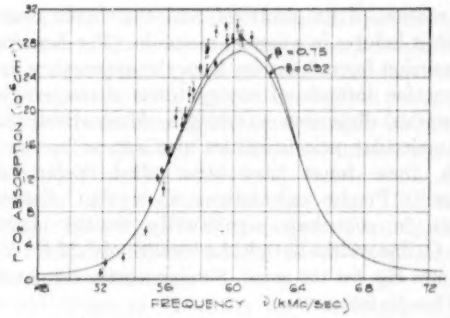

FIG. 6. Microwave absorption in dry air at 1 atmosphere pressure and 300° Kelvin by oxygen.

$\beta=0.90$ the O_2-N_2 breadth corresponds to a $b(O_2-N_2)$ of 4.24A [or to a $b(O_2-N_2)$ of 3.88A for $\beta=0.75$]. From viscosity data[20] the collision diameters are $b(O_2-O_2)=3.60$A, $b(O_2-N_2)=3.38$A. Hence it is likely that O_2-O_2 and O_2-N_2 interactions are much the same and caused by forces of rather short range.

Since $(O^{16})_2$ has no electric dipole moment, the longer-range Van der Waals interactions, usually found to account for microwave line breadth, do not occur. Oxygen interactions that should be examined include magnetic dipole, molecular electric quadrupole, London dispersion, and exchange.

Oxygen molecular magnetic-dipole interaction is readily shown to contribute insignificantly toward line breadth—the collision diameter caused solely by this effect (estimated by determining the distance of closest approach at which the change in phase is one radian) is only 0.238A. This interaction is of course not present in O_2-N_2 collisions.

Oxygen broadening caused by molecular electric quadrupole interaction alone has been calculated by Mizushima[18] using the methods of adiabatic collision theory.[21] From the more appropriate semidiabatic approach of Anderson the O_2-O_2 collision diameter caused by quadrupole interactions is estimated (in the same fashion as in the previous case) to be less than 1.71A. Although the nitrogen molecular quadrupole is at least three times as large as that of oxygen,[22] O_2-N_2 as well as O_2-O_2 molecular quadrupole broadening is probably quite small.

Anderson[3] has made a calculation for O_2 broadening caused by London dispersion forces.[23] This type of force may be described as an interaction between the fluctuating dipole moment of one molecule, associated with

[20] E. H. Kennard, *Kinetic Theory of Gases* (McGraw-Hill Book Company, Inc., New York, 1932), p. 149.
[21] In Appendix B the distinction between the adiabatic and Anderson pressure-broadening theories is made clear. For the case of O_2 the results of these two theories are compared in some detail.
[22] R. R. Howard and W. V. Smith, Phys. Rev. **79**, 128 (1950); W. V. Smith and R. Howard, Phys. Rev. **79**, 132 (1950).
[23] Anderson's final formulas for London dispersion force broadening were found to be in error and have been corrected.

the motion of its electrons, and the dipole moment which it induces in a second molecule. (The description "dispersion forces" derives from the appearance in the interaction formula of energy terms characteristic of the optical dispersion wavelength. Alternatively, since the molecular polarizabilities also appear in the formula, these forces have been called "polarizibility forces.") Precise calculations show that dispersion forces do contribute significantly toward observed O_2-O_2 line widths but yield a breadth of 1.27 (Mc/sec) per mm Hg, far too small. Similar results are obtained for O_2-N_2 interaction.

The exchange repulsion between two molecules arises from the interaction of their electronic wave functions. Examination shows that exchange interaction contributes substantially toward oxygen line breadth. Since exchange and polarization are by far the largest contributors to broadening, the line breadth resulting from the combination of these forces alone will be calculated.[24]

The polarizability interaction is specified in terms of parameters known from optical measurements. The exchange interaction is much more difficult to treat theoretically. Although a reasoned assumption as to the form of this interaction can be made, the exchange oxygen parameters in general are not known. Some information can be gleaned from O_2 gas-kinetic collision diameter data; exchange parameters for other substances have been determined from the study of the structure of solids and from the investigation of repulsive forces between molecules in gases. Oxygen exchange parameters were selected that appeared plausible in view of these data and which resulted in calculated exchange-polarizability line widths agreeing closely with observed values.

The exchange interaction[25] is taken to be of the form

$$H_{\text{exchange}}=\frac{3}{3+\epsilon}\frac{4}{\pi}kTe^{-[(r-b_{kT})/a]}[1+\epsilon\cos^2\Theta],$$

in which the parameters are defined as: a=exchange force range, b_{kt}=gas-kinetic collision diameter, ϵ=measure of geometric anisotropy of O_2, Θ=angle between figure axis of radiator and the radiator-perturber distance r, k=Boltzmann constant, and T=temperature in °K. From the data on page 149 of Kennard's book,[20] b_{kT} for O_2 is 3.60A at 300°K. Epsilon is estimated by Miller (verbal communication and reference 26) to be 0.85 with an uncertainty of no more than 15 percent. With these parameters fixed, $a(O_2-O_2)$ was chosen to be 0.420A in matching theoretical polarizability-exchange widths to observed line breadths.

To fit alkali halide energies and lattice constants in solids, Born and Mayer[27] chose an a of 0.345A (this and other early work is summarized by Seitz[28]). Rittner,[29] in a recent paper investigating repulsive forces in alkali halide molecules, selected the smaller value 0.31A. Since the interionic diameters of alkali halide molecules are less than those of the corresponding crystals, Rittner[29] suggested that a rough proportionality exists between interaction range a and intermolecular diameter b.

Repulsive forces between rare gas molecules have been considered theoretically by Slater,[25] who obtained a range of 0.217A for He. Bleick and Mayer[30] calculated a range of 0.209A and a collision diameter of 2.058A for Ne. Kunimine[31] determined a to be 0.272A for argon. Since the oxygen molecule is larger than the alkali halide molecules and the rare gas atoms, the selection of 0.420A for $a(O_2-O_2)$ does not appear unreasonable. In these references the exponential dependence of the exchange interaction on r is shown to correspond roughly to $1/r^{10}$ or $1/r^{11}$. The power of r is approximated by the ratio of the gas-kinetic collision diameter b to the intermolecular force range a:

$$H_{\text{exchange}}\propto e^{-r/a}\simeq A/r^n;\quad n\simeq b_{kT}/a.$$

For a b_{kT} value of 3.60A and an a value of 0.420A, $n\simeq 8.6$, which is reasonably close to 10.

The temperature variation of gas-kinetic collision diameters can be expressed by the relation $(b_{kT})_T=(b_{kT})_{T_0}(T_0/T)^m$. It can be shown that m is approximated by a/b. For O_2-O_2 collisions, m is 0.155, (see Kennard, reference 20, p. 149) in reasonable agreement with 0.117, the ratio of $a(O_2-O_2)$ (0.420A) to $b(O_2-O_2)$(3.60A).[32]

Only a rough estimate can be made of the exchange parameters for O_2-N_2 collisions. The O_2-N_2 diffusion diameter is 3.38A at 300°K (see Kennard, reference 20, p. 201). Following the suggestion of Rittner[29] $a(O_2-N_2)$ can be estimated from the relation

$$a(O_2-O_2)/b_{kT}(O_2-O_2)\sim a(O_2-N_2)/b_{kT}(O_2-N_2)$$

to be 0.394A.

For these O_2-O_2 exchange-polarizability collision parameters, the impact parameter,[33]

$$\Delta\nu/P=(n\nu/P\sqrt{2})(b_{\text{eff}}^2)$$

[24] Contribution of the so-called resonance interactions to oxygen line breadth is negligible. These effects are discussed in Appendix C.

[25] J. C. Slater, Phys. Rev. **32**, 349 (1928).

[26] Miller, Townes, and Kotani, Phys. Rev. **90**, 542 (1953).

[27] M. Born and J. E. Mayer, Z. Physik **75**, 1 (1932).

[28] F. Seitz, *The Modern Theory of Solids* (McGraw-Hill Book Company, Inc., New York, 1945).

[29] E. S. Rittner, J. Chem. Phys. **19**, 1030 (1951).

[30] W. E. Bleick and J. E. Mayer, J. Chem. Phys. **2**, 252 (1934).

[31] M. Kunimine, J. Chem. Phys. **18**, 754 (1950); Progr. Theoret. Phys. (Japan) **5**, 412 (1950).

[32] Temperature dependence of line widths is discussed in Appendix D.

[33] If all terms involving exponentials are set equal to zero the correct formulas for pure polarizibility line breadth are obtained.

is found from

$$b_{\text{eff}}^2=b^2+(fg_{\pm})\left[\frac{1.071\times10^5}{b^8}+12.94e^{-2(b-3.60)/a}\times a^2b^2\left(1+\frac{a}{b}+\frac{a^2}{2b^2}\right)+\frac{9.419\times10^3a^4}{b^{7/2}}\times e^{-(b-3.60)/a}\left\{1-\frac{7}{2}\frac{a}{b}+\frac{7\cdot9}{4}\left(\frac{a}{b}\right)^2-\frac{7\cdot9\cdot11}{8}\left(\frac{a}{b}\right)^3+\frac{7\cdot9\cdot11\cdot13}{16}\left(\frac{a}{b}\right)^4\cdots\right\}\right],$$

where a and b are in A, $a=0.420$, and b is determined from the relations:

$$\tfrac{1}{2}\eta^2(b)=1,$$

$$\eta(b)=\left[\frac{9.258}{b^5}\times10^2+5.087(ab)^{\frac{1}{2}}e^{-(b-3.60)/a}\right](fg_{\pm})^{\frac{1}{2}}.$$

Also

$$f=\frac{K(K+1)}{(2K-1)(2K+3)},$$

$$g_+=1-\left[1-\frac{3}{K(K+1)}\right]\frac{(2K+5)(2K+4)(2K)(2K-1)}{[(2K+1)(2K+3)]^{\frac{1}{2}}(2K+2)^2}\quad(+\text{lines}),$$

$$g_-=1-\left[1-\frac{3}{K(K+1)}\right]\frac{(4K^2-9)(4K^2-4)}{(4K^2-1)^{\frac{1}{2}}(2K)^2}\quad(-\text{lines}).$$

The $fg_{\pm}$ functions are substantially *independent* of K (see Appendix B). The results of this $\Delta\nu/P$ calculation are displayed in Fig. 2 and tabulated in Table I.

By performing a similar analysis β, the ratio $[(\Delta\nu/P)$ for $O_2-N_2]/[(\Delta\nu/P)$ for $O_2-O_2]$, is found to be 0.88.

SUMMARY

The spin reorientation spectrum of O_2 in the millimeter wavelength region has been investigated both at high and low pressures with the untuned cavity spectrometer.

The resolved O_2 lines observed at low pressures corresponded to values of the rotational quantum number K extending from 1 to 19. The line breadth parameters were found to be fairly independent of the value of K, averaging to 1.94 (Mc/sec) per mm Hg. For several lines both the peak intensity γ_p and the line breadth parameter $\Delta\nu/P$ were independently determined. The product $\gamma_p(\Delta\nu/P)$ was found to agree to ±5 percent with theoretical values which are expressed in terms of known physical constants. Beta, the ratio of the O_2-N_2 broadening parameter to the O_2 self-broadening parameter, was determined by observations on a number of individual lines to be 0.90 ± 15 percent.

Applicability of various proposed theories to oxygen broadening has been examined in detail. The line breadth can be most reasonably interpreted as resulting from Van der Waals interactions of the London dispersion and exchange types. Although the dispersion interaction constants are known from optical measurements there are no direct determinations of the exchange parameters. The choice of exchange parameters agrees qualitatively, however, with what is known about the properties of oxygen and other molecules. The line breadths computed by following the general formulation of P. W. Anderson match most of the observed values within experimental error.

The absorption of O_2 in dry air was measured at pressures of $\frac{1}{4}$, $\frac{1}{2}$, and 1 atmos. At these pressures, absorption is caused by the addition of the many overlapping individual lines. A good fit to the experimental data was obtained by simply adding the contributions from the various lines, using the Van Vleck-Weisskopf line shape formula with an oxygen self-broadening parameter value of 1.94 (Mc/sec) per mm Hg and an oxygen-nitrogen broadening ratio β of 0.75. This value of β is somewhat more accurate than the low-pressure value, and is the appropriate parameter for use in calculating line breadths at pressures near one atmosphere; the data obtained are useful in predicting atmospheric absorption of oxygen under various conditions.

Absorption on the far wings of the oxygen lines may perhaps be lower than that expected from extrapolation from the central region.

ACKNOWLEDGMENTS

The research described in this paper would not have been possible without use of the facilities and cooperation of the personnel of the Columbia Radiation Laboratory. Dr. P. W. Anderson lent a copy of his thesis and responded to many of our questions.

The authors wish to acknowledge their indebtedness to Professor C. H. Townes for his continued interest, guidance, and encouragement.

APPENDIX A. MEASUREMENT OF ABSOLUTE MICROWAVE ABSORPTION WITH THE NONRESONANT CAVITY SPECTROMETER

If the response of the detectors in the cavity is proportional to the cavity Q, the inverse of the detector response is proportional to the cavity losses which are additive.

$$1/A_1^0=K_1\alpha_{\text{tank}},$$

and

$$1/A_2^0=K_2(\alpha_{\text{tank}}+\alpha_{\text{window}}),$$

where A_1^0 is the detector response in the empty cavity with the microwave window *closed*, A_2^0 is the detector response in the empty cavity with the window *open*. K_1 and K_2 represent unknown proportionality factors. If the microwave generator is supplying energy at the *same* rate during both window-open and window-closed measurements, $K_1=K_2=K$ and

$$\alpha_{\text{tank}}=[A_2^0/(A_1^0-A_2^0)]\alpha_{\text{window}}.$$

Similarly if A_1^g, A_2^g denote window-closed, window-open detector readings when additional gas absorption α_{gas} is present,

$$\alpha_{tank}+\alpha_{gas}=\left(\frac{A_2^g}{A_1^g-A_2^g}\right)\alpha_{window}.$$

Hence,

$$\alpha_{gas}=\alpha_{window}\left[\left(\frac{A_2^g}{A_1^g-A_2^g}\right)-\left(\frac{A_2^0}{A_1^0-A_2^0}\right)\right].$$

If the detector input when the cavity is evacuated is the same as when it is empty (which was not demanded in the analysis above) then three measurements suffice. For instance, from A_1^0, A_2^0, A_1^g:

$$\alpha_{gas}=\alpha_{window}\left[\left(\frac{A_2^0}{A_1^0-A_2^0}\right)-\left(\frac{A_1^0}{A_1^g}-1\right)\right].$$

APPENDIX B. COMPARISON OF ADIABATIC AND SEMIDIABATIC PRESSURE-BROADENING THEORIES

The more appropriate semidiabatic theory used by Anderson[3] gives not only different numerical results from those of the adiabatic theory, but also a different dependence of the line-width parameter on K.

The adiabatic theory, used by Mizushima[18] in a calculation for O_2, gives the rms phase shift α as $\langle(\eta_i-\eta_f)^2\rangle_{Av}^{\frac{1}{2}}$, η_i and η_f referring to the phase shifts of the initial and final levels of the radiating molecule. If η_i equals η_f, then α vanishes. Anderson in calculating the rms phase shift considers neither $\langle(\eta_i-\eta_f)^2\rangle_{Av}$ as in adiabatic analysis, nor $\langle\eta_i^2+\eta_f^2\rangle_{Av}$ corresponding to the pure adiabatic case, but a quantity between these two extremes. This semidiabatic phase shift is roughly approximated by $\eta_{rms}^2=\langle\eta_i^2-\eta_i\eta_f+\eta_f^2\rangle_{Av}$. When η_i equals η_f, η_{rms} is not zero.

In the case of oxygen, the strong interactions are of the form $f(r)\cos^2\theta$. For this type of interaction $\eta_i\cong\eta_f$, so that while the adiabatic theory gives rms phase shifts varying inversely as K, the rms phase shifts of the diabatic or semidiabatic theories are essentially independent of K.[34] Since the K variation of the phase shift and hence $\Delta\nu/P$ depends on the method of averaging $\cos^2\theta$, these results are quite general for all oxygen Van der Waals interactions.

[34] The matrix elements of $\cos^2\theta$, which are to be suitably averaged when determining the rms phase shift, are:

$$\langle\cos^2\theta\rangle_{J=K,M}=\frac{2K^2+2K-1-2M^2}{(2K+3)(2K-1)}-\frac{2[K^2+K-3M^2]}{K(K+1)(2K+3)(2K-1)},$$

$$\langle\cos^2\theta\rangle_{J=K+1,M}=\frac{2K^2+2K-1-2M^2}{(2K+3)(2K-1)}-\frac{2[K^2+K-4KM^2-M^2]}{(2K+1)(K+1)(2K+3)(2K-1)},$$

$$\langle\cos^2\theta\rangle_{J=K-1,M}=\frac{2K^2+2K-1-2M^2}{(2K+3)(2K-1)}-\frac{2[K^2+K+4KM^2+3M^2]}{K(2K+1)(2K+3)(2K-1)}.$$

For example, for broadening caused solely by quadrupole interaction, the adiabatic theory gives

$$\frac{\Delta\nu}{P}=\frac{N_0}{P}\frac{1}{T}\left[\frac{9}{10}\frac{Q^2}{\hbar}\frac{1}{K}\right]^{\frac{1}{2}}1.41\left[\frac{kT}{\pi m(O_2)}\right]^{\frac{1}{2}};$$

$$\frac{N_0}{P}=0.9660\times10^{19}\frac{\text{deg K}}{\text{cm}^3\text{ mm Hg}}.$$

(Several algebraic and arithmetical errors made by Mizushima have been corrected.)

The semidiabatic theory gives

$$\frac{\Delta\nu}{P}=\frac{N_0}{P}\frac{1}{T}\left[\frac{\sqrt{21}}{20}\frac{Q^2}{\hbar}\right]^{\frac{1}{2}}1.30\left[\frac{kT}{\pi m(O_2)}\right]^{\frac{1}{2}}.$$

From O_2 broadening of the NH_3 inversion line Howard and Smith[22] have set an upper bound of 0.09×10^{-16} cm^2 to Q.

Numerically,

$$\left(\frac{\Delta\nu}{P}\right)_{\text{adiabatic}}<\frac{0.720}{K^{\frac{1}{2}}}\frac{\text{Mc/sec}}{\text{mm Hg}},$$

and

$$\left(\frac{\Delta\nu}{P}\right)_{\text{semidiabatic}}<0.335\frac{\text{Mc/sec}}{\text{mm Hg}}.$$

APPENDIX C. RESONANCE INTERACTIONS CAUSED BY POLARIZABILITY AND EXCHANGE FORCES

Oxygen collisions generally are accompanied by transitions between the spin multiplets of a given K rotational level. In addition, rotational level transitions are possible. The most probable of these K transitions are the resonance interactions in which a K transition of the radiator is accompanied by a K transition of the perturber between the same two levels in the opposite sense, the total energy of the radiator-perturber system being preserved. These resonance collisions necessarily can occur in only a small fraction of the total number of collisions. For this small fraction of collisions the rms phase shift would be calculated from the expression:

$$\eta_{rms}^2=(\eta_{pol}+\eta_{exch})_{rms}^2+(\eta_{res\ pol}+\eta_{res\ exch})_{rms}^2.$$

From an analysis by P. W. Anderson (private communication), the additional polarizability resonance contribution to phase shift has been estimated to be 0.02 of the usual effect. The exchange contribution to the phase shift is modified in a similar manner. Upon computation of the collision diameters, resonance is found to be unobservable for O_2-O_2 broadening. Resonance does not occur of course for O_2-N_2 broadening.

APPENDIX D. TEMPERATURE DEPENDENCE OF LINE WIDTHS

The pressure normalized impact parameter is expressed as: $\Delta\nu/P=(n\nu/P\sqrt{2})b_{\text{eff}}^2$. In the classical kinetic gas theory model b is independent of temperature. Since $n/P\propto T^{-1}$, $v\propto T^{\frac{1}{2}}$, it follows that $\Delta\nu/P\propto T^{-\frac{1}{2}}$. From the more sophisticated line-breadth theories $b\propto T^{-1/2(n-1)}$, therefore $\Delta\nu/P\propto T^{-(n+1)/2(n-1)}$, for $n\to\infty$, $\Delta\nu/P\propto T^{-\frac{1}{2}}$. The temperature dependence of polarizability-exchange line breadths is found to be $\Delta\nu/P\propto T^{-0.63}$. This corresponds to an interaction varying as $1/r^3$ or $1/r^9$, which is not unexpected since $H_{\text{pol}}\propto 1/r^6$, $H_{\text{exch}}\propto 1/r^9$. The agreement between this theoretical value and several recent measurements[35,36] which yielded results near $T^{-0.9}$ is not too good.

[35] R. Beringer and J. G. Castle, Jr., Phys. Rev. **81**, 82 (1951).
[36] R. M. Hill and W. Gordy, Phys. Rev. **91**, 222 (1953).

PHYSICAL REVIEW VOLUME 96, NUMBER 5 DECEMBER 1, 1954

Diffusion Parameters of Thermal Neutrons in Water

G. VON DARDEL* AND N. G. SJÖSTRAND
Department of Physics, AB Atomenergi, Stockholm, Sweden
(Received July 29, 1954)

A method is described for the determination of neutron diffusion parameters by measurements of the decay of thermal neutrons in a finite moderator with a pulsed-neutron source and a time analyzer. In the theory for the method one takes into account the "diffusion cooling" effect, which decreases the temperature of thermal neutrons below the temperature of the moderator. Measurements are reported on a cylindrical geometry, involving between 1 and 4 liters of distilled water. Analysis of the result yields a value of 0.333 $\pm$0.003 barns for the neutron-proton capture cross section, in good agreement with other measurements, and $(36\,340\pm750)[1-(0.20\pm0.04)\kappa_0^2]$ cm^2/sec for the diffusion constant of thermal neutrons in water. The term involving the "buckling" κ_0^2 of the geometry is due to the diffusion cooling effect. The value of the diffusion constant for $\kappa_0^2=0$ leads to a value for the diffusion length in excellent agreement with the result of other measurements. The diffusion cooling effect is larger by a factor of 3.5 than the theoretical value, calculated for the model of a monatomic gas.

ONE of us[1] had previously suggested a detailed study, using a pulsed neutron source, of the decay rate of the neutron flux from a moderator as a means of determining the mean life for absorption, the diffusion constant, and the related diffusion length for neutrons in the moderator. The present article reports the result of such measurements on distilled water in a cylindrical geometry.

THEORY

When the diffusion theory approximation is used the decay of the thermal neutron flux from a finite homogeneous moderator can be described as the exponential decay of a number of modes, each corresponding to a different neutron distribution in the moderator. Each of these modes vanishes on the extrapolated boundary of the moderator, which lies at the extrapolation distance $0.71l_t$ outside the true boundary. The transport mean free path of the neutrons is l_t.

For the decay constant of the νth mode we obtain, using the diffusion theory,

$$\lambda_\nu=\lambda_a+D\kappa_\nu^2, \tag{1}$$

where λ_a is the absorption probability per unit time (the inverse of the mean life for absorption θ). In a moderator containing n_i nuclei of type "i" per cm^3 with the absorption cross section σ_{ai}, the absorption probability λ_a is $\Sigma n_i\sigma_{ai}v$ and since, as is mostly the case, σ_{ai} varies as $1/v$, it follows that λ_a is independent of the velocity of the neutrons.

In Eq. (1) κ_ν^2 is the geometric buckling coefficient for the geometry in the νth mode. In the cylindrical geometry used in the present investigation we have for the buckling coefficient of the lowest, fundamental, mode:

$$\kappa_0^2=(2.405/R')^2+(\pi/H')^2, \tag{2}$$

where R' and H' are the extrapolated radius and height of the cylinder.

D in Eq. (1) is the diffusion constant of the neutrons in the moderator, which is proportional to the transport mean free path and the velocity of the neutrons. D will thus depend on the "temperature" T_n of the neutrons and is related to the diffusion constant D_0 at a standard temperature T_0 by the formula:

$$D=D_0[1+\beta(T_n-T_0)-\gamma(T_n-T_0)^2]. \tag{3}$$

It is usually assumed that thermal neutrons have a Maxwellian velocity distribution of the moderator temperature T_0, irrespective of the size of the moderating geometry. In reference 1 it was shown, however, that diffusion cooling will decrease the temperature T_n of thermal neutrons below the temperature T_0 of the moderator. The temperature difference increases in

* Now at CERN, Laboratory Group, Geneva, Switzerland.
[1] G. von Dardel, Trans. Roy. Inst. Technol. **75**, 1 (1954).

the first approximation proportionally to the geometric buckling of the geometry. In the second approximation we obtain, by an obvious extension of the formulae in reference 1 for the special model of a monatomic moderating gas of nuclei of mass M:

$$T_0-T_n=T_0\frac{2l_il_b}{9\pi^{\frac{1}{2}}C}\kappa_0^2 \times\left[1-\left(1-\frac{1}{2(1+m/M)}\right)\frac{2l_il_b}{9\pi^{\frac{1}{2}}C}\kappa_0^2\right], \quad (4)$$

where l_b is the neutron mean free path if the nuclei were rigidly bound, and C is a constant which depends on M/m and is listed in reference 1. Because of the variations in neutron temperature the diffusion constant will also depend on the buckling of the geometry:

$$D=D_0\left\{1-E\kappa_0^2+E^2\kappa_0^4 \times\left[\frac{1}{\beta T_0}\left(1-\frac{1}{2(1+m/M)}\right)-\frac{\gamma}{\beta^2}\right]\right\}, \quad (5)$$

where

$$E=\beta T_0(2l_il_b/9\pi^{\frac{1}{2}}C). \quad (6)$$

APPARATUS

A schematic view of the apparatus is shown in Fig. 1. Neutrons are generated in a heavy-ice target bombarded by the pulsed deuteron beam[2] of a 150-kv accelerator.[3] Fast neutrons from the target penetrate a cadmium shield into a cylindrical aluminum vessel containing the moderator, where the neutrons are slowed down to thermal energies. The flux of thermal neutrons which emerges from the moderator is detected with $B^{10}F_3$ counters of 150-cc sensitive volume and the time distribution of the pulses from the detectors is investigated by means of a multichannel time analyzer.[4] A shield of cadmium sheet next to the container and the detectors, tanks filled with boric acid solution below and around the container, and boron and paraffin bricks on top of the measuring space decrease the background of stray neutrons so effectively that the neutron flux can in most cases be followed over a factor of 10^5.

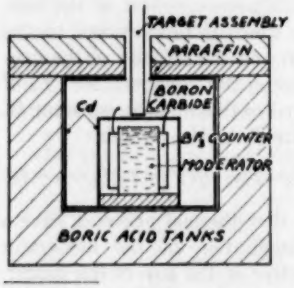

FIG. 1. A schematic view of the experimental arrangement.

Measurements were made with two cylindrical containers for the water moderator, of 18 and 14.5 cm diameter respectively. The water level was varied between 3.5 and 15 cm above the bottom of the container. Before and after a measurement the amount of water was determined by weighing and the temperature was measured. For each water level a run of 2–4 hours was made, which was sufficient to register about 10^6 pulses in the usable portion of the decay curve. The length of the neutron burst and the channel width were for each measurement chosen so that the decay was followed over at least a factor of 10^3 before the advent of the next neutron burst.

SUPPRESSION OF HARMONIC MODES

The presence of harmonic modes in the neutron distribution will make the decay curve depart from the pure exponential decay of the fundamental mode, and will make the measurements more difficult to interpret. In geometries of the small sizes studied in the present investigation, the amplitude of the harmonic modes will be considerably reduced during the slowing-down process. Their influence on the experimental results can be reduced further by a suitable choice of the experimental conditions. The target of the accelerator is situated on the axis of symmetry of the arrangement. Hence, for symmetry reasons, no harmonic modes having radial nodal planes through the axis will be excited.

By a suitable arrangement of the detector it is possible to eliminate the influence of one further set of harmonic modes, and this possibility should be used to suppress the harmonic mode with the smallest decay constant. If the water level in the container is high, this will be the mode with one nodal plane perpendicular to the axis. This mode is suppressed if the BF_3 chambers are placed along the cylindrical surface of the container symmetrically with respect to the nodal plane. For lower water levels the dominant harmonic modes have cylindrical, concentric nodal surfaces. These modes are eliminated by putting the detector below the bottom of the container, behind an opening in a cadmium mask, cut according to the function $rJ_0(2.405r/R')$.

With these precautions the experimentally determined decay curves which had first been corrected for counting rate losses (up to 3 percent in the first channels) are exponential except for the first time intervals. During about 40 μsec after the end of the neutron burst, the neutron spectrum and thus the diffusion constant changes with time, as the neutrons approach thermal equilibrium. This part of the decay curve was therefore always discarded.

In the remaining curve a small residual exponential component with a fast decay was usually found superimposed on a main exponential decay. The period of

[2] von Dardel, Hellstrand, and Taylor, Appl. Sci. Research. **B3**, 35 (1952).
[3] E. Blomsjö and G. von Dardel, Appl. Sci. Research **B4**, 49 (1954).
[4] G. von Dardel, Appl. Sci. Research **B3**, 209 (1953).

this component agreed with the calculated period for the lowest harmonic mode not eliminated by the above precautions.

TREATMENT OF DATA

The harmonic component and in a few cases a small background, were subtracted from the decay curve. The decay constant λ_0 of the corrected curve which is due entirely to the decay of the fundamental mode was calculated by the method of Peierls.[5]

The experimentally determined decay constants, corrected to a temperature of 22°C, are shown as a function of the buckling in Fig. 2. The curvature of the experimental points is apparent, showing that the diffusion constant in Eq. (1) decreases with increasing buckling, as expected theoretically, because of the diffusion cooling effect.

The experimental data have been fitted to a 3-term power series expression in κ_0^2,

$$\lambda_0=\lambda_a'+D_0'\kappa_0^2(1-E'\kappa_0^2), \tag{7}$$

by the method of least squares. The best values for the parameters are

$$\lambda_a'=4907\pm6 \text{ sec}^{-1},$$
$$D_0'=36\,160\pm50 \text{ cm}^2/\text{sec},$$
$$E'=0.175\pm0.002 \text{ cm}^2.$$

In Fig. 2 are also shown the deviations of the experimental points from the best parabolic curve (7).

ERRORS AND CORRECTIONS

The errors of the experimental points in Fig. 2 include the statistical errors in λ_0, as calculated by Peierls'[5] method, and the uncertainty in the water level due to the evaporation of water during the experiment. The errors given in the values for the parameters λ_a', D_0', and E' are calculated on the basis of these errors alone. The spread of the experimental points in Fig. 2 is about twice as large as would be expected on the basis of the calculated random errors, indicating the presence of other, unknown, sources of random errors. We take these into account by increasing the uncertainty limits of the parameters λ_a', D_0' and E' by a factor of two.

We further have to take into account various systematic errors. The electronic apparatus was frequently checked during the measurements and was found very reliable. The calibration and stability of the oscillator in the time analyzer is better than 10^{-4}. We have confidence that no significant systematic errors are introduced by malfunctioning of the apparatus.

The measured decay constants would be too small if some of the neutrons which emerge from the moderator are reflected back into the geometry. For thermal neutrons the effect of neutrons reflected by the moderating material outside the cadmium screen will be very small, since these neutrons have to pass twice through the cadmium in order to affect the measurements. We verified this point by measuring the decay rate with and without paraffin blocks on the outside of the cadmium shield and found the same result within the error of the measurement. Some neutrons will be reflected by the aluminum wall of the container and by the cadmium shield but this will have a negligible effect on the decay constant.

For the extrapolation length we used the value 0.32 cm as calculated from the transport mean free path. The uncertainty in this value is probably 10 percent, which will give rise to uncertainties of ±35 sec^{-1} in λ_a', ±650 cm^2/sec in D_0', and ±0.018 cm^2 in E'.

Additional errors are due to the theoretical assumptions which have to be made in interpreting the data. In the first place we have used ordinary diffusion theory. This is permissible since even for the lowest water level the dimensions of the geometry are much larger than the mean free path. We further checked this point by making calculations for the most unfavorable case by the spherical harmonic method,[6] taking into account the first four spherical harmonics, and found negligible deviations from the results of simple diffusion theory with the ordinary choice of extrapolated boundaries.

Before the experimentally determined parameters λ_a', D_0', and E' can be identified with the corresponding quantities of Eqs. (1) and (5), we have to consider the effect of the higher terms in the expression (5) for the diffusion constant D. From published curves[7] of the scattering cross section we estimate for the first and second temperature coefficients of the diffusion constant the values $\beta=2.4\times10^{-3}$ per °C and $\gamma=0.2\beta^2$. Assuming the mass of the scattering centers to be large compared to the neutron mass we find from Eq. (5)

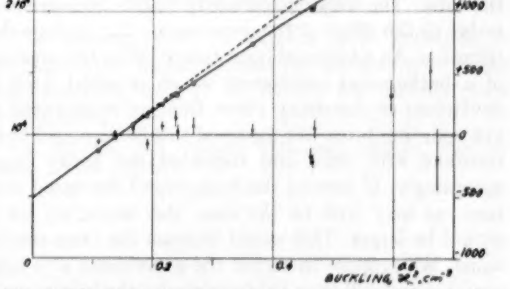

FIG. 2. Measured decay constant λ_0 and deviations $\Delta\lambda_0$ from the parabola $\lambda_0=4907+36\,160\kappa_0^2(1-0.175\kappa_0^2)$ sec^{-1} as functions of the buckling κ_0^2. Vertical lines on the $\Delta\lambda_0$ points indicate the calculated random errors.

[5] R. Peierls, Proc. Roy. Soc. (London) **A149**, 467 (1935).

[6] B. Carlson, U. S. Atomic Energy Commission declassified report MDDC-236 (LA-571) (unpublished).

[7] *Neutron Cross Sections*, U. S. Atomic Energy Commission Report AECU-2040 (Office of Technical Services, Department of Commerce, Washington, D. C., 1952).

for the second-order term in D the value $0.5E^2\kappa_0^4$. Since this is a rough estimate only we assign correspondingly generous uncertainty limits $\pm E^2\kappa_0^4$. The presence of a cubic term,

$$(0.5\pm1.0)D_0'E'^2\kappa_0^6,$$

in the expression (1) will influence the determination of the coefficients of the first three terms from the experimental data. If we approximate the cubic term by a parabola, using the method of least squares in the same way as for the experimental data, we find the following corrections to the parameters λ_a', D_0' and E':

$$\Delta\lambda_a' = -15\pm30 \text{ sec}^{-1},$$
$$\Delta D_0' = 180\pm350 \text{ cm}^2/\text{sec},$$
$$\Delta E' = 0.02\pm0.03 \text{ cm}^2.$$

With these corrections and combining the various sources of errors we obtain as our final result

$$\lambda_a = 4892\pm50 \text{ sec}^{-1},$$
$$D_0 = 36\,340\pm750 \text{ cm}^2/\text{sec},$$
$$E = 0.20\pm0.04 \text{ cm}^2.$$

THE ABSORPTION PROBABILITY

From the value for the absorption probability per unit time λ_a, we derive the mean life for absorption $\theta = 204.4\pm2.0$ μsec and the neutron-proton absorption cross section 0.333 ± 0.003 barns at 2200 m/sec in excellent agreement with the values 0.329 ± 0.004 obtained by Hamermesh, Ringo, and Wexler,[8] and 0.332 ± 0.007 barns obtained by Harris *et al.*[9] A previous measurement in our laboratory, by von Dardel and Waltner,[10] who also used a pulsed-neutron method, yielded the somewhat lower value 0.321 ± 0.005 barns. In this investigation the decay of the neutron flux was measured in a large water tank, so that the leakage of neutrons was negligible. The effects of diffusion were eliminated by integrating over the whole volume of the tank. The major uncertainty in this measurement is due to the effect of the detectors on the neutron distribution. An additional uncertainty lies in the presence of a background component which revealed itself in deviations of the decay curve from an exponential at low counting rates. We assumed this background to be constant with time and corrected the decay curve accordingly. If instead the background decreased with time, as may well be the case, the correction for it should be larger. This would increase the cross-section value. We propose to repeat the experiment at a later occasion and will then try to minimize the background.

The two pulsed-neutron methods have the advantage over most other methods in that the absorption cross section is determined directly without an intermediate determination of, for example, the boron absorption cross section. The method described in the present article has the advantage over our previous method that the target and the detectors are positioned outside the moderator and thus have no influence on the measurement. Very efficient detectors can therefore be used so that the counting rate is high, and any background will be negligible. The larger geometry used in the other method is also more difficult to screen efficiently.

On the other hand, we must in the present method apply diffusion theory in order to correct the measured decay for the leakage out of the tank. Furthermore, the interpretation is complicated by the diffusion cooling effect. If a firmer theoretical basis for the interpretation could be established, the uncertainty of the result of the present method would be decreased appreciably. Extending the measurements to smaller values of the buckling κ_0^2 (i.e., to larger geometries), would also increase the accuracy in the determination of λ_a, since the influence of the uncertainty in extrapolation length and in the correction for the cubic term in κ_0^2 would then be decreased. On the other hand, the harmonic modes will increase when the buckling is decreased and an optimum will soon be reached.

Scott, Thomson and Wright[11] have recently performed measurements very similar to ours using a pulsed fission neutron source. Their value for the neutron-proton absorption cross section, 0.323 ± 0.008 barn, is somewhat lower than ours, and the measurements extend over a range of buckling below the lowest value investigated by us. As discussed above, the presence of harmonic modes may make the experimental results uncertain in this region.

THE DIFFUSION CONSTANT D_0

The diffusion constant D_0 has not previously been determined directly. However, from D_0 and θ we can calculate the diffusion length $L=(D_0\cdot\theta)^{\frac{1}{2}}$, which has been studied extensively in the past. We find for L the value 2.725 ± 0.03 cm at 22°C. The most reliable result of a direct measurement of the diffusion length is probably the value 2.763 ± 0.015 cm found by DeJuren and Rosenwasser.[12] The effect of the buckling on the neutron temperature was, however, not taken into account in their measurements. While in our measurement the buckling is positive and equal to the geometric buckling, in their measurements it will be negative and equal to the material buckling L^{-2}. Thus in their case the temperature of thermal neutrons is higher than the moderator temperature. Using Eq. (5) and the value of E, we find that their diffusion constant is larger by 2.6 percent and their diffusion length by 0.035 cm than for the case where the buckling is zero. Correcting for this effect leads to excellent agreement with our result.

[8] Hamermesh, Ringo, and Wexler, Phys. Rev. **90**, 603 (1953).
[9] Harris, Muehlhause, Rose, Schroeder, Thomas, and Wexler, Phys. Rev. **91**, 125 (1953).
[10] G. von Dardel and A. W. Waltner, Phys. Rev. **91**, 1284 (1953).
[11] Scott, Thomson and Wright, Phys. Rev. **95**, 582 (1954).
[12] J. A. DeJuren and H. Rosenwasser, J. Research Natl. Bur. Standards **51**, 203 (1953).

We have also investigated the temperature dependence of the decay constant over the interval 10–35°C. The absorption probability λ_a is temperature-independent apart from a small effect due to the density change. From the results we can therefore calculate the temperature coefficient of the diffusion constant D. We find a value of $+(2.4\pm0.4)\times10^{-3}$ per °C in agreement with the value calculated from the scattering cross section curves. This value leads to a temperature coefficient of the diffusion length of +0.003 cm per °C, a factor of two smaller than the value quoted by Fermi.[13]

DIFFUSION COOLING

From the experimentally determined parameter E we can, knowing the temperature coefficient β of the diffusion constant, calculate the temperature decrease of the neutrons with increasing buckling. By Eqs. (4) and (6) we obtain in the first approximation:

$$T_n = T_0 - 83\kappa_0^2, \quad (\kappa_0^2 \text{ in cm}^{-2},\ T_n \text{ and } T_0 \text{ in °K}), \quad (8)$$

which indicates a by no means negligible temperature difference between neutrons and moderator for the region of κ_0^2 investigated.

Using an independent method, we have demonstrated this decrease in neutron temperature by measurements of the transmission through a pyrex absorber.[1] The experimentally determined neutron temperatures are shown in Fig. 3 as a function of the buckling and are in good agreement with the theoretical curve predicted by Eq. (8). In interpreting the transmission measurements in terms of neutron temperature, the tables for perpendicular incidence given in reference 1 were used, and the neutron temperature for zero buckling was made to agree with the moderator temperature by normalizing the transmission data. It was shown that other assumptions concerning the angular distribution of the neutrons do not influence the result materially.

Finally, we can compare the experimentally determined value for the diffusion-cooling parameter E with the theoretical value given by (6). This expression is valid for the simple model of a monatomic gas consisting of nuclei of mass M. If we regard the water molecules as rigid scattering centers and neglect the bonds between them, we have $M=18m$. For this case

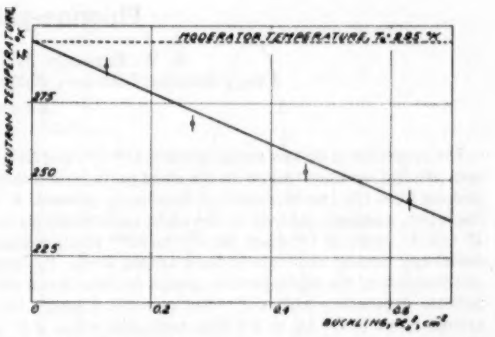

FIG. 3. Neutron temperature as a function of buckling calculated by Eq. (8) (solid line) and from transmission measurements.

we have $C=0.1383$ according to reference 1. With $l_b=0.2$ cm and $l_t=0.45$ cm, we obtain the theoretical value 0.059 cm² for E which is considerably lower than the experimental value 0.20 ± 0.04 cm². This disagreement would indicate that the model of the monatomic gas is not very accurate for water of room temperature. As the temperature of the neutrons falls to the neighborhood of the Debye temperature, about 300°K for water,[14] we would expect the bonds between the molecules to become effective. This will tend to decrease the energy transfer per collision, and consequently the diffusion cooling will increase, as we observe experimentally.

On the other hand, the theoretical results for the monatomic gas model were in fairly satisfactory agreement with the measurements described in reference 1, on the approach to equilibrium of the neutron temperature, a process which is closely related to the diffusion-cooling effect. More theoretical and experimental work is obviously needed for the detailed understanding of the phenomena, and will probably also allow the limits of error on the results of the present investigation to be narrowed.

ACKNOWLEDGMENTS

The authors wish to express their gratitude to O. Nicolaysen for his invaluable assistance with the measurements, and to A. Rentze for the numerical calculations.

[13] E. Fermi, Los Alamos Report LADC-255, 1946 (MDDC-320) (unpublished).

[14] N. Bjerrum, Kgl. Danske Videnskab. Selskab, Mat.-fys. Medd. 27, No. 1 (1951).

Fluorine-plus-Proton Reactions*

R. W. Peterson, W. A. Fowler, and C. C. Lauritsen
Kellogg Radiation Laboratory, California Institute of Technology, Pasadena, California
(Received August 16, 1954)

The properties of certain energy levels in O^{16}, F^{19}, and Ne^{20} have been studied by observations on the alpha particles and inelastic protons from the bombardment of fluorine by protons. A high-resolution magnetic analysis of the alpha-particle groups to the 2^+ and 1^- levels in O^{16} from the $F^{19}(p,\alpha)O^{16*}$ reaction failed to reveal any doublet structure in these known levels. The angular distributions of the alpha-particle groups to these levels did not indicate degeneracy with a 2^- level, nor did a search for new excited levels in O^{16} up to 8.7-Mev excitation reveal a 2^- level. These results are not in agreement with the alpha-particle model of the O^{16} nucleus which predicts a 2^- state close in energy to the 2^+ state.

Angular distributions of the alpha particles were measured at proton bombarding energies of 873, 935, 1290, 1355, and 1381 kev. The distributions at 1355 kev indicated that the corresponding Ne^{20} resonance level at 14.16 Mev has spin 2 and odd parity. The spin and parity assignments previously found for the other levels were confirmed.

A study of the inelastic proton groups from the $F^{19}(p,p')F^{19*}$ reaction gave 108.8 ± 0.8 and 196.0 ± 1.4 kev for the excitation energies of the two lowest excited levels of F^{19}. The cross sections at the 1431-kev resonance for these groups in the center-of-mass system were 0.187 ± 0.015 barn for the first group and 0.007 ± 0.002 barn for the second group. At 1381 kev the cross section was 0.0427 ± 0.0040 barn for protons to the second excited level.

Angular distributions of the proton groups were measured and, in conjunction with other studies made in this laboratory, resulted in spin and parity assignments of $\frac{1}{2}^-$ and $\frac{3}{2}^+$ for the first and second excited states of F^{19}, respectively.

INTRODUCTION

IN the work reported in this paper the alpha particle and inelastic proton groups from the bombardment of fluorine by protons have been studied in an effort to gain information concerning certain states in O^{16}, F^{19}, and Ne^{20}. In particular, the $F^{19}(p,\alpha)O^{16*}$ reaction has been investigated to determine whether or not there exists an energy level in the O^{16} nucleus in the range of excitation energy 7.1 to 8.7 Mev just above the four known levels[1,2] at 6.05 Mev with spin and parity (0^+), 6.13 Mev (3^-), 6.91 Mev (2^+), and 7.12 Mev (1^-). The alpha-particle model of the O^{16} nucleus[3,4] indicates that levels with these spins and parities could be expected to be the lowest excited states of this nucleus, and that in addition a 2^- state should lie near to the 2^+ state, differing from it only in the "inversion" energy of the tetrahedral structure of the four alpha particles. None of the experiments previous to these studies had been done with high enough resolution to resolve a very narrow doublet in the known level structure, nor had the region just above 7.1 Mev been carefully investigated. Therefore, it appeared worthwhile to use the high resolution equipment available in this laboratory to investigate the region near and above the 2^+ level, the region of lower excitation energy having been covered by Chao *et al.*[2] Special attention was paid to the alpha-particle groups leading to the 2^+ level and the nearby 1^- level in O^{16} to make certain that a 2^- level was not degenerate with one of them. In the first place, the groups were studied with the highest possible energy resolution. Secondly, the angular distributions of these particles relative to the direction of the incident proton beam were studied at various resonance levels of the compound nucleus Ne^{20}. Since these distributions depend in part upon the spin and parity of the final state of the residual nucleus, it was expected that a 2^- state which could not be resolved from either of these levels might be revealed by deviations from the angular distributions expected for either a pure 2^+ or 1^- level. Special high resolution and angular distribution studies of the groups leading to the 3^- and 0^+ states were not made, since it was considered unlikely that the 2^- state would be degenerate with either of these states which lie some 1 Mev lower than the 2^+ state.

In the second part of these studies the inelastic protons from the reaction $F^{19}(p,p')F^{19*}$ were observed in an attempt to find groups corresponding to excited levels in F^{19} reported at 113 and 192 kev by Mileikowsky and Whaling[5] from studies of the $Ne^{21}(d,\alpha)F^{19*}$ reaction. The same two excited levels were also reported by Day,[6] who observed the de-excitation gamma rays following the reaction $F^{19}(n,n')F^{19*}$. The inelastic proton groups leading to these two levels in the bombardment of fluorine by protons had not been previously reported, and our experiment was undertaken to observe these groups and measure their energies. In addition, their angular distributions were studied in order to aid in the determination of the spins and parities of these levels.

The results have been briefly reported in a Letter to the Editor of this journal[7] along with other studies on

* This work was assisted by the joint program of the U. S. Office of Naval Research and the U. S. Atomic Energy Commission.

[1] J. Seed and A. P. French, Phys. Rev. **88**, 1007 (1952); see also J. M. Freeman, Phil. Mag. **41**, 1225 (1950).

[2] Chao, Tollestrup, Fowler, and Lauritsen, Phys. Rev. **79**, 108 (1950); C. Y. Chao, Phys. Rev. **80**, 1035 (1950).

[3] J. A. Wheeler, Phys. Rev. **52**, 1083 (1937); D. M. Dennison, Phys. Rev. **57**, 454 (1940).

[4] D. R. Inglis, Revs. Modern Phys. **25**, 390 (1953).

[5] C. Mileikowsky and W. Whaling, Phys. Rev. **88**, 1254 (1952).

[6] R. B. Day, Phys. Rev. **89**, 908(A) (1953).

[7] Peterson, Barnes, Fowler, and Lauritsen, Phys. Rev. **94**, 1075 (1954).

these levels carried out concurrently in this laboratory.[8–10]

APPARATUS AND EXPERIMENTAL PROCEDURE

The 2-Mv electrostatic generator of this laboratory was used to accelerate the protons, which were then passed through an 80-degree electrostatic analyzer of 1-meter radius which made them homogeneous in energy to ±0.05 percent. The outgoing reaction products were analyzed by a 180-degree variable angle double-focusing magnetic spectrometer of 10½-in. radius. A regulator on the magnet held the current constant to ±0.02 percent. The detection was done either with a thick emulsion photographic plate or with a scintillation counter consisting of a zinc sulfide screen followed by a 931-A photomultiplier tube.

In the high resolution study of the alpha-particle groups to the 2^+ and 1^- O^{16} levels (usually designated α_2 and α_3) thin, uniform targets of sodium fluoride were evaporated in vacuum onto a thin aluminum foil (0.2 mg/cm²) which was supported on an aluminum frame. Target thicknesses were determined by measuring the gamma-ray intensity and excitation curve at resonances of known width and cross section, and by using methods of analysis which have been previously described.[11]

The detection in this part of the experiment was done with photographic plates in order to obtain higher resolution than is possible with the scintillation counter arrangement for the same amount of target bombardment. Ilford C_2 plates (1 in.×3 in.) were used, with a 100-micron emulsion thickness. A camera was built which placed the long axis of the plate in the exit focal plane of the spectrometer; the short axis made an angle of 30 degrees with the incident alpha particles. The plate could be withdrawn from this position and exit slits moved into the focal plane without loss of vacuum. Just to the rear of the focal plane was the zinc sulfide screen, followed by the photomultiplier tube.

Momentum spectra of moderate resolution were taken, with the scintillation counter as detector, on the alpha-particle groups under study before and after each run with a photographic plate. This procedure served to locate the groups and to check on the over-all stability of the target, analyzer, and spectrometer. Continuous monitoring of the gamma-ray yield was also carried out. There was no evidence of a shift in the peak positions of the alpha-particle groups indicating that surface contamination was not building up on the targets. A liquid nitrogen cold trap between the target and oil diffusion pump was employed to trap out oil vapors.

[8] Thirion, Barnes, and Lauritsen, Phys. Rev. **94**, 1076 (1954).
[9] Sherr, Li, and Christy, Phys. Rev. **94**, 1076 (1954).
[10] R. F. Christy, Phys. Rev. **94**, 1077 (1954).
[11] Fowler, Lauritsen, and Lauritsen, Revs. Modern Phys. **20**, 236 (1948).

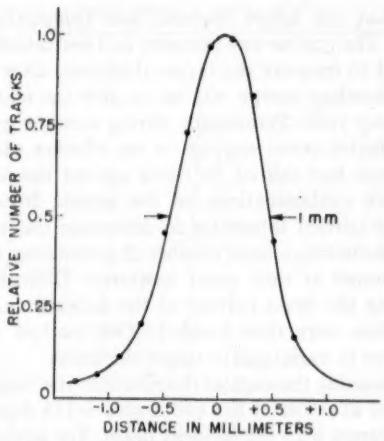

FIG. 1. Distribution in number of particles in the focal plane of the spectrometer normal to the direction of deflection.

After exposure and development of the plates, the alpha-particle tracks were counted employing a microscope which was fitted with a mechanical stage driven by two micrometer screws at right angles, capable of reproducing any setting to ±3 microns. A 25× objective and 8× eyepiece with counting reticle were used. At this magnification the reticle covered an area approximately ½ mm × ⅓ mm on the plate. The position of the tracks measured parallel to the long axis of the plate was a measure of the momentum and thus of the energy of the particles. All tracks in a band ⅓ mm wide and length 6 mm parallel to the short edge of the plate were counted as due to particles with the same energy. The 6 mm corresponds to a distance of 3 mm in the focal plane normal to the direction of deflection. The distribution of tracks in the focal plane normal to the deflection is shown in Fig. 1. It will be noted that the line image has a half width of only one millimeter. The change in energy per unit length along the photographic plate can be calculated from the expression[12]

$$\delta P/P=\delta E/2E=\delta r/3.6r_0,$$

where P and E are the momentum and energy of a particle in the equilibrium orbit, r_0 is the radius of the equilibrium orbit (10.5 in.), and δr is the distance in the focal plane through which a particle of energy $E+\delta E$ is displaced from one of energy E. For the spectrometer used, $\delta E=E\delta r/480$, for δr in millimeters. For $\delta r=\frac{1}{3}$ mm, $\delta E/E=1/1440$. Although a magnetic spectrometer essentially measures momentum spectra, it is sometimes convenient in the analysis to convert these to energy spectra and in what follows we will refer to the one most appropriate to the discussion.

In measuring the angular distributions of the alpha particles, uniform targets of the order of 5-kev stopping power for the proton energy used were made as described

[12] Snyder, Rubin, Fowler, and Lauritsen, Rev. Sci. Instr. **21**, 852 (1950).

above, but the target material was principally zinc fluoride. The gamma-ray intensity and excitation curve was used to measure the target thickness, after which the bombarding energy was set to give the maximum gamma-ray yield. Periodically during runs the gamma-ray excitation curve was run to see whether the resonance peak had shifted, to check against the buildup of surface contaminations on the target. Instead of using the current integrator to determine the amount of bombardment, a fixed number of gamma-ray counts were counted at each point measured. Difficulties in measuring the beam current at the forward angles of observation were thus avoided. This method also is insensitive to variations in target thickness.

In measuring the angular distributions the target was held fixed at either of the two angles +135 degrees or −135 degrees with the incident beam. The angle given is that between the direction of the incident protons and the normal drawn outwardly from the fluorided side of the target. The angle is considered positive when the normal points toward the spectrometer entrance. The target was set at +135 degrees for angles of observation greater than 90 degrees and at −135 degrees for angles less than 90 degrees. In this way, the target thickness was the same for all angles of observation. This method also had the advantage, since the upper energy limit of the spectrometer was 2 Mev for alpha particles, that those particles emitted in forward directions passed through the target backing foil before entering the spectrometer. In addition to this foil, up to two additional foils were inserted in the path of the alpha particles just after leaving the target at the higher energy resonances and at forward angles. The loss in energy of the alpha particles in these aluminum foils (0.2 mg/cm²) was 200 kev. A correction factor for loss of alpha particles due to scattering and large energy loss in the foils was determined experimentally by comparing yields which could be obtained with and without foils.

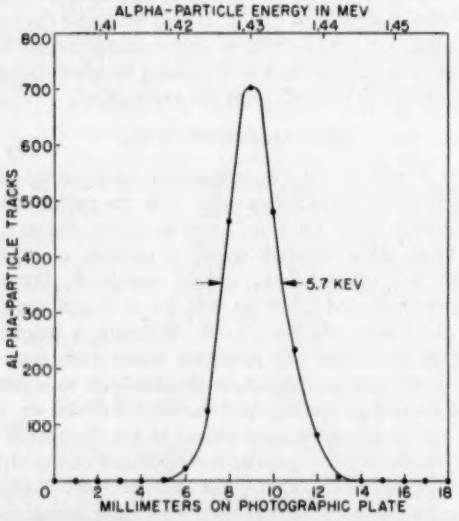

FIG. 2. Energy spectrum of the α_2 group from the $F^{19}(p,\alpha)O^{16*}$ reaction at $\theta_{lab}=137.8°$ and a bombarding energy of 873 kev. In the figure, 5.7 kev should read 8.1 kev.

The angles of observation were chosen in order to divide the interval of $\cos^2\theta_{c.m.}$ from zero to one into eight equal parts. All distributions were plotted *vs* $\cos^2\theta_{c.m.}$ for ease in comparison with the theoretical distributions. When plotted in this way, all distributions obtained were fitted reasonably well with either straight lines or parabolas.

The method of obtaining an angular distribution was to determine the momentum-spectrum of the desired alpha-particle group at each angle. The total number of counts at each angle was then obtained by integrating graphically the area under each curve. After dividing this quantity by the momentum corresponding to the peak reading,[12] and transforming the resulting quantity to the center-of-mass system, small corrections were made for the losses due to singly charged alpha particles and to the foils, and the data were then normalized to unity at 90 degrees. It was plotted *vs* $\cos^2\theta_{cm}$, forward and back angle points being plotted separately to display fore and aft symmetry if observed.

In studying the inelastic proton groups to the first two known excited levels of F^{19}, the target materials used were principally aluminum fluoride (Al_2F_6) and lithium fluoride (LiF). Here, different target backing materials were also used. Since the Q-values for these reactions (equal to the negatives of the excitation energies of the levels) are so small in magnitude, the inelastic groups fell quite close in energy to the elastically scattered group from F^{19}, and even closer to the elastically scattered groups from O^{16} and C^{12}, which are always present in very thin layers (~10 atoms deep with good trapping) on the target surfaces. In addition to these groups, there were always protons elastically scattered from the target backing material as well as from the other element which made up the fluorine compound used, and from the carbon and oxygen on the rear side of the target support, if this was thin. These groups had lower energy than the groups from O^{16} and C^{12} on the front surface because they traversed the target supporting foil before reaching the spectrometer (see Fig. 7 of reference 12). Because the recoil energy of the scattering nucleus varies with its mass, the various elastically scattered proton groups differ somewhat in energy, the effect being largest at backward angles of observation. Thus very high resolution must be employed to isolate the protons inelastically scattered by F^{19} from the various elastically scattered groups. Two different target backings were used for this purpose. One backing used was a thick layer of lithium deposited in vacuum on copper, the target material in turn being evaporated onto the lithium surface from a second furnace. The protons scattered

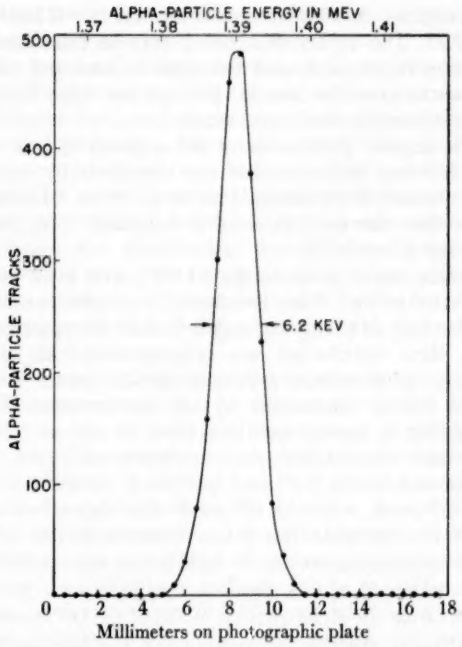

FIG. 3. Energy spectrum of the α_2 group from the $F^{19}(p,\alpha)O^{16*}$ reaction at $\theta_{lab}=157.7°$ and a bombarding energy of 873 kev.

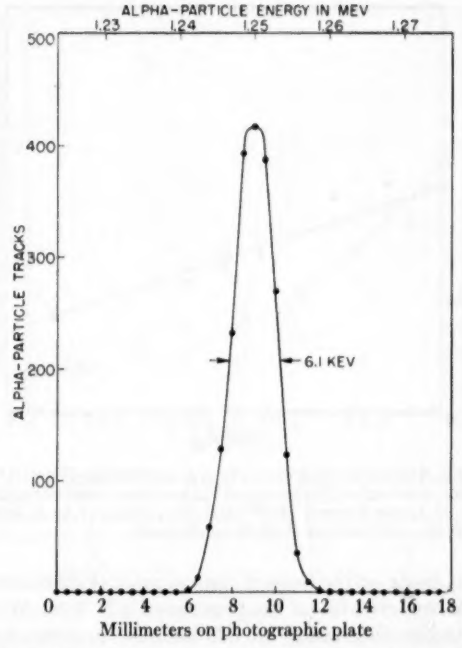

FIG. 4. Energy spectrum of the α_3 group from the reaction $F^{19}(p,\alpha)O^{16*}$ at $\theta_{lab}=157.7°$ and a bombarding energy of 873 kev.

elastically from the lithium had much less energy than the inelastic groups at angles of observation greater than 90 degrees, and the lithium deposit was thick enough to prevent the incident protons from striking the copper and its surface contaminations. A second target backing was thin aluminum leaf (0.2 mg/cm^2). Protons scattered elastically from the aluminum were at higher energies than the two inelastic groups. However, due to the finite foil thickness and straggling, protons scattered from the rear surface fell too close in energy to the first inelastic group at some angles of observation; in addition, there were always four elastic groups from the carbon and oxygen on the two surfaces of the aluminum leaf. All of these undesired elastic groups made it impossible to observe the inelastic groups separately at all angles in determining angular distributions and the data suffer from incompleteness in this regard. (See Fig. 1 of reference 7.)

DISCUSSION OF RESULTS

(a) $F^{19}(p,\alpha)O^{16*}$

Good energy spectra were obtained with the photographic plates at a bombarding energy of 873 kev for the α_2 group from $F^{19}(p,\alpha)O^{16*}$ at $\theta_{lab}=90$, 137.8, and 157.7 degrees, and for the α_3 group at $\theta_{lab}=157.7$ degrees (Figs. 2–4). There is no evidence of doublet structure in any of the curves, and all of the curves are quite symmetrical. In addition, in the best case for each group, the width at half maximum of the peak is about 6 kev. This leads to the conclusion that if a 2^- level exists, its separation from either the 1^- or 2^+ levels is less than 3 kev or more than 100 kev, the energy range covered by the photographic plate. We assume that groups separated by half their width will be clearly resolved.

In searching for a 2^- level separated by more than 100 kev from the known levels, the region of excitation energy higher than the 1^- level at 7.12 Mev was examined, the region of lower energy having been investigated by Chao *et al.*[2] The proton energy was set at 873 kev and a search made for lower energy alpha particles than the α_3-group. The excitation range in O^{16} from 7.12 to 8.7 Mev was covered in this way without finding any new alpha-particle groups. Since there is no simple selection rule which will prevent an alpha-particle transition from the 2^- level in Ne^{20} at 873-kev bombarding energy to a 2^- level in O^{16}, and since the penetration factor is most favorable for s-wave alpha particles which can make the transition, we conclude that a 2^- level does not exist in O^{16} in this region. We cannot completely rule out the existence of levels of other spin and parity values.

In order to determine if there was a 2^- level closer than 3 kev to the 2^+ or 1^- levels, the angular distributions of the alpha particles to these levels were studied in detail. Seed and French[1] had already measured the angular distributions for the α_1, α_2, and α_3 groups at the 873-kev resonance for the three angles 90, 120, and 135 degrees, and found agreement with their assign-

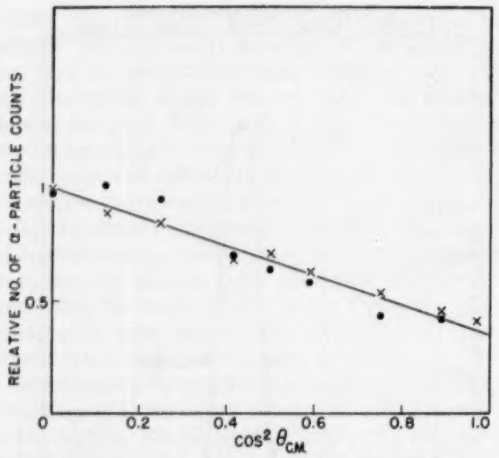

FIG. 5. Angular distribution of the α_3 group from the $F^{19}(p,\alpha)O^{16*}$ reaction at a bombarding energy of 873 kev; the crosses are points taken at angles forward of 90° and the circles are back angle points; the solid curve is $W(\theta)=1-0.65\cos^2\theta$.

ments made on the basis of the α-γ angular correlation measurements without the presence of a 2^- level. With the bombarding energy at 873 kev, the α_3 group was observed at forward and back angles, and an angular distribution described by $1-0.65\cos^2\theta$ obtained with fore and aft symmetry (Fig. 5). As noted previously, the 873-kev resonance level in Ne^{20} is a 2^- level.[1] The theoretical angular distribution for the transition $Ne^{20}(2^-)\rightarrow O^{16}(2^+)$, considering only the lowest values for the orbital momenta of the reacting particles ($l_p=1$, $l_\alpha=1$), is $1-7/9\cos^2\theta=1-0.78\cos^2\theta$. The observed coefficient of $\cos^2\theta$ is lower in magnitude than the predicted one by some 17 percent. If there were a 2^- level, almost or completely degenerate with the 2^+ level, s-wave ($l_\alpha=0$) alpha particles would be permitted, and their angular distribution would be isotropic. This would tend to reduce the coefficient of the $\cos^2\theta$ term as was observed. However, the barrier penetration factor would greatly favor the s-wave alpha particles to the 2^- level, and one would expect an even greater lowering of this coefficient. This is not a conclusive argument since the barrier penetration factor is not the only factor determining transition rates. However, the reduced value of the coefficient may be accounted for without resorting to a new level, simply by taking into account the other two orbital momentum values possible in this transition; $l_p=3$, $l_\alpha=3$. The distributions which consider these next higher values have been calculated by Seed and French.[1] If the relative amplitude of protons with orbital momentum $l+2$ to those with orbital momentum l is A, and their phase difference is α, and if B and β are the same quantities for the alpha particles, then the observed distribution may be fitted with $A=0.06$, $\cos\alpha=0.439$, $B=0.29$, and $\cos\beta=-0.244$. These values of A and B are in agreement with those obtained by Seed and French[1] from the α-γ angular correlation measurements: $A=0.1\pm0.1$, $B=0.35$. The values of α and β may be calculated[18] up to a factor of π, and the signs of $\cos\alpha$ and $\cos\beta$ chosen to give the best fit. We use the same values as calculated by Seed and French.

The angular distribution of the α_3 group (Fig. 6) at the 873-kev resonance was also satisfactorily fitted with the use of the known 1^- level in O^{16} at 7.12 Mev only. Here the same value of A was used (0.06), but only $l_\alpha=2$ is possible.

Finally the α_1 group to the $6.13(3^-)$ level in O^{16} was measured at the 873-kev resonance. Since these particles are too high in energy to be deflected by the spectrometer, their distribution was only measured at back angles, and aluminum foils employed to reduce them to an energy measurable by the spectrometer. The straggling in energy was less than 10 percent. The measured distribution was consistent with the 2^- assignment to the Ne^{20} level and the 3^- assignment to the O^{16} level, with the effects of the higher l-values taken into account. Here B was determined to be 0.37.

These results show that at least in this reaction there is no evidence of a 2^- level in the region one would expect from the alpha-particle model of the O^{16} nucleus. This model predicts the positions of the four known levels only with rather anomalous values of the parameters involved,[4] and from the present results seems to fail in an important respect unless the inversion frequency of the tetrahedral structure is much larger than can be reasonably expected. The implications of these results were anticipated independently by Inglis who has discussed the matter in considerable detail in reference 4, page 433. Our results would seem to

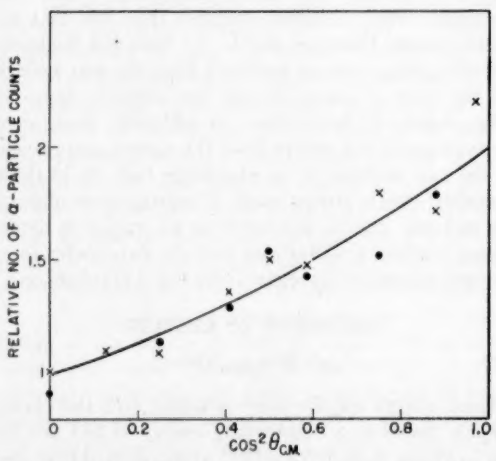

FIG. 6. Angular distribution of the α_3 group from the $F^{19}(p,\alpha)O^{16*}$ reaction at a bombarding energy of 873 kev; the crosses are points taken at angles forward of 90° and the circles are back angle points; the solid curve is $W(\theta)=1+0.61\cos^2\theta+0.39\cos^4\theta$.

[18] Bloch, Hull, Broyles, Bouricius, Freeman, and Breit, Revs. Modern Phys. 23, 147 (1951).

indicate two or four particle excitation for the 2^+ state and probably also for the 0^+ state in O^{16}.

The angular distribution of the α_3 group was measured at the 935-kev resonance as a check on the experimental techniques used, and on the previous assignment[1,2] of spin and parity for this level in Ne^{20}. The 935-kev resonance corresponds to a 1^+ level in Ne^{20} and may be formed by *s*-wave protons. The expected distribution should be mainly isotropic, with *d*-wave protons modifying the distribution slightly. The measured distribution was quite isotropic and served as a satisfactory check. No attempt was made to measure the angular distribution of the α_2 group at this resonance as the yield is very small.

The next distributions measured were those at the 1355-kev resonance. Chao,[2] analyzing the data of Day *et al.*[14] on the de-excitation gamma rays found that satisfactory agreement could be had by assuming the level in Ne^{20} to be either 2^- or 3^+. The alpha-particle distributions, measured for the α_2 and α_3 groups, and shown in Figs. 7 and 8, lead to a 2^- assignment for the Ne^{20} level. The assumption of *p*- and *f*-wave protons leading to a 2^- Ne^{20} level, which decays by *p*- and *f*-wave alpha particles to the O^{16} 2^+ level, and by *d*-wave alpha particles to the O^{16} 1^- level gave a very satisfactory fit to the data. The analysis gave values of $A=0.14$; $B=0.43$ for the α_2 group.

The yields of the α_2 and α_3 groups at the 1290-kev resonance were quite small, and made accurate analysis impossible without more extensive data. The background yield is roughly of the same order of magnitude as the alpha-particle intensity from the resonance itself. The distributions obtained are not inconsistent with the assignment of 3^+ made to the level by Chao.[2]

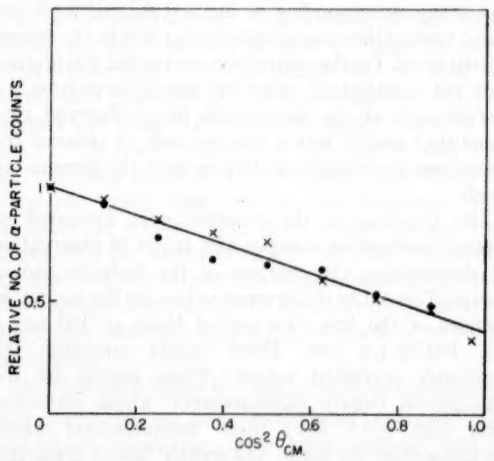

FIG. 7. Angular distribution of the α_3 group from the $F^{19}(p,\alpha)O^{16*}$ reaction at a bombarding energy of 1355 kev; the crosses are points taken at angles forward of 90° and the circles are back angle points; the solid curve is $W(\theta)=1-0.63\cos^2\theta$.

[14] Day, Chao, Fowler, and Perry, Phys. Rev. **80**, 131(A) (1950).

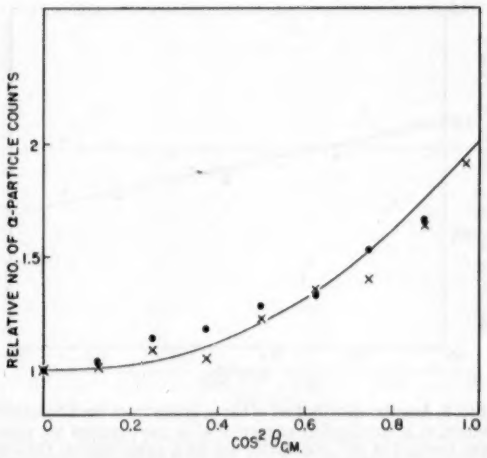

FIG. 8. Angular distribution of the α_3 group from the reaction $F^{19}(p,\alpha)O^{16*}$ at a bombarding energy of 1355 kev; the crosses are points taken at angles forward of 90° and the circles are back angle points; the solid curve is $W(\theta)=1-0.19\cos^2\theta+1.19\cos^4\theta$.

The 1381-kev resonance was previously studied by Day *et al.*[14] The gamma rays were observed with Geiger-Müller counters and no attempt was made to resolve the three high-energy gamma rays which follow the emission of the α_1, α_2, and α_3 groups. All distributions were fitted with curves of the form $1+a\cos^2\theta$. However, as the bombarding energy was varied across the resonance, the coefficient a was found to vary linearly from -0.2 to 0.1, with the value -0.073 at the resonance. This behavior suggests the possiblity of interference, although it could result merely from the change in the relative intensities of the gamma rays as the bombarding energy was changed. On the basis of the smallness of the coefficient at resonance, and of the ratio of gamma-ray intensity at 90 degrees to alpha-particle intensity at 138°, Chao[2] made the assignment of 1^+ to this Ne^{20} resonance level.

Sanders[15] separated the 6.14-Mev gamma ray from the 6.91- and 7.12-Mev gamma rays, using a deuterium-filled ionization chamber. Measurements of the angular distributions of the 6.14-Mev gamma ray and the combination of the 6.91- and 7.12-Mev gamma rays led to a 2^- assignment for the Ne^{20} level. This assignment is in agreement with a preliminary analysis of the data from the elastic scattering of protons studied in this laboratory[16] at this resonance.

The alpha-particle angular distributions obtained at resonance (Figs. 9 and 10) are difficult to fit with either a 1^+ or 2^- assignment, even with the higher *l*-values taken into account. Considering the number of levels in this region, it seems likely that interference effects are modifying the distributions one would expect from a 2^- level. Besides the level in question,

[15] J. E. Sanders, Phil. Mag. **44**, 1302 (1953).

[16] Webb, Hagedorn, Fowler, and Lauritsen, Phys. Rev. **96**, 851 (1954).

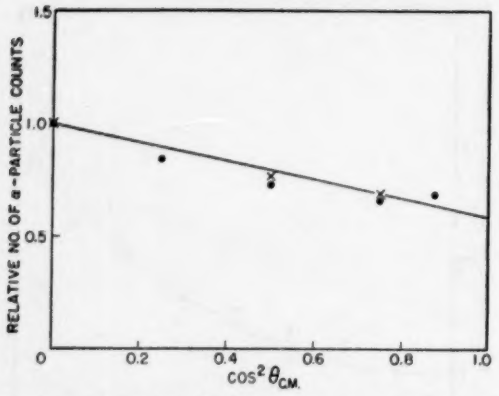

FIG. 9. Angular distribution of the α_2 group from the $F^{19}(p,\alpha)O^{16*}$ reaction at a bombarding energy of 1381 kev; crosses are points taken forward of 90° and circles are back angle points; the solid curve is $W(\theta)=1-0.43\cos^2\theta$.

there is the 2^- gamma-ray resonance at 1355 kev, the 2^+ pair and long-range alpha-particle resonance[17] at 1365 kev, the 1^+ inelastic scattering resonance[16] at 1431 kev, and a nonresonant background.

In order to determine whether interference effects were modifying the alpha-particle angular distributions, the bombarding energy was set at the energies where the gamma-ray yield was equal to one-half its value at the maximum, since the distributions should be quite sensitive to bombarding energy if they are the result of the interference of two or more levels. There was very little change in the α_3 distribution at either bombarding energy, and in the α_2 distribution at the lower bombarding energy. However, at the higher bombarding energy the α_2 distribution was almost isotropic.

A preliminary analysis of the data to determine if any of the above distributions could result from the interference of a 2^- level with one of the other known levels was unsuccessful. Interference with an even parity level seems unlikely since the observed distributions at resonance had fore and aft symmetry at the points measured. The assignment to the level appears to be known with certainty from the elastic scattering[16] and gamma-ray measurements;[15] more extensive data is necessary for complete analysis of the alpha-particle results. The results of the angular distribution measurements of this section are summarized in Table I.

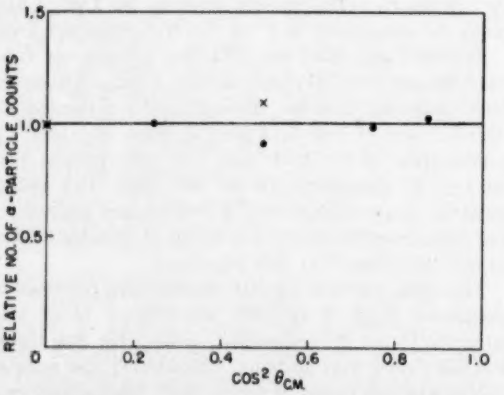

FIG. 10. Angular distribution of the α_3 group from the $F^{19}(p,\alpha)O^{16*}$ reaction at a bombarding energy of 1381 kev; the crosses are points taken at angles forward of 90° and the circles are back angle points; the solid curve is $W(\theta)=1$.

[17] Paul, Clarke, and Sharp, Phys. Rev. **90**, 381(A) (1953); and private communication.

(b) $F^{19}(p,p')F^{19*}$

After finding the two inelastic proton groups corresponding to the two lowest excited levels of F^{19} at a proton energy of 1381 kev, a brief excitation curve was run from just below 1355 kev to about 1500 kev. Both groups were observed to follow the well-known resonances at 1355 and 1381 kev, and in addition there was a much stronger resonance for the first group at 1431 kev, a proton capture resonance reported by Sinclair.[18]

TABLE I. Measured angular distributions of the $F^{19}(p,\alpha)O^{16*}$ reaction.

Resonance energy (kev)	Excitation in Ne^{20} (Mev)	Alpha-particle group[a]	Ne^{20}-level assignment	Measured distribution
873	13.70	α_1	2^-	$1-0.49\cos^2\theta$
		α_2		$1-0.65\cos^2\theta$
		α_3		$1+0.61\cos^2\theta+0.39\cos^4\theta$
935	13.76	α_3	1^+	1
1290	14.10	α_1	$3^+(?)$	1
		α_2		$1+\cos^2\theta$
1355	14.16	α_2	2^-	$1-0.63\cos^2\theta$
		α_3		$1-0.19\cos^2\theta+1.19\cos^4\theta$
1381	14.18	α_1	2^-	$1-0.43\cos^2\theta$
		α_2		1

[a] The α_1 group leads to the 6.13-Mev (3^-) level in O^{16}; the α_2 group to the 6.91-Mev (2^+) level; and the α_3 group to the 7.12-Mev (1^-) level.

The group corresponding to the first excited level was about twenty times as intense as that due to the second excited level. Further excitation curves for the protons were not investigated, since the gamma rays from the de-excitation of the levels were being observed concurrently,[7] and it was a simpler task to observe the resonances for inelastic scattering from the gamma-ray yields.

The Q-values of the reaction were measured at several bombarding energies and angles of observation by determining the energies of the inelastic proton groups. This led to the average values for the excitation energies of the first two excited levels of 108.8 ± 0.8 and 196.0 ± 1.4 kev. These values supercede the previously published values.[7] These results are the averages of twenty measurements, whose statistical error was ±0.4 kev; three measurements whose deviation from the mean was greater than 5 times this value were discarded in the averaging. As a check on these values, calculated by standard methods using the calibrated scales of our analyzer and spectrometer,

[18] R. M. Sinclair, Phys. Rev. **93**, 1082 (1954).

a difference method of calculating Q for inelastic scattering was used in those cases where the F^{19} elastic group was observed at the same time as the inelastic groups. The nonrelativistic expression which may be used for Q in these cases is

$$Q=E_1\left[\frac{M_0+M_1}{M_0}k(r-1)-2\cos\theta\frac{M_1}{M_0}k^{\frac{1}{2}}(r^{\frac{1}{2}}-1)\right],$$

where E_1 is the bombarding energy, M_0 the mass of the target nucleus, M_1 the mass of the incident particle, θ the angle of observation in the laboratory system, $k=E_{el}/E_1$ and $r=E_{inel}/E_{el}=I_{el}^2/I_{inel}^2$.

Here I is the observed fluxmeter setting of the magnetic spectrometer and is inversely proportional to the momentum of the particles observed. The quantity k was calculated using the conservation of energy and momentum for the elastic scattering in which $Q=0$. E_1 was taken as the standard resonance energy and θ was measured on the vernier protractor which has been checked as reliable in numerous previous measurements. The primary measurements involved $r-1$ and $r^{\frac{1}{2}}-1$ and these differences could be determined with high precision independent of extensive calibrations of the spectrometer. This method of calculation cancels out many sources of error but neglects target surface layer corrections to second order in that the elastic and inelastic groups have slightly different energies and hence have different energy losses in the layers. This check was satisfactory, the values 109.5 and 196.1 kev being obtained in those cases where the F^{19} elastic group was observed simultaneously with the inelastic groups, and these values agreed very closely with the values calculated for these cases using our standard calibrations and surface layer corrections. The average values of all the measurements which we give in the previous paragraph are considered to be the best results.

TABLE II. Measured coefficient in the angular distribution, $1+a\cos^2\theta$, for the reaction $F^{19}(p,p')F^{19*}$.

Resonance energy (kev)	Excitation in Ne^{20} (Mev)	Ne^{20} level assignment	Value of a To 109-kev level	Value of a To 196-kev level
873	13.70	2^-	...	0±0.1
1355	14.16	2^-	...	0±0.1
1381	14.18	2^-	...	−0.45±0.04
1431	14.23	1^+	0±0.1	...

The cross sections for the inelastic scattering processes were measured at two bombarding energies. The method of calculating these cross sections was to observe the momentum spectrum of the fluorine elastic group along with the two inelastic groups, and to calculate the area under each of these graphically. The cross section for each of these processes is proportional to this number divided by the momentum reading at the peak. The ratios of the inelastic scattering cross sections to the elastic scattering cross section were thus obtained. The absolute cross sections for the inelastic scattering were determined by using the absolute differential cross section for the elastic scattering process which were measured in this laboratory.[16] The values obtained in this manner were in good agreement with those obtained from the gamma-ray yields.[19]

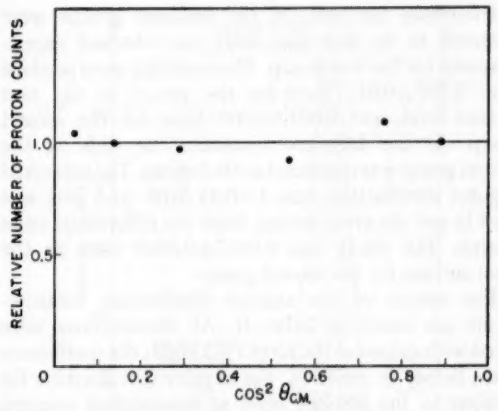

FIG. 11. Angular distribution of the inelastic proton group to the 196-kev excited level of F^{19} at a bombarding energy of 1355 kev; all points were taken at angles greater than 90°; the solid curve is $W(\theta)=1$.

The cross sections for both groups were measured at the 1431-kev resonance. The measurements were made at 159.7 degrees in the laboratory system; the elastic scattering measurements[16] indicated that this resonance level in Ne^{20} had spin and parity 1^+. Since this state may be formed by s-wave protons, angular

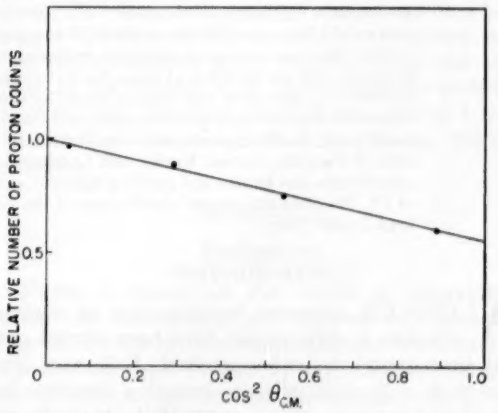

FIG. 12. Angular distribution of the inelastic proton group to the 196-kev excited level of F^{19} at a bombarding energy of 1381 kev; all points were taken at angles greater than 90°; the solid curve is $W(\theta)=1-0.45\cos^2\theta$.

[19] Barnes, Fowler, Lauritsen, and Peterson, Phys. Rev. **96**, 851 (1954).

distributions for both of the inelastic groups were expected to be isotropic. This was checked experimentally for the first group. The resulting cross sections were 0.187 ± 0.015 barn for the group to the first excited level, and 0.007 ± 0.002 barn for the second group. At the 1381-kev resonance the yield of the second group was measured at 90 degrees. The measured angular distribution was $1-0.45\cos^2\theta$, and this was used to get the cross section from the differential cross section. The result was 0.0427 ± 0.0040 barn as the cross section for the second group.

The results of the angular distribution measurements are listed in Table II. All distributions were fitted with curves of the form $1+a\cos^2\theta$; the coefficients a are listed. In addition, the angular distributions for protons to the 196-kev level at bombarding energies of 1355 kev and 1381 kev are shown in Figs. 11 and 12. The angular distribution data is meager, due to the difficulties involved in isolating the groups from elastically scattered groups. In addition, the 935- and 1431-kev resonances were not useful in attempting to determine the spins and parities of the two F^{19} excited levels as both are 1^+ levels formed by s-wave protons. The results are made more difficult to analyze due to the presence of the proton spin, making two outgoing channel spins possible in general.

Unique assignments for the excited levels of F^{19} could not be made on the basis of the inelastic proton results alone due to the reasons discussed above. However, measurements on the de-excitation gamma ray and on the $F^{19}(\alpha,\alpha')F^{19*}$ reaction did result in the assignments $\frac{1}{2}^-$ and $\frac{5}{2}^+$ for the first and second excited states respectively. These assignments are discussed in detail in an accompanying publication.[20] Our results are consistent with those assignments.

In conclusion we wish to express our appreciation to C. A. Barnes, R. F. Christy, R. Sherr, and J. Thirion for many discussions of these results.

Note added in proof.—In a recent paper, Dennison [Phys. Rev. **96**, 378 (1954)] has extended his original calculations[3] on the tetrahedral alpha particle model of O^{16} and has made two different identifications of the theoretically predicted energy levels with those observed experimentally. In the first identification the 6.91-Mev level is identified with a 2^+ level of the first excited state of the triply degenerate normal mode of vibration of the alpha particles (ω_1). A 2^- level is not associated with this level. In the second identification, which corresponds to our previous discussion based on the original paper,[3] the 6.91-Mev level is identified with a 2^+ level of the first excited state of the doubly degenerate mode of vibration (ω_2). In the light of these considerations, our results stand as a strong argument in favor of Dennison's first identification unless, as indicated above, the inversion frequency separating the 2^+ and 2^- states in the second identification is much larger than can be reasonably expected.

[20] Sherr, Li, and Christy (following paper).

PHYSICAL REVIEW VOLUME 96, NUMBER 5 DECEMBER 1, 1954

Coulomb Excitation of F^{19} by Alpha Particles*

R. Sherr,† C. W. Li,‡ and R. F. Christy
Kellogg Radiation Laboratory, California Institute of Technology, Pasadena, California

(Received August 16, 1954)

Gamma rays emitted in the excitation of F^{19} by α particles of 0.6 to 2.8 Mev have been studied. Resonances are found in the reaction $F^{19}(\alpha,p)Ne^{22*}$ at α particle energies greater than 1.3 Mev and in the inelastic excitation of 109-kev and 196-kev levels in F^{19} at energies greater than 2.2 Mev. At bombarding energies below 2 Mev, the cross sections for inelastic excitation of F^{19} decrease much too slowly for compound nucleus formation and are identified as being due to Coulomb excitation. The observed cross sections in the region 0.6 Mev to 2 Mev agree well with the theory for Coulomb excitation. The electromagnetic transition probabilities for decay of these states deduced from the excitation cross sections are in good agreement with those found from direct measurement of the lifetimes by Thirion, Barnes, and Lauritsen. Together with the results of Peterson, Barnes, Fowler, and Lauritsen on the inelastic excitation of fluorine by protons, these experiments lead to spin and parity assignment of $\frac{1}{2}^-$ for the 109 kev state and $5/2^+$ for the 196-kev state of F^{19}. The observed angular distributions of the γ rays from Coulomb excitation by α particles are also in accord with theory.

I. INTRODUCTION

ALTHOUGH extensive investigations of nuclear reactions in light nuclei have been carried out with protons and deuterons, relatively little work has been done with artificially accelerated α particles. In the present paper we wish to summarize our results on several reactions induced in F^{19} by α particles in the energy range 0.6 to 2.8 Mev. We have studied only those reactions yielding γ radiation. These are the $F^{19}(\alpha,p)Ne^{22*}$ reaction leading to the excited state of Ne^{22} at 1.28 Mev ($Q=426$ kev) and the excitation of F^{19} states at 109 kev and 196 kev[1] in the reaction $F^{19}(\alpha,\alpha')F^{19*}$.

The first and second excited states of F^{19} are particularly interesting insofar as they are exceptionally

* Assisted by the joint program of the Office of Naval Research and the U. S. Atomic Energy Commission.

† On sabbatical leave from Princeton University.

‡ Present address: Department of Radiology, City of Hope, Duarte, California.

[1] The energies of the low states of F^{19} quoted in this paper are somewhat lower than those in references 6–9 and reflect revised estimates based on private communication from R. B. Day, recent measurements by Mills, Hilton, and Barnes (unpublished); and new calculations of data of Peterson, Barnes, Fowler, and Lauritsen.

close to the ground state. The spin of the ground state is known to be 1/2; this value has been considered anomalous in the usual coupling schemes in the $j-j$ model if one assumes the $1d_{5/2}$ orbit to have lower energy than the $2s_{1/2}$ or $1d_{3/2}$. Furthermore the simplest unmixed configuration $[(d_{5/2})^2; s_{1/2}]$ for F^{19} is excluded by the superallowed β decay of Ne^{19}. The determinations of the spins and parities of the nearby excited states may eventually clarify these questions.

The low states of F^{19} were first observed by Whaling and Mileikowsky[2] in the reaction $Ne^{21}(d,\alpha)F^{19}$. Day[3] has found these levels in the inelastic scattering of neutrons by fluorine. The observation of their excitation by α particles has also been reported by Heydenburg and Temmer[4] and by Jones and Wilkinson.[5] These levels have been intensively studied in this laboratory by the inelastic scattering of protons, and their lifetimes have been measured. Summaries of these experiments and of the present results have been published in Letters to the Editor.[6-9] The conclusions reached in the proton experiments are that the 196-kev state is $5/2^+$ and that the spin of the 109-kev state is 1/2. The α particle work, in conjunction with the lifetime measurements, confirms the $5/2^+$ assignment, and leads to the assignment of odd parity to the 109-kev state.

We found no evidence for a 400-kev γ ray which could correspond to a reported state in Ne^{22} at 0.4 Mev.[10] While we have used α particle energies up to 2.8 Mev, we observed no γ rays attributable to the reaction $F^{19}(\alpha,n)Na^{22}$.* These last two (negative) findings are in agreement with the results of Heydenburg and Temmer.[4] They also found no evidence of a 0.4-Mev γ ray. However they did observe a 592-kev γ ray at bombarding energies in excess of 3.05 Mev; they assign this γ ray to an excited state of Na^{22} at 592 kev. We did not look carefully for γ rays corresponding to the level at 3.4 Mev[11] in Ne^{22} which might have been excited at a bombarding energy as low as 2.06 Mev, but we found no indication of it in our spectra.

II. EXPERIMENTAL ARRANGEMENT

Singly charged helium ions were accelerated by an electrostatic generator. The ion beam impinged on the target after passing through a calibrated electrostatic analyzer of high resolution.

The γ rays were observed with a scintillation spectrometer[12] using a NaI(Tl) cylindrical crystal 1½ in. long and 1½ in. in diameter. The pulse spectrum was analyzed with the aid of a 10-channel discriminator. A lead cylinder enclosed the counter fairly closely, leaving room however for an additional shield around the crystal. A house of 2-in. thick lead bricks was built around the entire counter-target assembly to improve the shielding, chiefly against low energy x-radiation coming from the generator.

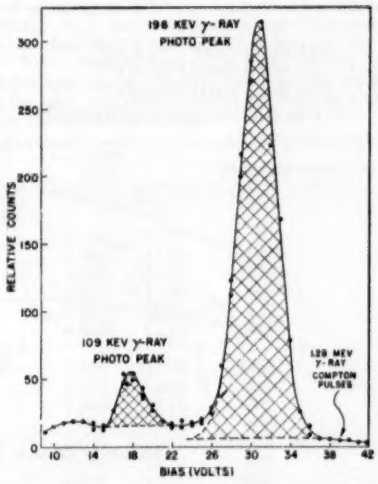

FIG. 1. Scintillation counter pulse height spectrum in the low-energy region produced by inelastic excitation of F^{19} by α particles. The target was a thick CaF_2 crystal and the bombarding energy was 2.35 Mev.

Yield curves were obtained for a variety of thick and thin targets of CaF_2, AlF_3, and ZnF_2. A typical low-energy scintillation spectrum is shown in Fig. 1; the target was a thick CaF_2 crystal and the bombarding energy 2.35 Mev. This spectrum was taken with a ¼-in. copper cylinder around the crystal to remove lead fluorescent radiation which otherwise gives rise to a peak in the vicinity of 80 kev comparable with the 109-kev peak. The cross hatched areas of Fig. 1 were taken to represent the yields of the 109- and 196-kev radiation.

III. RESULTS

Resonances

Figure 2 summarizes the results of observations made with three thin targets. Here we were primarily interested in the location and magnitudes of resonances. The ordinates give the yield for the 1.28-Mev, 196-kev, and 109-kev radiations, while the abscissa is the energy of the incident beam. Target A was ZnF_2 evaporated onto a copper foil; target B was CaF_2 evaporated on copper; and target C was AlF_3 made by exposing an aluminum foil to HF fumes. The yields for target C were multiplied by ⅓ for convenience in plotting.

In obtaining these points, the 10-channel discriminator was set to cover the 109-kev photopeak (see Fig. 1).

[2] C. Mileikowsky and W. Whaling, Phys. Rev. **88**, 1254 (1952).
[3] R. B. Day, Phys. Rev. **89**, 908(A) (1953).
[4] N. P. Heydenburg and G. M. Temmer, Phys. Rev. **94**, 1252 (1954).
[5] G. A. Jones and D. H. Wilkinson (pre-publication report).
[6] Peterson, Barnes, Fowler, and Lauritsen, Phys. Rev. **94**, 1075 (1954).
[7] Thirion, Barnes and Lauritsen, Phys. Rev. **94**, 1076 (1954).
[8] Sherr, Li, and Christy, Phys. Rev. **94**, 1076 (1954).
[9] R. F. Christy, Phys. Rev. **94**, 1077 (1954).
[10] B. J. Jolley and F. C. Champion, Proc. Phys. Soc. (London) **A64**, 88 (1951).
[11] F. Ajzenberg and T. Lauritsen, Revs. Modern Phys. **24**, 321 (1952).
[12] H. J. Woodbury, Thesis, California Institute of Technology, 1953 (unpublished).

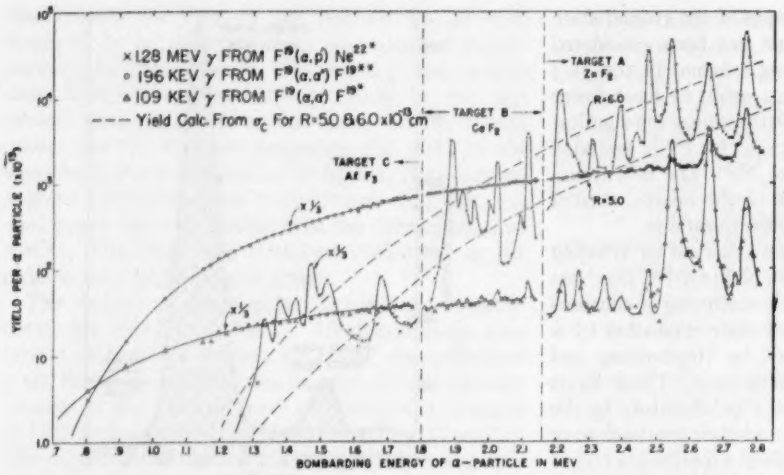
×1.28 MEV γ FROM F19(α,p) Ne22*
○ 196 KEV γ FROM F19(α,α') F19**
△ 109 KEV γ FROM F19(α,α) F19*
Yield Calc. From σc For R=5.0 & 6.0 x10-5 cm
TARGET A ZnF2
TARGET B CaF2
TARGET C AlF3
R=6.0
R=5.0
YIELD PER α PARTICLE (x10-5)
BOMBARDING ENERGY OF α-PARTICLE IN MEV

FIG. 2. Yield of the reactions $F^{19}(\alpha,p')Ne^{22*}$, $F^{19}(\alpha,\alpha')F^{19*}$ and $F^{19}(\alpha,\alpha'')F^{19**}$.

The 196-kev yield was obtained at the same time by taking the difference between two integral discriminators, one coinciding with the end of the 109-kev spectrum and the other set slightly beyond the 196-kev photopeak. The latter reading was taken as a measure of the yield of the 1.28-Mev γ ray. (The positions of the 1.28-Mev resonances were checked by observations on the 1.28-Mev photopeak using thin and thick targets.)

The observed counts were converted to yield per α particle, using the known calibration of the current integrator and approximate values for the scintillation counter efficiency for the various radiations. For the 196-kev data correction was made for the Compton pulses arising from the 1.28-Mev radiation which fell in the region of the 196-kev photopeak. This generally small correction was determined empirically using a Co^{60} source to give the shape of a pulse spectrum similar to that of the 1.28-Mev radiation in this region.

It is seen in Fig. 2 that the 196-kev curves for the three targets join smoothly. Recalling that the yields for target *C* were reduced by a factor of 3 in plotting, it is seen that the number of F atoms per unit area are in the approximate ratio of 1:1:3 for targets *A*:*B*:*C*. The target thickness was estimated to be 19, 15, and 33 kev (for *A*, *B*, *C*) at an α particle energy of 1.7 Mev.

It is estimated that the absolute scale of Fig. 2 is correct to 20 or 30 percent for the 1.28-Mev and 196-kev radiation. The absolute yield of the 109-kev radiation is much less certain as is evident from Fig. 2 at 2.16 Mev where the 109-kev curves for targets *A* and *B* should join. This discrepancy in yield reflects a major problem in determining the correct yield of the 109-kev radiation. This yield is quite small relative to that for the other radiations, except at the lowest energies.

Our procedure in finding the 109-kev yield was to draw a line joining the valleys above and below the peak in the pulse spectrum and to take the area above this line to represent the yield (Fig. 1). This procedure has the virtue of simplicity and reproducibility for a given geometry and choice of shielding. The apparent magnitude of the 109-kev yield relative to the 196-kev yield was, however, quite sensitive to the geometry, target and shielding. In Fig. 3(a) we have plotted the 109-kev spectrum obtained with a thick CaF_2 target at a bombarding energy of 2.07 Mev with and without a $\frac{1}{4}$-in. copper cylinder around the crystal. Using the procedure outlined above for finding the 109-kev photopeak area and comparing it with the corresponding 196-kev photopeak areas, we find for the ratio of the latter to the former, 12.1 with the copper shield, and 14.7 with the copper removed. It is clear that the $\frac{1}{4}$-in. copper shield increases the number of 109-kev counts by back-scattering the γ rays which reach it, most probably the 196-kev radiation. For the measurements to be discussed below, we used 15-mil Ta foil to remove the lead x-rays which would otherwise be bothersome

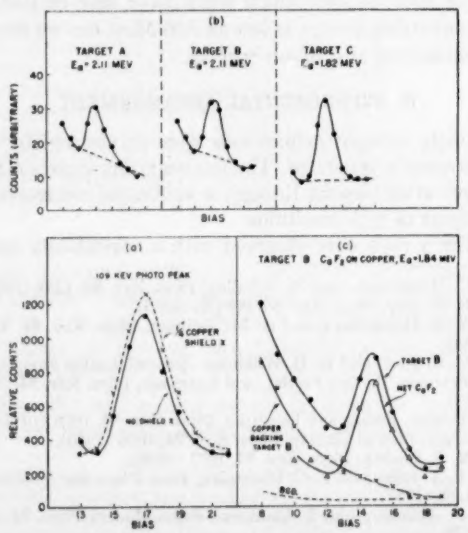

FIG. 3. Pulse height spectra in the neighborhood of 109 kev obtained under different conditions (see text).

when using thin targets. The tantalum shield gave spectra similar to the "no shield" curve of Fig. 3(a).

The choice of target also affected the analysis of the 109-kev γ ray. Figure 3(b) shows typical 109-kev photopeaks obtained with targets *A*, *B*, and *C*. The dotted lines are the ones used in the analysis. It is evident that the copper-backed targets (*A* and *B*) exhibit a low energy radiation not attributable to fluorine. Figure 3(c) shows the spectra obtained from the front and back of target *B*; the copper backing is seen to contribute an appreciable continuous spectrum. This radiation is probably bremsstrahlung[13] from the α particles. Mr. W. J. Karzas in this laboratory has calculated the bremsstrahlung to be expected and, finds approximate agreement with the data of Fig. 3(c). Thick CaF_2 and thin CaF_2 on Al gave spectra similar to that of target *C*.

In addition to the effects of shielding and target, there are also uncertainties arising from the low counting rates and from possible variations in width of the channels of the discriminator, especially those channels which register the valleys. The analysis is particularly sensitive to the latter, since the subtractions are relatively large.

The above remarks indicate the difficulties involved in an accurate determination of the yield of the 109-kev radiation. However, the yield of the bothersome radiations is smooth enough not to interfere with the detection of resonances for the 109-kev radiation.

The positions and yields of the resonances are tabulated in Table I. For the former we have taken the center of the observed peaks minus one half of the target thickness. All of the peaks observed have widths comparable with the (only approximately known) target thickness and therefore the true widths are less than, or comparable with, the target thickness. Additional correction for surface contamination might lower the resonance energies by 10 or 20 kev. The results of the present measurements are on the whole in good agreement with the observations of Heydenberg and Temmer.[4]

The rapid decrease of resonant yield of the 196- and 109-kev radiations relative to the 1.28-Mev yield with decreasing α particle energy is to be expected because of the much lower penetration factor for inelastically scattered α particles in comparison with that for the protons from the $\alpha-p$ reaction. The energy dependence (averaged over resonances) of the yield of the 1.28-Mev radiation is determined primarily by the penetrability of the incident α particle. The dotted curves in Fig. 2 correspond to the yield to be expected on the basis of the continuum theory if we assume the yield is determined by the cross section for formation of the compound nucleus:

$$\sigma_c=\pi\lambda^2\sum_l(2l+1)T_l(E_\alpha),$$

where T_l is the transmission coefficient. The latter depends on the choice of a model. We have used the tabulations of Feshbach, Shapiro, and Weisskopf[14] to evaluate σ_c for various values of the interaction radius. The two dotted curves shown in Fig. 2, correspond to radii of 5.0 and 6.0×10^{-13} cm. The correspondence of shape between the calculated and experimental curves is quite good. It is, of course, not possible to choose an interaction radius from this comparison. The smaller radius corresponds to one of the conventional prescriptions $(1.5A^{\frac{1}{3}}+1.2)\times10^{-13}$ cm, while the larger radius is given by $1.4(A_1^{\frac{1}{3}}+A_2^{\frac{1}{3}})\times10^{-13}$ cm. Qualitatively the latter might be preferred, since the penetrability for the outgoing proton would lower the theoretical yield curve, while the cross section for protons to the ground state (unobserved here) would raise the actual total yield.

TABLE I. Resonances in $F^{19}+\alpha$ reactions. E_α is the resonant α particle energy, E_c is the corresponding excitation energy in the compound nucleus Na^{23} if one uses 10.50 Mev for the mass difference $F^{19}+He^4-Na^{23}$. Columns 4, 5, and 6 list the peak yields per 10^{13} α particles for the 1.28-Mev, 196-kev, and 109-kev radiations; for the latter two the continuous yield has been subtracted. "*U*" marks unresolved resonances.

	E_α (Mev)	E_c (Mev)	Gamma-ray yields per 10^{13} α's 1.28 Mev	196 kev	109 kev
Target *C* AlF_3	1.315	11.59	79		
	1.362	11.63	128		
	1.408	11.66	138		
	1.455	11.70	345		
	1.501	11.74	225		
	1.662	11.87	245		
Target *B* CaF_2	1.879	12.05	3140		
	1.914	12.08	817		
	1.948	12.11	607		
	1.994	12.15	606		
	2.017	12.17	1730		10
	2.083	12.22	420		
	2.109	12.24	3800		20
Target *A* ZnF_2	2.207	12.32	12 000		40
	2.257	12.36	*U*	(100)	55
	2.298	12.40	3200		
	2.337	12.43	*U*		48
	2.383	12.47	8000		14
	2.428	12.50	3702		
	2.463	12.53	34 000	200	60
	2.533	12.59	46 000	400	3000
	2.648	12.69	24 000	1800	4500
	2.728	12.75	*U*	*U*	25
	2.758	12.78	55 000	4700	600

Coulomb Excitation

The nonresonant yields of the 196-kev and 109-kev radiation at energies below 2.5 Mev vary much too slowly with energy to be ascribed to processes involving the barrier penetration of ingoing and outgoing α particles associated with formation of the compound nucleus. Results qualitatively similar to these were obtained by Heydenberg and Temmer[4] and were ascribed to Coulomb excitation. In this process the

[13] C. Zupancic and T. Huus, Phys. Rev. **94**, 205 (1954).

[14] Feshbach, Shapiro, and Weisskopf, Nuclear Development Associates Report 158B-5 (NYO 3077) June 15, 1953 (unpublished).

incident α particle excites the F^{19} nucleus by virtue of the electromagnetic field associated with the passage of the α particle externally to the nucleus. From the yield curves we note that the cross section for formation of the compound nucleus, as inferred from the yield of the 1.28-Mev gamma ray, is comparable with the cross section for Coulomb excitation of the 109-kev level at as low an energy as 1.3 Mev. While the formation of the compound nucleus will not contribute directly to the excitation process (because of the extremely low probability that the α particle can escape), it might be expected to modify the calculation of the cross section for Coulomb excitation.

In order to compare the observed Coulomb excitation with theory, a series of measurements were carried out to determine the absolute cross sections accurately. Yield curves for the 196-kev and 109-kev radiations were taken with a semithick target (~100 kev)of CaF_2 evaporated on a 15-mil aluminum disk. At each energy a series of readings were taken with different channel settings of the multichannel discriminator in order to average out fluctuations in channel widths. These curves agreed in shape very closely (within 10 percent) with the curves for Target *C* (Fig. 3). Measurements were made at several energies with a Ta-lined lead collimator which restricted the passage of γ rays to be near the axis of the NaI crystal. With these "good geometry" measurements, the absolute yield was determined. In order to determine the absolute cross section, a target of CaF_2 was used whose width for protons was determined[15] by observing the $F^{19}(p,\gamma)$ resonance at 873 kev. The width was found by comparing the integrated thin target yield with the yield of a (nearly) thick target.[16] The corresponding number of F^{19} atoms was determined taking 11.9×10^{-15} ev cm^2 per F^{19} atom for the stopping cross section of CaF_2 for 880 kev protons. The error in the calibration due to uncertainty in target thickness and stopping power is probably less than 20 percent. The final results of these absolute determinations are shown in Fig. 4 in which the absolute cross section is plotted *versus* α particle bombarding energy (corrected for target thickness). For purposes of clarity, the weak resonances shown in Fig. 2 have been omitted. The curves in Fig. 4 are theoretical and will be discussed later.

Corrections for counter efficiency, absorption, and angular distribution were considered. We assumed that the photopeak areas measured the number of quanta entering the crystal (through the collimator). Although some of the 196-kev quanta give rise to Compton pulses, this loss is balanced by inscattering of gamma rays by the surroundings. A reasonable estimate would be that both are of the order of a few percent. The accuracy of the determination of the photopeak area of the 109-kev radiation is more difficult to evaluate because of effects discussed previously. However, a comparison was made of the ratio of the differential yields of 196- and 109-kev radiations as determined from the thin-target data and from calibrated thick-target yields at 1.96 Mev. These agreed within 7.5 percent. Since the intensity of the 196-kev radiation relative to the 109-kev radiation varied by a factor of 1.5 between these two determinations, we estimate that the error in the photopeak area for the 109-kev radiation arising from improper allowance for the 196-kev spectrum is less than 20 percent at 2 Mev and is smaller at lower energies where the yields approach each other.

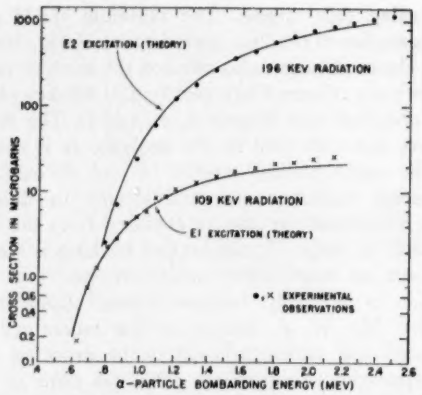

FIG. 4. Cross section for the inelastic excitation of the 109-kev and 196-kev states of F^{19} as a function of bombarding α particles energy. The points are experimental, the curves are theoretical.

Absorption corrections were negligible, while for the effect of angular distribution we used the results of the next section (below). This latter correction was 14 percent for the 196-kev radiation and zero for the 109-kev radiation. In summary we estimate that the errors in absolute cross section are no larger than 25 percent for the 196-kev radiation and no larger than 35 percent for the 109-kev radiation.

In addition to the possible sources of error in the cross sections discussed above, there is also uncertainty in the correct value of E_α arising from the presence of surface deposits on the targets and from the lack of precise information regarding the thickness of the targets for α particles. The surface deposits may have been as thick as 10 to 20 kev with the result that the points may be plotted at too high an energy. The errors in target thickness (for α particles) is estimated to be ±10 kev. The theoretical curves in Fig. 4 were chosen for best fit in the intermediate energy region to minimize this uncertainty in the energy scale.

Angular Distributions

Knowledge of the angular distributions of the 196-kev and 109-kev radiations relative to the α particle beam is necessary in order to establish the total cross sections. Furthermore, the theory for Coulomb excita-

[15] We are indebted to Dr. C. A. Barnes and Dr. W. A. Fowler for preparation and calibration of this target.

[16] Fowler, Lauritsen, and Lauritsen, Revs. Modern Phys. **20**, 236 (1948).

tion predicts the magnitude of the anisotropy to be expected for various spin assignments to the levels involved. The angular distributions predicted vary slowly with energy. Because of the low inelastic reaction cross section we investigated the yields at 0°, 45°, and 90° from a thick CaF_2 target at a bombarding energy of 1.84 Mev.

The CaF_2 was evaporated onto a 15-mil aluminum disk, which was then mounted in a lucite target chamber so that the target could be rotated about a vertical axis (the beam being horizontal). The counter was mounted on a stand which could be rotated around the target in a horizontal plane. A lead collimator (half-angle 10°) was mounted in front of the counter. The aperture-target distance was 2.0 in. Lead bricks were piled up to shield the counter as much as possible from the generator-produced background.

As a check on the geometry of the apparatus we used the angular distribution of the 478-kev gamma radiation produced in the inelastic scattering of α particles by Li^7. The 478-kev level has spin 1/2 and therefore the radiation should be emitted isotropically. Our procedure then was to bombard LiOH which had been put on the back of the CaF_2 target, and measure the yield at 0°, 45°, and 90°. The target was then rotated through 180° and the yield for the fluorine was measured. (The target was placed at 45° to the beam so that the 0° and 90° positions were symmetrical with respect to the target.)

From the Li results we found that the yields at 90° and 45° were larger than the 0° yield by factors 1.04 $\pm$0.01 and 1.02$\pm$0.02 respectively. These agreed with measurements of the geometry. We used these factors to correct the F^{19} results. For the 196-kev radiation the final results were $W(0°)/W(90°)=1.22\pm0.02$ and $W(0°)/W(45°)=1.08\pm0.03$, where $W(\theta)$ is the relative counting rate at an angle θ between the directions of the beam and the γ rays.

Using our usual prescription for finding the yield of the 109-kev radiation, we obtained $W(0°)/W(90°)=1.09\pm0.06$ and $W(0°)/W(45°)=1.08\pm0.08$. These results indicate a slight forward peaking. However, since the geometry for back scattering from the beam tube, target chamber, and shielding were not identical for the three angles, we investigated the back scattering effect. The pulses arising from the 196-kev radiation in the vicinity of the 109-kev photopeak can have their origin (a) externally to the counter assembly, (b) in scattering by the material surrounding the crystal, (c) in the crystal itself. Effects (b) and (c) would be the same for the three angles, while (a) would be expected to vary. Our procedure was to measure first the pulse spectrum with a $\frac{3}{16}$-in. diameter disk of 30-mil Ta and 17-mil Cd placed directly behind the beam spot on the back side of the target. This absorber reduced the 196-kev radiation from the target by a factor of 4, and the 109-kev radiation by a factor of 400. The absorber was sufficiently small in diameter not to change

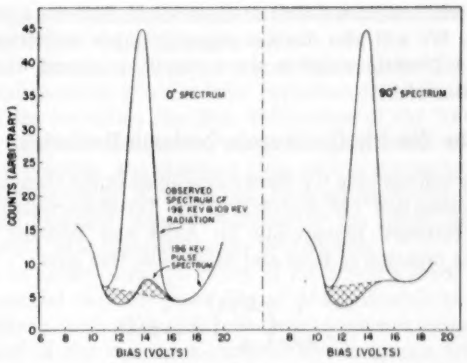

FIG. 5. Pulse height spectra (schematic) in the neighborhood of 109 kev obtained in the measurement of the angular distribution of the 109-kev radiation.

the amount of the backscattered radiation appreciably from its intensity in the angular distribution measurements. Thus the pulse spectrum obtained was that due to transmitted 196-kev radiation plus backscattered radiation from the surroundings. The measurements were repeated, with the same thickness of absorbers placed over the counter aperture to determine the magnitude of effects (b) and (c). Finally we reconstructed the pulse spectrum at 109 kev to be expected from the 196-kev radiation in the angular distribution measurements. The results are shown schematically in Fig. 5 for 0° and 90°. The dotted lines in each figure correspond to our standard prescription for finding the photopeak area. The cross-hatched areas indicate the errors in this procedure. For the 0° case it is evident that an underestimate on the lower side of the peak is practically balanced by an overestimate on the upper side. For the 90° case, however, our procedure leads to an underestimate of (9$\pm$5) percent. No similar measurements were made at 45°, but from the appearance of the bias curve we feel justified in taking an intermediate value of (-5 ± 3) percent for the correction at 45°.

With these corrections the angular dependence is given by $W(0°)/W(90°)=0.99\pm0.08$ and $W(0°)/W(45°)=1.03\pm0.09$. Thus the emission of the 109-kev radiation appears to be isotropic. These results on the angular distributions of the 109-kev and 196-kev radiation will be discussed in the following sections.

IV. COMPARISON WITH THEORY

In this section we will discuss the theoretical Coulomb excitation functions to be compared with the experimental excitation functions of the 196-kev and 109-kev radiations at α particle bombarding energies below those which show pronounced resonance phenomena. We have compared the excitation of the 196-kev state with calculated electric quadrupole excitation of a $5/2^+$ state (the ground state of F^{19} is taken to be $1/2^+$). In the case of the 109-kev state, we have compared the

data with calculated electric dipole excitation of a $1/2^-$ state. We will also discuss magnetic dipole excitation of a $1/2^+$ state which is not, however, in accord with experiment.

The Electric Quadrupole Coulomb Excitation

We will use here the theory developed in the classical approximation ($2Z_1Z_2e^2/\hbar v \gg 1$) by Ter-Martyrosian[17] and extended numerically by Alder and Winther.[18] In the notation of Bohr and Mottelson,[19] we have

$$\sigma = \frac{2\pi^2}{25}\frac{1}{Z_2^2e^2}\left(\frac{Mv}{\hbar}\right)^2 B_{e\frac{1}{2}\to\frac{1}{2}} g(\xi), \qquad (1)$$

where M is the reduced mass of the α particle and F^{19}, $Z_1=2$, $Z_2=9$, v is the relative velocity, and $\xi=(\Delta E/2E)\times(Z_1Z_2e^2/\hbar v)$. ΔE is the excitation energy in question (196 kev) and E is the bombarding energy. The quantity $g(\xi)$ has been calculated numerically and is given by Alder and Winther. In using this form for σ we note that the classical condition is fairly satisfactory since $2Z_1Z_2e^2/\hbar v > 8$ up to 2 Mev. However the additional requirement of the calculation, namely $\Delta E/E \ll 1$ is not sufficiently satisfied to give accurate results for $E \approx 1$ Mev. The extreme evidence of this failure lies in the way in which σ behaves in the neighborhood of threshold at 238 kev where σ should vanish exponentially, whereas ξ is finite as is $g(\xi)$. The simplest modification of the theory which introduces the proper exponential behavior at threshold is to replace ξ by n_2-n_1, where $n_2=Z_1Z_2e^2/\hbar v_2$, $n_1=Z_1Z_2e^2/\hbar v_1$, and v_1 and v_2 are the relative velocities of colliding and separating nuclei respectively. Then

$$n_2-n_1=\frac{Z_1Z_2e^2}{\hbar}\left(\frac{1}{v_2}-\frac{1}{v_1}\right)=\frac{Z_1Z_2e^2}{\hbar}\left(\frac{v_1^2-v_2^2}{v_1v_2(v_1+v_2)}\right)$$

$$\approx\frac{Z_1Z_2e^2}{\hbar v}\frac{\Delta E}{2E}=\xi.$$

Thus for $\Delta E \ll E$, $n_2-n_1\approx\xi$ but near threshold, $n_2-n_1\to\infty$ and $g(n_2-n_1)\to 0$ as it should. Although this substitution (which is suggested in ref. 17) produces presumably the correct exponential behavior near threshold, it could readily be in error by a power of $(n_2-n_1)/\xi$. Consequently, we will assume our calculated σ to be in error by up to a factor of 2 around 1 Mev where $(n_2-n_1)/\xi=1.5$. On the other hand, compound nucleus formation is apparently relevant near 2 Mev, which can also modify the theory which neglects the finite nuclear size. Thus there is no energy range in which the existing calculations are entirely satisfactory for as light a nucleus as fluorine, and the calculated σ will be presumed to contain errors of order a factor 2 either in absolute magnitude or in the ratio of σ at high to σ at low energy.

We have calculated σ from Eq. (1) with n_2-n_1 replacing ξ. The calculations were fitted to the observed σ at $\sim$1.4 Mev by suitable choice of $B_{e\frac{1}{2}\to\frac{1}{2}}=7.8\times10^{-70}$. The resulting curve is shown as the solid line in Fig. 5. The agreement with experiment is good.

From the value of $B_{e\frac{1}{2}\to\frac{1}{2}}$ so determined we predict a value of the lifetime τ, since

$$\frac{1}{\tau}=T=\frac{4\pi}{75}\frac{1}{\hbar}\left(\frac{\omega}{c}\right)^5 B_{e\frac{1}{2}\to\frac{1}{2}},$$

$$B_{e\frac{1}{2}\to\frac{1}{2}}=(2/6)B_{e\frac{1}{2}\to\frac{1}{2}}.$$

There results a predicted lifetime $\tau=2.5\times10^{-7}$ sec. This is in satisfactory agreement with the measured[7] value $\tau\approx0.8\times10^{-7}$ sec. The assumption of $3/2^+$ for the spin would have led to a predicted E_2 decay time τ less by a factor 1.5, and also in good agreement with the measured value. This possibility is, however, excluded by the argument in the next section.

The theory of Coulomb excitation also predicts the angular distribution of the γ rays. In this case, at a mean energy of 1.6 Mev we expect[18] $W(\theta)=1+0.67B_2P_2(\cos\theta)+0.025B_4P_4(\cos\theta)$. For a $5/2^+$ state, $B_2=0.285$ and $B_4=0.381$. However, associated with the long lifetime, it has been found[6,9] that the coefficient of $P_2(\cos\theta)$ is reduced by a factor of about 0.6; the coefficient of P_4 should show an even larger reduction of $\sim$0.4. The observed ratios $W(0°)/W(90°)=1.22\pm0.02$ and $W(0°)/W(45°)=1.08\pm0.03$ are consistent with the formula above if the reduction of the coefficient of P_2 is between 0.6 and 0.8. A $3/2^+$ state being excited and decaying by $E2$ radiation would also give an angular distribution consistent with experiment. However, if it decayed by $M1$ radiation the coefficient of P_2 would be negative, in disagreement with observation.

The value of B_e may be compared with a calculated one-particle (proton) matrix element for a $d_{5/2}-s_{1/2}$ transition, although we would not propose that the ground state configuration can be so simply treated. We get

$$B_{e\frac{1}{2}\to\frac{1}{2}}=\frac{e^2}{4\pi}\left(1-\frac{Z}{A^2}\right)^2\times\frac{6}{2}\times\langle i|r^2|f\rangle^2.$$

Taking $\langle i|r^2|f\rangle=\frac{3}{5}R_0^2$, we get a calculated R_0 from the experimental value of B. It is $R_0\approx5\times10^{-13}$, which is rather larger than conventional values for the nuclear radius, suggesting the possibility of some collective motion contribution to the matrix element.

The Electric Dipole Coulomb Excitation

The theory of the electric dipole excitation has been worked out by Mullin and Guth[20] and also by Ter-

[17] K. A. Ter-Martyrosian, J. Exptl. Theoret. Phys. (U.S.S.R.) **22**, 284 (1952).
[18] K. Alder and A. Winther, Phys. Rev. **91**, 1578 (1953).
[19] A. Bohr and B. R. Mottelson, Kgl. Danske Videnskab. Selskab, Mat.-fys. Medd. **27**, No. 16 (1953).
[20] C. J. Mullin and E. Guth, Phys. Rev. **82**, 141 (1951).

Martyrosian.[17] In this case, exact formulae[20] have been developed for $\sigma(\theta)$ and σ in the approximation that the finite size of the nucleus can be neglected. However, the exact formula involves hypergeometric functions which have been evaluated only in the limit $n_2 \to \infty$ (near threshold) and $n_2 - n_1$ small. The experimental data in this case extend from 600 kev where $n_2 - n_1 \approx 1$ to about 2 Mev where $n_2 - n_1 \approx 0.15$. The lower energy is still not low enough to make the threshold approximation good and at the higher energy the neglect of the finite size of the nucleus can hardly be accurate since compound nucleus formation is important. As a result, we again cannot apply the results of theory with high precision. We have, following Ter-Martyrosian, joined smoothly the limiting forms for σ in the comparison with experiment which was fitted at $\sim$1.0 Mev. The resulting value of the dipole moment D^2 should be correct within a factor $\sim$1.5.

The electric dipole excitation has been calculated from the expression

$$\sigma = \frac{32\pi^2}{9e^2}\left(\frac{n_1}{Z_2}\right)^2 e^{-2\pi(n_2-n_1)} B_{\frac{1}{2}\to\frac{1}{2}} f(E),$$

where $B_{\frac{1}{2}\to\frac{1}{2}}$ is the electric dipole operator as defined by Bohr and Mottelson. $f(E)$ is a slowly varying factor which approaches $\pi/\sqrt{3}$ near threshold and varies logarithmically with E at high energies; at 2 Mev it is ≈ 3 and varies approximately linearly with E between $\pi/\sqrt{3}$ and 3. The curve so calculated is shown as a solid line in Fig. 4. The correspondence with the experimental excitation function is quite good.

The value of $B_{\frac{1}{2}\to\frac{1}{2}}$ derived from this excitation function is $B_{\frac{1}{2}\to\frac{1}{2}} = 2.3\times10^{-30} e^2$. From this a lifetime τ can be predicted from

$$\frac{1}{\tau} = T = \frac{16\pi}{9}\frac{1}{\hbar}\left(\frac{\omega}{c}\right)^3 B_{\frac{1}{2}\to\frac{1}{2}}.$$

This gives $\tau = 2.1\times10^{-9}$ sec, whereas the directly measured lifetime $\tau = 1.0\pm0.3\times10^{-9}$ sec.[7] The combined uncertainties in the two experiments, together with the approximations in the theory, are sufficient to account for the discrepancy of $\sim$2.

The observed angular distribution of the 109-kev γ ray is, of course, consistent with the spherical symmetry to be expected for a $\frac{1}{2}^-$ (or $1/2^+$) state. It also serves, however, to exclude the possibility that it is a $3/2^+$ state which is excited by $E2$ and decays by $M1$. Such a possibility would give $W(\theta) = 1 - 0.24\cos^2\theta$ which is inconsistent with observation.

The value of B can be compared to a calculated one-particle matrix element for a $p_{\frac{1}{2}}\to s_{\frac{1}{2}}$ transition for orientation purposes. We find

$$B_{\frac{1}{2}\to\frac{1}{2}} = \frac{3}{64\pi} e^2\left(1 - \frac{9}{19}\right) R_0^2,$$

which, for $R_0 = 1.4\times A^{\frac{1}{3}}\times10^{-13}$ cm, gives $B = 5.8\times10^{-28} e^2$ which is 250 times larger than the observed value. This suggests that the transition involves the change of more than a single particle orbit.

In general it would be possible to determine the multipolarity of a Coulomb excitation from the shape of the excitation function. In the case of the 109-kev γ ray, however, in the range $0.6 \le E \le 2$ Mev this is not possible. The observed cross section is equally well represented by $E2$ excitation. Such an interpretation is not, however, possible because of the other experiments. It is discussed in the next section.

In ascertaining the parity of the 109-kev state, it is essential that the possibility of $M1$ excitation be discussed. Such excitation will proceed via the magnetic field of the moving α particle. The magnetic field is less than the electric field by a factor v/c and in the high-velocity realm, the magnetic excitation should be less than the electric by v^2/c^2 [21] if the magnetic dipole moment of the nucleus is substituted for the electric dipole moment. Thus, to fit the observed cross section would require a magnetic moment $\approx c^3/v^2 \approx 1000$ times the electric moment and a lifetime $\approx 10^{-12}$ sec. This latter value is in disagreement with observation.

V. DISCUSSION

In this section we review all of the experiments[6-9] recently carried out in the Kellogg Radiation Laboratory on the low excited states of F^{19}.

The assignment of $5/2^+$ as the spin of the 196-kev state of F^{19} is relevant to the further discussion of the problem, so its basis is outlined below. First, the 196-kev gamma-ray angular distributions from the inelastic scattering of protons at the 2^- resonances in Ne^{20} lead to $5/2^+$ assignment. A $3/2^+$ state decaying by magnetic dipole radiation would require the coefficient A_γ in $1 + A_\gamma\cos^2\theta$ to be zero or negative in contradiction to the experimental data. On the other hand, the $E2$ decay of a $3/2^+$ state would give $0 \le A_\gamma \le 14/22$ which is consistent with the data. ($3/2^+$ is also consistent with the angular distribution observed in Coulomb excitation.) The angular distribution for $E2$ decay of $5/2^+$ state is also consistent with the data. On *a priori* grounds, a $3/2^+$ state should decay by $M1$ radiation in about 10^{-11} sec compared to 10^{-6} to 10^{-7} sec by $E2$ decay so that the assumption of $E2$ decay of a $3/2^+$ state implies a forbiddeness of $M1$ decay by a factor $\sim10^4$ which is very unlikely. The measurement of the lifetime of 10^{-7} sec confirms the assumption that the state is decaying by $E2$ radiation. Finally, the cross section for Coulomb excitation is in good numerical agreement with the observed lifetime if $E2$ excitation and $E2$ decay are assumed. In principle this agreement could distinguish between $3/2^+$ and $5/2^+$ since there is a difference of a factor of $6/4 = 1.5$ in the statistical weights. However, the inaccuracies in present theory of the excitation process probably preclude such a fine

[21] K. Alder and A. Winther have calculated the magnetic dipole excitation and find it given by $0.055v^2/c^2$ times the expression for electric dipole excitation (private communication).

distinction. In conclusion, the facts on the 196-kev state are most reasonably explained by a $5/2^+$ assignment, which, moreover, is expected from the shell model. It should be noted, however, that a $3/2^+$ assignment is not directly disproved but only made unreasonable by the fact that the $M1$ transition to the ground state (and also the transition to the 109-kev state) would have to be suppressed by apparently accidental factors of many powers of ten. Since a $3/2^+$ assignment for the 196-kev state at best makes the explanation of the 109-kev state only more difficult, it will not be considered further.

In discussing the 109-kev state we note that the lifetime of 10^{-9} sec requires that the transition be dipole. The expected lifetime for an $E2$ transition would be about 10^{-5} sec, whereas the lifetime for $E1$ could be 10^{-11} to 10^{-12} sec and for $M1$ it could be $\sim 5\times 10^{-11}$ sec. Thus the spin of this state must be $1/2^{\pm}$ or $3/2^{\pm}$. Since the unexpected feature of these assignments is the negative parity, the real problem is to decide if $1/2^+$ or $3/2^+$ is possible. If these are not reasonable, then $1/2^-$ is the only choice since the $3/2^-$ would permit the cascade 87-kev γ ray at too rapid a rate and would not automatically give isotropy to the γ rays.

The $1/2^+$ Possibility

This assignment would be in satisfactory agreement with the lifetime for decay and with the isotropy of the γ rays. However, the Coulomb excitation can then not be understood. From the lifetime, we can compute the $M1$ matrix element. Coulomb excitation by α particles of a $1/2^+$ state should be smaller than the $E1$ excitation by a factor $\sim 10^4$ for the same dipole moment. Consequently, the state cannot be excited as observed by magnetic Coulomb excitation and the spin is not $1/2^+$.

The $3/2^+$ Possibility

The decay must be predominantly $M1$. On the other hand, as we see above, the excitation must be $E2$. From the Coulomb excitation cross section, we calculate the (matrix element)^2 as 35 times smaller than for the 196-kev transition (the fit to the data is fairly good to $\sim$1.5 Mev). Thus the calculated $E2$ lifetime would be $35/1.5\times(196/109)^5\times 2\times 10^{-7}$ sec so $\tau(E2)$ would be 7.7×10^{-6} sec. As a result, the ratio of $E2$ to $M1$ in the decay is $1.0\times 10^{-9}/7.7\times 10^{-6}=1.3\times 10^{-5}$. Thus the $E2$ admixture would perturb the calculated angular distributions for the $M1$ decay by only $\sim$1 percent, which is negligible. We are left with a direct contradiction with experiment in the angular distribution of the 109-kev radiation as given by Coulomb excitation. The observed distribution is spherical and cannot be brought into agreement with $1-0.25\cos^2\theta$ calculated for $E2$ excitation and $M1$ decay. Further, the expected $M1$ decay rate for the $5/2^+\rightarrow 3/2^+$ 87-kev transition would be 10^{10} sec^{-1}. It is observed to be $\leq 10^6$ sec^{-1}, a discrepancy of at least 10^5; this is also regarded as a major failure of this supposition. Finally the universal isotropy of the 109-kev radiation finds no explanation, although isotropy from a $3/2^+$ state formed from a 2^- resonance is a possible result.

The $1/2^-$ Possibility

This assignment explains both the isotropy of the radiation and the lack of the 87-kev transition ($5/2^+\rightarrow 1/2^-$ would be $M2$ with a transition rate $\sim 10^3$ sec^{-1}). In addition, however, the fact that the lifetime calculated from $E1$ excitation agrees with that observed is an exceedingly strong argument in its favor.

In conclusion we think the only reasonable explanation of the facts is that the states are $5/2^+$ and $1/2^-$, taking the ground state to be $1/2^+$.

The authors take pleasure in acknowledging the many discussions of these problems with C. A. Barnes, W. A. Fowler, C. C. Lauritsen, and J. Thirion of the Kellogg Radiation Laboratory.

Elastic Scattering of 9.7-Mev Protons by He^4

BRUCE CORK AND WALTER HARTSOUGH
Radiation Laboratory, Department of Physics, University of California, Berkeley, California

(Received August 5, 1954)

The differential cross section for the scattering of 9.7-Mev protons from helium has been measured over the range from 17° to 154° in the center-of-mass system. The new 9.9-Mev proton linear accelerator, which is now used as an injector for the Bevatron, was used as a source of incident protons. A scattering chamber has been used that has the solid angles at the various scattering angles determined by fixed slits. The scattered particles were detected with sodium iodide scintillators and RCA 6199 photomultiplier tubes.

The detectors were conveniently arranged so that each scintillator could be well shielded, and background runs could be made easily. The counters were arranged so that they could be interchanged and three angles have been measured simultaneously, with a statistical accuracy in the forward direction of better than ±1 percent. The differential cross-section measurements of the forward angles are in good agreement with published data in this energy region. However, the cross section for protons scattered in the backward direction is approximately 75 percent of the published value.

I. INTRODUCTION

THE elastic scattering of protons from helium has been measured at low energies,[1–6] and a phase-shift analysis has recently been made.[7,8] This is a many-body problem because of nuclear forces. However, to simplify the problem, it has been treated with the alpha particle regarded as acting as a tightly bound unit. On the basis of the previously published data, calculations by Breit[8] tend to favor a Gaussian type of potential well in preference to a long-tailed exponential well or a short-tailed square well. The 9.9-Mev proton linear accelerator,[9] which is now used as an injector for the Bevatron, has been used to measure both the differential proton-proton[10] cross section and the elastic proton-alpha cross section. The same scattering apparatus (see Fig. 3 of reference 10) was used for both experiments.

II. APPARATUS AND PROCEDURE

The scattering chamber has the solid angles at the various scattering angles determined by fixed rectangular slits. The scattered protons were detected with sodium iodide scintillators and RCA 6199 photomultiplier tubes. The detectors were conveniently arranged so that each scintillator could be well shielded, and background runs could be made easily. The counters were arranged so that they could be interchanged, and three angles were measured simultaneously.

The beam current was measured with a Faraday cup arranged with an automatic type of feedback integrator.[11]

Before a scattering experiment was started, the chamber was evacuated, flushed, and again evacuated to less than 10^{-5} mm mercury. Grade A helium, 99.95 percent pure, was admitted to the chamber through an activated charcoal trap which was cooled to liquid-nitrogen temperature. Most of the scattering experiments were done with a helium pressure of approximately 10 cm mercury.

The proton-beam energy was measured by determining the range in aluminum of the elastically scattered protons. A set of triple-coincidence proportional counters was used at the 30° angle, with the third counter connected in anticoincidence. The amount

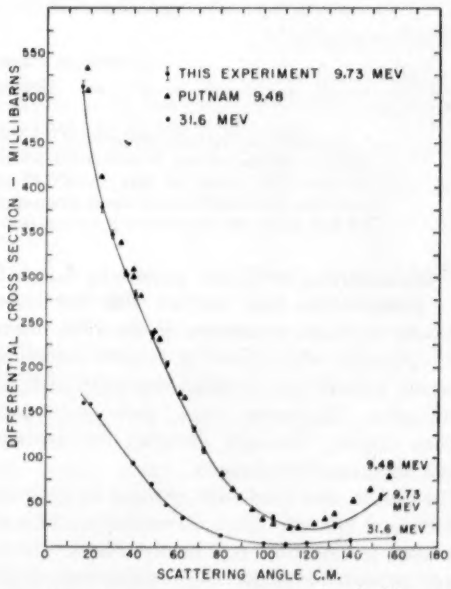

FIG. 1. Elastic scattering of 9.7-Mev protons by helium.

[1] Freier, Lampi, Sleator, and Williams, Phys. Rev. **75**, 1345 (1949).
[2] C. L. Critchfield and D. C. Dodder, Phys. Rev. **76**, 602 (1949).
[3] M. Heusikveld and G. Freier, Phys. Rev. **85**, 80 (1952).
[4] R. K. Adair, Phys. Rev. **86**, 155 (1952).
[5] Kreger, Kerman, and Jentschke, Phys. Rev. **86**, 593 (1952).
[6] T. M. Putman, Phys. Rev. **87**, 932 (1952).
[7] D. C. Dodder and J. L. Gammel, Phys. Rev. **88**, 520 (1952).
[8] Sack, Biedenharn, and Breit, Phys. Rev. **93**, 321 (1954).
[9] Bruce Cork, University of California Radiation Laboratory Report No. UCRL-2385, October, 1953 (unpublished).
[10] B. Cork and W. Hartsough, Phys. Rev. **94**, 1300 (1954).
[11] J. Benveniste and B. Cork, Phys. Rev. **89**, 422 (1953).

TABLE I. Elastic scattering of 9.73-Mev protons by helium.

$\theta_{c.m.}$	$d\sigma/d\Omega_{c.m.}$ (10^{-27} cm^2)
17°10′	512.6±7.2
25° 8′	374.9±4.5
30°56′	346.9±5.5
36°57′	305.0±3.6
37°16′	303.3±5.5
42°14′	281.2±3.1
49° 5′	236.9±3.1
55°40′	204.3±2.4
68°17′	132.5±1.6
72°27′	108.6±1.4
89°21′	57.0±1.6
104°23′	32.2±1.5
132°55′	24.5±0.7
154°15′	58.4±1.1

of aluminum absorber required to stop the scattered protons in the foil that separated the second and third counters was a measure of the proton energy. The incident proton beam was calculated to have an energy of 9.73±0.05 percent.

III. RESULTS

The uncertainties are estimated to be as follows: integrated charge, ±0.4 percent; solid-angle calculations, ±0.5 percent; pressure and temperature, ±0.3 percent; and proton energy, ±0.5 percent. Estimates were made of the loss in counts caused by multiple scattering in the helium; also, the pressure of the helium in the scattering chamber was changed over the range from 5 to 15 cm mercury and no corrections appear necessary. No corrections were made for scattering caused by contamination in the helium.

The differential cross section is plotted in Fig. 1 and tabulated in Table I. Some of the lower-energy data and the higher-energy data are shown on the same plot. It is observed that the measured cross section for 9.73-Mev protons scattered in the forward direction is lower but in good agreement with the 9.48-Mev data of Putnam. However, the cross section for protons scattered in the backward direction is approximately 75 percent of the value published by Putnam. Each of these deviations is in the direction which would be expected by extrapolation from lower and from higher energies,[12] but the deviation of the large-angle scattering is greater than the extrapolated value.

[12] Bruce Cork, Phys. Rev. **89**, 78 (1953).

PHYSICAL REVIEW VOLUME 96, NUMBER 5 DECEMBER 1, 1954

Scattering of 9.5-Mev Protons by Nitrogen

R. G. FREEMANTLE, *University of Birmingham, Birmingham, England*
D. J. PROWSE, *University of Bristol, Bristol, England*
AND
J. ROTBLAT, *University of London, London, England*

(Received August 16, 1954)

The elastic and inelastic scattering of 9.5-Mev protons by N^{14} nuclei has been studied by means of photographic emulsions. Groups of inelastically scattered protons have been observed due to the excited states of N^{14} at 2.3, 3.9, 4.9, and 5.1 Mev; the first of these was excited in a very low intensity. Angular distributions have been determined for the elastic group of protons as well as for the inelastic group corresponding to the 3.9-Mev state; the latter curve is symmetrical about 90°.

THE scattering of 9.5-Mev protons by various light elements has been studied with the beam of molecular hydrogen accelerated in the 60-in. Birmingham cyclotron; the scattering camera described by Burrows, Powell, and Rotblat[1] was used, after slight modification. Exposures were made with various gaseous targets; this note describes the preliminary results obtained with nitrogen.

The camera was filled with nitrogen at pressures of 19.9 cm and 14.8 cm. Ilford C2 emulsions, 200μ thick, were used to detect the scattered particles. The mean energy calculated from the ranges of elastically scattered protons was 9.45±0.01 Mev. Levels in N^{14} at 2.3, 3.9, 4.9, and 5.1 Mev have been observed as well as levels of higher excitation. The 2.3-Mev level was excited in surprisingly low intensity. Only after prolonged search over a large area of emulsion was it possible to detect the protons due to this level; we are able to set an upper limit of 7.0 millibarns for the total cross section for the inelastic scattering of protons from this state. The major contribution to this value comes from difficult measurements at forward angles, where the background of tracks due to elastically scattered protons penetrating the scattering gap wall is relatively high. At 45°, 65°, 115°, and 130°, where accurate measurements of the cross section were possible, we obtained values: 0.68±0.20, 0.26±0.08, 0.32±0.07,

[1] Burrows, Powell, and Rotblat, Proc. Roy. Soc. (London) **A209**, 461 (1951).

and 0.54 ± 0.12 millibarns per steradian respectively. This level has previously been observed in the same reaction at other bombarding energies, as shown in Table I, which also gives comparable information for the 3.9-Mev state.

It appears that transitions to the 2.3-Mev level are becoming less probable as the proton energy increases. Moreover, the observed intensity relative to that of elastic scattering for 9.5-Mev protons, is not much greater than the upper limit set for the corresponding group in (d,d') scattering by Bockelman *et al.* at 7 Mev. This last experiment would at first sight appear to give excellent confirmation of the isotopic spin selection rules, but the present similar result, to which these rules do not apply, suggest that such observations must be interpreted with caution.

The angular distribution of the elastically scattered protons is shown in Fig. 1. It is more complicated than the corresponding distribution found for C^{12} and O^{16} by Burcham *et al.*[2] In addition to the statistical uncertainties shown, there is a possibility that the absolute values of the cross sections are about 5 percent too low.

The angular distribution observed for protons inelastically scattered from N^{14}, leading to the 3.9-Mev level is shown in Fig. 2. Measurements could not be made at angles less than 30° but the evidence from all

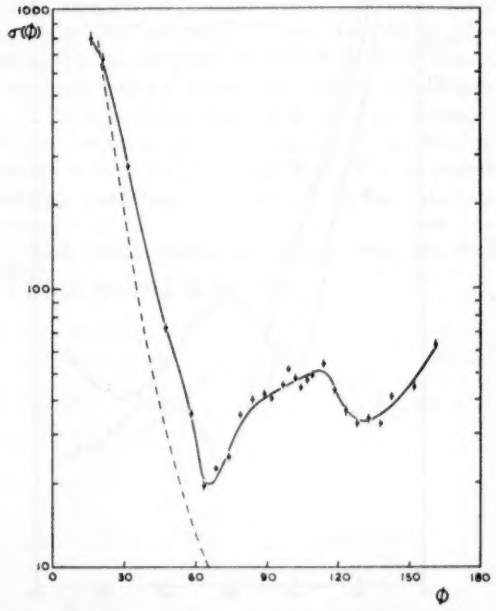

FIG. 1. Angular distribution in the center-of-mass system of protons elastically scattered by N^{14}. $\sigma(\phi)$ is given in millibarns per steradian. The dashed line is the Rutherford scattering curve.

[2] Burcham, Gibson, Hossain, and Rotblat, Phys. Rev. **92**, 1266 (1953).

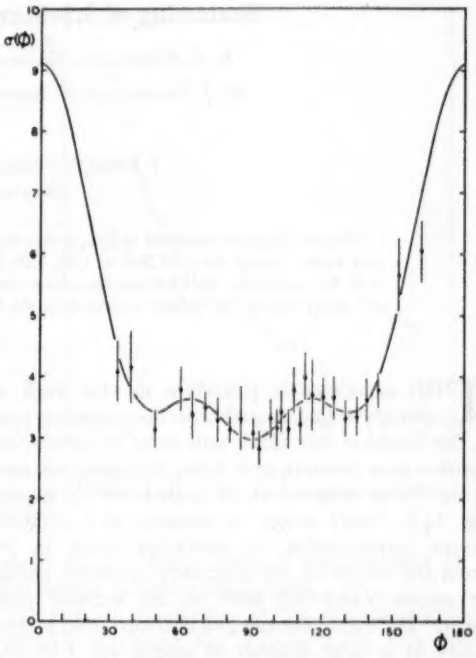

FIG. 2. Angular distribution in the center-of-mass system of protons inelastically scattered from nitrogen, leading to the 3.9-Mev state of N^{14}. $\sigma(\phi)$ is given in millibarns per steradian. The solid curve is the best fit in terms of even Legendre polynomials up to $P_4(\cos\phi)$.

higher angles is that the curve is symmetrical about 90° in the c.m. system. The result can be expressed as:

$$\sigma(\phi)=3.91P_0(\phi)+2.12P_2(\phi)+1.83P_4(\phi)+1.47P_6(\phi)-0.21P_8(\phi).$$

TABLE I. The cross sections for the inelastic scattering of protons from the 2.3- and 3.9-Mev levels of N^{14}, relative to those for scattering from the ground state (g.s.).

Reference	E_p(Mev)	Angle	2.3/g.s.	3.9/g.s.
Bockelman *et al.*[a]	6.92	90°	5%	10%
Cowie *et al.*[b]	7.4	90°	5%	13%
Arthur *et al.*[c]	8.0	150°	2%	4%
Present work	9.5	90°	<1%	7%
		150°	<2%	12%
Fulbright and Bush[d]	15.0	...	not observed	

[a] Bockelman, Browne, Buechner, and Sperduto, Phys. Rev. **92**, 665 (1953).
[b] Cowie, Heydenburg, and Phillips, Phys. Rev. **87**, 304 (1952).
[c] Arthur, Allen, Bender, Hausman, and McDole, Phys. Rev. **88**, 1291 (1952).
[d] H. W. Fulbright and R. R. Bush, Phys. Rev. **74**, 1323 (1948).

One would expect a symmetrical distribution if only one level in the compound nucleus, O^{15}, of unique spin and parity were involved. But this is unlikely to be the case with the high excitation given by 9.5-Mev protons, and some other cause for symmetry must presumably be sought.

Scattering of 9.5-Mev Protons by Neon and Argon

R. G. FREEMANTLE, *University of Birmingham, Birmingham, England*

D. J. PROWSE AND A. HOSSAIN, *University of Bristol, Bristol, England*

AND

J. ROTBLAT, *University of London, London, England*

(Received August 16, 1954)

The photographic emulsion technique was employed to study the scattering of 9.5-Mev protons by neon and argon. Energy levels of Ne^{20} at 1.58, 4.20, 4.95, and 5.62 Mev have been observed as well as of A^{40} at 1.48 Mev. Angular distributions have been determined for the protons elastically scattered by Ne^{20} and A^{40}, as well as for the inelastic groups from the 1.58-Mev level of Ne^{20} and the 1.48-Mev level of A^{40}.

THE experimental procedure in this work was similar to that described in the preceding paper. The chamber was filled with neon of normal composition at a pressure of 6.2 cm. A typical histogram of the tracks observed at an angle of 80° is shown in Fig. 1; it clearly shows the presence of a number of groups corresponding to excitation levels in Ne^{20}. From the ranges of the elastically scattered particles we obtain 9.51±0.01 Mev as the incident proton energy. The excitation energies obtained from measurements at a large number of angles are 1.58±0.01, 4.20±0.01, 4.95±0.02, and 5.62±0.02 Mev. The first two agree within experimental error with those given by Ajzenberg and Lauritsen,[1] while the two states at 4.95 and 5.62 Mev replace the quoted level at 5.4 Mev; it would appear that previous measurements, on the reaction $F^{19}(d,n)Ne^{20}$, had not resolved this doublet.[2] The possibility that one or both of these levels might be due to Ne^{22} rather than to Ne^{20} has been ruled out by the variation of range with angle.

Figure 2 shows the angular distribution of the protons elastically scattered by neon (Curve A). It bears a marked similarity to both the carbon and oxygen curves obtained at the same energy.[3] The angular distribution of the protons arising from the 1.58-Mev level is shown in Fig. 3; it fits the equation:

$$\sigma(\phi)=14.0P_0(\phi)-10.4P_2(\phi)+3.2P_4(\phi).$$

There is a slight tendency to asymmetry at about 60° which may just be significant. This distribution may be compared with that obtained by Burcham *et al.*[3] for protons inelastically scattered from carbon, leading to

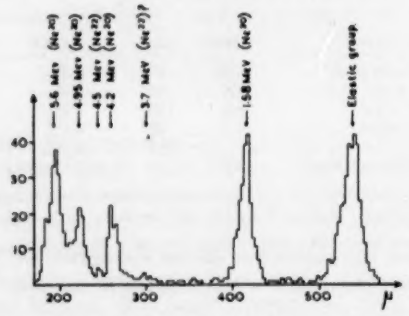

FIG. 1. Histogram of the tracks found at an angle of 80° (lab) in the neon experiment. A few tracks due to levels in Ne^{22} are visible but are not sufficient in number to enable accurate excitation energies to be given. All ranges should be reduced by 125 microns.

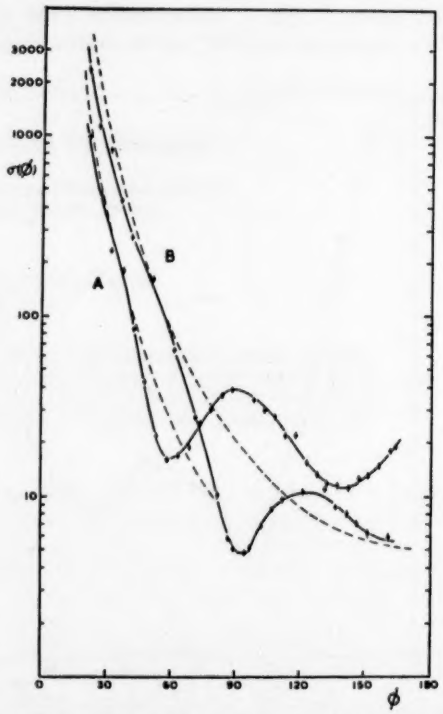

FIG. 2. Angular distributions of protons elastically scattered from (*A*) neon and (*B*) argon. $\sigma(\phi)$ is given in millibarns per steradian. The dashed lines are the curves to be expected from Rutherford scattering only.

[1] F. Ajzenberg and T. Lauritsen, Revs. Modern Phys. **24**, 321 (1952).

[2] T. W. Bonner, Proc. Roy. Soc. (London) **174**, 339 (1940).

[3] Burcham, Gibson, Hossain, and Rotblat, Phys. Rev. **92**, 1266 (1953).

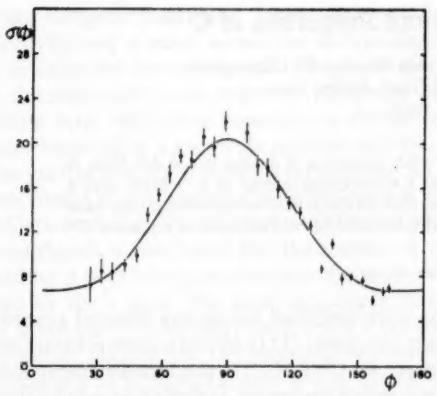

FIG. 3. Angular distribution of protons inelastically scattered from 1.58-Mev level of Ne^{20}. The solid line is the best fit in terms of even Legendre polynomials up to $P_4(\cos\phi)$. $\sigma(\phi)$ is given in millibarns per steradian.

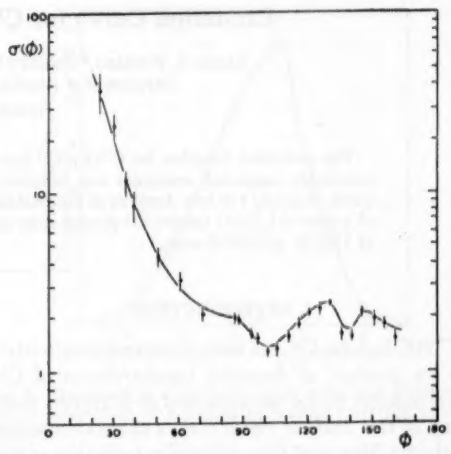

FIG. 4. Angular distribution of protons inelastically scattered from the 1.48-Mev level of A^{40}. $\sigma(\phi)$ is given in millibarns per steradian.

the excited state at 4.4 Mev. We have fitted a series of Legendre polynomials to this carbon distribution and obtained:

$$\sigma(\phi)=15.9P_0(\phi)+10.1P_2(\phi)-6.0P_4(\phi).$$

The constant terms in these two expressions are similar, but the coefficients of $P_2(\phi)$ while numerically indistinguishable from each other are of opposite sign. Since the spins and parities of the first excited states of C^{12} and Ne^{20} are both[4,5] 2^+ and those of the ground states 0^+, the difference between the angular distributions must be due to some other property of these states.

In the experiment with argon (at a gas pressure of 9.5 cm) we found in addition to the elastic group, one due to a level at 1.48 ± 0.02 Mev. This is probably identical with that reported by Heitler, May, and Powell[6] at 1.46 Mev. Further investigations of the other energy levels are being made.

The angular distribution of the elastically scattered protons is shown in Fig. 2 (Curve B). The nuclear effect is much less marked in this curve than in those obtained from nitrogen or neon. At 90° the cross-section is 4 times less than that of Rutherford scattering. The general shape is similar to the other curves obtained, but the minimum has moved up to 95° and the maximum up to 125°. The angular distribution of the protons leaving A^{40} in its excited state at 1.48 Mev is shown in Fig. 4; in contrast to those obtained for carbon, nitrogen, and neon it is not symmetrical. It bears a generic resemblance to the curve obtained by Davis[7] for the inelastic scattering of 7.1-Mev protons from Be^9.

[4] Kraus, French, Fowler, and Lauritsen, Phys. Rev. **89**, 299 (1953).
[5] J. Seed, Phil. Mag. **44**, 921 (1953).
[6] Heitler, May and Powell, Proc. Roy. Soc. (London) **190**, 180 (1947).
[7] K. E. Davis, Phys. Rev. **88**, 1433 (1952).

Excitation Curve for $C^{14}(d,p)C^{15}$ and Properties of C^{15}†

JAMES A. RICKARD,* EMMETT L. HUDSPETH, AND WILLIAM W. CLENDENIN
Department of Physics, University of Texas, Austin, Texas

(Received August 4, 1954)

The excitation function for $C^{14}(d,p)C^{15}$ has been studied with deuterons of energy 0.6 to 3.0 Mev. A previously suspected resonance was definitely established at a bombarding energy of 2.15 Mev, with a width of nearly 400 kev. Analysis of the excitation curve shows that its shape may be explained on the basis of a spin of 5/2(+) for the C^{15} ground state and a Q value of 0.15±0.15 Mev. This leads to a mass of C^{15} of 15.0141 ±0.00015 amu.

I. INTRODUCTION

THE isotope C^{15} has been observed previously[1,2] as a product of deuteron bombardment of C^{14}. It has a half-life of 2.4 seconds, and it is known that the decay of this nucleus yields β rays of maximum energy nearly 8.8 Mev and that delayed γ radiation of energy approximately 5.5 Mev[3] (with possibly other components) is present. The Q value for $C^{14}(d,p)C^{15}$ has not previously been established, since the decay scheme of C^{15} is not definitely known and the protons from the reaction have not been observed thus far. It is certain, however, that the 8.8-Mev β rays cannot be in coincidence with the observed 5.3-Mev γ rays; if such were the case, C^{15} would be unstable against heavy particle emission. An excitation curve for $C^{14}(d,p)C^{15}$, based on nine bombarding energies in the range 1.4 to 2.8 Mev, has been reported,[2] and the existence of one resonance in this region (near 2 Mev) was thought probable.

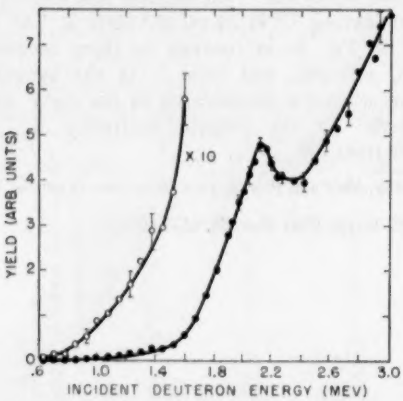

FIG. 1. Experimentally observed excitation curve for $C^{14}(d,p)C^{15}$. Target thickness about 15 kev for 1-Mev deuterons.

The work described herein was directed toward two primary purposes: (1) to obtain a more accurate excitation curve for $C^{14}(d,p)C^{15}$ over a broader energy interval of bombarding deuterons, including especially the low-energy region; and (2) to analyze the resultant curve in order to determine the Q value for the reaction and to deduce the probable value for the spin of C^{15}. The experimental work described herein has been briefly reported,[4] and some additional analysis is included in this note.

II. EXPERIMENTAL PROCEDURE

The Van de Graaff generator at the University of Texas was used in these experiments for the bombardment of a $BaCO_3$ target, enriched 18.6 percent in C^{14}. A uniform target was prepared by painting a thick slurry of water and $BaCO_3$ on a silver disk. The target used in most of the present work had a weight of 0.124 mg/cm², or a thickness of about 15 kev for 1-Mev deuterons.

The deuteron beam was regulated to about 0.3 percent by a slit system and probe current control; higher resolution is possible but was not considered necessary in this experiment.

The activity of the target was measured by a scintillation counter. A sodium iodide crystal was used in conjunction with a 5819 photomultiplier tube, a linear amplifier, pulse height selector, and appropriate scaling and counting circuits.

Deuteron bombardment of $BaCO_3$ results in the formation of several radioactive nuclides, including B^{12}, N^{13}, and F^{17}, as well as C^{15}. (F^{17} is produced only at bombarding energies greater than about 1.6 Mev.) A bombarded target also emits neutrons and γ rays from excited states of stable elements, but ordinarily these are emitted almost instantaneously. It is most convenient to measure the activity of C^{15} in the presence of the other radioactive nuclides by bombarding the target for a known time with a known current, stopping the bombardment and allowing the B^{12} (of half-life only about 25 milliseconds) to decay almost entirely, and then to begin counting the radiations from C^{15}. This was accomplished by setting the pulse-height selector so as to discriminate against radiation which

† Experimental work assisted by the U. S. Atomic Energy Commission; the analysis was assisted by the Office of Scientific Research of the Air Research and Development Command.

* Present address: Humble Oil and Refining Company, Houston, Texas.

[1] Hudspeth, Swann, and Heydenburg, Phys. Rev. **77**, 736 (1950).

[2] Hudspeth, Swann, and Heydenburg, Phys. Rev. **80**, 643 (1950).

[3] Hudspeth, Rose, and Heydenburg, Phys. Rev. **85**, 742(A) (1952). The first excited state in N^{15} consists of a doublet near 5.3 Mev; we therefore assume that this is a more precise value for the energy of the delayed γ radiation.

[4] J. A. Rickard and E. L. Hudspeth, Austin Meeting of the American Physical Society [Phys. Rev. **94**, 806 (A) (1954)].

was less energetic than about 2 Mev, leaving only the C^{15} activity and a small cosmic-ray background. The final evidence for the validity of the methods of timing and discrimination came from an inspection of the counting rate, which was observed to decline in the manner expected of 2.4-seconds half-life activity.

The yield of both the 8.8-Mev β rays and the 5.3-Mev γ rays from C^{15} was measured with the sodium iodide scintillation counter. By taking counts with and without various shields, it was found that the number of counts caused by β rays was approximately the same as that caused by the γ rays. The equal magnitude measurement is not particularly significant, being a function of the relative efficiency of the counting equipment for detecting β and γ radiation and of the discriminator setting, but the fact that the curves were identical in shape made it possible to improve statistical accuracy by measuring both types of radiation simultaneously. The data represented by the excitation curve of Fig. 1 were taken in this manner.

In obtaining points on the excitation curve, the following steps were taken: (1) The beam of the statitron was turned on and allowed to continue for a 30-second time interval, during which the number of beam integrator counts was recorded; (2) at the end of the chosen time interval, the high voltage on the statitron was cut off (by stopping the spray-on current), an interrupter was pushed into the deuteron beam, and, after about 0.1 second (to allow decay of B^{12} formed during bombardment), the scintillation counter was allowed to feed into a scaler for twenty seconds. This 20-second interval represents about eight half-lives of C^{15}, and hence the decay was virtually complete.

TABLE I. Possible l values.

Spin of 1/2(+)		Spin of 5/2(+)	
Deuterons	Protons	Deuterons	Protons
$l=0$	$l'=0$	$l=0$	$l'=2$
0	2	1	1
1	1	2	0
2	0		

III. RESULTS AND DEDUCTIONS

The experimental excitation curve for $C^{14}(d,p)C^{15}$ is shown in Fig. 1. The existence of the suspected resonance at a bombarding energy of about 2 Mev is confirmed.

Figure 2 shows the resonance in N^{16} in greater detail. This curve was obtained by the graphical subtraction of a postulated smooth excitation curve from the observed curve in the resonance region. The peak is estimated from the graph to lie at 2.15-Mev bombarding energy, which corresponds to an excitation of 12.8±0.5 Mev of N^{16}. This calculation uses a reported[5] mass of N^{16} of 16.010740±0.0005 amu. As should be expected from the large excitation energy involved, the resonance is quite broad, having a width of nearly 400 kev.

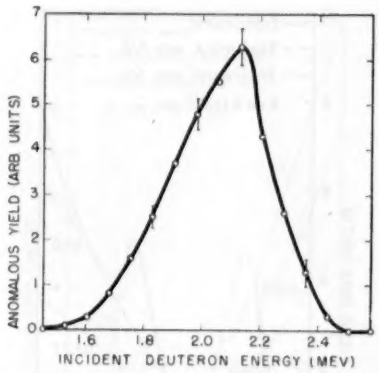

FIG. 2. Resonance in $C^{14}(d,p)C^{15}$. This curve was obtained by graphical subtraction of a postulated smooth excitation curve in this region.

The sharp rise in the experimental excitation curve starting at about 1.5 Mev suggests strongly that deuterons of higher angular momentum than $l=0$ play an important part in the reaction. For this reason it seemed interesting to compare the data with theoretical excitation functions calculated along standard lines by one of the authors (WWC). It was assumed that Coulomb barrier penetrability was the determining factor in the energy range considered. Of interest here is the fact that the shape of the excitation curve depends strongly on the spin of C^{15}. Comparison with experiment thus should give a determination of the spin.

On the basis of the shell model[6] the most probable spin and parity values for C^{15} are 1/2(+) and 5/2(+). In Table I are shown possible l values for the incoming deuterons and outgoing protons which obey the angular momentum and parity conservation laws.

In order to conserve parity the difference between l and l' must be an even integer [assuming 0(+) for the C^{14} ground state[7]]. The pairs of values in the table are all those possible such that $l+l'$ is 0 or 2. Possible pairs with higher l values, e.g., $l=1$, $l'=3$, contribute much less to the cross section because of their lower penetrability. The significant difference between the two possible spin values for C^{15} is that an $l=0, l'=0$ reaction which is most favored on a penetrability basis is possible for a spin of 1/2 but not for a spin of 5/2.

The cross section of the interaction is given by Bethe and Placzek's generalization[8] of the Breit-Wigner

[5] *Experimental Nuclear Physics*, edited by E. Segrè (John Wiley and Sons, Inc., New York, 1953), Vol. 1.
[6] M. G. Mayer, Phys. Rev. **78**, 16 (1950).
[7] D. R. Inglis, Revs. Modern Phys. **25**, 390 (1954).
[8] H. A. Bethe and G. Placzek, Phys. Rev. **51**, 450 (1937).

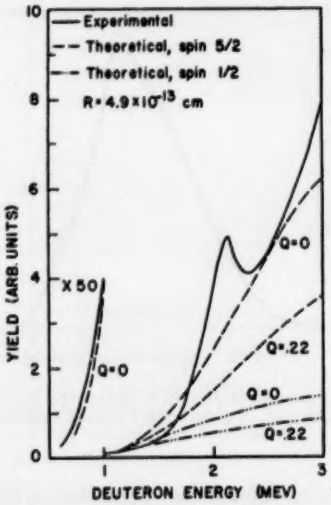

FIG. 3. Comparison of experimental and theoretical excitation curves for $C^{14}(d,p)C^{15}$ assuming C^{14} radius of 3.6×10^{-13} cm. Below 1 Mev all curves lie between the experimental curve and that shown for $Q=0[5/2(+)]$.

formula,[9]

$$\sigma=\frac{\pi\lambda^2}{(2i+1)(2s+1)}\sum_{ljl'j'J}(2J+1)\times\left|\sum_r\frac{\mathfrak{U}_{lj}{}^{rJ}\mathfrak{U}_{l'j'}{}^{rJ}}{E_1-E_r+\frac{1}{2}(-1)^{\frac{1}{2}}\gamma_{rJ}}\right|^2,$$

where i is the spin of the initial nucleus and s is the spin of the incident particle. The quantities $\mathfrak{U}_{lj}{}^{rJ}$ and $\mathfrak{U}_{l'j'}{}^{rJ}$ are matrix elements of the interaction between the system "initial nucleus plus incident particle" and the compound nucleus in the first case, and between the compound nucleus and the system "final nucleus plus outgoing particle" in the second case. The letter r refers to all quantum numbers of the compound nucleus except its total angular momentum J. E_r is the energy of the state r, and E_1 is the total energy of the system initial nucleus plus incident particle. The quantum numbers of orbital and total angular momentum are l,j, respectively, for the incident particle and l',j' for the outgoing particle. The half-width of the level r,J is

$$\gamma_{rJ}=\sum_{q'}\sum_{l'j'}\gamma_{l'j'}{}^{rJ},$$

where the sum over q' is over the states of the various particles which can be emitted by the compound nucleus and

$$\gamma_{l'j'}{}^{rJ}=(\mathfrak{U}_{l'j'}{}^{rJ})^2.$$

Penetrabilities have been computed using the WKB method as outlined in Bethe's review article.[10] The penetrability may be expressed as $e^{-2C_l(E)}$, C_l being a function of the energy E in the center-of-mass system of particle and nucleus, and of l. The quantity e^{-C_l} appears as a factor in the wave function and hence in the matrix element $\mathfrak{U}_{lj}$. If $\mathfrak{W}_{lj}$ is defined by

$$\mathfrak{U}_{lj}=e^{-C_l}\mathfrak{W}_{lj},$$

the cross section may be written

$$\sigma=\frac{\pi\lambda^2}{(2i+1)(2s+1)}\sum_{ljl'j'J}(2J+1)e^{-2C_l(E)}e^{-2C_{l'}(E')}\times\left|\sum_r\frac{\mathfrak{W}_{lj}{}^{rJ}\mathfrak{W}_{l'j'}{}^{rJ}}{E_1-E_r+(-1)^{\frac{1}{2}}\gamma_{rJ}}\right|^2,$$

where $C_l(E)$ refers to the incident particle of energy E and $C_{l'}(E')$ to the outgoing particle of energy E'. The factor in absolute brackets involves the "partial half-widths without penetrability." This has been assumed to be a slowly varying function of the energy and also of the quantum numbers $ljl'j'J$. Since λ^2 is proportional to $1/E$, the energy dependence of the cross section becomes

$$\sigma=KE^{-1}\sum_{ljl'j'J}(2J+1)e^{-2C_l(E)}e^{-2C_{l'}(E')},$$

where K is essentially constant over the energy range considered

For the pairs of ll' values in Table I, the sum over $jj'J$ leads to the weighting factors for $e^{-2C_l(E)}e^{-2C_{l'}(E')}$ given in Table II.

Comparison of calculated curves with the experimental data is shown in Figs. 3 and 4. The assumptions made about the internal conversion probability do not, of course, apply to the part of the cross section arising from the resonance at 2.15 Mev. The theoretical curves are conceived to describe the part of the cross section not caused by this level. Theoretical curves are shown for both possible spin values of C^{15}, for possible Q values of the reaction between $Q=0$ and $Q=0.29$ Mev ($Q=E'-E$), and for two values of the nuclear radius R. The smaller of these values, 3.6×10^{-13} cm, is $(1.5\times10^{-13}\text{ cm})A^{\frac{1}{3}}$, where A is 14. The higher of the values, 4.9×10^{-13} cm, is this plus about half the deuteron radius. All curves are normalized at 1 Mev. The difference in shape between the curves for spin 1/2 and those for spin 5/2 is caused mainly by the contribution of the $l=0$, $l'=0$ term. This term is larger than the remaining ones but has a fairly flat energy dependence. When the spin 1/2 curve, dominated by this term, is normalized to fit the low-energy data, it falls well below the experimental points at high energies.

It is clear that the curves for an assumed 5/2(+) ground state fit the data much better than those for an assumed 1/2(+) ground state. The best fit is for a

[9] G. Breit and E. P. Wigner, Phys. Rev. **49**, 519 (1936).
[10] H. A. Bethe, Revs. Modern Phys. **9**, 69 (1937).

Q value between 0 and 0.29 Mev.[11] A probable spin value of 5/2(+) for C^{15} compares with the same spin value for the ground state of O^{17}, which also has nine neutrons and an even number of protons. It contrasts with the 1/2(+) ground state of F^{19} with nine protons and ten neutrons. In all three cases there is a single odd nucleon outside closed shells. Apparently there is some tendency here for high angular momentum neutron states to lie lower, relatively, than high angular momentum proton states.

A spin of 5/2(+) is also indicated by the decay scheme of C^{15}, as Inglis[7] has pointed out. There appear to be two β rays, one with maximum kinetic energy of about 8.8 Mev and the other with about 3.3 Mev. If there is a branching ratio of 1:1, the log ft values for these are 5.6 and 3.6, respectively. The transition to the lower state thus seems to be first forbidden and that to the higher state allowed. The ground state of N^{15} is 1/2(−) and the first excited state is a doublet at about 5.3 Mev, which is probably 5/2(+), 7/2(+). A spin of 5/2(+) agrees with a first forbidden transition to the ground state and an allowed transition to the first excited state. A 1/2(+) spin would not lead to an allowed transition to the first excited state. The energy of the observed γ rays, about 5.5 Mev,[3] is in good agreement with the energy level difference between ground and first excited states.

Note added in proof.—The assumption of compound nucleus formation rather than an Oppenheimer-Phillips process is suggested by the resonance at 2.15 Mev, but it is certainly possible that the part of the cross section treated here, i.e., excluding the resonance, might be largely due to stripping. The cross section for an Oppenheimer-Phillips process, however, rises less steeply as a function of energy than the compound nucleus cross section [H. A. Bethe, Phys. Rev. **53**, 39 (1938)], and would fit the experimental data less well in the spin 1/2 case than the compound nucleus cross section. A spin of 1/2 thus seems unlikely in the case of either mechanism. Consistency of a spin of 5/2 with a reaction taking place by compound nucleus formation is indicated by the similar situation in the 5.3-Mev excited state of N^{15} produced by $N^{14}(d,p)N^{15}$ where the reaction is dominated by compound nucleus formation [S. T. Butler, Proc. Roy. Soc. (London) **208A**, 559 (1951)]. In the nitrogen case there is thought to be an angular momentum transfer (Butler's l_n) of 2 or more; in the carbon case l_n would have to be at least 2. It seems probable that this would discriminate against stripping in the carbon case as it does in the nitrogen case, especially since the Coulomb barrier for compound nucleus formation is lower for carbon.

TABLE II. Weighting factors.

Spin of 1/2			Spin of 5/2		
l	l'	Weight	l	l'	Weight
0	0	3	0	2	6
0	2	3	1	1	13
1	1	12	2	0	12
2	0	3			

[11] The protons from the reaction have recently been observed by Dr. K. R. Spearman. The Q value which he obtains is 0.12 Mev, with a tentatively estimated error of about 0.05 Mev (to be published).

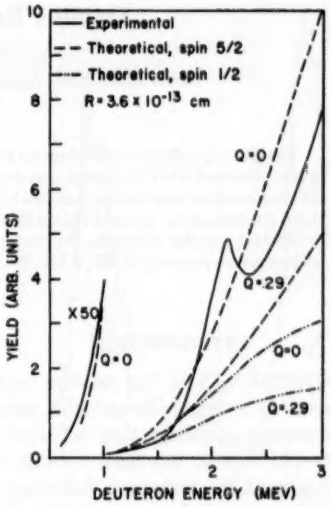

FIG. 4. Same as Fig. 3, except that the radius of C^{14} is assumed to be 4.9×10^{-13} cm.

IV. CONCLUSIONS

(1) The results of the present analysis of the excitation curve for $C^{14}(d,p)C^{15}$ lead to a Q value between 0 and 0.3 Mev; it appears probable that Q is 0.15±0.15 Mev, consistent with certain unpublished work[11] from this laboratory.

(2) On the basis of the above Q value and measured masses[5] of C^{15}, H^2, and H^1, the mass of C^{15} is 15.0141 ±0.00015 amu. This yields a $C^{15}-N^{15}$ mass difference of 8.6 Mev, which is consistent with the maximum energy of the observed β rays (8.8±0.5 Mev).

(3) The resonance in the $C^{14}(d,p)C^{15}$ excitation curve at a bombarding voltage of 2.15 Mev indicates a level of excitation in N^{15} at 12.8±0.5 Mev, with an experimentally observed width of about 400 kev.

(4) The most probable spin and parity value for the ground state of C^{15} is 5/2(+).

ACKNOWLEDGMENTS

The technical assistance of Joseph T. Peoples and the computational work of P. M. Clayton are gratefully acknowledged.

Gamma Radiation from Ce^{144} and Pr^{144}

W. E. Kreger and C. Sharp Cook
United States Naval Radiological Defense Laboratory, San Francisco, California

(Received August 17, 1954)

The gamma radiation following the decay of Ce^{144} and Pr^{144} has been studied with a 4-in. diameter, 4-in. high cylindrical NaI(Tl) crystal, and single-channel and twenty-channel pulse-height analyzers. With the aid of photopeak to total ratios, previously determined for this crystal, the relative gamma-ray intensities have been determined in terms of the 0.134 Mev gamma ray of Ce^{144}. If an intensity of unity is assumed for the 0.134-Mev gamma radiation, the photon radiation intensities for the 0.081, 0.696, 1.49, and 2.185-Mev transitions are respectively 0.287, 0.116, 0.023, and 0.059.

INTRODUCTION

MEASUREMENTS of the relative intensities of gamma-ray transitions[1] and the determination of the consequent disintegration schemes[2,3] for the $Ce^{144} \rightarrow Pr^{144} \rightarrow Nd^{144}$ chain has been difficult because of the low energies of the radiations following the decay of Ce^{144}, and because of the low intensity of the radiations following the decay of Pr^{144}. The relative transition probabilities have been determined primarily from observations of the electron spectra (beta ray plus internal conversion). The study described in this paper is concerned primarily with the spectral distribution of the gamma quanta and attempts to fit these measurements with the information obtained in the previous investigations.

APPARATUS

The availability of large NaI(Tl) crystals has produced great improvements in gamma-ray scintillation spectrometry techniques. An appreciable fraction of the gamma quanta incident upon the crystal can be totally absorbed within it, thereby enhancing the intensity of the total absorption peaks (sometimes called photopeaks) recorded for these quanta. As a result there is a suppression of the lower-energy continuous Compton distribution.

The particular experiment arrangement used here utilizes a packaged 4-in. diameter by a 4-in. high cylindrical NaI(Tl) crystal surrounded by lead to reduce background. Inserts which fit into a stair-step well in that portion of the lead separating the crystal and the cerium-praseodymium source provide cylindrical apertures, either 1.4 cm or 2.6 cm in diameter, or no aperture when a background record is desired. A DuMont type 6292 photomultiplier tube is used as detector for the scintillations produced in the crystal.

The sources were dried by evaporation from solution in the end of a 0.5-cm inside diameter closed glass tube. When the source was being studied, careful alignment

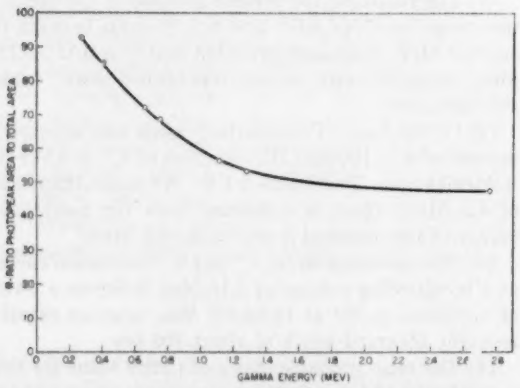

FIG. 1. Plot of the ratio of total absorption peak area to total pulse-height spectrum area as a function of gamma-ray energy, for a 4-in. diameter, 4-in. high cylindrical NaI(Tl) crystal, with a source on the axis of the crystal whose radiations are collimated by a cylindrical aperture in the lead shield which surrounds the crystal.

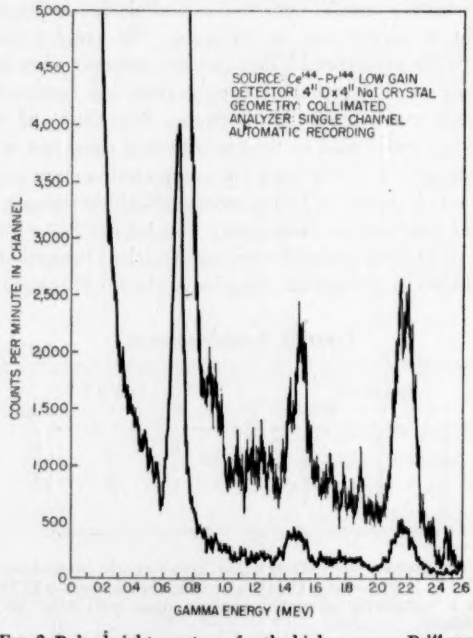

FIG. 2. Pulse-height spectrum for the higher-energy Pr^{144} gamma radiations as recorded in the single-channel analyzer. The upper curve is ×5.

[1] D. Alburger and J. Kraushaar, Phys. Rev. **87**, 448 (1952).
[2] F. T. Porter and C. S. Cook, Phys. Rev. **87**, 464 (1952).
[3] Emmerich, Auth, and Kurbatov, Phys. Rev. **94**, 110 (1954).

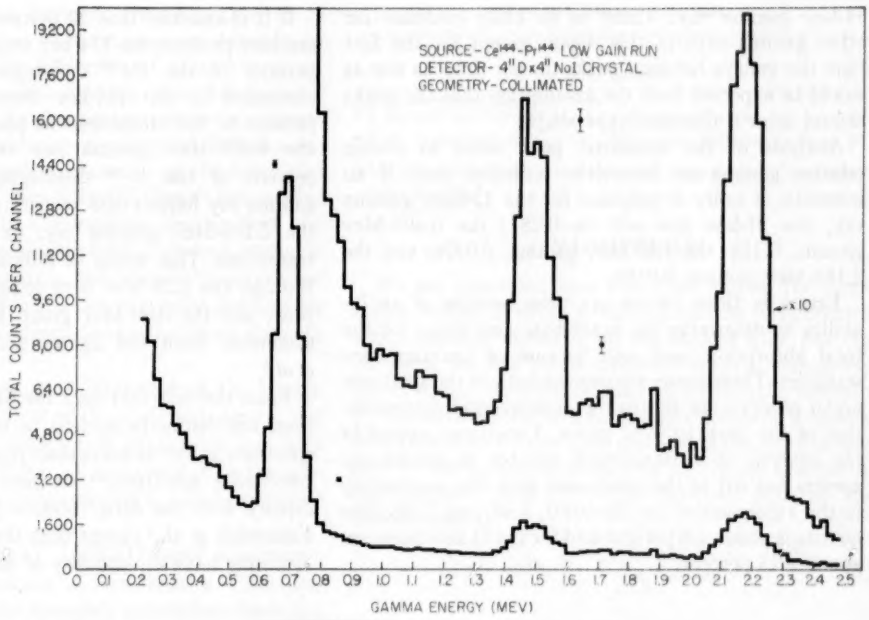
SOURCE - Ce144 - Pr144 LOW GAIN RUN
DETECTOR - 4" D x 4" NaI CRYSTAL
GEOMETRY - COLLIMATED
x 10
TOTAL COUNTS PER CHANNEL
GAMMA ENERGY (MEV)

FIG. 3. Same as Fig. 2 but recorded by means of a twenty-channel analyzer.

was made to ascertain that the NaI(Tl) saw the entire source through the aperture. A piece of aluminum 5 mm thick was placed over the aperture to absorb the energetic 2.97-Mev beta radiation from Pr^{144}.

The ratio of the area under the total absorption (photo) peak to the total area of pulse height distribution as a function of energy for a series of monoenergetic gamma rays has been determined,[4] and is plotted in Fig. 1, for the conditions used in this experiment. Thus, a measurement of the area of any total absorption peak from any single gamma-ray energy, corrected for the ratio of total area to peak area, for the relative number of quanta absorbed in the NaI(Tl) crystal and for the relative number of quanta absorbed in the aluminum beta-absorber, gives a figure proportional to the number of gamma quanta of that energy. The technique is similar to that used by Mijatovic and Wintersteiger[5] in their studies of the radiations from Xe^{131}.

The data were collected by means of either a single-channel analyzer or a Bell-Kelly-type twenty-channel analyzer, operated so as to record the spectrum under consideration in a total of 120 channels. In the case of the single-channel analysis, a channel of appropriate width was swept through the spectrum synchronously with the movement of recording paper through a Brown Recorder, on which the count rate (intensity) was plotted as a function of pulse height (energy). Recording of the data from the twenty-channel analyzer was made by means of scaling strips and mechanical registers.

[4] W. E. Kreger and L. McIsaac, Phys. Rev. **93**, 943 (1954).
[5] A. M. Mijatovic and V. Z. Wintersteiger, Bulletin of the Institute of Nuclear Sciences "Boris Kidrich" **3**, 57 (1953).

RESULTS

A typical pulse-height distribution from the single-channel analyzer, as recorded on the Brown strip chart, is shown in Fig. 2 for the 0.695, 1.48, and 2.185 Mev gamma rays. The same region as a histogram from the results of the twenty-channel analyzer is shown in Fig. 3. The low-energy pulse-height distribution is shown in Fig. 4. In this plot can be seen a peak associated with the 81- and 134-kev gamma rays and a peak produced by the x-rays resulting from the internal conversion, with possible additional effects from a

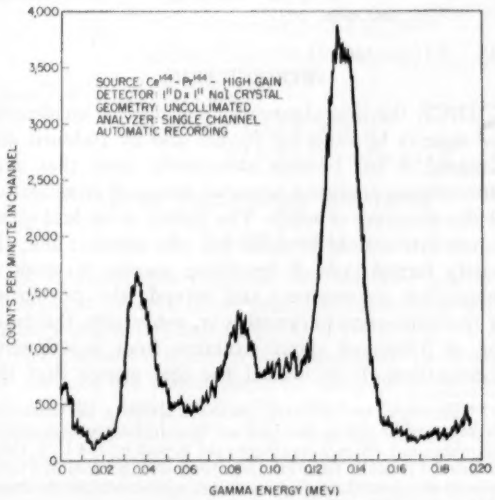
SOURCE Ce144 - Pr144 - HIGH GAIN
DETECTOR: 1" D x 1" NaI CRYSTAL
GEOMETRY: UNCOLLIMATED
ANALYZER: SINGLE CHANNEL
AUTOMATIC RECORDING
COUNTS PER MINUTE IN CHANNEL
GAMMA ENERGY (MEV)

FIG. 4. Single-channel analyzer recording of the pulse-height spectrum of the lower-energy photons from $Ce^{144}-Pr^{144}$.

34-kev gamma ray. There is no clear evidence for other gamma rays in this region except for the fact that the valleys between peaks do not drop as low as would be expected from the assumption that the peaks should show a Gaussian-type shape.

Analysis of the measured peak areas to obtain relative gamma-ray intensities indicates that, if an intensity of unity is assumed for the 134-kev gamma ray, the 81-kev line will be 0.287; the 0.695-Mev gamma, 0.116; the 1.48-Mev gamma, 0.0226; and the 2.185-Mev gamma, 0.0589.

Errors in these values can arise because of an inability to determine the exact base and shape for the total absorption peak and because of counting rate statistics. These errors are present both in the spectrum under observation and in the experimental determination of the peak to total ratios. Experience gained in the analysis of a considerable number of gamma-ray spectra has led to the conclusion that the uncertainty in the value quoted for the 0.695, 1.48, and 2.185 Mev quanta is about ± 8 percent and for the 81 kev quantum about ± 15 percent.

If it is assumed that 22 percent of the Ce^{144} disintegrations produce the 134-kev transition[2,3] and that 6.6 percent of the Ce^{144} disintegrations are internally converted in the 134-kev transition[2] (leaving 15.4 percent of the transitions as photon radiation), then the 0.695-Mev gamma ray occurs following 1.79 percent of the Pr^{144} disintegrations, the 1.48-Mev gamma ray follows 0.35 percent of the transitions and the 2.185-Mev gamma ray, in 0.91 percent of the transitions. This would be indicative that Pr^{144} decays through the 2.28-Mev beta group 1.44 percent of the time, and the 0.80-Mev group 1.26 percent, differing somewhat from the figures proposed by Emmerich *et al.*[3]

From the fact that only the 81- and 134-kev transitions are distinctly evident in the low-energy photon spectrum as well as being most prominent in the internal conversion spectrum,[2,3] we find no evidence contradictory with the decay scheme proposed for Ce^{144} by Emmerich *et al.*,[3] except that the 223-kev beta transition may have an intensity of as much as six percent.

PHYSICAL REVIEW VOLUME 96, NUMBER 5 DECEMBER 1, 1954

Nuclear Quadrupole Spectra in Solids*

M. H. COHEN
Institute for the Study of Metals, The University of Chicago, Chicago, Illinois
(Received July 8, 1954)

Numerical values for the energy levels, Zeeman splitting parameters, and intensity parameters of the pure quadrupole spectrum are given for ten values of the asymmetry parameter for spins 5/2, 7/2, and 9/2. The intensity parameters for the $m \rightarrow -m$ transition in a magnetic field for large asymmetric quadrupole interaction are given. They show that the corresponding lines should be observable. A method of increasing the accuracy of perturbation calculations is presented for the Zeeman splitting case and the strong magnetic field case.

INTRODUCTION

SINCE the first observations of nuclear quadrupole spectra in solids by Pound[1] and by Dehmelt and Kruger,[2] it has become abundantly clear that such observations provide a powerful means of investigation of the structure of solids. The theory of nuclear quadrupole interactions in solids has two aspects: first, the purely formal task of describing spectra in terms of interaction parameters; and second, the calculation of the interaction parameters or, conversely, the drawing of inferences about structure from experimental observations. It is toward the first aspect that this paper is addressed, in the hope of providing a broader theoretical basis for experiments which stress the second aspect.

The present state of the spectrum theory may be summarized as follows: (1) Pound has discussed the Hamiltonian; (2) Bersohn treated the broadening of a magnetic resonance line by a small quadrupole interaction;[3] (3) Pound gave third order perturbation formulae for the splitting of the magnetic resonance line by nuclear quadrupole interaction with a symmetric field gradient;[4] Bersohn treated the general case to third order; Volkoff *et al.*, have discussed the explicit orientational dependence of the first and second order formulas;[5] (4) Explicit numerical formulas giving the effect of small asymmetry on the pure quadrupole

* This work was initiated at the University of California, Berkeley, while the author held an Atomic Energy Commission fellowship and where it was supported in part by the U. S. Office of Naval Research. The work done there was included in a thesis submitted in partial satisfaction of the requirements for the degree of Doctor of Philosophy.

[1] R. V. Pound, Phys. Rev. **79**, 685 (1950).
[2] H. G. Dehmelt, Naturwiss. **37**, 111 (1950).
[3] R. Bersohn, J. Chem. Phys. **20**, 1505 (1952).
[4] See also E. F. Carr and C. Kikuchi, Phys. Rev. **78**, 470 (1950).
[5] Volkoff, Petch, and Smellie, Can. J. Phys. **30**, 270 (1952); G. M. Volkoff, Can. J. Phys. **31**, 820 (1953).

spectrum exist in the literature for $I=5/2$,[3] 3,[6] 7/2,[7] and 9/2;[8] Bersohn has given the general formula for small asymmetry; (5) Kruger[9] and Dean[10] have investigated the first order Zeeman effect for spin 3/2 for which the pure quadrupole spectrum can be obtained exactly for arbitrary asymmetry; Bersohn has given the effect of small asymmetry on the first order Zeeman splitting for spin 5/2; (6) Weiss[11] has studied a spin 3/2 nucleus in a symmetric electric field and simultaneously in a magnetic field of various strengths and orientations; Lamarche and Volkoff[12] have studied in detail the case of spin 5/2 in a particular asymmetric electric field for given orientation and arbitrary strength of magnetic field.

A detailed derivation and discussion of the Hamiltonian, of various aspects of the spectrum theory, and of the calculation of interaction parameters has been given by the author.[13] For an introduction to the subject of nuclear quadrupole resonance, see the paper of Dehmelt.[14]

Experimentally, spins 7/2 and 9/2 are of importance, for example, in the study of ferroelectrics.[15] Further, inspection of the above summary shows that there is a need for the study of the pure quadrupole spectrum and its first order Zeeman splitting for electric fields of arbitrary asymmetry. Section I of this paper consists, then, of a review of the Hamiltonian; Sec. II gives a numerical analysis of the pure quadrupole spectrum for spins 5/2, 7/2, 9/2 in electric fields of arbitrary asymmetry; and Sec. III deals with the first order Zeeman splitting of that spectrum. For splittings of the magnetic resonance line as great as those observed by Knight and Cotts for Nb in $KNbO_3$,[15] third order calculations are not adequate. For that reason, Sec. IV contains a method of obtaining fourth order accuracy from third order calculations. A similar method of increasing the accuracy of calculations of the first order Zeeman splitting of the pure quadrupole spectrum is also presented.

Much of the work in this paper can be applied directly to the study of ferroelectrics and antiferroelectrics by nuclear resonance techniques.[15] For such substances the quadrupole coupling can be large, the field gradients asymmetric, and the orientation of the principal axes of primary importance.

[6] H. G. Dehmelt, Z. Physik **133**, 528 (1952).
[7] H. G. Dehmelt and H. Kruger, Z. Physik **130**, 385 (1951).
[8] Robinson, Dehmelt, and Gordy, Phys. Rev. **89**, 1305 (1953).
[9] H. Kruger, Z. Physik **130**, 371 (1951).
[10] C. Dean, Phys. Rev. **86**, 607 (1952).
[11] P. R. Weiss, Phys. Rev. **73**, 470 (1948); **74**, 1478 (1948).
[12] G. Lamarche and G. M. Volkoff, Can. J. Phys. **31**, 1010 (1953).
[13] M. H. Cohen, thesis, University of California, Berkeley, 1952 (unpublished).
[14] H. G. Dehmelt, Am. J. Phys. **22**, 110 (1954).
[15] R. M. Cotts and W. D. Knight, Phys. Rev. **93**, 940 (1954) and following paper [Phys. Rev. **96**, 1285 (1954)].

TABLE I. Secular equations.

I	Secular equation	Units of E
5/2	$E^3-7(3+\eta^2)E-20(1-\eta^2)=0$ [a]	$2L$
7/2	$E^4-42(1+\eta^2/3)E^2-64(1-\eta^2)E+105(1+\eta^2/3)^2=0$ [b]	$3L$
9/2	$E^5-11(3+\eta^2)E^3-44(1-\eta^2)E^2+\frac{44}{3}(3+\eta^2)^2E+48(3+\eta^2)(1-\eta^2)=0$	$6L$

[a] See reference 3.
[b] See reference 7.

I. HAMILTONIAN

We are concerned here with that part of the interaction energy between a nucleus and its environment which depends explicitly on the nuclear spin. For our purposes, we may characterize the nucleus completely by its spin I, its g-factor, and its quadrupole moment Q. The environment is specified by a constant magnetic field $\mathbf{H}_0$ and by $\partial E_i/\partial x_j$, the gradient of the electrostatic field at the nucleus produced by all charge exterior to the nucleus ($\nabla\cdot\mathbf{E}=0$). The relevant part of the Hamiltonian is

$$\mathcal{H}=-g\beta\mathbf{H}_0\cdot\mathbf{I}-K\sum_{\mu=-2}^{2}F_\mu Q_{-\mu}, \tag{1}$$

$$K=eQ/4I(2I-1), \tag{2}$$

$$F_0=\frac{\partial E_z}{\partial z},\quad F_{\pm1}=(2/3)^{\frac{1}{2}}\left(\frac{\partial E_z}{\partial x}\pm i\frac{\partial E_z}{\partial y}\right), \tag{3}$$

$$F_{\pm2}=\frac{1}{\sqrt{6}}\left(\frac{\partial E_x}{\partial x}-\frac{\partial E_y}{\partial y}\pm 2i\frac{\partial E_x}{\partial y}\right).$$

The operators Q_μ are such that the nonzero matrix elements of $\mathcal{H}$ in the representation diagonalizing I_z are

$$(m|\mathcal{H}|m)=-g\beta H_0{}^z m-KF_0[3m^2-I(I+1)], \tag{4a}$$

$$(m\pm1|\mathcal{H}|m)=-\tfrac{1}{2}g\beta(H_0{}^x\mp iH_0{}^y)\times[I(I+1)-m(m\pm1)]^{\frac{1}{2}}-KF_{\mp1}(3/2)^{\frac{1}{2}}\times(2m\pm1)[I(I+1)-m(m\pm1)]^{\frac{1}{2}}, \tag{4b}$$

$$(m\pm2|\mathcal{H}|m)=-KF_{\mp2}(3/2)^{\frac{1}{2}}\times[I(I+1)-(m\pm1)(m\pm2)]^{\frac{1}{2}}\times[I(I+1)-m(m\pm1)]^{\frac{1}{2}}. \tag{4c}$$

II. PURE QUADRUPOLE SPECTRUM

A. Energy Levels

In this case, the magnetic field vanishes and it is convenient to work in the principal axis system of the tensory $\partial E_i/\partial x_j$. Then $F_0=-eq$, $F_{\pm1}=0$, $F_{\pm2}=-(1/\sqrt{6})eq\eta$, where η is called the asymmetry parameter. If the axis are chosen so that $|\partial E_x/\partial x|\leq|\partial E_y/\partial y|\leq|\partial E_z/\partial z|$, then $0\leq\eta\leq1$. Now $(-m'|\mathcal{H}|-m)=(m'|\mathcal{H}|m)$, and $(m'|\mathcal{H}|m)=0$ unless $\Delta m=0$, ±2, so that the secular equation factors into two identical ones of degree $I+\frac{1}{2}$. We shall speak of each set of $I+\frac{1}{2}$ levels as a group of levels. If we denote E_m as that eigenvalue which goes over continuously into $-L[3m^2-I$

TABLE II. Eigenvalues E^0 and Zeeman-splitting parameters A, B, C of the pure quadrupole Hamiltonian.

I	m	η	E^0	A	B	C
5/2	5/2	0.1	5.00278	6.2469	—	—
		0.2	5.01113	6.2375	0.0002	—
		0.3	5.02512	6.2215	0.0011	—
		0.4	5.04481	6.1982	0.0035	0.0002
		0.5	5.07034	6.1670	0.0086	0.0007
		0.6	5.10185	6.1268	0.0179	0.0018
		0.7	5.13952	6.0767	0.0332	0.0039
		0.8	5.18353	6.0154	0.0567	0.0075
		0.9	5.23412	5.9417	0.0907	0.0136
		1.0	5.29150	5.8545	0.1379	0.0229
	3/2	0.1	−0.985095	2.2206	0.1565	0.0026
		0.2	0.941470	2.1387	0.5870	0.0182
		0.3	0.872088	2.0202	1.1959	0.0510
		0.4	0.781033	1.8830	1.8751	0.0942
		0.5	0.672723	1.7416	2.5387	0.1353
		0.6	0.551343	1.6048	3.1340	0.1620
		0.7	0.420564	1.4768	3.6373	0.1652
		0.8	0.283469	1.3587	4.0435	0.1399
		0.9	0.142591	1.2496	4.3583	0.0846
		1.0	0	1.1480	4.5918	—
	1/2	0.1	−4.01768	0.2409	9.0955	−1.1827
		0.2	4.06966	0.2162	9.3570	2.2692
		0.3	4.15303	0.1824	9.7237	3.1952
		0.4	4.26378	0.1464	10.1289	3.9390
		0.5	4.39762	0.1131	10.5222	4.5125
		0.6	4.55051	0.0850	10.8752	4.9437
		0.7	4.71895	0.0626	11.1772	5.2640
		0.8	4.90006	0.0454	11.4283	5.5010
		0.9	5.09153	0.0325	11.6339	5.6771
		1.0	5.29150	0.0230	11.8008	5.8086
7/2	7/2	0.1	7.00233	12.2467	—	—
		0.2	7.00935	12.2369	—	—
		0.3	7.02106	12.2203	—	—
		0.4	7.03753	12.1966	—	—
		0.5	7.05881	12.1656	0.0002	—
		0.6	7.08501	12.1265	0.0005	0.0001
		0.7	7.11622	12.0786	0.0013	0.0002
		0.8	7.15260	12.0210	0.0030	0.0004
		0.9	7.19432	11.9521	0.0063	0.0009
		1.0	7.24157	11.8704	0.0121	0.0020
	5/2	0.1	1.00834	6.2360	0.0005	—
		0.2	1.03351	6.1925	0.0078	0.0003
		0.3	1.07589	6.1154	0.0386	0.0019
		0.4	1.13601	5.9991	0.1183	0.0078
		0.5	1.21447	5.8383	0.2762	0.0228
		0.6	1.31176	5.6295	0.5395	0.0527
		0.7	1.42809	5.3736	0.9249	0.1035
		0.8	1.56325	5.0765	1.4331	0.1784
		0.9	1.71652	4.7485	2.0456	0.2762
		1.0	1.88669	4.4025	2.7277	0.3900
	3/2	0.1	−2.96971	2.1575	0.9293	−0.0138
		0.2	2.88628	1.9362	3.0617	0.0618
		0.3	2.76651	1.6823	5.3001	0.0564
		0.4	2.62743	1.4480	7.0760	+0.1041
		0.5	2.48217	1.2436	8.3145	0.4516
		0.6	2.33975	1.0632	9.1305	0.9604
		0.7	2.20609	0.8998	9.6656	1.5779
		0.8	2.08487	0.7493	10.0346	2.2449
		0.9	1.97813	0.6112	10.3166	2.9078
		1.0	1.88669	0.4870	10.5589	3.5256
7/2	1/2	0.1	−5.04097	0.2220	16.6392	−3.8223
		0.2	5.15658	0.1512	18.1007	6.7962
		0.3	5.33044	0.1023	19.6395	8.7475
		0.4	5.54610	0.0607	20.8895	9.9385
		0.5	5.79112	0.0349	21.8100	10.6626
		0.6	6.05702	0.0198	22.4699	11.1165
		0.7	6.33822	0.0112	22.9450	11.4133
		0.8	6.63098	0.0063	23.2926	11.6162
		0.9	6.93270	0.0036	23.5518	11.7604
		1.0	7.24157	0.0020	23.7490	11.8664
9/2	9/2	0.1	6.00143	20.2463	—	—
		0.2	6.00572	20.2319	—	—
		0.3	6.01289	20.2166	—	—
		0.4	6.02297	20.1902	—	—
		0.5	6.03598	20.1557	—	—
		0.6	6.05199	20.1125	—	—
		0.7	6.07105	20.0602	—	—
		0.8	6.09323	19.9977	0.0001	—
		0.9	6.11864	19.9242	0.0003	—
		1.0	6.14738	19.8382	0.0008	0.0001
	7/2	0.1	2.00467	12.2369	—	—
		0.2	2.01870	12.1973	—	—
		0.3	2.04218	12.1301	0.0005	—
		0.4	2.07524	12.0332	0.0028	0.0002
		0.5	2.11809	11.9033	0.0105	0.0009
		0.6	2.17102	11.7354	0.0308	0.0031
		0.7	2.23440	11.5227	0.0760	0.0089
		0.8	2.30867	11.2568	0.1648	0.0219
		0.9	2.39434	10.9286	0.3222	0.0480
		1.0	2.49193	10.5297	0.5783	0.0952
	5/2	0.1	−0.989724	6.2123	0.0060	0.0001
		0.2	0.958469	6.0899	0.0919	0.0031
		0.3	0.905221	5.8615	0.4324	0.0212
		0.4	0.829081	5.5122	1.2157	0.0767
		0.5	0.730171	5.0528	2.5141	0.1840
		0.6	0.610259	4.5232	4.2069	0.3252
		0.7	0.472749	3.9750	6.0338	0.4426
		0.8	0.322087	3.4495	7.7273	0.4615
		0.9	0.163016	2.9670	9.1118	0.3227
		1.0	0	2.5310	10.1240	—
	3/2	0.1	−2.96512	2.0395	3.3607	0.0329
		0.2	2.87966	1.6461	9.0311	0.1116
		0.3	2.77647	1.2968	13.0116	0.9467
		0.4	2.67805	1.0101	15.3151	2.4522
		0.5	2.59608	0.7637	16.7710	4.2783
		0.6	2.53541	0.5518	17.9117	6.0693
		0.7	2.49670	0.3794	18.9414	7.6018
		0.8	2.47833	0.2493	19.8877	8.8013
		0.9	2.47766	0.1578	20.7274	9.6920
		1.0	2.49193	0.0970	21.4437	10.3376
	1/2	0.1	−4.05126	0.1885	27.4244	9.0014
		0.2	4.18630	0.0957	31.5395	14.3040
		0.3	4.37338	0.0417	34.5446	16.8182
		0.4	4.59107	0.0176	36.3957	18.0484
		0.5	4.82782	0.0075	37.5463	18.7207
		0.6	5.07734	0.0033	38.2989	19.1300
		0.7	5.33599	0.0014	38.8170	19.4010
		0.8	5.60149	0.0006	39.1894	19.5917
		0.9	5.87231	0.0003	39.4661	19.7318
		1.0	6.14738	0.0001	39.6770	19.8380

$\times(I+1)]$ as η goes to zero, then $E_m=E_{-m}$ for all η. Here $L=e^2qQ/4I(2I-1)$.

The factored secular equations, listed in Table I, have been solved numerically for ten values of η for spins 5/2, 7/2, 9/2. The resulting eigenvalues are listed in Table II under E^0. Values for E^0 for spin 9/2 have been obtained previously to five significant figures.[13]

B. Intensities

Each line in the spectrum is a superposition of the four transitions $\pm m \leftrightarrows \pm m'$. The sum of the four

transition probabilities will be proportional to

$$WH'^2=\sum_{(\pm)}|(\pm m'|\mathbf{H}'\cdot\mathbf{I}|\pm m)|^2, \quad (5)$$

where $\mathbf{H}'$ is the rf-field exciting the transitions. If θ and ϕ are the polar angles of $\mathbf{H}'$ with respect to the principal axes, then

$$W=2D\cos^2\theta+\tfrac{1}{2}\sin^2\theta[G+2J\cos2\phi], \quad (6)$$

$$D=(I_{m,m'}{}^z)^2, \quad G=(I_{-m,m'}{}^+)^2+(I_{-m,m'}{}^-)^2,$$

$$J=(I_{-m,m'}{}^+)(I_{-m,m'}{}^-). \quad (7)$$

In the above formulas we have taken m and m' to be one of the two pairs belonging to the same group among the four levels $\pm m$, $\pm m'$ and have set $I^\pm=I^x\pm iI^y$.

We note that W contains all of the orientation dependence of the intensity of a given line. Hence, fitting the observed dependence on orientation of the relative intensity of a line to Eq. (6) will serve as a check on the assignment of mm' values to that line.

Values of D, G, and J are given in Table III for the transitions of observable intensity. In selecting the transition listed in the table, ν^2W has been used as a measure of the signal to noise ratio of a line and hence its observability. Also tabulated are the averaged transition probabilities $\bar{W}$ appropriate to a polycrystalline or powdered sample:

$$\bar{W}=\tfrac{2}{3}D+\tfrac{1}{3}G. \quad (8)$$

The results embodied in Table III show that the allowed transitions, $|\Delta m|=1$, are dominant for all values of η. There are several "forbidden" transitions for which the breakdown of the selection rule $|\Delta m|=1$ may be sufficiently strong to permit observation. These are the (5/2,1/2) transition for $I=5/2$, 7/2, 9/2, and the (7/2,3/2) transition for $I=7/2$, 9/2, both for various values of η. Similar results have been obtained in the special case considered by Lamarche and Volkoff.[12] For all lines except those with $I=9/2$, $(m,m')=(1/2, 5/2)$, $\eta\geq0.5$, the intensity is a maximum when $\mathbf{H}'$ is parallel to the x axis and for the exceptional cases when $\mathbf{H}'$ parallels the y axis.

If the observed frequency ratios of a pure quadrupole spectrum are drawn as horizontal lines on a plot of calculated frequency ratios *vs* η, one set of their intercepts with the calculated curves should lie on a vertical line. One thus obtains η and then qQ. Observations of the directional dependence of intensities in a single crystal yields the orientation of the principal axes. One can then determine the frequency of, and optimum orientation of $\mathbf{H}'$ for the "forbidden" lines if these are not observed at first.

III. ZEEMAN SPLITTING

A study of the Zeeman splitting of the pure quadrupole spectrum in a single crystal as a function of the orientation of the magnetic field will yield simply and immediately the orientation of the crystalline field axes[10] as well as a check on the assignment of transitions in the zero field pattern. The large quadrupole moments of some nuclei, e.g., Ta, have prevented the measurement of their magnetic moments by the usual magnetic resonance or induction techniques. The Zeeman splitting[16] can probably give the magnetic moment to greater accuracy than can be obtained at present by optical means.[17] The case of the symmetric field gradient is by far the simplest to analyze. The results for $\eta\neq0$ presented below will be useful, however, when the nucleus in question cannot be found in a site of tetragonal, hexagonal, or rhombohedral symmetry.

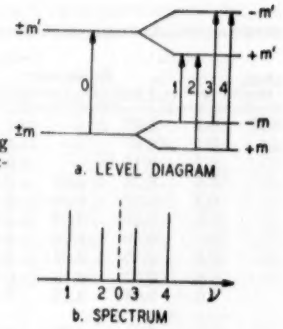

FIG. 1. Zeeman splitting of pure quadrupole spectrum.

A. Energy Levels

A magnetic field $\mathbf{H}_0$ at arbitrary orientation to the principal axes connects the degenerate states $\pm m$. Solution of the resulting secular problem yields, to first degree in the field strength,

$$E_{\pm m}=E_{\pm m}{}^0\mp g\beta H_0[A\cos^2\theta+\tfrac{1}{4}\sin^2\theta(B+2C\cos2\phi)]^{\frac{1}{2}}, \quad (9)$$

$$A=(I_{mm}{}^z)^2, \quad B=(I_{m,-m}{}^+)^2+(I_{m,-m}{}^-)^2, \quad C=I_{m,-m}{}^+I_{m,-m}{}^-. \quad (10)$$

In Eq. (9), θ and ϕ are the polar angles of $\mathbf{H}_0$. Values of A, B, and C are listed in Table II. Figure 1 shows schematically the fourfold splitting of each component of the pure quadrupole spectrum. The four members of the multiplet are symmetric about the original line in frequency and intensity.

B. Intensities

The intensity formulas for arbitrary orientation of the rf-field $\mathbf{H}'$ are extremely complicated. One can, however, show that the intensities of the Zeeman pattern are symmetric in the general case, as noted above. Examination of the general formulas shows that all lines of a multiplet are of comparable, but not necessarily equal, intensity. Hence those multiplets which contain allowed transitions $|\Delta m|=1$ are dominant.

[16] H. Kruger and V. Meyer-Berkhout, Z. Physik **132**, 221 (1952).
[17] B. M. Brown and D. H. Tomboulian, Phys. Rev. **88**, 1158 (1952); Phys. Rev. **91**, 1580 (1953).

TABLE III. Intensity parameters, pure quadrupole spectrum.

Quantity	η	$I=5/2$ Transitions (1/2,3/2)	(3/2,5/2)	(1/2,5/2)
D	0.1	0.02	···	···
	0.2	0.07	···	···
	0.3	0.15	···	0.01
	0.4	0.24	0.01	0.02
	0.5	0.33	0.01	0.02
	0.6	0.41	0.02	0.03
	0.7	0.49	0.04	0.03
	0.8	0.56	0.07	0.04
	0.9	0.62	0.10	0.04
	1.0	0.68	0.14	0.05
G	0.1	7.87	4.99	0.01
	0.2	7.51	4.97	0.04
	0.3	7.01	4.95	0.08
	0.4	6.44	4.93	0.13
	0.5	5.88	4.92	0.17
	0.6	5.36	4.92	0.21
	0.7	4.91	4.93	0.23
	0.8	4.53	4.95	0.25
	0.9	4.21	4.99	0.26
	1.0	3.95	5.03	0.26
J	0.1	0.48	0.11	···
	0.2	0.90	0.22	···
	0.3	1.24	0.33	···
	0.4	1.47	0.44	0.01
	0.5	1.62	0.56	0.01
	0.6	1.70	0.67	0.02
	0.7	1.74	0.79	0.02
	0.8	1.74	0.91	0.03
	0.9	1.72	1.03	0.03
	1.0	1.70	1.16	0.04
$\bar{W}$	0.1	2.64	1.66	···
	0.2	2.55	1.66	0.02
	0.3	2.44	1.65	0.03
	0.4	2.31	1.65	0.05
	0.5	2.18	1.65	0.07
	0.6	2.06	1.66	0.09
	0.7	1.97	1.67	0.10
	0.8	1.88	1.70	0.11
	0.9	1.82	1.73	0.11
	1.0	1.77	1.77	0.12

Quantity	η	$I=7/2$ Transitions (1/2,3/2)	(3/2,5/2)	(5/2,7/2)	(1/2,5/2)	(3/2,7/2)
D	0.1	0.06	···	···	0.01	···
	0.2	0.21	0.01	···	0.02	···
	0.3	0.37	0.02	···	0.03	0.01
	0.4	0.52	0.06	···	0.05	0.01
	0.5	0.65	0.13	···	0.06	0.02
	0.6	0.75	0.23	···	0.06	0.03
	0.7	0.85	0.36	···	0.06	0.04
	0.8	0.93	0.51	0.01	0.06	0.06
	0.9	1.01	0.69	0.02	0.05	0.07
	1.0	1.08	0.88	0.03	0.05	0.09
G	0.1	14.20	11.93	7.00	0.08	···
	0.2	12.35	11.78	7.01	0.27	···
	0.3	10.38	11.64	7.03	0.45	0.01
	0.4	8.76	11.55	7.04	0.57	0.02
	0.5	7.57	11.49	7.06	0.62	0.04
	0.6	6.72	11.43	7.08	0.61	0.07
	0.7	6.12	11.31	7.11	0.56	0.11
	0.8	5.69	11.12	7.13	0.50	0.16
	0.9	5.37	10.85	7.17	0.43	0.21
	1.0	5.12	10.50	7.21	0.35	0.27

Quantity	η	$I=7/2$ Transitions (1/2,3/2)	(3/2,5/2)	(5/2,7/2)	(1/2,5/2)	(3/2,7/2)
J	0.1	1.40	0.36	0.14	···	···
	0.2	2.36	0.72	0.28	0.01	···
	0.3	2.81	1.09	0.42	0.02	···
	0.4	2.95	1.48	0.56	0.03	···
	0.5	2.93	1.87	0.71	0.03	···
	0.6	2.85	2.27	0.85	0.03	0.01
	0.7	2.76	2.65	1.00	0.03	0.01
	0.8	2.66	2.99	1.15	0.02	0.02
	0.9	2.58	3.27	1.30	0.01	0.03
	1.0	2.50	3.50	1.45	···	0.04
$\bar{W}$	0.1	4.77	3.98	2.33	0.03	···
	0.2	4.26	3.93	2.34	0.10	···
	0.3	3.71	3.90	2.34	0.17	0.01
	0.4	3.27	3.89	2.35	0.22	0.02
	0.5	2.96	3.92	2.35	0.24	0.03
	0.6	2.74	3.96	2.36	0.24	0.04
	0.7	2.60	4.01	2.37	0.23	0.07
	0.8	2.52	4.05	2.38	0.21	0.09
	0.9	2.46	4.08	2.40	0.18	0.12
	1.0	2.42	4.08	2.42	0.15	0.15

Quantity	η	$I=9/2$ Transitions (1/2,3/2)	(3/2,5/2)	(5/2,7/2)	(7/2,9/2)	(1/2,5/2)	(3/2,7/2)
D	0.1	0.14	···	···	···	0.01	···
	0.2	0.40	0.03	···	···	0.04	0.01
	0.3	0.63	0.12	···	···	0.06	0.03
	0.4	0.80	0.29	···	···	0.07	0.06
	0.5	0.95	0.54	0.01	···	0.07	0.09
	0.6	1.08	0.83	0.04	···	0.06	0.12
	0.7	1.20	1.14	0.08	···	0.04	0.15
	0.8	1.30	1.43	0.15	···	0.03	0.17
	0.9	1.39	1.69	0.27	···	0.02	0.19
	1.0	1.47	1.92	0.43	···	0.02	0.19
G	0.1	21.05	20.71	16.00	9.01	0.32	···
	0.2	16.02	20.24	16.01	9.01	0.83	0.02
	0.3	12.37	19.89	16.00	9.05	1.08	0.08
	0.4	10.19	19.47	15.97	9.08	1.07	0.20
	0.5	8.90	18.76	15.92	9.13	0.92	0.37
	0.6	8.10	17.73	15.87	9.18	0.73	0.57
	0.7	7.56	16.49	15.85	9.25	0.56	0.76
	0.8	7.15	15.22	15.87	9.32	0.42	0.91
	0.9	6.83	14.05	15.94	9.40	0.31	1.00
	1.0	6.56	13.06	16.04	9.49	0.23	1.03
J	0.1	3.08	0.84	0.39	0.17	···	···
	0.2	4.34	1.72	0.78	0.31	0.02	···
	0.3	4.49	2.66	1.17	0.52	0.02	···
	0.4	4.14	3.61	1.57	0.69	0.01	0.01
	0.5	4.10	4.46	1.97	0.87	−0.01	0.03
	0.6	3.89	5.10	2.37	1.05	0.04	0.05
	0.7	3.70	5.50	2.80	1.23	0.05	0.08
	0.8	3.54	5.69	3.24	1.42	0.06	0.11
	0.9	3.40	5.73	3.70	1.61	0.06	0.12
	1.0	3.27	5.68	4.18	1.80	0.06	0.13
$\bar{W}$	0.1	7.11	6.90	5.33	3.00	0.12	···
	0.2	5.61	6.77	5.34	3.00	0.30	0.02
	0.3	4.54	6.71	5.33	3.02	0.40	0.05
	0.4	3.93	6.68	5.33	3.03	0.40	0.10
	0.5	3.60	6.61	5.32	3.04	0.35	0.18
	0.6	3.42	6.46	5.31	3.06	0.28	0.27
	0.7	3.32	6.25	5.34	3.08	0.22	0.35
	0.8	3.25	6.02	5.39	3.11	0.16	0.42
	0.9	3.20	5.81	5.49	3.13	0.12	0.46
	1.0	3.17	5.63	5.63	3.17	0.09	0.47

Orientation of the rf-field parallel to the x axis again appears to be favorable in the majority of cases. One cannot be certain without detailed numerical analysis.

For this simplest case the transition probabilities for the multiplet $|m|$, $|m'|$ become

$$W=\frac{\frac{1}{4}(G+2J)}{(1+|r|^2)(1+|s|^2)}M, \tag{11}$$

where

$$r=-\frac{\sin\theta[I_{m,-m}{}^{+}e^{i\phi}+I_{m,-m}{}^{-}e^{-i\phi}]}{2[|I_{mm}{}^{z}|\cos\theta+|\Delta E_m|]}. \tag{12}$$

In Eq. (11), s is the same quantity for the levels $\pm m'$ as r is for the levels $\pm m$. Further, M is a 2×2 matrix, the indices of which indicate the signs of m and m'. In Eq. (12), $|\Delta E_m|$ is the magnitude of the Zeeman shift (i.e., half the level separation) in units of $g\beta H_0$. We must distinguish two cases before writing M explicitly: in case I, $|m|$ and $|m'|$ belong to the same group; in case II, they do not. Noting that $M_{++}=M_{--}$ and $M_{+-}=M_{-+}$, we obtain

$$\begin{aligned} M_{++}{}^{\mathrm{I}}&=|r^*+s|^2, \quad M_{++}{}^{\mathrm{II}}=|1+r^*s|^2,\\ M_{+-}{}^{\mathrm{I}}&=|1-rs|^2, \quad M_{+-}{}^{\mathrm{II}}=|r-s|^2. \end{aligned} \tag{13}$$

The quantities needed to evaluate W through Eqs. (11), (12), and (13) may be found in Tables II, III, and IV.

As examples of the use of the matrix M, consider the multiplets $\pm7/2$, $\pm5/2$ and $\pm7/2, \pm3/2$. In the former case, $7/2$ and $5/2$ are in different groups and we must use M^{II}; in the latter case, $7/2$ and $3/2$ are in the same group and we must use M^{I}. Let $W=ZM$. Then

$$\begin{aligned} W_{7/2,5/2}&=W_{-7/2,-5/2}=Z_{7/2,5/2}M_{++}{}^{\mathrm{II}},\\ W_{-7/2,5/2}&=W_{7/2,-5/2}=Z_{7/2,5/2}M_{+-}{}^{\mathrm{II}},\\ W_{7/2,3/2}&=W_{-7/2,-3/2}=Z_{7/2,3/2}M_{++}{}^{\mathrm{I}},\\ W_{-7/2,3/2}&=W_{7/2,-3/2}=Z_{7/2,3/2}M_{+-}{}^{\mathrm{I}}. \end{aligned}$$

All "allowed" transitions are of type I; all observable "forbidden" transitions are of type II.

C. Large Quadrupole Coupling

There are cases when the quadrupole coupling is so large that the frequencies of the pure quadrupole spectrum lie beyond the reach of conventional nuclear resonance or induction equipment, say greater than 10^8 cps. Then, however, it becomes possible to observe in single crystals transitions between the levels $\pm m$ in a strong magnetic field, the frequencies of which are $2|\Delta E_m|$. Such measurements could yield a value for the magnetic moment, for η, and for the orientation of the principal aces. The mixing of the $\pm m$ states by $\mathbf{H}_0$ is sufficiently strong for intermediate and large values of η that all $I+\frac{1}{2}$ transitions $m\rightarrow-m$ should be observable. Depending on the values of m and η, it is sometimes favorable to have $\mathbf{H}'\|z$ and sometimes paral-

TABLE IV. Matrix elements of the angular momentum.

Quantity	η	$I=5/2$ $m=1/2$	$3/2$	$5/2$	$I=7/2$ $m=1/2$	$3/2$	$5/2$	$7/2$
$I_{mm}{}^{z}$	0.1	0.49	1.49	2.50	0.47	1.47	2.50	3.50
	0.2	0.46	1.46	2.50	0.39	1.39	2.49	3.50
	0.3	0.43	1.42	2.49	0.32	1.30	2.47	3.50
	0.4	0.38	1.37	2.49	0.25	1.20	2.45	3.49
	0.5	0.34	1.32	2.48	0.19	1.12	2.42	3.49
	0.6	0.29	1.27	2.48	0.14	1.03	2.37	3.48
	0.7	0.25	1.22	2.47	0.11	0.95	2.32	3.48
	0.8	0.21	1.17	2.45	0.08	0.87	2.25	3.47
	0.9	0.18	1.12	2.44	0.06	0.78	2.18	3.46
	1.0	0.15	1.07	2.42	0.04	0.70	2.10	3.45
$I_{m-m}{}^{+}$	0.1	2.99	0.40	···	3.96	0.96	0.02	···
	0.2	2.96	0.77	0.01	3.88	1.75	0.09	···
	0.3	2.92	1.09	0.03	3.78	2.30	0.20	···
	0.4	2.87	1.37	0.06	3.70	2.66	0.34	0.01
	0.5	2.82	1.59	0.09	3.63	2.88	0.52	0.01
	0.6	2.78	1.77	0.13	3.59	3.00	0.73	0.02
	0.7	2.73	1.91	0.18	3.55	3.07	0.96	0.04
	0.8	2.69	2.01	0.24	3.53	3.08	1.19	0.05
	0.9	2.66	2.09	0.30	3.52	3.07	1.42	0.08
	1.0	2.63	2.14	0.37	3.51	3.03	1.63	0.11
$I_{m-m}{}^{-}$	0.1	−0.40	0.01	···	−0.96	0.01	···	···
	0.2	0.77	0.02	···	1.75	0.04	···	···
	0.3	1.09	0.05	···	2.31	0.02	0.01	···
	0.4	1.37	0.07	···	2.69	−0.04	0.02	···
	0.5	1.60	0.09	0.01	2.94	0.16	0.04	···
	0.6	1.78	0.09	0.01	3.10	0.32	0.07	···
	0.7	1.93	0.09	0.02	3.21	0.51	0.11	···
	0.8	2.04	0.07	0.03	3.29	0.73	0.15	0.01
	0.9	2.13	0.04	0.05	3.34	0.95	0.19	0.01
	1.0	2.21	···	0.06	3.38	1.16	0.24	0.02

Quantity	η	$I=9/2$ $m=1/2$	$3/2$	$5/2$	$7/2$	$9/2$
$I_{m,m}{}^{z}$	0.1	0.43	1.43	2.49	3.50	4.50
	0.2	0.31	1.28	2.47	3.49	4.50
	0.3	0.20	1.14	2.42	3.48	4.50
	0.4	0.13	1.01	2.35	3.47	4.49
	0.5	0.09	0.87	2.25	3.45	4.49
	0.6	0.06	0.74	2.13	3.43	4.48
	0.7	0.04	0.62	1.99	3.39	4.48
	0.8	0.03	0.50	1.86	3.36	4.47
	0.9	0.02	0.40	1.72	3.31	4.46
	1.0	0.01	0.31	1.59	3.24	4.45
$I_{m,-m}{}^{+}$	0.1	4.90	1.83	0.08	···	···
	0.2	4.73	3.00	0.30	0.01	···
	0.3	4.61	3.60	0.66	0.02	···
	0.4	4.53	3.86	1.10	0.05	···
	0.5	4.49	3.95	1.58	0.10	···
	0.6	4.47	3.94	2.04	0.17	···
	0.7	4.47	3.89	2.45	0.27	0.01
	0.8	4.47	3.82	2.77	0.40	0.01
	0.9	4.47	3.75	3.02	0.56	0.02
	1.0	4.47	3.68	3.18	0.75	0.03
$I_{m,-m}{}^{-}$	0.1	−1.84	−0.02	···	···	···
	0.2	3.02	0.04	0.01	···	···
	0.3	3.65	0.26	0.03	···	···
	0.4	3.98	0.64	0.07	···	···
	0.5	4.17	1.08	0.12	0.01	···
	0.6	4.28	1.54	0.16	0.02	···
	0.7	4.34	1.96	0.18	0.03	···
	0.8	4.39	2.31	0.17	0.05	···
	0.9	4.42	2.59	0.11	0.09	···
	1.0	4.44	2.81	···	0.13	···

lel to x or y.

$$W_z=\frac{4|r|^2}{[1+|r|^2]^2}A, \tag{14}$$

$$W_x=\frac{|1-r^2|^2}{[1+|r|^2]^2}(B+2C), \tag{15}$$

$$W_y=\frac{|1+r^2|^2}{[1+|r|^2]^2}(B-2C). \tag{16}$$

Again the intensity formulas for arbitrary orientation of $\mathbf{H}'$ are extremely complicated. Unless some knowledge of the orientation of the principal axes is available, say from symmetry considerations, the above intensity formulas will not be of use until after analysis of the orientation dependence of the frequencies.

IV. ACCURACY OF PERTURBATION THEORY

A. Zeeman Splitting

We take as the unperturbed Hamiltonian the pure quadrupole energy; the perturbation energy is $-g\beta\mathbf{I}\cdot\mathbf{H}_0$. Let $E_m^{(n)}$ be the nth order term in the perturbation theoretic expansion of the energy levels. It can be shown that

$$E_{-m}^{(n)}=(-1)^n E_m^{(n)}, \tag{17}$$

by induction on the general form of the nth order term. The proof rests on the behavior with respect to change of sign of m of the matrix elements of the Hamiltonian in the representation diagonalizing it to first order. A demonstration of Eq. (17) will not be given here; the corresponding theorem for the strong field case will be discussed more fully in Sec. B.

For accurate determination of the first order Zeeman parameters one needs as wide a range of field strengths as possible. At first glance it would appear that the magnetic field strength can be increased only until the second order effect is of the order of the experimental error. However, Eq. (17) shows that the second order term cancels out of $\nu_{m,m'}-\nu_{-m,-m'}$, and hence first order calculation of the separation between a symmetric pair in a multiplet gives second order accuracy. The working range of field strength extends until third order terms are of the order of the experimental error when first order calculations are used.

B. Strong-Field Case

Let R signify reflection of the coordinate system in the $x-y$ plane. Then in the expressions 4(a), 4(b), and 4(c) for the matrix elements of $\mathcal{H}$, $H_0{}^z\rightarrow -H_0{}^z$, $F_{\pm 1}\rightarrow -F_{\pm 1}$ upon application of R. Inspection of the matrix elements shows that

$$\mathcal{H}_{-m-m'}(\mathbf{H}_0,F_\mu)=\mathcal{H}_{mm'}(R\mathbf{H}_0,RF_\mu). \tag{18}$$

Therefore

$$E_{-m}(\mathbf{H}_0,F_\mu)=E_m(R\mathbf{H}_0,RF_\mu). \tag{19}$$

In the strong-field case, we take $\mathbf{H}_0\|z$ and $-g\beta I^z H_0$ as the unperturbed Hamiltonian. The latter is nondegenerate and hence perturbation theory yields an expansion in powers of F_μ and inverse powers of H_0 for the energy. The dependence on F_μ of a typical term might be

$$(F_0)^a(F_{-1})^b(F_{+1})^c(F_{-2})^d(F_{+2})^e, \tag{20}$$

with the condition that[18]

$$b-c+2d-2e=0. \tag{21}$$

Therefore $b-c$ must be even and the sign change in each term caused by R is determined by the sign change of $H_0{}^z=\pm H_0$. We conclude, therefore, that

$$E_{-m}{}^{(n)}=(-1)^{n-1}E_m{}^{(n)}. \tag{22}$$

Thus the third order calculations of Bersohn[3] give fourth order accuracy when the results of theory and experiment for $\nu_{m,m'}-\nu_{-m,-m'}$ are compared. This increased accuracy becomes important for quadrupole interactions of the order of that observed for Nb^{93} in $KNbO_3$ where $|e^2qQ/h|=23.1$ Mc/sec.[15] In most ferroelectrics and antiferroelectrics one could expect to encounter similarly large couplings.

ACKNOWLEDGMENTS

I wish to thank Professor Charles Kittel for helpful discussions concerning this project. A part of the work was carried forward at the Westinghouse Research Laboratories; it is a pleasure to acknowledge their hospitality. I am very grateful to the Laboratory of Molecular Structure and Spectra of the University of Chicago for its cooperation and assistance in computational matters. W. Jaunzemis, G. Lenkersdorf, and H. Resnikoff performed the bulk of the numerical calculations. My thanks go to W. D. Knight and R. Cotts for their helpful comments. The work performed at the University of Chicago was supported in part by Contract No. N-6ori-02004, U. S. Office of Naval Research.

[18] Equations (20) and (21) become especially clear when one uses the perturbation techniques described in reference 13.

Nuclear Resonance of Nb^{93} in $KNbO_3$†

R. M. Cotts and W. D. Knight
Department of Physics, University of California, Berkeley, California
(Received July 8, 1954)

The nuclear resonance of Nb^{93} in a single crystal of $KNbO_3$ has been studied in magnetic fields of approximately 5000, 100, and zero oersteds, and at temperatures between −196°C and +460°C. The quadrupole splitting of the magnetic resonance line in strong fields is found to be a sensitive function of crystal structure and, hence, of temperature. Temperatures of the phase transitions found in this way at about −50, +220, and +430°C are in agreement with other known data for this substance. The splitting $\Delta\nu$ of one satellite line is a continuous function of temperature between 220 and 430°C; near 430°C $\Delta\nu$ changes abruptly, indicating a first-order phase change. Below the Curie temperature (430°C) $KNbO_3$ is ferroelectric, with noncubic crystal structure. Above 430° it is cubic and a single resonance line is observed.

Four lines have been identified in the pure quadrupole spectrum in zero magnetic field, and at 20°C. From the four frequencies the quadrupole coupling constant and asymmetry parameter are evaluated to be 23.1 Mc/sec and 0.80, respectively. At −196°C, the frequencies are different from the room temperature values, and the quadrupole coupling is evaluated to be 16.0 Mc/sec and the asymmetry parameter 0.0, the latter appropriate to the rhombohedral crystal structure at this temperature. The Zeeman effect in magnetic fields up to about 100 oersteds is shown to be an aid in identifying the absorption lines and in locating the principal axes of the crystalline electric field gradient. The value of the quadrupole coupling constant is consistent with the existence of a strong covalent character in the chemical bonding to the Nb.

I. INTRODUCTION

PRIOR to the present experiments,[1] the crystal structure of $KNbO_3$ was studied extensively by both x-ray and optical means,[2] and four modifications of the perovskite structure (Fig. 1) are known. These are, in order of decreasing temperature, cubic, tetragonal, orthorhombic, and rhombohedral, where one may think of the latter three modifications as being respectively generated by elongations along an edge, face diagonal or body diagonal of the cell shown in Fig. 1. The transition temperatures are about 430, 220, and −50°C. In addition, a large body of data on the electrical properties of this substance is available. Below the Curie point (430°C) it is ferroelectric, and discontinuities in the dielectric constant appear at the three transition temperatures.[3,4] Around each transition temperature the measured dielectric constant shows a marked hysteresis, and latent heats of transition are observed.[4] It is known further that a natural twinning[2] during growth of the crystal prevents one from obtaining a large crystal of one domain only. Thus, any measurements of electrical properties on single crystals are somewhat complicated.

Now, although a good deal of theoretical work[5] has been done in an attempt to understand the microscopic local field which results in the spontaneous polarization in such ferroelectrics, the theoretical treatments are limited by lack of direct experimental information about the polarizing forces. It is generally agreed that the ferroelectric state is associated with a displacement of the central ion (in this case Nb) from the center of symmetry of the surrounding oxygen octahedron. This is a complicated cooperative phenomenon, and depends on the potential well affecting the central ion; the surrounding oxygen ions are also supposed to be polarized in such a way as to enhance the Nb polarization by a Lorentz type of local field interaction. Whether or not it is possible to describe this interaction accurately will depend to a large extent on whether or not direct experimental evidence can be found not only for the geometrical displacement of the Nb ion in the crystal, but also for the electrical forces actually causing this displacement.

Since the measurement of the coupling between the nuclear quadrupole moment and the crystalline field gradient should be helpful in this respect, we have undertaken the present series of experiments on the nuclear magnetic resonance (NMR) and the nuclear quadrupole resonance (NQR) in hopes of shedding light

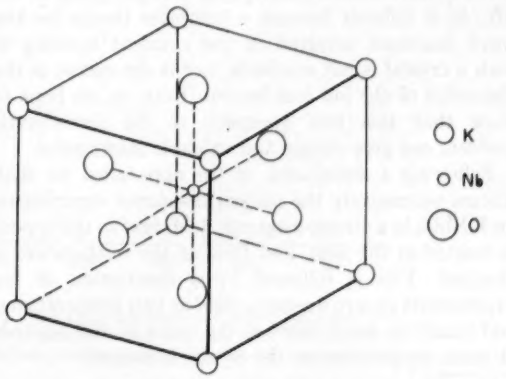

FIG. 1. The perovskite structure.

† Supported in part by the Office of Naval Research.
[1] R. M. Cotts and W. D. Knight, Phys. Rev. **93**, 940 (1954); W. D. Knight, Phys. Rev. **94**, 1408 (1954).
[2] E. A. Wood, Acta Cryst. **4**, 353 (1951).
[3] B. T. Matthias and J. P. Remeika, Phys. Rev. **82**, 727 (1951).
[4] Shirane, Danner, Pavlovic, and Pepinsky, Phys. Rev. **93**, 672 (1954).
[5] See, for example, E. T. Jaynes, *Ferroelectricity* (Princeton University Press, Princeton, 1953).

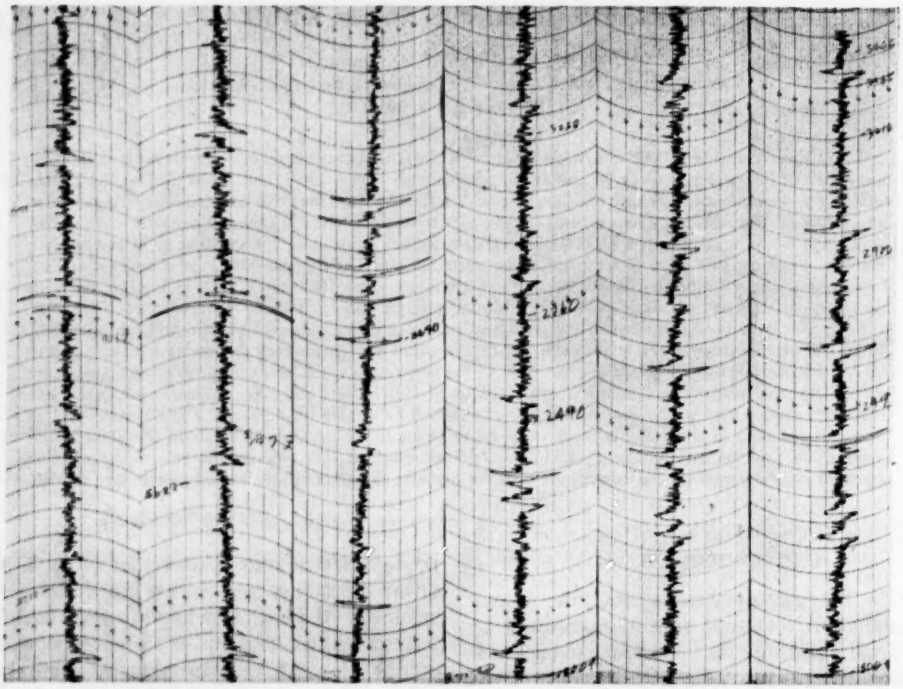

FIG. 2. Nuclear magnetic resonance absorption peaks at several orientations of a single crystal of $KNbO_3$. The limits of the spectrum are from about 6 to 8 Mc/sec.

on the problem. To be sure, the interpretation of these results will not be an easy matter, but one may, as we shall show, reasonably expect to extract results which will roughly indicate the relative strength and direction of bonding to the Nb ion in the crystal. The difficulties are briefly the following: The quadrupole coupling constant $e^2qQ/h=(\partial E_z/\partial z)/h$ and asymmetry parameter $\eta=(\partial E_x/\partial x-\partial E_y/\partial y)/(\partial E_z/\partial z)$ are evaluated directly in the experiments, but in order to calculate $eq=\partial E_z/\partial z$, one needs to know Q for the Nb nucleus. At present no experimental value is available and one can only estimate[6,7] the value for Q. Furthermore, even if the Q were known exactly, the interpretation of the $\partial E_z/\partial z$ is difficult because a complete theory for the wave functions involved in the covalent bonding in such a crystal is not available; nor is the extent of the distortion of the ion core known. Even so, we hope to show that this new approach to the ferroelectric problem can give unique and valuable information.

Following a description of the apparatus, we shall discuss successively the nuclear resonance experiments on $KNbO_3$ in a strong magnetic field, first as the crystal is rotated in the field, and then as the temperature is changed. This is followed by a description of the experiments in zero magnetic field at two temperatures, and finally in small fields of the order of 100 oersteds at room temperature as the crystal is rotated.

[6] Townes, Foley, and Low, Phys. Rev. **76**, 1415 (1949).
[7] K. Murakawa and T. Kamei, Phys. Rev. **92**, 325 (1953).

II. APPARATUS

A Pound spectrometer[8] was used as a detector of both the NMR and NQR. The NMR of Nb^{93} was observed in a permanent magnet field of 5250 oersteds[9] which was sine wave modulated at 100 cps with an amplitude about equal to one-half the resonance line width. Temperatures up to 460°C were reached in a stainless steel Dewar with a power dissipation of 70 watts in a heater coil which was wound around the rf head. For low-temperature work, the space below the heater was partially filled with liquid nitrogen and the current through the heater coil was adjusted to obtain an intermediate steady-state temperature.

The 29-turn rf-coil (12.5 mm in diameter and 20 mm long) was held together with Sauer Eisen cement, and was suspended by two 0.100-in.-diameter ceramic tubes which fit inside two 0.125-in.-diameter stainless steel tubes extending downward from the top of the Dewar. One end of the coil was grounded to the tubing and the other ran through the ceramic piece, thus forming a coaxial line. Leads to the heater were carried in double-hole ceramic insulators from the top of the Dewar. Iron and constantan thermocouple wires extended down the inside of a third tube which held the sample crystal in the coil. Because of the magnetic effects of the iron,

[8] R. V. Pound and W. D. Knight, Rev. Sci. Instr. **21**, 219 (1950).
[9] The field was about 7000 oersteds during the rotation experiments. For most of the other high-field experiments, the gap was increased, which resulted in the lower field of about 5000 oersteds.

the thermocouple was kept about 1 cm above the coil and crystal during a run. A separate calibration run was performed later to determine temperature at this location in terms of the temperature in the sample.

The NQR was modulated by an on-off antisymmetric square wave H-field[10] of about 100 oersteds amplitude.

Small dc fields for Zeeman splitting were generated by two coils of 9-in.-diameter, spaced 4.5 in. apart. The rf coil, shield, and modulating coils were mounted together as a unit on a turn table between the Zeeman coils. With this arrangement, the angle between the crystal axes and the modulating coils was kept constant at an orientation of the modulating field most effective in splitting the line.

III. ROTATION SPECTRUM IN STRONG MAGNETIC FIELDS

The energy levels for a nucleus of spin 9/2 in strong magnetic fields have been calculated to the third order of perturbation.[11] However, explicit expressions for the orientational dependence have not yet been deduced beyond the second order. One expects in general to see $2I=9$ absorption lines, unequally spaced with respect to the unperturbed Larmor frequency, where the frequencies of all components will vary in a complicated way with the orientation of the crystal in the magnetic field. Furthermore, the relative intensities are expected to be functions of orientation. Since the Larmor frequency in a 7000-oersted field will be about 7000 kc/sec, and the absorption spectrum (see Fig. 2) extends over a 2000–3000 kc/sec range, one expects that any evaluation of the quadrupole coupling must be made on the basis of a third-order theory. It was, in fact, found that second-order calculations do not agree with the experimental results. Figure 3 shows the results of a 180° rotation of the crystal at 5° intervals, where the polar axis (assumed tentatively to coincide with the axis of symmetry of the crystalline field gradient tensor) was at right angles to the axis of rotation, the latter being perpendicular to the external magnetic field. The following qualitative features are to be noticed. Figure 3 shows two groups of 9 lines which tend toward a partial convergence near 7.2 Mc/sec which is the Larmor frequency. The convergences occur at angles of approximately 70° and 140° of the chosen polar axis with respect to the magnetic field. We see, further, that three pairs of lines, one of each pair apparently being associated with each of the domain twins, cross at 100°. This crossing apparently represents respective orientations for the two domains for which the quadrupole perturbations are the same. The above result is consistent with that of Mrs. Wood,[2] that the crystals are predominantly of only two domains.

Since any more detailed examination of the above results seemed too difficult to warrant the necessary labor involved, we temporarily abandoned the high-field rotation experiments (until a larger magnetic field is available) in favor of three other lines of investigation. *First*, it was clear from the results shown in Figs. 1 and 2 that the quadrupole splittings are large enough to allow a measurement of the effects of thermally induced changes in crystal structure which produce appropriate variations in the crystalline field gradient. Thus, if the lattice parameter changes continuously as a function of temperature in a given crystal phase, the quadrupole splitting should exhibit a corresponding

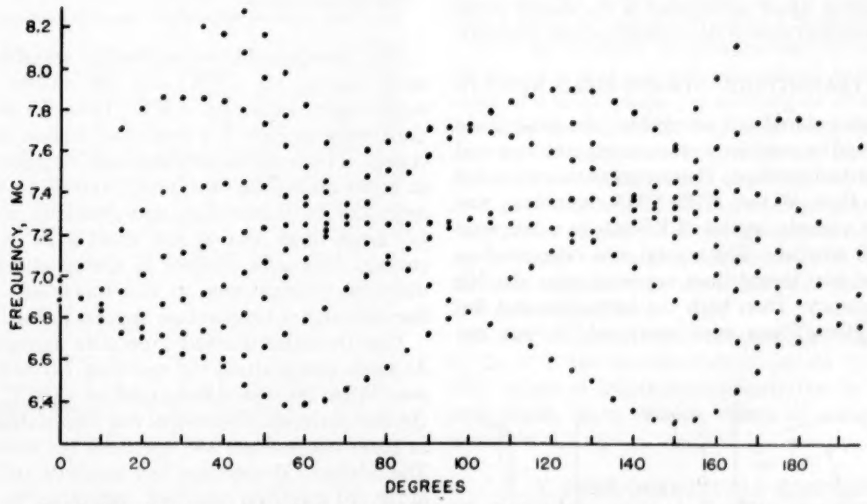

FIG. 3. Rotation pattern for a single crystal of $KNbO_3$. Each circle represents an absorption peak. Zero degrees represents an orientation for which the polar axis is parallel to the magnetic field. The rotation is made about an axis perpendicular to the dc magnetic field but parallel to the oscillating (rf) magnetic field.

[10] F. Reif and E. M. Purcell, Phys. Rev. **91**, 631 (1953).
[11] R. Bersohn, J. Chem. Phys. **20**, 1505 (1952).

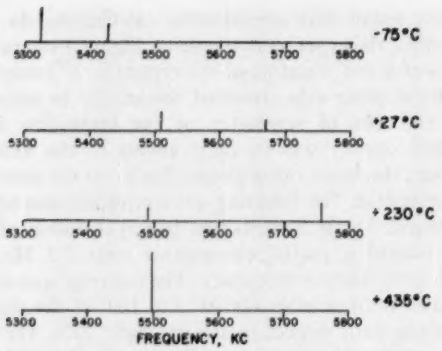

FIG. 4. Partial magnetic absorption spectrum of $KNbO_3$ at four different temperatures, showing the effects of crystal structure on the quadrupole splitting.

behavior. Also, if the lattice parameter changes more abruptly at a phase transition, the quadrupole splitting would be expected to behave accordingly, the sharpness of the transition being easily observed as a function of temperature in this way. It was clear at the outset that any such changes would be meaningful, even if the value of the quadrupole coupling constant for the crystal was not known. *Second*, the quadrupole splitting seemed large enough so that one could predict that a successful observation of the NQR in zero magnetic field would be possible. In the absence of a strong magnetic field the number of absorption lines to fit into the theoretical spectrum would be smaller (i.e., 4) and the effects of domain structure should become less important. *Third*, the application of a small Zeeman field should split the NQR lines in a predictable way and, except for ambiguities introduced because of the crystal twinning, allow verification of the energy levels and of the principal axes of the crystalline field gradient.

IV. PHASE TRANSITIONS—STRONG-FIELD RESULTS

As we have pointed out previously, the quadrupole coupling should be sensitive to the crystal structure and hence to the temperature. The experiments proceeded as follows. Part of the Nb^{93} NMR spectrum was recorded for a single crystal of $KNbO_3$ in a magnetic field of 5250 oersteds. The crystal was orientated so that at least two strong lines appeared near the Nb Larmor frequency. Then both the intensities and frequencies of these lines were measured. It was not necessary to scan the whole Nb spectrum since any change in the quadrupole coupling would, of course, affect all the lines in the spectrum. At temperatures between phase transitions, the splittings of the lines were observed, while at both sides of the −50°C transition and the low-temperature side of the 430°C transition a combination of change in intensity and frequency occurred. At the −50°C transition the change occurred over a temperature range wide enough to allow measurement of an increase in intensity of lines appropriate to the new phase while the corresponding decrease was measured in lines of the old phase. The crystal was assumed to be in thermal equilibrium during these measurements. At both sides of the 220°C transition and the high-temperature side of the 430°C transition the structure change occurred in range of temperature so small that the intermediate intensities were not seen. Then the change in frequencies alone served as an indicator of phase transitions. The magnitude of frequency changes in the spectrum can be seen in Fig. 4.

In Table I will be found comparative data on the transition temperatures as found by x-ray, optical,[2] and dielectric measurements,[3,4] and in our experiments.

TABLE I. Phase transition temperatures (°C) in $KNbO_3$ as measured by various methods.

Method	rhombohedral—	orthorhombic —	tetragonal —	cubic
X-ray, optical[a]	—	225	435	
Dielectric constant[b]	−55 to −10	210 to 220	410 to 435	
Nuclear magnetic resonance	−52 to −27	207 to 222	426 to 431	

[a] See reference 2.
[b] See references 3 and 4.

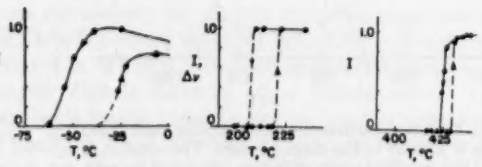

FIG. 5. Hysteresis effects in the $KNbO_3$ magnetic absorption spectrum near the three phase transitions.

The rhombohedral-orthorhombic transition occurs upon heating at −27°C and the reverse transition occurs upon cooling at −52°C. Here the intensity of the absorption lines was used as a criterion of structure change. The temperatures were held constant to ±2°C or better during the runs, which were 20 to 30 minutes long. The line intensity changes gradually over about a 12° range upon heating and about a 20° range upon cooling. This is in contrast to abrupt changes in the dielectric constant seen at this transition.[4] A plot of line intensity *vs* temperature appears in Fig. 5.

This transition showed a peculiar annealing effect. At room temperature, the spectrum (a) in Fig. 6 was seen. When the crystal was cooled to −196°C, spectrum (b) was observed. The crystal was then warmed rapidly to room temperature and spectrum (c) was observed. The original (a) spectrum had vanished and a vestige of the (b) spectrum remained, indicating that the low-temperature rhombohedral phase persisted in part. The room-temperature orthorhombic phase is not visible in (c). The crystal was then recooled to −196°C and the spectrum (b) appropriate to the rhombohedral

phase reappeared. Then, when the crystal was heated *slowly* to room temperature, the rhombohedral spectrum disappeared and the original orthorhombic spectrum (a) reappeared in (d) with reduced intensity. The crystal was originally clear, but the above treatment produced a cloudy appearance indicating the presence of gross imperfections in the crystal. The crystal was then used for observations of high-temperature phase transitions where this annealing effect was not observed.

After the high-temperature runs were completed, the exact $-50°C$ transition temperatures were measured. Repeated thermal cycling through this transition increased the cloudiness and actually caused minor splittings in the crystal surface. The persistence of the rhombohedral pattern above $-50°C$ was not again observed after the first runs shown in Fig. 6. Apparently a serious fracturing took place throughout the crystal so that it never completely regained the original structure it had before the first cooling to $-196°C$.

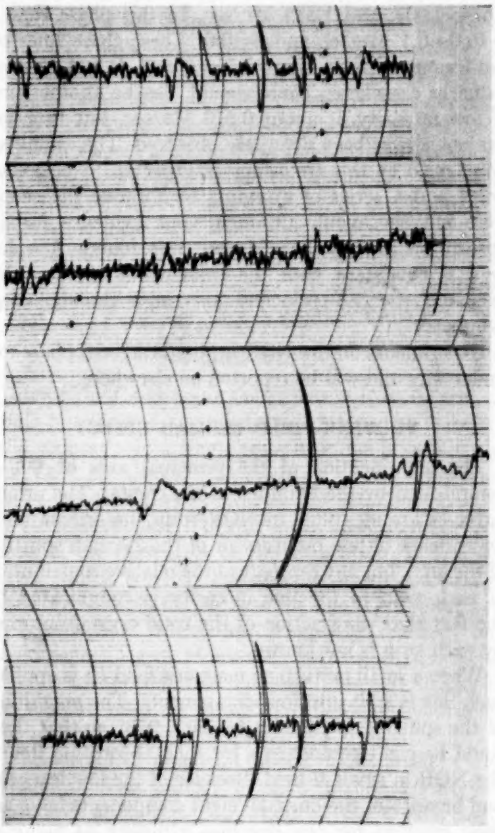

FIG. 6. Partial magnetic absorption spectrum at a single orientation and at temperatures above and below the orthorhombic-rhombohedral transition. (a) 27°C, (b) −196°C, (c) 27°C after rapid heating, (d) 27°C after recooling to −196°C and subsequent slow heating.

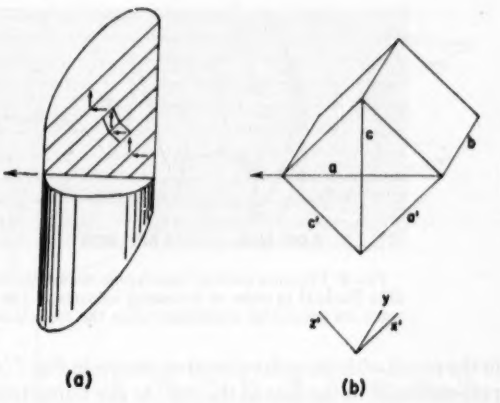

FIG. 7. (a) Cut-out section of the single crystal II, showing direction of laminar twinning. Arrows indicate the polar direction. Two adjacent unit cells are also indicated. (b) Orthorhombic unit cell referred to monoclinic axes $a, b, c. a', c'$ include the obtuse angle 90° 21′, not drawn to scale here; a and c are orthorhombic cell edges.

The orthorhombic-tetragonal transition, Fig. 5, occurs at $222°\pm3°C$ upon heating and at $207°\pm3°$, on cooling. Here the line intensities change less gradually than in the $-50°$ transitions. Within a range of 5°C, the new lines appeared at full strength and the old lines disappeared. In these runs, the temperature was held constant to $\pm2°$ and did not vary faster than about 0.2°C/min. Each run required several minutes.

The transition at the Curie point occurs at $430\pm1°$ upon heating and at $425\pm2°$ upon cooling (Fig. 5). The spectrum changes were observed while the temperature changed less than 1°C per minute. Upon heating, the transition covers a range of less than 2°C and, upon cooling, the transition covers a range of about 7°C.

Since considerable importance may be attached to the behavior of the crystal over the whole temperature range of a single phase, the splitting $\Delta\nu$ of one satellite line from the Nb NMR frequency was measured as a function of temperature throughout the tetragonal phase. $\Delta\nu$ was found to be a smoothly varying function of T up to within 5° of the Curie temperature, in which range about 50 percent of the change in $\Delta\nu$ occurs. This rapid change indicates a discontinuity in $\nabla\boldsymbol{E}$ and we therefore suppose that the Curie-point transition is a first-order transition.

It will be interesting to compare the relative change in $\Delta\nu$ with the lattice-constant values $(c/a-1)$ and with values of spontaneous polarization in the tetragonal phase, when reliable values of c/a and P_s are available.

V. PURE QUADRUPOLE SPECTRUM

The pure NQR was observed in the crystal (I) described in Sec. IV as well as in another single crystal (II) which had not been subjected to the fracturing effects of the $-50°C$ transition. Crystal II was placed

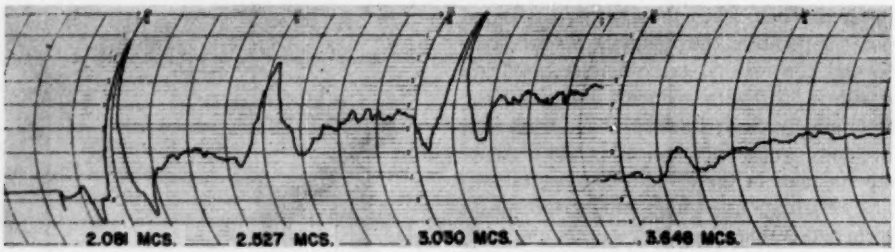

FIG. 8. The pure nuclear quadrupole resonance absorption spectrum at 25°C. The lines are labeled *A* through *D* in Table II in order of increasing frequency. The symmetrical wings on the negative side of the no-resonance trace are caused by absorption when the modulating field is on.

in the rf coil with the polar direction, shown in Fig. 7(a), perpendicular to the axis of the coil. In the unfractured crystal II, four lines, Fig. 8, appropriate to a spin of 9/2, were found at the frequencies given in Table II. The temperature of the crystal was slightly higher than 25°C because of heat generated by the modulating current. A small-temperature coefficient for the resonance frequencies was noticed and is now being studied.

The measured frequencies were fitted to a graph of frequency ratios *vs* axial asymmetry parameter η, and the energy levels for $I=9/2$ as calculated by Cohen[12] (Fig. 9) were used to plot Fig. 10. In Fig. 10 the ratio of the second-lowest frequency to the lowest frequency was plotted as one line. This procedure was followed for each pair of lines at successively higher frequencies. The transition frequencies associated with each ratio are shown on the graph. The measured frequency ratios intersect the calculated ratios in a straight line at constant $\eta=0.806\pm0.002$. From the measured frequencies and the energy-level parameter of Cohen, the quadrupole coupling constant is found to be $e^2qQ/h=23.120\pm0.05$ Mc/sec. With the fit of measured and calculated frequency ratios, the transitions can be identified. The identification is shown in Table II. These lines correspond to $|\Delta m|=1$. Possible $|\Delta m|=2$ lines would be predicted[12] at 4.62 and 5.14 Mc/sec with lower intensities. However, careful search over the range from 3.7 to 5.7 Mc/sec did not show these lines.

TABLE II. Identification of zero field nuclear quadrupole spectrum of Nb^{93} in $KNbO_3$.

Crystal structure	Line	Frequency (Mc/sec)	Measured ratio	Calculated ratio $\eta=0.806$	Identification
Orthorhombic	*D*	3.648	1.204	1.204	(9/2, 7/2)
	C	3.030	1.198	1.196	(3/2, 1/2)
	B	2.527	1.214	1.213	(7/2, 5/2)
	A	2.085			(5/2, 3/2)
Rhombohedral	*H*	2.674	1.335	1.333 ($\eta=0.0$)	(9/2, 7/2)
	G	2.004	1.503	1.500	(7/2, 5/2)
	F	1.335			(5/2, 3/2)

The NQR in the rhombohedral phase was observed in crystal I at −196°C. Before cooling this crystal, the fractured one, the NQR was observed at room temperature and found to agree with crystal II, which has never been taken through the −50°C phase transition. At −196°C, absorption lines are seen in crystal I at 2.674, 2.004, and 1.335 Mc/sec. In this phase $e^2qQ/h=16.0\pm0.1$ Mc/sec and $\eta=0.0$. These three lines fit the frequency ratio chart at $\eta=0$ and do not fit consistently elsewhere. There should also be another line of low intensity at about 0.670 Mc/sec, but this line has not as yet been definitely observed. The signal-to-noise ratio at this frequency is expected to be about unity and a series of attempts to improve the signal were not successful, although some evidence for an absorption around 0.68 Mc/sec was found. A value $\eta=0$ is consistent with the coincidence of the polar axis and the ∇E principal axis in a rhombohedral symmetry.

Experiments on the NQR in the tetragonal phase are under way and will be reported on elsewhere.

VI. WEAK-FIELD ZEEMAN EFFECT

The identification of the principal axes of ∇E is complicated by the twinning of the crystal. The principal axes are identified in NQR from the orientational dependence of line intensity or of the Zeeman splitting of the lines, but any estimate of the relative contribution of each twin to the line intensity is complicated by the fact that the fraction of the total crystal occupied by each twin is not known.

When a small perturbing magnetic field H_0 is applied, each line is split into four components. The magnitude of the splitting is different for each twin, so that there could be eight components for each absorption line in the NQR in small *H* field. Because of the low intensity and breadth of the lines, all eight components have not been resolved for any one line, although as many as four have been observed.

The transition having the simplest Zeeman dependence is the (9/2, 7/2) 3.65-Mc/sec line. Although this is the weakest line of the four, a measurable symmetric

[12] M. H. Cohen, preceding paper [Phys. Rev. 96, 1278 (1954)].

splitting was observed. For $I=9/2$ and $\eta=0.8$ as for Nb in $KNbO_3$, Cohen's results may be used to show that the Zeeman splitting for the (9/2, 7/2) transition has essentially only θ dependence, where θ is the angle between the Zeeman field H_0 and the z principal axis of ∇E. The calculation gives

$$|\Delta\nu| = (g\beta H_0/h)(4.47\pm3.34)|\cos\theta|$$

as the splitting from the pure NQR. The + and − signs go with the outer and inner satellites, respectively. For Nb^{93}, $g\beta/h=1.045$ Kc/sec/oersted. In a dc field of 89 oersteds, the inner satellite lines followed the relation,

$$|\Delta\nu| = (100\pm6)|\cos\theta| \text{ Kc/sec},$$

which is within 6 percent of the predicted dependence at all angles. Analysis shows that the z principal axis of ∇E lies within 5° of the plane $a'c'$ in Fig. 6 and within 20° of the polar direction of the crystal. This Zeeman pattern was somewhat complicated by an outer component of the (3/2, 1/2) transition which, for this H_0, lies near the (9/2, 7/2) frequency. This satellite, which was of low intensity and tended to broaden the (9/2, 7/2) lines, was a major cause of uncertainty in the assignment of the direction of the z axis of ∇E.

If the polar direction of one domain is the z direction, the z direction of the other domain will always be at 90° with respect to H_0 and the modulating field for the axis of rotation used. Thus the absorption line from the latter domain is not split by either Zeeman or modulation fields, and is not seen at all.

Attempts to analyze the splitting of other lines have so far proved unsatisfactory. No Zeeman splittings have yet been tried in the rhombohedral phase.

VII. LINE WIDTHS

Above the Curie point the structure is cubic and, as would be expected, the quadrupole interaction is drastically reduced and a single resonance line is seen at the Nb NMR frequency. The intensity of this absorption line is about 5 times as large as the individual lines in the tetragonal phase. The line width, measured between peaks of the derivative of the absorption, is 5.0±0.5 kc/sec, which is about half the line width observed in the tetragonal phase. Because the line is narrower and the quadrupole interaction is greatly reduced, one would expect a greater intensity increase than a factor of 5. It is expected that imperfections and strains in the crystal resulted in enough random quadrupole interactions to "wash out" some of the signal.

The calculated magnetic dipolar width given by the formula of Van Vleck[13] is from 1.6 to 3.6 kc/sec, depending upon the orientation of the crystal axes. Since an arbitrary orientation was used, the direction of the crystal axes was not known. The observed extra width is partially attributed to random static quadrupole interactions from crystal imperfections. Also, since the resonance could not be saturated with the available rf power from the spectrometer, it is assumed that the spin-lattice relaxation time T_1 is rather short, and that there is probably a line-width contribution from the relaxation mechanism. The contribution to T_1 from thermally induced random quadrupole interactions[14] has been estimated, and this is in reasonable agreement with the observed width, which indicates that T_1 at 450°C is perhaps as short as 10^{-4} sec. The large intensity of the lines at −196°C [Fig. 6(b)] is also evidence for the existence of a strong spin-lattice relaxation mechanism.

The line widths in zero field were found to be three to four times the widths at 5000 oersteds. In the orthorhombic phase the zero field widths at half maximum were 27 kc/sec, 45 kc/sec, 30 kc/sec, 45 kc/sec for lines A, B, C, D, respectively, in Table I, and in the

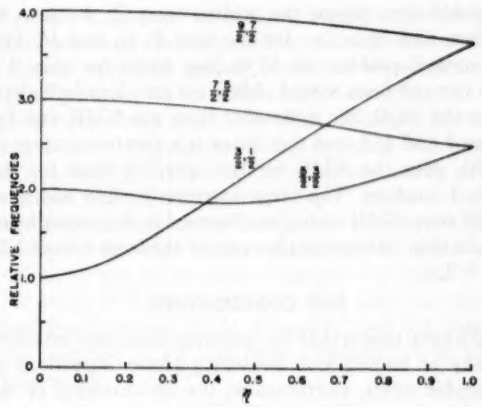

FIG. 9. Pure quadrupole absorption frequencies calculated as a function of the asymmetry parameter, η. (See reference 12.) The ordinates are in units of $6e^2qQ/4I(2I-1)h$.

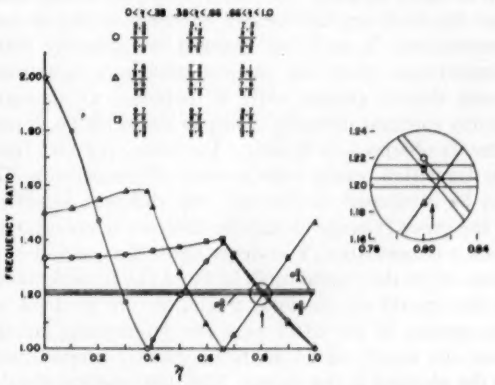

FIG. 10. Determination of the asymmetry parameter, η, from measured frequency ratios. The insert at the right is an expanded view in the region of $\eta=0.8$.

[13] J. H. Van Vleck, Phys. Rev. 74, 1168 (1948).

[14] N. Bloembergen, *Nuclear Magnetic Relaxation* (Martinus Nijhoff, The Hague, 1948), pp. 118–121.

rhombohedral phase the widths were 25 kc/sec, 30 kc/sec, and 30 kc/sec for the lines F, G, and H. The theoretical problem of NQR line width for spin 9/2 has not yet been solved. Abragam and Kambe[15] show that the NQR line is broader than the NMR line for spins 1 and 3/2, and that there is a greater increase in width over the NMR for the spin 3/2 than for the spin 1 nucleus. The large increase in line width of NQR over NMR which we observed in this experiment might then be expected because of the large spin of Nb, $I=9/2$.

VIII. CONCLUSIONS

We have shown that the quadrupole interaction offers a way of finding and measuring phase transitions in noncubic solids. Furthermore, the measurement of the quadrupole coupling provides a new piece of information, useful in calculations of the microscopic structure of such solids.

With good temperature control, accurate phase-transition temperatures, and associated hysteresis effects can be measured. In addition, information can be gained on the qualitative nature of phase transitions. The quadrupole interaction, being very sensitive to crystal structure, shows whether the transition occurs continuously or discontinuously. A gradual change in quadrupole interaction would indicate a second-order transition, while a discontinuity in the interaction would indicate that the transition was of the first order.

In all of the phase transitions observed the frequency changes and, hence, the quadrupole interaction changes were abrupt. However, the changes in line intensity were not always discontinuous. In the -50°C transition the intensity changed gradually over a range, δT, of about 15°C, Fig. 5. This effect was also seen at the 430°C transition where $\delta T \sim 5$°C. The intensity change in the 220° transition occurred within a 5°C range.

This means that the transition of any given unit cell or small region in the crystal is discontinuous, and that the whole crystal does not change structure at one temperature. If each cell changed continuously with temperature, then the nuclear resonance spectrum would show a gradual shift in frequency at approximately constant intensity. This, as stated above, is not what is observed in $KNbO_3$. Therefore, the fact that the transition occurs over a range of temperature δT can be attributed to the fact that different localities of the crystal change at slightly different temperatures. Such a temperature dependence upon the position of a given cell in the crystal could be caused by imperfections in the crystal or, possibly, a temperature gradient in the crystal. If the latter were the determining factor, then one would expect δT to be directly proportional to the gradient in the crystal. Also, the gradient should be, to first approximation, proportional to the difference between the transition temperature and the room temperature. This would give a much bigger δT for the 430°C transition than for the -50°C transition. This certainly is not the case in these measurements.

Local activation energies for nucleation could depend on imperfection concentration. Then if there is some average energy E_I, associated with an imperfection, it will have a greater relative effect on a transition for which the normal activation energy is small. This mechanism would suggest that the temperature range δT decreases as the activation energy increases. The latent heats of these transitions have been measured,[4] and it is found that the latent heat increases as the transition temperature increases. This would predict a decrease in δT as T increases, in agreement with the observations. Similar arguments may also apply to the widths ΔT of the temperature hysteresis curves.

The problem of accounting for the observed quadrupole coupling for Nb in $KNbO_3$ in a nearly cubic structure must now be faced. Investigations of atomic hyperfine structure of Nb do not show a deviation from the interval rule because of quadrupole interaction.[16] As yet no upper limit, based on a calculated field gradient in atomic Nb, has been placed on the quadrupole moment of Nb. We estimate however, from the plots of Townes[6] and of Murakawa,[7] that Q is of the order of 0.1×10^{-24} cm^2. In order to account for the measured quadrupole coupling in the orthorhombic phase of $KNbO_3$, then, the field gradient eq should be about 3×10^{15} esu/cm^3.

Also, any model for this crystal should give an estimate of η and for the direction of the principal axes of ∇E as well as for the magnitude of eq.

In the orthorhombic phase, the calculated field gradient produced a charge of 2 esu in the position of the each six nearest-oxygen neighbors to Nb does not agree with the experimental measurements. The calculated gradient is about $eq\sim2\times10^{13}$ esu/cm^3, which is too small by a factor of about a hundred. The calculated principal axis of the gradient caused by the oxygens is perpendicular to the rhomb face and the axial asymmetry parameter is about 0.5, neither of which results agrees with experiment. This calculation was made for both a displaced and an undisplaced Nb ion.

Another kind of lattice-point calculation based on the covalent bonding suggested by Megaw[17] was tried. She suggests that Nb forms covalent tetrahedral bonds with the four oxygen atoms nearest to the displaced position of Nb. In this calculation it was assumed that there is an average concentration of charge halfway between niobium and each oxygen atom. Approximately the right magnitude, 2×10^{15} esu/cm^3, for eq results, but the asymmetry parameter, $\eta\sim0.1$, and the principal axis of ∇E is perpendicular to the rhomb face. So we see that neither of these crude approximations to the measured field gradient fits the observed data at all. An important conclusion to be drawn is that simple lattice-point calculations for ∇E in such a complicated

[15] A. Abragam and K. Kambe, Phys. Rev. 91, 894 (1953).

[16] W. W. Meeks and R. A. Fisher, Phys. Rev. 72, 451 (1947); F. A. Jenkins (private communication).

[17] H. Megaw, Acta Cryst. 5, 739 (1952).

crystal are not capable of giving even qualitative results. Furthermore, it is not expected that a complete lattice-point calculation using appropriate dipole-field factors will be significantly better. It is therefore felt that the large size of the quadrupole coupling which we observe can only be the result of covalent bonding, where the ∇E is generated by valence electrons which penetrate the ion core. Magnification effects[18] may contribute significantly.

It should be pointed out that the large observed quadrupole coupling in the tetragonal phase and the single magnetic resonance line in the cubic phase are inconsistent with the Mason-Matthias[19] model of six equilibrium positions for the central ion.

Perhaps a better correlation between the quadrupole interaction and ferroelectric properties could be made if there were more data available on the ferroelectric properties in the tetragonal phase. A comparison of this interaction, with the lattice constants $(c/a-1)$ and with the spontaneous polarization (P_s) would be appropriate. These properties are well known for $BaTiO_3$ but not for $KNbO_3$. The $(c/a-1)$ measurements involve extensive x-ray work and the measurement of P_s seems to be inhibited by the high conductivity of $KNbO_3$ near the Curie temperature[4] as well as by the twinning.

In order to indicate the range of applicability of the nuclear resonance techniques to problems of this sort, we note that the Curie temperature of $NaNbO_3$ is not known. (X-ray measurements[2] indicate a cubic structure above 470°C, while optical data would make this temperature 640°C.) Furthermore, there is evidence that this substance may be antiferroelectric. Both of these questions can, in principle, be resolved by doing a careful series of nuclear resonance experiments. It will not be easy to do satisfactory experiments on the nuclear resonance in $BaTiO_3$. First, it would be necessary to grow crystals containing enriched Ti isotopes. Second, large $BaTiO_3$ single crystals are usually grown with too much paramagnetic "dope" to expect to see good nuclear resonances. Third, even these crystals are usually in the form of thin plates, which is not convenient for use in the nuclear resonance rf coils.

A study of $YAlO_3$ would be useful since the nuclear quadrupole moment of Al is known,[20] and the quadrupole coupling of Al has been measured[21,22] in other compounds.

[18] Foley, Sternheimer, and Tycko, Phys. Rev. **93**, 734 (1954).
[19] W. P. Mason and B. T. Matthias, Phys. Rev. **74**, 1622 (1948).

ACKNOWLEDGMENTS

We are happy to express our thanks to Professor C. Kittel, who suggested that we undertake this problem, for many stimulating discussions, and to Dr. M. H. Cohen for his continuing assistance with the theoretical work. We are greatly indebted to Dr. E. A. Wood and Mr. J. P. Reimeika of the Bell Telephone Laboratories for providing us with the $KNbO_3$ crystals and to Professor A. Pabst of the Department of Mineralogy at the University of California for making an x-ray analysis of a small chip of one of the crystals. Mr. D. F. Abell assisted with some of the measurements on the high-field rotation pattern.

[20] Davis, Feld, Carrol, Zabel, and Zacharias, Phys. Rev. **76**, 1076 (1949); Hin Lew, Phys. Rev. **76**, 1086 (1949).
[21] R. V. Pound, Phys. Rev. **79**, 685 (1950).
[22] Hatton, Rollin, and Seymour, Phys. Rev. **83**, 672 (1951).

Upper Limit on the Neutrino Magnetic Moment*

C. L. COWAN, JR., F. REINES, AND F. B. HARRISON
University of California, Los Alamos Scientific Laboratory, Los Alamos, New Mexico

(Received August 18, 1954)

A liquid scintillation detector and neutrinos from a fission reactor were employed to set a new upper limit of 10^{-7} Bohr magnetons for the neutrino magnetic moment.

IF a neutrino possesses a magnetic moment, then on passing through matter it will undergo elastic collisions with atomic electrons. The cross section $\sigma(W)dW$ (cm²) for the target electrons to appear in an energy range dW at energy W as a result of such a process has been calculated by Bethe[1] to be

$$\sigma(W)dW = Af^2 \frac{1}{1+W}\left(1-\frac{W}{E}\right)\frac{dW}{W}, \qquad (1)$$

where A = classical electron area (2.5×10^{-25} cm²) obtained by taking $r_0=e^2/mc^2$, E = energy of the incident neutrino in units of the electron rest energy (mc^2 units), W = target electron energy (in mc^2 units) resulting from collision ($W\gg$ionization potential), and f = neutrino magnetic moment in Bohr magnetons (Bm). The rest energy of the neutrino is taken to be negligible compared to the incident neutrino energy.[2]

On the basis of Bethe's theory, Nahmias[3] has shown experimentally that $f<2\times10^{-4}$ Bm, corresponding to a cross section less than 10^{-30} cm² per "air atom" for neutrinos from radium. Barrett,[4] in an experiment similar to that of Nahmias, but using tritium, obtained an upper limit of 4×10^{-34} cm²/electron, corresponding to $f<10^{-5}$.

Houtermans and Thirring,[5] using data of Kulp and Tyron[6] and assuming that the sun provides a flux at the earth of 6×10^{10} neutrinos/cm² sec, deduce the neutrino collision cross section to be $<8\times10^{-34}$ cm²/"air atom," giving $f<2\times10^{-6}$ Bm. Crane[7] rules out cross sections down to 10^{-36} cm² on the basis of geophysical arguments, with the result that $f<2\times10^{-7}$ Bm.

In the course of an experiment to measure backgrounds for use in an improved version of the free neutrino experiment,[8] data were collected which permit the setting of a new upper limit on the neutrino magnetic moment.

The neutrinos from the reactor were incident on a liquid scintillation detector which provided electrons as targets for the neutrinos. In this detector the liquid is viewed by several 5-in. DuMont photomultiplier tubes. The counting rate difference due to the reactor in the 0.44–2 Mev energy range was $30(\pm4)$ counts/sec. In order to obtain an upper limit on the neutrino-electron interaction via a neutrino magnetic moment, we attribute this difference to the neutrino. The detection efficiency for electrons in this energy range is very nearly unity. We assume, perhaps conservatively, that the mean energy of the fission neutrinos is 2 Mev. Integrating Eq. (1) from the upper limit E to a lower limit W_0, we obtain a cross section for these recoil electron energies,

$$\sigma = Af^2 \ln\left[\frac{E}{W_0}\left\{\frac{1+W_0}{1+E}\right\}^{(1+1/E)}\right]. \qquad (2)$$

Inserting the energy limits $E=4$, $W_0=0.86$, and the value of A, we find

$$\sigma = 7.5\times10^{-26} f^2 \text{ (cm}^2\text{)}. \qquad (3)$$

Combining this equation with numbers for the estimated net reactor neutrino flux, the upper limit on the observed difference in counting rate, and the number of target electrons, we obtain $f<10^{-7}$ Bm. This result is $\sim10^3$ short of the theoretical estimate,[8] $f_{th}\sim10^{-10}$ Bm, based on the virtual dissociation of the neutrino into neutron, antiproton, and electron.

The data obtained can also be used to establish an upper limit on the electron-neutrino interaction without specifying the origin of the interaction. Table I gives upper limits to the cross section for the scattering of fission neutrinos by electrons resulting in an electron energy in the ranges cited. It seems likely that a further reduction in this interaction cross section will be made incidental to the improved neutrino experiment mentioned above.

TABLE I. Upper limit on electron neutrino interaction for fission neutrinos resulting in the production of electrons with energies above those listed.

Minimum energy in units of mc^2	$\sigma\times10^{46}$ (cm²)
0.45	14
0.9	6
1.3	3
1.7	2

* Work performed under the auspices of the U. S. Atomic Energy Commission.

[1] H. A. Bethe, Proc. Cambridge Phil. Soc. **31**, 108 (1935).
[2] L. M. Langer and R. J. D. Moffat, Phys. Rev. **88**, 689 (1952); Hamilton, Alford, and Gross, Phys. Rev. **92**, 1521 (1953).
[3] M. E. Nahmias, Proc. Cambridge Phil. Soc. **31**, 99 (1935).
[4] J. H. Barrett, Phys. Rev. **79**, 907 (1950).
[5] F. G. Houtermans and W. Thirring, Helv. Phys. Acta **27**, 81 (1954).
[6] J. L. Kulp and L. E. Tyron, Rev. Sci. Instr. **23**, 296 (1952).
[7] H. R. Crane, Revs. Modern Phys. **20**, 278 (1948).
[8] F. Reines and C. L. Cowan, Jr., Phys. Rev. **92**, 830 (1953); Cowan, Reines, Brousseau, Harrison, and Ronzio, Atomic Energy Commision Report AECU-2924 (unpublished).

We wish to thank M. P. Warren for help in making the measurements at Savannah River, A. T. Brousseau for his valuable assistance with the electronics, and the Savannah River Plant personnel of the du Pont Company for their cooperation.

Energies of the Radiations from Ce^{144} and Pr^{144}†

J. M. Cork, M. K. Brice, and L. C. Schmid
Department of Physics, University of Michigan, Ann Arbor, Michigan

(Received August 16, 1954)

With scintillation and magnetic photographic spectrometers the energies of the gamma rays from Ce^{144} have been re-evaluated. Several previously reported gamma rays are believed not to exist, while certain others not reported are found to occur. Gamma energies of 33.4, 40.8, 53.2, 59.0, 79.9, 95.0, 133.5, and 145.2 kev are found. Coincidence measurements together with a consideration of energy relationships indicate a reasonable level scheme for the Pr^{144} nucleus. The energies of the three high-energy gamma rays in Nd^{144} following beta decay of Pr^{144} are 0.688, 1.49, and 2.18 Mev. Some relative intensity measurements are made of the conversion electron lines, leading to a prediction of the multipolarities for three of the gamma transitions. The beta spectrum from Ce^{144} resolves into components with upper energies of 327, 258, and 160 kev. The beta radiation from Pr^{144} has an upper energy limit at 3.12 Mev with a lower energy component whose maximum energy is 0.92 Mev.

A LONG-LIVED radioactive cerium isotope was first isolated from fission products by Hahn and Strassman[1] in 1940. Many subsequent investigations[2] assigned the activity to the isotope of mass 144 and fixed the half-life at about 300 days. No evidence for the existence of gamma rays was presented in the earlier reports. When stronger sources became available from the Oak Ridge National Laboratory it was found that several gamma rays accompany the beta decay of Ce^{144} to Pr^{144}. The Pr^{144} decays mainly by beta emission (~3 Mev) with a half-life of 17 minutes to the ground state of Nd^{144}. Weak high-energy gamma radiation accompanies this disintegration through a competing process with a very low percentage.

In the present investigation a fission source of high specific activity was used with both scintillation and magnetic photographic spectrometers to check the previously reported results. The energies of the observed electron conversion lines are presented in Table I, along with their interpretations. By carefully considering each electron line in relation to its neighboring lines, it now appears reasonably certain that in several cases the gamma energies are not correct as previously published. In Table II, the results of previous investigations are shown together with the conclusions of the present investigation.

It seems quite definite that gamma rays of energy 46.8, 60.3, 100, and 231 kev do not exist and that others at 59.0 and 145.2 do occur. This change in interpretation may be illustrated by the electron lines at 52.2, 53.0, and 57.6 kev which form a reasonable L_1, L_3, M group for a gamma ray at 59.0 kev. Previously the line at 53 kev was not resolved and had been assumed to be simply a K line for a gamma ray at 95 kev. Similarly the M line at 57.6 kev had been assumed to be a K line for a gamma ray at 100 kev. The line at 53 kev is as strong as that at 52.2 kev so it is probably both an L_3 line for the 59.0-kev gamma as well as a K line for the 95.0-kev gamma radiation.

There is evidence for Auger lines at low energy, but the electron line at 26.6 kev is too low in energy to be of this nature. The electron lines which yield the gamma ray at 40.8 kev could conceivably be of Auger origin as they correspond in energy to the difference in Pr work functions, K minus L minus M, and K minus M minus M. However, if these rather strong electron lines are of this nature then other stronger lines should be expected but are not found at lower energies, corresponding to such more probable transitions as K minus L_1 minus L_2.

TABLE I. Electron energies from Ce^{144}.

Electron energy	Interpretation	Energy sum	Electron energy	Interpretation	Energy sum
26.6 kev	L_1 (59)	33.4 kev	57.6 kev	M	59.1 kev
28.5	Auger KL_1L_1		73.1	L_1	79.9
31.7	M	33.4	73.9	L_3	79.9
34.0	L_1	40.8	78.4	M	79.9
38.1	K	80.1	88.2	L	95.0
39.3	M	40.8	91.6	K	133.6
46.4	L_1	53.2	103.2	K	145.2
52.2	M	53.7	126.7	L	133.5
or	L_1	59.0	131.9	M	133.4
53.0	L_3	59.0	138.6	L	145.4
or	K	95.0	143.7	M	145.3

TABLE II. Summary of gamma energies from Pr^{144}, in kev.

EJK[a]	Observer KC[b]	LJK[c]	PC[d]	Present
33.6	34.0		33.7	33.4
41.0	41.3			40.8
	46.8			
53.0	53.7	54.7	53.5	53.2
			60.3	59.0
80.2	80.9	79.4	80.7	79.9
94.8	95.0			95.0
99.6	100.5		100.3	
134.0	134.5	134	134.2	133.5
				145.2
		231		

† This investigation received the joint support of the U. S. Atomic Energy Commission and the Office of Naval Research.

[1] D. Hahn and F. Strassman, Naturwiss. **28**, 543 (1940).

[2] See Hollander, Perlman, and Seaborg, "Table of Isotopes," Revs. Modern Phys. **25**, 469 (1953).

[a] Emmerich, John, and Kurbatov, Phys. Rev. **82**, 968 (1951).
[b] H. Keller and J. Cork, Phys. Rev. **84**, 1079 (1952).
[c] Lin-Sheng, John, and Kurbatov, Phys. Rev. **85**, 487 (1952).
[d] F. Porter and G. Cook, Phys. Rev. **87**, 464 (1952).

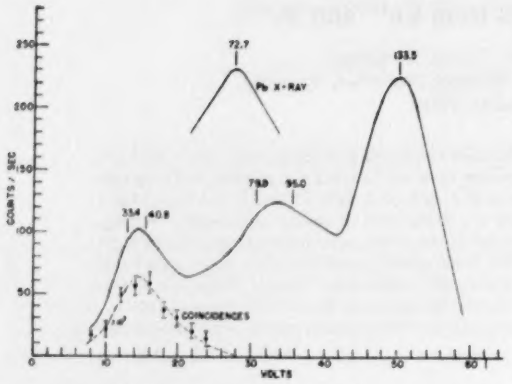

FIG. 1. Low-energy gamma rays in Pr^{144}, scintillation spectrometer.

The beta spectrum for Ce^{144} has been resolved by the aid of the double-focusing, constant-radius, magnetic spectrometer. The high-energy electrons due to the decay of Pr^{144} are always present and must be subtracted from the over-all distribution. The residual curve is complex and yields components with upper energy limits at 327 ± 7 kev and 160 ± 15 kev, whose relative abundances are 75 percent and 20 percent, respectively. There is good indication of another component with an upper energy limit of 258 ± 15 kev and a relative abundance of about 5 percent. There could possibly still be some lower-energy component that is not seen because of the many conversion electrons.

With the scintillation spectrometer the low-energy peaks are not completely resolved. The 133.5-kev peak is relatively strong as shown in the singles curve of Fig. 1. The gamma-gamma coincidence curve between the 133.5-kev gamma ray and others at lower energies is also shown in Fig. 1. It is quite apparent that coincidence exists and hence the upper energy level representing the Pr^{144} nucleus must be higher than 134 kev as had been previously proposed.[2] The 133-kev gamma is in coincidence with both the 33- and 40-kev gammas.

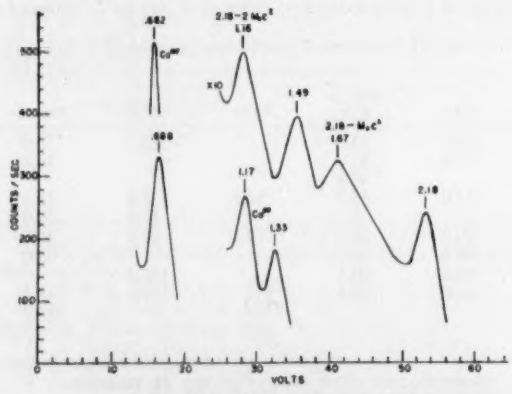

FIG. 2. High-energy gamma rays in Nd^{144}, scintillation spectrometer.

The 80-kev peak is also found to be in coincidence with both the 33- and 40-kev gamma with some evidence for a coincidence peak at 145 kev.

For the 133.5-kev gamma ray the K/L conversion ratio is found to be 5.8 ± 0.5 and the L_3/L_1 ratio is small (~0.1) with no L_2 line present. It thus appears that this corresponds to an $M1$ transition although the K/L ratio is less than that expected from the empirical curves of Goldhaber and Sunyar. For the 79.9-kev gamma ray the K/L ratio is 3.0 ± 0.5 and the L_3/L_1 ratio is small (~0.15), so that this is probably an $M2$ transition. The 59.0-kev gamma ray has a K/L ratio smaller than unity. If the L_3 line did not have a double interpretation the L_3/L_1 ratio would be about unity, since the L_3 line is almost as strong as the L_1 with no L_2 line present. This would then be a high-order magnetic multipole transition, probably designated as

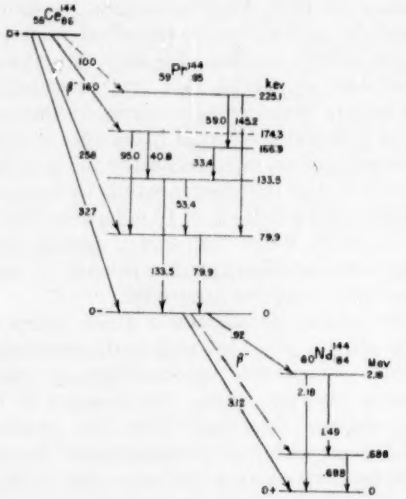

FIG. 3. Proposed nuclear level scheme for mass 144.

$M3$. In this event it should not be a prompt emission but the half-life of the initial state should be of the order of 100 seconds. This is presumably not the case.

No conversion electron lines are observed that have energy differences corresponding to that of the work functions for neodymium. It is quite certain that the 60-kev gamma previously reported does not exist in this nucleus. Scintillation spectrometer observations of the high-energy region confirm, with some adjustment in energies, the previous reports.[3] The singles curve shown in Fig. 2 for this region yields energies at 0.688, 1.49, and 2.18 Mev. For the 2.18-Mev gamma ray, peaks due to the loss of both single and double annihilation radiation quanta are apparent. The upper energy limit of the beta spectrum is found to be at 3.12 Mev, a value somewhat higher than the previously

[3] D. Alburger and J. Kraushaar, Phys. Rev. **87**, 448 (1952); C. Cook and W. Kreger, Bull. Am. Phys. Soc. **29**, No. 6, 20 (1954).

reported value of 2.97 Mev. A lower-energy component with a relative abundance of 1.5 percent has its upper energy limit at 0.92 Mev. No strong evidence appeared for the existence of a beta ray at an intermediate energy, as previously reported.[3]

The energies of certain gamma rays are observed to be equivalent to the sum of others, suggesting cross-over transitions. It is possible to postulate a reasonable nuclear level scheme for Pr^{144}, as shown in Fig. 3, which satisfies most of the observed data. The intensity relations as well as the coincidence data are about as would be expected from the level scheme.

PHYSICAL REVIEW VOLUME 96, NUMBER 5 DECEMBER 1, 1954

Slow Neutron Cross Sections of Gold, Silver, Indium, Nickel, and Nickel Oxide

R. G. Allen,* T. E. Stephenson, C. P. Stanford, and Seymour Bernstein
Oak Ridge National Laboratory, Oak Ridge, Tennessee

(Received March 1, 1954)

The total reflection and selective attenuation properties of mirrors for neutrons were used to obtain essentially higher order free reflections of a beam of reactor neutrons from a quartz crystal. An arrangement of mirror, crystal, and sample, in series was used to measure the total cross section of Au, Ag, In, Ni, and NiO as a function of neutron wave length over intervals in the region between 0.7A and 4.6A. The results on the strong absorbers Au, Ag, and In were analyzed into absorption and scattering contributions. The absorbers exhibited essentially the $1/v$ characteristic expected. The scattering and absorption cross sections of Au, Ag, and In are compared with previously reported values. For the strong scatterers Ni and NiO, the total scattering, ordered scattering, and disordered scattering cross sections, and the Debye temperature were derived from the energy dependence of the total cross section. The ordered scattering cross section per Ni nucleus was found to be 13.1 ± 0.3 barns. The capture and ordered elastic contributions were subtracted from the experimental curve of total cross section *vs* energy. This residual scattering function of energy was compared to that theoretically expected from a Debye independent-oscillator model and the one-phonon incoherent scattering approximation of Kleinman. In the case of Ni, at the longer wavelengths, both models fit the data well, and at the shorter wavelengths, where multiple phonon processes occur, the independent oscillator model continues to fit the data. For NiO, measurements fit the independent oscillator model at the shorter wavelengths, and lie above the values calculated from either model at the longer wavelengths. Additional measurements of the total cross section of NiO as a function of temperature would be needed to attribute the difference between measured and calculated values at the longer wavelengths definitely to inelastic scattering processes.

I. INTRODUCTION

THE development of high-intensity neutron sources, such as chain reactors, and the utilization of the wave properties of neutrons for diffraction from single crystals provide a relatively simple instrument, the neutron spectrometer, for obtaining nearly monoenergetic neutron beams of usable intensities. The intensity distribution in the neutron spectrum from slow neutron chain reactors is such that, for most commonly used crystals, higher order reflections from the crystal must be considered in certain regions of the spectrum. Bragg's law $n\lambda=2d\sin\theta$ states that for a fixed angle of incidence, wavelengths λ, $\lambda/2$, $\lambda/3$, $\cdots$, having energies E, $4E$, $9E$, $\cdots$, will be present in the beam reflected from a crystal. Since the energy spectrum from a chain reactor is approximately Maxwellian, the presence of the higher orders may not be troublesome at glancing angles corresponding to first order energies E greater than the most probable energy, because the neutron flux decreases rapidly with increasing energy. For energies less than the most probable energy, the presence of higher orders can be very troublesome. The higher order crystal reflections can be removed by use of the total reflection properties of mirrors. (We find that a mirror was used briefly for this purpose in 1945 by L. B. Borst and associates.[1])

The reflectivity of a plane mirror for neutrons of wavlength λ is given by

$$R=\left\{\frac{1-[1-(\lambda/\lambda_f)^2]^{\frac{1}{2}}}{1+[1-(\lambda/\lambda_f)^2]^{\frac{1}{2}}}\right\}^2, \tag{1}$$

where λ_f, the cut-off or critical wavelength is related to the glancing angle of incidence on the mirror, α, by the expression:

$$\lambda_f=\frac{\alpha}{(N\bar{f}/\pi)^{\frac{1}{2}}}. \tag{2}$$

Here, N is the number of nuclei per cm^3 of the mirror material and $\bar{f}$ is the average ordered (coherent) scattering amplitude, due regard being taken of the signs of the individual scattering amplitudes. For a fixed angle of incidence, wavelengths greater than the cut-off wavelength will be totally reflected, whereas the inten-

* Present address: Airforce Special Projects Office, P. O. Box E, Oak Ridge, Tennessee. This work was done at Oak Ridge National Laboratory in partial fulfillment of the requirements for the Ph.D. degree at the University of Texas, while the author was on active duty with the United States Air Force. This arrangement was made through the cooperation of the Oak Ridge Institute of Nuclear Studies.

[1] Borst, Ulrich, Osborne, and Hasbrouck, Atomic Energy Commission Report MDDC 15 (unpublished).

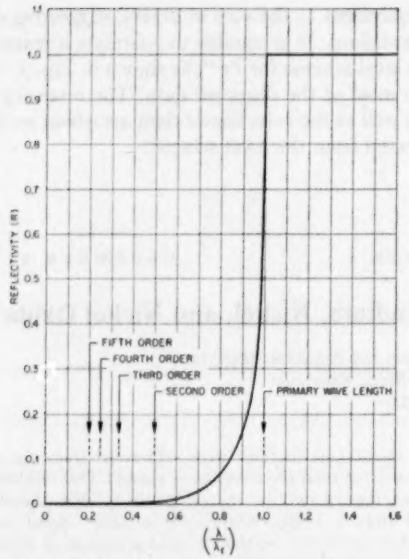

FIG. 1. Reflectivity of a mirror for neutrons incident at a fixed angle of incidence.

sities at wavelengths less than the cut-off wavelength will be attenuated. Equations (1) and (2) apply rigorously when absorption by the mirror is zero, but they are sufficiently accurate for most purposes when the average absorption cross section per atom is less than about 10^4 barns.[2]

Figure 1 gives the reflectivity as a function of λ/λ_f for the case of a perfectly collimated neutron beam. It shows the attenuation of the higher orders when the primary wavelength is taken as λ_f. In practice, the proper choice of mirror angle for acceptable elimination of the higher orders will be influenced by the intensity distribution of the incident spectrum. Figure 2 shows the counting rate obtained from the series arrangement of mirror and quartz crystal of Fig. 3, as a function of wavelength for several mirror angles of incidence α, using as the neutron source the approximately Maxwellian energy spectrum of the Oak Ridge Graphite Reactor. The curves of Fig. 2 can be used to select the proper mirror angle for a desired upper limit to the amount of higher order content in the beam reflected by the crystal.

II. DESCRIPTION OF APPARATUS

Figure 3 shows a schematic diagram of the arrangement of the spectrometer and mirror used for neutron cross section measurements in the wavelength region from 0.7 to 4.6A. In this arrangement, the beam is first collimated by a slit system in the reactor shield. The collimated beam strikes the mirror at a very small glancing angle, is reflected and passes through another slit before reaching the crystal. The beam from the crystal then passes through the sample and into the detector. The collimating slit system in the reactor limits the horizontal beam divergence to approximately ten minutes of arc. The slit adjacent to the crystal is used for further collimation and also to shield the crystal from any portion of the direct beam that was not reflected from the mirror. The additional collimation introduced by the slit at the crystal was variable depending upon the mirror angle and the beam intensity. The mirror consists of four Pyrex glass blocks, each 11.5 in. long by 3.75 in. high by 2 in. thick with the reflecting surfaces polished to optical flatness. These four Pyrex blocks were adjusted as accurately as possible to place the polished surfaces in the same plane. The mirror assembly is equipped with adjustments for positioning it in the beam and for varying the angle between the neutron beam and the mirror.

The spectrometer was an x-ray spectrometer modified to support the heavy paraffin shield surrounding the BF_3 detector tube. Angular settings were reproducible to within 0.5 to 1.0 min of arc. The entire spectrometer was mounted on ways so the crystal could be placed in the beam reflected at different mirror angles. The crystal used with the spectrometer was quartz, oriented to give reflections from the (100) planes. Neutron detection was accomplished with a $B^{10}F_3$ enriched proportional counter and a small $B^{10}F_3$ tube, located at the end of the mirror, served to monitor the beam. Because of the length of time required to obtain the data with the desired accuracy, features were incorporated into the equipment which allowed it to collect and record the required data automatically.

III. CRYSTALLINE SCATTERING OF NEUTRONS

The scattering of neutrons from polycrystalline material, as a function of neutron energy, may be described qualitatively as follows: For neutron energies large compared to the energy binding the atoms in the lattice, the scattering takes place from nuclei that are effectively free. In this case, the collisions are predominantly "inelastic," energy being exchanged with the individual nuclei in dislocating them from their

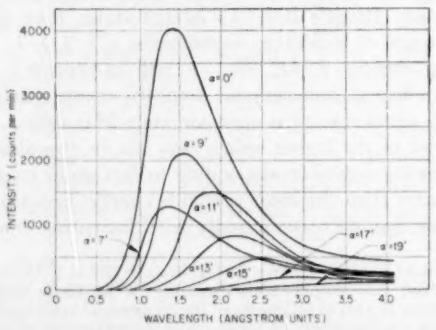

FIG. 2. Intensity reflected from series arrangement of mirror and quartz crystal as a function of neutron wavelength for various mirror angles (α).

[2] M. L. Goldberger and F. Seitz, Phys. Rev. 71, 294 (1947).

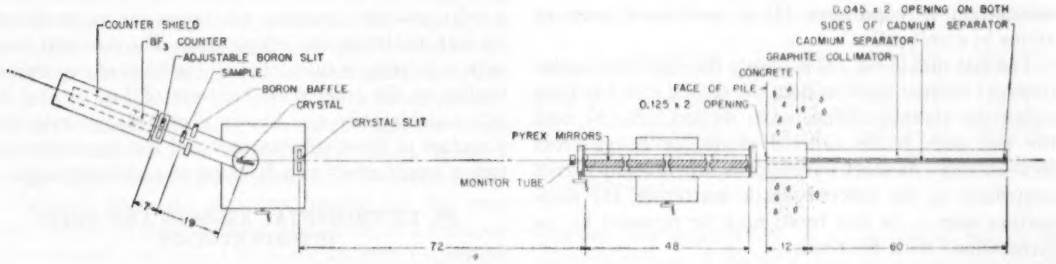

FIG. 3. Schematic diagram of the arrangement of the apparatus.

positions in the lattice. For neutron energies of the order of the crystal binding energy, the collisions are still predominately inelastic, but at these energies, the energy exchange occurs between the neutrons and the lattice as a whole through processes involving the emission or absorption of several sound quanta in the excitation or extinction of elastic vibrations of the crystal lattice. As the energy of the incident neutron decreases, the elastic scattering increases and inelastic scattering processes involving only single phonons predominate. In this energy region, the scattering is characterized by interference effects arising from coherent scattering by the crystal planes. These effects become quite appreciable for materials possessing large ordered (coherent) nuclear scattering cross sections and relatively small capture cross sections. For energies such that the neutron wavelength is greater than twice the maximum plane spacing for which crystal reflections are possible, the ordered elastic or Bragg scattering disappears. Finally, for sufficiently low energies, the incident neutrons have insufficient energy to excite crystal vibrations, but inelastic scattering is still present as a result of the absorption of phonons by the neutrons.

An expression for the total scattering cross section for slow neutrons can be obtained in a rather simple manner following the method used for x-rays[3] where the change in energy upon scattering is assumed negligible in comparison to the incident energy. In the case of neutrons, the effects of isotopes and nuclear spins must be included. In this approximation, a crystal composed of independent oscillators having the same average energy is assumed. Such a model is admittedly a crude approximation since the coupling between atoms is neglected. However, the results obtained under these assumptions are interesting in that, in the case of nickel and nickel oxide, at least, the predicted values for the total scattering cross section for this model are in close agreement with our measured values in the higher energy region where expressions which are limited to single phonon processes do not adequately represent the total inelastic scattering.

On the basis of this "independent oscillator" model the total nuclear scattering cross section per molecule may be written as follows:

$$\sigma_{\text{scattering}}=\sum_a n_a s_a+\sum_a n_a S_a\left[1-\frac{\lambda^2}{P}[1-\exp(-P/\lambda^2)]\right]+\frac{N\lambda^2}{2}\sum_{\tau<2/\lambda}\frac{j_\tau}{\tau}|F_\tau|^2\exp(-\tfrac{1}{4}P\tau^2). \quad (3)$$

In this expression,

$$P=\frac{12h^2}{\bar{M}k_0\Theta}\left[\frac{\phi(x)}{x}+\frac{1}{4}\right], \quad (4)$$

$$\phi(x)=\frac{1}{x}\int_0^x\frac{\beta d\beta}{e^\beta-1}, \quad (5)$$

$$x=\Theta/T, \quad (6)$$

$$F_\tau=\frac{1}{n}\sum_j \bar{f}_j\exp(2\pi i[h_1x_j+h_2y_j+h_3z_j]), \quad (7)$$

$$\bar{f}=(S/4\pi)^{\frac{1}{2}}. \quad (8)$$

Here, h is Planck's constant, k_0 is Boltzman's constant, Θ is the Debye or characteristic temperature of the scattering material, T is the absolute temperature of the scattering material, x_j, y_j, and z_j are the coordinates of the jth nucleus in a unit cell in terms of the lattice constants, $\tau=[d(h_1h_2h_3)]^{-1}$ is the reciprocal of the spacing of the planes designated by the Miller indices $h_1h_2h_3$, S and s are respectively the ordered (coherent) and disordered (incoherent) nuclear scattering cross sections,[4] λ is the neutron wavelength, j_τ is the multiplicity of the $h_1h_2h_3$ reflection, n represents the number of molecules per unit cell, N is the number of molecules per unit volume of crystal, n_a is the number of atoms of type a per molecule and $\bar{M}$ is the average atomic mass of the molecule. If the cross section per nucleus is desired, in the case of a substance consisting of only one element, the index a and the summation over this index are neglected and n and N refer to atoms rather than molecules. The τ summation in expression (3) is performed over all values of τ less than $2/\lambda$ and the j

[3] R. W. James, *The Optical Principles of the Diffraction of X-rays* (G. Bell and Sons, Ltd., London, 1948).

[4] J. M. Cassels, *Progress in Nuclear Physics* (Academic Press, Inc., New York, 1950), p. 185.

summation in expression (7) is performed over all atoms in a unit cell.

The first sum in Eq. (3) is simply the disordered or incoherent nuclear cross section, the second sum has been called the thermal diffuse cross section,[5] $E_{td}(S)$, and the last sum is the ordered elastic or Bragg cross section, $E(S)$. At short wavelengths, where many planes contribute to the ordered elastic scattering, the summation over τ, in this term, may be replaced by an integration,[6] with the result:

$$E(S)=\sum_a n_a S_a\{(\lambda^2/P)[1-\exp(-P/\lambda^2)]\}. \quad (9)$$

Thus, at short wavelengths for the independent oscillator approximation, the total nuclear scattering cross section reduces to the constant value

$$\sigma_{\text{scattering}}=\sum_a n_a(s_a+S_a). \quad (10)$$

Weinstock[7] considered the scattering of neutrons from a Debye crystal consisting of a single spinless isotope, taking into consideration only zero phonon and single phonon processes. Cassels[4] extended Weinstock's calculation to include the effects of isotopes and nuclear spins. The use of the explicit expressions deduced by Weinstock and Cassels is laborious. Kleinman[8,9] calculated the total cross section for inelastic scattering from a Debye crystal for one phonon processes by treating the inelastic scattering as incoherent (disordered). This approximation replaces the summation over crystal planes by an integral. Kleinman has tabulated values of the functions involved, so that a numerical computation of a specific total inelastic scattering cross section can be done simply. Finkelstein[10] has calculated the inelastic scattering cross section for an Einstein crystal for collisions in which a single oscillator changes its energy by one or more phonons and an approximate calculation of the inelastic scattering cross section for events in which more than one oscillator simultaneously change their energy by one phonon has been made by Squires[11] for a Debye crystal.

We have calculated the total nuclear scattering cross section as a function of wavelength for Ni and NiO in the region in which our measurements were made using both Kleinman's "incoherent scattering" approximation and the independent-oscillator model for the nuclear scattering. Since Ni is ferromagnetic and NiO is antiferromagnetic at room temperature, the effects of coherent magnetic scattering were included in the calculated values of the total cross section using the theory of magnetic scattering described by Halpern and Jonhson.[12] For unpolarized neutrons incident upon a polycrystalline magnetic substance, the magnetic and nuclear scattering are independent. The coherent magnetic scattering is calculated on the basis of expressions similar to the ordered elastic term of Eq. (3), taking into consideration the known chemical and magnetic structure of these substances,[13] and the magnetic scattering amplitudes[14] as a function of scattering angle.

IV. EXPERIMENTAL RESULTS AND THEIR INTERPRETATION

The total cross section for neutrons is a measure of the loss of neutrons from the incident beam due to all causes, including absorption and scattering, and is expressed through the relation

$$\sigma_{\text{total}}=-(1/Nt)\ln T, \quad (11)$$

in which N is the number of interacting centers per cm^3, and t is the thickness of the scatterer in cm. T is the sample transmission, the ratio of the transmitted intensity, I, to the incident intensity, I_0.

Neutron cross section measurements were made for various materials in the energy region 0.17 to 0.0038 ev, corresponding to wavelengths 0.7 to 4.6A. These materials can be divided into two groups, absorbers and scatterers. The absorbers were gold, indium, and silver in the form of thin foils and the scatterers were nickel and nickel oxide in the form of very fine powders. Spectrographic analysis of the samples showed negligible amounts of impurities in all samples. Sufficient counts were collected for the measured values of the cross sections so that their statistical probable errors are, in most cases, less than about 1 percent.

A. Absorbers

Figure 4 shows the measured values for the total cross section of gold made with and without the mirror. The falling off, with increasing wavelength, of the curve obtained without the mirror shows clearly the effect of

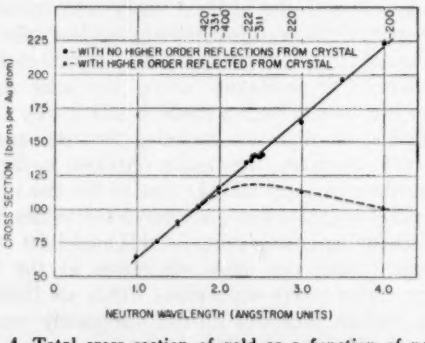

FIG. 4. Total cross section of gold as a function of neutron wavelength measured with and without mirror, showing effectiveness of the mirror in elimination of higher order reflections from crystal.

[5] E. O. Wollan and C. G. Shull, Phys. Rev. **73**, 830 (1948).
[6] Halpern, Hamermesh, and Johnson, Phys. Rev. **59**, 981 (1941).
[7] R. Weinstock, Phys. Rev. **65**, 1 (1944).
[8] D. A. Kleinman, dissertation, Brown University, 1951 (unpublished).
[9] D. A. Kleinman, Phys. Rev. **81**, 326 (A) (1951).
[10] R. J. Finkelstein, Phys. Rev. **72**, 907 (1947).
[11] G. L. Squires, Proc. Roy. Soc. (London) **A212**, 192 (1952).
[12] O. Halpern and M. H. Johnson, Phys. Rev. **55**, 898 (1939).
[13] Shull, Strauser, and Wollan, Phys. Rev. **83**, 333 (1951).
[14] Shull, Wollan, and Koehler, Phys. Rev. **84**, 912 (1951).

higher orders on the values obtained for the total cross section if no corrections are made for the presence of the higher order wavelengths. The effectiveness of the mirror in eliminating the higher order reflections can be judged by the fact that, with the mirrors present, the values measured at long wavelengths and the values measured at short wavelengths fall closely along a straight line, as would be required by a $1/v$ relationship.

Figure 5 gives the measured results for the total cross section of gold, indium, and silver as a function of wavelength from about 1A to 4A. In order to consider the effect of the nearest resonance, these data were fitted by least squares to an equation of the form

$$\sigma_t = c_1(\lambda + 2\lambda_0^2/\lambda) + c_2, \tag{12}$$

where λ is the neutron wavelength and λ_0 is the wavelength of the nearest resonance. The values 4.8 ev, 5.1 ev, and 1.45 ev, respectively were used for the nearby resonance levels in Au, Ag, and In. The values of c_1 and c_2 determined by this method are given in Table I along with the value of the capture cross section for neutrons of velocity 2200 meters per second. The term $c_1[\lambda + (2\lambda_0^2/\lambda)]$ represents the absorption cross section, and is obtained as an approximation to the Breit-Wigner one-level resonance formula. Its accuracy depends upon the neutron energy being much less than the resonance energy, and upon $|E-E_0|$ being greater than the total width of the level. For In, Ag, and Au, the expression should be accurate to one or two percent in the interval covered by the data.

In principle, discontinuities in the total cross section should occur at wavelengths satisfying $\lambda = 2d(h_1h_2h_3)$ for these materials as expressed by the term for the ordered elastic cross section. However, the ordered elastic cross section for these materials is small compared to the capture cross section and the crystalline effects are difficult to observe. The inset in Fig. 5 shows the measured values for gold in the region of the (311) discontinuity at 2.45A on an expanded scale. The data exhibit the presence of this discontinuity but measurement of the height is impractical. In order to observe this small effect, a discontinuity height of about 2 percent of the total cross section at this wavelength, sufficient data were collected to give a probable error less than 0.7 percent for each cross section value. The inset for Ag covers the region of the (222) discontinuity. It does not show a discontinuity because of the small ordered cross section of Ag.

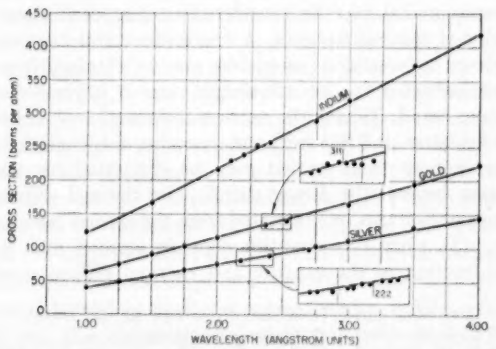

FIG. 5. Total cross section of gold, indium, and silver as a function of neutron wavelength.

TABLE I. Measured constants for absorbers.

Element	c_1 barns/atom angstrom	c_2 scattering barns/atom	σ_a barns/atom (2200 m/sec)	σ_a barns/atom (2200 m/sec)*
Gold	53.1±0.4	8.7±0.9	96.5±0.7	94±1
Silver	35.2±0.3	4.2±0.7	64.0±0.5	60±3
Indium	102.3±1.0	8.6±2.4	190.2±1.8	190±10

* See reference 15.

Our values of the absorption cross sections of Au, Ag, and In at 2200 m/sec agree quite well with the best available estimates of these cross sections as determined by the Atomic Energy Commission Neutron Cross Section Advisory Group,[15] which are given in the last column of Table I. A recent value[16] of 98.7±0.7b for the absorption cross section of Au at 2200 meters per second has been derived from measurements in the region 1.5 to 10A.

B. Scatterers

The samples of nickel and nickel oxide consisted of circular disks pressed from fine powder and placed in sealed aluminum containers having thin windows. The average particle size for each of these powders was estimated to be between one half and one micron from photographs of the particles under a magnification of 2000 diameters. For particles of this size, extinction effects may be considered negligible.[17] The samples were pressed in order to prevent density changes resulting from the frequent movement and inevitable slight jars which they receive in being positioned in the neutron beam. Because of intensity requirements, the samples were fairly large, approximately two inches in diameter. Several sample thicknesses, from about $\frac{1}{8}$ in. to $\frac{1}{2}$ in. were used. Table II gives the physical properties of the various specimens. Efforts were made to prepare the samples from dry material, samples being exposed to the atmosphere only during the time necessary to load the powder into the press. In preparing the nickel oxide sample, the powder was heated to 300°C and maintained at this temperature for four hours in an effort to eliminate any adsorbed water. The powder was then cooled in a dry atmosphere before pressing. Water analyses failed to show detectable amounts of water in the nickel oxide powders. However, it is difficult to

[15] *Neutron Cross Sections*, Atomic Energy Commission Report, AECU-2040 (Technical Information Division, Department of Commerce, Washington, D. C., 1952).

[16] Carter, Palevsky, Myers, and Hughes, Phys. Rev. **92**, 716 (1953).

[17] R. J. Weiss, Phys. Rev. **86**, 271 (1952).

TABLE II. Physical properties of powder samples.

Sample	Thickness (inches)	No. atoms or molecules per cm³	Apparent density (g per cm³)
Nickel No. 1	0.465	7.67×10^{22}	6.33
Nickel No. 2	0.127	2.00×10^{22}	6.06
Nickel oxide No. 1	0.477	3.00×10^{22}	3.07
Nickel oxide No. 2	0.401	3.18×10^{22}	2.62

make accurate chemical analyses for water in samples of this kind. Neutron measurements at low energies will be affected strongly by even small amounts of water. Since a departure from a random orientation of the particles in the powder sample could have a serious effect on the value obtained for the ordered elastic scattering cross section determined by the method of these measurements, a search for departure of the particle orientations from a random distribution was made by measuring the scattered intensity at various points on a Debye ring. Results showed no evidence of a preferred orientation.

1. Nickel

Since Ni has a face-centered cubic structure, the crystal structure factor, F_r, becomes for Ni simply $\bar{f}_{\mathrm{Ni}}$ for all Miller indices odd or all indices even, and becomes zero for any combination of odd and even indices. Discontinuities in the cross section will occur at values of λ satisfying $\lambda=2d(h_1h_2h_3)$, where $d(h_1h_2h_3)$ may be written as a_0/L with $L=(h_1^2+h_2^2+h_3^2)^{\frac{1}{2}}$ and $a_0=3.517$A. From Eq. (3) an expression for the height of the discontinuity, H_L, for a particular value of L may be written in the form:

$$\frac{H_L}{(8j_L/L^2)}=|\bar{f}|^2\exp[-A\Phi(x)L^2]. \tag{13}$$

Here,

$$A=\frac{3h^2}{Mk_0Ta_0^2},\quad \Phi(x)=\frac{1}{x}\left[\frac{\phi(x)}{x}+\frac{1}{4}\right].$$

Equation (13) represents a linear relationship between $\ln(H_LL^2/8j_L)$ and L^2. The slope of this line is a known function of Θ, and its intercept with the axis of ordinates at $L^2=0$ is equal to $\ln|\bar{f}|^2$. Such a plot, using the measured discontinuity heights, is exhibited in Fig. 6 with the straight line shown determined from the data

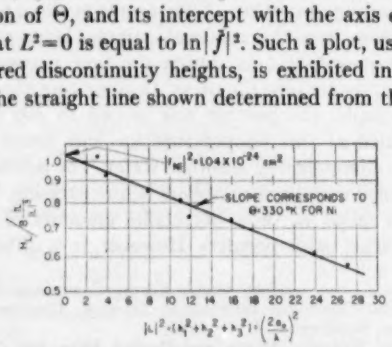

FIG. 6. Determination of the ordered scattering amplitude and Debye temperature for nickel.

by the procedure of least squares. The values obtained for the ordered scattering cross section per nickel nucleus and the Debye temperature are: $S=13.1\pm0.3$ barns/atom; $\Theta=330$°K. Table III gives the measured heights and compares them with those calculated from Eq. (13) using the experimentally determined values of S and Θ. Our value of 13.1 ± 0.3 barns compares very well with the value 13.4 barns obtained from powder diffraction patterns.[18] The value of this quantity has special practical significance since it is generally used as a secondary standard in neutron diffraction work. The value, 13.4 barns, was determined by comparison of the intensity of scattering from a normal nickel sample to the intensities scattered from a set of calibrated scatterers,[18] one of which was diamond dust. An independent absolute measurement of $\bar{f}$ for nickel, such as that obtained from these measurements, confirms the absolute measurement on diamond and the nickel-carbon comparison. Our value for the Debye temperature may be compared with the value 370°K, obtained from neutron diffraction measurements[19] and the values

TABLE III. Nickel discontinuity heights.

Plane $(h_1h_2h_3)$	L^2	Wavelength A^0	Calculated height, barns/atom	Measured height, barns/atom
111	3	4.06	12.0	12.7
200	4	3.52	5.7	5.5
220	8	2.49	3.7	3.6
311	11	2.12	4.3	4.3
222	12	2.03	1.2	1.2
400	16	1.76	0.5	0.6
331	19	1.61	1.6	···
420	20	1.57	1.4	···
422	24	1.44	1.0	1.0
333, 511	27	1.35	1.0	1.1

400°K and 413°K, determined by specific heat measurements.[20]

The cross section at wavelengths greater than the Bragg cutoff, 4.016A for nickel, should be due entirely to capture, inelastic scattering and disordered scattering resulting from the presence of isotopes. There is negligible disordered scattering due to nuclear spins, since normal nickel may be considered as composed essentially of spinless isotopes. A first estimate of the disordered cross section per nucleus may be obtained from measurements in the wavelength region beyond the Bragg cutoff. Taking the capture cross section of nickel as 4.5 barns at 0.025 ev,[21] and assuming a $1/v$ relation, the capture cross section may be computed for the region beyond the Bragg cutoff. The thermal diffuse cross section can be calculated from the second term in Eq. (3), since this quantity depends upon S and Θ. Subtraction of the capture and thermal diffuse cross

[18] C. G. Shull and E. O. Wollan, Phys. Rev. **81**, 527 (1951).
[19] C. G. Shull and E. O. Wollan (unpublished).
[20] M. W. Zemansky, *Heat and Thermodynamics* (McGraw-Hill Book Company, Inc., New York, 1950).
[21] H. Pomerance, Phys. Rev. **83**, 641 (1951).

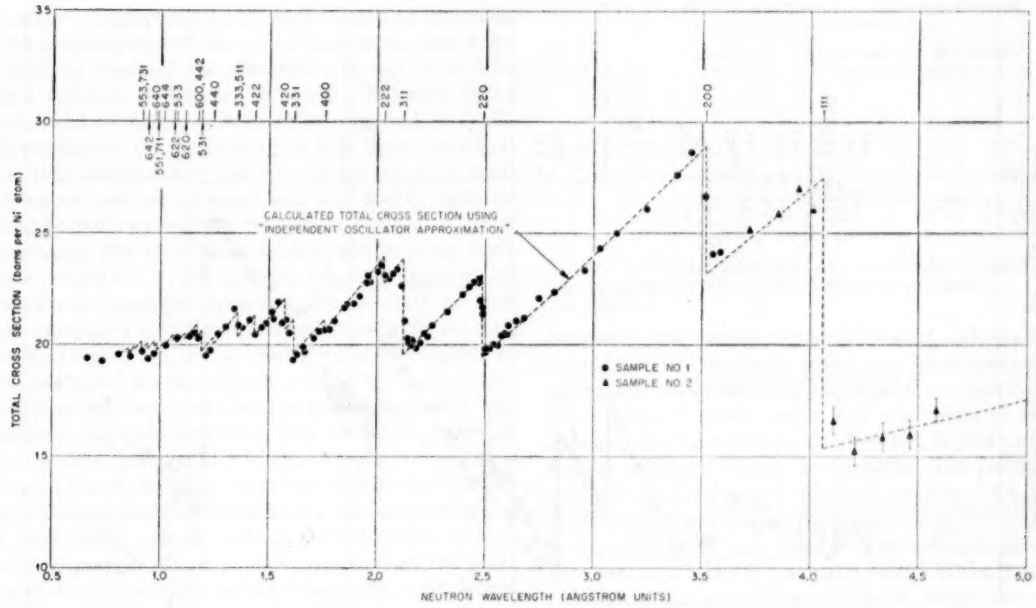

FIG. 7. Total cross section of nickel as a function of neutron wavelength.

sections from the measured values in this region leaves only the disordered scattering cross section. The value of s obtained in this manner should be in accord with the value obtained by an extrapolation of the total cross section to $\lambda=0$ which gives $\sigma_{\text{scattering}}=S+s$. Finally, the values of S and s should be consistent with the measured total cross section over the entire range of measurements. From these considerations the value of s which best fits the data was found to be 4.8 barns.

Figure 7 shows the measured total cross section as a function of wavelength compared to the values for the total cross section calculated on the basis of the independent oscillator model, using the values of S, s, and Θ derived from our data. The capture and ordered elastic contributions were subtracted from the experimental values of the total cross section *vs* energy. Since the quantities subtracted from the measured values are the same for either the independent oscillator approximation or the incoherent approximation, the residual experimental function of energy, represented by the points of Fig. 8, was compared to the scattering function of energy expected from each of these approximations. The incoherent approximation fits the data only at the longer wavelengths, as is to be expected from a one phonon theory. The independent oscillator approximation fits the data over the entire region of observation on the basis of values for S, s, and Θ derived entirely from these measurements alone. This agreement with the independent oscillator approximation is interesting in that this simple approximation seems to account for the total scattering, for Ni, over this range of measurements, and for NiO at the short wavelengths. At longer wavelengths, i.e., beyond the Bragg cut off, the independent oscillator approximation fails to predict the linear increase in scattering cross section with wavelength that is predicted by the more rigorous approach and which is experimentally observed. From these measurements, the total inelastic scattering cross section, $e(s,S)$, can be represented semi-empirically by an expression of the form

$$e(s,S)=(s+S)\{1-(\lambda^2/P)[1-\exp(-P/\lambda^2)]\}, \quad (14)$$

which agrees with the generally accepted conclusion that the sum of the elastic and inelastic nuclear scattering is constant for the shorter wavelengths.

The ferromagnetic scattering of the powdered Ni sample was calculated for $\lambda=2d(111)$ where the magnetic scattering is greatest, and found to be only 0.15 barn, or about one percent of the (111) discontinuity height due to nuclear scattering. Consequently the effects of magnetic scattering for Ni were considered

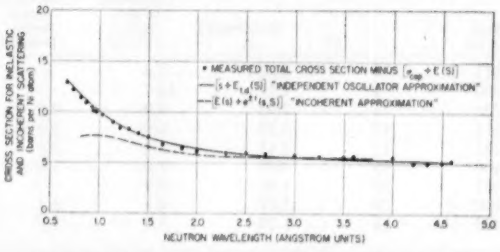
CROSS SECTION FOR INELASTIC AND DISORDERED SCATTERING (barns per Ni atom)
NEUTRON WAVELENGTH (ANGSTROM UNITS)
"INDEPENDENT OSCILLATOR APPROXIMATION"
"INCOHERENT APPROXIMATION"

FIG. 8. Inelastic plus disordered cross section of nickel as a function of neutron wavelength.

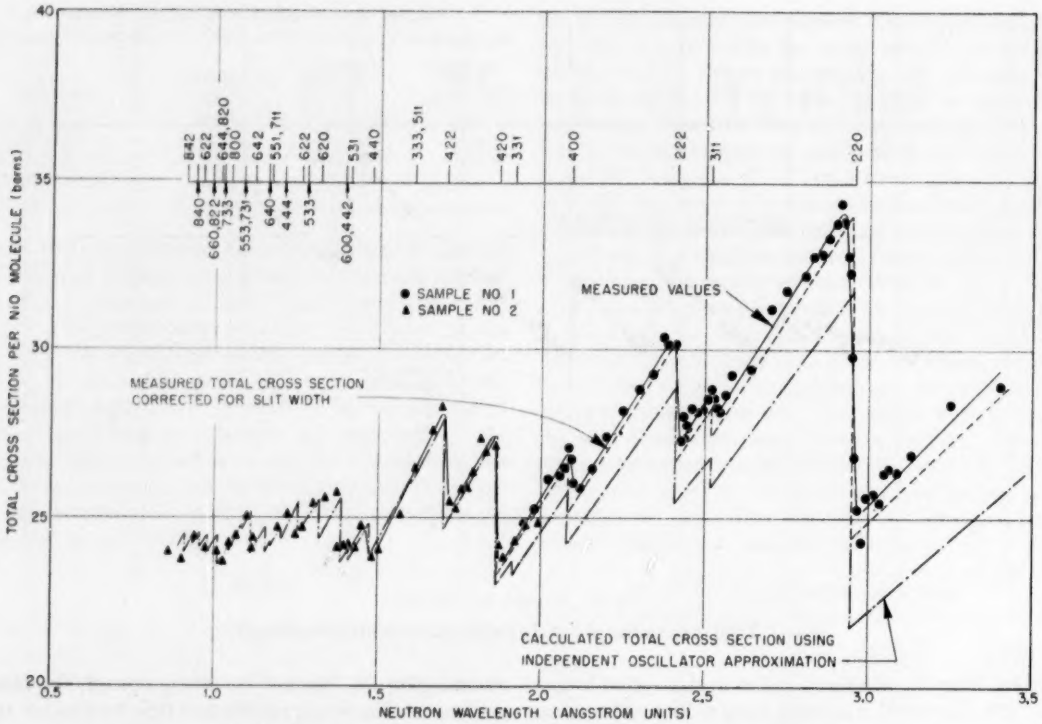

FIG. 9. Total cross section of nickel oxide as a function of neutron wavelength.

negligible. In these calculations the magnetic form factor for Ni was approximated by that for iron.[22]

2. *Nickel oxide*

Measurements were made with a nickel oxide sample in the same fashion as those described for nickel. At room temperature nickel oxide is a face centered cubic with NaCl structure. The crystal structure factor per molecule was taken as $(\bar{f}_{Ni} \pm \bar{f}_O) \exp(-\frac{1}{4}P\tau^2)$, where the positive sign applies to all indices even, the negative sign to all indices odd. The structure factor is zero for any combination of odd and even indices. Taking the spins of the nickel and oxygen isotopes as zero, and treating oxygen as essentially mono-isotopic, the disordered cross section may be taken simply as that due to the isotopes in nickel, i.e., 4.8 barns. Employing the same methods used for nickel, the quantity $|\bar{f}_{Ni}+\bar{f}_O|^2$ and Θ can be determined from the measured heights of the discontinuities resulting from planes characterized by even Miller indices. In principle, $|\bar{f}_{Ni}-\bar{f}_O|^2$ and Θ could be determined from the odd reflections. Since the discontinuities resulting from these planes are much smaller than those from the even planes, such a procedure is impractical. Using 4.2 barns[18] for the ordered scattering cross section, S_O, of oxygen, the value obtained for S_{Ni} was 13.2 barns, and the measured Debye characteristic temperature was 495°K. Using the height of the (311) discontinuity, both S_{Ni} and S_O can be found. This procedure gives $S_{Ni}=13.4$ barns and $S_O=4.1$ barns. This method uses only one odd discontinuity height, however, and it is felt that the value of 13.2 barns represents the better measurement in the case of NiO. The calculated discontinuity heights for nickel oxide are compared with the measured values in Table IV.

TABLE IV. Nickel oxide discontinuity heights.

Plane ($h_1k_1l_1$)	L^2	Wavelength A	Calculated height, barns/molecule	Measured height, barns/molecule
111	3	4.82	2.3	...
200	4	4.17	14.7	...
220	8	2.95	9.9	9.8
311	11	2.52	0.9	1.0
222	12	2.41	3.4	3.5
400	16	2.09	1.6	1.6
331	19	1.91	0.4	...
420	20	1.87	4.4	4.2
422	24	1.70	3.2	3.2

In Fig. 9, the points represent the values of the total cross section deduced from the actually measured values of the sample transmission. The solid curve is drawn through these points. The NiO data were the first to be taken. After it had been taken, it was found that the detector window had not been quite wide

[22] J. Steinberger and G. C. Wick, Phys. Rev. **76**, 994 (1949).

enough to accept all small angle scattered neutrons. The necessary corrections to the solid curve were determined by studying the effective cross section at 3.4A as a function of detector slit width. The solid curve value at 3.4A had to be reduced by 3 percent, or 0.75b. Corrections at other wavelengths were made by assuming that the necessary correction for small angle scattering was zero at 1.6A and less, and that it increased linearly with wavelength. The dashed curve of Fig. 9 represents the total cross section which would have been measured if the detector slit had accepted all small angle scattered neutrons. The dot-dash curve is the calculated total cross section. It includes capture, ordered elastic scattering, disordered scattering due to Ni isotopes, thermal diffuse scattering on the independent oscillator model, and magnetic scattering. The ordered magnetic scattering was computed following the methods previously mentioned[13] with the magnetic form factor of the Ni ion approximated by that for Mn ion. The magnetic contribution to the total scattering is appreciable, about 0.9b at $\lambda=3.4$A. The experimental and calculated curves agree well at the short wavelengths, but disagree quite markedly at the longer wavelengths.

The good agreement between the calculated and observed ordered elastic scattered effects in Ni alone, and in NiO alone, and the agreement between the values of S from the Ni data and the NiO data, suggest that the difference between calculated and observed total cross section of NiO of Fig. 9 can not be attributed to ordered elastic scattering. It seems unlikely that it is due to the use of an incorrect value for the capture cross section. The presence of water in the sample does not seem a likely candidate to account for the difference between the observed and calculated values, since great care was taken to remove the water. Furthermore, if one assumes the sample to have contained an amount of water sufficient to give agreement between calculated and observed values at some one energy, the agreement fails to persist at other wavelengths.

In Fig. 10, the plotted points represent the measured total cross section values minus the contributions from capture, coherent nuclear and coherent magnetic scattering as a function of wavelength. The solid curve

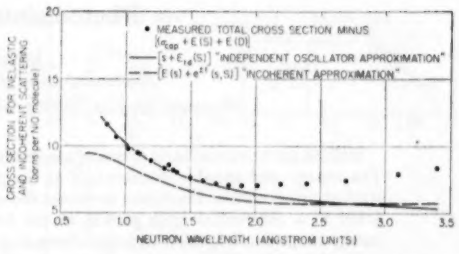

FIG. 10. Inelastic plus disordered cross section of nickel oxide as a function of neutron wavelength.

represents the corresponding calculated values using the independent oscillator model and the dashed curve represents the values from the incoherent approximation. This first model agrees with the points at short wavelengths, the second model does not. Neither model fits the data at the long wavelengths. The points lie about 3 barns above the calculated curves at 3.4A. The incoherent approximation should show a minimum due to lattice inelastic scattering at a wavelength greater than that at which the minimum occurs in the data.

Simultaneous one phonon processes, which were not included in the calculated cross section curves, should decrease slightly the difference between the measured and calculated values of Figs. 9 and 10. There is also the possibility that the difference may be due, in part, to magnetic inelastic scattering[23–25] as well as to lattice inelastic scattering. Additional measurements of the cross section of NiO as a function of temperature are needed to relate the difference definitely to inelastic scattering of either or both types. Measurements in the region beyond the Bragg cutoff should also be helpful.

We wish to acknowledge our appreciation to Drs. C. G. Shull, E. O. Wollan, and S. Tamor for helpful discussions on neutron scattering. We are indebted to Miss T. Arnette for help in taking the data, to R. M. Steele for x-ray studies of our samples, and to C. Feldman for spectroscopic analyses of the samples.

[23] R. G. Moorhouse, Proc. Phys. Soc. (London) **A64**, 1097 (1951).
[24] H. Palevsky and D. J. Hughes, Phys. Rev. **92**, 202 (1953).
[25] L. Van Hove (unpublished).

Photodisintegration of Helium

EVERETT G. FULLER
National Bureau of Standards, Washington, D. C.

(Received May 18, 1954; revised manuscript received August 24, 1954)

Helium gas at atmospheric pressure was irradiated with 26-, 29-, 32-, and 40-Mev bremsstrahlung spectra. The energy and angular distributions of the protons produced by the photodisintegration of He^4 were studied using nuclear emulsions to detect the charged particles. Angular distributions of the protons are fitted to a differential cross section of the form $\sigma(\theta_{c.m.})\sim(a/b)+\sin^2\theta_{c.m.}[1+(\gamma/b)\cos\theta_{c.m.}]$. Over the energy range studied, the interference term may increase slowly with energy but is approximately constant $(\gamma/b=0.2\pm0.1)$; the isotropic term increases rapidly with energy from 0 to 0.33 ± 0.2 at a mean photon energy of 32.5 Mev. The (γ,p) cross section reaches a peak value of about 1.8 mb at about 26 Mev. $\int_{20}^{40}\sigma dE=0.016\pm0.005$ Mev barns.

DURING the last few years it has been suggested that a modified α-particle model of the nucleus might possibly lead to an explanation of some of the features of the "giant resonances" observed in the experimental studies of the (γ,p) and (γ,n) processes.[1] Any such theory would require some information about the nuclear absorption of photons by the helium nucleus. For this reason, and also because it was felt that the structure of the alpha particle was simple enough to make possible a theoretical interpretation of the results, it was thought that an experimental study of the photodisintegration of He^4 would be worthwhile.

There have been very few experimental studies made of the photodisintegration of helium. Two studies have been made of the high-energy protons (energies greater than 45 Mev) produced by 300-Mev bremsstrahlung spectra. Benedict and Woodward[2] measured the cross section for the production of monoenergetic protons having energies between 45 and 100 Mev at 90 and 60 degrees with respect to the direction of the photon beam in the laboratory system. Kikuchi[3] has obtained the distribution in energy of the protons produced by a 320-Mev bremsstrahlung spectrum at laboratory angles of 45, 90, and 135 degrees. Both of these experiments indicate that there is a strong forward peaking in the angular distributions of the high-energy photoprotons in the center-of-mass system.

In addition to these high-energy measurements Gaerttner and Yeater[4] have made measurements with a cloud chamber using the General Electric 100-Mev betatron. Although these data suffer from a lack of statistics, they do indicate that there is a peak in the (γ,p) cross section around 27 Mev. The angular distribution of these data is compatible with a $\sin^2\theta$ center-of-mass angular distribution.

The experiment described below is an attempt to study in some detail the (γ,p) process in He^4 by photons having energies between about 20 and 40 Mev. Some of the preliminary results of this work have been reported.[5]

THE EXPERIMENTAL ARRANGEMENT

The NBS 50-Mev betatron was used as a photon source in the experiment. The target in this machine is a tungsten wire 10 mils in diameter. The effective target thickness, however, as determined by a measurement of the x-ray beam width, is only of the order of one mil.[6] Nuclear emulsions were used to detect the charged particles produced by the bombardment of a helium gas sample by various bremsstrahlung spectra produced by the betatron. The emulsion thickness was 200 microns and the helium gas was at atmospheric pressure. The geometry used in exposing the plates was the same as that used in a previous study of the photodisintegration of deuterium.[7] All exposures were measured with a 100-r Victoreen thimble chamber surrounded by a $\frac{1}{8}$-inch lead cap.

When helium is bombarded by photons having energies greater than 28 Mev, there are five reactions that can take place. These reactions and their thresholds are:

(1)	$He^4(\gamma,p)H^3$,	19.8 Mev
(2)	$He^4(\gamma,n)He^3$,	20.6 Mev
(3)	$He^4(\gamma,d)D$,	23.7 Mev
(4)	$He^4(\gamma,pn)D$,	25.9 Mev
(5)	$He^4(\gamma,2p2n)$,	28.1 Mev.

If He^4 is bombarded by a bremsstrahlung spectrum having a peak energy from 30 to 40 Mev, a great many tracks are produced in the emulsion whose ranges are so short it is impossible to determine the type of particle producing the track. This means that a range distribution of "proton" tracks produced in such a bombardment will not only include tracks due to the (γ,p) reaction but also those due to reactions 3 through 5 and the recoil H^3 and He^3 from reactions 1 and 2. If a short-range cut-off of about 8 microns is used,

[1] H. A. Bethe and J. S. Levinger, Phys. Rev. **78**, 115 (1950).
[2] T. S. Benedict and W. M. Woodward, Phys. Rev. **83**, 1269 (1951).
[3] S. Kikuchi, Phys. Rev. **86**, 126 (1952).
[4] E. R. Gaerttner and M. L. Yeater, Phys. Rev. **83**, 146 (1951).
[5] E. G. Fuller and M. Wiener, Phys. Rev. **83**, 202 (1951).
[6] H. W. Koch *et al.*, Natl. Bureau Standards Handbook 55 (U. S. Government Printing Office, Washington, D. C., 1954).
[7] E. G. Fuller, Phys. Rev. **79**, 303 (1950).

range-energy and geometry considerations indicate that for a recoil He^3 to be included in a range distribution it must be produced by a photon having an energy greater than 32 Mev. Similar arguments indicate that recoil tritons are included in the distribution if they are produced by photons having energies greater than 25 Mev.

The (γ,d) reaction is not expected to lead to any confusion, since it has a higher threshold, and since it cannot take place in the dipole approximation. Both reactions 4 and 5, however, can take place by dipole transitions. These reactions are discriminated against both because of their higher thresholds and because of the dynamics of the three- and four-particle disintegrations. For example, in the (γ,pn) reaction if all three disintegration products have equal momenta, the proton energy in the center-of-mass system is $(1/2.5)E_a$, where E_a is the energy available for the disintegration products. The maximum possible energy for the proton is $\frac{2}{3}E_a$. For a disintegration produced by a 40-Mev photon the maximum proton energy will be the same as the energy of the proton produced in reaction (1) by a 32-Mev photon.

An attempt to sort out the effects of the various reactions listed above was made by making four different exposures with 25-, 29-, 32-, and 40-Mev bremsstrahlung spectra. In addition to the exposures made with the chamber filled with helium, background exposures were made with the chamber evacuated. In all cases the background was negligible.

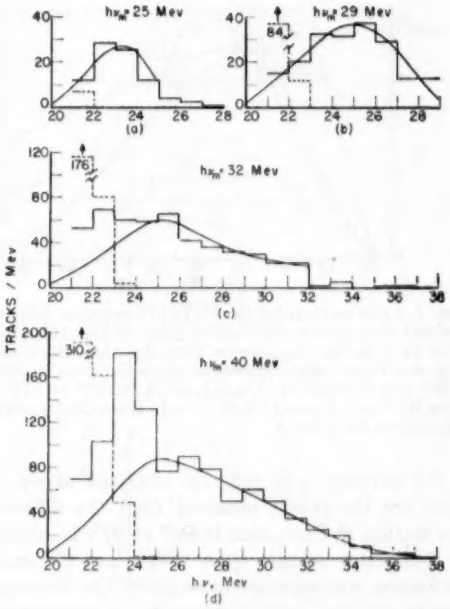

FIG. 1. Energy distributions of photoprotons. The solid histograms are the distributions corrected for recoil tritons. The dashed histograms are the recoil triton corrections. Smooth curves are free hand estimates of proton distributions (see text).

TREATMENT OF THE DATA AND RESULTS

A. Proton Energy Distribution

In analyzing the data each track was treated initially as a proton. The energy of each "proton" was obtained from the observed range in the emulsion after correcting this range for a mean range in the helium gas for each track. The size of this range correction depended upon the energy and direction of each "proton." Assuming a two-body breakup for the helium nucleus, the energy of the proton producing the disintegration was calculated from the observed "proton energy" and direction. For each exposure a distribution was made of the numbers of "protons" as a function of photon energy. Assuming that for each high-energy proton there was a corresponding recoil triton, a triton distribution was calculated based on the observed high-energy proton distribution and the observed angular distributions. This calculated triton distribution was used to correct the low-energy region of the corresponding "proton" distribution.

The proton distributions for the four exposures are shown in Fig. 1, (a) through (d). The solid histograms are the distributions after correction for recoil tritons. The dashed histograms are the calculated recoil triton distributions that have been used to correct the original data. It is obvious that the triton correction becomes increasingly important as the bremsstrahlung energy is increased.

Uncertainties in the triton corrections and in the shape of the high energy tip of the bremsstrahlung spectrum make it impossible to obtain the exact shape of the (γ,p) cross section near threshold. The smooth curves drawn in Fig. 1 are free-hand estimates of proton distributions. These curves were drawn on the basis of the following considerations. All of these data represent the effect of the product of a cross section and the bremsstrahlung spectrum. When allowance is made for the bremsstrahlung spectrum the data in Fig. 1(a) and (b) indicate a peak in the (γ,p) cross section above 23 Mev, while those of Fig. 1(c) and 1(d) place the peak below 27 Mev. Threshold considerations show that the yield curves in Fig. 1(a) and 1(b) are free from the effects of processes other than the (γ,p) process. For this reason the general shape of the proton yield curves drawn in Fig. 1(c) and 1(d) below 25 Mev has been taken to be the same as that given in Fig. 1(a) and 1(b) when consideration is made for the differences in the bremsstrahlung spectra used in the four exposures.

The solid curve given in Fig. 2 is the result of dividing the smooth curve of Fig. 1(d) by a Schiff thin-target bremsstrahlung spectrum.[6] The normalization to an absolute cross section was obtained using the ν-chamber response given in reference 6. The curve given in Fig. 3 is that obtained for the total cross section for the $T(p,\gamma)He^4$ as a function of proton energy using the principle of detailed balancing and the cross section

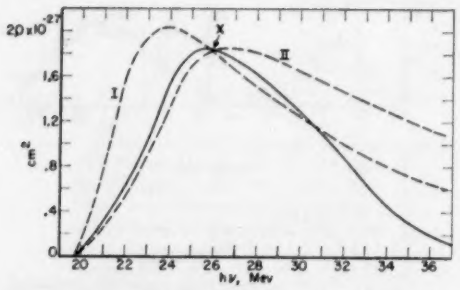

FIG. 2. Cross sections for the $He^4(\gamma,p)T$ reaction. Solid curve calculated from proton distribution given in Fig. 1(d). Dashed curves have energy dependence given by the calculations of Irving and Gunn using exponential wave functions to describe the He^4 and T nuclei (I: $1/\mu_\alpha = 1/\mu_T = 2.5\times10^{-13}$ cm; II: $1/\mu_\alpha = 2.0\times10^{-13}$ cm, $1/\mu_T = 2.5\times10^{-13}$ cm). Theoretical curves are normalized at the point ×.

for the inverse (γ,p) reaction obtained above. The circles are the points obtained from the differential cross section of Perry and Bame[8] at 90°. In obtaining the total cross section from these data the angular distribution was assumed to be $\sin^2\theta$. The discrepancy between the two measurements is not thought to be significant.

B. The (γ,d) or (γ,pn) Process

When the shape of the bremsstrahlung spectrum is taken into consideration, the distributions given in Fig. 1(c) and 1(d) have a relatively large number of short range tracks (under 25 Mev) compared to the number in the distributions of Fig. 1(a) and 1(b). These tracks could be produced by either the (γ,d) or the (γ,pn) reactions. The data are consistent with the cross section for this process having a peak at about 32 Mev. (A 32-Mev photon producing a (γ,pn) reaction in which the three disintegration products have equal momenta would give a proton having the same energy as that produced by a 23.2-Mev photon in the (γ,p) reaction.) Around 30 Mev the cross section for this process seems to be of the order of the (γ,p) cross section at 30 Mev.

C. Angular Distributions

The data from the four exposures were divided into three energy intervals and angular distributions plotted corresponding to each energy group. The lowest energy used (23 Mev) was high enough so that recoil tritons could produce only a negligible effect. These data are plotted in Fig. 4 as a function of the angle θ. As indicated in Fig. 4(a), the angle θ is the projection into the plane of the emulsion of the angle θ_1 between the direction of the photon and the direction of emission of the proton in the laboratory system. The projection angle β is 15 degrees.

In analyzing these data the angular distribution in the center-of-mass system was assumed to be of the form:

$$\sigma(\theta_{c.m.})d\Omega_{c.m.} = b\left[\frac{a}{b}+\sin^2\theta_{c.m.}\left(1+\frac{\gamma}{b}\cos\theta_{c.m.}\right)\right]d\Omega_{c.m.}. \quad (1)$$

This differential cross section when transformed to the laboratory system and projected into the plane of the emulsion gives the following approximate expression for the number of events to be expected as a function of the angle θ:

$$N(\theta)d\theta \simeq [a\sin\theta(1+2c\cos\beta\cos\theta+\sin^2\beta\cos^2\theta) + b\sin^3\theta(1+4c\cos\beta\cos\theta+2\sin^2\beta\cos^2\theta) + \gamma\cos\beta\sin^3\theta\cos\theta(1+4c\cos\beta\cos\theta+5/2\sin^2\beta\cos^2\theta]d\theta. \quad (2)$$

In this expression c is the ratio of the velocity of the center of mass to the velocity of the proton in the center-of-mass system ($c\simeq\hbar\omega/[24Mc^2(\hbar\omega-B)]^{\frac{1}{2}}$, where B is the proton binding energy), and β is the projection angle indicated in Fig. 4(a). The constants a, b, and γ and the probable errors in these constants were determined by fitting (2) to the experimental data by the method of least squares. The values obtained by this procedure are given in Table I. These data are not sufficiently accurate to determine the form of the angular distribution function. If, however, the differential cross section is assumed to be of the form given by (1) the data do indicate the general trend of the constants in this expression over the energy interval studied. The dashed histograms in Fig. 4 are those obtained using (2) and the constants determined from the least-squares fit of the data.

DISCUSSION

The integrated cross section from threshold to 40 Mev determined from Fig. 2 is $\int\sigma dE = 0.016\pm0.005$ Mev barns. The error quoted is principally due to uncertainties in the geometry and in the determination of the absolute photon flux. Within the experimental errors this value is in agreement with the value estimated by Gaerttner and Yeater[4] from their data. It is in very

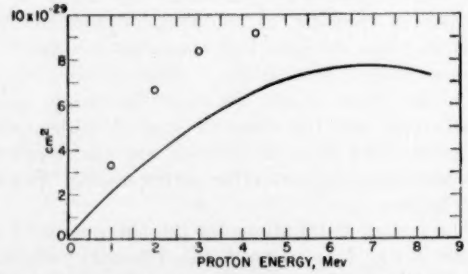

FIG. 3. Cross section for $T(p,\gamma)He^4$ reaction. Solid curve is that obtained from the photodisintegration cross section using the principle of detailed balancing. Circles are total cross sections from the work of Perry and Bame assuming a differential cross section of the form $\sigma(\theta_{c.m.})\sim\sin^2\theta_{c.m.}$.

[8] J. E. Perry, Jr., and S. J. Bame, Jr., Phys. Rev. **90**, 380 (1953).

good agreement with the value of 0.015 Mev barns obtained by Nicolai and Goldwasser.[9] In agreement with the recent measurements made of the inverse $T(p,\gamma)He^4$ reaction,[8,10] the data given in Fig. 2 do not show any indication of a "resonance level" in He^4 around 21 Mev.[11] Rather, the data seem to indicate a "resonance" curve similar to those obtained for the photon processes in the heavier nuclei.

The errors in the constants determined for the angular distributions are large. Some general conclusions, however, can be drawn about the trend of the angular distribution with increasing photon energy. The "isotropic term" a/b increases rapidly with energy over the energy range considered. The coefficient of the "interference term" γ/b, however, is either constant or only increases slowly with energy. The value obtained for the "interference term" is in agreement with that found by Perry and Bame in their study of the inverse reaction.

The theoretical curves giving the (γ,p) cross section as a function of photon energy as given by the calculations of Flowers and Mandle[12] and by the work of Gunn and Irving[13] can be brought into qualitative agreement with the curve given in Fig. 2 by making the proper choice of a parameter used in these calculations which determines the radial extent of the He^4 nucleus. The calculations of Flowers and Mandle make use of Gaussian wave functions to describe the helium and tritium nuclei. Gunn and Irving made calculations using both Gaussian and exponential type wave functions. For reasonable values of the nuclear parameter involved, the energy dependence of the (γ,p) cross section given in Fig. 2 is in better agreement with the calculations made by Gunn and Irving using the exponential type wave functions than with those using Gaussian functions. The theoretical curves given in the work of Gunn and Irving that best fit the experimental data are given in Fig. 2. The theoretical curves are normalized to the experimental data at the points indicated. Although the statistics are poor and there are uncertainties in the shape of the bremsstrahlung spectrum it is felt that, for energies above 26 Mev, the experimental shape of the cross-section curve given in Fig. 2 is much more reliable than the shape indicated below 26 Mev. In the region above 26 Mev a discrepancy is indicated between the energy dependence given by Gunn and Irving and that given by the experimental curve. Although it is not considered likely, this may be entirely due to the crudeness of the experiment. It may also be due to the crudeness of the approximations used in the calculations (i.e., exponential wave functions for the triton and helium nuclei and plane waves to describe the motion of the proton and triton in the final state) or due to the neglect of noncentral forces in the calculations. The neglect of noncentral forces results in the omission of transitions from ground state components that are not present in the pure central force approximation. Irving[14] points out the need for the inclusion of a tensor force in the nuclear interaction in order to obtain the correct binding for the helium nucleus. It may also be necessary to include a tensor force to explain the behavior of the angular distributions.

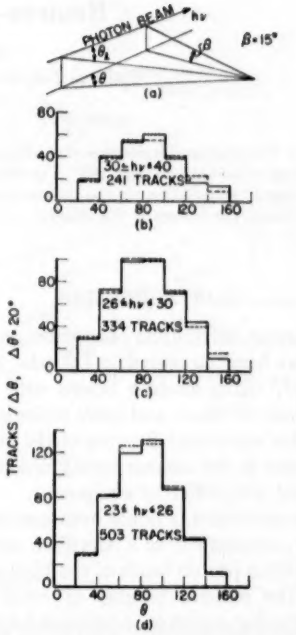

FIG. 4. Proton angular distributions. In (a) the angle θ is in the plane of the emulsion, the angle β is in a plane perpendicular to the emulsion. Solid histograms are experimental results. The energy interval for each distribution as well as the numbers of tracks in each distribution are indicated. Dashed histograms are calculated for a differential cross section in the center-of-mass system of the form

$$\sigma(\theta_{c.m.})=b\left[\frac{a}{b}+\sin^2\theta_{c.m.}\left(1+\frac{\gamma}{b}\cos\theta_{c.m.}\right)\right].$$

Values of the constants are taken from Table I.

TABLE I. Values of the parameters in Eq. (1).

Photon energy range (Mev)	23–26	26–30	30–40
$\langle\hbar\omega\rangle_{Av}$ (Mev)	24.5	28	32.5
a/b	0.004±0.05	0.21±0.08	0.33±0.2
γ/b	0.13 ±0.05	0.25±0.09	0.35±0.2

The author wishes to acknowledge the help of M. Wiener and J. Godfrey in the analysis of the nuclear emulsions. He gratefully acknowledges the many helpful discussions of the work held with members of the Radiation Physics Laboratory, in particular those with Dr. C. H. Blanchard.

[9] V. O. Nicolai and E. L. Goldwasser, Phys. Rev. **94**, 755 (1954).
[10] C. E. Falk and G. C. Philips, Phys. Rev. **83**, 468 (1951).
[11] H. Argo *et al.*, Phys. Rev. **78**, 691 (1950).
[12] B. H. Flowers and F. Mandle, Proc. Roy. Soc. (London) **A206**, 131 (1951).
[13] J. C. Gunn and J. Irving, Phil. Mag. **42**, 1353 (1951).
[14] J. Irving, Proc. Phys. Soc. (London) **66**, 17 (1953).

Neutron-Proton Scattering at 91 Mev*

R. H. Stahl† and N. F. Ramsey
Cyclotron Laboratory, Harvard University, Cambridge, Massachusetts
(Received June 23, 1954)

The angular distribution of neutrons scattered by protons has been measured for center-of-mass scattering angles between 60° and 180°. The effective neutron energy was 91±1 Mev. A liquid hydrogen scatterer and plastic scintillation proton counters were used. The experimental results are in good agreement with previous experiments at this energy.

I. INTRODUCTION

THE angular distribution of neutron-proton scattering has been measured in the past at Berkeley[1] and Harvard,[2] using neutron beams with an effective energy of about 90 Mev, and more recently at Harwell using 104-Mev neutrons.[3] Because of the importance of this experiment to the nuclear force problem, it has now been repeated with different equipment.

In this measurement, a liquid hydrogen scatterer was irradiated by neutrons from a beryllium target inserted in the circulating proton beam of the Harvard synchrocyclotron. The relative number of recoil protons at various scattering angles was measured by a movable scintillation telescope. A similar, fixed, telescope facing a CH_2 radiator monitored the neutron flux. Since the effective thickness of the liquid hydrogen target varied from one angle to another, the energy interval of protons accepted by the telescope was varied to keep the effective energy of measurement constant at 91 Mev. The results were also corrected for variation of the telescope efficiency with proton energy. The resultant relative cross sections, transformed to the center-of-mass coordinate system, were normalized to the $n-p$ total cross section.

The notation for the scattering angles follows the practice introduced by Hadley *et al.*[1] Θ and Φ are, respectively, the laboratory system neutron and proton scattering angles, and ϑ and φ the corresponding angles in the center-of-mass system. The kinematic transformation equations are given by Hadley.[1]

II. EXPERIMENTAL EQUIPMENT

A schematic diagram of the equipment used in this experiment is shown on Fig. 1. Neutrons from the $\frac{1}{8}$-in. beryllium target were collimated by a 6-ft long tapered brass collimator inserted in the water shielding tank. This defined a cone of neutrons 4 cm wide and 10 cm high at the hydrogen target about 7 meters from the source. A lead shielding block 24 in. thick, piled against the cyclotron tank, shielded against stray radiation from the cyclotron. Another lead block, 18 in. thick, at the outside of the water tank, shielded against particles scattered by the collimator walls.

Since liquid hydrogen is not normally available at this laboratory, a helium-hydrogen converter has been constructed to liquefy the small amounts of hydrogen actually needed for scattering purposes, and to keep these targets liquid for a period of several days which is required to perform an experiment. This cryostat will be described in detail elsewhere.[4] The target used in the $n-p$ experiment consisted of a 3-cm diameter cylinder of liquid hydrogen in a foil tube of 0.0006-in. thick beryllium copper. A second, evacuated tube was mounted on the same plate, and could be bombarded alternately by rotating the cryostat. In this way background scattering was measured. The copper foils did not contribute very much to the background.

The targets were kept in a large steel scattering chamber.[5] Neutrons entered, and recoil protons left through 0.005-in. aluminum windows. The targets were surrounded by a radiation shield at near liquid nitrogen temperature, having windows of 0.0005-in. aluminum in the beam direction. The counter telescope was placed on one of two I-beams attached to the chamber base. This entire assembly rotated about an axis through the liquid hydrogen target, and could be positioned by remote control to within $\pm\frac{1}{8}°$. It was convenient to use one of the counter positions (on the beam 15° from a line perpendicular to the chamber face) for recoil proton angles $\Phi=0°$ to 30°. To reduce the scattering of the protons by a long air path, a helium balloon about 2 meters long was placed between the vacuum chamber and the counter telescope. Angles from $\Phi=20°$ to 60° were measured with the counter telescope on the 45° arm. Since protons here had lower energy it was necessary to extend the vacuum chamber to the counters. The telescope was closer to the target in this position

* Supported by the joint program of the Office of Naval Research and the U. S. Atomic Energy Commission.

† U. S. Atomic Energy Commission Predoctoral Fellow, now at the University of California, Radiation Laboratory, Livermore, California.

[1] J. Hadley *et al.*, Phys. Rev. **75**, 351 (1949); K. A. Brueckner *et al.*, Phys. Rev. **75**, 555 (1949); R. H. Fox, University of California Radiation Laboratory Report UCRL-867 (unpublished); R. Wallace, Phys. Rev. **81**, 495 (1951); O. Chamberlain and S. W. Easley, Phys. Rev. **94**, 208 (1954); W. M. Powell and Chih (private communication); W. M. Powell, Phys. Rev. **94**, 786 (1954).

[2] Selove, Strauch, and Titus, Phys. Rev. **92**, 724 (1953).

[3] R. Wilson (private communication) and *Proceedings of the Fourth Annual Rochester Conference on High-Energy Physics*, (University of Rochester Press, Rochester, 1954), p. 5.

[4] C. A. Swenson and R. H. Stahl, Rev. Sci. Instr. **25**, 608 (1954).

[5] Built by J. M. Teem and U. E. Kruse.

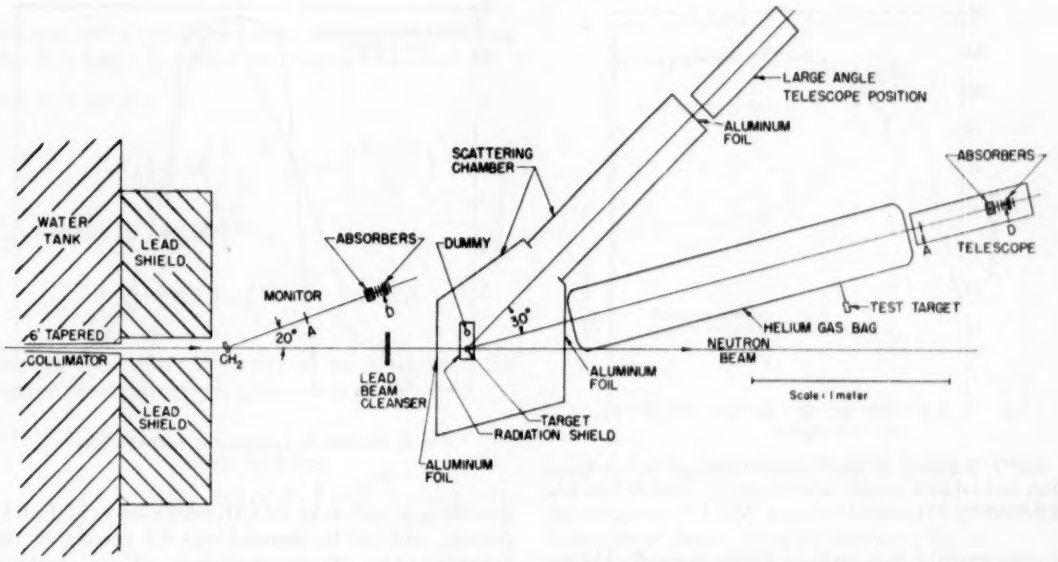

FIG. 1. Schematic diagram of $n-p$ experiment.

to improve counting rates at large proton scattering angles.

The monitor telescope with its CH_2 radiator, and a lead beam cleanser were located between the shielding and the scattering chamber. No charged particle in the neutron beam emerged from the lead with an energy above the telescope threshold.

All counters used in this experiment were plastic scintillators[6] attached to 1P21 photomultipliers tubes. Usually five scintillator telescopes were used; the fourth (D) was the defining crystal, and had the same size as the active portion of the hydrogen target -3 cm$\times$10 cm. The rest were larger, 4.4 cm$\times$11.5 cm. CH_2 absorbers were placed in front of the B crystal and behind the D crystal. The protons of interest were those which penetrated into D but not E. Different absorbers were used at each angle, calculated as described below in Sec. III, using the range energy curves of Aron, Hoffman, and Williams.[7] Polyethylene was selected as absorber material in order to keep the range telescope, of which the absorber forms a variable part, relatively homogeneous. At large recoil angles, at which the recoil proton energy is low, first C and then also B scintillators were removed from the telescope. Overlapping portions of the $n-p$ curve were taken using all states of the recoil telescope.

The amplifiers and coincidence circuits used in this experiment have been described by Strauch.[8] The only change has been the addition of a one-stage limiting preamplifier immediately following the phototubes, built around a Phillips EFP 60 secondary emission tube. The high transconductance of this tube makes it possible to build a conventional amplifying circuit with a rise time of about 10^{-8} second. Use of this amplifier improved the plateaus of the counters, while the resolution of the circuits became slightly poorer. Tests were made for accidental coincidences by displacing one counter laterally until no true coincidences could occur. It was found that at the counting rates of this experiment the accidental rate was negligible.

Individual counter efficiency was checked by inserting defining scintillators in front and back of the telescope, and requiring agreement of TT, $TABCDET$ counting rates. Efficiencies exceeded 99 percent, and were rechecked at least daily in the course of the cyclotron runs. No great variation of efficiency over the area of these rather large scintillators was noted.

The efficiency with which the telescope counted protons was checked experimentally, using cyclotron external proton beams with energies between 20 Mev and 90 Mev. A two scintillator monitor was used (the second crystal of defining size) and the telescope was set up in the external proton beam, about 1½ meters from the monitor. The strength of the beam was reduced to eliminate chance coincidences. The variation of the monitor—D coincidence counting rate was then observed as a function of absorber thickness. The results of the calibration are shown on Fig. 2. It is seen that the efficiency is quite uniform above 35 Mev. Below that, the outscattering by the A scintillator increasingly exceeds the in-scattering. The A crystal had been placed about 16 in. in front of the D crystal in order to reduce background counting rates at large Φ.

When the telescope is set up at an angle Φ, it is of

[6] Pilot Chemicals Inc., Waltham, Massachusetts; Larco Nuclear Instruments Company, Palisades Park, New Jersey.

[7] Aron, Hoffman, and Williams, Atomic Energy Commission Report AECU 663, 1949 (unpublished).

[8] K. Strauch, Rev. Sci. Instr. 24, 283 (1953).

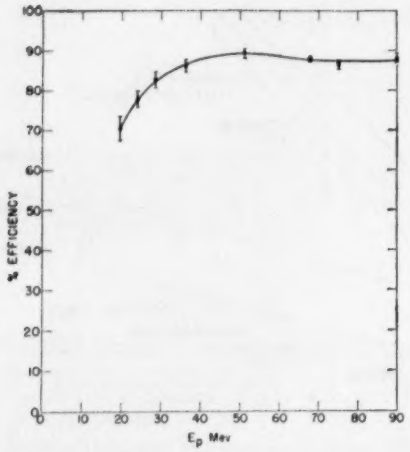

FIG. 2. Efficiency of recoil counter telescope. ×—computed from initial slope of integral range curves; ○—directly from integral range curves.

course sensitive to a range of angles about Φ. The angular resolution of the equipment is conveniently defined as the full width at half height of the angular sensitivity function. It depends on a number of factors: (1) the divergence of the incident neutron beam, (2) the size and separation of the counter-scatterer system, and (3) scattering of protons in the hydrogen, the surrounding foils, and in the telescope. Assuming each of these to yield a roughly Gaussian distribution, the angular resolution may be computed and has been shown in Fig. 3. The rise at large θ, i.e., at the smallest recoil proton angles, is caused by the long vertical shape of the counters and the active target.

The neutron monitor consisted of a telescope of the same size as the main telescope, operating as a permanent $\Phi=20°$ channel. It faced a CH_2 radiator of the same thickness to protons as the liquid hydrogen target at 20 (0.408 g/cm²). The angular resolution was poorer. The

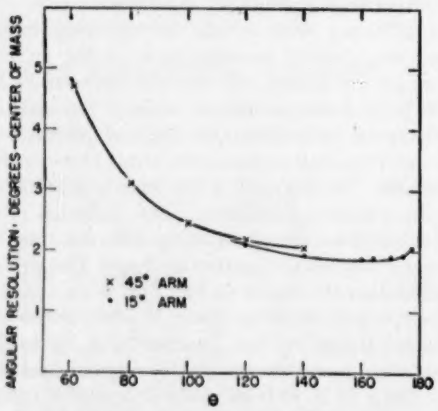

FIG. 3. Approximate angular resolution of equipment at various angles.

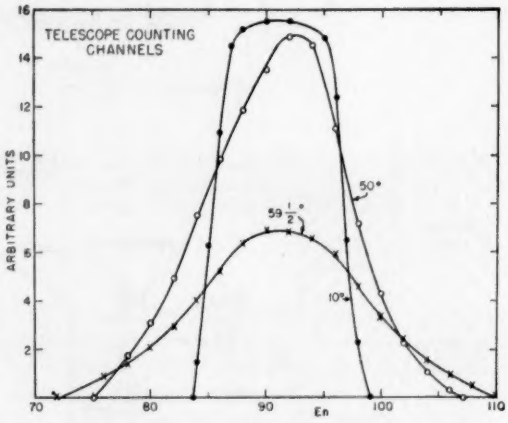

FIG. 4. Effective flux counted at various angles—typical *BF* curves.

scattering by carbon in the CH_2 amounted to (7.2±0.5) percent, and the background was 0.5 percent of the hydrogen rate. These corrections of the monitor counting rate were not normally made.

III. COUNTING CHANNEL CALCULATIONS

In all $n-p$ experiments, the incident neutron beam contains a considerable spread of energies, only a protion of which is used. The interpretation of the experimental data therefore depends on a precise knowledge of the effective flux. The energy of the recoil protons decreases rapidly with angle ($E_p(\Phi)\simeq E_n\cos^2\Phi$) while the scatterer dE/dx increases. However, in experiments using CH_2-C targets, it is customary to use at each angle scatterers designed to have the same stopping power on a neutron energy scale. On such a scale, therefore, the energetics of the experiment are then kept constant for all angles. In this experiment the same 3-cm diameter liquid hydrogen scatterer was used throughout since it was not feasible to replace the liquid hydrogen target frequently. The target thickness as seen by a proton recoiling at the center of the cylinder from a neutron of a certain energy increased rapidly with Φ. If the energy interval of protons accepted by the telescope (on the neutron energy scale) had remained constant for all Φ, then at larger Φ recoils from higher-energy neutrons would have been counted preferentially. The telescope counting channel was therefore varied to keep the energy of measurement constant.

If $C(\Phi)$ is the counting rate at an angle Φ, then

$$C(\Phi)=NVg\int\sigma(\Phi,E_n)F(E_n)B(E_n,\Phi)dE_n,$$

where N is the proton density in the scatterer, V the scatterer volume, g the solid angle intercepted by the telescope, $\sigma(\Phi,E_n)$ the $n-p$ differential cross section, $F(E_n)$ the incident neutron flux, and $B(E_n,\Phi)$ the probability of counting a proton recoiling anywhere in

the scatterer at an angle Φ from a neutron with energy E_n. It is useful to expand the cross section about E_0.

$$\sigma(\Phi,E)=\sigma(\Phi,E_0)$$
$$\times\left\{1+\alpha_\Phi\left(\frac{E-E_0}{E_0}\right)+\beta_\Phi\left(\frac{E-E_0}{E_0}\right)^2+\cdots\right\}.$$

If we define E_0' such that

$$\int B(E_n\Phi)F(E_n)\left(\frac{E-E_0'}{E_0'}\right)dE_n=0,$$

then E_0', the center of gravity of the BF curve, is the energy of measurement.

$$C(\Phi)=NVg\sigma(\Phi,E_0')$$
$$\times\left\{\int BFdE+\beta_\Phi\int BF\left(\frac{E-E_0'}{E_0'}\right)^2dE\right\}.$$

The calculation of $B(E_n,\Phi)$ falls into two parts:

$$B(E_n,\Phi)=\bar{\eta}(\Phi)B'(E_n,\Phi).$$

Here $\bar{\eta}(\Phi)$ is the average telescope efficiency for proton energies encountered at an angle Φ. It has been measured experimentally as described in the previous section. The theoretical counting efficiency $B'(E_n,\Phi)$ was computed for each angle, and the telescope limits fixed to keep the center of gravity of the $B'F$ curve at 91 Mev. Corrections were made for the circular cross section of the scatterer. $\int BFdE$ was then measured graphically. A number of these curves are shown on Fig. 4.

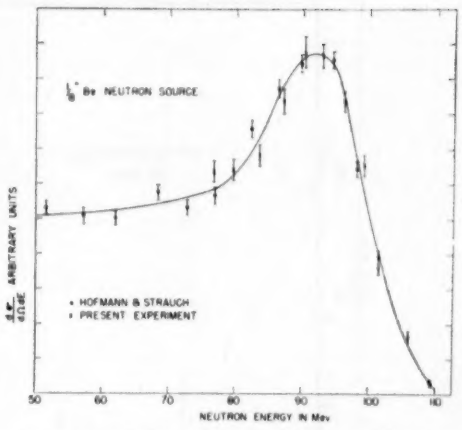

FIG. 5. Energy distribution of the ½-inch Be neutron beam.

The neutron energy spectrum used in these calculations is shown on Fig. 5. It has been measured in the past by Hofmann and Strauch,[9] and again as part of this experiment. Small variations of the neutron energy distribution could be detected by the change in the fraction AE/AD in the monitor. No changes corresponding to a shift of the neutron spectrum leading edge by more than ¾ Mev were noticed when cyclotron operation was steady.

The reliability of this correction has been investigated

TABLE I. Differential $n-p$ scattering cross section in the center-of-mass system. Neutron energy = 91 Mev (lab).

Proton angle (lab) Φ(deg)	Neutron angle (c.m.) θ(deg)	Run No. 2 mb/sterad	±%	Run 4a mb/sterad	±%	Run 4b mb/sterad	±%	Run 4c mb/sterad	±%	Run 5 mb/sterad	±%	Weighted average mb/sterad	±%
1½	176.6	13.07	3.0					13.06	4.6	13.01	3.7	13.08	3.1
2	175.6	12.90	3.2					13.01	3.6	13.45	3.7	13.09	2.9
3	173.7	13.20	4.5	13.41	3.4			13.09	3.6	13.38	2.6	13.30	2.5
4	171.7	13.36	3.0					13.32	3.1	13.08	2.7	13.24	2.6
5	169.7	13.09	3.0					12.26	2.7	13.14	2.7	12.61	2.5
6½	167.3	11.94	3.0	11.62	3.4			11.66	3.5	12.01	2.9	11.84	2.5
7½	164.5	11.82	2.7	12.10	3.4			11.50	4.4	11.74	2.9	11.82	2.6
8¾	162.0	11.02	3.3	10.24	6.2			10.93	3.5	10.72	4.3	10.85	2.8
10	159.4	10.09	3.2	10.60	2.5			10.33	3.9	10.60	3.7	10.42	2.5
−10	159.4							10.84	3.6			10.84	4.0
12	154.9	10.26	3.1	9.47	3.8					10.05	3.7	9.97	3.0
15	149.3			8.53	3.0			8.61	3.6	9.72	2.3	9.13	2.6
20	139.1	7.48	2.6	7.72	3.8	7.86	2.2			7.82	2.6	7.74	2.5
20A	139.1					8.28	3.1			7.94	2.6	8.08	3.5
25	129.0	6.16	2.2	6.40	3.9					6.98	2.4	6.51	2.6
30	118.8	5.92	2.0			6.10	3.0			6.05	2.2	5.99	2.5
35	108.7	4.90	2.9							4.98	3.5	4.93	3.3
40	98.7	4.60	2.3			4.52	3.4			4.33	4.4	4.53	3.0
45	88.7	4.17	2.7							4.40	3.0	4.19	3.5
47½	82.7					3.79	4.5			4.06	3.4	3.96	3.3
50	78.7	4.08	3.8			4.20	3.1			4.22	2.9	4.17	3.7
52	74.7									4.08	3.5	4.08	4.7
54½	69.7	3.82	5.6			4.06	4.1			4.50	3.0	4.26	4.3
57	64.8									4.89	4.6	4.88	5.9
59½	59.8									5.61	3.8	5.61	5.9

[9] J. A. Hofmann and K. Strauch, Phys. Rev. **90**, 449 (1953).

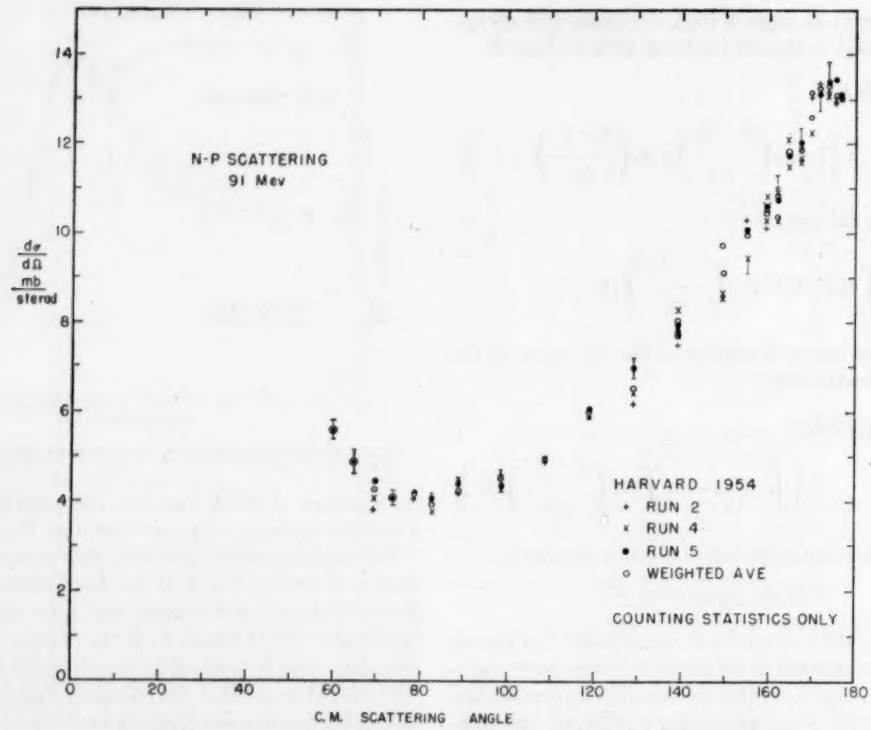

FIG. 6. Results of the individual runs of this experiment, and weighted averages. Errors shown are counting statistical mean deviations.

by varying some of the parameters. Both E_0' and $\int BFdE$ were found quite insensitive to the small variations in the target diameter which occurred when leaky foils were replaced. The integral, but not its center of gravity, was affected by variations in the neutron energy flux, especially at the largest Φ. Raising the leading edge by $2\frac{1}{2}$ Mev changed the ratio of areas at 10° and 59.5° by 5.6 percent. The uncertainty of the neutron flux is thus the chief uncertainty of this correction. As an additional check, two channels were designed for $\Phi=20°$, one using a much larger portion of the neutron spectrum. Cross sections taken in this manner have agreed within counting statistics.

The second order correction was small, a maximum of 1.3 percent at $\Phi=59\frac{1}{2}°$. The factor β was estimated using $n-p$ data at 40 Mev[10] and at 156 Mev,[11] and the integral computed from the BF curve. The error introduced by the uncertainty in this correction should be less than $\pm\frac{1}{2}$ percent for all angles.

IV. NORMALIZATION

The procedure outlined above gave relative differential cross sections in the laboratory system. These were transferred to the center-of-mass system by multiplying by $d\cos\Phi/d\cos\vartheta$. The total neutron cross section of hydrogen (78.5±3 mb)[12] was then used to place an absolute value on the cross sections. For the region $\Phi=0-60°$, not covered in this experiment, other $n-p$ experiments[1,3] were consulted. This normalization is believed accurate to ±5 percent.

V. RESULTS

The results of the various individual runs, as well as the weighted averages, are given on Table I and on Fig. 6. Errors for the individual runs are counting statistics only, while those of the weighted average are total errors compounded from the following sources:

(1) Counting statistics.

(2) Fitting errors. The counter-monitor ratios, which are the experimental numbers of this experiment, will have the same absolute values only if the equipment is set up precisely the same way each time. This was not done for runs No. 2 and No. 4b, and so an error is introduced fitting these curves to the others. This was taken to be about half the counting statistics.

(3) Error in the correction for telescope efficiency. See Fig. 2. This varies from 1 percent at 180° to 3 percent at 60°.

[10] J. Hadley *et al.*, reference 1.
[11] Randle, Taylor, and Wood, Proc. Roy. Soc. (London) **A213**, 392 (1952).
[12] A. E. Taylor and E. Wood, Phil. Mag. **44**, 95 (1953); J. de Juren and N. Knable, Phys. Rev. **77**, 606 (1950); L. J. Cook *et al.*, Phys. Rev. **75**, 7 (1949).

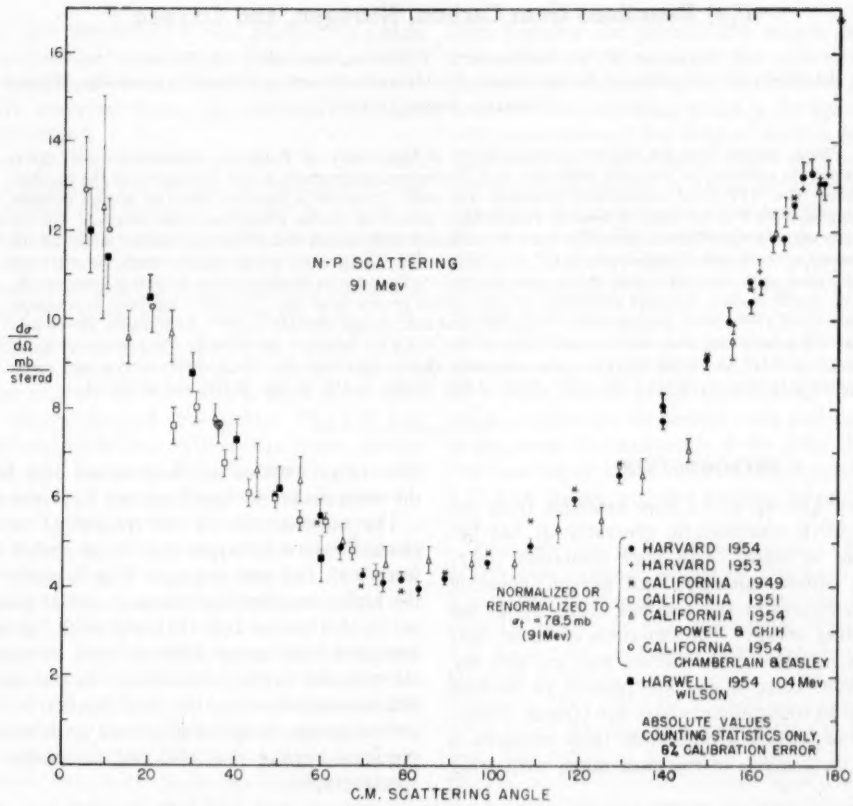

FIG. 7. Summary of $n-p$ scattering results in the neutron energy range 85–105 Mev. The California data of 1949 have been renormalized to a total cross section of 78.5 mb, and the 1951 California and 1953 Harvard experiments have been refitted to the n curve. Errors shown are those listed by each experiment (see Sec. V).

(4) Error in the counting channel computation, caused primarily by uncertainty in the neutron energy distribution. This was taken to be either 1½ percent or the error arising from a 1 Mev shift of the neutron spectrum leading edge, whichever was larger. It rose to 3 percent at 60°.

VI. CONCLUSIONS

A summary of the results of various $n-p$ experiments[1–3] in the energy region 85–105 Mev is given on Fig. 7. For this graph, the results of Hadley *et al.*[1] (California, 1949) have been renormalized to a more recent value of the $n-p$ total cross section. The results of Selove, Strauch, and Titus[2] (Harvard, 1953) and of Wallace[1] (California, 1951) have been renormalized to give a closer fit to the more complete $n-p$ angular distribution curve which is now available. The errors shown for the present experiment are the total errors discussed in the previous section.

These results are seen from Fig. 7 to be in good agreement. The $n-p$ curve is at this energy only slightly asymmetric about 90°. It becomes flat for scattering angles greater than 170°, and may dip again at the largest scattering angles measured, although the uncertainties of the experiment do not permit a definite conclusion on this subject. The ratio of cross sections at $\theta=\pi$ and $\theta=\pi/2$ is 3.15 ± 0.10.

We should like to acknowledge with thanks the cooperation of Earl Wilkie, who operated the Collins helium liquefier, and of R. Wharton and the cyclotron crew. The advice and assistance of P. Hillman, R. L. Smith, J. M. Teem, U. E. Kruse, J. Weiss, and P. Cooper were greatly appreciated.

(d,p) Reactions from Carbon, Nitrogen, and Oxygen*†

A. Sperduto, W. W. Buechner, C. K. Bockelman, and C. P. Browne
Physics Department and Laboratory for Nuclear Science, Massachusetts Institute of Technology, Cambridge, Massachusetts

(Received August 25, 1954)

Proton groups from the deuteron bombardment of thin targets of Formvar, polyethylene, and nylon have been analyzed by magnetic deflection in a 180-degree spectrograph and at 90 degrees to the incident beam. The MIT–ONR electrostatic generator was used to provide a deuteron beam at several energies ranging from 5 to 8.5 Mev. A total of twenty-eight individual proton groups has been observed. On the basis of both the relative intensities from the different targets and the differential energy shift, all the groups were identified with levels in C^{13}, C^{14}, N^{15}, or O^{17}. The present investigation covers the region of excitation up to energies corresponding approximately to the neutron binding energy in each of these nuclei. The results confirm previous knowledge of four proton groups from the $C^{12}(d,p)C^{13}$ reaction; two groups from $C^{13}(d,p)C^{14}$; seven groups from $N^{14}(d,p)N^{15}$; and four groups from $O^{16}(d,p)O^{17}$. In addition, eleven new particle groups were observed, two arising from the $C^{13}(d,p)C^{14}$ reaction and corresponding to energy levels in C^{14} at 6.723 and 6.894 Mev, and the remaining nine groups from the $N^{14}(d,p)N^{15}$ reaction and corresponding to levels in N^{15} at 7.575, 8.571, 9.062, 9.834, 10.069, 10.458, 10.544, 10.705, and 10.811 Mev.

I. INTRODUCTION

WITH energies up to 8.5 Mev available from the MIT–ONR electrostatic generator, it has become possible to study, with high resolution, (d,p) reactions on carbon, nitrogen, and oxygen, covering regions of excitation in the residual nuclei up to the neutron binding energy. The reactions of these light nuclei are of interest in themselves and are also important because these nuclei are present in backing materials and as contaminants on other targets. Hence, a knowledge of particle groups from these elements is essential for an analysis of the data taken with other target nuclei.

The present investigation has been confined to the analysis of the (d,p) groups leading to information on the excited states of C^{13}, C^{14}, N^{15}, and O^{17}. Alpha particles from (d,α) reactions were also observed but are not reported here. Earlier work in this Laboratory on these reactions, at bombarding energies of about 1.5 Mev, covered the excitation region from the ground state up to 3.4 Mev in C^{13},[1] 6.2 Mev in C^{14},[2] 8.4 Mev in N^{15},[3] and 2.9 Mev in O^{17}.[1] The information on C^{14} was mostly obtained in the course of bombardments of other target materials on which C^{13} was present only in its natural abundance. In addition, the excitation region between 5.1 and 6.2 Mev had been explored with targets in which the C^{13} content was enriched to 52 percent.[2] In the present work, these regions are now extended up to 4.9 Mev in C^{13}, 8.1 Mev in C^{14}, 10.8 Mev in N^{15}, and 4.1 Mev in O^{17}. A summary of the results from other workers on these nuclei may be found in the compilation of Ajzenberg and Lauritsen.[4]

The uncertainties in the present Q values are in general somewhat larger than those stated in previous work with this spectrograph. This is partly because of the higher bombarding energies used at present and is partly due to the fact that the results given here are compiled from many different runs on many targets, taken under varying conditions. As the main point of this investigation was the identification of the various proton groups, no great effort was made to increase the precision beyond that obtained in routine use of the spectrograph.

II. APPARATUS AND EXPERIMENTAL PROCEDURE

The experimental arrangement in connection with the MIT–ONR generator has been described in a recent paper.[5] Further details associated with the use of the 180-degree magnetic spectrograph and analysis of the data are treated in earlier publications.[1,2,6]

To aid in the identification of the target nucleus responsible for the various proton groups observed, three different target materials were used: Formvar, polyethylene, and nylon. A mass analysis of thin films of these targets was made by measuring the momenta of elastically scattered deuteron groups. The results showed that, aside from hydrogen and negligible amounts of sulfur and calcium or potassium, all three materials contained only carbon, nitrogen, and oxygen in varying proportions. The nylon targets were rich in all three elements; the Formvar targets contained carbon and oxygen with only traces of nitrogen; while polyethylene was predominantly carbon with traces of oxygen and nitrogen. By comparing the intensities of the individual proton groups when each target was

* This work has been supported in part by the joint program of the Office of Naval Research and the U. S. Atomic Energy Commission.

† A portion of these results was presented at the 1953 Washington Meeting of the American Physical Society [Phys. Rev. **91**, 473 (1953)].

[1] Buechner, Strait, Sperduto, and Malm, Phys. Rev. **76**, 1543 (1949).

[2] Sperduto, Holland, Van Patter, and Buechner, Phys. Rev. **80**, 769 (1950).

[3] R. Malm and W. W. Buechner, Phys. Rev. **80**, 771 (1950).

[4] F. Ajzenberg and T. Lauritsen, Revs. Modern Phys. **24**, 321 (1952).

[5] Buechner, Sperduto, Browne, and Bockelman, Phys. Rev. **81**, 1502 (1953).

[6] Strait, Van Patter, Buechner, and Sperduto, Phys. Rev. **81**, 747 (1951).

bombarded with deuterons, it was possible to assign the group in question to the responsible nucleus. However, final identification was based on the differential energy shift observed when the incident deuteron energy was changed.

Thin films of Formvar were prepared in the usual manner[7] by dissolving the powder in dichloro-ethylene in the proportion of 4 grams of powder to 100 cc of solution. A small droplet of this solution was deposited on the surface of distilled water. After the dichloro-ethylene evaporated, the thin film of Formvar remaining on the surface was raised with a wire frame, $\frac{1}{2}$ in.$\times\frac{3}{4}$ in. Nylon targets were made by dissolving Type 8 nylon resin DV-55[8] in isopropyl alcohol. A thin film of the solution was allowed to flow onto a glass plate and, when dry, was stripped off under water. The film was then floated and picked up with a wire frame similar to that used with Formvar. Polyethylene targets were prepared in the same manner from a solution made by dissolving small polyethylene chips in warm xylene.

Self-supporting targets thus prepared could be made in thicknesses ranging from a few hundred to several thousand angstroms. A typical target used in these experiments had a thickness of approximately 5 kev for 5-Mev deuterons. Despite this small energy loss, these targets were incapable of withstanding beam currents of the order of 0.1 μa. With thin metallic layers, such as gold, supporting these films, the targets survived long exposures with beam currents as high as 0.3 μa. For this reason, most of the work was done with targets on which a thin layer of gold had been evaporated. Unfortunately, a low background of protons was observed which appeared to originate in the gold layer. The problem of preparing thin self-supporting targets remains a serious one.

III. ASSIGNMENT OF THE PROTON GROUPS

Figure 1 shows a typical momentum spectrum of the proton groups, observed at 90 degrees to the incident deuteron beam, obtained from a series of exposures at different field settings of the spectrograph, for a deuteron bombarding energy of 7.0 Mev. The upper plot shows the number of protons in a 0.5 mm$\times$18 mm strip of emulsion *vs* $H\rho$ for a Formvar target, while the lower plot gives the number of protons *vs* $H\rho$ when the target was nylon. A similar spectrum for a polyethylene target (not shown) appeared much like that from Formvar, except that the four oxygen peaks were appreciably reduced in height.

An examination of these plots shows clearly how, on the basis of intensity considerations alone, assignment of the target nucleus responsible for most of the peaks is a simple matter. All of the prominent proton groups from Formvar and polyethylene targets were identified with either carbon or oxygen; the additional prominent groups observed from nylon targets were attributed to nitrogen. The individual peaks in the figure are labeled with the symbol of the residual nucleus formed in the (d,p) reaction. The number above each peak refers to the excitation energy in Mev; for example, O^{17} 3.055 designates the particle group corresponding to the 3.055-Mev level in O^{17}. Each of the peaks appearing in Fig. 1 has been observed many times at several bombarding energies ranging from 5 to 8.5 Mev. For the range of masses of interest in this work, unambiguous assignment of a particular peak can generally be made from a measurement of the change in proton energy observed for a given change in deuteron energy. For the energy range available in the present work and an uncertainty in the energy measurements of the order of 0.1 percent, the uncertainty in the residual mass varies from about 0.25 amu to 0.4 amu for residual masses between 13 and 17.

Two new groups attributed to the $C^{13}(d,p)C^{14}$ reaction were assigned wholly on the basis of measurements from a voltage shift. These are discussed in Sec. IV below. In the momentum region shown in Fig. 1, a total of twenty-seven proton groups were assigned as follows: four to the $C^{12}(d,p)C^{13}$ reaction, three to the $C^{13}(d,p)C^{14}$ reaction, sixteen to the $N^{14}(d,p)N^{15}$ reaction, and four to the $O^{16}(d,p)O^{17}$ reaction. The region of excitation covered in each of the residual nuclei involved extends approximately up to the neutron binding energy in these nuclei. The positions of these neutron thresholds are indicated in Fig. 1. The sharp rise of the proton count just below $H\rho=270$ kilogauss-centimeters is caused by protons elastically scattered from the gold target backing. There is present with the atomic deuteron beam a small percentage of molecular hydrogen ions. These have nearly the same momentum as the deuterons, and, as a result of small variations in generator voltage, some pass through the slits and strike the target. Many of these are scattered from the target as protons of approximately half the energy of the incident deuterons. The momentum region below $H\rho=270$ is complicated, then, by the presence of scattered protons from the target nuclei in addition to the (d,p) groups. The region of excitation above the neutron binding is currently being investigated and will be reported at a later date.

IV. DISCUSSION OF RESULTS

The $C^{12}(d,p)C^{13}$ Reaction

The four groups attributed to this reaction have all been observed previously. The Q values determined from the present work are 2.717, -0.373, -0.967, and -1.138 Mev and the corresponding excitation energies in C^{13} are 3.090, 3.684, and 3.855 Mev. These values are in good agreement with previous measurements.[4] The probable errors in the measurement of the Q values for

[7] L. M. Fry and R. T. Overman, Atomic Energy Commission Report AECD-1800, 1948 (unpublished).

[8] The nylon resin was supplied by E. I. du Pont de Nemours and Company.

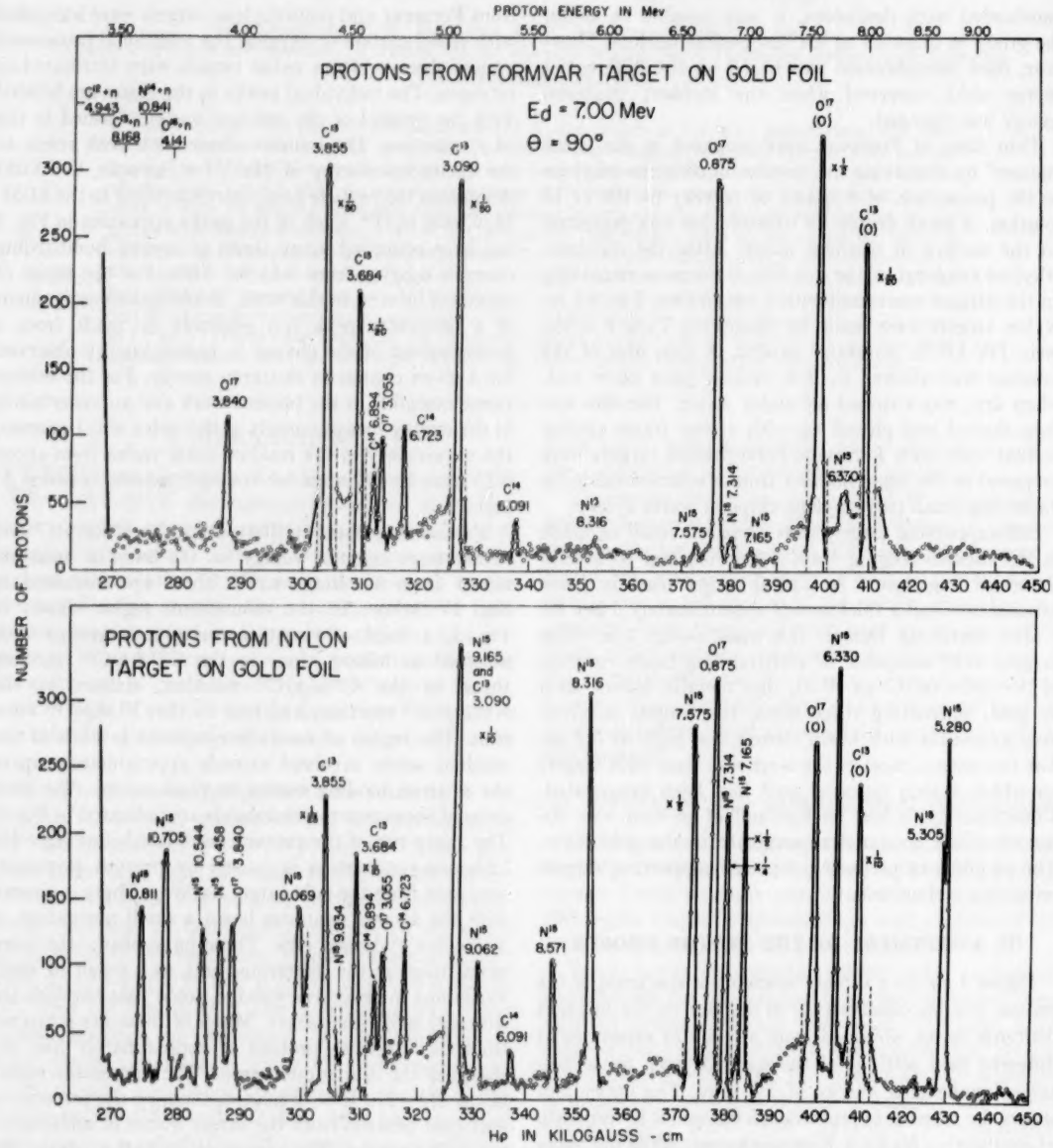
PROTON ENERGY IN Mev
PROTONS FROM FORMVAR TARGET ON GOLD FOIL
Ed = 7.00 Mev
θ = 90°
NUMBER OF PROTONS
PROTONS FROM NYLON TARGET ON GOLD FOIL
Hρ IN KILOGAUSS - cm

FIG. 1. Spectrum of proton groups from deuteron bombardment of Formvar and nylon targets.

this reaction range from 10 kev for the ground-state group to 7 kev for the 3.855 group. Our earlier measurement[6] at lower bombarding energy for the ground-state group was 2.716±0.005 Mev. In a number of cases where two adjacent particle groups are close enough in energy to be observed on the same plate, the separation can be measured to within a few kilovolts. Thus, the spacing between the 3.684- and 3.855-Mev levels has been determined as 170±3 kev. In the excitation region from the ground state up to 4.9 Mev in C^{13}, no other group has been observed with intensity greater than about 0.5 percent of the ground-state group. Proton groups corresponding to levels at 0.70 and 4.6 Mev reported[4] from the $B^{10}(\alpha,p)C^{13}$ reaction have not been observed. An energy-level diagram for C^{13} showing only the region investigated is presented in Fig. 2. The vertical arrows represent gamma-ray transitions that have been reported from the two reactions $C^{12}(n,\gamma)C^{13}$ and $C^{12}(d,p\gamma)C^{13}$. The observed gamma-ray energies are indicated along the vertical lines.

The two gamma-rays with energies of 4.948 and 3.68

Mev have been observed by Bartholomew and Kinsey[9] from slow neutron capture experiments, while the 3.082-Mev gamma has been reported by a number of workers[4] from the deuteron bombardment of C^{12}. No gamma ray that can be associated with the 3.855-Mev level has been reported.

The $C^{13}(d,p)C^{14}$ Reaction

Three of the four groups assigned to this reaction are shown in Fig. 1 at $H\rho=313$, 318, and 337 kilogauss-centimeters, the ground-state group falling outside the range of the spectrograph at the 7.0-Mev bombarding energy. However, the latter group was observed at incident energies of 5.00, 5.16, and 5.65 Mev. From measurements at these energies, the ground-state Q value was determined to be 5.942 ± 0.011 Mev. This is in excellent agreement with the previous measurement[6] as is also the case for the first excited state, for which a Q value of -0.149 ± 0.007 Mev was found in the present work.

The two groups at $H\rho=313$ and 318 kilogauss-centimeters have not been previously reported. It is clear from a comparison of the two spectra of Fig. 1 that nitrogen is not the target nucleus responsible for these groups. The assignment to C^{14} was made on the basis of results obtained at bombarding energies of 5.008 and 8.064 Mev. The expected change in proton energy over this range is (a) 2.396 Mev for a $C^{12}(d,p)C^{13}$ group; (b) 2.441 Mev for a $C^{13}(d,p)C^{14}$ group; and (c) 2.478 Mev for a $N^{14}(d,p)N^{15}$ group. The observed shift in energy was 2.436 ± 0.010 Mev.

The Q values determined from these measurements were -0.781 and -0.952 Mev, which correspond to levels in C^{14} at 6.723 and 6.894 Mev, respectively. The separation of the two new groups has been determined as 171 ± 3 kev. An energy-level diagram for C^{14} is shown in Fig. 2. The gamma-ray transitions shown here indicate the possible assignment of two gamma rays, among others, resulting from the deuteron bombardment of enriched C^{13} targets. The 6.11-Mev gamma was originally reported by Thomas and Lauritsen[10] and by others recently.[4] Mackin *et al.*[11] have reported a gamma ray of energy 6.730 ± 0.030 Mev. Bent *et al.*[12] also observed a 6.72-Mev gamma ray. This may well correspond to the 6.723-Mev level in C^{14} observed in our work. No gamma ray with an energy corresponding to the 6.894-Mev level has been reported. It should be noted here that all four groups have been observed from bombardment of the 1.1 percent C^{13} occurring in natural carbon. One measurement of the ground-state group was made with a KCN target enriched in C^{13}. The remaining survey on up through 8.1 Mev in C^{14} was explored only from bombardments of the natural carbon present on the various targets. The region below about 2-Mev excitation in C^{14} is not shown in Fig. 1 but was investigated at other bombarding energies between

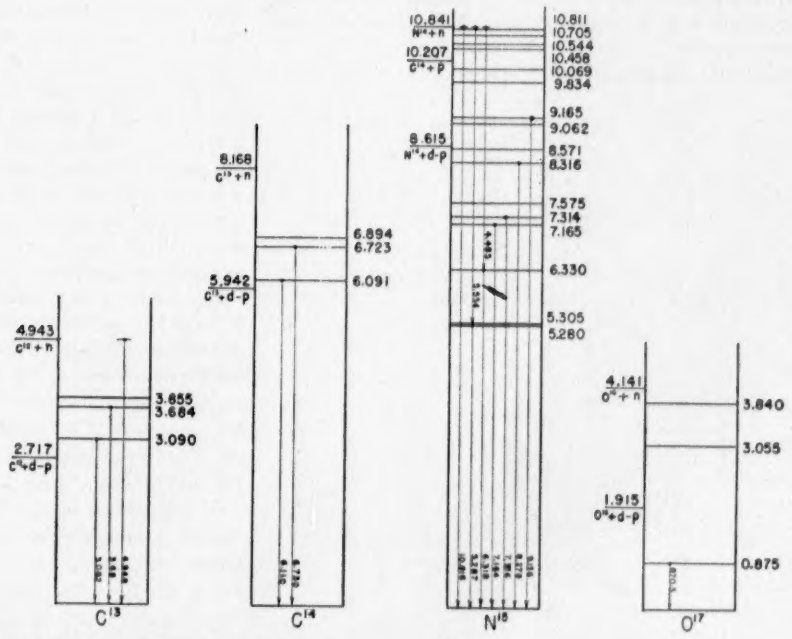

FIG. 2. Energy-level diagrams for C^{13}, C^{14}, N^{15}, and O^{17}.

[9] G. A. Bartholomew and B. B. Kinsey, Can. J. Phys. **31**, 49 (1953).
[10] R. G. Thomas and T. Lauritsen, Phys. Rev. **78**, 884 (1950).
[11] Mackin, Mims, and Mills, Phys. Rev. **93**, 950 (1954).
[12] Bent, Bonner, and Sippel, Phys. Rev. **95**, 649 (1954).

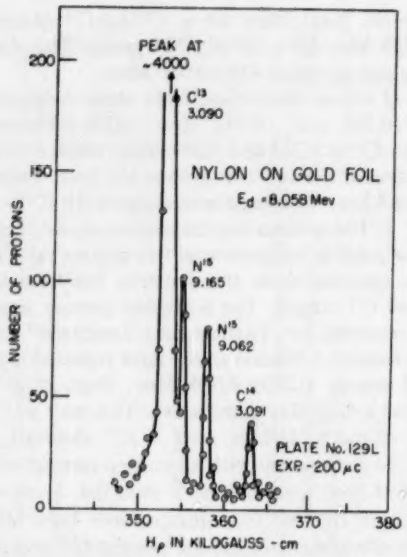

FIG. 3. Proton spectrum from 8-Mev deuteron bombardment of a nylon target showing the N^{15} 9.165 group resolved from the C^{13} 3.090 group.

5 and 6 Mev. The region between 2 and 8.1 Mev represented in Fig. 1 shows only the three groups mentioned above. Within this region, a group with intensity less than 20 percent of the intensity of the group corresponding to the 6.091-Mev level would not have been observed. A group corresponding to the reported[4] pair-emitting state at 4.1 Mev in C^{14} should occur in Fig. 1 at about 400 kilogauss-centimeters. Because of the background from gold and the intense C^{13} and O^{17} groups, a weak group here from C^{14} could easily have been obscured.

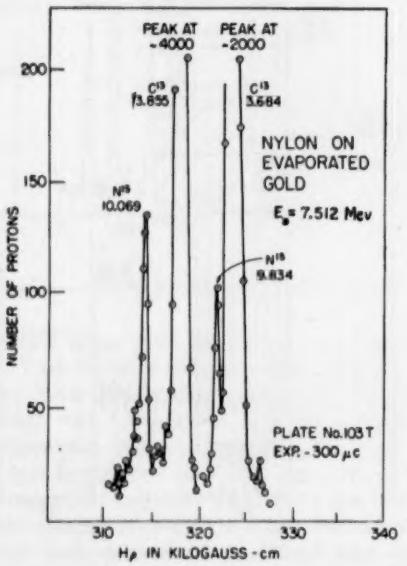

FIG. 4. Proton spectrum of a 7.5-Mev deuteron bombardment of a nylon target showing the N^{15} 9.834 group.

The $N^{14}(d,p)N^{15}$ Reaction

The present study of the reaction $N^{14}(d,p)N^{15}$ combined with the earlier investigation at lower bombarding energy covers the complete region of excitation from the ground state up to the neutron binding energy in N^{15}. Of a total of seventeen proton groups attributed to this reaction, fourteen are clearly shown in the lower part of Fig. 1. The highest-energy group corresponding to the ground-state transition was not analyzed in the present work since it fell outside the range of the spectrograph even at the lowest (5.0 Mev) bombarding energy used. The single peak at $H\rho = 327$ kilogauss-centimeters is a superposition of a N^{15} 9.165 group with the strong C^{13} 3.090 group at the 7.0-Mev bombarding energy. That this is so can be seen from Fig. 3, where this same region of the spectrum is reproduced for a bombarding energy of 8.0 Mev. The N^{15} 9.165 group here appears completely resolved from the C^{13} 3.090 peak. A group reported by Gibson and Thomas[13] at 9.22 Mev from photographic-plate range measurements is probably due to the pair of levels at 9.062 and 9.165 Mev observed here.

The remaining group not prominent in Fig. 1 should appear at $H\rho$ of 306 kilogauss-centimeters. The spectrum between 295 and 320 kilogauss-centimeters was obtained from two exposures at different field settings which were not sufficiently overlapped. The N^{15} 9.834 group was thus mostly obscured in the background of the prolific C^{13} groups, close to an edge of both photographic plates. Figure 4 shows a more adequate exposure of this region of the spectrum obtained at a bombarding energy of 7.5 Mev.

The group corresponding to the level at 7.575 Mev was not observed in the previous MIT work because of the high background of protons from the O^{17} 0.875 group. With this exception, the two investigations are in excellent agreement where they overlap.

In Table I are summarized the Q values for $N^{14}(d,p)N^{15}$ and the excitation energies in N^{15} determined from the present work, together with the previous MIT measurements. The ground-state Q value of 8.615 Mev was used in calculating the excitation energies in both cases. Also tabulated are excitation energies derived from the gamma-ray energies observed from the $N^{14}(n,\gamma)N^{15}$ reaction by Kinsey *et al.*[14]

A comparison of the three sets of data where the observations overlap shows excellent agreement, except for the two gamma rays assigned to the levels at 7.314 and 8.316 Mev. The deviations from the present (d,p) results amount to $+42$ and -38 kev, respectively,

[13] W. M. Gibson and E. E. Thomas, Proc. Roy. Soc. (London) **A210**, 543 (1952).

[14] Kinsey, Bartholomew, and Walker, Can. J. Phys. **29**, 1 (1951).

whereas the average difference for the remaining four level positions is 5 kev. The reason for this discrepancy has not been found.

A level diagram for N^{15}, incorporating all the data from Table I, is included in Fig. 2. The set of vertical arrows represent the possible gamma-ray transitions that can be correlated with the nitrogen capture radiations reported by Kinsey *et al.*[14] The values of their gamma-ray energies are indicated along the vertical line. The absence of a gamma ray that can be associated with the 7.575 level may indicate the operation of selection rules forbidding such a transition. However, because of the presence of a strong background radiation of 7.7 Mev from aluminum, it appears possible that a weak 7.6-Mev gamma ray from nitrogen might not have been observed.

TABLE I. Q values for the $N^{14}(d,p)N^{15}$ reaction and excited states in N^{15}.

Q values (Mev)		Excitation energies in N^{15} (Mev)		
Present work $E_d=5$ to 8 Mev ±0.010	Previous MIT work[a] $E_d=1.5$ Mev ≤ ±0.010	Present work	Previous MIT work[a] ±0.006	Kinsey *et al.*[b] $N^{14}(n,\gamma)N^{15}$ ~±0.015
	8.615		0	
3.335	3.339	5.280	5.276	5.275
[c]	3.310	...	5.305	...
2.285	2.287	6.330	6.328	6.325
1.450	1.451	7.165	7.164	7.164
1.301	1.306	7.314	7.309	7.356
1.040	...	7.575	...	...
0.299	0.300	8.316	8.315	8.278
0.044	...	8.571	...	...
−0.447	...	9.062	...	...
−0.550	...	9.165	...	9.156
−1.219	...	9.834	...	...
−1.454	...	10.069	...	...
−1.843	...	10.458	...	...
−1.929	...	10.544	...	...
−2.090	...	10.705	...	...
−2.196	...	10.811	...	...

[a] See reference 3.
[b] See reference 14.
[c] Not sufficiently resolved.

From a recent study of gamma-ray resonances from proton bombardment of C^{14}, Bartholomew *et al.*[15] have observed resonances at proton energies of 0.36, 0.53, and 0.64 Mev, corresponding to levels in N^{15} at 10.567, 10.737, and 10.847 Mev, respectively, in excellent agreement with our measurements.

Because of the close spacings of a number of the new groups, two or more appeared on the same photographic plate. This made possible a more accurate determination of their separation. In Table II are listed the separations of those adjacent groups that were observed on the same plate. It should be noted that the data on separations were not used in computing the excitation energies.

There has been considerable speculation regarding the closely spaced pair of levels at 5.3 Mev.[16] A study, now under way, of the angular distributions of the proton groups from this reaction may help in determining the nature of these levels.

[15] Bartholomew, Brown, Gove, Litherland, and Paul, Phys. Rev. **95**, 649 (1954).

TABLE II. Spacings for some adjacent groups from the $N^{14}(d,p)N^{15}$ reaction.

Group interval (Mev) From	To	Spacing in kev
7.165	7.314	149±4
7.314	7.575	263±5
8.316	8.571	258±4
9.062	9.165	103±4
9.834	10.069	239±6
10.458	10.544	85±3
10.544	10.705	160±4
10.705	10.811	105±3

The $O^{16}(d,p)O^{17}$ Reaction

The four groups from the $O^{16}(d,p)O^{17}$ reaction have all been observed previously. In earlier measurements in this Laboratory at lower bombarding energies, only the ground-state group and the group corresponding to the 0.875 level were observed. The present work extends the survey to include the groups corresponding to the levels in O^{17} at 3.055 and 3.840 Mev. Burrows, Powell, and Rotblat[17] have previously reported these groups in addition to groups from the $F^{19}(d,\alpha)O^{17}$ reaction leading to the same levels in O^{17}. Watson and Buechner[18] have also investigated the $F^{19}(d,\alpha)O^{17}$ reaction in this region of excitation.

A summary of these results appears in Table III. The slight discrepancies in the excitation energies of O^{17} between the present results from the $O^{16}(d,p)O^{17}$ reaction and those of Watson and Buechner from the $F^{19}(d,\alpha)O^{17}$ reaction are within the experimental errors. However, the fact that the level positions from the latter reaction are consistently higher than the new values is presumably due to the uncertainty mentioned in the earlier work regarding target contamination. An

TABLE III. Q values for the $O^{16}(d,p)O^{17}$ reaction and excitation energies in O^{17}.

Q values (Mev), $O^{16}(d,p)O^{17}$			Excitation energies (Mev) in O^{17}			
Present work $E_d=5$ to 8.5 Mev ±0.010	Previous MIT results[a] $E_d=1.5$ Mev ±0.005	Burrows *et al.*[b] ±0.02	Present work $E_d=5$ to 8 Mev ±0.012	Previous MIT results[a] $O^{16}(d,p)O^{17}$	Previous MIT results[a] $F^{19}(d,\alpha)O^{17}$	Burrows *et al.*[b] $O^{16}(d,p)O^{17}$ $F^{19}(d,\alpha)O^{17}$
1.915	1.917	1.93	0	0	0	0
1.040	1.037	1.06	0.875	0.880±0.005	0.883±0.012	0.87±0.02
−1.140		−1.14	3.055		3.069±0.012	3.06±0.02
−1.925		−1.94	3.840		3.856±0.012	3.85±0.02

[a] See references 1 and 18.
[b] See reference 17.

[16] D. R. Inglis, Revs. Modern Phys. **25**, 390 (1953).
[17] Burrows, Powell, and Rotblat, Proc. Roy. Soc. (London) **A209**, 478 (1951).
[18] H. A. Watson and W. W. Buechner, Phys. Rev. **88**, 1324 (1952).

energy-level diagram for O^{17} is included in Fig. 2, which also shows the 870.5±2.0 kev gamma ray reported by Thomas and Lauritsen.[10]

The authors wish to express their appreciation for the assistance they received in the course of this work from the various members of the ONR Generator Group. We are indebted to Dr. M. M. Elkind, Mr. Walter J. Fader, and Mr. C. M. Braams for their help in obtaining preliminary data. We wish especially to thank those who read the photographic plates, particularly Mr. W. A. Tripp, Miss Janet Frothingham, and Miss Sylvia Darrow.

PHYSICAL REVIEW VOLUME 96, NUMBER 5 DECEMBER 1, 1954

Proton-Proton Scattering at 5.77 Mev*

E. J. Zimmerman,† R. O. Kerman,‡ Sidney Singer, P. Gerald Kruger, and W. Jentschke
Physics Department, University of Illinois, Urbana, Illinois

(Received August 30, 1954)

Absolute differential scattering cross sections for proton-proton scattering at laboratory energies of 5.77 and 5.86 Mev (±1 percent) have been obtained with an accuracy of about one percent at many angles (23° to 110° c.m.) by two independent experiments, one employing nuclear emulsion plates as detectors and the other employing proportional counters. Reduced to the same energy, the average indicated S-wave nuclear phase shift is in excellent agreement with other data for this energy region. However, at small scattering angles, important for determining a P-wave phase shift, the measured cross sections differed originally by 3 to 5 percent, the nuclear emulsions method indicating a P-wave shift of -0.08 ± 0.05 degree, and the original counter data indicating -0.34 ± 0.05 degree. After the beam collimation was improved and the energy spectrum of the incident proton beam was examined, check runs with the counters at six scattering angles failed to indicate the large P-wave effect, giving -0.08 ± 0.07 degree, in agreement with the emulsion data. It therefore appears likely that the P-wave shift at this energy is small (less than 0.1 degree) and negative, in agreement with other determinations in this energy region.

I. INTRODUCTION

RESULTS of the proton-proton scattering experiments carried out over a period of several years at the University of Illinois Cyclotron Laboratory will be reported here. While some of the data have already been published in preliminary form,[1,2] this report gives a complete analysis of the experiments, together with some additional information.

Two separate methods were used to measure the differential scattering cross sections. The two experiments were almost completely independent, only the device for measuring the charge being common to both. One experiment employed the scattering chamber constructed by Rodgers, Meagher, and Leiter[3–5] in which the scattered protons were recorded in nuclear emulsions. The second method used a scattering chamber in which scattered protons were detected by proportional counters used in coincidence to eliminate the effect from background radiation produced by the cyclotron.

A number of studies of proton-proton scattering in the low-energy region (below about 10 Mev) have been made. Reference will be made here only to some fairly recent theoretical analyses which contain references to early theoretical and experimental work.[6–11] Reference will also be made to some very recent experimental papers,[12–17] most of which also contain bibliographies.

II. NUCLEAR EMULSION EXPERIMENT[18]

The scattering chamber, used previously by Rodgers,[3] Leiter,[4] Meagher,[5] and concurrently by Kreger,[19] is constructed so that particles scattered over a wide range of angles are recorded simultaneously on six

* Assisted by the joint program of the U. S. Office of Naval Research and the U. S. Atomic Energy Commission.

† U. S. Atomic Energy Commission Predoctoral Fellow, 1948–1950, now at the University of Nebraska.

‡ Now at Kalamazoo College.

[1] E. J. Zimmerman and P. G. Kruger, Phys. Rev. **83**, 218 (1951).

[2] Kerman, Kreger, and Kruger, Phys. Rev. **89**, 908 (1953).

[3] Rodgers, Leiter, and Kruger, Phys. Rev. **78**, 656 (1950).

[4] Leiter, Rodgers, and Kruger, Phys. Rev. **78**, 663 (1950).

[5] R. E. Meagher, Phys. Rev. **78**, 667 (1950).

[6] G. Breit and R. D. Hatcher, Phys. Rev. **78**, 110 (1950).

[7] R. S. Christian and H. P. Noyes, Phys. Rev. **79**, 85 (1950).

[8] J. D. Jackson and J. M. Blatt, Revs. Modern Phys. **22**, 77 (1950).

[9] Yovits, Smith, Hull, Bengston, and Breit, Phys. Rev. **85**, 540 (1952).

[10] A. Martin and L. Verlet, Phys. Rev. **89**, 519 (1953).

[11] H. H. Hall and J. L. Powell, Phys. Rev. **90**, 912 (1953).

[12] James Rouvina, Phys. Rev. **81**, 593 (1951).

[13] K. B. Mather, Phys. Rev. **82**, 133 (1951).

[14] F. L. Fillmore, Phys. Rev. **83**, 1252 (1951).

[15] Bondelid, Braden, Battat, and Bohlman, Phys. Rev. **87**, 699 (1952).

[16] Allred, Armstrong, Bondelid, and Rosen, Phys. Rev. **88**, 433 (1953).

[17] Worthington, McGruer, and Findley, Phys. Rev. **90**, 899 (1953).

[18] The work of this section was aided in part by a grant from the Research Corporation. This section is part of a thesis submitted by R. O. Kerman in partial fulfillment of the requirements for the degree of Doctor of Philosophy at the University of Illinois, 1953.

[19] Kreger, Jentschke, and Kruger, Phys. Rev. **93**, 837 (1954).

50-micron Ilford nuclear plates mounted around the periphery of the cylindrical chamber. The slit system is such that all particles striking a certain region of the nuclear plate have been scattered through nearly the same laboratory angle. Consequently the incident angle and range of the particles in the emulsion need not be measured; to obtain cross sections it is only necessary to count all the tracks on a given swath of the plate and to measure precisely all the different dimensions which enter into the geometry.

The construction and operation of the chamber, the details of the various annular slits used, and the method used to measure the total charge are all described by Kreger.[19] The technique by which the uncorrected cross sections are calculated from the nuclear emulsion data is discussed by Leiter.[4]

A. Experimental Procedure

Hydrogen gas was admitted to the chamber through a heated palladium thimble to a pressure of about 5 cm Hg. Liquid nitrogen traps were not used because of the findings of Rouvina[12] concerning their effect on the cross sections. The low-angle annular slit was used in recording protons scattered through a laboratory angle of from 11.5° to 30°, while the high-angle slit was used for the range 21° to 55°. In addition, a background run was taken, and also a run using a "closed slit"[19] (identical with the high-angle annular slit except that the two slit edges were just closed) to check effects due to slit penetration. A drawing of the annular slits and a table of their geometrical dimensions are given in Fig. 3 and Table I, respectively, of reference 19.

The number of incident protons was determined by collecting the undeflected particles in a Faraday cup to which was attached a bank of polystyrene capacitors.[20] A vibrating reed electrometer[21,22] was used to measure the capacitor voltage.

The energy of the incident protons was determined (in connection with a different experiment[19]) by measuring their range in the emulsion of an Ilford C2 nuclear plate, and was found to be 5.80 Mev±0.7 percent probable error with an actual spread in energy corresponding to a Gaussian distribution with a half-width of about 30 kev. The energy was decreased by 0.03 Mev to allow for the energy loss in the hydrogen gas before scattering occurs. In order to enter the scattering chamber, the proton beam from the cyclotron must be bent through an angle of 37° in an analyzer magnet whose field was stabilized by means of a proton nuclear magnetic resonance device. The proton magnetic resonance frequency was measured for each data run and was used to indicate any small changes in the proton energy.

[20] Manufactured by John E. Fast and Company, Chicago, Illinois.

[21] Manufactured by Applied Physics Corporation, Pasadena, California.

[22] Palevsky, Swank, and Grenchik, Rev. Sci. Instr. **18**, 298 (1947).

B. Determination of Corrected Cross Sections

Four corrections to the measured cross sections are required before comparison with the theory can be made.

1. Penetration Correction

The closed slit run was made to measure experimentally the correction for effects caused by slit penetration in the annular slit. The measured correction agreed with that obtained from the theoretical expression;[3,19] both are listed in Table I. Values of the penetration correction used in the present experiment are given in column 4 of Table II.

An additional check on the validity of the penetration correction was carried out by counting five angles of one of the low angle data runs using two different minimum track lengths. After making the background and penetration corrections, both cross sections should be the same. The cross section obtained by using the smaller minimum track length came out $\frac{1}{4}$ percent higher on the average. This difference was probably not significant, but it did suggest the possibility that some of the short tracks were due to protons which had been scattered out of the emulsion before coming to rest. A recount of these angles using a higher microscope magnification failed to show such an effect. In the error analysis the probable error in the penetration correction was taken to be 15 percent in order to take into account the $\frac{1}{4}$ percent difference.

2. Background Correction

A background run was made to measure the correction needed to account for slit-scattered or impurity-scattered protons which reached the photographic plates. The run was exactly like a low-angle data run, except that no gas was admitted to the chamber. The run was started after a length of time equal to the time required to admit the hydrogen, and was continued for twice the length of a regular data run. The background correction was measured to be less than 0.1 percent except at the three lowest angles, where corrections up to 1.3 percent were required. The tracks comprising the background at the lowest angles were considerably shorter than would be expected from contaminant scattering and were evidently due to penetration through or scattering from one of the anti-scattering baffles in the collimation system. The background correction is recorded in Table II.

To check the high-angle background, two plates in one of the high-angle data runs were covered with aluminum foil sufficiently thick to almost stop protons scattered by protons; protons scattered from heavy nuclei would manifest themselves by their long track lengths. The number of such tracks was negligible, and

TABLE I. Comparison of theoretically and experimentally determined penetration corrections. Values are the percentage ratios of the number of penetration particles to the number of particles passing through the annular slit opening, for a given minimum track length used in counting.

Laboratory angle	23°	25°	30°	35°	40°	45°	50°
Experimental correction (%)	0.50±0.05	0.65±0.06	1.06±0.07	1.09±0.07	1.05±0.06	0.96±0.06	0.58±0.04
Theoretical correction (%)	0.50	0.74	1.10	1.24	1.08	0.89	0.59

no background correction was made for the high angle run.

3. Second Order Geometry Correction

The finite size of the proton beam, its divergence, and the variation of angle and cross section over the swath area were neglected in deriving the formula used for calculating the uncorrected cross sections. These were taken into account by considering the scattering from an element in the scattering volume to an element of area in the nuclear plate swath and integrating over the scattering volume and the swath area, as was done by Critchfield and Dodder[23] for a different geometry. The result[24] was an expression consisting of three parts: the first represented a correction to the expression for the solid angle; the second part represented the correction necessary because the average scattering angle was slightly different from the angle determined by a line from the center of the scattering volume to the center of the swath area; and the third part took into account the change in cross section over the angular interval accepted by the detector. The geometry corrections, never greater than 0.9 percent, are listed in Table II.

4. Energy Correction

The scattering chamber is so constructed that the position of the scattering volume changes with scattering angle. For example, a particle scattered through 55° (lab) must travel about 14 cm farther along the axis of the chamber before being scattered than a particle scattered through 11.5°. Thus, the energy at the scattering volume changes with scattering angle. In addition, it was found that the incident proton energy was slightly smaller for one of the data runs than for the others. It was therefore necessary to correct the cross sections obtained from that run to the same energy as those obtained from the other runs; and it was also desired to correct the cross sections for the slight energy dependence on the scattering angle. Accordingly, a number of curves of cross section *vs* energy for various laboratory angles from 10° to 45° were plotted for energies up to 7.5 Mev using published results. The slope of each curve was measured graphically at 5.75

TABLE II. Corrections and final cross sections for plates at 5.77 Mev.[a]

Angle (c.m.)	Angular[d] resolution	No. of counts[b]	Penetrat.[e] correction %	Background correction[c] %	Geom. correct., %	Cross section (c.m.) mb/steradian	App. *S*-wave phase shift
23.00°	±32′	24 427	1.11	0.16	0.13	118.0 ±0.8	55.23±0.48°
			1.89	1.28			
23.87	±32′	11 390	1.27	0.31	0.33	110.0 ±0.9	55.18±0.48
			1.66	0.81			
26.00	±34′	19 558	1.11	0.09	0.63	95.91±0.70	54.75±0.40
			1.96	0.21			
27.85	±37′	10 540	1.70	0.07	0.64	91.73±0.79	55.67±0.40
30.00	±40′	22 651	1.07	0.06	0.67	87.30±0.64	55.68±0.35
31.84	±44′	10 185	1.91	0.05	0.77	83.53±0.73	55.10±0.37
35.00	±46′	22 766	1.43	0.05	0.88	81.98±0.58	55.17±0.32
			2.17	0.05			
40.00	±49′	21 564	1.53	0.05	0.92	82.82±0.60	55.57±0.32
			2.01	0.05			
45.00	±53′	12 391	1.71	0	0.86	81.12±0.67	54.55±0.35
50.00	±56′	31 417	1.0	0	0.78	83.28±0.64	54.98±0.34
54.76	±57′	22 614	1.48	0	0.68	85.00±0.62	55.23±0.36
60.00	±58′	35 480	0.82	0	0.58	85.70±0.65	55.17±0.35
69.70	±58′	12 188	1.23	0	0.38	86.86±0.71	55.08±0.37
79.68	±59′	11 606	1.08	0	0.16	86.73±0.70	54.73±0.38
84.73	±59′	10 733	1.52	0	0.05	86.51±0.72	54.57±0.38
89.68	±60′	10 576	0.87	0	−0.09	87.18±0.70	54.90±0.37
94.71	±63′	11 617	1.08	0	−0.18	87.28±0.68	54.87±0.37
99.68	±52′	10 564	0.66	0	−0.28	87.87±0.70	55.18±0.37
109.69	±52′	10 454	0.41	0	−0.49	86.01±0.69	54.72±0.37

[a] Errors listed are probable errors.
[b] The value listed is the total of all runs counted at that angle.
[c] Two values are listed where two different minimum track lengths were used.
[d] The angular resolution is in the laboratory system.
[e] Values of the penetration correction in Table II differ from those in Table I because different minimum track lengths were used.

[23] C. L. Critchfield and D. C. Dodder, Phys. Rev. 75, 419 (1949).
[24] R. O. Kerman, Ph.D. thesis, University of Illinois, 1953 (unpublished).

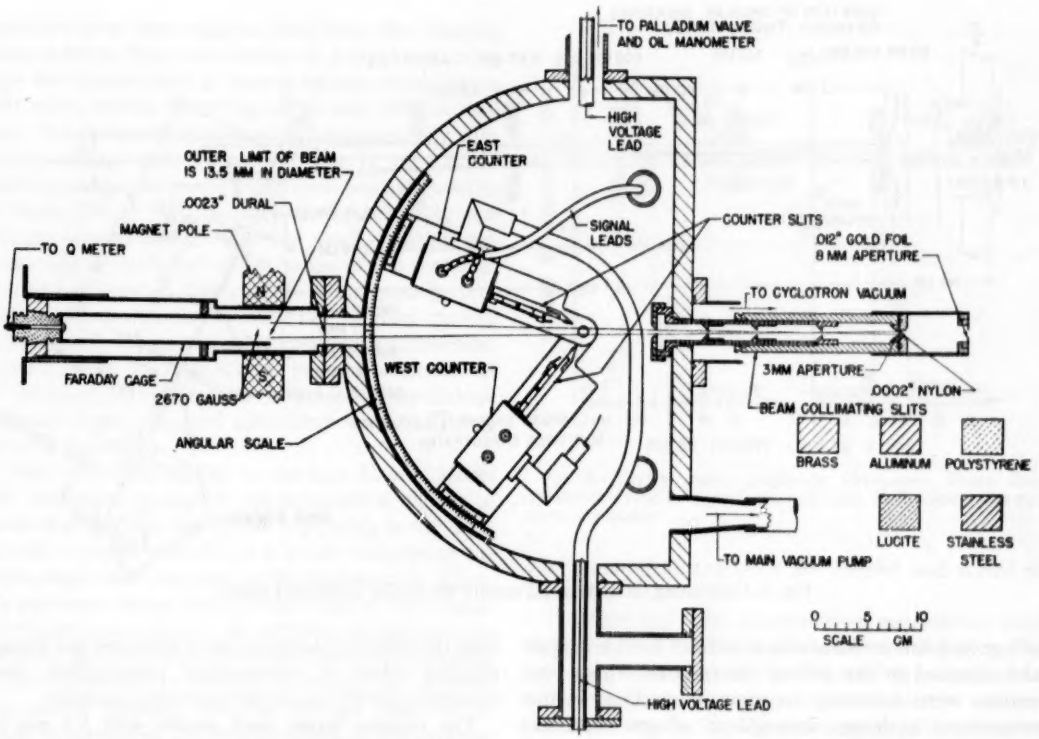

FIG. 1. Horizontal view of counter scattering chamber. Depth perpendicular to drawing is about 10 cm.

Mev. Finally, a plot of $\partial\sigma/\partial E$ *vs* angle was made; this curve was the basis of all energy corrections.

The corrected center-of-mass cross sections together with the estimated probable errors are listed in Table II. These errors were calculated in the usual way and include those due to statistics, uncertainty in measurements of angles, geometrical dimensions, total charge, and gas pressure and temperature, as well as a 0.4 percent probable error in counting tracks and an assumed 15 percent error in each correction. The average angular resolution in the laboratory system as defined by Kreger *et al.*[19] is recorded in column 2 of Table II. The corrected center-of-mass cross sections are plotted against the center-of-mass scattering angle in Fig. 5.

III. PROPORTIONAL COUNTER EXPERIMENTS[25]

A. Scattering Chamber

Concurrently with the use of nuclear plates to detect scattered protons, a scattering chamber for use with gas-filled counters was completed, and is shown in Fig. 1. It was placed adjacent to the photographic scattering chamber at the end of the exit tube making an angle of 51° with the particles emerging from the cyclotron.[3] After being deflected in the analyzer magnet, the proton beam passed through a round 8-mm aperture in an insulated gold foil used for monitoring the intensity of the analyzed beam, and entered the scattering chamber through a collimating slit system and a 0.0002-in. nylon foil. The slit geometry in a horizontal plane is shown in Fig. 2. The first and last of the collimating slits defined the angular spread of the beam in the chamber; the others prevented protons scattered from the slit-holder walls from entering the scattering volume. The proton beam left the rear of the chamber through a 0.0023-in. Dural foil and entered the Faraday cup, which was maintained at 10^{-5} mm Hg by a separate vacuum system. The Faraday cup construction and the charge measurement technique were similar to those used with the photographic chamber.

Scattered protons were detected on either side of the incident beam by one of two double proportional counters movable in the horizontal plane (the East and West counters). These counters were mirror images, and Fig. 3 shows the construction of one of them. The single high-voltage electrode containing the two separate counting volumes was designed so that all particles entering the counter would have equal ionization paths. The electrode was supported by three Kovar-glass seals which were modified from commercial seals by clipping off the stem and spotting glass over the exposed metallic portion of the seal. The high-

[25] Part of the material in this section is from a thesis submitted by E. J. Zimmerman in partial fulfillment for the requirements for the Ph.D. at the University of Illinois, 1951.

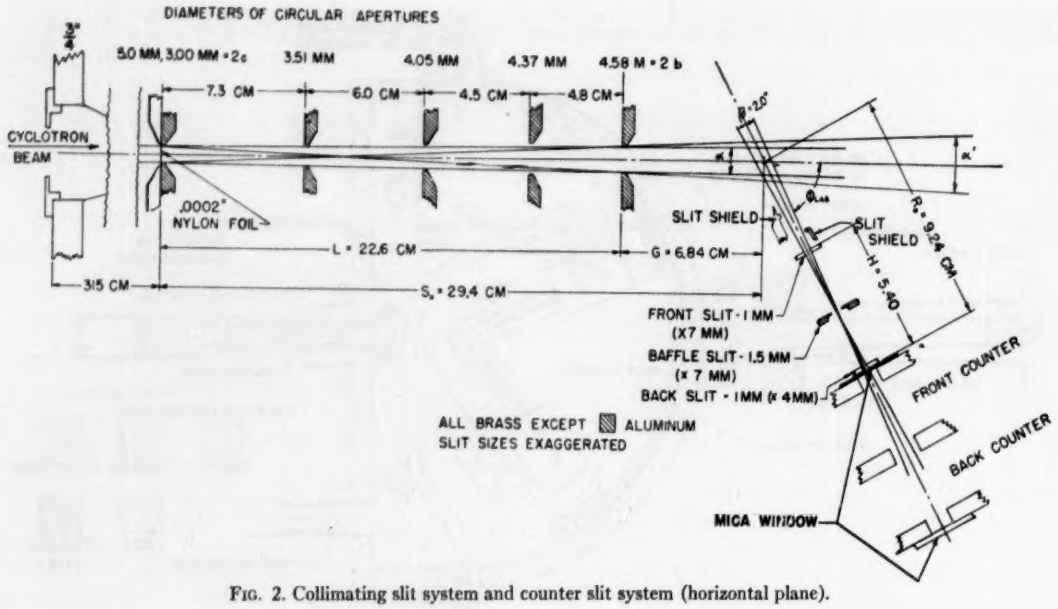

FIG. 2. Collimating slit system and counter slit system (horizontal plane).

voltage lead was enclosed in a re-entrant flexible copper tube attached to the side of the counter. These precautions were necessary to prevent sparking in the low-pressure hydrogen atmosphere of the chamber. Pulses from the counters were taken at ground level from the 0.002 in. platinum center wires and fed through shielded cables to conventional preamplifiers shock mounted directly below the scattering chamber.

The counter boxes were sealed with 1.5 mg/cm² mica foils and filled with pure methane at 35 cm Hg.[26]

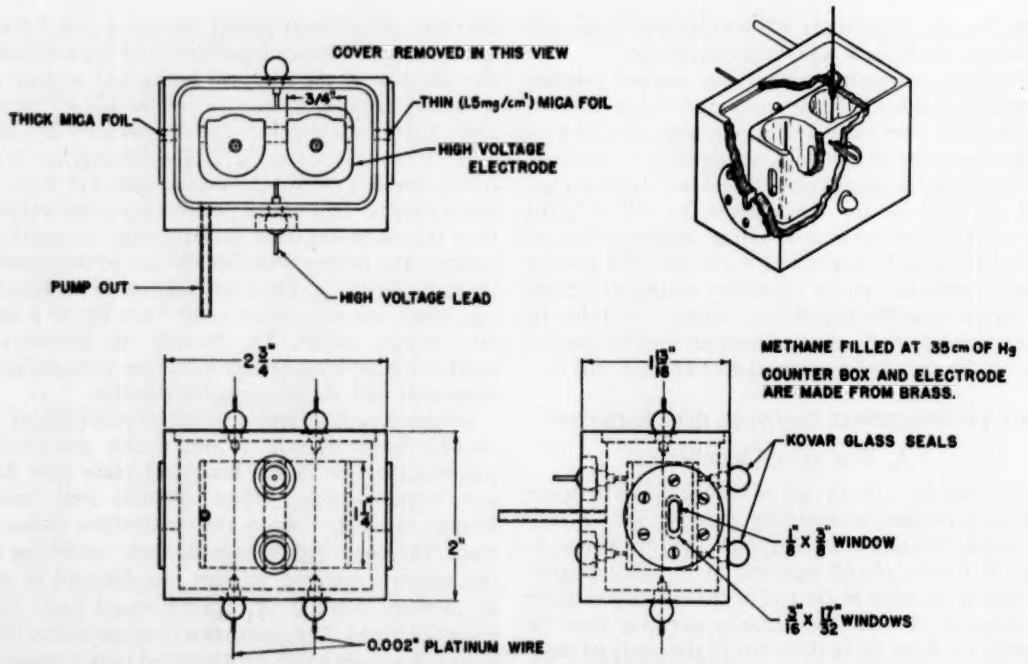

FIG. 3. Construction of the double proportional counter.

[26] The sealing and filling were done by Radiation Counter Laboratories, Chicago, Illinois.

Extensive tests were made to determine the counting characteristics. The cross section at a fixed scattering angle was independent of counter voltage from 1400 to 2100 volts; normal operating range was 1700 to 1900 volts. The gas multiplication varied exponentially with counter voltage over the same range. In the normal operating range, the gas multiplication was measured to be about 250 to 900. Because of the relatively low methane counter gas pressure and small counting volumes, only a small part of the range of the scattered protons was spent in the counters. Consequently, protons of different energies could not be very readily distinguished. There was some energy discrimination, however, since the low-energy protons scattered at 55° (lab) had nearly 2.5 times the pulse heights of those scattered at 13°, in good agreement with the Bragg curve for protons.

Linear amplifiers similar to the Los Alamos Model 100[27] were used to amplify the preamplifier signals to a level of about 75 volts. Pulses originating in the front and rear counters were fed to a stable coincidence circuit having a resolving time of 80 microseconds. Thus, only particles coming from the direction of the scattering volume were counted. In addition, coincidence signals from the front counter were pulse-height analyzed so that pulses due to protons of energy far removed from that of properly scattered protons could be rejected. By analyzing the counter pulses in this manner, background was reduced to a negligible amount; and since the singles counting rate never exceeded 10 counts per second, no correction was needed for the resolving time of the coincidence circuit. Test runs with the proton beam stopped in front of the chamber, or with no hydrogen in the chamber, showed that differences (about 0.2 percent) between the singles and coincidence counting rates could be traced to transient sparks and arcs in the cyclotron control room, and possibly to neutron recoils in the methane counter gas. This type of background was small, and no correction was made for it.

Typical pulse amplitude analyses are shown in Fig. 4. In computing the "proton count" for each scattering run, both very large and very small pulses were discarded. Perhaps the largest source of error in the experiment was due to personal factors involved in deciding where to cut off the pulse distribution; the average estimated uncertainty in the proton count from this cause was 0.8 percent. This uncertainty, estimated for each run, was combined with the statistical standard deviation for that run, and the result used as the standard deviation in the proton count.

As shown in Fig. 2, the scattering volume was defined by two rectangular slits in front of each counter. The dimensions of the various slits were measured with a comparator, and their spacing with a micrometer.

[27] W. C. Elmore and M. Sands, *Electronics* (McGraw-Hill Book Company, Inc., New York, 1949), p. 166.

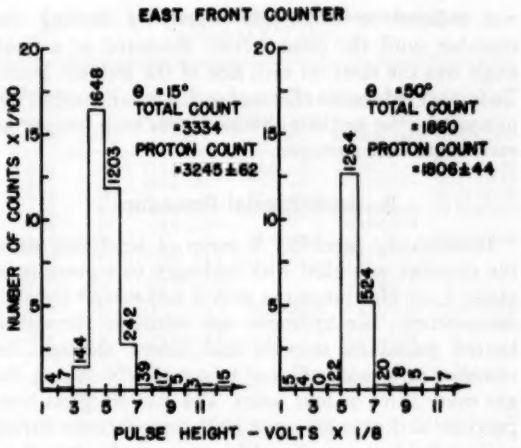

FIG. 4. Typical pulse amplitude histograms. Front East counter analyzed in coincidence with back East counter, for two scattering angles.

The geometrical constants are defined and stated in Table III.

The East and West counters were mounted on arms which could be rotated from outside the chamber. The scattering angle could be read to 0.05° by means of an angular scale and verniers mounted on the counter arms. The angular misalignment of the entire chamber

TABLE III. Notation and geometrical constants for counter experiment.

Symbol	
$\sigma_{c.m.}, \sigma_L$	Differential scattering cross section in center-of-mass, laboratory system.
$\theta_{c.m.}, \theta_L$	Scattering angle in center-of-mass, laboratory system
N_s	Number of scattered protons observed at θ_L
ω	Solid angle subtended by back counter slit at the center of the scattering volume $=fd/R_0^3$
τ	Gas target thickness for counter slit system at 90° to the incident beam of protons $=2wR_0/H$
H_1	Difference in heights of oil columns in manometer
m	Temperature coefficient of density of Octoil-S; $d_t=d_0[1-m(t-25)]$
V	Vibrating Reed Electrometer output voltage, difference before and after a run
R_s	Vibrating Reed Electrometer calibration
T	Absolute temperature in scattering chamber
H	Distance between counter slits
R_0	Distance from scattering volume to back counter slit
$2w$	Width of front counter slit
d	Width of back counter slit
f	Height of back counter slit
E	Energy of incident protons
$E(\theta_L)$	Energy of proton scattered through a laboratory angle θ_L

Quantity		East counter	West counter
H	(cm)	5.397 ±0.003	5.398 ±0.003
R_0	(cm)	9.238 ±0.004	9.250 ±0.003
$2w$	(cm)	0.9418±0.00014	0.9570±0.00014
d	(mm)	0.9566±0.00014	0.9658±0.00014
f	(mm)	4.032 ±0.004	4.099 ±0.004
τ	(cm)	0.1612±0.0003	0.1640±0.0003
$\omega\times10^4$	(sterad)	4.520 ±0.008	4.627 ±0.008

was reduced to 0.02±0.05 degree by moving the chamber until the cross section measured at a fixed angle was the same on each side of the incident beam. To further reduce the effects of such a misalignment, the measured cross sections obtained from each counter at each angle were averaged.

B. Experimental Procedure

Immediately preceding a series of scattering runs, the chamber was filled with hydrogen to a pressure of about 5 cm Hg (measured with a calibrated[28] Octoil-S manometer). The hydrogen was admitted through a heated palladium thimble and flowed through the chamber at a rate sufficient to completely change the gas every three or four hours. The scattering gas temperature and pressure were read several times during each individual run. For laboratory angles less than 45°, a particular run was terminated when 2500 scattered protons were recorded (about 20 minutes); above 45° only 1500 scattered protons were counted per run.

Protons were counted alternately in the East and West counters, and the order in which the scattering angle was changed was varied from day to day. One hundred usable scattering runs were made during which 10 000 scattered protons were detected by each counter at each scattering angle.

The energy of the incident protons was measured in connection with a previous experiment.[29] The range of the protons in air was measured using a scintillation counter technique and the proton energy was found to be 5.93 Mev±1 percent, with a 65-kev spread about the mean energy. The energy of the protons was degraded by their passing through the 0.0002-in. nylon foil and 29.5 cm of gas in the chamber before reaching the scattering volume. The energy loss was calculated from available data[30,31] and was found to be 70±10 kev, so that the energy at scattering was 5.86 Mev±1 percent.

During the data runs, as in the photographic plates experiment, both the cyclotron magnet and analyzer magnet fields were stabilized by use of a proton-moment automaton control.

Most of the data were taken using liquid nitrogen cold traps which were connected to the chamber. However, during the analysis of these data, it was learned that Rouvina,[12] using photographic plates as detectors, found that the use of liquid nitrogen traps during the experiment gave incorrect results, apparently because of the less efficient pumping action of the traps with hydrogen in the chamber as compared to background runs taken with no gas in the chamber. While investigations of contaminant scattering (described below) had convinced us of the absence of any contaminant vapors in our scattering chamber, it was thought desirable to check for a liquid nitrogen effect. Accordingly, a series of runs were made at several small scattering angles (where contaminant errors are largest) in an effort to compare cross sections taken with liquid nitrogen with those taken without liquid nitrogen. No appreciable effect was found. Since these data were in agreement with those taken in the initial series of runs, they are included in Table V.

TABLE IV. Corrections and energy reduction data for the counter cross sections. The coincidence and finite geometry corrections were used in obtaining the final counter cross sections, while the derivatives listed in the last three columns were used to reduce these data to an equivalent energy of 5.77 Mev.

$\theta_{c.m.}$	Coincidence correction East counter %	Coincidence correction West counter %	Finite geometry correction (%)	$-\frac{\Delta\sigma}{\Delta E}$ mb/Mev	$\frac{E\Delta\theta_0}{\Delta E}$ (deg)	$\sigma\frac{\Delta\theta_0}{\Delta\sigma}$ (deg)
24	0.20	0.16	1.8	25	50	44
26	0.20	0.16	1.4	20	43	37
28	0.20	0.16	1.2	15.5	38	35
30	0.20	0.16	0.9	14.5	36	33
40	0.23	0.19	0.4	11.5	31.5	33
45	0.27	0.22	0.3	11.5	31	33
50	0.31	0.25	0.2	11.7	32	34
60	0.43	0.35	0.2	12.0	33	35
70	0.63	0.51	0.1	12.7	34	35.5
80	0.98	0.80	0.1	13	34	36
90	1.62	1.32	...	13	34	36
100	3.26	2.68	...			
110	7.12	5.84				

C. Calculation of Corrected Cross Sections

Upon inserting values for the fundamental constants and constants of the apparatus, the formula for the center-of-mass cross section in terms of the laboratory scattering angle takes the form:

$$\sigma_{c.m.}(\theta_L)=3.0198\times10^{-33}\left(\frac{1}{\tau\omega}\right)\left[\frac{T}{1-m(t-25)}\right]\left(\frac{N_s\tan\theta_L}{H_1VR_s}\right),$$

with notation and constants tabulated in Table III. Two corrections were made to the experimental cross sections: a "missed coincidences" correction, and a correction for finite geometry. The former was necessary because some protons which had correctly passed through the counter slit system were so scattered in the mica foil that they failed to enter the rear counter. This effect was studied with a collimated beam of protons as a function of proton energy, and the measured correction was then expressed in terms of the laboratory scattering angle by means of the relation $\cos^2\theta_L=E/E(\theta_L)$. That this effect was actually due to scattering in the mica foils was verified by observing that the ratio of the measured correction for the East Counter

[28] See reference 3, p. 658.
[29] Taylor, Jentschke, Remley, Eby, and Kruger, Phys. Rev. 84, 1034 (1951).
[30] Aron, Hoffman, and Williams, University of California Radiation Laboratory Report No. 121, revised, 1948 (unpublished).
[31] M. S. Livingston and H. Bethe, Revs. Modern Phys. 9, 245 (1937).

to that for the West Counter was the same as the ratio of the thicknesses of the corresponding foils. The uncertainty of the measured corrections was as much as 15 percent in some cases, but the correction itself was small except for large scattering angles. The corrections are listed in Table IV.

The other correction was one for the second order geometry effect due to the finite size of the proton beam and counter slits. The method of Critchfield and Dodder[24] was applied and carried out to third order terms.[32] These corrections are also given in Table IV; they are largest at the smallest scattering angles (1.8 percent) and decrease with increasing angle.

The possibility that multiple scattering and contaminant scattering were occurring was also checked. Earlier tests by Meagher[5] had indicated that multiple scattering effects in this chamber were unimportant for pressures up to at least 5 cm Hg. To check this, the scattering cross section (at 20° lab) of protons on unpurified tank oxygen was measured as a function of pressure up to 3 cm Hg. Multiple scattering effects in oxygen at 3 cm Hg should be about 15 times as great as in hydrogen at 5 cm; and since the proton-oxygen cross sections were observed to be independent of pressure, no correction was applied to the proton-proton cross sections.

To investigate contaminant scattering, the chamber was pumped down to its base pressure, then closed off from the pumps for 36 hours. At the end of this time a "scattering" run was started, and the accumulated gas produced less than 0.2 percent background at all scattering angles. No background correction was made.

After correcting the cross section for each run as described above, the final corrected East and West cross sections at each angle were obtained by a weighted averaging over all the individual cross sections at that angle. Since no consistent difference between the East and West cross sections were observed, these too were averaged.

In order to compare the results of the counter and plates experiments, a correction must be applied to one or both sets of data because the incident proton energy was different for each experiment. The comparison can be carried out in two different ways. One might reduce the cross sections from the two experiments to the same energy using published data to calculate $(\partial\sigma/\partial E)\theta$ as described in Sec. II. Or, since the ultimate comparison of the data is to be made in terms of a partial wave analysis, the data given in Jackson and Blatt[8] can be used to calculate the apparent S-wave phase shift: their values of $E(\partial\delta_0/\partial E)_{\sigma,\theta}$ and $\sigma(\partial\delta_0/\partial\sigma)_{E,\theta}$ can then be used to correct this phase shift over the energy interval ΔE. The results of the two methods are consistent within 0.1 percent in all cases. For comparison, the counter data were reduced to the energy used in the plates experiment, 5.77 Mev. Values of the derivatives used for this reduction are shown in Table IV, and the resulting cross sections at 5.77 Mev are given in Table V. The uncertainties attached to these cross sections include, in addition to the statistical error defined earlier, those incurred in the measurement of the counter solid angle, scattering angle, total charge, gas temperature, and pressure.

[32] G. R. Briggs, Ph.D. thesis, University of Illinois, 1953 (unpublished).

TABLE V. Final cross sections of counter experiments reduced to 5.77 Mev.

Values of the functions $P_1(E,\theta)$	$\theta_{c.m.}$ (deg)	$\sigma_{c.m.}$ (mb/sterad) Original runs (%)	Check runs (%)	Apparent S-wave phase shift (deg) Original runs	Check runs
−5.64	24	114.8 ±2	109.9 ±2	57.46±0.75	55.76±0.75
−4.71	26	102.2 ±1	99.26±1	57.19±0.51	56.02±0.52
−4.05	28		93.07±0.9		56.35±0.50
−3.44	30	89.89±0.7	87.88±0.9	56.70±0.43	55.90±0.47
−1.66	40	84.9 ±0.9		56.40±0.48	
−1.19	45		85.24±0.9		56.19±0.43
−0.84	50	84.8 ±1.0		55.57±0.48	
−0.42	60	87.6 ±1.0		55.89±0.49	
−0.15	70	88.0 ±1.0		55.53±0.50	
−0.04	80	89.3 ±0.8		55.80±0.46	
−0.00	90	88.5 ±0.8	88.05±0.8	55.34±0.46	55.17±0.46
−0.04	100	88.4 ±0.8		55.38±0.46	
−0.15	110	88.8 ±0.8		55.86±0.44	
−0.04	Av 80 and 100	88.8 ±0.6		55.59±0.33	
−0.15	Av 70 and 110	88.4 ±0.7		55.70±0.33	

D. Check Runs

When it became apparent that the counter data were to a certain extent in conflict with the data taken from the photographic plates, in other laboratories as well as our own, an intensive effort was made to locate the source of the discrepancies. Because the missed coincidences correction was angle-dependent, an effort was made to avoid it by operating the proportional counters in the scattering chamber without windows. As expected, however, when the counters were operated in very pure hydrogen at about 5 cm pressure, the pulses were quite small and the spread of pulse amplitudes was so large that no reliable proton count could be obtained. The counters could be stabilized by the addition of small amounts of methane, but this would have necessitated a different experiment to obtain the proton-proton cross sections. It was therefore decided to work with the original counters. The missed coincidences correction was remeasured, and was found to agree with the previous measurement.

The possibility of scattering from the collimation and counter slits was also investigated since it would have produced apparent cross sections too large at small scattering angles. A polonium alpha source was mounted at the scattering volume (with the chamber evacuated) and two sets of runs were made: one with the counter slit system in place and one with the slit system replaced by a single aluminum slit sufficiently thick to just stop the alpha particles. A sufficient number of counts was recorded so that as few as 3 percent low-energy scattered alpha particles could have been easily

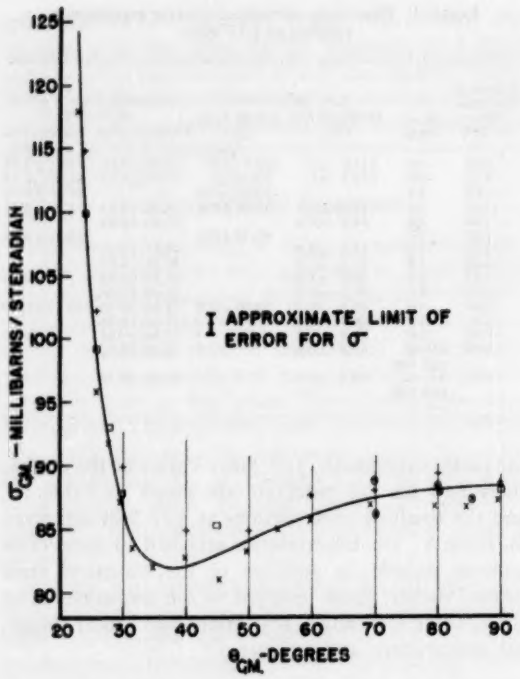

FIG. 5. Proton-proton center-of-mass cross section *vs* center-of-mass scattering angle at an energy of 5.77±0.05 Mev. × Nuclear plates; + original counter runs; □ check runs with counters; ○ means $\sigma(180-\theta_{c.m.})$ is plotted. Solid curve is calculated for pure *S*-wave scattering for $\delta_0=55.29°$. Approximate error in cross sections is indicated; for individual values see Tables II and V.

detected. No such low-energy particles were observed, and the two pulse amplitude analyses did not appear to be different. This was considered to be a significant test since the problem of slit-scattering is expected to be much more severe for the alpha particles than for the protons used in the experiments.

Further investigations were made by replacing one of the counters with a nuclear plate camera so that virtually all protons leaving the rear counter slit were recorded in the emulsion. It was hoped to obtain a measure of the slit scattering occurring with protons by comparing plates taken with and without the counter slit system in place, but no conclusive results were obtained because small-angle Coulomb scattering in the emulsion obscured the effect under investigation. However, these investigations did yield valuable information concerning the "purity" of the proton beam. A deuteron component in the beam would have increased the apparent low-angle cross sections because both the elastically scattered deuterons and protons would have given pulses in the counters indistinguishable from pulses due to properly scattered protons. In the many nuclear plates exposed to the cyclotron beam, not a single deuteron track (easily detected since its length would be twice as great as a proton track) was observed. The purity of the proton beam used in the original counter measurements was not investigated.

It was finally decided to repeat the counter experiment at several scattering angles. The incident proton energy was remeasured using a nuclear emulsion technique[19] and was found to be 5.84 Mev±1 percent at the scattering volume; otherwise the procedure of the original experiment was followed as closely as possible. The results of these check runs were reduced to an equivalent energy of 5.77 Mev and are given in Table V; they are plotted with the other data in Fig. 5.

The check runs were taken with an elliptical aperture $\frac{3}{8}$ in.×$\frac{9}{16}$ in. (and sufficiently thick to just stop 6-Mev protons) placed at the exit of the analyzer magnet chamber (about 3.6 meters from the scattering volume). The slit was not used for the original counter runs. It improved the energy homogeneity of the incident proton beam by reducing the number of particles entering the scattering volume which had been scattered in the beam collimation system. The energy measurement for the check runs showed that the energy spread in the incident proton beam was essentially the same as for the photographic plates experiment, and that there was no low-energy component in the beam, either proton or deuteron.

IV. DISCUSSION OF RESULTS

In Fig. 5 all measured cross sections are plotted as a function of scattering angle in the center-of-mass system. The solid curve is theoretically calculated for a pure *S*-wave phase shift of 55.29°. It is evident that there are some differences between the cross sections measured with the nuclear plates and those measured with the counters. Above about 50°, the original counter cross sections are consistently higher than the plate values by about 1.7 percent; as the scattering angle decreases, the differences increase to about 5 percent at the smallest angles measured. The check runs with counters failed to show the larger discrepancies at the small angles, but were still generally about 2 percent larger than those measured in the emulsion experiment. The consistent difference could be explained by assuming an error in one or both of the energies so that the actual energies in the two experiments differed by about 1.7 percent. Since the separate determinations of energy claim precisions of 1 percent (counters) and 0.7 percent (plates), this is not impossible, but in view of the agreement of the energy measurements between themselves, it does not seem likely. Considering the large number of geometrical measurements required and the uncertainties in the number of proton counts indicated by the pulse height histograms in the counter experiment, it is more likely that the differences are due to small systematic errors in one or both of the experiments. We believe the results based on the weighted averages should be accurate generally within about 1 percent.

Further discussion of the results is best done by the method of phase shift analysis described by Jackson and Blatt.[8] One calculates the nuclear phase shift on the assumption that only the S-wave contributes to the scattering. If there exists some contribution from states of higher angular momentum, this "apparent S-wave phase shift," δ_a, varies with the scattering angle. In the special case where only a small P-wave contributes, Jackson and Blatt showed that to a good approximation,

$$\delta_a = \delta_0 + P_1(E,\theta)\delta_1,$$

where δ_1 is the P-wave phase shift and δ_0 the true S-wave phase shift; the function $P_1(E,\theta)$ is tabulated in their Table V. Values of δ_a for our data are given with the final cross sections in Tables II and V. The uncertainties in the phase shifts are based on the errors in the cross sections and in the energy as given here and are calculated by the method given in Jackson and Blatt.[8] The apparent S-wave phase shifts are plotted as a function of P_1 for all our data in Figs. 6a and 6b. For each set of runs, the above equation was fitted to the phase shifts by a weighted least squares computation with the results tabulated in Table VI, and shown on Fig. 6.

The values of the true S-wave phase shift, δ_0, obtained from the two experiments reflect the consistent difference in the measured cross sections. The counter check runs are in excellent agreement with the original counter runs, but their average δ_0 is greater than δ_0 from the plates data by almost three times the sum of the separate probable errors. This again is evidence for a small systematic error. As can be easily seen from Fig. 6, δ_0 depends essentially on the measured values of the cross sections near $P_1=0$, that is, for $|P_1|<0.2$. For these values of P_1, the difference between δ_a and δ_0 is less than 0.02° in all cases. Hence it makes sense to average the thirteen phase shifts calculated from the cross sections measured in the angular range 70° to 110° (center of mass) corresponding to $|P_1|$-values less than 0.2. This gives a "direct" value of the S-wave phase shift, which, as indicated in Table VI, has been averaged with the values obtained from the separate experiments. The final value for the S-wave shift is 55.29°±0.30°, the error being calculated from the weighted deviations of the four separate values of δ_0 given in Table VI from their weighted average.

TABLE VI. Phase shifts for the plates and counter experiments.

	S-wave phase shift (deg)	P-wave phase shift (deg)
Plates	54.96±0.11	−0.08±0.05
Original counter runs	55.57±0.12	−0.34±0.05
Check runs (counters)	55.63±0.25	−0.08±0.07
Average (plates and counters) for $\|P_1\|<0.2$	55.08±0.30	
Weighted average	55.29±0.30	

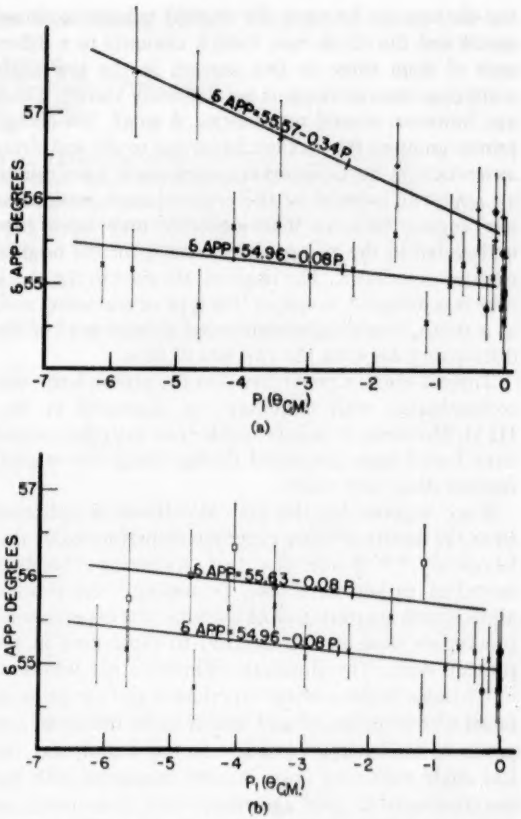

FIG. 6. Apparent S-wave phase shifts vs $P_1(\theta_{c.m.})$ for proton-proton scattering at 5.77 Mev. (a) Comparison of plates data with original counter data. (b) Comparison of plates data with those of counter check runs. Symbols are identified with experiments as in Fig. 4. Least-squares determinations of δ_1 are indicated. For individual values of δ_{app} see Tables II and V.

This value of the S-wave phase shift can be compared with those from other experiments by use of the K-function of Jackson and Blatt.[8] Analysis of a number of proton-proton scattering experiments in the low energy region[33] shows that K is a linear function of the energy according to the equation

$$K=3.755+0.4603E.$$

From this equation, and at a laboratory energy of 5.77 Mev, we calculate $K=6.41$. The value of K calculated from our S-wave phase shift is 6.39±0.05.

The results of the P-wave analysis are more ambiguous. The original counter experiment indicated a fairly large P-wave shift (−0.34°), while the check runs as well as the plates experiment gave small P-wave shifts (−0.08°). In view of the agreement between the last two values we are inclined to believe that the indicated P-wave effect at 5.77 Mev is small and negative, and probably less than 0.1° in magnitude. The source of

[33] Bruce Cork, Phys. Rev. 80, 321 (1950).

the discrepancy between the original counter measurements and the check runs (which amounts to a difference of from three to five percent in the low angle scattering cross sections) is not definitely known. There are, however, several possibilities. A small, low-energy proton group in the incident beam due to slit scattering somewhere in the collimation system could have caused an apparent increase in the counter cross sections at low angles; such an inhomogeneity may have gone undetected in the energy measurement for the original counter experiment. The elliptical slit used in the check runs was designed to reduce this type of scattering and, as a result, would have eliminated at least part of the discrepancy between the two sets of data.

There is also the possibility that the proton beam was contaminated with deuterons, as discussed in Sec. III D. However, it is improbable that the effect would have lasted over the period during which the original counter data were taken.

Some support for the first hypothesis is indicated from the results of other experiments performed at this laboratory.[19,34] There the two scattering chambers described earlier were used to measure the proton-alpha elastic scattering cross sections: the experimental procedures were almost identical to those used in the present work. The elliptical collimation slit was used at all times in the counter experiment and the primary beam was investigated and shown to be free from any group of low energy particles. It was found that the low angle scattering cross sections measured with the counters were in good agreement with those measures using nuclear emulsions.

At these energies, theory would lead one to expect that the higher angular momentum states should begin to contribute appreciably to the nuclear scattering. The extremely precise experiments performed at Wisconsin[11,17] gave almost indisputable evidence that a *P*-wave contribution does exist even at the somewhat lower energies used there. It has already been noticed that our data from the original counter runs give a *P*-wave phase shift in excellent agreement with the Wisconsin data extrapolated to 5.77 Mev[11] provided the Wisconsin data measurements at 4.2 Mev are heavily discounted. On the other hand, the Wisconsin data at 4.2 Mev imply less of a *P*-wave effect than occurs at even as low an energy as 2.4 Mev;[11] if the measurements at 4.2 Mev are weighed equally with the lower energy results, then the Wisconsin data extrapolated to our energy are consistent with a *P*-wave phase shift of about $-0.10°$. Taking the data at their face value, one would have to conclude that the *P*-wave scattering does indeed contribute about to the extent theoretically predicted (on the basis of a static potential) but that some other effect or effects, beginning at the unexpectedly low energy of 4 Mev, tend to mask the *P*-wave scattering. Most probably a final interpretation will have to await further precise experiments at higher energies and possible future advances in the theoretical treatment.[35,36]

[34] A. L. Atkins, Ph.D. thesis, University of Illinois, 1953 (unpublished).

V. ACKNOWLEDGMENTS

The authors would like to express their appreciation to William E. Kreger in the plate work and to Andrew L. Atkins, Jr. in the counter work, for their close collaboration and assistance in every phase of the experiments; to the entire staff of the Cyclotron Laboratory for assistance in carrying out the experiments; to Howard Hirschy, Milton Meux, and Cynthia Kerman, who counted some of the tracks; and to the members of the Cyclotron shop for the skillful construction of the apparatus used in the experiments. It is a real pleasure to acknowledge the valuable aid of all of these persons.

[35] An analysis (see reference 36) of recent proton-proton scattering data at 9.7 Mev shows that the experimental results were not accurate enough to allow definite conclusions about the existence of a *P*-wave shift at this energy.

[36] H. H. Hall, Phys. Rev. 95, 424 (1954).

Determination of Alpha-Alpha Scattering Phase Shifts

JAMES N. SNYDER
Department of Physics, University of Illinois, Urbana, Illinois
(Received July 2, 1954)

A program is described which makes it possible to carry out a phase shift analysis of alpha-alpha scattering on the ILLIAC (University of Illinois Graduate College High Speed Electronic Digital Computer). In approximately 5–10 min the program can carry out the analysis in terms of up to 6 phase shifts ($\delta_0, \delta_2, \cdots, \delta_{10}$) with a precision comparable to an extremely careful human analysis. The number of scattering angles and the energy of the scattering are limited by 32 and 1–150 Mev, respectively.

THE method usually used to determine a set of phase shifts for alpha-alpha scattering from an experimental measurement of the differential cross section $\sigma^{\text{exp}}(\theta)$, is the graphical one originally used by Wheeler.[1] This method is beset by several limitations. (a) Only the three lowest phase shifts δ_0, δ_2, and δ_4 can be obtained directly because of the limitation of two-dimensional graph paper. Higher phase shifts must be obtained by trial and error involving laborious computation, curve fitting, and adjustment. (b) Only part of the experimental data is directly used, since the cross section at three angles is sufficient for the determination of the three phase shifts. The data at other angles are used only in adjusting the higher phase shifts and in making a choice between the several sets of alternate solutions that arise, both of which again involve fitting a theoretical curve to the experimental data. (c) No consistent account is taken of the different experimental errors at the different angles. (d) Although implied above, explicit mention should be made of the lengthy and tedious hand computation involved. A careful fit at 20 experimental angles using four phase shifts can take two to four weeks of steady, conscientious work. Hence, it is very laborious to investigate extensively the energy variation of the phase shifts since many such analyses at different energies must be made.

To facilitate such an investigation,[2] the Digital Computer, Graduate College, University of Illinois (ILLIAC) has been programmed to carry out the phase shift analysis. The program finds the phase shifts δ_l which minimize the function:

$$f(\delta_0, \delta_2, \cdots, \delta l_{\max}) \equiv \sum_{i=1}^{n} \frac{[\sigma^{\text{exp}}(\theta_i) - \sigma^{\text{th}}(\theta_i; \delta_0, \delta_2, \cdots, \delta l_{\max})]^2}{\Delta_i^2}, \quad (1)$$

where $\sigma^{\text{exp}}(\theta_i)$ and Δ_i are the observed cross section and root-mean-square error at θ_i in the laboratory system and

$$\sigma^{\text{th}}(\theta; \delta_0, \delta_2, \cdots, \delta l_{\max}) = \left(\frac{z^2e^2}{mv^2}\right)^2 \Bigg| \csc^2\theta \exp(-i\alpha \log \sin^2\theta) + \sec^2\theta \exp(-i\alpha \log \cos^2\theta) + \frac{2i}{\alpha} \sum_{l=0\ (\text{even})}^{l_{\max}} e^{2i(\xi_l - \xi_0)} \times (e^{2i\delta_l} - 1)(2l+1) P_l(\cos 2\theta) \Bigg|^2, \quad (2)$$

with

$$\xi_l - \xi_0 \equiv \sum_{s=1}^{l} \tan^{-1}(\alpha/s), \quad (3)$$

$$\alpha = 4e^2/\hbar v, \quad (4)$$

where v is the speed of the incident alpha particle. The capacity of ILLIAC and the scaling provided by the program allow wide limits to be placed on the energy of the incident alpha particles, the number n and position θ_i of the experimental observations, and the number of phase shifts used in analyzing the data. These quantities are all adjustable within the ranges:

$$\begin{aligned} 10.5^\circ \leq \theta_i\ (\text{lab}) \leq 45^\circ \\ 0 \leq\ n\ \leq 32 \\ 0 \leq\ l_{\max}\ \leq 10 \\ 0.1 \leq\ \alpha\ \leq 1.4 \end{aligned} \quad (5)$$

i.e.,

$$1\ \text{Mev} \leq E\ (\text{lab}) \leq 150\ \text{Mev}.$$

The numerical minimization program used by the machine[3] first computes the gradient of the function f in δ space, and then alters the δ's so as to approach the

TABLE I. A comparison between the first four phase shifts for α-α scattering at 22.9 Mev as computed by Briggs and as computed by ILLIAC.

	Solution I		Solution II	
	Briggs[a]	ILLIAC	Briggs[a]	ILLIAC
δ_0	−10.5°	−10.7°	86.5°	86.4°
δ_2	94.1°	94.0°	−61.5°	−61.8°
δ_4	59.1°	59.2°	−52.0°	−51.3°
δ_6	0.95°	1.09°	1.10°	1.62°
ϵ	···	∼1.5	···	∼2.1

[a] See reference 5.

[1] J. A. Wheeler, Phys. Rev. 59, 16 (1941).
[2] Nilson, Briggs, Jentschke, Kerman, and Snyder (to be published).
[3] James N. Snyder, ILLIAC Program Library, Programs H3–H6 (unpublished).

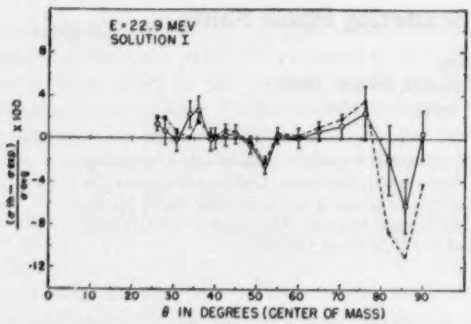

FIG. 1. Comparison of the phase shift analysis of Briggs (see reference 5) (solid lines) and ILLIAC (broken lines). Best solution.

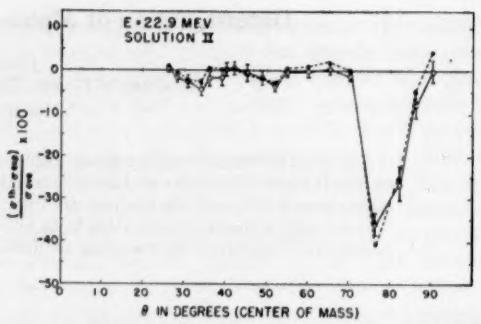

FIG. 2. Comparison of the phase shift analysis of Briggs (see reference 5) (solid lines) and ILLIAC (broken lines). Alternate solution.

minimum of the function in the most efficient manner. This procedure is repeated with ever decreasing mesh size until some predetermined mesh size is reached. It is known from tests on various functions that such a method of steepest descent can be deceived by functions of complicated structure. To eliminate this possibility in the case at hand the program, at the conclusion of the minimization process outlined above, makes another attempt to minimize the function by treating it as a function of only one of the δ_i at a time, proceeding through all the δ_i cyclically again and again with ever decreasing mesh size. In all of the cases run to date, this precaution has proved superfluous. To use the program the experimenter must spend about one-half hour preparing a teletype tape of input data consisting of several parameters which instruct the program how to proceed, the list of experimental angles, the list of cross sections and a list of weighting factors w_i such that:

$$\sum_{i=1}^{n} w_i = 1, \quad w_i = k/\Delta_i^2, \tag{6}$$

where k is a normalizing constant. ILLIAC then carries out the phase shift analysis in the order of 5 min and prints the best set of phase shifts, the numerical value of the minimum of the function, and a table of the cross section at the experimental angles computed using this set of phase shifts.

It is necessary to provide the machine with a set of initial phase shifts $\delta_i^{(0)}$ from which it proceeds to the nearest minimum. These initial values may be chosen in several ways, e.g., educated, intuitive guesses or rough results from a preliminary analysis. Usually the initial $\delta_i^{(0)}$ for the analysis at a given energy were chosen to be the final δ_i from an already completed analysis at a nearby energy. The function being minimized has many local minima in δ space representing possible alternate solutions to the problem. Since the machine carries out an analysis so rapidly, it is possible to start at many different initial points which form a rough net in the δ space and find thereby the various alternate solutions. The most suitable of these can then be chosen by examining which set best fits the energy dependence of the phase shifts and by examining which set yields the best visual fit of the experimental curves. When the alpha-alpha scattering data taken at Illinois were processed by this program, it was invariably found that the best set of phase shifts on these two bases also yielded the absolute minimum value of the function f out of the various relative minima found.

According to the Theory of Least Squares,[4] the root-mean-square error to be feared in a measurement of unit weight is

$$\epsilon \equiv (f_{\min}/n-m)^{\frac{1}{2}}, \tag{8}$$

where n is the number of observations and m is the number of parameters used in an attempt to fit them. Since the rms error associated with the numerical fit σ^{th} is given by $\epsilon\Delta$, a fit commensurate with the accuracy of the experimental data demands that ϵ be of order 1. The cases run to date have been characterized by ϵ in the range 1–3. Hence, it is possible for ILLIAC to quickly carry out a phase shift analysis which is comparable in accuracy to that obtainable by a most careful human.

As an illustration, the 22.9-Mev data taken by Briggs[5] and analyzed by him with extreme care were analyzed by ILLIAC. The comparative results of Briggs and ILLIAC for the best solution (I) and an alternate solution (II) are shown in Table I and Figs. 1 and 2.

The author is grateful for the continued encouragement of W. Jentschke and R. Nilson of the University of Illinois Nuclear Radiations Laboratory and for the continued cooperation of R. E. Meagher, J. P. Nash, and the rest of the staff of the University of Illinois Digital Computer Laboratory.

[4] See, for example, E. T. Whittaker and G. Robinson, *The Calculus of Observations* (Blackie, London, 1944), fourth edition, Chap. IX.

[5] Briggs, Singer, and Jentschke, Phys. Rev. 91, 438 (1953).

Classical Theory of the Temperature Dependence of Magnetic Anisotropy Energy*

C. ZENER
Westinghouse Research Laboratories, East Pittsburgh, Pennsylvania
(Received May 7, 1954; revised manuscript received August 26, 1954)

The consequences are analyzed of the following two assumptions: (1) the effect of temperature upon magnetic anisotropy arises solely from the introduction of local deviations in the direction of magnetization; and (2) the local deviation in an elementary region is the resultant of a very large number of independent deviations. The influence of these local deviations upon the magnetic anisotropy is most conveniently expressed by representing the magnetic energy as a series of surface harmonics. The coefficient of the nth harmonic is found to vary with temperature as $\{J_s(T)/J_s(0)\}$ raised to the power $n(n+1)/2$. The first two exponents for cubic crystals have values of 10 and 21, respectively. The exponent 10 expresses almost precisely the observed temperature dependence of K_1 in iron. In nickel the anisotropy decreases much more rapidly than predicted. It is deduced that the above two assumptions are applicable to iron but not to nickel.

1. INTRODUCTION AND RESULTS

THE magnetization energy of a ferromagnetic crystal is usually dependent to some extent upon the relative orientation of the magnetization vector with respect to the crystalline axes. It is customary to describe this anisotropy of magnetic energy in terms of the coefficients in a Fourier-like expansion of the magnetic energy. Thus, K_1, K_2, $\cdots$, are the first, second, $\cdots$, coefficients which symmetry requirements do not require to be precisely zero. As an example,

$$E_{\text{mag}}=E_0+K_1(\alpha_1^2\alpha_2^2+\alpha_2^2\alpha_3^2+\alpha_3^2\alpha_1^2)+K_2\alpha_1^2\alpha_2^2\alpha_3^2+\cdots \quad (1)$$

for a crystal with cubic symmetry, and

$$E_{\text{mag}}=E_0+K_1\sin^2\theta+K_2\sin^4\theta+\cdots \quad (2)$$

for a crystal with hexagonal symmetry. Here α_1, α_2, α_3 are the cosines of the magnetization vector with respect to the cubic axes, and θ is the angle which the magnetization vector makes with the hexagonal axis.

As is illustrated in Fig. 1 for iron, cobalt, and nickel, the anisotropy coefficients of metals decrease very rapidly with increasing temperature. One is tempted to interpret this marked temperature dependence somewhat as follows: the anisotropy energy must have its origin in a coupling between the spins and the orbital motion, which in turn is coupled to the crystallographic axes, and we then interpret the temperature dependence of the anisotropy coefficients as simply a manifestation of the gradual weakening of this coupling with rising temperature. The fallacy of this naive interpretation is evident upon observing the temperature dependence of the saturation magnetostriction, λ_s. Magnetostriction also arises from a spin-orbit coupling. It decreases with temperature but at a much slower rate than does anisotropy. The fallacy of this naive interpretation is also evident upon observing that the deviation of g from 2 is a measure of the spin-orbit coupling, and experimentally this deviation is found to be essentially constant in nickel up to the Curie temperature.[1]

This paper presents an attempt to understand this marked temperature dependence of the crystal anisotropy. In this attempt we proceed in a classical manner, no quantum mechanical effects being introduced. Two basic assumptions are made. The first assumption is that the sole effect of temperature is to introduce local fluctuations in the direction of the magnetization vector **J**. This assumption implies that the local magnitude of **J** is independent of temperature, and that Eqs. (1) and (2) represent correctly the local density of magnetization energy, the coefficients K_1, K_2, $\cdots$ being independent of temperature. The second assumption is that the deviation in the direction of the local **J** from the direction of the macroscopic **J** is the resultant of a large number of very small deviations having independently random directions. This second assumption is in accord with the spin wave description of the influence of temperature upon magnetization, each independent small deviation being associated with a particular spin wave. A consequence of this second assumption is that the probability that the angle θ between the local and the macroscopic **J** lie within a certain range is given by a random walk function appropriate to a spherical surface.

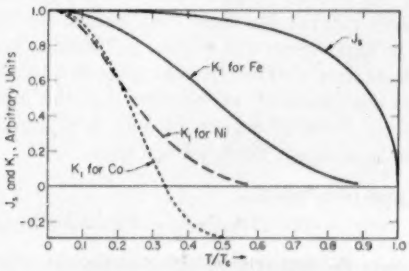

FIG. 1. Temperature dependence of anisotropy energy in Fe, Co, and Ni.

* This paper is a contribution from a magnetics program supported by an Air Force contract.

[1] N. Bloembergen, Phys. Rev. **78**, 572 (1950); Bagguley and Harrick, Proc. Phys. Soc. (London) **A67**, 648 (1954).

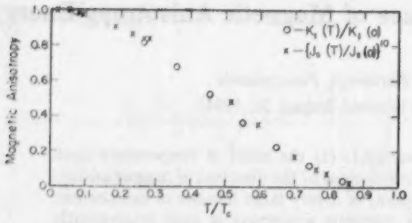

FIG. 2. Comparison of experimental and theoretical temperature dependence of K_1 for iron. Experimental values of $K_1(T)$ from Bozorth (see reference 2). Experimental data for $J_s(T)/J_s(0)$ at low temperature after Bozorth (see reference 3), at high temperatures after Potter (see reference 4).

The consequences of the above assumptions are analyzed in Sec. (2). In order to be able to express the results succinctly, we rewrite Eqs. (1) and (2) in the form

$$E_{mag}=\sum_n E_n S_n(\alpha_1,\alpha_2,\alpha_3), \tag{3}$$

where S_n is a surface harmonic of order n having the appropriate symmetry. The result of this analysis is that $E_{mag}(\alpha_1,\alpha_2,\alpha_3)$ averaged over the random walk function satisfies an equation identical to Eq. (3) except that now $\alpha_1, \alpha_2, \alpha_3$ refer to the direction cosines of the macroscopic $\mathbf{J}$, and the coefficients $E_n(T)$ are related to the original coefficients $E_n(0)$ by the relation

$$E_n(T)/E_n(0)=\{J_s(T)/J_s(0)\}^{n(n+1)/2}, \tag{4}$$

where J_s is the magnetic saturation. In particular,

$$E_4(T)/E_4(0)=\{J_s(T)/J_s(0)\}^{10}. \tag{5}$$

Since

$$S_4(\alpha_1,\alpha_2,\alpha_3)=\alpha_1^2\alpha_2^2+\alpha_2^2\alpha_3^2+\alpha_3^2\alpha_1^2-\tfrac{1}{5},$$

we are tempted to compare theory with experiment[2-4] by comparing the right member of Eq. (5) with the observed value of $K_1(T)/K_1(0)$ for a crystal with cubic symmetry. Such a comparison is made for iron in Fig. 2. The essentially perfect agreement indicates that our two basic assumptions correspond rather closely to reality, at least for this metal.

Upon reference to Fig. 1, we see that K_1 decreases at least twice as rapidly with T/T_c in the case of nickel as in the case of iron. Since J_s decreases in approximately the same manner for these two metals, we conclude that the same agreement will not be obtained for nickel as was obtained for iron. In seeking for an interpretation of this disagreement, we observe that the expression $\alpha_1^2\alpha_2^2+\alpha_2^2\alpha_3^2+\alpha_3^2\alpha_1^2$ occurs not only in $S_4(\alpha_1,\alpha_2,\alpha_3)$ but also in $S_6(\alpha_1,\alpha_2,\alpha_3)$. Thus, we find that

$$S_6(\alpha_1,\alpha_2,\alpha_3)=\alpha_1^2\alpha_2^2\alpha_3^2 - (1/11)(\alpha_1^2\alpha_2^2+\alpha_2^2\alpha_3^2+\alpha_3^2\alpha_1^2)+(2/231).$$

If E_6 were the first nonvanishing coefficient, other than E_0, in the expansion of Eq. (3), the coefficient of $\alpha_1^2\alpha_2^2+\alpha_2^2\alpha_3^2+\alpha_3^2\alpha_1^2$ would vary as the 21st power of $J_s(T)/J_s(0)$. Such a variation would indeed agree quite well with the observed variation of $K_1(T)/K_1(0)$. Such an interpretation would, of course, imply a large value of the coefficient $K_2(0)$ compared to $K_1(0)$. The writer is indebted to Dr. H. Sato of this laboratory for a careful analysis of the low-temperature data for nickel,[5] from which analysis one must conclude that $K_2(0)$ cannot be sufficiently large compared to $K_1(0)$ to render acceptable the above interpretation of the discrepancy for this metal. We must conclude that our two basic assumptions, while valid for iron, are invalid for nickel.

Two attempts have been made to compute the temperature dependence of K_1 by quantum mechanical methods. The first, by Akulov,[6] proceeds somewhat in the spirit of the present paper. He found that at low temperatures, $K_1(T)/K_1(0)$ decreased ten times as rapidly as $J_s(T)/J_s(0)$, and recognized that a reasonable generalization of this variation was a tenth power law. He showed that the experimental data for iron were consistent with a power of 10.03. The second attempt was by Van Vleck.[7] His computed values of $K_1(T)/K_1(0)$ varied between the fifth and sixth power of $J_s(T)/J_s(0)$.

2. ANALYSIS

In this section, our objective is to compute the average of $S_n(\alpha_1,\alpha_2,\alpha_3)$ with respect to the appropriate random walk function. The origin of the random walk will be taken at $(\bar\alpha_1,\bar\alpha_2,\bar\alpha_3)a$ on the surface of a sphere of radius a.

The random walk distribution function will have symmetry about $(\bar\alpha_1,\bar\alpha_2,\bar\alpha_3)$. We shall, therefore, find the average of $S_n(\alpha_1,\alpha_2,\alpha_3)$ as the direction $(\alpha_1,\alpha_2,\alpha_3)$ describes a cone about $(\bar\alpha_1,\bar\alpha_2,\bar\alpha_3)$. Towards this end, we let $\theta\varphi$ be the polar coordinates of $(\alpha_1,\alpha_2,\alpha_3)$ with respect to $(\bar\alpha_1,\bar\alpha_2,\bar\alpha_3)$. We then expand

$$S_n(\alpha_1,\alpha_2,\alpha_3)=\sum_{m=-n}^{n} C_m Y_n^m(\theta,\varphi). \tag{6}$$

When we now take the average of both sides with respect to φ, all terms vanish on the right side except that corresponding to $m=0$.

$$\langle S_n(\alpha_1,\alpha_2,\alpha_3)\rangle_\varphi = C_0 P_n(\cos\theta). \tag{7}$$

The constant C_0 is found by giving θ the particular value of zero. We thereby obtain

$$\langle S_n(\alpha_1,\alpha_2,\alpha_3)\rangle_\varphi = P_n(\cos\theta) S_n(\bar\alpha_1,\bar\alpha_2,\bar\alpha_3). \tag{8}$$

Our second and final step is to obtain the average of $P_n(\cos\theta)$ with respect to the appropriate random walk distribution function. This distribution is a function of

[2] R. M. Bozorth, *Ferromagnetism* (D. Van Nostrand Company, Inc., New York, 1951), pp. 569–578.
[3] Reference 2, p. 720.
[4] H. H. Potter, Proc. Roy. Soc. (London) **146**, 362 (1934).
[5] Honda, Masumoto, and Shirakawa, Sci. Rpts. Tohoku Imp. Univ. **24**, 391 (1935–36).
[6] N. Akulov, Z. Physik **100**, 197 (1936).
[7] J. H. Van Vleck, Phys. Rev. **52**, 1178 (1937).

θ and of some parameter τ which determines the spread of the distribution function. Upon recalling that diffusion is a random walk process, we recognize that the distribution function $RW(\theta,\tau)$ will obey the standard diffusion differential equation if we associate τ with time, or more appropriately, with the dimensionless quantity tD/a^2, where D is the diffusion coefficient, a the radius of the spherical surface upon which diffusion is imagined to be occurring. Thus, we have

$$\frac{\partial}{\partial\tau}RW(\theta,\tau)=\frac{1}{\sin\theta}\frac{\partial}{\partial\theta}\sin\theta\frac{\partial}{\partial\theta}RW(\theta,\tau). \quad (9)$$

The solution of this differential equation, subject to the boundary condition that $RW(\theta,\tau)$ approaches a delta function about $\theta=0$ as $\tau\rightarrow 0$, is

$$RW(\theta,\tau)=\sum_{n=0}^{\infty}\left\{\int_{-1}^{1}P_n^2(\cos\theta)d\cos\theta\right\}^{-1}\times e^{-n(n+1)\tau}P_n(\cos\theta). \quad (10)$$

We thereby obtain

$$\int_{-1}^{+1}RW(\theta,\tau)P_n(\cos\theta)d\cos\theta=e^{-n(n+1)\tau}, \quad (11)$$

or

$$\langle P_n(\cos\theta)\rangle_{RW}=e^{-n(n+1)\tau}, \quad (12)$$

where $\langle\ \rangle_{RW}$ denotes an average with respect to the random walk function. We now eliminate the parameter τ by observing that

$$J_s(T)=J_s(0)\langle P_1(\cos\theta)\rangle_{RW}, \quad (13)$$

which equation, combined with (12) leads to

$$\langle P_n(\cos\theta)\rangle_{RW}=\{J_s(T)/J_s(0)\}^{n(n+1)/2}. \quad (14)$$

Upon combining Eqs. (8) and (14), we obtain our final equation,

$$\langle S_n(\alpha_1,\alpha_2,\alpha_3)\rangle_{RW}=\{J_s(T)/J_s(0)\}^{n(n+1)/2}S_n(\bar{\alpha}_1,\bar{\alpha}_2,\bar{\alpha}_3). \quad (15)$$

PHYSICAL REVIEW VOLUME 96, NUMBER 5 DECEMBER 1, 1954

Angular Distribution of 12- and 16-Mev Gamma Rays from the Proton Bombardment of a Thin Boron Target*

H. H. Givin, G. K. Farney, T. M. Hahn,† and B. D. Kern
Department of Physics, University of Kentucky, Lexington, Kentucky

(Received August 3, 1954)

The angular distribution of 12- and 16-Mev gamma rays from proton bombardment of thin boron targets has been obtained for proton energies ranging from 0.6 to 2.0 Mev. The angular distribution may be represented by the equation $w(\theta)=1+A\cos\theta+B\cos^2\theta$, indicating interference between at least two levels of opposite parity. An analysis of the energy dependence of the coefficients A and B for the 16-Mev gamma rays indicates the interference to be between more than two levels.

INTRODUCTION

GAMMA-RAY resonances in the yield from the proton bombardment of boron have been observed by various investigators at 163,[1] 680,[2,3] 1388, 2650,[4] and 3550 kev,[5] all except the first having very large widths. The excited states of C^{12} may decay directly to the ground state with the emission of gamma rays of energy equal to the excitation energy ($Q=15.949$ Mev) or to the 4.43-Mev excited state and then to the ground state with the emission of cascade radiation. These gamma-rays are called, in the following, the "16-Mev," "12-Mev," and "4.43-Mev" radiations. Earlier work[6] has shown a $\cos\theta$ term in the angular distribution of the gamma radiation from this reaction over the energy region from 300 to 1100 kev. This indicates interference between at least two states of opposite parity. Since the spin and parity are known for the C^{12} level corresponding to the 163-kev resonance, this investigation of the angular distribution of the 16-Mev gamma rays was undertaken so that the spins and parities of the interfering levels could be determined. Although the theoretical analysis of the angular distribution of the 12-Mev gamma rays is more complex, the experimental determination of this angular distribution was also undertaken since the spin and parity of the 4.43-Mev excited state of C^{12} are known.

EXPERIMENTAL PROCEDURE

Protons were accelerated in the University of Kentucky 3-Mev electrostatic accelerator to energies

* Sponsored by the Office of Ordnance Research, U. S. Army.
† Now at Virginia Polytechnic Institute, Blacksburg, Virginia.
[1] R. Tangen, Kgl. Norske. Videnskab. Selskabs, Skrifter No. 1 (1946).
[2] Cochran, Ryan, Givin, Kern, and Hahn, Phys. Rev. **87**, 672 (1952).
[3] T. Huus and R. Day, Phys. Rev. **91**, 599 (1953).
[4] H. E. Gove and E. B. Paul, Phys. Rev. **91**, 463 (A) (1953).
[5] H. B. Willard (private communication).
[6] Jenkins, Cochran, Kern, and Hahn, Phys. Rev. **91**, 915 (1953).

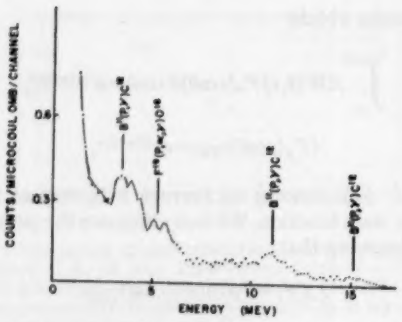

FIG. 1. Gamma-ray spectrum from the proton bombardment of boron at 0.873 Mev. The gamma rays from fluorine are caused by fluorine contamination of the target backing.

ranging from 600 to 2000 kev, with an energy resolution of 0.25 percent. Beam currents of from 1 to 5 microamperes were used.

The gamma-ray detector was a NaI(Tl) crystal $1\frac{1}{2}$ inches in diameter and 1 inch thick mounted on the face of a selected Dumont 6292 photomultiplier tube. The crystal, surrounded by magnesium oxide,[7] was housed in a thin-wall aluminum case and slipped over the end of the photomultiplier tube. The detector had an energy resolution of 10 percent at 0.661 Mev. The front face of the crystal was 7 cm from the target, and the detector could be rotated about an axis through the target and perpendicular to the beam direction to 135° on either side of the beam direction. The photomultiplier tube was magnetically shielded and operated at a potential of 750 volts supplied by series-connected 45-volt batteries. The pulses from the photomultiplier tube were sorted by a twenty-channel pulse-height analyzer.

The angular distribution data were obtained using a thin boron film deposited on tantalum backing by the diborane process.[8] The target was made available by the Van de Graaff group at the California Institute of Technology.

By use of the twenty-channel pulse-height analyzer it was possible to obtain the gamma-ray spectrum at each of seven angles (225°, 270°, 315°, 0°, 45°, 90°, and 135°) and at proton bombarding energies of 600, 700, 800, 1000, 1200, 1400, 1600, 1800, and 2000 kev. The projection of the beam through the target is defined as 0°. Figure 1 shows a spectrum taken at 0° for a proton bombarding energy of 873 kev.

Inasmuch as the degree of anisotropy in the distribution was not large it was most important that all extraneous sources of anisotropy be eliminated. The symmetry of the target-detector geometry was carefully checked by mechanical measurements and using radioactive sources.

TABLE I. Coefficients in the expression $W(\theta)=1+A\cos\theta+B\cos^2\theta$ for the yield of 16-Mev gamma rays from the proton bombardment of boron.

E_p (Mev)	A	B
0.600	−0.01±0.01	0.09±0.02
0.700	−0.04±0.01	0.15±0.03
0.800	−0.02±0.01	0.16±0.02
1.000	−0.05±0.01	0.13±0.02
1.200	0.01±0.01	0.20±0.02
1.400	0.05±0.02	0.26±0.04
1.600	−0.01±0.01	0.27±0.02
1.800	0.02±0.01	0.26±0.02
2.000	0.05±0.02	0.16±0.04

[7] C. S. Borkowski and R. L. Clark, Rev. Sci. Instr. **24**, 1046 (1953).

EXPERIMENTAL RESULTS

The twenty-channel pulse-height analyzer was adjusted such that the twenty channels covered the energy region from approximately 8 to 17 Mev. This adjustment was maintained throughout the experiment. The upper seven channels covered the region above 14 Mev. After absorption and finite solid angle corrections, the variation in the total count from these seven channels as a function of angle and energy yielded the angular distribution of the 16-Mev gamma rays.

The lower seven channels of the analyzer covered the the energy region between 8 and 11 Mev, the plateau seen just below the 12-Mev pair peak in the spectrum of Fig. 1. The total count in these seven channels was caused by both 16- and 12-Mev radiation, and it was necessary to separate the two contributions. Campbell and Boyle[8] have theoretically determined the energy resolution up to 18 Mev of NaI(Tl) scintillation counters. Their results are in good agreement with experiment. Using their results, the contribution from the 16-Mev gamma rays to the portion of the spectrum between 8 and 11 Mev was obtained and subtracted from the total count in the lower seven channels. The remainder was attributed to 12-Mev gamma radiation, and from its variation with angle and energy the angular distribution was obtained.

The absorption of 16-Mev gamma rays caused by the 10-mil tantalum target backing was calculated theoretically[9] and found to be in excellent agreement with experimental results. An absorption correction of

TABLE II. Coefficients in the expression $W(\theta)=1+A\cos\theta+B\cos^2\theta$ for the yield of 12-Mev gamma rays from the proton bombardment of boron.

E_p (Mev)	A	B
0.600	0.18±0.01	0.14±0.02
0.700	0.12±0.02	0.01±0.04
0.800	0.19±0.02	0.18±0.03
1.000	0.39±0.03	0.33±0.05
1.200	0.50±0.03	0.44±0.05
1.400	0.48±0.04	0.45±0.08
1.600	0.60±0.05	0.33±0.09
2.000	0.47±0.03	0.76±0.06

[8] J. G. Campbell and A. J. F. Boyle, Australian J. Phys. **6**, 171 (1953).

[9] C. M. Davisson and R. D. Evans, Revs. Modern Phys. **24**, 79 (1952).

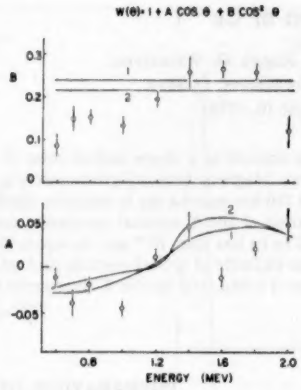

FIG. 2. Energy dependence of the coefficients A and B in the expression $W(\theta)=1+A\times\cos\theta+B\cos^2\theta$ for the yield of 16-Mev gamma rays from the proton bombardment of boron. Curves 1 and 2 show the poor agreement obtained under the assumption that the two interfering levels are 163 kev (2+) and 1388 kev (1−) or 1388 kev (1−) and 3550 kev (2+), respectively.

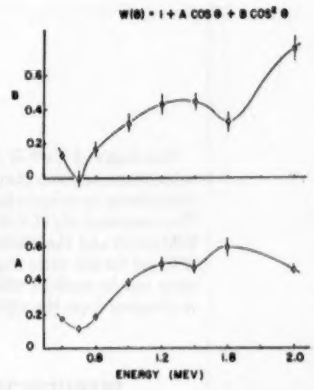

FIG. 3. Energy dependence of the coefficients A and B in the expression $W(\theta)=1+A\times\cos\theta+B\cos^2\theta$ for the yield of 12-Mev gamma rays from the proton bombardment of boron.

3.4, 2.4, and 2.4 percent was applied to the data at 0°, 45°, and 315°, respectively.

In the case of the 12-Mev gamma rays, the total count in the chosen seven channels is reduced because of absorption in the target backing at the angles 315°, 0°, and 45° and is increased because of the degradation in energy of some of the 16-Mev gamma rays. The correction for the latter was found to be negligible. The calculated correction for the former is 2 percent. Since the uncertainty in the contribution from the 16-Mev gamma rays is of this order of magnitude, this correction was not actually applied.

A least-squares fit of the equation $W(\theta)=1+A\cos\theta+B\cos^2\theta$ to the data was made following the method of Rose.[10] Solid angle corrections were made and the angular distributions transformed to center-of-mass coordinates. Values of the coefficients for various bombarding energies are shown in Tables I and II.

DISCUSSION

A comparison of the coefficients with the values obtained by other investigators shows good agreement with the work of Gove and Paul,[4] Jenkins,[11] and Cross.[12] The results do not agree with those of Glattli and Stoll[13] at low bombarding energies. The energy dependence of the coefficients is clearly indicated in Figs. 2 and 3.

A theoretical analysis of the angular distributions of the 16-Mev radiation was made following the method of Devons and Hine[14] with the assumption of two-level interference. Curves 1 of Fig. 2 indicate the theoretical variation of the coefficients with energy under the assumption[3] that the interfering levels are 163 kev with spin 2 and even parity (2+) and 1388 kev with spin one and odd parity (1−). The agreement is not within the experimental errors. Curves 2 in Fig. 2 indicate the theoretical results for the assumption of interference between the 1388-kev level (1−) and the 3550-kev level (2+). Various choices of the values of the parameters t and δ, in the notation of Devons and Hine, did not materially alter this disagreement.

Calculations were made for other combinations of the 1388, 2650, and 3550-kev levels for two-level interference. The results are shown in Table III. None of the calculations agreed within experimental errors. It is, therefore, concluded that more than two interfering levels are involved in the problem.

TABLE III. Calculated values of the coefficients in the expression $W(\theta)=1+A\cos\theta+B\cos^2\theta$ for the yield of gamma rays from the proton bombardment of boron. Interference between two levels is assumed, and various choices of spin and parity are made for the levels corresponding to bombarding energies of 1.388, 2.650, and 3.550 Mev.

E_p (Mev)	1.388 (1−) 2.650 (2+)[a]		1.388 (2+)[a] 2.650 (1−)		1.388 (2+) 3.550 (1−)	
	A	B	A	B	A	B
0.600	−0.045	0.625	−0.060	0.625	−0.100	0.625
0.700	−0.035	0.625	−0.048	0.625	−0.073	0.625
0.800	−0.023	0.625	−0.022	0.625	−0.054	0.625
1.000	−0.012	0.625	−0.006	0.625	−0.021	0.625
1.200	−0.005	0.625	0.000	0.625	0.000	0.625
1.400	0.001	0.625	0.003	0.625	0.011	0.625
1.600	0.003	0.625	0.005	0.625	0.023	0.625
1.800	0.003	0.625	0.008	0.625	0.032	0.625
2.000	0.002	0.625	0.012	0.625	0.040	0.625

[a] See reference 4.

ACKNOWLEDGMENT

The authors wish to express their gratitude to K. Schneider, K. Ilens, and J. L. Ryan for their willing assistance in the constructing of experimental apparatus.

Note added in proof.—Grant, Flack, Rutherglen, and Deuchars [Proc. Roy. Soc. (London) **A417**, 751 (1954)] have obtained angular distribution data in the proton energy region from 175 to 680 kev. They conclude that the 163-kev resonance has $J=2+$ and the 1388-kev resonance has $J=1-$.

[10] M. E. Rose, Phys. Rev. **91**, 610 (1953).
[11] G. L. Jenkins, Ph.D. dissertation, Department of Physics, University of Kentucky, 1953 (unpublished).
[12] W. G. Cross (private communication).
[13] H. Glattli and P. Stoll, Helv. Phys. Acta **25**, 455 (1952).
[14] S. Devons and M. G. Hine, Proc. Roy. Soc. (London) **A199**, 73 (1949).

Disintegration of Ce^{139}†

CHARLES H. PRUETT AND ROGER G. WILKINSON
Indiana University, Bloomington, Indiana
(Received August 16, 1954)

The decay of Ce^{139} is shown to proceed by *s*-electron capture to a single excited state of La^{139} with the subsequent emission of an internally converted gamma ray. Magnetic beta-ray spectrometry and scintillation coincidence techniques have been used to show that the 166-kev gamma ray is magnetic dipole in character. The measured $K/(L+M)$ ratio is 6.6 ± 0.3. An estimation of the K internal conversion coefficient yields 0.20 ± 0.05 and the lifetime of the excited level is found to be less than 10^{-6} sec. An upper limit of 315 kev is found for the total disintegration energy. Although no estimate of orbital electron capture to the ground state can be made, a small amount is probable. A value of 0.94 ± 0.02 for the K fluorescent yield at $Z=57$ is obtained from the experiment.

INTRODUCTION

THE decay of Ce^{139} (140 days) occurs by orbital electron capture[1-3] and leads to an excited state of La^{139}. The subsequent gamma-ray spectrum, although simple, has not been clearly established by previous investigations. The presence of a strong internally converted 166-kev gamma ray is certain,[4-6] but there is considerable variance concerning the nature of additional radiations. Pool and Krisberg,[3] for example, have reported an 0.8-Mev gamma ray, while Keller and Cork[6] have suggested a 275-kev gamma ray in cascade with the 166-kev radiation. Further progress in the study of this element apparently has been hampered by the lack of strong sources and the problem of contaminants.

In the present paper the results of a detailed study of this element are given. Intense cyclotron bombardments and improved chemical procedures have yielded reliable and reasonably strong sources. The radiations have been studied with a small 180° shaped-field beta-ray spectrometer (~1 percent transmission, ~1 percent resolution), with a flat-field permanent magnet spectrometer (126 gauss), and with a scintillation coincidence spectrometer. The decay is found to involve a single gamma ray. The multipolarity of the gamma ray has been determined from a measurement of the K/L ratio. An upper limit to the lifetime of the excited state has been obtained as well as an estimation of the internal conversion coefficient. An upper limit to the energy released in the decay has been established from the L_I/K capture ratio. The upper limit on the ft value which results, together with the multipole assignment of the gamma transition, allow an assignment of spins which is in agreement with the shell model. As a by-product, the K fluorescent yield of the x-rays for $Z=57$ has been obtained.

† Supported by the joint program of the Office of Naval Research and the U. S. Atomic Energy Commission.

[1] M. L. Pool and J. D. Kurbatov, Phys. Rev. **63**, 463 (1943).
[2] D. E. Mathews and M. L. Pool, Phys. Rev. **72**, 163 (1947).
[3] M. L. Pool and N. L. Krisberg, Phys. Rev. **73**, 1035 (1948).
[4] J. B. Chubbuck and J. Perlman, Phys. Rev. **74**, 982 (1948).
[5] R. D. Hill, Phys. Rev. **82**, 449 (1951).
[6] H. B. Keller and J. M. Cork, Phys. Rev. **84**, 1079 (1951).

PREPARATION OF SOURCES

Ce^{139} was produced by bombarding lanthanum oxide with 11-Mev deuterons. Targets received from 500 to 1000 microampere hours. For the initial survey, the cerium was separated from the target material by oxidation to the +4 valence state and precipitated as the iodate. For quantitative measurements requiring higher specific activity the cerium in the +4 state was extracted into tributyl phosphate without the addition of cerium carrier.[7] Source material prepared in this way was not entirely carrier-free, owing to the presence of a small amount of cerium in the target material. Spectrometer sources were mounted in the usual manner on zapon (or aluminum coated zapon) films. Source thickness, including backing, ranged from 0.1 to 0.2 mg/cm².

MAGNETIC SPECTROMETER MEASUREMENTS

A survey of the electron spectrum from 2 kev to 2 Mev in a small shaped-field spectrometer (7.5-cm radius) yielded only the Auger electrons and the K, L, and M conversion lines corresponding to a gamma ray of energy 166.5 kev. A search for positrons gave negative results. The Auger and conversion lines as obtained with a source of about 0.1 mg/cm² thickness are shown in Fig. 1. The counter window cut-off occurred at approximately 1.5 kev. Calibration and window transmission in the region of the Auger electrons were checked by comparison with the well-known A and F conversion lines of ThB. The values of the $K/(L+M)$

TABLE I. Summary of experimental data.

Ratio	Notation	Measured value
K/L conversion	···	8.20 ± 0.40
L/M conversion	···	4.00 ± 0.20
$K/(L+M)$ conversion	R_1	6.60 ± 0.30
Augers/K-conversions	R_2	0.34 ± 0.03
K-captures/K-conversions	$2R_3-1$	4.40 ± 0.20
K x-rays/gamma rays	R_4	1.00 ± 0.20

[7] This procedure is described in detail by J. C. Warf, Iowa State College, U. S. Atomic Energy Commission Report AECD-2524 (unpublished).

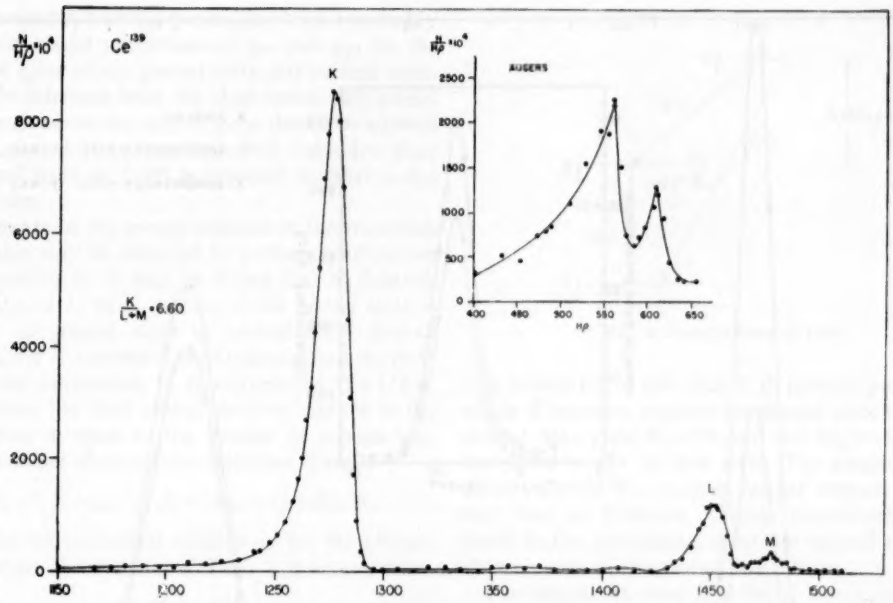

FIG. 1. Negatron spectrum of Ce^{139}.

conversion ratio R_1, and the Auger/K-conversion ratio R_2, which are listed in Table I, are the result of a number of runs.

As a further check on these results the electron spectrum was obtained in a permanent-magnet spectrometer utilizing photographic detection. A long exposure taken 10 months after the irradiation did not bring to light any additional features of the negatron spectrum in the region 0.01 to 0.5 Mev. The energy of the gamma ray obtained from these data is 165.5 kev.

SCINTILLATION SPECTROMETER MEASUREMENTS

Additional information concerning the radiations of Ce^{139} was obtained from scintillation spectrometry. Two scintillation spectrometers in a coincidence arrangement having a coincidence resolving time of 2×10^{-7} sec were used. This apparatus is a modification of one described by Roggenkamp.[8] The detectors in this case were 1-in. $\times$1-in. cylindrical canned NaI(Tl) crystals mounted on DuMont 6292 photomultiplier tubes.

A survey of the photoelectron spectrum in a single channel from 25 kev to 1.6 Mev showed only peaks due to La K x-rays and the 166-kev gamma ray. Higher-energy gamma rays, if present at all, have an intensity of less than 10^{-3} of the intensity of the 166-kev radiation. The pulse-height distribution taken in channel 2 is shown in Fig. 2 (squares). The Compton electron distribution is very small in this case since almost total absorption takes place in the detector at these energies.

With channel 1 set to accept only the x-ray, the coincidences which occurred as channel 2 scanned the spectrum are shown in Fig. 2 (circles). The x-x and x-γ coincidence peaks are expected if the decay of Ce^{139} occurs by s-electron capture to the 166-kev level in La^{139} followed by the emission of an internally converted gamma ray. The inset of Fig. 2 shows the coincidence peak which resulted when channel 1 was set to register the gamma ray as channel 2 surveyed the spectrum.

If the coincidence curve shown in Fig. 2 is normalized to the singles curve at the gamma ray peak, the ratio of the singles x-ray counting rate to the coincidence x-ray counting rate for corresponding pulse-height settings near the peak will not depend on the over-all efficiency factor of either counter. In terms of the coincidence rates, $N_{x\gamma}$ and N_{xx}, and the singles counting rates, N_x and N_γ, in channel 2, this ratio is

$$R_3=\frac{N_{x\gamma}}{N_\gamma}\Big/\frac{N_{xx}}{N_x}.$$

By an extension of the analysis described by Mitchell,[9] it may be shown that $(2R_3-1)$ represents the ratio of the total K-shell captures to the number of K conversions. The quantity R_3 as determined at a number of corresponding points on the curves near the peaks was found to be constant. The value given in Table I represents the average over a number of points and includes a small correction for coincidences in the neighborhood of the x-ray due to the gamma-ray Compton distribution.

[8] Roggenkamp, Pruett, and Wilkinson, Phys. Rev. **88**, 1262 (1952).

[9] A. C. G. Mitchell, Revs. Modern Phys. **20**, 296 (1948).

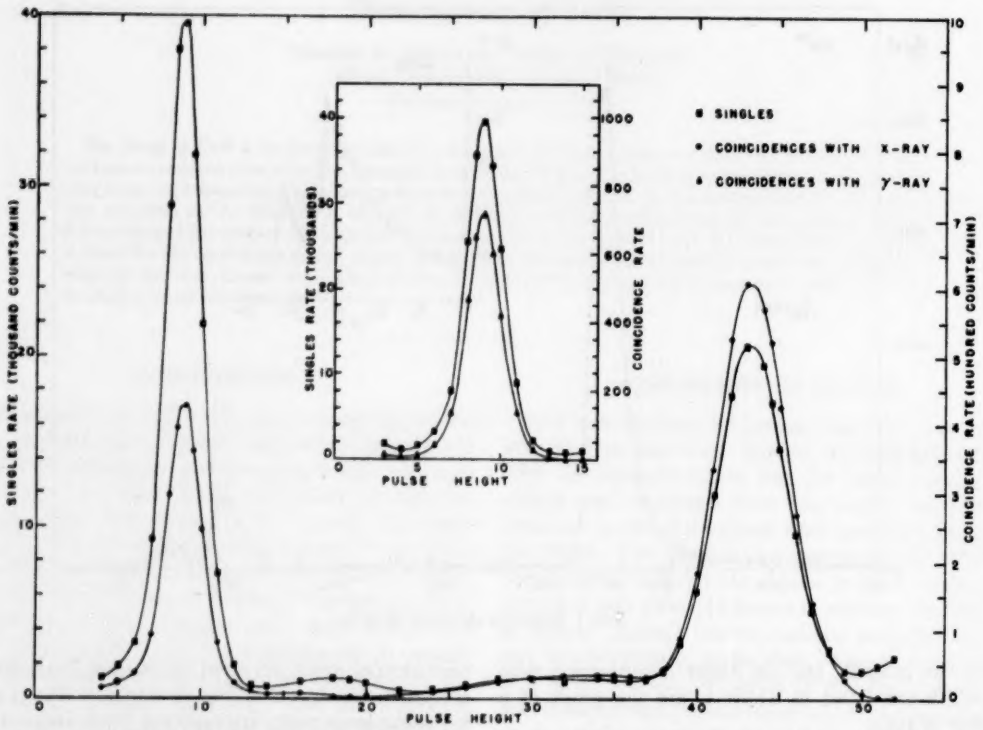

FIG. 2. A scintillation coincidence spectrum of the gamma radiation of Ce^{139}. A single-channel pulse height distribution is also plotted. Peaks are due to the 33-kev x-ray and the 166-kev gamma ray.

The ratio, R_4, of the number of K x-rays to the number of gamma rays is also of interest. The single-channel pulse-height distribution in this case was taken with a well-collimated source. The figure listed in Table I was obtained after applying corrections for energy dependence of counter efficiencies, absorption in the crystal holder, and escape of the iodine x-ray. Unfortunately, the last mentioned correction is not straightforward and consequently the number R_4 is the most uncertain of any in Table I. In fact, the K x-ray of La gives rise to a very pronounced "escape peak" in NaI. This is due to the fact that the K absorption edge of iodine lies between the energies of the $K_{\alpha 1}$ and $K_{\alpha 2}$ x-rays of lanthanum.[10] The correction applied involved the data of McGowan[11] and the known relative intensities of the La K x-ray components.

In addition to the measurements described above, a delayed coincidence experiment was performed to check the lifetime of the 166-kev excited state in La^{139}. The plot of coincidence rate *vs* artificial delay was a curve characteristic of "prompt" radiation. From the slope of the curve it is estimated that the lifetime of this state is less than 10^{-8} sec. A small asymmetry in the delayed coincidence curve was ascribed to difference in energy between the gamma ray and x-ray.

[10] Hill, Church, and Mihelich, Rev. Sci. Instr. **23**, 523 (1952).
[11] F. K. McGowan, Phys. Rev. **93**, 163 (1954).

RESULTS

The data given in Table I establish most of the features of the decay scheme of Ce^{139}. The K/L ratio when compared with empirical curves similar to those of Sunyar and Goldhaber[12] incorporating the more recent data of Graham and Bell,[13] is found to lie directly on the $M1$ curve. The presence of an $E2$ admixture, if any, must be small. The upper limit of 10^{-8} sec on the lifetime of the 166-kev state, while not a definitive check on the assignment of $M1$, is consistent with it. As a further check the internal conversion coefficient may be derived from the data. It may be verified that, with no assumptions involved, the K conversion coefficient is

$$\alpha_K = R_4/(2R_3 - R_2) = 0.20 \pm 0.05.$$

Within the experimental uncertainties, especially in R_4, this is consistent with the theoretical value[14] of 0.24 for $M1$ radiation of 166-kev energy at $Z=57$. Since the $E2$ conversion coefficient differs very little from that for $M1$, no estimate of mixing can be made on this basis. The decay scheme is shown in Fig. 3. The measured spin of the ground state[15] is 7/2, hence

[12] M. Goldhaber and A. W. Sunyar, Phys. Rev. **83**, 906 (1951).
[13] R. L. Graham and R. E. Bell, Can. J. Phys. **31**, 377 (1953).
[14] Rose, Goertzel, Spinrad, Harr, and Strong, Phys. Rev. **83**, 79 (1951).
[15] J. E. Mack, Revs. Modern Phys. **22**, 64 (1950).

the assignment $M1$ for the gamma ray leads reasonably to the shell model predictions of $g_{7/2}$ and $d_{3/2}$ for the respective spins of the ground state and excited state. By further inference from the shell model, the orbital electron capture to the excited state should be allowed and the ground state transition 2nd forbidden since the ground state of Ce^{139} is expected to have a $d_{3/2}$ configuration.

An estimate of the energy released in the transition and ft value may be obtained by a closer examination of the quantity R_3. It may be shown that R_3 depends on the ratio of L_I to K capture to the *excited* state ϵ, the ratio of ground state to excited state K-shell capture β, the K conversion coefficient α_K, and the ratio of the total conversions to K conversions $(1+1/R_1)$. In fact, since the total orbital electron capture to the excited state is equal to the number of gamma rays plus the number of conversion electrons, then

$$(2R_3-1)(1+\epsilon)/(1+\beta)=1/\alpha_K+(1+R_1)/R_1.$$

If one uses the theoretical value of α_K for the 166-kev $M1$ transition and the data of Table I, it follows that

$$\epsilon=0.21+1.21\beta.$$

According to Rose and Jackson,[16] the value of the ratio of L_I to K electron densities at the nuclear radius is 0.124 for $Z=57$. If the energy available for electron capture to the *excited* state W_0 is large compared to the K binding energy this quantity should be essentially equal to ϵ. It will be noted that even with $\beta=0$, i.e., no K capture to the ground state, the value of ϵ is almost double Rose's theoretical value for $(\psi_{LI}/\psi_K)^2$. It is to be concluded that the magnitude of the K binding energy cannot be neglected. In this case the upper limit to W_0 corresponds to $\beta=0$. If the transition to the excited state is assumed to be allowed and the value of Rose given above as well as the current electron binding energies[10] for La are used, an upper limit of $W_0=147$ kev results. The corresponding upper limit to $\log ft$ is 6.0, a somewhat large value for an allowed transition. The presence of a small amount of ground state K capture would lower both W_0 and $\log ft$. While no estimate of β can be made from these experiments

[16] M. E. Rose and J. L. Jackson, Phys. Rev. **76**, 1540 (1940).

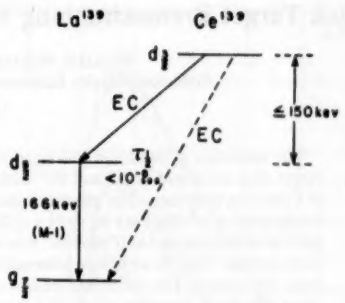

FIG. 3. Decay scheme of Ce^{139}.

it is interesting to note that if 10 percent, for example, of the K captures occur to the ground state the experimental data yield $W_0=94$ kev and $\log ft=5.3$ for the transition to the 166-kev level. The assignment of a small value of W_0 receives further support from the fact that no evidence of inner bremsstrahlung was found in the scintillation spectrum beyond the photoelectron peak of the gamma ray.

The fluorescent yield f_k of the K x-rays for $Z=57$ is contained implicitly in the foregoing analysis of the data. Reference to Table I shows that this auxiliary piece of information may be obtained. It is readily seen that

$$f_k=1-(R_2/2R_3)=0.94\pm0.02.$$

It would appear that the curve of Broyles *et al.*[17] is somewhat low in this region. The spread in R_2 and R_3 necessary to bring f_k below 0.90 is considerably greater than the most generous limits which the uncertainties of the experiment allow. Evidence for this conclusion has been previously reported by Browne *et al.*[18] Their data lead to a value of 0.99 for $Z=58$ and 59 with little likelihood of experimental limitations reducing this figure below 0.90.

The authors are indebted to Dr. Milo B. Sampson and the cyclotron group for many effective bombardments and to Mr. Arthur Lessor for the chemical separations.

[17] Broyles, Thomas, and Haynes, Phys. Rev. **89**, 715 (1953).
[18] Browne, Rasmussen, Surls, and Martin, Phys. Rev. **85**, 146 (1952).

Thick Target Bremsstrahlung Spectra for 1.00-, 1.25-, and 1.40-Mev Electrons*

WILLIAM MILLER, J. W. MOTZ, AND CARMEN CIALELLA†
Radiation Physics Laboratory, National Bureau of Standards, Washington, D. C.

(Received August 23, 1954)

The spectrum of radiation produced by 1.0-, 1.25-, and 1.40-Mev electrons incident on a thick tungsten target was measured at 0° and 90° with the incident beam by a method involving the magnetic analysis of Compton electrons. The effects of electron scattering and energy loss in the target preclude any simple interpretation of this data to yield a differential bremsstrahlung cross section. However, an estimate of the spectra to be expected at 0° and 90° was obtained by combining the Sauter expression for the bremsstrahlung cross section with the available information on electron scatter and energy loss in the target and backscatter from the target. The reliability of the estimate is limited because the Sauter formula was calculated by using the Born approximation, the electron scattering calculations are applicable to an infinite medium only, and the backscatter was estimated empirically from Bothe's experimental data which were obtained with lower energy electrons (370 kev). Furthermore electron energy straggling was neglected. Nevertheless, the predicted spectral shapes at 0° and 90° and the relative intensities at these two angles are in qualitative agreement with the measured values. The absolute magnitudes of the measured intensities at both angles are about a factor of two greater than the predicted values.

I. INTRODUCTION

EXPERIMENTAL investigations of the bremsstrahlung radiation from electrons in an energy range from 1.0 to 2.0 Mev have produced information about the angular distribution of the radiation from thick targets for different atomic numbers.[1] However information about the spectrum of photons produced by electrons in this energy range has been incomplete.[2]

This study was undertaken as part of a program to provide detailed information about the bremsstrahlung radiation for electrons with initial kinetic energies of the order of the electron rest energy. The present measurements[3] are concerned only with the radiation from the 2.8-mm tungsten target of the National Bureau of Standards 1.4-Mev accelerator.[4] The photon energy distribution for electrons with initial kinetic energies of 1.00, 1.25, and 1.40 Mev was measured with a magnetic Compton spectrometer.[5,6] The radiation was examined in directions parallel and perpendicular to the direction of the incident electron beam.

Previous estimates[1] of the spectrum to be expected from a thick target for electrons in this energy range, have depended on the theory developed by Kramers.[7] However, the validity of the Kramers' theory in the present case is limited: (a) the theory estimates the photon energy distribution integrated over all directions of the emitted photons, (b) the theory is nonrelativistic, (c) the effect of electron energy loss in the target is estimated on the basis of the Thomson-Whiddington law which is not valid for energies as high as those considered here, and (d) no account is taken of electron backscatter from the target. A more recent estimate of the spectrum to be expected from a thick target has been made by Wilson,[8] but his results also are in the form of an average over the direction of photon emission. In the present case, it is necessary to use the differential form (differential in photon energy and angle of photon emission) of the bremsstrahlung cross section, and then to estimate the modification produced in the radiation emitted from the target by electron energy loss and scattering in the target (including electron backscattering).

II. EXPERIMENTAL PROCEDURE

A schematic diagram of the experimental arrangement is shown in Fig. 1. Electrons with a given energy are focused on the thick tungsten target. Pinhole pictures indicate that the focal spot on the target has a diameter of approximately 5 mm. The target assembly shown in Fig. 1 is separated from the end of the vacuum chamber by a porcelain spacer. With this Faraday cup arrangement, target currents are measured with an accuracy of one percent. The electrostatic potential across the accelerator is determined with an accuracy of approximately one percent from measurements made with a high resistance voltmeter.[4]

The radiation passes from the target and the surrounding material shown in Fig. 1 to the lead collimator. The angle, ϕ, between the collimator-spectrometer axis and the direction of the incident electrons was adjusted for two separate values: $\phi=0°$ and $\phi=90°$. During a set of measurements, the radiation intensity was monitored by the integrated current output from an

* This work was supported by the U. S. Atomic Energy Commission.

† Present address: U. S. Geological Survey.

[1] Petrauskas, Van Atta, and Myers, Phys. Rev. **63**, 389 (1943); Buechner, Van de Graaff, Burrill, and Sperduto, Phys. Rev. **74**, 1348 (1948); Goldstein, Fano, and Wyckoff, J. Appl. Phys. **22**, 417 (1951).

[2] W. B. Lasich and L. Riddiford, J. Sci. Instr. **24**, 177 (1947); W. C. Miller and B. Waldman, Phys. Rev. **75**, 425 (1949).

[3] Other measurements involving the radiation from thin targets are now in progress.

[4] E. E. Charlton and H. S. Hubbard, Gen. Elec. Rev. **43**, 272 (1940).

[5] Motz, Miller, Wyckoff, Gibson, and Kirn, Rev. Sci. Instr. **24**, 929 (1953).

[6] Motz, Miller, and Wyckoff, Phys. Rev. **89**, 968 (1953).

[7] H. A. Kramers, Phil. Mag. **46**, 863 (1923).

[8] R. Wilson, Proc. Phys. Soc. (London) **A66**, 645 (1953).

ionization chamber placed in the photon beam at the back end of the spectrometer.

The collimated photon beam is incident on a beryllium foil, 0.96 cm long, 0.31 cm wide, and 0.0040 cm thick, and a magnetic analysis is made of the Compton electrons ejected from the foil into a small solid angle in the direction of the incident photon beam. A detailed description of the spectrometer and the method of data analysis have been given elsewhere.[5,6]

The spectrometer was calibrated with γ-ray sources of Co^{60} (1.17 Mev, 1.33 Mev), Cs^{137} (0.661 Mev) and Au^{198} (0.411 Mev).[9] The intensity of these sources was determined from measurements made with an extrapolation type ionization chamber.[10] The line shapes of the electron counting rate *versus* the magnetic field, which were obtained with the monoenergetic photons from these sources showed a resolution (full width at half maximum) of 4 percent.

III. RESULTS OF MEASUREMENTS

The spectra of the bremsstrahlung radiation emitted from the 2.8 mm tungsten target at angles of 0 degrees and 90 degrees to the incident electron direction are shown in Figs. 2 and 3 respectively, for tube voltages of 1000, 1250, and 1400 kilovolts. For each of the voltages, the measured target current was 0.5 ma. The values of the photon energy flux density, $P(k)$, are given at a position one meter from the target, and

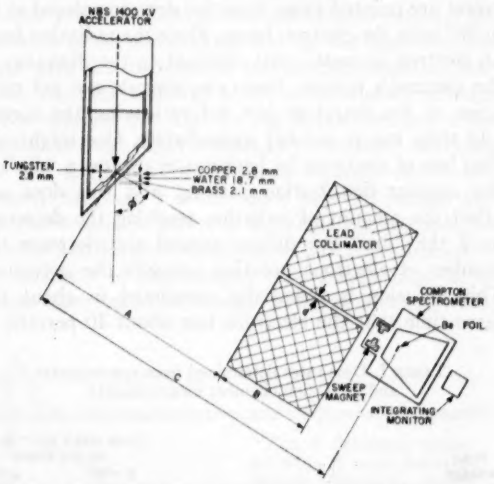

FIG. 1. Experimental arrangement for the bremsstrahlung measurements. Data were obtained for $\phi=0°$ and $\phi=90°$. The tungsten target was at an angle of 45° to the incident electron beam so that the filtration produced by the materials surrounding the target was the same in both the horizontal and vertical directions. For $\phi=0$ degrees; $A=31.1$ inches, $B=11.5$ inches, $C=54$ inches, and $d=0.308$ inch. For $\phi=90$ degrees; $A=34.5$ inches, $B=15$ inches, $C=58.5$ inches, and $d=0.541$ inch.

[9] *Nuclear Data*, National Bureau of Standards Circular 499 (U. S. Government Printing Office, Washington, D. C., 1950).
[10] G. Failla, Radiology **24**, 262 (1937).

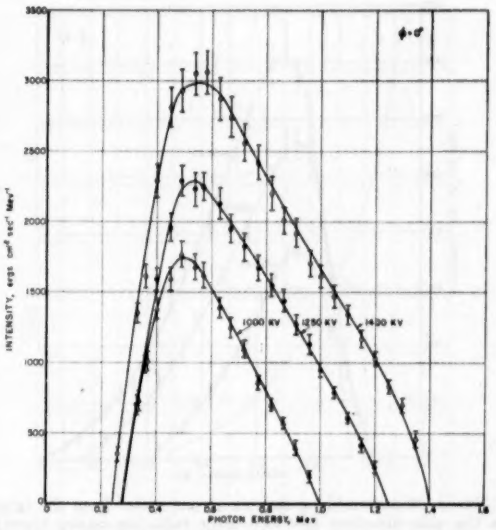

FIG. 2. Bremsstrahlung spectra at one meter from the target in the forward direction ($\phi=0°$), after radiation passes through materials surrounding target. The photon intensity was measured at a point 54 inches from the target (Fig. 1) and corrected for inverse square. The target current was 0.5 ma.

represent the photon energy distribution after filtration by the materials surrounding the target (see Fig. 1).

The dose rate which is produced at the position of the spectrometer foil by the photon energy flux density integrated over all photon energies for the spectra shown in Figs. 2 and 3, was computed by the use of true air absorption coefficients.[11] For comparison, the dose rate produced by the radiation at the foil position was measured with an extrapolation ionization chamber with $\frac{1}{4}$-inch Lucite walls. The measured dose rates were corrected for wall absorption and for the difference in stopping power of Lucite relative to air.[12] The dose rates determined by the above two methods are given in Table I, and show an agreement of approximately 10 percent.

IV. COMPARISON WITH THEORY

With a monoenergetic, monodirectional beam incident on a thick target, the spectral and angular distributions of the radiation leaving the target results from a superposition of several complex processes. These are:

(1) Radiation by monoenergetic, monodirectional electrons incident on a thin target; this is given by the differential bremsstrahlung cross section (i.e., differential in photon energy, photon angle, and electron energy).

(2) Electron penetration into a semi-infinite medium;

[11] Gladys R. White (private communication).
[12] A 3 percent correction was applied for the difference in Lucite to air stopping power. See T. J. Thompson, University of California thesis, UCRL—1910, Aug. 11, 1952 (unpublished); and G. N. Whyte, Nucleonics **12**, No. 2, 19 (1954).

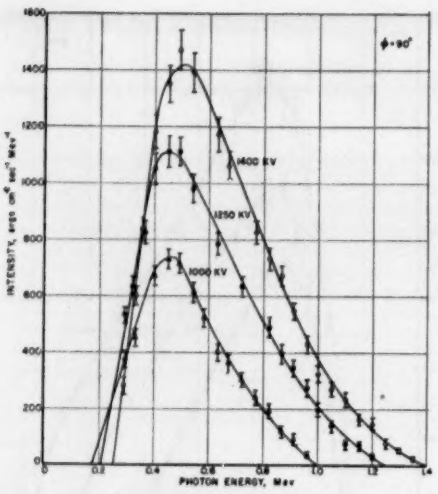

FIG. 3. Bremsstrahlung spectra at one meter from the target in the side direction ($\phi=90°$) after radiation passes through materials surrounding target. The photon intensity was measured at a point 58.5 inches from the target (Fig. 1) and corrected for inverse square. The target current was 0.5 ma.

this includes (a) angular dispersion of electron velocities, (b) backscatter out of the target, (c) energy loss.

(3) Absorption of photons in the target and surrounding materials.

Unfortunately, information on these individual processes is far from complete at present. The differential bremsstrahlung cross section has been computed in Born approximation by Sauter,[13] but the results are not strictly applicable here because of the high atomic number of the target material. Estimates have been made[14] of the error resulting from the use of the Born approximation in the nonrelativistic energy range, and Bethe and Maximon[15] have determined the correction which is applicable above 20 Mev. Interpolation between these corrections indicates that the Sauter formula underestimates the bremsstrahlung cross section for incident electrons with energies of approximately 1 Mev, but no quantitative estimate of the error is available. We shall use the Sauter formula to describe process (1) above, with these possible errors in mind.

With regard to process (2a), theories have been developed[16] to describe the angular distribution of electron velocities as a function of electron energy, for an initially monodirectional monoenergetic electron beam. However, these results apply to an infinite medium, and assume that the electron energy is a unique function of path-length (i.e., energy straggling is neglected). It is possible to get around the restriction to an infinite medium by considering the experimental results of Bothe[17] on backscattering. These show that (for the type of geometry in Fig. 1) very few electrons are backscattered until they have lost at least 10 percent of their energy. On the other hand, the electron scattering theories predict that in a heavy element like tungsten an initially monodirectional beam of electrons will have become almost completely isotropic by the time the electrons have lost about 10 percent of their energy.[18] This means that the angular diffusion process is essentially complete before a significant number of electrons get back to the surface. It seems plausible, then, that the electron scattering results obtained for an infinite medium will provide an approximate description for the semi-infinite medium.

The effect of electron backscatter (2b), is to cut down the number of electrons which can radiate. Bothe's[17] results indicate that well over half of the electrons incident at 45° on a high Z material like tungsten will eventually be backscattered. Furthermore, a large fraction of the backscattered electrons leave the target with at least 50 percent of their incident energy. It is apparent that backscatter causes a significant reduction in the total amount of radiation produced in the target. We shall account for backscattering by specifying that the number of electrons in the target decreases as the electron energy decreases.

The actual rate of decrease can be obtained from Bothe's data on the spectrum of backscattered electrons, with one modification. Electrons leaving the target are pointed away from the detector placed at 0° or 90° with the electron beam. Since the radiation from an electron is pretty well confined to the direction of the electron's motion, these electrons do not get radiation to the detectors just before leaving the target, and their loss is not felt immediately. One might say that loss of electrons by backscatter creates a "dip" in the angular distribution pattern, and this does not affect the amount of radiation reaching the detectors until the "dip" can diffuse around and decrease the number of electrons pointing towards the detectors. This diffusion is essentially completed in about the same time that the electrons lose about 10 percent of

TABLE I. Dose rates determined from spectrometer and ionization chamber measurements.

Tube voltage		Dose rate r min^{-1} ma^{-1} at one meter $\phi=90°$	$\phi=0°$
1400 kv	Ion. chamber	26±1	76±3
	Spectrometer	28±3	80±8
1250 kv	Ion. chamber	19±1	51±2
	Spectrometer	21±2	50±5
1000 kv	Ion. chamber	10±0.5	27±1
	Spectrometer	11±1	29±3

[13] F. Sauter, Ann. Physik **20**, 404 (1934).
[14] See W. Heitler, *The Quantum Theory of Radiation* (Oxford University Press, London, 1954), third edition, p. 246.
[15] H. A. Bethe and L. C. Maximon, Phys. Rev. **93**, 768 (1954).
[16] S. Goudsmit and J. L. Saunderson, Phys. Rev. **57**, 24 (1940); H. W. Lewis, Phys. Rev. **78**, 526 (1950).
[17] W. Bothe, Ann. Physik **6**, 44 (1949).
[18] This has been pointed out by U. Fano. See *Radiation Biology*, edited by A. Hollaender (McGraw-Hill Book Company, Inc., New York, 1954), Chap. I.

their energy. To allow for this, the distribution of backscattered electrons, as given by Bothe, has been scaled in energy. Thus, if Bothe's data indicate that a certain number of electrons are backscattered from the target with 80 percent of their initial energy, then in estimating the decrease in the number of electrons getting radiation to the detectors, these electrons are assumed to have been backscattered 10 percent later in energy, i.e., when they have $(0.9)\times 80$ percent, or 72 percent of their initial energy.

The main processes which cause the incident electrons to lose energy in the target are excitation and ionization of the target atoms (which results from collisions with atomic electrons) and radiation (which results mostly from collisions with nuclei). A comparison of the stopping power formula based on ionization and excitation[19] with the Sauter formula shows that a 1-Mev electron incident on a material with a high Z like tungsten will lose only a few percent of its energy by radiation. We shall make the simplifying assumption that the stopping power formula describes the energy loss of the electron, and that straggling may be neglected.

With regard to absorption of the radiated photons in the target and surrounding materials, it will be assumed that the photons of any energy are attenuated in a simple exponential manner. For the absorber thicknesses and Z values involved here it is sufficiently accurate to neglect "build-up" caused by Compton scattered photons ultimately reaching the detectors.

With the simplifying assumptions just outlined it is possible to carry through a calculation to estimate the spectrum of bremsstrahlung leaving the target at any angle with the direction of the incident beam of electrons. The kinetic energy of the incident electron beam will be taken as 1.4 Mev. In Fig. 4, the direction of the incident electron beam is taken as the forward direction, ϵ is the angle between electron velocity vector and forward direction, θ is the angle between photon and electron velocities, and φ is the angle between photon velocity and forward direction. If $I(k,\varphi)$ is defined as the intensity of photons per unit energy interval at energy k per steradian at angle φ, per incident electron,

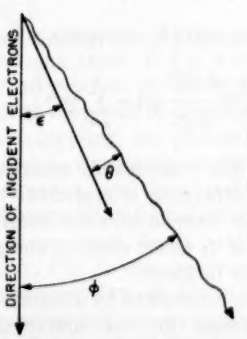

FIG. 4. Schematic representation of angles between photon direction (wavy line), direction of motion of an electron about to radiate, and the direction of the electron beam incident on the target.

[19] See W. Heitler, *The Quantum Theory of Radiation* (Oxford University Press, London, 1954), third edition, p. 386, Eq. (1).

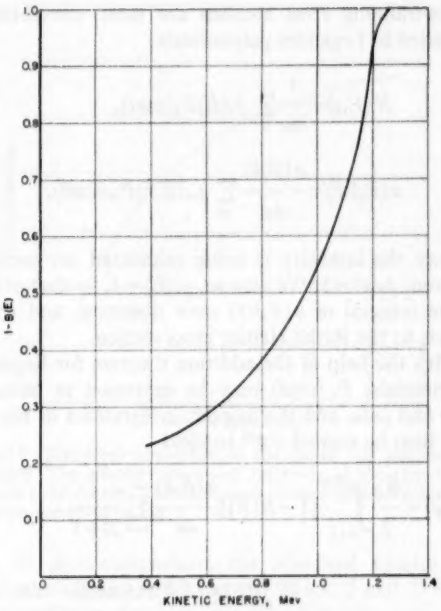

FIG. 5. The function $1-B(E)$.

then

$$I(k,\varphi)=N_A\int_{k+1}^{E_M}\int_0^{2\pi}\int_0^{\pi}N(E,\epsilon)\{1-B(E)\}\times k\sigma(E,k,\theta)\sin\epsilon\,d\epsilon\,d\psi\frac{ds}{dE}dE, \quad (1)$$

where N_A is the number of target atoms/cc, $B(E)$ corresponds to the fractional number of electrons of energy E which have been backscattered out of the target, $N(E,\epsilon)$ represents the angular distribution of the electron velocities as a function of electron energy, $\sigma(E,k,\theta)$ is the differential bremsstrahlung cross section, and ψ is the angle between the planes containing the angles ϵ and φ (Fig. 4), dE/ds is the stopping power, and E_M is the total energy of the incident electrons. The angle φ appears implicitly in Eq. (1) through the relationship $\cos\theta=\cos\epsilon\cos\varphi+\sin\epsilon\sin\varphi\cos\psi$. The kinetic energy of the incident electron has been set at 1.4 Mev for this calculation, so E_M is approximately $3.7mc^2$. The function $B(E)$ was empirically estimated from Bothe's data which was scaled in energy as described above. The resulting function $1-B(E)$ is shown in Fig. 5. Because the stopping power for electrons is a slowly varying function of energy at 1.4 Mev, dE/ds has been assigned a constant value. The value used is $43mc^2$/cm, and corresponds to the stopping power of a 1.4-Mev electron in tungsten, as calculated from the Bloch formula. The distributions $N(E,\epsilon)$ and $\sigma(E,k,\theta)$ have been approximated in the manner described above.

The angular distributions of the electrons and of the

bremsstrahlung cross sections are most conveniently expanded in Legendre polynomials:

$$N(E,\epsilon)=\frac{1}{4\pi}\sum_l f_l(E)P_l(\cos\epsilon), \tag{2}$$

$$\sigma(E,k,\theta)=\frac{\sigma(E,k)}{4\pi}\sum_m g_m(E,k)P_m(\cos\theta). \tag{3}$$

Since the intensity is being calculated per incident electron, $f_0(e)=1$. We also set $g_0(E)=1$, so that $\sigma(E,k)$ is the integral of $\sigma(E,k,\theta)$ over direction, and corresponds to the Bethe-Heitler cross section.

With the help of the addition theorem for Legendre polynomials, $P_m(\cos\theta)$ may be expressed in terms of $\cos\varphi$ and $\cos\epsilon$, and the angular integrations in Eq. (1) may then be carried out[20] to yield

$$I(k,\varphi)=\frac{N_A}{2}\int_{k+1}^{E_M}\{1-B(E)\}\frac{\sigma(E,k)}{4\pi}\sum_{l=0}^{\infty}\frac{2}{2l+1}$$
$$\times f_l(E)g_l(E,k)P_l(\cos\varphi)\frac{ds}{dE}dE. \tag{4}$$

For electrons with energies in the range 0.4 to 1.4 Mev the Bethe-Heitler cross section may be approximated by

$$\sigma(E,k)\cong 11.5\left(1-\frac{k}{E-1}\right), \tag{5}$$

which is good to about 5 percent.

At this point it is easy to make a rough estimate of the average photon intensity spectrum to be expected, by assuming that all the electrons in the target are isotropic, and by neglecting backscatter effects. This means all f_l for $l>0$ are set equal to zero, as is $B(E)$. The spectrum calculated in this manner is shown in Fig. 6 as the dotted curve.

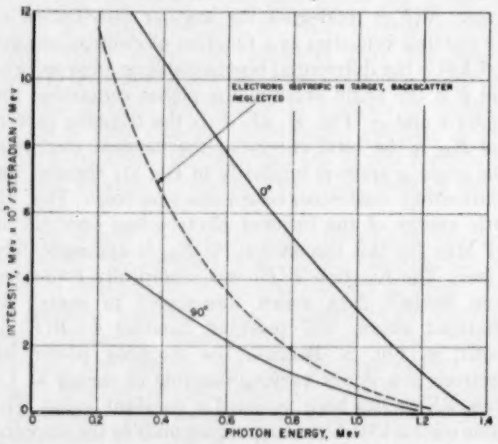

FIG. 6. Calculated spectral intensities per incident electron. (No adjustment has been made for photon absorption in the target and surrounding materials.)

[20] This integration is discussed in greater detail by O. Blunck, Ann. Physik 9, 25 (1951).

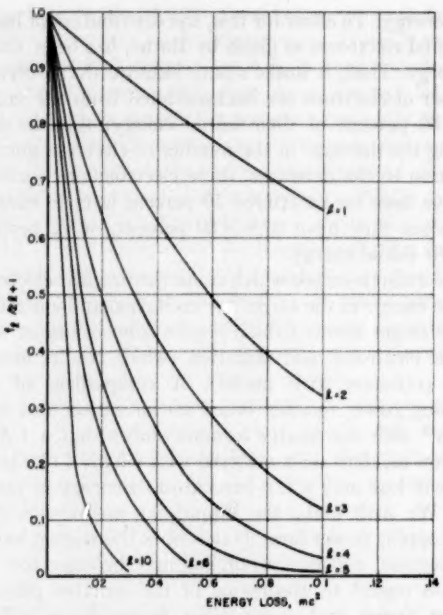

FIG. 7. Legendre coefficients for the angular distribution of electrons in tungsten. The incident electrons are monenergetic and have a kinetic energy of 1.4 Mev.

To determine the intensity and spectral dependence on angle, it is necessary to insert the values f_l and g_l into Eq. (4). The f_l have been determined by Lewis[16] who expanded the angular distribution of the electron velocity vectors in Legendre polynomials, and integrated the transport equation over the position variable. Using a relativistic, screened single scattering cross section calculated in Born approximation he obtained an expression for the Legendre coefficients of the form:

$$f_l=(2l+1)\exp\left(-\int_0^s K_l ds\right), \tag{6}$$

where s = total path length travelled by the electron, and

$$K_l\cong\frac{1}{2}\frac{2\pi N_A Z^2 e^4}{p^2v^2}l(l+1)\left\{\ln\frac{4a_0^2p^2}{\hbar^2Z^{\frac{1}{3}}}+1-\sum_{m=1}^{l}m^{-1}\right\},$$

where a_0 is the Bohr radius. The f_l are readily expressed in terms of energy loss (if straggling is neglected) by inserting the stopping power formula into the integral over S. Figure 7 is a plot of f_l *versus* electron energy loss, for 1.4-Mev electrons in tungsten.

In principle, the g_l could be determined by integration over the analytical expression for the differential bremsstrahlung cross section. An alternative procedure is to actually plot the angular dependence of the

differential cross section, and numerically integrate to find the Legendre polynomial expansions for these curves. The latter procedure is much simpler than the analytic method because of the complexity of the differential cross-section formula. The graphical method was actually used to determine the g_l, and although the numerical work was only carried to an accuracy of about 5 percent, this is not inconsistent with the uncertainty in the backscatter estimate. Figure 8 is a representation of the values obtained for the g_l for selected values of electron and photon energies. Interpolations were carried out to supply the values necessary to complete the integrations and sums in Eq. (4). The distributions thus obtained were multiplied by photon energy to yield the spectral intensity distributions at

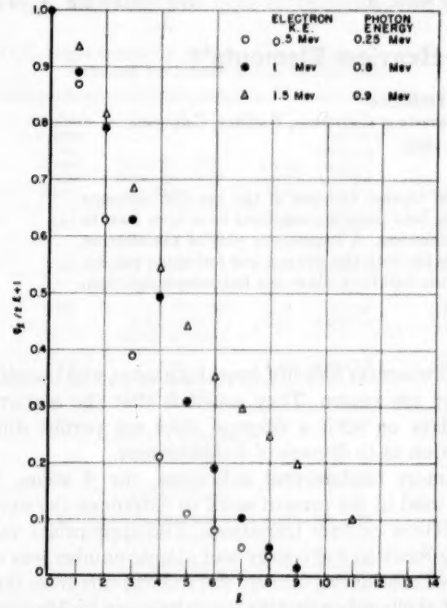

FIG. 8. Legendre coefficients for the angular distribution of bremsstrahlung, for selected values of electron and photon energies.

0° and 90°. These are indicated by the solid lines of Fig. 6.

The computed spectra at 0° and 90°, for 1.4-Mev electrons, shown in Fig. 6 must be modified to account for attenuation in the target and surrounding media, before they can be compared with measured spectra. In computing the attenuation, the thickness of the target was estimated to be 2.8 mm on the basis of a radiograph, and the absorbing thickness was taken as 2.4 mm to allow for the fact that the x-rays are produced at some small depth in the target. The absorption curve, Fig. 9, was constructed from the narrow beam absorption data of White,[11] and absorber thicknesses corresponding to dimensions shown in Fig. 1. The 1.4-Mev spectra of Fig. 6 multiplied by the attenuation curve of Fig. 9, are indicated by the solid curves in

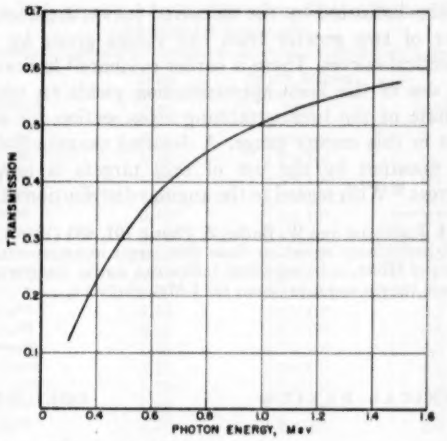

FIG. 9. Estimated absorption in the target and surrounding materials. The effective absorbing thickness of the target was assumed to be 2.4 mm. The thicknesses of the additional absorbing materials are given in Fig. 1.

Fig. 10. For comparison, the observed spectra for 1.4-Mev electrons at 0° and 90° (Figs. 2 and 3) have also been plotted in Fig. 10. The intensity scale per incident electron is in units of 2.1×10^{-3} (Mev/Mev) per steradian for the experimental data, and 10^{-3} (Mev/Mev) per steradian for the computed curves. These scale factors were chosen so that the computed and experimental data at 0° would agree at their peak values.

A comparison of the measured and computed curves in Fig. 10 shows that the energy distributions and the relative intensities of the radiation at 0° and 90° are in qualitative agreement. However, the absolute in-

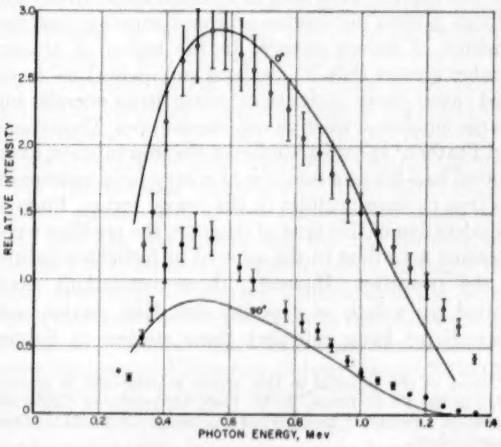

FIG. 10. Computed and experimentally determined relative spectral intensities at 0° and 90°. The solid curves were obtained by applying the transmission curve (Fig. 9) to the computed spectra (Fig. 6). The experimental points correspond to the 1400-kev data on Figs. 2 and 3. To obtain absolute spectral intensities, in Mev per steradian per Mev per incident electron, the ordinate should be multiplied by 10^{-3} for the computed curves, and by 2.1×10^{-3} for the experimental points.

tensities indicated by the measured curves are about a factor of two greater than the values given by the theoretical curves. There is earlier evidence[21] indicating that use of the Born approximation yields an underestimate of the bremsstrahlung cross section for electrons in this energy range. A detailed examination of this question by the use of thin targets is now in progress.[22] With regard to the angular distribution of the radiation, it is interesting to note the extent to which the angular diffusion of the electrons in the target smear the radiation pattern. This smearing is evident when one compares the intensity ratio at 0° and 90° for thin and thick targets; the Sauter formula gives an intensity ratio of about 200, while the thick target results give an intensity ratio of about three.

The writers wish to thank Dr. H. O. Wyckoff for his advice during the course of this work, and F. H. Attix for his help in carrying out the ionization chamber measurements.

[21] H. Klarmann and W. Bothe, Z. Physik **101**, 489 (1936).

[22] A preliminary report on these thin target measurements by Motz and Miller, to be published, indicates a similar disagreement between theory and experiment for 1-Mev electrons.

PHYSICAL REVIEW VOLUME 96, NUMBER 5 DECEMBER 1, 1954

Orbital Electron Capture in the Heaviest Elements*†

R. W. Hoff and S. G. Thompson
Radiation Laboratory and Department of Chemistry, University of California, Berkeley, California

(Received August 20, 1954)

Log*ft* values have been calculated for 30 orbital electron capture isotopes in the heaviest elements ($Z=89$–97). The average values of log*ft* products for negative beta particle transitions have been used to classify the electron capture transitions studied as to forbiddenness. A logarithmic plot of the electron capture partial half-life *versus* neutrino energy has been made for both the allowed and forbidden species. These diagrams can be used in the prediction of electron capture half-lives where one has some insight into the amount of decay energy available.

THE orbital electron capture process can be studied with particular effectiveness in the heaviest elements since decay energies may be calculated from closed decay cycles. Because of inherent experimental difficulties, only a limited number of decay energies for electron capture have been determined either from continuous gamma ray spectra or from competing positron emission of known energy. In the region of atomic number greater than 82, Seaborg and co-workers[1] have used closed decay cycles to calculate decay energies for a large number of electron capture isotopes. Thompson[2] and Feather,[3] in earlier studies of electron capture, have plotted half-life as a function of energy for a number of electron capture nuclides in the heavy region. From a consideration of this type of diagram, the nuclides were classified according to the allowed or forbidden nature of the transition. However, these correlations were limited by a lack of experimental data. Major and Biedenharn[4] have extended these studies to lighter nuclei wherever half-life, branching ratio, and transition energy are known. They conclude that the scatter of the data on such a diagram does not permit differentiation as to degrees of forbiddenness.

A more fundamental indication, the *ft* value, has been used in the present work to determine the nature of electron capture transitions. The appropriate value of the function *f* of energy and atomic number was calculated considering allowed electron capture from the *K* and *L* shells only using the formulas given by Marshak.[5] This value was multiplied by the electron capture half-life to form the *ft* product. Table I lists log*ft* values for nuclides whose electron capture decay schemes are known or can be inferred from the negative beta particle or alpha decay of an isotope to the same daughter nucleus. In certain cases where relative intensities of gamma and x-rays are not known, it has been assumed that the majority of the electron capture decay proceeds to the excited levels in the daughter nuclei. Log*ft* values calculated for these transitions will not be affected greatly by a certain amount of branching decay to the ground states of the daughter nuclei.

Another group of nuclides exists for which decay schemes are not known. Log*ft* values have been calculated for these isotopes under the assumption of ground state transitions. Obviously this assumption is not realistic, but it is the only method of treating the data

* Most of the material in this article is presented in greater detail in the Ph.D. thesis, R. W. Hoff, University of California Radiation Laboratory Declassified Document UCRL-2325, 1954 (unpublished).

† This work was performed under the auspices of the U. S. Atomic Energy Commission.

[1] Seaborg, Glass, and Thompson (to be published); R. A. Glass, Ph.D. thesis, University of California Radiation Laboratory Unclassified Document UCRL-2560, April 1954 (unpublished).

[2] S. G. Thompson, Phys. Rev. **76**, 319 (1949).

[3] N. Feather, Proc. Roy. Soc. (London) **A63**, 242 (1952).

[4] J. K. Major and L. C. Biedenharn, Phys. Rev. **94**, 779 (1954).

[5] R. E. Marshak, Phys. Rev. **61**, 431 (1942).

at the present time. These logft values are listed in Table II.

A more detailed grouping of beta transitions than those following from Gamow-Teller selection rules has been given by Mayer *et al.*[6] In this case the logft products for allowed transitions were noted to be in general less than 6.0. In addition, King and Peaslee[7] have recently observed that most first-forbidden transitions have logft values averaging 6.5 and 7.5 for $\Delta I=0$ or 1, respectively, and logf_1t values averaging 8.5 for $\Delta I=2$.

These average values of ft products for negative beta particle transitions are used to classify the electron capture transitions studied here. None of the above-mentioned nuclei are here classified as l-forbidden, since the logft limits for this type of transition are quite broad and knowledge of exact orbital assignments is lacking for the heavy elements. It is also noted that most of the nuclides can be considered as either allowed or first forbidden $\Delta I=0$, 1 yes.

The isotope Cm^{241} has logft values for its transitions that are large enough to suggest assignment of $\Delta I=2$, yes. It is more appropriate in the case of the pure Gamow-Teller $\Delta I=2$, yes transitions to use a special first-forbidden f_1 for the f_1t product.[5] These logf_1t values, listed in Table I, are somewhat lower than the average of 8.5 for negative beta particle emitters. This result indicates that $\Delta I=0$, 1 yes is a preferable assignment for the Cm^{241} decay.

The apparent lack of highly forbidden transitions is not surprising, since the precise amount of electron capture branching to various excited levels is often very difficult to determine and the highly forbidden transitions would be masked by the more predominant allowed decay. The logft values, 3.8 for U^{228} and 3.2 for Am^{240}, are definitely low even for allowed transitions in this region. However, a small increase in the calculated decay energies for U^{228} and Am^{240} would raise the ft values to within the limits for allowed electron capture.

For the isotopes studied, i.e., those with atomic number greater than 82, the nuclear shell model predicts that the odd proton and the odd neutron will generally be in orbitals of different parity, although the many low-energy $E1$ gamma transitions in the heavy region cast doubt on the generality of this parity change assumption. Ground state transitions would involve parity changes, and therefore allowed transitions would be expected to populate excited levels of daughter nuclei. In this region many odd-odd nuclei decay to highly excited levels in their even-even daughter nuclei. For example, Ac^{228}, Pa^{232}, Pa^{234}, Np^{234}, Np^{238}, Am^{240}, and others decay to levels at least one Mev above the ground state of the daughter nucleus. Therefore, it may be expected that transitions to highly excited levels will be observed when enough decay energy is available in

TABLE I. Logft values for nuclides whose electron capture decay schemes are known or can be inferred.

Isotope	Available energy from closed cycles (Mev)	Level to which decay proceeds[a] (Mev)	Decay energy (Mev)	Partial electron capture half-life (sec)	Logft
Pa^{228}	2.07	1.03 (decay of Ac^{228})	1.04	8.1×10^{4}	6.6
Pa^{230}	1.32	0.94 (γ ray observed)	0.38	1.7×10^{6}	6.9
U^{231}	0.34	Ground state—50% 0.23—50% (decay of Th^{231})	0.34 0.11	7.4×10^{5} 7.4×10^{4}	6.4 4.7
Np^{232}	2.67	1.05 (γ ray observed, decay of Pa^{232})	1.62	7.8×10^{2}	5.1
Np^{233}	1.09	0.30 (conv. e^-'s observed, decay of Pa^{233})	0.79	2.1×10^{3}	4.8
Np^{234}	1.86	1.57[b] (γ ray observed)	0.29	3.8×10^{5}	6.1
Np^{235}	0.17	Ground state[b] (no γ rays observed)	0.17	3.5×10^{7}	6.6
Pu^{234}	0.48	Ground state[b] (no γ rays observed)	0.48	3.4×10^{4}	5.6
Am^{236}	2.26	1.03 (decay of Np^{236})	1.23	7.6×10^{2}	5.8
Am^{239}	0.78	0.277 (γ ray observed, decay of Np^{239})	0.50	4.3×10^{4}	5.7
Am^{240}	1.46	0.92—14%[c] 1.02—70% 1.40—15%	0.54 0.44 0.06	1.2×10^{6} 2.4×10^{5} 1.1×10^{6}	7.4 6.6 3.2
Am^{242m}	0.69	0.041[b] (conv. e^-'s observed)	0.65	2.6×10^{5}	6.7
Cm^{241}	0.89	0.47—28%[c] 0.59— 7% Ground state—65%	0.42 0.30 0.89	4.7×10^{6} 1.1×10^{7} 4.3×10^{7}	8.2 logf_1t=6.5 8.2 logf_1t=6.4 8.3 logf_1t=7.7
Bk^{245}	0.70	0.245[d] (γ ray observed)	0.46	4.3×10^{5}	6.7

[a] Data on decay schemes have been taken from Hollander, Perlman, and Seaborg, "Table of Isotopes," Revs. Modern Phys. **25**, 469 (1953) unless otherwise noted.
[b] Experimental work by authors.
[c] R. A. Glass, Ph.D. thesis, University of California Radiation Laboratory Unclassified document UCRL-2560, April, 1954 (unpublished).
[d] E. K. Hulet, Ph.D. thesis, University of California Radiation Laboratory Unclassified document UCRL-2283, July, 1953 (unpublished).

TABLE II. Logft values for nuclides whose electron capture decay schemes are not known.

Isotope	Decay energy (Mev)	Partial electron capture half-life (sec)	Logft
Ac^{223}	0.64	1.3×10^{4}	5.3
Ac^{224}	1.39	1.2×10^{4}	6.0
Th^{226}	0.55	4.8×10^{3}	4.7
Pa^{227}	1.08	1.5×10^{4}	5.9
Pa^{229}	0.37	1.3×10^{5}	5.8
U^{225}	0.30	2.8×10^{5}	3.8
U^{229}	1.29	4.4×10^{3}	5.6
Np^{236}	0.91	1.2×10^{5}	6.8
Pu^{232}	0.99	2.2×10^{5}	5.1
Pu^{235}	1.14	1.6×10^{5}	5.1
Pu^{237}	0.23	3.5×10^{6}	6.8
Am^{237}	1.48	4.7×10^{3}	5.9
Cm^{238}	1.12	1.0×10^{4}	6.0
Cm^{239}	1.79	1.1×10^{4}	6.4
Bk^{243}	1.46	1.7×10^{4}	6.5
Bk^{244}	2.20	1.8×10^{4}	6.8

[6] Mayer, Moszkowski, and Nordheim, Revs. Modern Phys. **23**, 315 (1951); L. W. Nordheim, Revs. Modern Phys. **23**, 322 (1951).
[7] R. W. King and D. C. Peaslee, Phys. Rev. **94**, 1284 (1954).

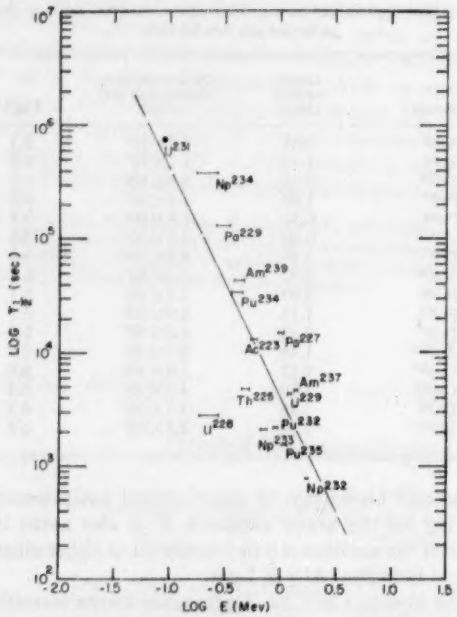

FIG. 1. Logarithm of the partial electron capture half-life *versus* logarithm of the neutrino energy for allowed electron capture.

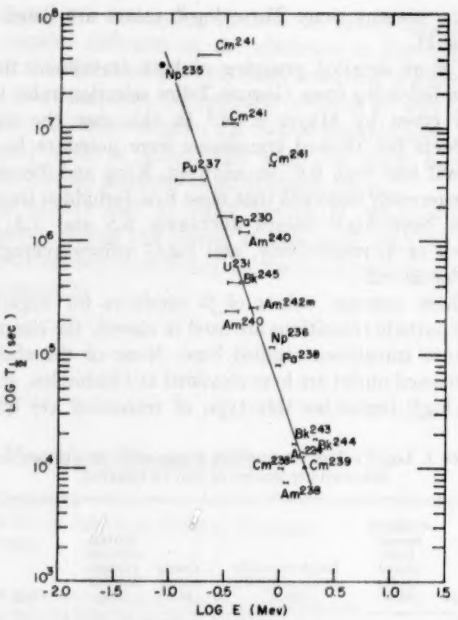

FIG. 2. Logarithm of the partial electron capture half-life *versus* logarithm of the neutrino energy for forbidden electron capture. (In the figure, Pa^{238} should read Pa^{228}.)

certain odd-odd nuclei for which no experimental data are yet available.

A plot of the logarithm of the partial electron capture half-life *versus* the logarithm of the neutrino energy for allowed species is shown in Fig. 1. This type of plot may be used with confidence, for the variation of electron capture probability with atomic number in this limited range is not great. The limits on the neutrino energy indicate K and L electron capture energies, the average decay energy lying somewhere between the limits, depending on the ratio of K to L electron capture. The theoretical expression for the probability of allowed electron capture predicts a slope of two for such a plot. A reference line has been drawn with the predicted slope. The data indicate a line of slope slightly greater than two.

A similar plot for the forbidden electron capture transitions is shown in Fig. 2. Although theory does not predict a unique slope in this type of plot for $\Delta I = 0, 1$ yes transitions, the slope should be between two and three. The data fit a line of slope of approximately three as indicated in the figure. Curium-241 with its larger logft values falls well away from the line.

These diagrams can be used in the prediction of electron capture half-lives when one has some insight as to the amount of decay energy available. This is especially true in a search for new isotopes in the heaviest elements where electron capture energies may be calculated from closed-decay cycles. In addition, a continuation of this type of study may eventually lead to the prediction of decay schemes for new isotopes in the region.

The continued interest and helpful suggestions of Professor G. T. Seaborg throughout this investigation are gratefully acknowledged. The authors also wish to express appreciation to Dr. J. O. Rasmussen, Jr. for his most helpful discussion of the problem.

Energy Levels of Be^{10}* †

J. J. JUNG‡ AND C. K. BOCKELMAN
Physics Department and Laboratory for Nuclear Science, Massachusetts Institute of Technology, Cambridge, Massachusetts

(Received August 23, 1954)

A magnetic spectrograph has been employed to measure the momenta of proton groups emitted at 90 degrees from a thin beryllium target bombarded by deuterons. Groups were observed corresponding to the ground state of Be^{10}, as well as known levels at 3.37, 5.96, 6.26, 7.35, and 7.54 Mev. A new level at 6.18 Mev was also seen.

THE energy-level spectrum of Be^{10} below 3.5-Mev excitation, which includes the first excited state at 3.37 Mev, is well known from a number of studies of the $Be^9(d,p)Be^{10}$ reaction.[1–4] Between 3.5 Mev and the neutron binding energy of 7.2 Mev, the earlier work of Boyer[5] has been supplemented by the more recent experiment of Rhodes and McGruer.[6] These authors report levels at 5.94 and 6.24 Mev. Above 7.2 Mev, the latter work is augmented by measurements of the total neutron cross section of Be^9, which indicate levels at 7.37, 7.54, and 9.27 Mev.[7,8]

The levels were observed as proton groups emerging at 90 degrees from thin beryllium targets bombarded by deuterons. Charged particles were analyzed in momentum by a 180-degree magnetic spectrograph and recorded on Eastman NTA plates. The position of the tracks in the emulsion is a measure of the radius of curvature of the particles which, when combined with magnetic field measurements obtained with a resonance fluxmeter, allows a comparison with the momenta of polonium alpha particles. A rough range measurement of the nuclear tracks is sufficient to distinguish protons from other charged particles of the same momentum. The deuteron beam was furnished by the MIT–ONR electrostatic generator. Currents of 0.1 μa with energy spreads of 0.1 percent were used. Further details of the experimental arrangement have been given in a recent article.[9]

For accurate measurement of Q-values, a number of targets were prepared from several sources of beryllium metal by evaporation from a wolfram filament onto a Formvar film supported by a wire frame. With spectrograph entrance slits open $\frac{1}{2}$ mm, the targets produced peaks about 0.7 mm wide, equivalent to an instrumental energy resolution of about 250. Examination of elastically scattered groups from these targets showed the presence of a heavy contaminant, perhaps mercury or wolfram picked up in the evaporator, but only traces of other nuclei, except beryllium, carbon, and oxygen.

Figure 1 shows the proton momentum spectrum observed with 7-Mev deuteron bombardment. The peaks are labeled by the state of the residual nucleus to which they correspond. All the groups attributed to the $C^{12}(d,p)C^{13}$, $C^{13}(d,p)C^{14}$, and $O^{16}(d,p)O^{17}$ reaction are associated with well-known levels. Since the deuterium used in the ion source contains a small amount of ordinary hydrogen, a weak beam of singly ionized hydrogen molecules exists which has nearly the same momentum as the atomic deuterium beam. Small variations in generator voltage allow some molecular hydrogen through the energy defining slits. Each molecule yields two protons of one-half the incident energy when it strikes the target. The intensity of this beam was sufficient to produce a series of elastically scattered groups seen in Fig. 1 between $H\rho=238$ and $H\rho=268$ kilogauss-centimeters. The exposure was insufficient in this particular set of plates to bring out the elastic O^{16} peak.

The assignment of the remaining groups to Be^{10} was verified by observations at different bombarding energies between 5.4 and 7.4 Mev. For a 2-Mev change in incident energy, the change in energy of a (d,p) group resulting in a nucleus of mass 10 differs from that resulting in a nucleus of mass 11 by 40 kev, and the energy change is greater if the mass difference is greater. A 40-kev difference was easily measurable. At a deuteron energy of 7 Mev, the groups from $O^{16}(d,p)O^{17*}$ (5.39) and $Be^9(d,p)Be^{10*}$ (7.37) happen to coincide, as noted in Fig. 1; they were well separated at other energies.

The Be^{10} groups shown were obtained from the same target and are normalized to the same deuteron bombardment. The areas under the peaks may be taken as a rough indication of their relative intensity at this energy and angle. The least intense group (6.18-Mev level) is about 5 percent of the strongest (the 6.26-Mev level). From the survey, it appears that there are no

† This work has been supported in part by the joint program of the Office of Naval Research and the U. S. Atomic Energy Commission.

‡ While on leave from the University of Strasbourg, Strasbourg, France.

[1] Lattes, Fowler, and Cuer, Proc. Phys. Soc. (London) **59**, 883 (1947).
[2] Strait, Van Patter, Sperduto, and Buechner, Phys. Rev. **81**, 747 (1951).
[3] E. D. Klema and G. C. Phillips, Phys. Rev. **86**, 951 (1952).
[4] A. J. Salmon, Proc. Phys. Soc. (London) **A64**, 848 (1951).
[5] K. Boyer, Massachusetts Institute of Technology, Laboratory for Nuclear Science, Progress Report, July 1950 (unpublished).
[6] K. Rhodes and J. M. McGruer, Phys. Rev. **92**, 1328 (1953).
[7] R. Ricamo and W. Zunti, Helv. Phys. Acta **24**, 419 (1953).
[8] Bockelman, Miller, Adair, and Barschall, Phys. Rev. **84**, 69 (1951).
[9] Buechner, Sperduto, Browne, and Bockelman, Phys. Rev. **91**, 1502 (1953).

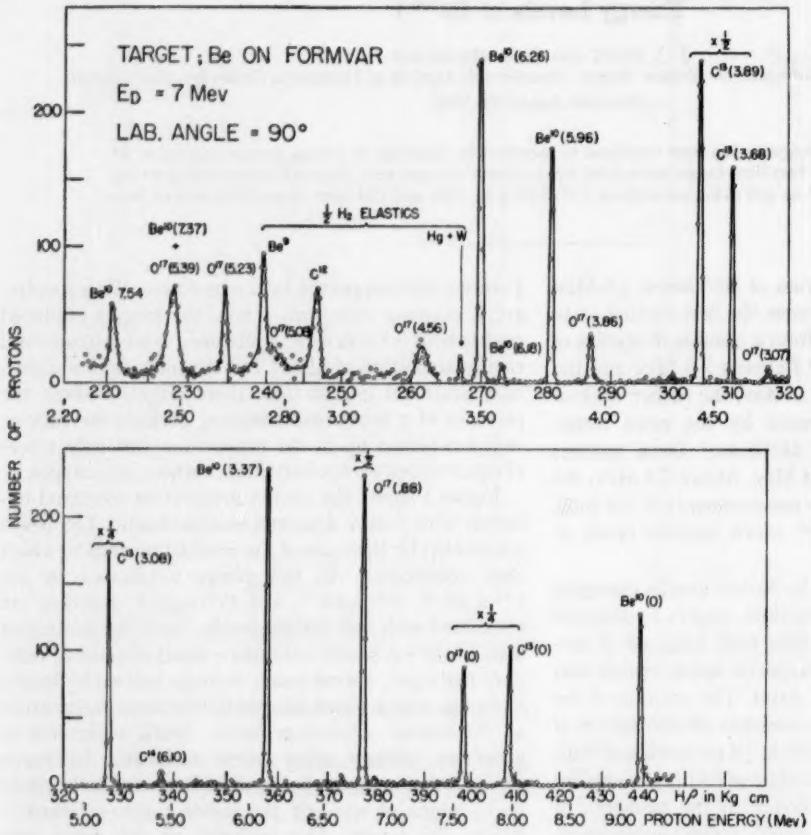

FIG. 1. Proton momentum spectrum observed at 90 degrees from a beryllium target bombarded by 7-Mev deuterons. The number of proton tracks in a $\frac{1}{2}$-mm strip across the nuclear emulsion is plotted against the momentum measured in kilogauss-centimeters. The peaks are labeled by the state of the residual nucleus to which they belong. The beryllium peaks are from the same target and are normalized to a 200-microcoulomb exposure.

other groups attributable to Be^{10} which produce a peak more than 3 percent as strong as the 6.26-Mev level at this energy and angle. At the other deuteron energies investigated, the relative intensities do not seem to differ markedly. Peaks other than those assigned to Be^{10} were obtained from targets which differed in thickness; their intensities are not significant.

The observed width of the groups attributed to the 7.37-Mev level is consistent with a level width of about 25 kev, as observed in the neutron total cross section.[8] The 7.54-Mev Be^{10} level appears to be narrower and approaches the instrumental width of some 10 kev in this region. For these levels, the energies corresponding to the point on the high-energy side of the peak at which the count reaches one-third of its maximum give the most consistent Q-values, and agree to within 10 kev with level positions obtained from the neutron resonance energies. For narrow peaks, the one-third point appears least dependent on instrumental factors and is used as the reference point.

TABLE I. Measured Q-values of $Be^9(d,p)Be^{10}$ reaction.

Be^{10} excitation	Q in Mev
0	4.586±0.009
3.37	1.218±0.009
5.96	−1.373±0.008
6.18	−1.592±0.007
6.26	−1.676±0.007

The measured Q-values for the sharp levels are listed in Table I. Incident energies were obtained from the energy of deuterons elastically scattered from Be^9. Targets were changed frequently to avoid accumulating deposits on the beryllium. The measured energies were inserted in the 90-degree Q-equation, and relativity corrections were made. The values in Table I represent averages of at least three separate runs. It should be noted that, for the weak group corresponding to the 6.18-Mev level, exposures three times larger than that represented in Fig. 1 were necessary to obtain the positions of the high-momentum edge accurately. The reaction angle was measured as 90.0°±0.1° by comparing energies of alpha particles scattered from gold and lithium targets at constant input energy. Under the conditions of the present experiment, the errors arising from uncertainties in the fundamental constants, in the absolute value of $H\rho$ for polonium alpha particles, and

in the measurement of fluxmeter frequencies and reaction angle were smaller than the uncertainty in determining the position of one-third height of the peaks. The square root of the sum of the squares of all these errors for a typical set of measurements is quoted in Table I as the error.

These results confirm the existence of the levels at 5.96 and 6.26 Mev and show an additional level, previously unreported, at 6.18 Mev.

The authors thanks are tendered to Professor W. W. Buechner, Dr. C. P. Browne, and Mr. A. Sperduto for help and advice during the experiment, and to Mr. W. A. Tripp and Miss Janet Frothingham for scanning many of the numerous photographic plates.

PHYSICAL REVIEW VOLUME 96, NUMBER 5 DECEMBER 1, 1954

Angular Distribution of Protons from (d,p) Reactions on Be^9, N^{14}, and Zn^{68}†*‡

F. S. Eby§
University of Illinois, Urbana, Illinois
(Received August 4, 1954)

The (d,p) stripping theory of Butler has been employed in the interpretation of the angular distributions of protons resulting from the bombardment of foil targets of Be^9, N^{14}, and Zn^{68} by 11.9-Mev deuterons. A NaI(Tl) scintillation counter was used to detect protons emitted between angles of 5° and 90°, and pulses were recorded on a 35-mm film strip for pulse height analysis. The distribution of protons from the reaction $N^{14}(d,p)N^{15}$ leaving N^{15} in its doublet first excited state was found to have a peak in the forward direction, indicating that the conclusion previously reached, i.e., that high momentum transfers are involved in this reaction, is probably incorrect. Although it was not possible to do so in the present work, it appears that stripping theory might be used to account for the proton distribution from this reaction if deuterons of higher energy were used. The orbital momenta of a pair of isomeric levels in the nucleus Zn^{69} as determined from the proton distributions and stripping theory are in agreement with the shell model assignments of $p_{1/2}$ for the ground state and $g_{9/2}$ for the 436-kev level. Higher excited levels of Zn^{69} are indicated at about 770 kev and 1.6 Mev. The distribution of the proton group leaving the final nucleus with an excitation of 770 kev is characterized by a momentum transfer, $l_n=2$. The Q value for the reaction leaving Zn^{69} in the ground state was determined to be 4.16 ± 0.15 Mev.

I. INTRODUCTION

THE reaction chamber and experimental arrangement which are described in the first part of this paper have been used to study the angular distributions of proton groups resulting from the deuteron bombardment of thin targets of Be^9, N^{14}, and Zn^{68}. Previous investigations of proton distributions from (d,p) reactions on Be^9 have been made at deuteron energies of 3.6 Mev,[1] 7.7 Mev,[2] 8 Mev,[3] and 14.5 Mev,[4] as well as 18 energies between 300 kev and 1.3 Mev. The present work was carried out with 11.9-Mev deuterons, and the proton groups associated with the ground state and the first excited state of Be^{10} were observed at laboratory angles between 5° and 85°. In an earlier experimental study of the reaction $N^{14}(d,p)N^{15}$ with 8-Mev deuterons,[5] the proton group associated with the doublet first excited state of N^{15} was shown to have a nearly isotropic distribution. This result has been interpreted by Butler[6] as indicating that the reaction proceeds primarily through the formation of a compound nucleus with little or no contribution from a stripping process. It was considered worth-while to investigate this reaction again using a higher deuteron energy and to extend the measurements to lower angles.

The successful use of stripping theory in interpreting the angular distributions of protons from (d,p) reactions has been restricted almost entirely to relatively light nuclei. Reactions involving the target nucleus Sr^{88} have been investigated by Holt and Marsham[7] and were found to lead to complex proton distributions which could not be explained in a simple way in terms of stripping theory. In the present work (d,p) reactions on Zn^{68} were studied for the purpose of comparing the results obtained from an interpretation of the proton distributions in terms of stripping theory with information which can be inferred from other knowledge about

† This investigation was supported jointly by the U. S. Atomic Energy Commission and the Office of Naval Research.

* This paper is based on a thesis submitted in partial fulfillment of the requirements for the degree of Doctor of Philosophy at the University of Illinois.

‡ A preliminary report of part of this work was given at the Chicago meeting of the American Physical Society in November, 1953 [Phys. Rev. **93**, 925(A) (1954)].

§ Now at the University of California Radiation Laboratory, Livermore, California.

[1] Fulbright, Bruner, Bromley, and Goldman, Phys. Rev. **88**, 700 (1952).

[2] F. A. El-Bedewi, Proc. Phys. Soc. (London) **A65**, 64 (1952).

[3] J. R. Holt and T. N. Marsham, Proc. Phys. Soc. (London) **A66**, 1032 (1953) contains references to previous work.

[4] C. F. Black, Phys. Rev. **87**, 205(A) (1952). See also U. S. Atomic Energy Commission Report AECU 2128, 1952 (unpublished).

[5] W. M. Gibson and E. E. Thomas, Proc. Roy. Soc. (London) **A210**, 543 (1951).

[6] S. T. Butler, Proc. Roy. Soc. (London) **A208**, 559 (1951).

[7] J. R. Holt and T. N. Marsham, Proc. Phys. Soc. (London) **A66**, 565 (1953).

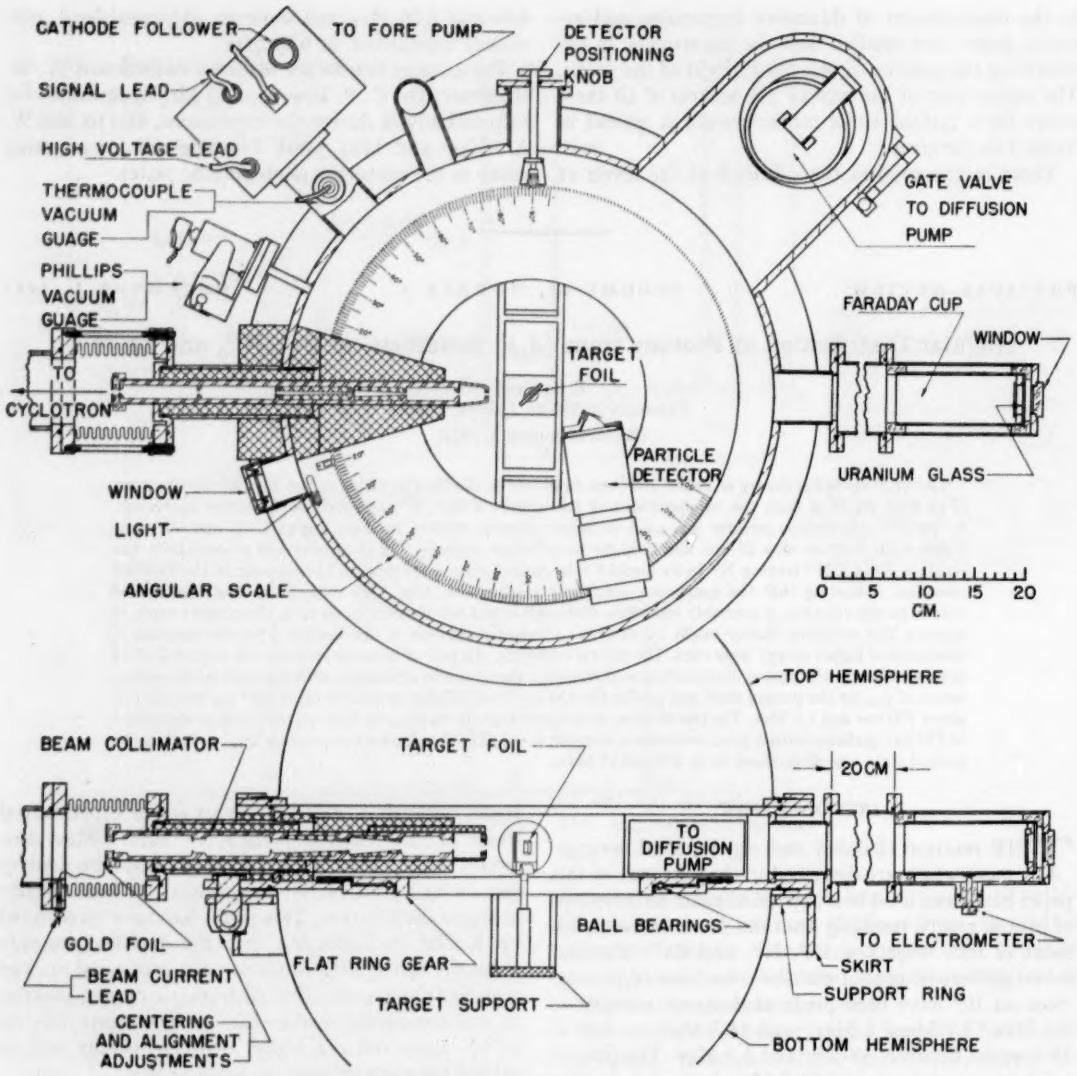

FIG. 1. Top and right-end cross-sectional views of the reaction chamber.

the nuclei involved in the reactions. On the basis of the assignment of zero spin to the ground state of Zn^{68} and the shell model assignments[8] of $p_{1/2}$ for the ground state and $g_{9/2}$ for the 436-kev isomeric level of Zn^{69}, it must be assumed that when Zn^{68} is bombarded by deuterons, p-wave neutrons are captured leading to the ground state of Zn^{69} and g-wave neutrons leading to the 436-kev level. The proton distributions are hence expected to be characterized by momentum transfers of $l_n=1$ for the ground state group and $l_n=4$ for the group leaving Zn^{69} in its first excited state. Direct comparison can be made with the results of stripping theory by fitting to the experimental angular distributions Butler's theoretical expression using these values for the parameter l_n.

[8] M. Goldhaber and R. D. Hill, Revs. Modern Phys. 24, 179 (1952).

II. EXPERIMENTAL APPARATUS AND PROCEDURE

Deuteron Beam

A reasonably monoenergetic beam of 11.9-Mev deuterons was obtained by selecting a narrow swath of the main beam at the end of the 180° deflection channel of the University of Illinois cyclotron. The beam emerged from the cyclotron through a tube containing a remotely operated shutter and entered a deflecting magnet where it was bent through an angle of about 37°. By means of

a proton spin resonance device the magnetic field in the deflecting magnet was held constant to within 0.1 percent and provided additional energy selection as well as deflection. The deuteron beam which reached the reaction chamber, about 4½ meters from the cyclotron exit port, had a mean energy of 11.9 Mev and an energy spread of approximately ±50 kev. The cyclotron was run continuously during data taking periods, and the beam was interrupted whenever necessary by operating the shutter in front of the deflecting magnet.

Reaction Chamber

Top and right-end cross-sectional views of the reaction chamber are shown in Fig. 1. The center section of the chamber is a cylindrical shell of ¼-inch thick brass, 19½ inches in diameter and 2½ inches high. Spun aluminum hemispheres (about $\frac{1}{32}$ inch thick) are used for the top and bottom. The top hemisphere is simply set in place on a rubber gasket in the upper flange of the cylindrical section and is easily lifted off to gain access to the inside. The chamber is supported by a tripod ring-stand which fits under the lower flange of the cylindrical section. Screw adjustments and a vertical shaft at the front of the ring permit translation of the front of the chamber in a direction perpendicular to the beam and rotation of the entire chamber about a vertical axis. Adjusting screws on the legs of the tripod provide for vertical positioning. The chamber is evacuated by a 100-liter/sec oil-diffusion pump backed up by a mechanical fore-pump.

Collimation of the Beam

The part of the collimating system which is located at the front of the chamber consists of seven rectangular apertures. The first six of these were milled in two pieces of stainless steel which are fastened together to form a bar of one-inch-square cross section. Two machined channels, centered on the beam axis of the chamber about eight inches apart, position the bar along a diameter to within 0.5 minute of arc. The first aperture, which was milled out of gold sheet inlaid in the steel, serves to minimize the gamma ray background by excluding divergent beam as far in front of the chamber as possible. The third (also of gold), together with the aperture at the exit of the deflecting magnet, defines the cross section and divergence of the primary beam which passes through the chamber. The other five apertures serve to limit the spray of particles scattered from the defining slit and the inside of the collimator. The final aperture, located about 4 cm from the target foil, is adjustable and mounts in a Dural frame which is fastened to the end of the steel bar.

The primary beam has a maximum divergence (half-angle) within the chamber of 13.5 minutes and a measured cross-sectional area at the target position of 1.6 mm×6.8 mm. In the plane of the particle detector the maximum half-angle of spray is 21 minutes for particles which have scattered once within the collimation system and 3°–20 minutes for particles which have scattered twice. A considerable decrease in the background gamma radiation at low angles was achieved by filling the spaces between slits with lead wherever possible.

The Target Holder

The target foil is mounted in a frame at the center of the chamber, the intersection of the beam with the foil defining the target volume. The frame, which slip-fits in a groove accurately milled in position along a diameter of the chamber, may be removed from the chamber for convenience in loading target foils. For detector angles in the range from 0° to 90° the plane of the target is set at 45° to the beam direction (as shown in Fig. 1). For detector angles greater than this the foil holder is rotated 90°.

The Particle Detector

A scintillation crystal and a selected RCA 5819 photomultiplier tube are used to detect particles emitted by the target. A NaI(Tl) crystal of approximate dimensions 6 mm×9 mm×0.8 mm is mounted in a channel near the end of a Lucite light pipe (Fig. 2). The Lucite is curved in such a way that the light from the crystal which strikes its inside surface is totally reflected toward the photocathode of the tube. The light pipe is joined to the multiplier tube by a strip of aluminum foil cemented to both members with Duco cement. The intervening space is filled with Dow Corning 703 fluid, a clear, thin, low vapor pressure oil, which optically couples the Lucite to the glass photomultiplier tube and minimizes light losses due to internal reflections. Crystals were freshly cleaved in a jet of dry helium immediately before mounting and were covered by 0.16 mg/cm² aluminum foil as soon as they were in place on the light pipe.

A rectangular slit defines the solid angle, and a Lucite absorber immediately in front of the crystal attenuates the energy of the incident particles. The slit has the dimensions 1.60 mm×6.35 mm and is situated 5.4 cm from the center of the target. Absorbers used in the

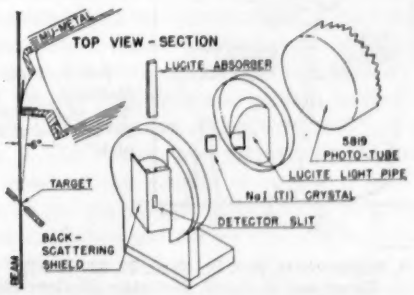

FIG. 2. Top cross-sectional and exploded isometric views of the particle detector.

present work were sufficiently thick to completely stop elastically scattered deuterons and low energy protons.

The detector is fastened to a ring-gear which is supported by ball bearings and can be rotated about a vertical axis through the center of the target by means of a shaft which passes through an *O* ring seal in the side of the chamber. The angular position of the detector slit can be read from a scale which is scribed on the ring-gear and is visible through a window near the front of the chamber. At angles lower than about 6° the side of the detector intercepts the main beam. At high angles the collimating system acts as a stop and limits the maximum detector angle to about 120°.

A cylindrical shell of several thicknesses of annealed mu-metal shields the photomultiplier tube from external magnetic fields. Electrical connections to the tube consist of a high voltage lead, a ground wire, and a signal lead, all of which pass through Stupakoff seals and terminate in a shielded box on the side of the chamber. A Higinbotham +500–1500-volt supply[9] is used for the high voltage, and positive signals from the last dynode of the photomultiplier tube are amplified by a Los Alamos model 100 pulse amplifier.[10]

Charge Collection and Measurement

A Faraday cup is supported by Lucite rings in a tube connected to the rear of the chamber along the beam axis. The rear of the cup is made of uranium glass and is shielded from the direct beam by a hinged sheet of mu-metal which can be raised by means of an external magnet. This construction provides a convenient means for checking the alignment of the chamber or estimating the thickness of target foils by noting the size of the beam spot on the uranium glass. The cup was electrically connected to two precision one-microfarad polystyrene condensers which were connected in parallel. The voltage across the condensers, as measured by a vibrating reed electrometer,[11] provided a measure of the integrated beam through the chamber during the 3 to 10 minute runs taken at each angle.

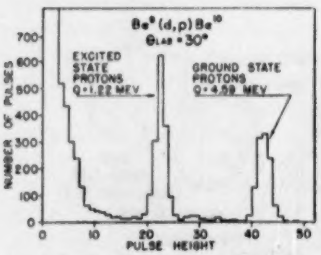

FIG. 3. Pulse height spectrum of protons from (d,p) reactions on Be^9 at a laboratory angle of 30°.

[9] W. A. Higinbotham, Rev. Sci. Instr. **22**, 429 (1952).

[10] W. C. Elmore and M. Sands, *Electronics* (McGraw-Hill Book Company, Inc., New York, 1949).

[11] Palevsky, Swank, and Grenchik, Rev. Sci. Instr. **18**, 298 (1947).

Pulse Recording and Discrimination

Since protons belonging to several different energy groups were simultaneously incident on the detector, it was necessary to perform a pulse height analysis in order to decompose the spectrum and obtain information on particles of a single energy group. This was done photographically. An oscillograph record camera (Du Mont type 314) employing 100-ft lengths of 35-mm film was used to record the signals on the cathode ray tube of a triggered sweep oscilloscope (Tektronix 511A). The signals were traced on the face of the tube parallel to an illuminated Lucite scale containing 100 equally spaced pulse-height divisions. Since the film ran continuously, the image of the scale on the film consisted of 100 equally spaced lines running the length of the film superimposed on the images of the pulses. For analysis, the films were projected on the screen of a micro-film reader (Diebold "Flowfilm") and magnified by a factor of about 18. When the particle groups were cleanly resolved, it was necessary only to count the pulses within the separated groups. For groups which were not resolved, the number of pulses whose peaks lay in each of the separate channels, was determined by counting the 10 channel swaths across the film. The use of a keyboard with 10 keys, each connected to a mechanical register, made it possible to read the films and sort the pulses at an average rate of about 2000 pulses an hour.

Determination of Foil Thickness

A thin-window, argon-filled ionization chamber and a Po alpha source were used to determine the air equivalent thickness of each target foil. The foil to be measured was interposed between the alpha source and the window of the ionization chamber and the pulse heights from the chamber noted. Upon withdrawal of the foil the alpha source was removed a distance equal to the air equivalent thickness of the foil in order to restore the pulse heights to their former level. In terms of the energy equivalent for 11.9-Mev deuterons the foils used in the present work had thicknesses of less than 50 kev.

III. (d,p) REACTIONS ON Be^9

Deuterons of 11.9 Mev were directed at a 0.43 mg/cm² free foil of beryllium metal,[12] and the reaction protons associated with the ground state and first excited state of Be^{10} were detected at 22 angles between 5° and 85°. Different absorber thicknesses were used in front of the crystal in each of three overlapping angular intervals. Absorbers were chosen of sufficient thickness to absorb completely the elastically scattered deuterons and to reduce the energy of the protons from the excited state group to about 5 or 6 Mev.

[12] The Be foil was generously sent to us several years ago by Dr. Hugh Bradner of the University of California. See H. Bradner, Rev. Sci. Instr. **19**, 662 (1948).

Figure 3 shows a number *versus* pulse height plot for a laboratory angle of 30°. After the absorber, the energies of the protons in the two groups shown are 11.7 and 6.3 Mev. The small pulse heights are due to gamma rays and are present to about the same extent with or without a target foil. More than half of the gamma-ray counts result from the high background in the experimental area when the cyclotron is accelerating deuterons. The rest originate in the collimator or the Faraday cup when the beam passes through the chamber. The large pulse heights not included in the peaks are due mostly to protons from the Lucite absorber, which are knocked into the crystal by neutrons from the competing $Be^9(d,n)B^{10}$ reaction.

Figure 4 shows the angular distributions in center-of-mass coordinates for the proton groups associated with the ground state and the 3.37-Mev excited state of Be^{10} along with theoretical curves calculated from Butler's expression with $l_n=1$ and $r_0=5.1\times10^{-13}$ cm. The vertical lines through the experimental points are standard deviations based on the number of counts at each angle. The discrepancies shown in Fig. 4 between the theoretical curves and the experimental points are typical of distributions chracterized by $l_n=1$. It is frequently the case, as has been noted by other workers,[13] that the agreement between theory and experiment is rather poor for $l_n=1$ distributions. Previously reported results have indicated that when the principal maximum occurs at angles lower than about 15° and the theoretical curve is constructed to have the same maximum value as the experimental peak, the best possible fit to the data becomes progressively poorer the lower the angle of the peak. The theoretical curves appear to be somewhat broader than the experimental distributions and are displaced toward smaller angles. The discrepancies between the experimental points and the theoretical curves in Fig. 4 are consistent with this trend.

A comparison of the distributions obtained from the $Be^9(d,p)Be^{10}$ reactions for different incident deuteron energies indicates that as the energy is increased the secondary maximum decreases in size relative to the primary and shifts toward smaller angles, eventually merging with the primary maximum. The work of El-Bedewi[2] at 7.7 Mev shows a well defined secondary maximum in the ground state distribution at about 75° to 80°. This peak is much less prominent in the present work, and in the distribution reported by Black[4] at 14.5 Mev it appears to have coalesced with the primary peak. Only a small secondary maximum seems to be present in the excited state distribution at 7.7 Mev, and it is not apparent at all in the present work or at 14.5 Mev. As the deuteron energy is increased the shape of the proton distribution becomes similar to that sug-

[13] See reference 3. See also the review article by R. Huby in the book edited by O. R. Frisch, *Progress in Nuclear Physics* (Pergamon Press Ltd., London, 1953), Vol. 3, Sec. 7.

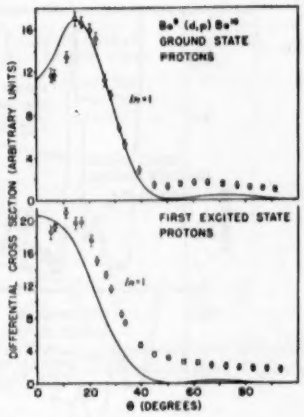

FIG. 4. The angular distributions of protons associated with the ground state and the first excited state of Be^{10} in the reaction $Be^9(d,p)Be^{10}$ for a deuteron energy of 11.9 Mev. Solid curves were calculated from Butler's theory with $r_0=5.1\times10^{-13}$ cm.

gested by Daitch and French,[14] in which the zero in Butler's curve is not present and the distribution decreases monotonically with angle, at least up to 90°.

IV. (d,p) REACTIONS ON N^{14}

A foil target containing nitrogen (99.6 percent N^{14}) was produced by vacuum evaporating a small quantity of a nitrogen-rich compound, and collecting the vapor on a thin, freshly prepared zapon film. The compound 1-cyano-guanidine ($C_2H_4N_4$), in the form of small white flakes was sublimed from a wolfram boat electrically heated to dull red in a vacuum of 10^{-5} mm Hg. The resulting target consisted of a 0.5 mg/cm² thickness of guanidine deposited on the zapon film backing (estimated thickness, 0.02 mg/cm²). Protons associated with the ground state and doublet first excited state (doublet separation about 30 kev) were counted at angles between 6° and 90° using absorbers sufficiently thick to completely stop elastically scattered deuterons and hydrogen nuclei from the target foil. Protons from the ground state carbon reaction $C^{12}(d,p)C^{13}$ are less energetic than protons associated with the N^{15} doublet level by about 600 kev. The carbon component of the target caused no difficulty except at low angles where, due to their great preponderance and the limited resolution of the detector, the pulses in the carbon group tended to spill over into the nitrogen peak and cause considerable uncertainty in the determination of the number of nitrogen pulses. Figure 5 shows pulse height spectra observed at laboratory angles of 6° and 45°.

The angular distributions of protons leading to the ground state and the first excited state of N^{15} are shown in Fig. 6. The vertical lines represent standard deviations based on the number of counts at each angle except for low angle points in the excited state distribution for which the uncertainties arising from the possible confusion with pulses from the carbon reaction are also included. The ground state proton group has a distri-

[14] P. B. Daitch and J. B. French, Phys. Rev. 87, 900 (1952).

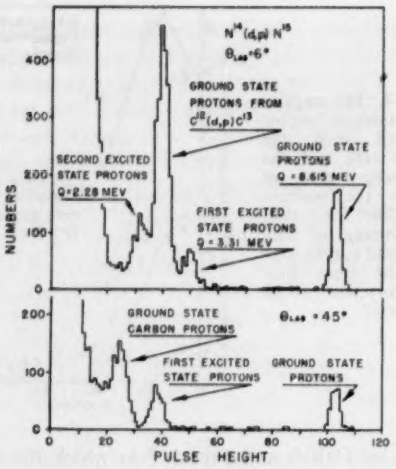

FIG. 5. Pulse height spectrum of protons from (d,p) reactions on N^{14} at laboratory angles of 6° and 45°.

bution characteristic of a momentum transfer $l_n=1$ in agreement with the work of Gibson and Thomas[5] at a deuteron energy of 8 Mev, and a reasonably good fit to the data is achieved using Butler's expression with $r_0=5.8\times10^{-13}$ cm. In the work at 8 Mev the distribution of the protons leaving N^{15} in its doublet first excited state showed no forward maximum. Hence, it has been inferred that the reaction takes place predominately by compound nucleus formation and that the levels have large spins. Since the present work shows a distinct maximum at low angles, it appears that the conclusion that the levels have large spins is probably not correct. In view of the large uncertainties in the low angle data, no definite statement can be made as to the spins of the levels or the momentum transfers involved. It seems possible, however, that bombarding with deuterons of higher energy might give rise to a distribution that is more typical of those from reactions which take place primarily by the stripping process.

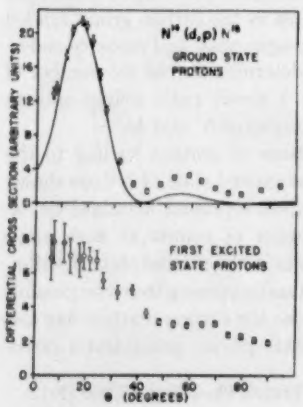

FIG. 6. The angular distribution of protons associated with the ground state and the first excited state of N^{15} in the reaction $N^{14}(d,p)N^{15}$ for a deuteron energy of 11.9 Mev. Solid curve was calculated from Butler's theory with $r_0=5.8\times10^{-13}$ cm.

V. (d,p) REACTIONS ON Zn^{68}

Targets were prepared by electrodepositing zinc metal, highly enriched in Zn^{68},[15] on thin metallic backings. Gold leaf and evaporated foils of copper were used as backing materials and both $Zn(CN)_2$ and $ZnSO_4$ were used as plating solutions. The proton spectrum was found to be the same for all of the targets, except that the copper backing gave a background approximately 20 times higher than the gold backing and a large contribution from carbon and nitrogen reactions occurred when the cyanide solution was used in plating, probably due to the presence of the AuCN which was formed.

The energies of the protons associated with the ground state and the second excited state of Zn^{69} were obtained by comparing their pulse heights with pulse heights due to protons of known energies from other reactions. Several different target materials were mounted in a foil holder whose position could be adjusted from outside the chamber. Pulse heights due to protons from reactions on Be^9, C^{12}, O^{16}, Al^{27}, and Zn^{68} were observed in succession and time exposures taken of the oscilloscope traces. Three sets of measurements were made at different detector angles and on different days. In each case photographs were taken of pulse heights due to protons from zinc targets and three or four other target materials. The unknown proton energies were obtained from curves of pulse height *versus* energy which were constructed using the pulses from protons of known energy. Q values for the reactions were calculated for each of the three energy determinations, and the resulting values averaged to give $Q=4.16\pm0.15$ Mev for the reaction leading to the ground state of Zn^{69} and $Q=3.39\pm0.15$ Mev for the second excited state. The Q value for the ground state reaction agrees within experimental accuracy with the value 4.39 ± 0.25 Mev which can be calculated from the measured masses[16,17] of Zn^{68} and Ga^{69} and Duffield and Langer's[18] values for the beta spectrum end point.

The spectrum of protons emitted by the target was observed at 23 angles between $7\frac{1}{2}°$ and 90°. Two different targets were used in the distribution measurements: a thin target (0.64 mg/cm² of Zn) for angles up to 60°, and a thick target (about 5 mg/cm² of Zn) for higher angles. Both targets were plated on 0.2 mg/cm² gold leaf from solutions of $ZnSO_4$. A Lucite absorber 1.7 mm thick was used in front of the detector at all angles.

Figure 7 shows, for 4 different angles, the pulse

[15] ZnO containing an isotopic abundance of 95.5 percent Zn^{68} was obtained on a loan basis from the Electromagnetically Enriched Isotopes Inventory of the Oak Ridge Laboratory of the Atomic Energy Commission by Professor R. D. Hill, to whom the author is indebted for making a quantity available for the present work.

[16] Collins, Nier, and Johnson, Phys. Rev. **86**, 408 (1952).

[17] B. G. Hogg and H. E. Duckworth, Phys. Rev. **92**, 848(A) (1953).

[18] R. B. Duffield and L. M. Langer, Phys. Rev. **89**, 854 (1953).

height distribution arising from protons which leave Zn^{69} in its ground state and excited states at 436 kev, 770 kev, and 1.6 Mev (denoted in the figure as Zn I, II, III, and IV, respectively). Protons in the peak Zn I have a laboratory energy of about 16 Mev at 7°. The low-angle spectrum illustrates the strong Z dependence of (d,p) reaction cross sections. The 0.2 mg/cm² of gold contributed only a few counts, while the 0.64 mg/cm² of Zn accounted for two large peaks. The highest peak, two and one-half times as high as the peaks from the Zn reactions, was caused mostly by a small carbon contaminant. The main source of the carbon was probably vacuum pump oil, and the contamination increased steadily while the beam was on. This possibly could have been avoided by more effectively baffling the pump or by using a liquid air trap in the pumping system. The pulse height distributions were corrected for the background due to the gold backing material which was found in an independent

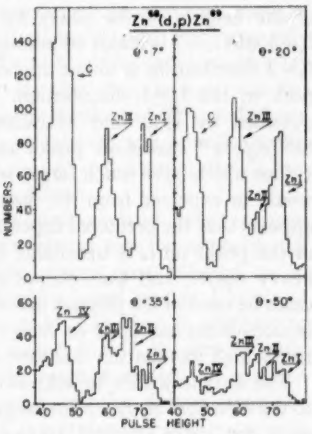

FIG. 7. Pulse height spectrum of protons from (d,p) reactions on Zn^{68} at laboratory angles of 7°, 20°, 35°, and 50°.

measurement. Protons from the gold accounted for less than 4 percent of the counts observed in the region of interest at any angle.

For the purpose of decomposing the number *versus* pulse height histograms into contributions from the individual groups (Zn I, II, and III), it was assumed that each of the groups gives rise to a normal "Gaussian" distribution of pulse heights whose root-mean-square width (standard deviation) is the same for each of the groups and is independent of angle. The value of the root-mean-square width was found from the reasonably well resolved individual peaks which are present in the low angle data by taking the second moments of the distributions and applying the parallel axis theorem. The separations of the centers of the assumed normal curves were taken as the weighted average values of the separations of the peaks in the histograms which were estimated at each angle. Using these values for the root-mean-square width and the separations of the centers, the amplitudes of the three assumed normal

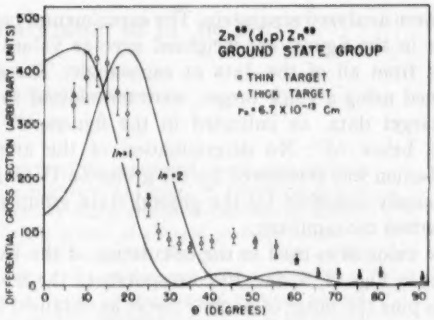

FIG. 8. The angular distribution of protons associated with the ground state of Zn^{69}. Solid curve was calculated from Butler's theory.

curves were calculated by fitting smooth curves to the number *versus* pulse height histograms by the method of averages.[19] A 24-channel range in pulse heights was used, and, in essence, the number of counts in each channel was equated to the sum of contributions from three normal distributions with unknown coefficients. At each angle the 24 linear algebraic equations so obtained were grouped into three sets and the equations in each set added to give three equations which were solved for the unknown coefficients (amplitudes of the component normal distributions).

Plots of the angular distributions of the proton groups leading to the ground state and to the 436-kev excited level of Zn^{69} are shown in Fig. 8 and Fig. 9, respectively. Figure 10 shows the distribution of the protons which leave the final nucleus with an excitation of 770 kev. The uncertainties drawn through the experimental points indicate the combined root-mean-square errors associated with the counting statistics and the calculation of the amplitudes of the assumed normal distributions from the pulse height histograms as determined by a detailed error analysis of the calculation. At least two runs were made at each angle below 60°, and the

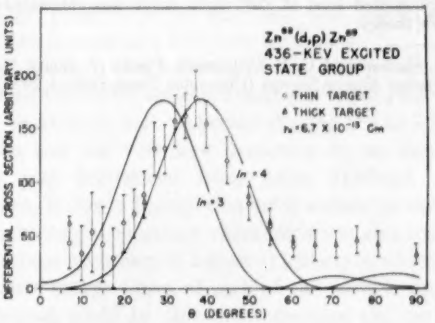

FIG. 9. The angular distribution of protons associated with the 436-kev excited level of Zn^{69}. Solid curve was calculated from Butler's theory.

[19] See, for example, J. B. Scarborough, *Numerical Mathematical Analysis* (The Johns Hopkins Press, Baltimore, 1950).

data were analyzed separately. The experimental points shown in the figures are weighted average values obtained from all of the data at each angle. The data obtained using a thick target, were normalized to the thin-target data, as indicated in the figures, at five points below 65°. No determination of the angular distribution was attempted for the group Zn IV since it was largely obscured by the ground state group from the carbon contaminant.

The value of r_0 used in the calculation of the Butler curves in Figs. 8, 9, and 10 corresponds to the nuclear radius plus the range of nuclear forces as obtained from fast neutron scattering experiments and was calculated from the general expression given by Gamow and Critchfield,[20] $r_0=(1.22A^{\frac{1}{3}}+1.7)\times10^{-13}$ cm. In agreement with the predictions mentioned earlier, the data shown in Figs. 8 and 9 are best fitted by theoretical curves with $l_n=1$ for the ground state group and $l_n=4$ for the 436-kev isomeric level. The momentum transfers obtained from an analysis of the proton distributions in terms of Butler's stripping theory are hence consistent with the level assignments inferred from shell theory and supported by the $M4$ character of the radiation from the 436-kev level, the allowed beta-decay of the ground state of Zn^{69}, and the measured spin of the ground state of Ga^{69}. The data shown in Fig. 10 are in reasonable agreement with a theoretical curve using $l_n=2$. The relatively large intensity of this group suggests that it is associated with a single particle level. A level assignment consistent with the shell model would require that the captured neutron go into the $d_{5/2}$ orbit in the next higher shell. Somewhat better fits to the experimental data for the excited state groups can be obtained by taking $r_0=7.1\times10^{-13}$ cm.

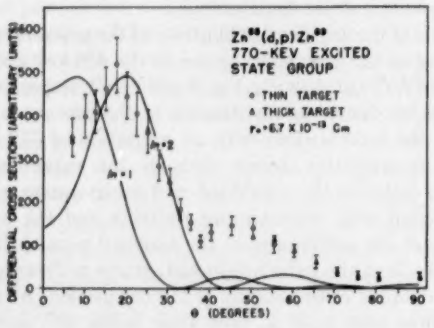

FIG. 10. The angular distribution of protons associated with the 770-kev excited level of Zn^{69}. Solid curve was calculated from Butler's theory.

A rather unexpected feature of these distributions is the relatively large intensities of the groups associated with high momentum transfers. The calculations of Butler have indicated that, other factors being equal, the magnitude of the peak in the angular distribution should decrease with increasing values of l_n by about an order of magnitude as l_n is increased by 2. Previously reported experimental results for a number of reactions involving target nuclei having mass numbers of 40 and lower[8] have, in general, shown this behavior. In the case of reactions on Zn^{68}, however, the observed ratio of the heights of the peaks for distributions having $l_n=4$ and $l_n=1$ is about 40 percent, and the peak in the $l_n=2$ distribution is about 25 percent higher than the peak in the $l_n=1$ distribution. Angular distributions obtained by Holt and Marsham[7] from the reaction $Sr^{88}(d,p)Sr^{89}$ also show peaks associated with high l_n values which have much larger relative intensities than would be expected from the theoretical calculations. It appears that the predicted dependence of the magnitude of the peaks on l_n is unreliable for reactions involving heavy nuclei, and that stripping theory can in some cases be used in the interpretation of the angular distributions from reactions on heavy nuclei in which relatively high momentum transfers are involved.

The author wishes to acknowledge his indebtedness to the members of the cyclotron group and the cyclotron shop for their cheerful cooperation and assistance. A debt of gratitude is due Professor W. K. Jentschke, who supervised this work, for his valuable advice and constant encouragement. The author is particularly grateful to Professor R. D. Hill for suggesting Zn^{68} as a suitable target nucleus and for his generous assistance and encouragement and to Professor G. F. Chew for helpful discussions of the theoretical aspects of the work.

[20] G. Gamow and C. L. Critchfield, *Theory of Atomic Nucleus and Nuclear Energy-Sources* (Clarendon Press, Oxford, 1950).

Charged Particles from the Bombardment of Li^7 by He^3

C. D. Moak, W. M. Good, and W. E. Kunz*
Oak Ridge National Laboratory, Oak Ridge, Tennessee
(Received July 23, 1954)

A $(Li^7)_2SO_4$ target was bombarded with He^{3++} ions at 720 kev, and the energies of the charged particles emitted were analyzed by means of a NaI spectrometer. The spectrum was found to consist in part of particles smoothly distributed in energy; and in part of relatively sharp groups of particles of defined energies. Evidence is presented that the five highest pulse height groups of charged particles consist of protons corresponding to defined energy states in Be^9. The observed proton energies are 10.51 ± 0.03, 8.9 ± 0.2, 8.3 ± 0.2, 7.6 ± 0.1, and 6.1 ± 0.10 Mev. In addition, group of particles were barely discernible at the lower half of the pulse height scale used for the protons. Although these groups of particles are not positively identified, it seems relatively certain that they are α-particles corresponding to Li^6 in its various energy states. A special attempt to identify groups of deuterons failed, indicating that for some reason the formation of Be^8 is discriminated against in this reaction.

INTRODUCTION

SOME time ago it was reported[1] that when Li^7 was bombarded by He^3 a pulse spectrum was observed in NaI which would correspond to particles, some of which were grouped and others of which were smoothly distributed in energy. Because of the very low counting rates, it was possible to say only that the spectrum was roughly consistent with the breakup of B^{10} into Be^9 and a proton, into Be^8 and a deuteron, and into the multibody breakups of two α's and a deuteron, and of two α's and a neutron plus a proton.

More recently with a multi-channel pulse analyzer available, it became feasible to seek to establish the identity of the particle groups just referred to in accordance with Be^8 having a broad level at 3 Mev and Be^9 having a narrow level at 2.43 Mev, in addition to the respective ground states. It will be seen in what follows that considerably more work will be required before definite conclusions can be drawn from the study to date. However, it seems reasonable to present, at this stage of the work, the body of evidence which indicates that each of the "relatively" sharp groups of particles arises from protons corresponding to associated states in Be^9.

EXPERIMENTAL APPARATUS AND PROCEDURE

As in previous studies with the He^3 beam, the spectrometer used to study the energy spectra of the reaction products consisted of a NaI crystal 2 mm thick coupled to a 5819 photomultiplier. A cut-away view of the essential features of this spectrometer and associated target arrangement is given in a previous paper.[2] The energy resolution of the spectrometer for 14.7-Mev protons was a little over 3 percent. Precision aluminum foils served to assist in spectrometer calibration and particle identification.

The Li^7 target consisted of $(Li^7)_2SO_4$ fused onto a tantalum backing. The Li^7 was of 99 percent purity with respect to Li^6. Spectral analysis showed that the $(Li^7)_2SO_4$ contained, in addition to sulfur and oxygen, only trace amounts of relatively high-Z elements. There was further assurance that the target was free from contamination and also that the beam contained no unwanted components, in the observation that when a $(Li^6)_2SO_4$ target, essentially identical with the $(Li^7)_2SO_4$ target, was bombarded with He^3 in an investigation of Be^8 there was no evidence of target contamination or of unwanted beam components.[3]

The experimental procedure was (a) to calibrate the crystal for pulse response *vs* energy for protons and deuterons, (b) to measure the pulse height spectrum and assign the particle identities on the basis of the expected energies, and (c) to check the particle assignment by measuring the energy loss of the various particles in their passage through aluminum absorbers. In order to obtain the proton and deuteron energy *vs* pulse height characteristic relation, there was mounted, together with the Li^7 target, a zirconium tritide target which contained, in addition, an appreciable amount of deuterium. The lithium and "zirconium" targets were so arranged that it was possible to quickly rotate from the Li^7+He^3 to the $H^2(He^3,p)He^4$ and $H^3(He^3,d)He^4$ reactions. These latter two reactions yield, respectively, 14.7-Mev protons and 9.99-Mev deuterons.

The absorber wheels shown in Fig. 1 of reference 2 were mounted with precision absorbers. These absorbers could be utilized, first, to permit slowing the 14.7-Mev protons and the 9.99-Mev deuterons by an amount which was determined from Aron, Hoffman, and Williams, Range *vs* Energy Charts[4] to obtain the respective pulse height *vs* energy characteristics; and second, to interpose absorbers of known thickness in which the respective energy losses of each of the particle groups in question could be obtained, assuming the particle identities were known. Figure 1 shows the pulse height *vs* energy characteristics for protons and deuterons

* Now at Naval Research Laboratory.
[1] Moak, Good, and Kunz, Oak Ridge National Laboratory Report ORNL-1496 (unpublished).
[2] C. D. Moak, Phys. Rev. **92**, 383 (1953).
[3] Kunz, Moak, and Good, Phys. Rev. **91**, 676 (1953).
[4] Aron, Hoffman, and Williams, Atomic Energy Commission Report AECU-663, 1951 (unpublished).

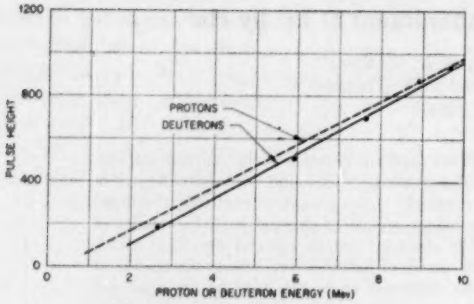

FIG. 1. Curves relating the NaI spectrometer pulse height to energy for protons and deuterons.

obtained from 14.7-Mev protons and 9.99-Mev deuterons in the manner just described.

Some three hours were required to run the entire Li^7+He^3 spectrum with 5 percent counting statistics, and consequently the possibility of instrumental drifts of the order of a few percent could not be ignored. However, such drifts could easily be kept negligible, if necessary, since with the high yields from the $H^2(He^3,p)He^4$, and $H^2(He^3,d)He^4$ reactions, a check on the calibration could be made in a matter of seconds. Likewise, in the data that will be given, the measurement of the shift in pulse height that accompanied the introduction of aluminum absorber was bracketed by a check on the calibration in the following way: The pulse height produced by the 9.99-Mev "calibration deuterons" was noted, the pulse height of a particular peak in question was then measured without absorber; after this the absorber was introduced and the new pulse height in question was redetermined followed by a recheck of the calibration with zero absorber. At one time a low-energy point on the deuteron pulse height *vs* energy characteristic was also rechecked and found to check well the earlier calibration characteristic. Finally, it should be noted that the high-energy proton group from Li^7+He^3 falling at 10.55-Mev constituted a proton calibration and this peak remained constant in pulse height for a fixed position of the 9.99-Mev calibration deuteron pulse height. The employment exclusively of the 9.99-Mev deuteron for instrumental checks obviated the changing of gain positions that would have been necessary had the 14.7-Mev proton been employed.

RESULTS AND CONCLUSIONS

In Fig. 2 is shown the pulse spectrum as it was obtained with a 0.1-mil absorber of nickel in order to identify the group at pulse height 340. Comparison of the pulse height of 340 with the corresponding pulse height at zero mils absorber showed the group in question to be α particles from the breakup of B^{10} into $Li^6+\alpha$. On the zero absorber spectrum there also appeared as just perceptible above the continuum, two other groups of particles in addition to the group just mentioned, presumably α particles associated with the excited states of Li^6. Lack of information on the pulse height *vs* energy characteristic of the crystal to α particles does not permit more to be said about the spectrum below pulse height 400.

Consider now the five highest energy groups in Fig. 2. The energy assignments will, as can be seen from Fig. 1, depend upon the identity of the particles. Let the groups be designated T_0, T_1, T_2, T_3, and T_4, respectively, from highest to lowest energy. Then group T_0 is identified with the breakup of B^{10} into a proton and Be^9 in its ground state by virtue of the fact that the measured energy of T_0, compared with the 14.7-Mev "calibration" proton, agrees well with the energy expected for the Be^9 ground state plus proton mode of breakup from mass values. In exactly analogous fashion T_2 is found to correspond to the state in Be^9 at 2.43-Mev.

The group of particles T_1 does not correspond to any well known state in Be^9 and hence is a logical choice for

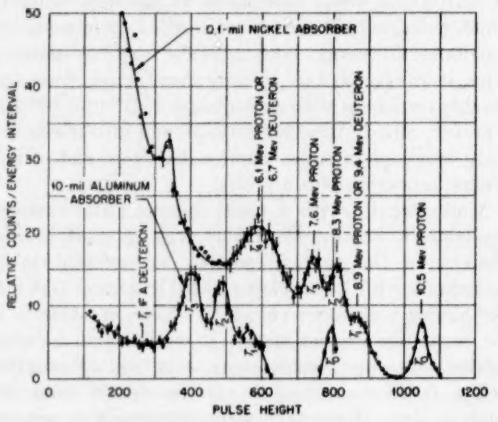

FIG. 2. Pulse spectrum produced in NaI by the reaction products from Li^7+He^3 for both a thick and a very thin absorber.

the deuteron corresponding to the breakup of B^{10} into Be^8 in its ground state and a deuteron. The other deuteron group corresponding to Be^8 at 3-Mev excitation would be expected to be broad in energy spread, and indeed group T_4 is just such a group. However, two irregularities occur, namely: (a) that while groups T_0 and T_2 are identified as the expected protons, and T_1 and T_4 may be the expected deuterons, T_3 is unaccounted for, and (b) that the measured energy interval for T_1 and T_4 is 2.7-Mev. This figure of 2.7-Mev in the laboratory system corresponds to 3.4-Mev in Be^8, and this latter figure is to be compared with 2.95-Mev from other experiments.[3,5–7] The statistical uncertainty in the present experiment is less than 10 percent and it seems unlikely that so large a discrepancy as that just indicated can exist.

[5] P. B. Treacy, Phil. Mag. 44, 326 (1953).
[6] R. Malm and D. R. Inglis, Phys. Rev. 92, 1326 (1953).
[7] C. C. Trail and C. H. Johnson, Phys. Rev. 95, 1363 (1954).

With a view to positively identifying groups T_1 and T_4, therefore, the corresponding portions of the spectrum were run, respectively, with 68-mg/cm² Al and 31.1-mg/cm² Al, and the shift in pulse height carefully noted. The two different values of absorber were chosen so as to optimize in each instance the distinction between deuterons and protons that was being sought. Figures 2 and 3 present the shift in pulse height of the particle groups in question, as produced by the 68-mg/cm² and 31.1-mg/cm² aluminum absorbers. In the instance of both groups T_1 and T_4, which were thought possibly to be deuterons, the groups lost energy in their respective absorbers as protons would. Hence, each of the five highest pulse height charged particle groups appears to consist of protons. Energy considerations show that it is not likely that these protons can arise from the breakup of B^9 subsequent to the decay of B^{10} into B^9 and a neutron, and, hence, must be associated with the alternative decay of B^{10} into Be^9 in various states of excitation and a proton. In Fig. 2 the proton

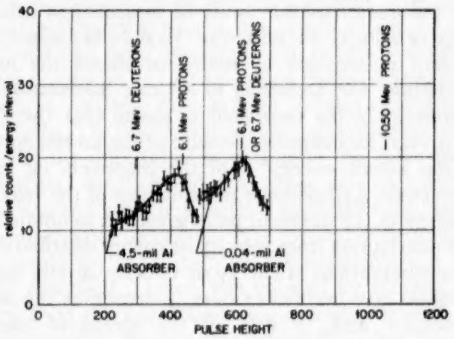

FIG. 3. Shift produced in the pulse height of the "broad peak" by a thick aluminum absorber.

energies are given, respectively, as 10.51, 8.9, 8.3, 7.6, and 6.1 Mev. These particular values were obtained from a single spectral determination in which special attention was given to instrumental stability. The energies obtained from four independent determinations showed a standard error in the determination of the energies of about 3 percent. The Be^9 energy level diagram, Fig. 4, summarizes the present experiment.

The existence of four excited states in Be^9 at excitations below 6 Mev is contradictory to careful experiments involving the reactions $B^{11}(d,\alpha)Be^9$ and $Be^9(p,p')Be^{9*}$.[8–11] The latter reaction, like $Li^7(He^3,p)Be^9$,

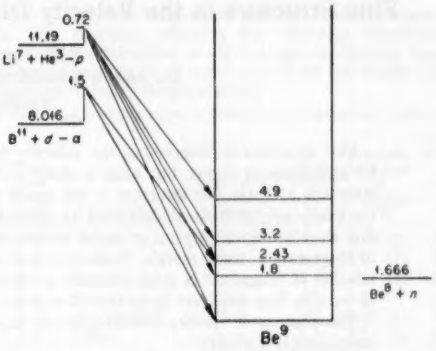

FIG. 4. Energy scheme of Be^9 suggested by the spectrum in Fig. 2.

involves the compound nucleus B^{10}. In spite of the fact that $Li^7(He^3,p)Be^9$ and $Be^9(p,p')Be^{9*}$ both involve B^{10}, the spectra of the B^{10} decay products differ, the first reaction from the second, not only in the absence of deuterons and the presence of more than two groups of protons but also in one other feature. The $Li^7(He^3,p)Be^9$ reaction is accompanied by an approximately equal amount of multi-body breakup such as two α's, a neutron and a proton, whereas, in the $Be^9(p,p')Be^{9*}$ reaction, the multi-body breakup seems of negligible proportions. It is interesting to note that in the neutron spectrum representing the reaction $Be^9(p,n)B^9$ as in the proton spectrum from the $Li^7(He^3,p)Be^9$ reaction, there is a conspicuous abundance of the multi-body process.[12]

In weighing the credibility of the results that the energy scheme for Be^9 is that given in Fig. 4, two other facts are worthy of note. As has already been reported[13] the proton spectrum from $Be^9(He^3,p)B^{11}$ is precisely that expected from knowledge of the well established states in B^{11}. This circumstance, accompanying as it does the fact that the same equipment has been employed for the $Li^7(He^3,p)Be^9$ and $Be^9(He^3,p)B^{11}$ studies, provides additional evidence that the groups observed in Li^7+He^3 are not spurious. Finally, it should be recalled that the yield with energy and the angular distribution of the Be^9 photoneutrons have suggested a state of Be^9 in the neighborhood of the neutron dissociation energy and perhaps other states of higher energies.[14–16]

[8] Van Patter, Sperduto, Huang, Strait, and Buechner, Phys. Rev. **81**, 233 (1951).
[9] Browne, Williamson, Craig, and Donahue, Phys. Rev. **83**, 180 (1951).
[10] K. E. Davis and E. M. Hafner, Phys. Rev. **73**, 1473 (1948).
[11] Cowie, Heydenburg, and Phillips, Phys. Rev. **87**, 304 (1952).
[12] Fay Ajzenberg and W. W. Buechner, Phys. Rev. **91**, 674 (1953).
[13] Moak, Good, and Kunz, Phys. Rev. **95**, 641 (1954).
[14] Russell, Sacks, Wattenberg, and Fields, Phys. Rev. **73**, 454 (1948).
[15] C. J. Mullin and E. Guth, Phys. Rev. **76**, 382 (1949).
[16] *Note added in proof.*—Dr. K. W. Allen, Nuclear Physics Laboratory, University of Liverpool (private communication), has obtained almost identical results from the bombardment of Li^7 with He^3.

Fine Structure in the Velocity Distributions of Slowed Fission Fragments*

R. B. LEACHMAN AND H. W. SCHMITT
Los Alamos Scientific Laboratory, Los Alamos, New Mexico

(Received August 13, 1954)

Fine structure is observed in the velocity distribution of U^{235} fission fragments that have been slowed by aluminum or nickel, but none is observed for unslowed fragments. Identification of this velocity fine structure with the fine structure in the fission mass yield confirms the influence of the 82-neutron shell in the fission act, as distinguished from its influence in post-fission neutron boil-off. The production of velocity fine structure by aluminum or nickel slowing is shown, by means of the measured range-velocity relation of fragments in these metals, to be the result of isobaric velocity bunching. The measured range-velocity relation of fragments in gold indicates no velocity bunching and therefore is consistent with the absence of velocity fine structure in measured velocity distributions of U^{235} fragments slowed in gold or platinum.

The absence of velocity fine structure in the velocity distribution of U^{233} and Pu^{239} fragments slowed by aluminum is discussed.

I. INTRODUCTION

FINE structure in the mass yield of the heavy-fragment group from U^{235} fission has been observed by Thode *et al.*[1-3] with mass spectograph measurements and by Pappas[4] by radiochemical measurements as an increase in the abundance of mass ~134 over the smooth mass yield curve. Mass spectograph measurement of the mass yield of the light-fragment group by Glendenin *et al.*[5] shows similar fine structure at the complementary mass ~100. The similarity of the fine structure peaks indicates the nuclear shell influence on the fission act itself, but the possibility of an additional influence on the post-fission neutron boil-off from the heavy-fragment group cannot be excluded from these data. The position of these fine structures at masses ~101 and ~135 in the primary-fragment (before neutron boil-off) yield indicates that the closed 82-neutron shell influences the fission act. It can be shown that, for the unstable fragments before decay, the 82-neutron shell is closed at a mass of approximately 135.

In the present work, the influence exerted by shell effects on the energy and velocity distributions of the fragments is of interest. The fission process is regarded initially as the separation of two fragments of equal and opposite momentum. The subsequent neutron emission from the moving fragments in various numbers and directions and with various energies disperses any fine structure initially existing in the distribution of fragment mass, velocity, or energy. The observed mass distribution is dispersed by the variation in the number of emitted neutrons. Further, it can be shown that the distribution in the fragment recoil momentum, resulting from neutron emission, causes a relatively greater spread in the velocity or energy distribution.

It is informative to neglect these dispersions and also any dispersion arising from the measurement and consider the quantities that must be measured to exhibit energy or velocity fine structure. To show fine structure, sufficient information is needed to obtain the mass distribution, for, according to existing information, it is primarily in the mass split of fission that the shell effects exert an influence. Because of the known spread of total kinetic energy[6-10] of the fragments for each fission mode, a coincidence measurement of the velocity or energy of the fragment pairs is needed to obtain the mass distribution from velocity or energy distributions. Thus, observations of energy or velocity of only single fragments give insufficient data to determine the mass distribution and, in view of the spread of masses associated with each fragment velocity, are not expected to follow the mass distribution closely enough to show fine structure. The lack of any fine structure in the good-resolution measurements[11] of the velocities of single fragments from U^{235} is in agreement with this expectation.

Several coincidence measurements[6-10] of fission fragment energies have been made by ionization chambers. Even though sufficient information is obtained to determine the mass distribution, no evidence of fine structure is observed in any of these measurements. A relatively large dispersion, which is presumably imposed by the statistics of the ionization process, was later shown[12] to exist in these energy measurements. This dispersion can be shown to be sufficient to eliminate any fine structure in these coincidence measurements of energy.

* This document is based on work performed under the auspices of the U. S. Atomic Energy Commission.

[1] H. G. Thode and R. L. Graham, Can. J. Research **A25**, 1 (1947).

[2] Macnamara, Collins, and Thode, Phys. Rev. **78**, 129 (1950).

[3] Wiles, Smith, Horsley, and Thode, Can. J. Phys. **31**, 419 (1953).

[4] A. C. Pappas, Massachusetts Institute of Technology, Laboratory for Nuclear Science Technical Report No. 63, 1953 (unpublished).

[5] Glendenin, Steinberg, Inghram, and Hess, Phys. Rev. **84**, 860 (1951).

[6] W. Jentschke and F. Prankl, Z. Physik **119**, 696 (1942).

[7] W. Jentschke, Z. Physik **120**, 165 (1943).

[8] Flammersfeld, Jensen, and Gentner, Z. Physik **120**, 450 (1943).

[9] M. Deutsch and M. Ramsey, U. S. Atomic Energy Commission Report MDDC-945, 1945 (unpublished).

[10] D. C. Brunton and G. C. Hanna, Can. J. Research **A28**, 190 (1950).

[11] R. B. Leachman, Phys. Rev. **87**, 444 (1952).

[12] R. B. Leachman, Phys. Rev. **83**, 17 (1951).

In this work it will be shown that the greater resolution of measurement afforded by observations of velocities by a time-of-flight method allows observation of the fine structure in the velocity distribution of U^{235} fragments, provided that the velocities of the fragments are decreased in such a way as to decrease the velocity spread associated with each fragment isobar. This results in an approach to the condition in which each fragment mass has associated with it a unique velocity. When such a condition is approached, the resulting velocity distribution follows the structure of the mass yield curve.

Regardless of this isobaric velocity (and energy) bunching, however, ionization-chamber measurements of slowed-fragment energies do not give any indication of fine structure.[13] Again, it can be shown that the large dispersion which apparently is inherent in ionization measurements prevents the observation of fine structure.

II. EQUIPMENT

In the present measurements fragments were slowed through thin metal foils on one side of which the fissile material had been deposited. The residual velocity of these fragments was measured, as shown schematically in Fig. 1, by their time of flight through an evacuated drift tube. The drift length for each absorber was chosen so that the drift times were roughly the same for all absorbers. The fragment drift times were recorded and the data analyzed by a method essentially the same as that previously described.[11] The method of determining the resolution of the velocity measurements was similarly described. Fission was induced by thermal neutrons from the Los Alamos homogeneous reactor. The background in the data was caused by pulses from the detector nearer the source foil followed by chance pulses from the remote detector. This background was measured with Po^{210} alpha sources substituted for the fissile foil in the beam from the reactor.

In the present efforts to observe fine structure in the velocity distribution of fragments it was important to maintain good velocity resolution both in measurement and in the slowing process. For the latter, particular attention was given to the uniformity of the slowing

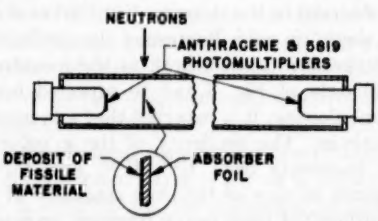

FIG. 1. Schematic diagram of the apparatus used to detect the time of flight of slowed fission fragments. Fragments were slowed by the metal backing of the fissile material. The longest of the drift lengths used was 199 cm and the shortest was 125 cm.

[13] H. W. Schmitt, dissertation, University of Texas, 1954 (unpublished).

TABLE I. Characteristics of the foils used to slow fission fragments. The numbers following the thickness nonuniformities represent (1) measurement of the foil used for slowing fragments and (2) measurement of an equal area of the foil neighboring the area used for velocity measurements.

Foil material	Thickness (mg/cm²)	Foil type	Method of U or Pu deposition	Foil diameter (in.)	Standard deviation of thickness (%)	Standard deviation of velocity (10^8 cm/sec)
Al	1.1	rolled	painted	1.5	0.93 (2)	0.023
Al	1.8	rolled	painted	1.5	2.0 (2)	0.060
Ni	1.1	plated	painted	1.5	2.7 (2)	0.050
Ni	2.6	plated	painted	1.5	3.9[a]	0.123
Au	5.15	evaporated	painted	1.0	0.90 (1)	0.042
Pt	5.1	rolled	evaporated	1.5	2.5 (2)	0.117

[a] One 1.24-mg/cm² foil and one 1.32-mg/cm² foil; uniformities measured by methods (1) and (2), respectively.

foils. Both thickness and uniformity were measured by means of a specially designed beta-ray thickness gauge. This gauge consisted of a 1.8-mm collimated beam of beta particles from a C^{14} source and a Geiger tube. Standard absorbers of the same element to be measured were used to calibrate the absorption of the beam and this calibration was combined with the beam attenuation at various positions on the unknown foil to determine uniformity. Tabulated in Table I are the characteristics of the foils used and the uniformity of these foils. The method for obtaining the velocity dispersion resulting from foil nonuniformity is explained in Sec. IV.

III. ISOBARIC VELOCITY BUNCHING

Velocity bunching occurs for a given fragment mass in slowing materials of which the absorption characteristics are such that the faster fragments of that mass are slowed more than the slower fragments. In this manner the spread of velocities associated with each fragment isobar will be decreased as the fragments are slowed. In view of the complexities in the velocity loss process of fission fragments in matter, we shall consider the loss expressed simply by the somewhat arbitrary expression,

$$dv/dx = -Av^n, \tag{1}$$

where, for each absorber, A and n are considered to be functions of only the fragment mass, the velocity v is in (10^8) cm/sec, and the thickness x is in mg/cm². It can be seen that isobaric velocity bunching occurs only when $n>0$.

Determinations[14–18] of the range-velocity relation needed for the evaluation of A and n in Eq. (1) have been made for several slowing elements. Those of Demers[18] are for slowing in photographic emulsion

[14] Bøggild, Brostrøm, and Lauritsen, Kgl. Danske Videnskab. Selskab, Mat. fys. Medd 18, No. 4 (1940).
[15] R. Sherr and R. Peterson, Rev. Sci. Instr. 18, 567 (1947).
[16] Bøggild, Arrøe, and Sigurgeirsson, Phys. Rev. 71, 281 (1947).
[17] N. O. Lassen, Kgl. Danske Videnskab. Selskab, Mat. fys. Medd. 25, No. 11 (1949).
[18] P. Demers, Can. J. Phys. 31, 78 (1953).

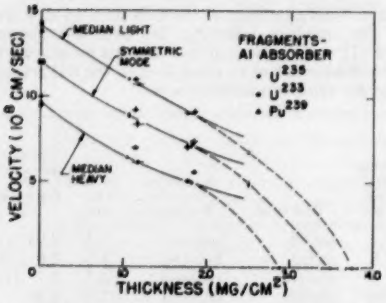

FIG. 2. Range-velocity data of fission fragments in aluminum. The velocities of unslowed fragments from U^{233} and Pu^{239} fission are from reference 11 and the end-point ranges are obtained from references 19 and 20. Solid curves are fits of the equation $dv/dx = -Av^n$ to the unslowed, 1.1-mg/cm^2, and 1.8-mg/cm^2 datum points of U^{235} fragments. The dashed curve represents experimental results. When no uncertainties are indicated they are smaller than the datum point.

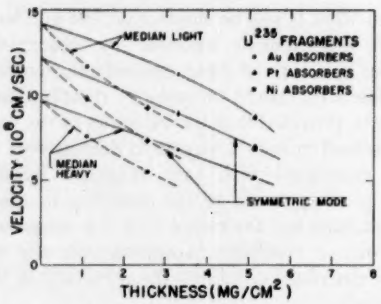

FIG. 3. Range-velocity data of fission fragments in nickel, gold, and platinum. A 3.3-mg/cm^2 gold foil was used in addition to the foils described in the text. Curves are fits of the equation $dv/dx = -Av^n$ to the data of nickel and gold. When no uncertainties are indicated they are smaller than the datum point.

and those of Sherr and Peterson[15] are known to be inaccurate near the beginning of the fragment range. Except for the end of the fragment range, which is not of importance in the present considerations, the data of Lassen are best fitted with a negative n for light fragments in all the slowing gases used; for heavy fragments in hydrogen and deuterium n is positive and for heavy fragments in argon n is zero. The data of Bøggild *et al.*[14,16] are consistent with the data of Lassen. From this limited information it appears that heavy fragments slowed in materials of low nuclear charge will undergo velocity bunching.

IV. VELOCITY LOSSES OF FRAGMENTS

In Figs. 2 and 3 are plotted the range-velocity data obtained from the present velocity measurements. These measurements are described in greater detail in the next section. Because of the uncertainties associated with any correlation of fragment velocity with fragment mass, the velocity distributions were used in this section only to obtain the median velocities of the heavy- and light-fragment groups and, with less accuracy, the velocity of the least probable yield, which corresponds to the symmetrical fission mode. For each of the mass groups and for each absorber, three range-velocity datum points are used in Eq. (1) to solve for A and n. The values of n are given in Table II.

TABLE II. The exponent n from range-velocity data of fission fragments. Data of Figs. 2 and 3 are fitted by the relation $dv/dx = -Av^n$. Uncertainties in the symmetrical fission data make the symmetrical fission results of n relatively uncertain. The n value for light fragments of Pu^{239} is similarly uncertain.

Fission source	Absorber	n for median heavy fragment	n for fragments from symmetrical fission	n for median light fragment
U^{235}	Al	1.3	1.2	0.6
U^{233}	Al	1.4	1.4	0.3
Pu^{239}	Al	0.9	−0.4	−0.4
U^{235}	Ni	0.9	1.0	1.4
U^{235}	Au	−0.1	−0.3	−1.7

The velocity dispersion resulting from the absorber nonuniformities is determined from these range-velocity relations and the magnitude of the foil nonuniformities. Equation (1) with the appropriate A and n values is used with the absorber nonuniformities of Table I to obtain the velocity dispersions listed in Table I.

It is to be emphasized that Eq. (1) is not necessarily expected to be a true representation of the actual range-velocity relation. The inadequacy of Eq. (1) in describing the range-velocity relation near the end of the fragment range is seen in Fig. 2, where points corresponding to a 2.5-mg/cm^2 aluminum absorber and to the end points of the fragment ranges[19,20] have been included. However, over the absorber thicknesses used in the velocity measurements to be discussed, Eq. (1) is an adequate approximation for the study of velocity bunching and velocity fine structure.

From the positive values of n in Table II velocity bunching of U^{233} and U^{235} fragments in aluminum, and of U^{235} fragments in nickel, is anticipated. Similarly, velocity bunching of the heavy Pu^{239} fragments in aluminum is anticipated. In contrast, the negative value of n for U^{235} fragments in gold implies a velocity expansion for fragment isobars rather than velocity bunching. On this basis, no fine structure is expected to be observed in the velocity distribution of U^{235} fragments slowed in gold. Because of the similarity of gold and platinum in respect both to the measured range-velocity data of Fig. 3 and to expected behavior in fragment slowing, it is expected that n is negative also for platinum. The similarity of the n values for the heavy fragments from U^{233}, U^{235}, and Pu^{239} is not unexpected in view of the close similarity of the mass distributions[21] of these heavy-fragment groups.

[19] F. Suzor, Ann. phys. 4, 269 (1949).
[20] Finkle, Hoagland, Katcoff, and Sugarman, *Radiochemical Studies: The Fission Products* (McGraw-Hill Book Company, Inc., New York, 1951), Paper No. 46, National Nuclear Energy Series, Plutonium Project Record, Vol. 9, Div. IV.
[21] See reference 19; appendix B.

It is noted in Table II that the decrease in the heavy-fragment value of n with the nuclear charge of the slowing material is consistent with the velocity data of Lassen.[17]

To illustrate the effect of isobaric velocity bunching we now calculate the velocity loss of each U^{235} fragment slowed by two different aluminum thicknesses. These calculations require the use of Eq. (1), where A and n values as functions of fragment mass are needed. For simplicity, the A and n values are assumed to be linear functions of the primary mass M of each fragment group. This yields $n=2.29(10^{-2})M-1.55$ and $A=-1.71(10^{-2})M+2.23$ for the light fragment group and $n=4.26(10^{-3})M+0.647$ and $A=1.07(10^{-3})M+0.080$ for the heavy fragment group.

These approximations of A and n as functions of mass are used in Fig. 4 with Eq. (1) and the probability $P(v,M)$ of occurrence as a function of mass and unslowed velocity. These latter data are obtained from a transformation we have made of the U^{235} data of Brunton and Hanna,[10] which give probability as a function of light- and heavy-fragment energies. However, before this transformation was made, 6.7 Mev was added to the heavy-fragment energies and 5.7 Mev to the light-fragment energies to bring the resulting velocities into agreement with measured unslowed velocities. It is to be noted that the transformed data of Fig. 4 do not indicate a preference for the primary masses ~101 and ~135, just as the energy data from which these contours were obtained did not show this preference. On the basis of the discussion of Sec. I, it must be assumed that the resolution of these original energy data was inadequate to resolve the fine structure which is known to exist. Similarly, the dispersion in the energy data is believed to have led to an increase in the velocity spread beyond the actual spread for each fragment isobar.

Velocity bunching is seen in Fig. 4, especially in the heavy-fragment group, as a contraction of the probability contours with increasing absorber thickness. Even the illustrated spread of isobaric velocities of the preferred mass ~135 decreases sufficiently to resolve the velocities of this mass, for example, from the velocities of the most probable mass ~140. In addition to the effect of velocity bunching, the increasing inclination of the light-fragment contours with absorber thickness aids in resolving the velocities of the complementary light-fragment masses. The observation, however, of the preferred mass ~101 as a velocity fine structure is difficult for the following reasons: the smaller n value for light fragments results in less velocity bunching in the light-fragment group and, further, the resolution of the velocity measurements is seen in the next section to be poorer for light fragments than for heavy fragments.

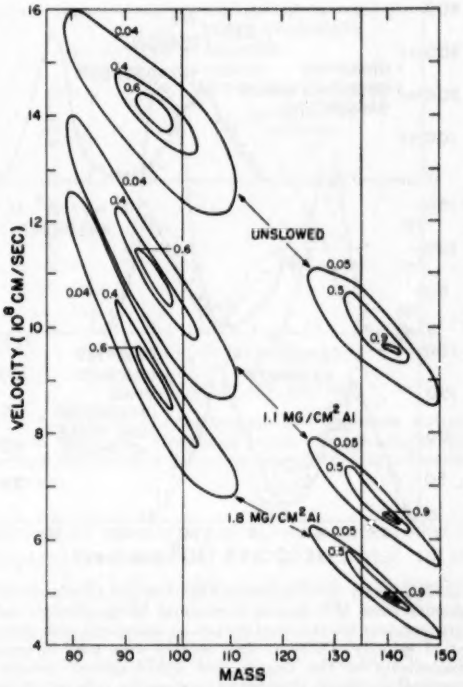

FIG. 4. Illustration of the contraction of mass-velocity probability contours for the slowing of U^{235} fragments by aluminum. The position of the known high yields at primary masses 101 and 135 are indicated by vertical lines. The probability contours of the unslowed fragments are obtained from a transformation of the data of reference 10 with the two groups normalized so that the integrated probability $\int\int P(v,M)dvdM$ for each group is the same. Velocity losses were calculated from the equation $dv/dx=-Av^n$, where A and n are given in Sec. IV of the text. The maximum $P(v,M)$ for each of the three light-fragment distributions are equal. Similarly, the maximum $P(v,M)$ for each of the three heavy-fragment distributions are equal.

V. VELOCITY DISTRIBUTIONS OF SLOWED FRAGMENTS

(a) U^{233}, U^{235}, and Pu^{239} Fragments; Al Absorbers

The velocity distributions of U^{235} fragments slowed by the aluminum thicknesses used in the calculations of the previous section were measured. They are shown in Fig. 5 in comparison with the velocity distribution of these fragments before being slowed. The latter measurement is a repeat of a previous measurement[11] and agrees with it within statistics. The expected fine structure in the heavy-fragment (low-velocity) group appears as a step on the high side of the slowed heavy-fragment distributions. Although smooth curves are drawn for the light-fragment (high-velocity) group, small but inconclusive indications of fine structure exist in the datum points on the low side of the slowed light-fragment distributions. As seen in Fig. 5, the decrease in velocity resolution with increasing velocity makes the observation of light-fragment fine structure more difficult than that of heavy-fragment fine structure.

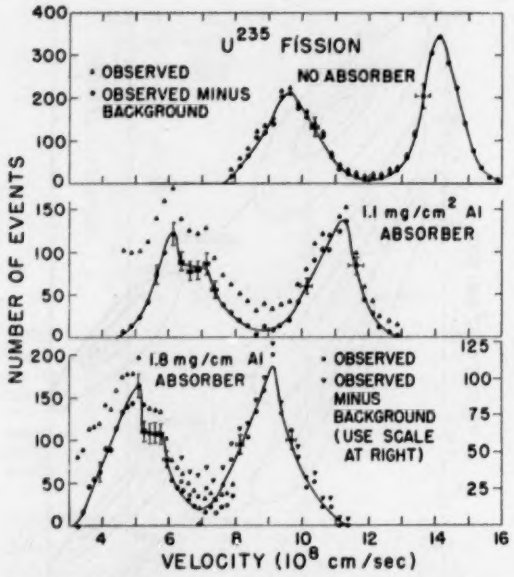

FIG. 5. Velocity distributions of unslowed and aluminum-slowed fragments from U^{235} fission. Horizontal wings through datum points represent the standard deviations associated with measurement of velocity. Different drift lengths were used in separate measurements of the heavy- and light-fragment groups for 1.8-mg/cm² aluminum absorber to improve the velocity resolution of the light fragment group.

Calculations, the results of which are shown in Fig. 4, predict that the fine structure in the velocity distribution should become more pronounced with increasing absorber thickness. However, no growth in the observed fine structure is noted in Fig. 5. The expected growth is presumably canceled by the greater velocity dispersion associated with the thicker absorber relative to the thinner absorber; the velocity dispersion for the 1.8-mg/cm² aluminum listed in Table I is appreciable compared with the velocity width of fine structure while that for the 1.1-mg/cm² aluminum absorber is small.

Mass fine structure, even after dispersion by the variation in the number of emitted neutrons, is about two mass numbers wide and so appears as a sharp spike on the mass distribution. Because of the larger dispersions associated with the velocity measurement of fine structure, on the other hand, the width of the velocity fine structure shown in Fig. 5 is appreciable compared with the width of the distribution. These dispersions in the velocity fine structure arise from measurement, from slowing, and from recoil momentum in neutron emission. It is doubtful if such a low-resolution detection of velocity fine structure would be seen if it occurs very near the peak of a velocity distribution. Accordingly, the velocity fine structure of U^{235} fragments is observed only because it occurs on the side of the velocity distribution.

Mass yield measurements indicate that the primary mass 135 occurs slightly nearer the center of the mass peak for U^{233} fission than for U^{235} fission[21,22] and still nearer the center for Pu^{239} fission.[21,23] As a consequence, the apparent lack of fine structure in the heavy-fragment velocity groups of U^{233} and Pu^{239} fragments shown in Fig. 6 may be the result of a relatively low-resolution detection of fine structure near the peak of the general velocity distribution. Since the position of the mass 135 is off the peak of the U^{233} mass distribution almost to the same extent as for U^{235} fission, we believe any fine structure in U^{233} fission that is comparable in magnitude to that of U^{235} fission would be observed in our velocity data. On this basis, the present results are in accord with those of Fleming *et al.*,[22] which indicate a smooth heavy-fragment mass yield from U^{233} fission. They are not, however, in accord with the results of Steinberg *et al.*,[24] which indicate mass fine structure in the light-fragment group. The failure of the velocity distribution to show the heavy-fragment fine structure[23] in the mass yield of Pu^{239} fission is attributed to the smaller magnitude of the fine structure compared to that of U^{235} and to its position near the peak of the general distribution.

These U^{233} and Pu^{239} data were taken under the same

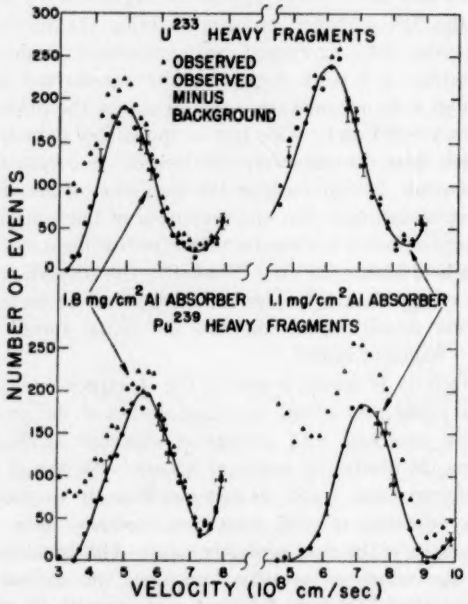

FIG. 6. Velocity distributions of U^{233} and Pu^{239} fragments slowed by aluminum. Horizontal wings through datum points represent the standard deviations associated with measurement of velocity.

[21] Fleming, Tomlinson, and Thode, Can. J. Phys. **32**, 522 (1954). The authors are indebted to Professor R. H. Tomlinson for information on these results and those of reference 23 in advance of publication and for suggesting the present measurements with U^{233} fragments.

[22] Fleming, Wanless, and Tomlinson, 1954 (private communication).

[24] Steinberg, Glendenin, Inghram, and Hayden, Phys. Rev. **95**, 867 (1954).

conditions of velocity bunching as the U^{235} data. With our method of measurement, fine structure is difficult to observe in the light-fragment distribution and so in these and the following data only the heavy-fragment data are included.

The possibility that velocity fine structure is the result of a discontinuity in the stopping power as a function of mass can be excluded by comparison of the velocity distributions of slowed fragments of U^{233} and U^{235} fission. The close similarity of these heavy fragments in mass, velocity, and nuclear charge results in essentially the same velocity loss characteristics for both. Thus, since the velocity distributions of slowed fragments from U^{233} fission are smooth and those of slowed fragments from U^{235} fission contain fine structure, the appearance of the velocity fine structure cannot be explained on the basis of a discontinuity in stopping power.

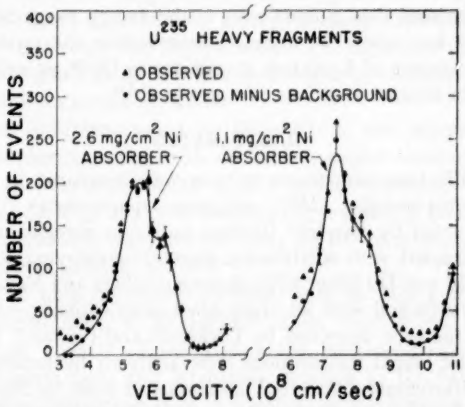

FIG. 7. Velocity distributions of U^{235} fragments slowed by nickel. Horizontal wings through datum points represent the standard deviations associated with measurement of velocity.

(b) U^{235} Fragments; Ni, Au, and Pt Absorbers

Slowed-fragment velocity distributions obtained when U^{235} fragments were slowed by nickel absorbers are similar to those obtained when U^{235} fragments were slowed by aluminum absorbers. These data of the heavy-fragment group for two nickel thicknesses are shown in Fig. 7. Although smaller than in the case of aluminum absorption, the velocity fine structures in these nickel data, when considered together, are well established. Indeed, fine structure is expected on the basis of the positive n values in Table II. The smaller

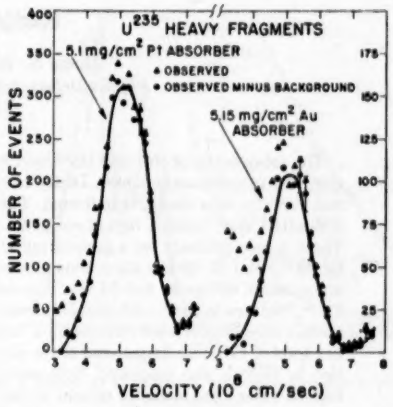

FIG. 8. Velocity distributions of U^{235} fragments slowed by platinum and gold. Horizontal wings through datum points represent the standard deviations associated with measurement of velocity.

extent of the velocity fine structure in these nickel data compared to aluminum data is attributed to three factors: For both nickel thicknesses, the smaller n values of Table II lead to less velocity bunching than for equivalent slowing by aluminum. For both nickel thicknesses, but especially in the case of the thicker absorber, the velocity dispersion from foil nonuniformity as listed in Table I is appreciable compared with the width of the velocity fine structure. Finally, the thinner nickel absorber is not thick enough to produce adequate velocity bunching.

In order to facilitate comparison of velocity data, foils of gold and platinum were selected to have similar stopping powers and somewhat smaller velocity dispersions compared to the thicker aluminum and nickel foils. As seen in Table I, the gold and aluminum foils are approximately equivalent in these respects, as are the platinum and nickel absorbers. The measured velocity distributions of heavy fragments from U^{235} fission slowed in these gold and platinum foils are shown in Fig. 8. The lack of fine structure in these velocity distributions is consistent with the negative n values for gold and platinum.

VI. ACKNOWLEDGMENTS

The authors are indebted to Miss E. Pierce for reading much of the velocity data and to Mr. W. D. Schafer for construction of the thickness gauge and for measurements with it.

Radiations from Ho^{164}†*

HUGH N. BROWN‡ AND ROBERT A. BECKER
Physics Department, University of Illinois, Urbana, Illinois
(Received May 3, 1954)

The decay modes of 36.7-min Ho^{164} have been studied with a magnetic spectrometer, scintillation spectrometer, and proportional counter. Decay to the two even-even daughters, Dy^{164} by orbital electron capture, and Er^{164} by beta decay, is indicated. The beta spectrum appears to be complex, with maximum energy 0.99±0.03 Mev. Gamma rays of energy 90.5, 72.8, and 37.3 kev, together with x-rays at 45.7 kev, are found. There is also evidence for a gamma ray at approximately 46 kev. Photon-photon coincidences are found for 46–73 and 37–46 kev approximate energies. Photon-beta coincidences are found to involve photons of approximate energy 91 and 50 kev. The data are interpreted in terms of first excited levels at 72.8 kev in Dy^{164}, 90.5 kev in Er^{164}, with probably a second level in Dy^{164} at 110 kev. Delayed photon-beta and photon-photon coincidences were found with a half-life of 1.4×10^{-9} sec. The former are associated with the 90.5-kev level of Er^{164}; the assignment of the photon-photon coincidences is uncertain. A possible isomeric transition in Ho^{164} is also suggested. Spin and parity assignments, on the basis of conversion coefficients and $\log(ft)$ value , are made for certain of the levels.

I. INTRODUCTION

HALF-LIVES for the beta decay of Ho^{164} of 47, 38.6, 41.5, and 35 and 34.0 minutes have been reported, respectively, by Pool and Quill,[1] Wäffler and Hirzel,[2] Wäffler,[3] and Wilkinson and Hicks.[4,5] Wilkinson and Hicks[5] reported a negative beta particle of 0.95-Mev maximum energy. The Al absorption curve indicated a simple spectrum. It was stated by the latter workers that if photons were present there would be fewer than 0.05 photon per beta particle. Moreover, no conversion electrons were found in their work.

The present investigation was undertaken because of several factors. At the present time, rare earth samples of a fairly high degree of purity are available in both the oxide form and the metal. Also, the activity can be produced readily in a rather pure state by means of a gamma-neutron reaction on the 100-percent isotope Ho^{165}. These considerations gave promise that the study of the Ho^{164} radiations might be a fruitful one to carry out by means of the probe technique[6] employed in this laboratory with the 22-Mev betatron. Further, it was expected that the decay might be more complicated than had been indicated by the work of previous observers, and that two even-even daughter nuclei might be involved. Previous work in this laboratory on the Ta^{180} decay scheme[7] and the discussion of even-even nuclei in general by Scharff-Goldhaber[8] suggested that gamma rays in the energy range 50 to 100 kev might be found, together with the possible occurrence of K-capture transitions to Dy^{164}, as well as beta minus transitions to states in Er^{164}.

II. APPARATUS

Electron momentum spectra were measured in the double-focusing 255° magnetic spectrometer constructed by Bendel.[9] Gamma radiation energies were measured with scintillation counters employing RCA 5819 and Du Mont 6292 photomultipliers and NaI(Tl) crystals and with an argon-filled proportional counter of the type described by Cockcroft and Curran.[10] The pulse height distributions were analyzed by means of a 10-channel differential discriminator built by Shore[11] and a single-channel analyzer similar to that described by Frankel.[12] A conventional coincidence circuit with a resolving time of 0.25 μsec and having a Rossi type crystal diode mixer was utilized. A fast coincidence circuit was also built for delayed coincidence measurements. The resolving time was $2\tau\simeq5\times10^{-9}$ sec. Again, a Rossi type mixer with 1N56 diodes was employed. The detectors were trans-stilbene crystals employed in combination with RCA 6199 phototubes. Hewlett-Packard distributed amplifiers and RG-62/U delay lines were used.

III. DATA

The half-life of Ho^{164} was determined to be 36.7±0.5 min from measurements of the particles by means of an end-window Geiger counter. This agrees well with

† This work was supported in part by the U. S. Atomic Energy Commission and the U. S. Office of Naval Research. The former is to be thanked for providing Sn^{113}, Cs^{137}, and Hg^{203}, the radiations from which were used to calibrate various pieces of equipment. In particular, thanks are due Professor F. H. Spedding and the Ames Laboratory of the U. S. Atomic Energy Commission for kindly providing pure samples of metallic holmium and holmium oxide, without which this work could not have been done.

* Part of the doctoral thesis of Hugh Needham Brown.

‡ National Science Foundation predoctoral fellow. Now on duty with the United States Armed Forces.

[1] M. L. Pool and L. L. Quill, Phys. Rev. **53**, 437 (1938).
[2] H. Wäffler and O. Hirzel, Helv. Phys. Acta **21**, 200 (1948).
[3] H. Wäffler, Helv. Phys. Acta **23**, 239 (1950).
[4] G. Wilkinson and H. G. Hicks, Phys. Rev. **74**, 1733 (1948).
[5] G. Wilkinson and H. G. Hicks, Phys. Rev. **79**, 815 (1950).
[6] R. A. Becker, Rev. Sci. Instr. **22**, 773 (1951).
[7] Brown, Bendel, Shore, and Becker, Phys. Rev. **84**, 292 (1951).
[8] G. Scharff-Goldhaber, Phys. Rev. **90**, 587 (1953).
[9] W. L. Bendel, Ph.D. thesis, University of Illinois, 1953 (unpublished).
[10] A. L. Cockcroft and S. C Curran, Rev. Sci. Instr. **22**, 37 (1951).
[11] F. J. Shore, Jr., Ph.D. thesis, University of Illinois, 1952 (unpublished); Shore, Bendel, Brown, and Becker, Phys. Rev. **91**, 1203 (1953).
[12] S. Frankel, Ph.D. thesis, University of Illinois, 1949 (unpublished).

certain of the previous measurements mentioned above. Weak long-lived components were noted, but their origins were not ascertained.

1. Particle Spectra

Sources for the magnetic spectrometer were prepared by depositing a few milligrams of irradiated Ho_2O_3 on a 0.6-mg/cm² rubber acetate film. These sources were necessarily rather thick, having an average surface density of about 15 mg/cm².

The momentum spectrum of the electrons emitted from Ho^{164} is shown in Fig. 1. The inset is a Kurie plot of the continuous spectrum, constructed with the aid of tables.[13] This analysis indicates that the maximum disintegration energy for the negatron decay is 990±30 kev. The nonlinearity of the Kurie plot near the end point is consistent with a complex beta spectrum consisting of two groups separated by about 90 kev. Subsequent experiments, to be mentioned later, will be seen to urge this interpretation. The departure from a straight line at 550 kev and below is assumed to arise from source thickness.

No positrons could be detected in the magnetic spectrometer, even with an intense source consisting of an irradiated chunk of Ho metal. Provided the kinetic energy available for positron emission is greater than 200 kev, there are less then 5×10^{-4} positron per negatron emitted by Ho^{164}.

The nine conversion electron lines in Fig. 1 were detected using a 130-μg/cm² zapon window on the Geiger counter. Table I lists the electron energies, interpretations, and intensities, relative to the betas, of these conversion lines. A small correction for counter window absorption (<20 percent) was applied to the data, but, because of the thick sources utilized, the intensities given are inaccurate. They were employed only as crude estimates or as lower limits.

The photon energies listed in the table are mean values derived from several determinations. The *K*, *L*, and *M* binding energies for the appropriate elements (to be assigned below) were taken from the table of Hill, Church, and Mihelich.[14]

TABLE I. Energies, interpretations, and relative intensities of conversion electrons.

Line	T(kev)	Interpretation	Intensity (e/β)
A	19.5	72.8-*K*	0.04
B	27.8	37.3-*L*	0.067
C	33.6	37.3-*M*, 90.5-*K*	0.017
D	37.1	46-*L*	0.20
E	44.6	46-*M*	0.10
F	64.5	72.8-*L*	0.24
G	71.2	72.8-*M*	0.036
H	82.1	90.5-*L*	0.19
J	88.2	90.5-*M*	0.024

[13] National Bureau of Standards, *Tables for the Analysis of Beta Spectra* (U. S. Government Printing Office, Washington, D. C., 1952).

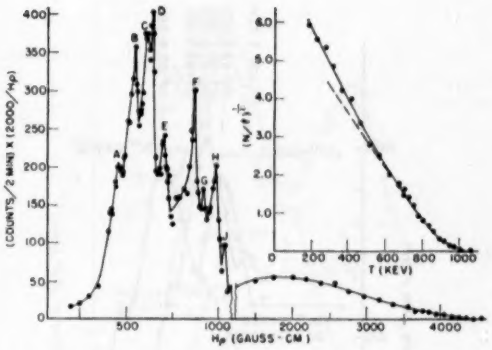

FIG. 1. Electron momentum spectrum and Kurie plot of the continuum.

2. Photon Spectra

The most prominent electromagnetic radiation from Ho^{164} has an energy of about 46 kev. Within experimental error, the energy is the same as the mean of the $K\alpha$ x rays from Dy, 45.7 kev. The evidence for this is contained in Fig. 2 which shows photon spectra observed with the argon-filled proportional counter. The 46-kev radiation from Ho^{164} is compared with the $K\alpha$ x rays from Hf and Gd. It is estimated that Ho or Er x rays, if present, contribute less than 30 percent or 20 percent, respectively, to the observed intensity.

This figure also shows the presence of a 37.3-kev gamma ray. After correction for counter detection efficiency, the intensity of this gamma ray, γ_3, relative to the x ray is $\gamma_3/x=0.040\pm0.003$.

Figure 3 illustrates the photon spectrum obtained with a NaI(Tl) crystal (1½ in. diam×1 in.) and a Du Mont 6292 photomultiplier. γ_3 is not resolved, but the 72.8- and 90.5-kev gammas, γ_2 and γ_1 respectively, show up clearly. (Energies indicated on this and other figures were derived from a calibration curve for the crystal, but may differ slightly from the "best" values given by the conversion electron data.) Relative to the x ray, the intensities of these two gammas are $\gamma_1/x=0.039\pm0.007$ and $\gamma_2/x=0.037\pm0.007$. Corrections were made in all cases for the "escape peak" intensities employing calculated values in those instances in which the escape peak was obscured by another line.

The ratio x/β was determined by comparison of the x-ray intensity detected by a NaI crystal and the β-ray intensity detected by an N. Wood end-window Geiger counter. The result, after correction for the variation in sensitivity of the Geiger counter across the window, was $x/\beta=0.90\pm0.20$, the uncertainty quoted arising mainly from the corrections to the beta intensity for absorption in the air and counter window.

[14] Hill, Church, and Mihelich, Rev. Sci. Instr. **23**, 523 (1952).

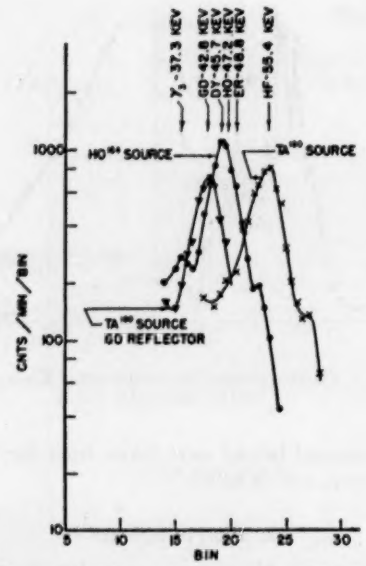

FIG. 2. Comparison of Ho^{164} photons with Hf and Gd $K\alpha$ x-rays in an argon filled proportional counter.

Possible discrepancies owing to the use of two separate counters have not been taken into account in the uncertainty quoted.

The photon spectrum at higher energies was also examined with the NaI crystal-photomultiplier combination. No radiation in the vicinity of 500 kev, other than bremsstrahlung, was found with a very active Ho metal source. The resulting upper limit on positrons from Ho^{164} is 8×10^{-4} positron per negative beta.

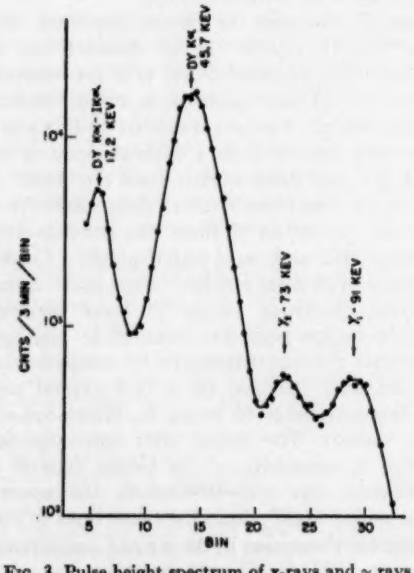

FIG. 3. Pulse height spectrum of x-rays and γ rays from Ho^{164} with a NaI(Tl) crystal.

Table II summarizes the data on photon energies and intensities.

3. Coincidence Experiments

Gamma-gamma coincidences in the vicinity of 500 kev were found to have a sharp maximum at 180°, indicating the presence of positrons. The decay of these coincidences did not, however, exhibit the proper lifetime. A half-life of about 93 minutes was measured. It is assumed that some impurity was responsible.

Coincidences involving the low-energy gammas were obtained. Beta-photon and photon-photon coincidences were observed. The pulse height spectra of the gammas involved are reproduced in Fig. 4. The gamma spectrum concerned with the beta-gamma coincidences was measured with a NaI crystal detector shielded from the betas by 940 mg/cm² of Be. The beta counter was an anthracene scintillation detector which was made to be insensitive below 150 kev in order to exclude low-energy photons and conversion electrons. The beta single counting rate was 8.81×10^5 per minute and the γ counter subtended 1.66 steradians at the source. A NaI detector, sensitive down to 15 kev, replaced the anthracene counter in the photon-photon coincidence experiment. The calculated accidental coincidences for the γ-γ curve indicate the shape of the single-count gamma-ray spectrum for comparison purposes. The accidentals in the β-γ case were slightly less in number.

TABLE II. Photon energies and relative intensities.

Photon	E(kev)	Int. (γ/β)
γ_1	37.3±0.5	0.036±0.01
x	45.7±0.5	0.90 ±0.20
γ_2	72.8±0.5	0.033±0.007
γ_3	90.5±0.5	0.035±0.007

Evidently, there are photons of about 50- and 91-kev energy in coincidence with the betas, and 46- and 70-kev photons coinciding with one another. It is to be noted that the low-energy end of the gamma-gamma spectrum does not fall away as sharply as either the beta-gamma or randoms spectra. One suspects a possible influence here of the 37.3-kev gamma ray. The gamma-gamma coincidences were therefore examined in more detail with pulse height selection in both channels. That is, spectra were recorded, with the 10-channel analyzer attached to counter No. 1, which were in coincidence with pulses from counter No. 2 in a narrow range selected by the single-channel analyzer. NaI crystals (1½ in. diam×1 in.) and Du Mont 6292 tubes were utilized.

Figure 5 contains three spectra taken with counter No. 2 set to select three different energy bands. The range covered by counter No. 2 for each curve is indicated by the correspondingly numbered shaded region. Accidental coincidences were negligible. These

curves show clearly that 46–73 and 37–46-kev coincidences occur. No noticeable evidence is given by this figure for 37–73-kev coincidences. The total number of coincidences observed are plotted in Figs. 4 and 5 and, hence, the statistical probable errors are very nearly equal to the square roots of the ordinates.

Beta—conversion-electron coincidences were looked for with the 255°, double-focusing magnetic spectrometer by placing an anthracene crystal near the source to detect beta particles and an anthracene crystal at the exit slit to detect conversion electrons. Definite evidence was obtained for such coincidences involving the conversion electrons associated with the 90.5-kev gamma ray. However, no evidence for coincidences of this kind was found for conversion electrons associated with photons of energy near 46 kev.

Another coincidence experiment measured the total energy of events coinciding within the resolving time of the 10 channel analyzer, about 3 μsec. A Ho_2O_3 source was placed between two NaI crystals, on a single RCA 5819, which absorbed completely all x rays and particles from the source. Since the 90.5-kev gamma and its conversion electrons are known from the preceding discussion to be in coincidence with a beta, pulses arising from these transitions were conveniently removed from the low-energy line spectrum and spread out over the beta continuum. Hence, the low-energy lines remaining were caused only by other decay branches or by decay of isomeric states produced by the beta decay. The ratio of such low-energy counts to the total beta continuum was found to be 1.3±0.15.

4. Delayed Coincidences

Beta-gamma and gamma-gamma coincidences were examined, with the fast-coincidence equipment already described, for possible measurable lifetimes. The resolving time was not low enough ($\sim 5\times10^{-9}$ sec) for a precise determination, but an analysis of the delayed coincidence curves employing the method of moments[15] yielded a half-life for both β-γ and γ-γ coincidences of $(1.4\pm0.5)\times10^{-9}$ sec (assuming a single period in each case). The β-γ result is deemed to be the more reliable since it is derived from a clearly discernable shift in the centroid of the delay curve. The γ-γ lifetime was derived from a broadening of the delay curve using the second moment.

IV. DISCUSSION

The obvious interpretations of the conversion electron lines were given in Table I. Lines *D* and *E* at 37.1 and 44.6 kev demand further attention. Their positions are, within experimental error, just what one would expect for Auger electrons owing to the conversion of the Dy x rays. However, the fluorescent yield of the *K* shell, ω_K, is about 0.92 for the elements of importance here.[16] Hence, the Auger intensity should

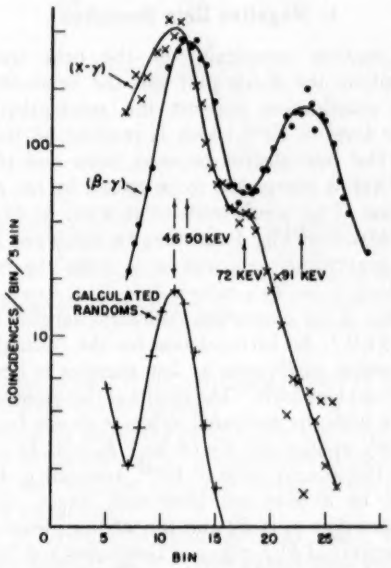

FIG. 4. Pulse height spectra of photons concerned with β-γ and γ-γ coincidences.

be less than 10 percent of the x-ray intensity or less than 9 percent of the beta intensity. The observed strength of these lines, from Table I, is 30 percent of that of the betas. Moreover, this value is a minimum because of the thick source employed. Hence, it is concluded that a part of the electrons at 37.1 and 44.6 kev arises from the conversion of a nuclear gamma ray of about 46-kev energy.

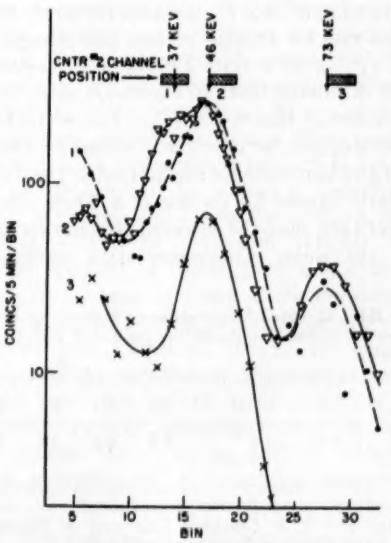

FIG. 5. Pulse height spectra of photons reaching counter No. 1 in coincidence with photons of selected energies detected by counter No. 2.

[15] Z. Bay, Phys. Rev. **77**, 491 (1950).
[16] Broyles, Thomas, and Haynes, Phys. Rev. **89**, 715 (1953).

1. Negative Beta Branches

The possible complexity of the beta spectrum suggested by the Kurie plot and the beta—90.5-kev gamma coincidences support the assumption of a 90.5-kev level in Er^{164} which is reached by the beta decay. The coincidences between betas and photons near 50 kev is interpreted to be caused by the K-shell conversion of γ_1, which leads to an x ray at 48.8 kev. The spectrum of Fig. 4 can then be employed to find the K conversion coefficient of γ_1 from the ratio of x rays to γ_1 rays. This ratio is $(x/\gamma_1)_{coinc}=\omega_K\alpha_{1K}=1.8$ where α_{1K} is the conversion coefficient sought. Hence, $\alpha_{1K}=1.9\pm0.2$. An extrapolation for the calculation of K-conversion coefficients at low energies is described by Axel and Goodrich.[17] The results of this extrapolation compare with the measured value as shown by Table III which applies for $Z=68$ and $E_\gamma=90$ kev. If γ_1 goes to the ground state of Er^{164}, assumed to be 0+, it must be a pure multipole and, hence, $\alpha_{1K}=1.9$ establishes that γ_1 is $E2$ and the 90.5-kev level is 2+.

The empirical K/L ratios of Goldhaber and Sunyar[18] and the observed L/M ratio, combined with α_{1K}, yield a total conversion coefficient of $\alpha_1=11\pm3$ for γ_1. The relative number of betas leading to the excited level in Er^{164}, β_1/β, then may be calculated from the observed γ_1/β ratio and, independently, from the β-γ coincidence experiment. The result is $\beta_1/\beta=0.38\pm0.08$. Since this ratio is significantly less than one, the assumption of a ground state transition is justified. Hence, the $Ho^{164}-Er^{164}$ atomic mass difference is taken to be 0.99 ± 0.03 Mev.

The delayed beta-gamma coincidences yield $(1.4\pm0.5)\times10^{-9}$ sec as the half-life of the 90.5-kev excited state. The γ-ray transition probability, corrected for conversion, is then $T_{exptl}=4.0\times10^7$ sec^{-1}. Now the transition rate for a single nucleon pair changing from a state $(j^2)_{J=2}$ to a state $(j^2)_{J=0}$ is $T_{calc}=9.65\times10^5$ sec^{-1}, as calculated from an expression given by Bohr and Mottelson.[19] Hence, $F=T_{exptl}/T_{calc}=41\pm13$. This is appreciably smaller than the F values ($\sim$150) given by Bohr and Mottelson for similar nuclei. The difference is evidently caused by the use of a larger conversion coefficient here, since the observed lifetimes are approximately the same. Conversion data published by McGowan[20] and by Mihelich and Church[21] for Dy^{160}, Er^{166}, and Yb^{170} also lead to F values on the order of 40 to 50.

TABLE III. Calculated K-conversion coefficients for $Z=68$ and $E=90$ kev for various multipolarities compared with the experimental value.

	$E1$	$E2$	$E3$	$M1$	$E4$	$M2$	$E5$
α_K(calc.)	0.37	1.6	5.4	6.4	18	54	54
α_{1K}(exptl.)		1.9 ± 0.2					

After subtracting the x-ray contribution associated with the conversion of γ_1 from the total x-ray intensity, the remainder may be assumed to represent decay by other branches. Making use of the β_1/β ratio, the f_0t values for the two transitions may be found by employing the tables of Feenberg and Trigg.[22] The results are $\log(f_0t)=5.76$ and 5.56, respectively, for β_1 and β_2. These values are compatible with either allowed or first forbidden transitions. Assignment of 0− or 2− to the 36.7-min level in Ho^{164} would be permitted by selection rules, but in that event the $\Delta I=2$ transition to the 2+ or 0+ state in Er^{164} would be expected to have $\log(f_0t)\approx8$. A 0+ or 2+ state in Ho^{164}, as well as spins higher than 2, require more highly forbidden transitions, with an estimated $\log(f_0t)\gtrsim10$. (See Blatt and Weisskopf[23] for a discussion of these points.) Hence, $1\pm$ seems to be the most likely assignment for the parent level. Coupling rules proposed by Nordheim[24] for odd-odd nuclei give odd parity for Ho^{164} and favor either a zero-spin or a high-spin state. A 1− level is excluded by these rules.

The conclusions reached above are contained in the proposed decay scheme of Fig. 6.

2. K Capture and Positron Branches

The 72.8-kev gamma ray γ_2 can be ascribed to Dy^{164} with a high degree of certainty. The energy sums for the K, L, and M conversion lines give the best agreement if Dy binding energies are used. In addition, the γ-γ coincidences prove that γ_2 coincides with a 46-kev photon, presumably Dy K x-rays following K capture to a 72.8-kev excited state in Dy^{164}. Figure 5 also shows that γ_3, 37.3 kev, is in coincidence with the x rays. Simple calculations verify that the 37.3-kev pulses do not arise from x-x coincidences degraded by Compton scattering in the beta absorbers, or by the escape of iodine x-rays from one crystal to the other. A consideration of the coincidence data makes the placement of γ_2 and γ_3 as shown in the decay scheme of Fig. 6 seem the most probable. The fact that no γ_2-γ_3 coincidences were observed does not invalidate this scheme since the conversion of γ_2 reduces the number of such events by a factor of $(1+\alpha)$, which is on the order of 20.

The K-conversion coefficient of γ_2 may be estimated from Fig. 5, corrections being made for contributions from γ_3 by using the known efficiencies of the single-

[17] P. Axel and R. F. Goodrich, University of Illinois, U. S. Office of Naval Research Report (unpublished).
[18] M. Goldhaber and A. W. Sunyar, Phys. Rev. **83**, 956 (1910).
[19] A. Bohr and B. R. Mottelson, Kgl. Danske Videnskab. Selskab, Mat.-fys. Medd. **27**, No. 16 (1953).
[20] F. K. McGowan, Phys. Rev. **85**, 151 (1952).
[21] J. W. Mihelich and E. L. Church, Phys. Rev. **85**, 690 (1952); **87**, 1144 (1952).
[22] E. Feenberg and G. L. Trigg, Revs. Modern Phys. **22**, 399 (1950).
[23] J. M. Blatt and V. F. Weisskopf, *Theoretical Nuclear Physics* (John Wiley and Sons, Inc., New York, 1952).
[24] L. W. Nordheim, Revs. Modern Phys. **23**, 322 (1951).

channel counter for various energies. The many possible combinations make the exact expression for the coincidence spectrum rather lengthy and it is not given here. The type of result obtained is illustrated more clearly by the simple case of K-capture decay to a single excited level in the daughter which then decays with the emission of a gamma ray. If it is assumed that the x-rays and γ rays are totally absorbed in the NaI crystals, that counter No. 2 is equally sensitive to all photon energies, and that the spectrum of coincident photons is observed in counter No. 1, then the ratio of x-rays to γ rays is $(x/\gamma)_{coinc}=1+2\alpha_K\omega_K$. The first term originates from coincidences between K-capture x-rays and the γ rays, while the second is caused by x-x coincidences arising from K capture followed by K-shell conversion of the γ. A factor of 2 appears since the x-rays may enter either counter.

For the case at hand, the final result, after making corrections using the complete expression for the coincidence spectrum, is $\alpha_{2K}=2.7\pm0.5$. This agrees well with the extrapolated theoretical value for an $E2$ transition which is 2.6. Hence, again assuming 0+ for the Dy^{164} ground state, the 72.8-kev level is 2+. Electron-gamma coincidences furnished qualitative support for the assumed cascade of γ_2 and γ_3 but, owing to poor electron energy resolution and calibration in the thin anthracene crystal, no reliable quantitative information was obtained from these data.

A very rough estimate of the L conversion coefficient of γ_3 may be found from the electron momentum spectrum, Fig. 1, and the measured ratio γ_3/β. The result is that α_{3L} is at least 2 and, guessing at the effect of source self-absorption, is probably not greater than 10 or 15. Gellman, Griffith, and Stanley[25] have calculated L conversion coefficients. Interpolated to $Z=66$ and $E_\gamma=37$ kev, it is found from their calculations that $\alpha_L=200$ for an $E2$ transition. Hence, a pure $E2$ transition would seem to be excluded for γ_3, although pure $E1$ or $M1$ could occur since the calculated L coefficients are about 0.8 and 9.0, respectively. Of course, $M1+E2$ is also possible.

With γ_3 placed as in Fig. 6, the second excited state of Dy^{164} therefore has a spin of 1, 2, or 3 and lies at 110 kev. This would not be consistent with the pure rotational spectrum predicted by the strong coupling approximation of the collective model[19] which would give a spin 4+ and an energy of 240 kev (assuming 73 kev for the first excited state). It is thought that the 110-kev level is probably 2+ since Scharff-Goldhaber[8] finds that about 50 percent of the second excited levels in even-even nuclei are 2+. This would also allow the transition to this level from the Ho^{164} level, which is thought to be 1±, to compete favorably with those to the ground and 72.8-kev states whereas a spin of 3 probably would not. The absence of a crossover gamma

[25] Gellman, Griffith, and Stanley, Phys. Rev. **85**, 944 (1952).

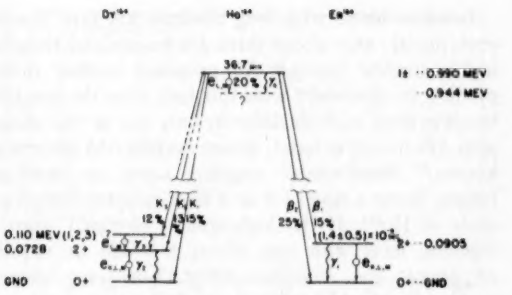

FIG. 6. A proposed decay scheme for Ho^{164}. The Ho^{164}-Dy^{164} mass difference is not specified in the figure.

to the ground state is not surprising in view of the work of Kraushaar and Goldhaber.[26]

It would be satisfying to attribute the 1.4×10^{-9}-sec half-life of the delayed γ-γ coincidences to the 72.8-kev gamma, but because of γ_3 this aspect of the problem remains undecided.

The K capture to positron ratio, $f_K/f_+>2\times10^3$, indicates that the $Ho^{164}-Dy^{164}$ atomic mass separation is less than 1.4 Mev,[22] if one assumes an allowed transition. The result should not be greatly different for a first forbidden decay. Mass spectrographic measurements by Hogg and Duckworth,[27] combined with 0.99 Mev as the $Ho^{164}-Er^{164}$ separation, give 2.1 ± 0.9 Mev for the $Ho^{164}-Dy^{164}$ difference. (The error quoted was not given explicitly for these nuclei but is the minimum uncertainty for their measurements in general.)

3. Long-Lived Isomer

The total-absorption experiment described in III suggests the possible existence of a long-lived isomeric transition. Entirely independent of the detailed decay scheme, if all multiple-step decay branches had mean lives less than 3×10^{-6} sec (the analyzer's resolving time), then in this experiment all K-capture processes would produce discrete, low-energy lines whereas all beta emission processes would produce a continuum. Now, as determined by separate measurements, $x/\beta=0.9$. When one corrects for conversion x rays and fluorescent yield, the maximum possible relative K-capture intensity is $(K/\beta)_{max}=0.9\pm0.2$. However, the ratio of the total intensity of the low-energy line structure to the beta continuum in the total absorption experiment was 1.3 ± 0.15. Hence, the excess was attributed to the existence of an isomeric level with $\tau>3\times10^{-6}$ sec. No further specific information was obtained on this point. The assignment of the remaining 46-kev gamma ray γ_4 to an isomeric transition in Ho^{164} is, at most, only a reasonable suggestion and therefore is indicated by broken lines in the figure.

[26] J. J. Kraushaar and M. Goldhaber, Phys. Rev. **91**, 1081 (1953).

[27] B. C. Hogg and H. E. Duckworth, Phys. Rev. **91**, 1289 (1953).

Isomeric levels with long lifetimes are rare in even-even nuclei; only about three are known and these are highly excited states.[23] All proposed nuclear models predict, in agreement with this fact, that the low-lying levels in such nuclides differ by only one or two units of spin. On the other hand, numerous odd-odd isomers are known.[23] Nordheim's[24] coupling rules, as mentioned before, favor a spin of 0 or a high spin for the ground state of Ho^{164}. If the high spin is obtained, then an isomeric level with spin about 1 would be required to permit the 36.7-min decay. Low-lying isomeric states in odd-odd nuclei are, in fact, predicted by the strong-coupling collective model of Bohr and Mottelson.[19] The parity of the isomeric state would be the same as that of the ground state in this case.

Of interest with regard to these considerations is the work of Butement[29] on Ho^{166}. This observer reports an activity with half-life greater than 30 years, in addition to the well known 27-hour decay. This indicates the probability of an isomeric pair similar to that hypothesized here for Ho^{164}. A long-lived activity decaying to the 90- and the 73-kev γ-ray emitting states was searched for in the present work with a source which had been irradiated for nine hours in the betatron. No evidence was found to support such a long-lived decay. However, it is felt that the inefficient method of activation here employed does not preclude its existence. Butement, in the course of his work, irradiated Ho with fast neutrons but found no long-lived activity which could not be attributed to neutron capture and Ho^{166}.

In conclusion, the 72.8- and 90.5-kev levels shown in the decay scheme are thought to be reasonably well established, as well as their spins and parities. The 110-kev state in Dy^{164} is probably correct but not absolutely forced by the present work. For instance, the existence of a level at about 36.5 kev would give rise to two gammas of almost the same energy. It would be difficult to completely rule out this possibility by the data described above, but the relative intensities in the γ-γ coincidence experiment are more consistent with the scheme proposed here. Furthermore, such a low-lying state (36.5 kev) has no precedent in the regular behavior of the many other even-even nuclei. The 36.7-min isomeric transition shown is not at all well established and must be considered to be highly tentative.

[23] M. Goldhaber and R. D. Hill, Revs. Modern Phys. **24**, 179 (1952).
[29] F. D. S. Butement, Proc. Phys. Soc. (London) **A65**, 254 (1952).

PHYSICAL REVIEW VOLUME 96, NUMBER 5 DECEMBER 1, 1954

Interaction of Heavy Primary Cosmic Rays in Lead*

Y. Eisenberg †
Cornell University, Ithaca, New York
(Received July 28, 1954)

The energy spectrum of heavy primary cosmic-ray nuclei was measured and found to be in agreement with the assumption that no primaries with energy below the geomagnetic cutoff enter the earth. The mean free path of the primary nuclei in lead was measured. If the transparency of nuclear matter is taken into account, the present results for lead and the measurements by others for lighter elements are in good agreement. If the expression $R_A = R_0 \times A^{\frac{1}{3}}$ is used for the radius of the nucleus, the data indicate for R_0 the value 1.3×10^{-13} cm. It is also shown that the ratio of the abundances of the charge groups $Z = 12$ to 17 and $Z = 18$ to 28 is ~ 2.1.

I. INTRODUCTION

An "emulsion cloud chamber" consisting of lead plates and photographic emulsions was flown[1] to an altitude of approximately 100 000 feet for about 10 hours. The box was made of aluminum, inside dimensions 4 in.$\times$6 in.$\times 5\frac{3}{4}$ in. In its walls $\frac{1}{8}$-in. grooves were cut so that 4 in.$\times$6 in.$\times\frac{1}{8}$ in. lead plates could slide in. The grooves were spaced accurately to within 0.002 in. and the lead plates were machined to the same accuracy.

Number G5 photographic emulsions, 100μ thick, mounted on 4-in.$\times$6-in. specially cut glass plates, were inserted below each lead plate. The position of a single particle going from plate to plate in the stack could be predicted to within 50–100μ. The total number of plates was 22. (In cases of distorted emulsions it was found that the correct angle to be used for the prediction of the position is that given by the part of the track near the air surface. Apparently, in the drying stage, the surface layers dry uniformly, and thus preserve the true angle.)

An ordinary Leitz binocular research microscope

* Assisted by the joint program of the Office of Naval Research and the U. S. Atomic Energy Commission.
† Now at the Weizmann Institute of Science, Physics Department, Rehovoth, Israel.
[1] The balloon flight was conducted by the Aero-Medical Field Laboratory, Hollaman Air Force Base, New Mexico (41.7°N geomagnetic latitude) on July 13, 1952.

clamped down on a steel base was used for following the tracks. Two depth gauges were connected to the microscope stage so that the x and y motions could be measured accurately to within 2 microns.

This arrangement was primarily used in studying the interactions of the heavy primaries. The top plate was scanned for primaries of charge $Z \geq 6$. The particles were followed through the entire "cloud chamber" until they left the stack or else suffered a nuclear interaction. In the latter case, the event was examined in more detail. Five hundred and eight primaries were traced, traversing a total amount of about 16 meters of lead. Of these, about 300 left the stack without interacting, and about 200 suffered nuclear interactions.

II. THE ENERGY SPECTRUM AND THE MAGNETIC CUTOFF

The energy of the interacting particles was estimated in the following way. The interaction of a heavy primary with the target nucleus gives rise to an ordinary star in the rest system of the incident particle. Such a star contains visible prongs which are, in general: a recoil, evaporation tracks (α particles and protons), "grey" tracks (protons of up to 200 Mev), and mesons, if sufficient energy is available. In the laboratory system the evaporation tracks will form a shower traveling in the forward direction. The average evaporation energy, T_α, of α particles from nuclei of charge $Z \sim 12$ is taken from Perkins'[2] work as ~ 10 Mev. The root-mean-square angle in the laboratory system of the α particles with the direction of motion of the primary is given[3] by:

$$\langle \Theta^2 \rangle^{\frac{1}{2}} = [\langle T_\alpha \rangle M / 3p^2]^{\frac{1}{2}} = 0.056/p \text{ radians},$$

where M is the proton mass and p the momentum per nucleon in Bev/c of the incident particle. (We call this the "opening angle" of the α shower.) Since no evaporation α particles are emitted with energy over 30 Mev,[2] the primary momentum cannot be underestimated by more than a factor of two.[3] In several cases the shower contained a heavy fragment (the "recoil" in the rest system) which stopped in the stack. In these cases it was possible to determine the energy accurately by the known range-energy relations, and to compare it to the energy obtained by the α-shower method. The agreement is quite good, as shown in Table I.

Since the cross section does not depend strongly upon the energy in the energy range considered here,[4] the sample of particles which suffered nuclear interactions is a random one, and therefore represents the energy spectrum of the heavy primaries.

The energy at the top of the atmosphere was obtained by adding to the value of the energy deduced from the analysis of the interaction, the energy lost in the residual atmosphere and in the apparatus up to the point of interaction, assuming that the particle is a primary particle. This assumption is indeed not justified, since probably about 40 percent of the ions observed in the stack (see Sec. IV) are heavy fragments of heavier primaries. Therefore, the energy loss in the atmosphere, and hence the energy at the top of the atmosphere, will occasionally be underestimated. Figure 1 shows the differential energy spectrum obtained. In about 20 percent of the cases, the energy is below the assumed geomagnetic cutoff (1.5 Bev/nucleon). However, using the fragmentation probabilities as given in Sec. IV, and the energy spectrum obtained beyond[5] $E = 1.5$ Bev per nucleon, one can predict that indeed about 20 percent of the particles will have to be found with energy below the cutoff. Our data, therefore, agree with the assumption that all primaries at latitude 41.7°N enter the earth with energy above 1.5 Bev per nucleon.

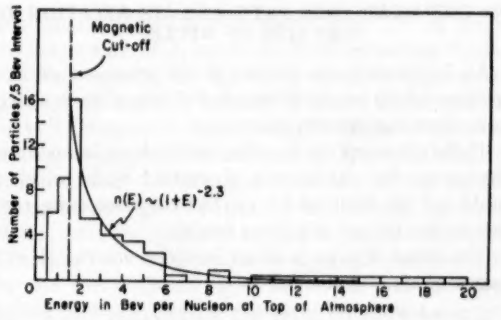

FIG. 1. Differential energy spectrum at the top of the atmosphere obtained by the α-shower method from opening angle measurements.

The spectrum obtained can be represented quite well by

$$n(E)dE \propto (1+E)^{-2.3}dE,$$

(where E is the kinetic energy in Bev/nucleon) and agrees with the integral spectrum obtained by Kaplon *et al.*[3]

TABLE I. Comparison between the energy obtained with the α-shower method and the residual-range method.

Primary	Shower particles	Energy in Bev/nucleon: Opening angle method	Residual range method
Fe^{26} [a]	$O^8+3\alpha+p$'s	0.69	0.40
Ca^{20}	$Al^{13}+3\alpha+p$	0.23	0.20
Mg^{12}	$N^7+\alpha+p$'s	0.14	0.23
Cr^{24}	$S^{16}+3\alpha+p$'s	0.33	0.57

[a] Reported by Kaplon *et al.* (see reference 3).

[2] D. H. Perkins, Phil. Mag. **41**, 138 (1950).
[3] Kaplon, Peters, Reynolds, and Ritson, Phys. Rev. **85**, 295 (1952).
[4] M. F. Kaplon (private communication).
[5] The shape of the spectrum beyond $E = 1.5$ Bev per nucleon will not be affected appreciably by the correction due to the fragmentation.

III. THE MEAN FREE PATH AND ITS RELATION TO THE SIZE OF NUCLEI

An interaction was defined in the present work as a collision which results in removal of one or more charge units from the primary particle.

There are examples of collisions in which no apparent change in the charge was observed.[6] Such collisions could not be detected by us, but they are quite rare, hence they do not affect our results.

The mean free path of an incident nucleus A in a target of mass number A' is

$$\lambda_A(A')=A'/[N\sigma_A(A')]\,\mathrm{g/cm^2}, \qquad (1)$$

where N is Avogadro's number, and $\sigma_A(A')$ is the cross section of particle A in the target A'. Assuming a geometric cross section (namely, 100 percent "black" nuclei), and taking radii of nuclei to be $R_A=R_0\times A^{\frac{1}{3}}$, we obtain

$$\sigma_A(A')=\pi(R_A+R_{A'})^2=\pi R_0^2(A^{\frac{1}{3}}+A'^{\frac{1}{3}})^2. \qquad (2)$$

If the target is composed of more than one element, the mean free path will be

$$\lambda(\mathrm{cm})=1/(\textstyle\sum_i\sigma_i n_i)=\{\pi R_0^2 N\sum_i m_i(A_i^{\frac{1}{3}}+A^{\frac{1}{3}})/A_i\}^{-1},$$

where m_i is the density in g/cm^3 of the element A_i of the target. The average atomic number of the target, $\bar{A}$, will depend upon A and is given by:

$$m(\bar{A}^{\frac{1}{3}}+A^{\frac{1}{3}})^2/\bar{A}=\textstyle\sum_i m_i(A_i^{\frac{1}{3}}+A^{\frac{1}{3}})^2/A_i,$$

where m is the density of the target, $m=\sum_i m_i$.

The mean free path of cosmic-radiation heavy primaries in glass was measured by Bradt and Peters[5] and in brass by Kaplon *et al.*[3] Both measurements indicated that the observed mean free path is longer than the expected one, obtained by using expression (2) above, and by using for R_0 the value 1.45×10^{-13} cm, which was widely accepted in 1951–1952. Recent experiments[7] indicate that the value of R_0 is about 1.2×10^{-13} cm, 20 percent smaller than it was believed to be.

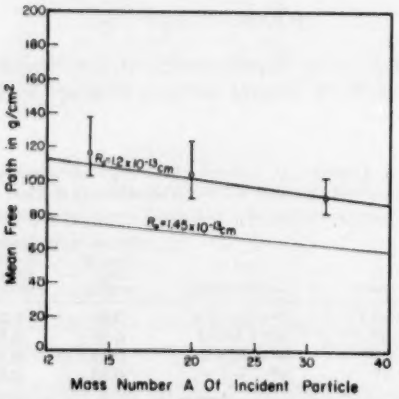

FIG. 2. The interaction mean free path in lead *vs* the mass number of the incident particles.

In Fig. 2 the mean free paths we obtained are plotted *vs* the mass number A of the incident particles. The present experimental points fall on the theoretical curve obtained by using $R_0=1.2\times10^{-13}$ cm, and assuming geometric cross sections. The interpertation of these results is not so clear, since it is known that nuclei are not completely "black." In the following calculations we have attempted to estimate the expected mean free path, taking into account the finite free path of a nucleon inside the nucleus. For a 100 percent "black" nucleus the cross section may be written as

$$\sigma=\int_0^{R_1+R_2}2\pi b\,db=\pi(R_1+R_2)^2.$$

Assuming the nucleus to be a uniform sphere, one may introduce the transparency of nuclear matter by writing the cross section as

$$\sigma=2\pi\int_0^{R_1+R_2}[1-P(b)]b\,db,$$

where $P(b)$ is the probability that for the impact parameter, b, none of the nucleons of A_2 will interact with any of the nucleons of A_1 (see Fig. 3). Such probability is

$$P(b)=\exp[-X(b)/\lambda],$$

where $X(b)$ is the integrated path length of all the nucleons of A_2 inside A_1 for the given impact parameter b, and λ is the mean free path of a nucleon in nuclear matter. We have used for λ the value[8]

$$\lambda=5\times10^{-13}\ \mathrm{cm},$$

which was derived from the analysis of nucleon-nuclei scattering experiments at machine energies. Lambda seems to be reasonably constant in the energy range from 0.2 to 1.5 Bev. The function $X(b)$ is given by

$$X(b)=\int_{b-R_1}^{R_2}\int_{-\Theta_0}^{\Theta_0}4\rho r_2(R_2-r_2)^{\frac{1}{2}}\times(R_1^2-r_2^2-b^2+2r_2b\cos\Theta)^{\frac{1}{2}}dr_2d\Theta,$$

where Θ_0 is determined by

$$\cos\Theta_0=(b^2+r_2^2-R_1^2)/(2br_2),$$

and R_1 and R_2 are the radii of the target and the incident nucleus, respectively. For a uniform distribution of nucleons, ρ, the density of nuclear matter, is $(4\pi R_0^3/3)^{-1}$. $X(b)$ was tabulated by numerical integration. It is a function of R_1 and R_2, hence of A_1 and A_2. For $A_2=25$ and $A_1=207$, 64, and 31, the

[6] H. Bradt and B. Peters, Phys. Rev. **77**, 54 (1950); H. Bradt and B. Peters, Phys. Rev. **75**, 1779 (1949); and J. Noon (private communication).

[7] F. Bittner and H. Feshbach, Phys. Rev. **92**, 837 (1953).

[8] T. Taylor, Laboratory of Nuclear Studies, Cornell University (private communication).

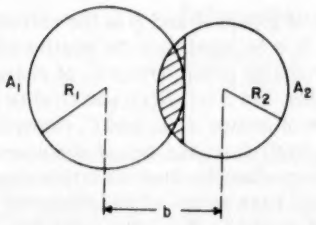

FIG. 3. Model used for calculating the mean free path and the fragmentation probability.

reduction in the cross section due to the transparency as introduced above comes out to be 16 percent, 23.2 percent, and 25.1 percent, respectively.

In Fig. 4 we plotted the calculated cross sections and the observed ones for incident primaries of $\bar{A}=25$, *vs* the mass number of the target nuclei. With this model of a transparent nucleus, the best fit to the experimental data is obtained if one chooses $R_0=1.3\times10^{-13}$ cm. This value of R_0 for a real "grey" nucleus is perhaps more significant than the value $R_0=1.2\times10^{-13}$ cm which would give the best fit to the data if one idealizes nuclei to be 100 percent "black."

Two additional experimental points have been obtained recently at the University of Rochester.[9] These are the mean free path in emulsion ($\bar{A}$ emulsion$\approx$38) of:
Medium Group

$$(6\leqslant Z\leqslant 10),\quad \bar{A}_M=14,\quad \lambda_M=59.6\pm6\ \text{g/cm}^2,$$

Heavy Group

$$(10<Z),\qquad \bar{A}_H=32,\quad \lambda_H=36.5\pm4.8\ \text{g/cm}^2.$$

If a correction is made for the difference in A_M of the incident particle, λ_H comes to be in agreement with the predicted value (circled point in Fig. 4), but λ_M seems to point to a much smaller value of R_0, namely $R_0=1.0\times10^{-13}$ cm, if the 100 percent "black" nucleus is assumed. However, taking into account the transparency in calculating λ_M and using $R_0=1.3\times10^{-13}$ cm, we have obtained $\lambda_M=52.5$ g/cm^2, in agreement with the observed value. The reduction in the cross section in this case is 31.5 percent.

In conclusion we may say that, taking into account the transparency of nuclear matter, and using $R_0=1.3\times10^{-13}$ cm, the calculated mean free paths agree with the observed ones for incident particles of $A=14$ to 32 and targets of mass numbers $A'=23$ to 207.

IV. RELATIVE ABUNDANCE OF COSMIC-RAY PRIMARIES

In order to extrapolate the relative abundance of the elements observed in the stack (under 25 g/cm^2 on the average from the top of the atmosphere) to the top of the atmosphere, the probability of fragmentation by collision with air nuclei had to be estimated. The fragmentation probability will depend upon (1) the size of the target nucleus A_1 and of the incident nucleus A_2, and (2) the energy of the incident nucleus. In general, the collision will involve "cutting" of a part of the incident particle (removal of the nucleons which are in the overlapping region, shaded area in Fig. 3) and subsequent evaporation of nucleons from the residual nucleus. In the extreme relativistic case, $E\gg Mc^2$, the side-scattering of the nucleons during the collision may be neglected. Therefore, the evaporation energy will come from the friction energy (breaking of the bonds between neighboring nucleons) and the change in the surface energy.[10] For an impact parameter b, the fractional number of nucleons contained in the overlapped region and lost in the "cutting" is

$$f_1=\tfrac{1}{4}[3(h/R_2)^2-(h/R_2)^3],$$

where h is the amount of overlap: $h=R_1+R_2-b$ if $R_1-b\leqslant R_2$, and $h=2R_2$ if $R_1-b\geqslant R_2$. The probability for such a collision is

$$P(h/R_2)=\frac{2[(R_1/R_2)+1-\frac{1}{2}(h/R_2)]h/R_2}{[(R_1/R_2)+1]^2}.$$

The friction energy is given by

$$U_F=1.5R_2^2[2(h/R_2)-(h/R_2)^2]\ \text{Mev},$$

and the surface energy is

$$U_S=4.12\pi R_2^2\{1-\tfrac{1}{4}(h/R_2)^2-[1-\tfrac{3}{4}(h/R_2)^2+\tfrac{1}{4}(h/R_2)^3]^{\frac{1}{2}}\}\ \text{Mev}.$$

The total excitation energy of A_2 is $U=U_F+U_S$. The average number of nucleons emitted in the evaporation process is[11]

$$N(U)=6.4\times10^{-2}U-2.4,\quad U>100\ \text{Mev}$$
$$N(U)=4.5\times10^{-2}U\qquad U<100\ \text{Mev}.$$

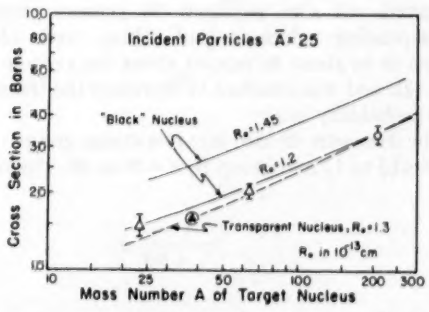

FIG. 4. The cross section for incident particles of $\bar{A}=25$ *vs* the mass number of the target used. Circle: present experiment; triangle: results of the Rochester group; solid line: calculated geometric cross section; and broken line: cross section calculated by using the transparent nucleus model.

[9] J. Noon (private communication).

[10] We have followed here the calculations of W. Heitler and Ch. Terreaux, Proc. Phys. Soc. (London) **A66**, 929 (1953).

[11] K. J. Le Couter, Proc. Phys. Soc. (London) **A63**, 259 (1950).

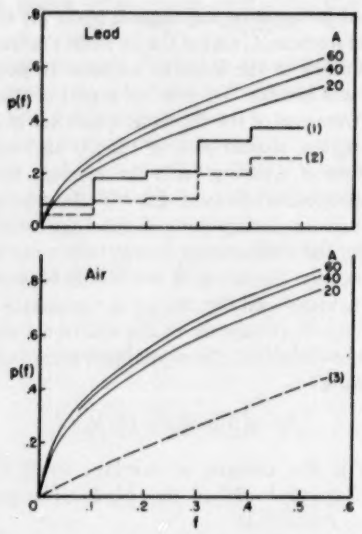

FIG. 5. The fragmentation probability for lead and air. $P(f)$, the probability of losing up to the fraction f of the number of nucleons in a collision, is plotted *vs* f.

The results of the above calculations are shown in Fig. 5. We have plotted $P(f)$, the integral probability of losing up to a fraction f of the number of nucleons, *vs* f for incident particles of $A=20$, 40, and 60, in lead and air targets. Histogram (1) (Fig. 5) represents 43 cases of particles interacting in lead, whose kinetic energy was $E\geqslant 1.3$ Bev/nucleon. Histogram (2) represents 92 cases of energy $E\geqslant 0.2$ Bev/nucleon. In both cases, the charge of the particles was $Z\geqslant 12$. One can see that indeed the higher the energy, the closer we get to the expected curve for the extreme relativistic case.

The expected curves for the extreme relativistic limit in air are about 40 percent higher than those for lead. We have, therefore, assumed that the fragmentation probability in air for the sample of particles which we observed will also be about 40 percent above the corresponding values in lead. Thus, curve (3) was drawn to be about 40 percent above the average of (1) and (2), and was assumed to represent the fragmentation probability in air.

The data were divided into two charge groups: group A, $Z=12$ to 17 and group B, $Z=18$ to 28. The natural abundance of groups A and B in the universe[12] is about the same. It is believed that the relative abundance of the higher charge group, group C, of charge $Z>28$, is much smaller. Let $A(x)$, $B(x)$, and $C(x)$ be the number of particles of groups A, B, and C, respectively, at the depth x(g/cm^2) from the top of the atmosphere. Let P_{BA} be the probability that an interacting particle of group B will have as one of its interaction products, a particle of group A. P_{AA}, P_{BB}, and P_{CB} are defined similarly. Then we get

$$\text{(a)}\quad dA(x)=-dx[A(x)/\lambda_A-P_{BA}B(x)/\lambda_B-0.55P_{AA}A(x)/\lambda_A]$$

and

$$\text{(b)}\quad dB(x)=-dx[B(x)/\lambda_B-P_{CB}C(x)/\lambda_C-P_{BB}B(x)/\lambda_B].$$

Forty-five percent of group A is presumably Mg^{12}, which leaves the group upon interaction. Therefore the factor 0.55 was introduced in (a) above. P_{AA}, P_{BA}, and P_{BB} were taken from curve (3) of Fig. 5, namely

$$P_{AA}=P(0.2)=0.20,$$
$$P_{BA}=P(0.55)-P(0.3)=0.20,$$
$$P_{BB}=P(0.3)=0.25$$

$C(x)$ can be neglected; thus (a) and (b) can be solved immediately and the relative abundance is found to be $A(0)/B(0)=2.1$. It should be noted however, that approximately the same relative abundance is obtained (by chance) if we do not introduce any fragmentation correction at all and use simple exponential decay, namely

$$A(x)=A(0)\exp(-x/\lambda_A),$$

and

$$B(x)=B(0)\exp(-x/\lambda_B).$$

The author is greatly indebted to Professor G. Cocconi for his continuous help during the analysis of the data, and for many invaluable discussions of the results obtained.

Most of the scanning work was done by Mrs. P. Eliash, Mr. J. Arkin, and Mrs. S. Eisenberg. Their effort is greatly appreciated.

[12] R. A. Alpher and R. C. Herman, Revs. Modern Phys. **22**, 153 (1950).

Interaction of a Negative Heavy Meson*

J. E. Naugle, E. P. Ney, P. S. Freier, and W. B. Cheston
University of Minnesota, Minneapolis, Minnesota

(Received August 16, 1954)

An interaction caused by a stopping heavy meson has been observed in emulsion. One of the four particles emitted in the interaction is interpreted as a nuclear fragment with a Λ^0 attached. The subsequent mesonic decay of this bound Λ^0 leads to a Q of 34.2±0.9 Mev. The measured mass of the heavy meson is $1010\pm200m_e$. The visible kinetic energy released in the interaction it causes is 50±8 Mev.

I. INTRODUCTION

THIS event was observed in G-5 600μ glass backed emulsion flown at $\lambda=10°$ at an altitude of 15.2 g/cm². The emulsions were flown horizontally in stacks of three plates. The event was observed in a routine examination of the 4-in.×10-in. emulsion by low-power hand lens. This "scan-by-eye" is made of all our plates before they are cut into pieces small enough for the microscope stages. Usually only nuclei of high Z, showers of great energy, and high-energy stars are seen in this scan. In this case the star was observed near the track of a carbon nucleus picked up during the "scan-by-eye."

The interaction is observed entirely in one emulsion with the exception of one particle which goes to a facing emulsion. Figures 1 and 2 show a sketch and a photomicrograph of the event. Table I lists the measurements made on the eight particles involved.

Particle a comes from glass and travels 1.635 cm before coming to the end of its range and being captured by an emulsion nucleus. Four particles are emitted in this interaction. Particles c and d have such small ranges that their mass cannot be determined. Their kinetic energies are assigned on the assumption that they are protons. Particle b travels 1 mm in the first emulsion and 1.6 mm in the facing emulsion before leaving the stack. By scattering, gap measurement and δ ray counts, it can be identified as a proton. Its kinetic energy as it leaves the star is 30±7 Mev. The energy was determined from scattering measurements.

Table I. Measurements made on the eight particles involved in the event shown in Fig. 1.

Track	Identification	Range in emulsion microns	Kinetic energy Mev	Momentum Mev/c
a	$M=1010\pm200m_e$	16 350		
b	proton	2600	30 ±7	237±27
c	p,d	167 ±3	4.9 ±0.1 if proton	96± 1
d	p,d	16.0±0.5	1.10±0.05 if proton	45± 1
e	$_3He^6$	97 ±1	14.1 ±0.2	324± 3
f	proton	450 ±5	8.9 ±0.2	129± 2
g	π	10 600	24.2 ±0.5	86± 2
h	$_3He^3$	2.9±0.4	1.1 ±0.2	78± 7

II. MASS MEASUREMENT OF HEAVY MESON

The mass of the heavy meson was measured by three methods; blob density, mean gap length, and multiple scattering. The variation of each of these quantities with range can be used as a measure of the mass provided their variation with range is known for particles of known mass.

The blob density of the heavy meson was measured over the first six millimeters of track. The variation of blob density with range for ending pions was measured over a range of values of blob density which included the values obtained on the heavy meson. The logarithm

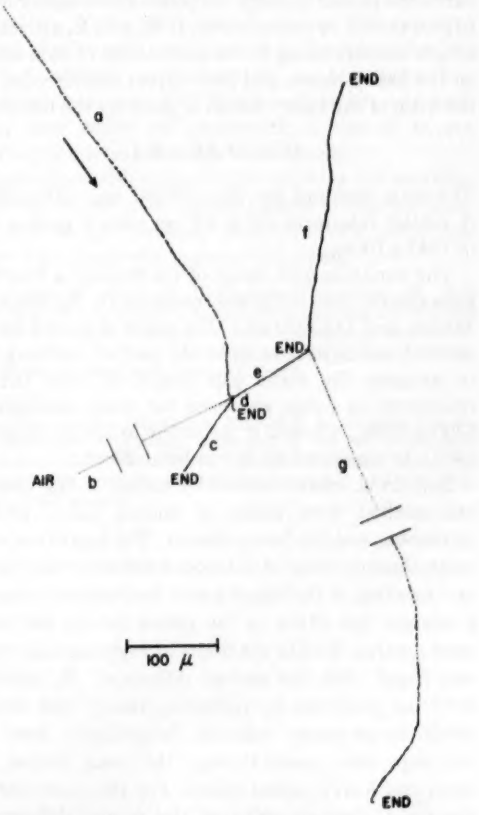

Fig. 1. A projection drawing of a star produced by an incoming heavy meson, a. Fragment e has a Λ^0 attached to it which subsequently suffers mesonic-type decay.

* This research supported in part by the joint program of the U. S. Atomic Energy Commission and the Office of Naval Research.

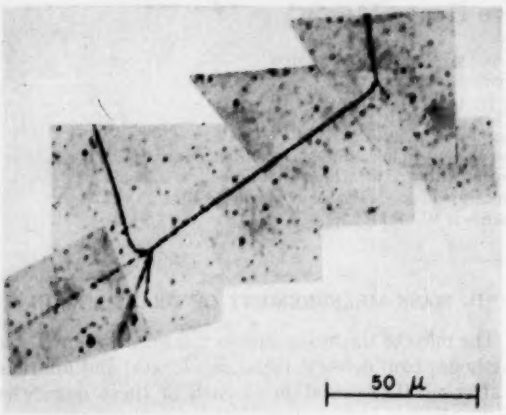

FIG. 2. A photomicrograph of the same event that is sketched in Fig. 1.

of the blob density was plotted as a function of the logarithm of the residual range. A straight line was fitted to the points of the pions by the method of least squares. A straight line with the same slope as the pion curve was passed through the points of the heavy meson to give the heavy meson curve. If R_H and R_π are residual ranges corresponding to the same value of blob density on the heavy-meson and pion curves respectively, then the mass of the heavy meson is given by the relation:

$$M_H = M_\pi(R_H/R_\pi). \tag{1}$$

The mass obtained by this method was $1030\pm200m_e$. A similar treatment for a 2.1 cm proton gave a mass of $1945\pm160m_e$.

The variation with range of the mean gap length for gaps greater than 0.82μ was measured by the method of Menon and O'Ceallaigh.[1] The mass obtained by this method was dependent upon the part of the track used to measure the mean gap length. If only the last centimeter of range was used the mass obtained was $1300\pm200m_e$, whereas if the entire available range was used, the measured mass was $840\pm200m_e$.

Scattering measurements by means of the constant cell method were made on ending pions, protons, deuterons, and the heavy meson. The logarithm of the mean absolute value of the second difference was plotted as a function of the logarithm of the residual range and a straight line fitted to the points by the method of least squares. Within the limits of experimental error it was found that the second difference, $\bar{D}$, varied as $R^{-0.58}$ as predicted by scattering theory and the empirical range-energy relation. Accordingly, lines with this slope were passed through the pions, proton, deuteron and heavy meson points. For the same size cell, the mean absolute value of the second difference is given approximately by:

$$\bar{D}(R) = K/M^{0.42}R^{0.58}, \tag{2}$$

where K is a slowly varying function of the cell length used and the velocity of the particle. Thus if we compare $\bar{D}_H$ of the heavy meson to $\bar{D}_M$ of a known particle at the same range, we have:

$$M_H = M(\bar{D}_M/\bar{D}_H)^{2.38}. \tag{3}$$

This method gave a mass of $970\pm200m_e$ for the heavy meson.

The constant sagitta method of scattering was used to measure the mass. The ranges proposed by Glasser[2] were employed, yielding a mass of $910\pm290m_e$.

The average of these methods is $1010\pm200m_e$, where the error quoted is about twice the standard deviation given by an analysis of the error.

III. THE Λ^0 FRAGMENT

Particle e ends in the emulsion with the emission of three charged particles. It is interpreted as the mesonic decay of a Λ^0 attached to the fragment e. At least 14 cases of the decay of such a fragment have been reported in the last eighteen months,[3] and all can be explained by the assumption that a Λ^0 is bound to the fragment. Its subsequent decay, mesonically or non-mesonically, results in the star at the end of the fragment.

Fragment e seems to be a fragment of charge 2 with a bound Λ^0 which decays mesonically. Preliminary measurements with a densitometer give a charge of 2 or 3 for particle e. The decay scheme which best satisfies all the measurements is:

$$_2\mathrm{He}^{4*} \rightarrow \pi^- + p + {}_2\mathrm{He}^3 + (34.2\pm0.9)\ \mathrm{Mev}. \tag{4}$$

The three emitted particles are coplanar to $13°\pm12°$, where the large error in angle is due to the extremely short range of particle h. Particle f is most probably a proton which stops in the emulsion. Particle g has been identified by gap measurement, blob counting, scattering-range, and scattering-ionization. Its measured mass compared to identified π's is $290\pm20m_e$. We therefore believe it is a π meson although there is neither a decay nor a σ star at the end of its range. However, there is approximately a 30 percent probability that a π^- makes a "zero-pronged" σ star.[4]

The momentum of the three particles emitted from the end of particle e conserve momentum to within 35 ± 25 Mev/c, the error being practically all in the Z direction where the error in measurement is large due to the emulsion shrinkage. The kinetic energy of the three emitted particles is 34.2 ± 0.9 Mev, where the energies are all determined from range measurements and Vigneron's range-energy curve.[5]

[1] M. G. K. Menon and C. O'Ceallaigh, Proc. Roy. Soc. (London) **221**, 292 (1954).

[2] R. G. Glasser (private communication).

[3] Notes of the Padua Meeting, April, 1954 (unpublished).

[4] W. B. Cheston and L. J. Goldfarb, Phys. Rev. **78**, 683 (1950).

[5] L. J. Vigneron, J. phys. et radium **14**, 145 (1953).

The difference between the kinetic energy of 34.2 $\pm$0.9 Mev and the Q of the decay of the free Λ^0 (37.3 $\pm$0.5 Mev) is 3.1$\pm$1.4 Mev. This represents the binding of the Λ^0 in the ${}_2He^{4*}$ nucleus and is much lower than the 20 Mev with which the last neutron is bound in ${}_2He^4$. The apparent low binding of the Λ^0 seems characteristic of Λ^0 hyperfragments which decay mesonically.[3] This is a somewhat surprising feature of hyperfragments if the Λ^0-nucleon force has the same field theoretic origin as the nucleon-nucleon force. The same choice of the Λ^0-nucleon well parameters as exist in the case of the nucleon-nucleon interaction would result in a greater binding of the Λ^0 because of its greater rest mass. In addition, in a hyperfragment containing two or more neutral particles, the Λ^0 would be bound more strongly than an equivalent neutron because of the nonoperation of the Pauli principle between the Λ^0 and a neutron. Although the role of many-body nuclear forces is not well understood, the apparent low binding of the Λ^0 in nuclear matter may be interpreted in terms of a Λ^0-nucleon interaction that is considerably weaker than the nucleon-nucleon interaction.

IV. THE HEAVY-MESON INTERACTION

The measured mass of the heavy meson initiating the primary event with the conservatively assigned limits of error encompasses the mass of the only certainly established heavy meson, the $\tau(m_\tau \sim 975 m_e)$. If it is assumed that the absorbed meson is a τ meson, the absorption schemes to be considered are:[6]

$$\tau^- + \text{“}p\text{+nucleons”} \rightarrow \text{“}\Lambda^0\text{+nucleons”} + \gamma \text{ (or } \nu) \quad (1a)$$

$$\rightarrow \text{“}\Lambda^0\text{+nucleons”} \quad (2a)$$

$$\rightarrow \text{“}\Lambda^0\text{+nucleons”} + \pi^0 \quad (2b)$$

$$\rightarrow \text{“}\Lambda^0\text{+nucleons”} + 2\pi^0 \text{ (or } \pi^+ \text{ and } \pi^-). \quad (2c)$$

In reaction scheme (1a), the maximum energy available in particles which interact strongly with nuclear matter is $\sim$35 Mev. This is well below the measured lower limit on the excitation energy and, therefore, this reaction mechanism must be discarded. Reaction mechanism (2a) releases $\sim$320 Mev in a particle which interacts strongly with nuclear matter. Only 50$\pm$8 Mev appears as a result of the absorption. Although this is a lower limit in the excitation since momentum is not conserved in the visible particles, the momentum unbalance is only 70$\pm$40 Mev/c. It therefore seems rather unlikely that the large fraction of excitation remaining undetected has been taken off by evaporation or recoil neutrons. The available energy in reaction scheme (2b) is 29 Mev, if the assumption is made that the π^0 produced in the absorption process escapes without further interaction with the nucleus in which it was produced. Since such an interaction cannot be ruled out, reaction scheme (2b) is a possible interpretation of the observed event. In a similar fashion, reaction scheme (2c) is also a possible interpretation if one or more of the mesons produced interacts with the nucleus. Indirect corroboration that one of reaction schemes (2)[7] is operative can be obtained by noting that there is some evidence that Λ^0's are produced in pairs with θ^0's in energetic π^- collisions in hydrogen. Copious production of Λ^0's via the above scheme automatically implies that the (τ, nucleon, Λ^0, π) interaction is strong. The apparent absence of τ^- stars in emulsions may be due to the fact that a Λ^0 particle is produced in the absorption act. This removes at least 180 Mev in excitation, and such events may easily go undetected if the Λ^0 is not fortuitously bound to an ejected fragment.

The authors wish to thank the people in the emulsion group who helped with various aspects of this problem; especially Dawn Copeland who found the event and Robert Danielson who exposed the plates.

Note added in proof.—H. DeStaebler [Phys. Rev. **95**, 1110 (1954)] has recently observed a stopping heavy meson in a multiplate cloud chamber. The absorption of the meson produces a Λ° and a L meson (π or μ). This cloud chamber event, therefore, parallels the emulsion event reported above.

[6] Emission of an additional γ ray (or neutrino) does not increase the energy available in interacting particles.

[7] In effect, reaction schemes 2a, 2b, and 2c are all aspects of the same interaction mechanism; in 2b and 2c the role of the pion field is assumed by one or more real mesons whereas in 2a, the pion field enters virtually through the interaction of the Λ^0 with the recoiling nucleons.

Search for the Production of μ-Meson Pairs by a 345-Mev Synchrotron Beam*

B. T. Feld, A. Julian, A. C. Odian, L. S. Osborne, and A. Wattenberg
Physics Department and Laboratory for Nuclear Science, Massachusetts Institute of Technology, Cambridge, Massachusetts
(Received August 9, 1954)

Observations made at 45° and 90° to a 345-Mev bremsstrahlung beam failed to indicate the production of pairs of μ^+-μ^- mesons from targets of Be and Al. From the run on Be at 45°, $\sigma(\mu \text{ pair}) < (4\times10^{-32}/16\pi^2)$ cm² (steradian)$^{-2}$ proton^{-1}. This upper limit is twenty times the value predicted by the Bethe-Heitler theory for a purely electromagnetic interaction. The result would seem to preclude any interaction between pairs of μ mesons and nucleons which is as large as 10^{-3} of the strength of the interactions of π mesons and nucleons.

I. INTRODUCTION

THERE is an increasing amount of quantitative evidence which shows that μ mesons are essentially heavy electrons.[1,2] Thus μ mesons do not appear to interact with other particles except through the electromagnetic field[3–5] or through a Fermi type of interaction (i.e., an interaction accompanied by the emission or absorption of neutrinos). From such experiments as those of Amaldi and Fidecaro[6] on the scattering of μ mesons, and those of Fitch and Rainwater[5] on μ mesonic atoms, it is possible to estimate that if there is a nonelectromagnetic interaction of *single* μ mesons with nuclei, its strength is less than 10^{-3} of the strength of the interaction of π mesons with nuclei.

The question arises as to what one can conclude concerning the possible interactions between nucleons and μ-meson *pairs*. Before the war, there was a considerable amount of theoretical work published on meson pair theories.[7,8] Several of these authors[8] showed that if there exists a nucleonic interaction of meson pairs, that the scattering of a single meson depends upon the type of coupling involved. Specifically, Jauch showed that one would not expect meson scattering if the pair was coupled by a pseudoscalar interaction. Therefore, from the data on the lack of scattering of mesons one can only say that if there is a μ-pair interaction (greater than 10^{-3} of the π interaction) it would have to be with pseudoscalar coupling.

After the war, Wentzel[9] and Tannenwald[10] explored theoretically some of the consequences of a pair theory model of π mesons. In Wentzel's model a charged π meson consisted of a charged muon bound to a neutral nuon, and the neutral π meson consisted of a pair of charged muons or neutral nuons.

One of the consequences of such a model is that from sufficiently excited nuclei one should observe the emission of μ mesons and of pairs of μ mesons. Peterson, Gilbert, and White[11] found that with a 322-Mev bremsstrahlung beam hitting a carbon target the number of μ mesons produced was 0.02±0.02 of the total production of π mesons. Wolff,[12] using Wentzel's model, calculated that for the spectrum employed in the experiment of Peterson *et al.*, they should have found the μ meson production was 6 percent of the total π-meson production. Mather, Martinelli, and Jarmie[13] looking for μ pairs found the production of such pairs was less that 6 percent of the production of π mesons. Therefore, there seems to be no experimental support for Wentzel's pair model of π mesons.

From the aforementioned data which set an upper limit on μ-meson production,[12,13] one can draw a more general conclusion, namely, if there is a nucleonic interaction with μ pairs, it is not commensurate with (and probably not even 10 percent of) the strength of the π-meson interaction. However, from these data, and in view of the ambiguity in interpreting the scattering data, one could not rule out the remote possibility that there is an interaction of μ-meson pairs with nucleons which is the order of several percent of the strength of the π-meson interaction. The present state of the π-meson theory of nuclear forces is certainly not sufficiently quantitative to rule out such a possibility. The experiments described here were undertaken to establish whether or not there was a nucleonic interaction of μ-meson pairs which was greater than 10^{-3} of the strength of the π-meson interaction.

It was mentioned at the very outset that μ mesons seem to be essentially heavy electrons. If they are simple Dirac particles, μ^+-μ^- meson pairs should be produced in a manner similar to the production of electron-positron pairs. The Bethe-Heitler[14] theory suitably

* This work was supported in part by the joint program of the Office of Naval Research and the U. S. Atomic Energy Commission.
[1] For a general discussion of the evidence up to 1951 see R. E. Marshak, *Meson Physics* (McGraw-Hill Book Company, Inc., New York, 1952), Chap. 6,
[2] Also see B. Rossi, *High Energy Particles* (Prentice Hall, Inc., New York, 1952), Chap. 4.
[3] W. D. Walker, Phys. Rev. **90**, 234 (1953).
[4] F. E. Driggers, Phys. Rev. **87**, 1080 (1952).
[5] V. L. Fitch and J. Rainwater, Phys. Rev. **92**, 789 (1953); L. N. Cooper and E. M. Henley, Phys. Rev. **92**, 801 (1953).
[6] E. Amaldi and G. Fidecaro, Phys. Rev. **81**, 339 (1951).
[7] For the literature up to 1945, see W. Pauli and N. Hu, Revs. Modern Phys. **17**, 267 (1945).
[8] For calculations on scattering, see R. Marshak and V. Weisskopf, Phys. Rev. **59**, 130 (1941); J. Weinberg, Phys. Rev. **59**, 130 (1941); J. M. Jauch, Helv. Phys. Acta **15**, 221 (1942).
[9] G. Wentzel, Phys. Rev. **79**, 710 (1950) and Progr. Theoret. Phys. (Japan) **5**, 584 (1950). The latter contains a survey of literature up to 1950.
[10] L. Tannenwald, Phys. Rev. **86**, 332 (1952).
[11] Peterson, Gilbert, and White, Phys. Rev. **81**, 1003 (1951).
[12] P. A. Wolff, Phys. Rev. **81**, 1056 (1951).
[13] Mather, Martinelli, and Jarmie, Phys. Rev. **82**, 973 (1951).
[14] W. Heitler, *The Quantum Theory of Radiation* (Oxford University Press, London, 1949), second edition, Chap. IV, pp. 194 ff.

modified for the heavier mass of the μ meson should give the cross section for the purely electromagnetic production of such pairs in the Coulomb field of a proton.[15] There is the interesting question of whether or not μ mesons have some complexity which reduces the probability of these particles being materialized in a purely electromagnetic field. From this point of view it would be extremely desirable to measure the purely electromagnetic production of μ^+-μ^- pairs. Unfortunately, the cross section predicted by the modified Bethe-Heitler formula is extremely small. Mather *et al.*[12] say that their result shows that the production of μ pairs is not greater than 10^5 times the cross section given by the Bethe-Heitler theory.

Although the experiments described here were undertaken as a search for a nucleonic interaction with μ pairs, it was felt that such a study would clarify the problems involved in trying to observe μ pairs from the purely electromagnetic interaction.

II. EQUIPMENT

A. Experimental Arrangement

A 345-Mev bremsstrahlung beam from the M.I.T. synchrotron was sent through a series of collimators and a clearing magnet. At the target the beam had a width of $\frac{3}{4}$ in. and was 2 in. high. The beam was monitored by two ionization chambers, one of which was in front and the other in back of the target. Targets of beryllium and aluminum metal were employed which were 4 in. and 1 in. long, respectively. One arrangement of the target, detectors, and their shielding is shown in Fig. 1.

Two detectors of the type shown in Fig. 2 were constructed especially for these measurements. The detectors consist of two tanks filled with cyclohexylbenzene containing 3 g of terphenyl and 18 mg of diphenylhexatriene per liter. The external tank (E) developed

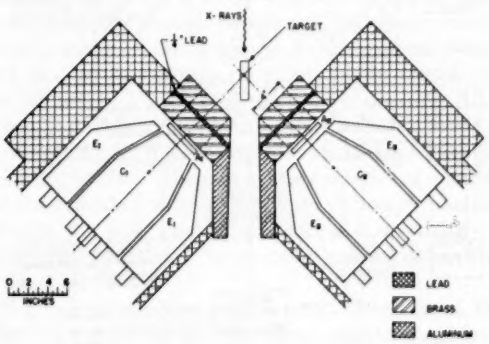

FIG. 1. μ^+-μ^- pair experimental arrangement. Detectors are at 45° to x-ray beam.

[15] For the case of $Z>1$, one has to consider the coherence in the production of the μ-meson pairs. This is discussed in the section on form factors under the heading of "Calculation of the Cross Section."

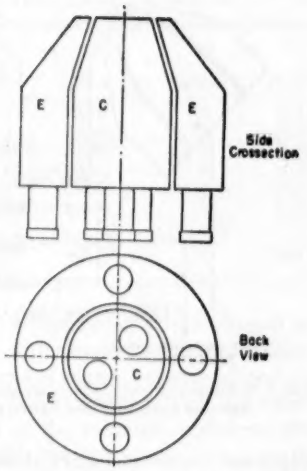

FIG. 2. μ-meson detector. Photomultipliers are RCA 5819.

from a desire to have a detector that did not have a direct view of the target, but which would observe the electrons following the decay of a μ meson in the central tank (C). Mu mesons were identified by the process $\mu^{\pm}\rightarrow e^{\pm}+2\nu$ with a mean life of about 2 μsec. It was required that the decay electron be observed in both the C and E detectors delayed relative to an event in C (see Sec. IIB).

The peculiar shape of these detectors arose from an attempt to optimize their efficiency and the solid angle they subtended at the target. The efficiency of these detectors was measured by counting the mesons arising from $\gamma+p\rightarrow\pi^++n$. The efficiency for detecting μ mesons that entered detector C was determined and found to be 60 percent, which checked the estimated design value.

In front of each special detector was a thin plastic scintillator (A) (Fig. 1) which was larger in diameter than C. The detectors A served dual purposes. Firstly, it was required that A and C be in coincidence (see Sec. IIB) for the incoming μ meson, and secondly, A had to be in anticoincidence with E and C at the time the decay electron was observed.

In order to decrease the spurious counting rate caused by scattered γ rays, a $\frac{1}{4}$-in. lead radiator was placed in front of detector A. With the above arrangement of the apparatus, and the biases employed on counters C, μ mesons which had a range of energies from 35 to 108 Mev were detectable.

B. Electronic Circuitry

The electronics can be looked upon as being separable into so-called fast electronics and conventional electronics. By fast electronics we mean coincidence circuits (and associated amplifiers, etc.) with resolving times of the order of 10^{-8} second; the conventional electronics was about ten times slower. Figure 3 shows a block diagram of the fast electronics. The circuitry was arranged so that counters AI and AII were in coinci-

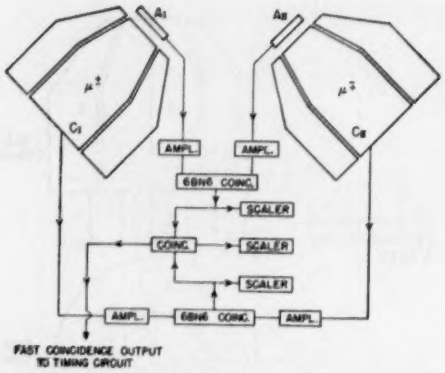

FIG. 3. Schematic of circuits for fast coincidences between μ mesons 200-ohm cable and distributed amplifiers are used.

dence and counters CI and CII were in coincidence. The resultant coincidences (AI and AII) and (CI and CII) were then put into fourfold coincidence. A pair of μ mesons would have triggered this fourfold coincidence circuit. The fast fourfold coincidence output was then sent through appropriate timing circuits to observe coincidences with delayed events. The operation of the fast fourfold coincidence circuitry and detectors was checked with electronically generated pulses and with the pulses arising from the conversion of the two γ rays from the decay of π^0 mesons.

The decay electron from a μ meson produced, as mentioned earlier, a coincidence of the type $(EI+CI-AI)$. If such an event occurred in detector I and was delayed relative to a fourfold coincidence $[(AI+AII)+(CI+CII)]$, it was recorded in one of five delayed channels. There was a similar five-channel delay circuit for such events from detector II. The first four of each of these sets of five channels were about 1.4 μsec long, and the fifth channel was about 10 μsec long.

If, following a fast fourfold coincidence, there were delayed events in both detectors I and II, then such an eightfold coincidence was recorded in one of a set of five delayed channels (see Fig. 4). The delay channel was determined by the time of arrival of the last of the two delayed events. With such an arrangement, the number of (spurious) accidental events increases linearly with delay time. One therefore obtains a large lever arm on the accidental events by using a delay as long as 20 μsec in the last channel. The first four channels were about 1.4 μsec long. If there were real μ-pair events, they would have appeared almost entirely in the first three channels.

III. DATA

The measurements were made over a rather long period of time, and the complexity of the equipment made frequent checking desirable. The individual scintillators had associated radium or cobalt standard. The timing of the circuits was checked by triggered synchroscopes and delay cables.

The most inclusive check on the proper functioning of the equipment was obtained by observing the $\mu^+ \rightarrow e^+$ decays from the π^+ mesons produced in the targets. The number of $\mu^+ \rightarrow e^+$ decays from the Be (or Al) target was measured about overy six hours during a long run. This standard checked the overall operation of everything except the two fast coincidence circuits. These latter were checked by the γ rays from a Co^{60} source.

Three separate measurements were made, each consisting of several runs lasting about eight to twelve hours each. With both detecting systems set at 90° to the beam and a Be target, no (eightfold coincidence) events were observed in a total of about 1.6×10^{11} equivalent quanta.[16] Similarly, with an Al target at 90°, no (eightfold coincidence) events were observed in a total of about 10^{11} equivalent quanta passing through the target. With the detecting systems set at 45° to the beam and a Be target and for a total of 5×10^{11} equivalent quanta, four (eightfold coincidence) events were observed in the first three delay channels (the channels where μ-pair events would appear). It can be estimated from the counting rates in the fourth and fifth delay channels (which arise from spurious accidental counts) that there should have been about 5.6 accidental counts in the first three channels, where we observed four. *Thus all events observed are attributable to an accidental (spurious) counting rate.* A check on this can be had from calculating the accidental counts that should have occurred in each of the eightfold delay channels from the registered events in the individual delay channels of detectors I and II. Such a calculation is based on the

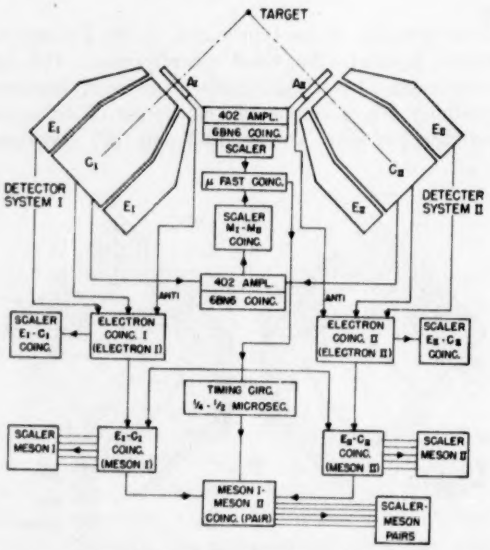

FIG. 4. Electronics for μ-pair detection. Five lines to scalers indicate five scalers for delay channels.

[16] The number of equivalent quanta, Q, in a beam is the energy in the beam divided by the maximum photon energy. Thus, for a $1/E$ spectrum, the number of quanta of energy E is $dN=QdE/E$.

TABLE I. Events observed in various delay channels and the estimated accidental events from the runs on Be at 45°.

Number of equivalent quanta	1		2		3		4		5	
	Observed	(Estimated accidental)	Obs	(Est.)	Obs	(Est.)	Obs	(Est.)	Obs	(Est.)
0.91×10^{11}	0	(0.05)	1	(0.25)	0	(0.43)	0	(0.48)	6	(7.1)
0.91×10^{11}	0	(0.36)	1	(0.27)	1	(0.40)	0	(0.38)	2	(3.0)
0.31×10^{11}	0	(0.05)	0	(0.06)	0	(0.04)	0	(0.17)	2	(1.7)
0.91×10^{11}	0	(0.18)	0	(0.40)	0	(0.51)	1	(0.70)	4	(4.4)
0.82×10^{11}	0	(0.15)	0	(0.40)	0	(0.72)	0	(0.65)	7	(4.8)
1.14×10^{11}	0	(0.27)	0	(0.47)	1	(0.63)	1	(0.69)	3	(3.4)
Total 5×10^{11}	0	(1.1)	2	(1.8)	2	(2.7)	2	(3.1)	24	(24.4)

assumption that all delayed events observed are purely random and that the fourfold fast coincidence arose from some real event such as two γ rays from a π^0 or a proton and π^- in coincidence. (The above assumption was corroborated by studies of counting rates as a function of beam intensity.)

Table I lists the events observed in various portions of the Be run at 45° and the calculated number of accidental events; the estimated accidental counts are in parentheses.

IV. CALCULATIONS OF CROSS SECTIONS

A. Cross Section per Atom

If we had observed any real events, the relationship between the cross section and the counting rate would have been given by

$$\text{counts/monitor unit} = (\Delta\omega)^2\epsilon^2\delta^2 N\int_{E_T}^{E_{\max}}\sigma\phi(E)g dE, \quad (1)$$

where $\Delta\omega$ is the solid angle subtended by each of the detecting systems; ϵ is the efficiency for counting the decay electrons from μ mesons that stop in the central tank; $(1-\delta)$ is the fraction of decay electrons which decay before the first delay channel goes on. N is the number of atoms per cm² in the target. σ is the double differential cross section which is a function of both angles. $\phi(E)$ is the number of photons of energy E (per monitor unit) which impinge on the target. E_T is the threshold energy and $E_{\max}$ is the maximum bremsstrahlung energy. g is the fraction of μ pairs that would be observable. All μ pairs are not observable because only a limited range of μ-meson energies (i.e., 35–105 Mev) are accepted by the detecting system. There is a broad spread of energies for the individual mesons even from monoergic photons because the pair production process is essentially a three-body reaction. (The recoiling nucleus or nucleon is the third body.)

We had an effective observational threshold of 290 Mev (i.e., $g\equiv0$ for $E<290$ Mev) even though it is energetically possible to produce μ-meson pairs as low as 220 Mev. Estimates of g were made on the assumption that the division of energy between the μ^+ and μ^- would be the same as the division of energy between e^+ and e^- as given by the Bethe-Heitler theory suitably scaled for the masses. A calculation of the integral in (1) was also performed with g evaluated on the assumption that all distributions of energy between μ^+ and μ^- were equally probable. This assumption leads to a value of the integral of half of the value calculated on the basis of the Bethe-Heitler theory.

The quantity g increases with energy from 0 at 290 Mev to about 0.75 at 345 Mev. The value of the other parameters in expression (1) are: $\Delta\omega=0.12$ steradian, $\epsilon=0.60$, $\delta=0.79$, $N=1.5\times10^{24}$ atoms/cm².

It is to be noted that the product $(\Delta\omega)\epsilon\delta$ was determined experimentally for each counter by measuring the number of π^+ mesons from the previously studied process $\gamma+p\rightarrow\pi^++n$.

In expression (1), the cross section of interest is contained in an energy integral. The integral was evaluated in two ways: one way was to assume that σ is a constant over the energy interval 295 to 345 Mev; the other way was to assume that σ varied as[17]

$$[(k-2)/k]^3,$$

where $k=$ photon energy divided by the rest energy of the particle. The value of the integral calculated on these two different assumptions differed by about 30 percent.

On the basis of the data previously described and summarized in Table I, it cannot be concluded that any μ-pair events were observed. Under the circumstances, all that one can do is set an upper limit on the cross section. The last column of Table II lists the values of the cross sections we would have obtained had we seen one real event in each of the 90° cases or one and a half

TABLE II. Summary of experimental results.

Angle of detectors	Target	Number of equivalent quanta	Number of events observed	Estimated accidental events	Upper limit to cross section[a] cm² sterad^{-1} atom^{-1}
90°	Be	1.6×10^{11}	0	0	5×10^{-33}
90°	Al	1.0×10^{11}	0	0	20×10^{-33}
45°	Be	5×10^{11}	4	5.6	6×10^{-33}

[a] These upper limits are based on the assumption that there is no angular correlation in the emission of the two mesons.

[17] P. V. C. Hough, Phys. Rev. **73**, 266 (1948). This paper gives a convenient approximation for the Bethe-Heitler formula in the region where $\hbar\omega\lesssim3mc^2$.

real events at 45°. (This latter comes from the experimental result -1.6 ± 3.1 events.)

B. The Cross Section per Proton and the Question of Coherent Production

It is of interest to try to convert the above values into upper limits on the cross section *per proton*. If we assume that there is no spin flip of a nucleon involved in producing a μ pair, and that only protons contribute, we find the cross section per atom from a nucleus of Z protons is given by

$$\sigma_A(\theta)=\sigma_p(\theta)[Z+Z(Z-1)F(KR)], \qquad (2)$$

where $\sigma_A(\theta)$ is the cross section per atom (for angle θ), σ_p is the cross section per proton, Z is the number of protons, and F is a form factor that depends on R, the nuclear radius, and K, which is the difference between the momentum of the incoming photon and the resultant momentum of the outgoing mesons.

As usual with form factors, F falls off very rapidly for $KR>2$ and is relatively independent of the charge distribution. For the runs at 90°, F is the order of 10^{-2} or less. For the run with Be at 45°, F has an average value of about 0.5 for the observable μ-meson energies. Therefore, if the production is coherent, the Be run at 45° is the most significant one. Using this value for the form factor, and assuming only the protons contribute, one obtains an upper limit to the cross section for the production of μ pairs at 45° of 6×10^{-34} cm^2 (sterad)$^{-2}$ proton^{-1}. This value appears misleadingly small because of the fact that it is the double differential; it is perhaps seen in better perspective when written in the form $(4\times10^{-32}/16\pi^2)$ cm^2 (sterad)$^{-2}$ proton^{-1}.

If the process involved in the production of μ pairs was an incoherent one (e.g., one that flipped the spin of a nucleon), one might look a little more closely into the kinematics. For incoherent production it is to be anticipated that a single nucleon probably takes up the entire recoil, and the rest of the nucleus would play a very minor role. For such processes, with the detectors at 90°, a single nucleon would have to take 50 Mev to balance momentum. As the maximum energy of the bremsstrahlung was at 345 Mev and the observational threshold for the μ meson was 290 Mev, there was very little probability for us to observe incoherent production at 90°. Measurements at large angles at such energies are therefore of very little significance in trying to detect μ-pair production; unfortunately, going to higher energies raises the possibility of π-meson pair production.

At 45°, if the production process were an incoherent one, the single nucleon would have 15 Mev of recoil energy. This reduces slightly the fraction of the spectrum from which production is observable. [The $Z(Z-1)$ term of expression (2) is zero for incoherent processes.] If the process were completely incoherent and if only the protons contributed, the upper limit to the cross section would be about $(1.5\times10^{-31}/16\pi^2)$ cm^2 (sterad)$^{-2}$ proton^{-1}. However, it would be very surprising if the neutrons, as well as the protons, did not contribute to a spin-dependent production process; in this case, the last value should be divided by approximately two.

V. DISCUSSION

A. Nuclear Forces

The upper limit obtained above is several orders of magnitude lower than those discussed in the introductory section. The first conclusion that one can draw is that the μ-pair model of pions[9] is not a correct one.

One can also set a crude upper limit on the contribution to nuclear forces that can arise from an interaction between μ pairs and nucleons. The upper limit for nuclear forces comes from comparing the upper limit for μ-pair production,

$$(4\times10^{-32}/16\pi^2) \text{ cm}^2 \text{ (sterad)}^{-2} \text{ proton}^{-1}$$

to the cross section for π-meson production [about $(2\times10^{-28}/4\pi)$ cm^2 sterad^{-1} proton^{-1}].[18] From these values it seems safe to say that if there is any contribution of μ-meson pairs to nuclear forces it is less than 10^{-3} of the strength of the π-meson interaction.

B. Electromagnetic Pair Production

As mentioned earlier, if μ mesons obey the Dirac theory, they should be produced in pairs according to a modification of the Bethe-Heitler theory. For the two detectors set at 45°, and for energies which were observable in our measurements, the Bethe-Heitler (modified for mass) predicts an average cross section of $(2\times10^{-33}/16\pi^2)$ cm^2 (sterad)$^{-2}$ proton^{-1}. Our upper limit of $(4\times10^{-32}/16\pi^2)$ cm^2 (sterad)$^{-2}$ proton^{-1} means that if we wished to study the electromagnetic production of μ-meson pairs, we would have to reduce our accidental counting rate by a factor of at least twenty.

ACKNOWLEDGMENT

We wish to thank J. S. Clark for the use of his detectors in the preliminary phases of these measurements. The authors are also indebted to A. Winston for assistance with the electronics and to H. Myers and P. C. Stein for help during many long runs.

[18] G. S. Janes and W. L. Kraushaar, Phys. Rev. 93, 900 (1954).

Composition of the Primary Cosmic Radiation at $\lambda = 10°$ N†

G. W. McCLURE
Bartol Research Foundation of The Franklin Institute, Swarthmore, Pennsylvania
(Received August 9, 1954)

A balloon-borne instrument comprising a fast ionization chamber interposed in a G-M counter train has been flown near the geomagnetic equator for the purpose of determining the fluxes of protons and He nuclei in the primary cosmic radiation. The apparatus measures the specific ionization of each particle that traverses the telescope, and contains a shower detector to aid in the identification of multiple-particle events of either local or external origin. Under the assumption that all telescope coincidences resulted from particles incident within the counter-defined solid angle, the total vertical flux, extrapolated to the "top of the atmosphere," is $I_{\text{total}} = 260$ sterad^{-1} m^{-2} sec^{-1}. The "top"-extrapolated fluxes of primary protons and He nuclei deduced from the ionization distributions recorded at various depths (17 g/cm^2 and greater) are as follows: $I_H < 145$ sterad^{-1} m^{-2} sec^{-1}; $I_{He} < 38$ sterad^{-1} m^{-2} sec^{-1}. The large difference between I_{total} and $(I_H + I_{He})_{\max}$ is believed to arise from air showers and/or nuclear events produced by particles incident from outside the telescope solid angle. The consequences of neglecting these spurious effects in interpretating counter-telescope measurements are discussed with particular reference to influences on the deduced form of the primary-proton energy spectrum, and the total energy flux associated with the primary radiation.

I. INTRODUCTION

THE primary cosmic radiation is believed to consist of protons, α particles and heavier nuclei roughly in the intensity ratio 85:15:1. While the protons are the most abundant component above the atmosphere, the heavier particles split up in atmospheric collisions yielding a total flux of proton and neutron fragments comparable to the primary proton flux at depths of the order of 40 g/cm^2. Because of their relatively large flux, the He nuclei play an especially important role in the atmospheric production of secondaries. In addition to contributing to our understanding of the cascade development of the cosmic radiation, knowledge of the absolute flux and energy spectrum of the primary α-particles may assist materially in establishing the origin of cosmic rays.

The α-particle flux has been measured at a number of latitudes by means of various devices including low-pressure G-M counters,[1-3] photographic emulsions,[4,5] scintillation counters,[6] proportional counters,[7,8] Čerenkov detectors,[9] and a combination cloud chamber, Čerenkov detector.[10] In general, the precision of the measurements has left much to be desired owing partly to large statistical uncertainties and partly to difficulties encountered in the interpretation of the experimental data.

The present work describes the results of an α-flux measurement conducted near the geomagnetic equator with an instrument which incorporates the best features of several of the methods employed earlier by other investigators. The method is similar in principle to that used by Perlow at $\lambda = 41°$, but utilizes a high-pressure ionization chamber instead of proportional counters to ascertain the specific ionization of individual incoming particles. The present method has no fundamental superiority over the proportional-counter method, but provides ionization resolution and stability equivalent to that of Perlow's arrangement with much simpler electronics.

An earlier form of the ion chamber instrument was designed for use in a cosmic-ray survey conducted in India in 1952–53.[11] Owing to time limitations and the small load-carrying capacity of the balloons available, it was necessary to make several sacrifices in the original design. The present refined version of the instrument overcomes many of the earlier inadequacies by including a pulse-height recorder and a multi-counter shower detector to aid in the identification of showers and other multiple-particle events which can yield ionization pulses of the same size as those produced by α particles.

With these refinements there still remains some ambiguity as to the identification of α-particle events, however it is possible to obtain with the instrument in its present form upper limits on both the primary proton and He intensities which probably do not differ appreciably from the true fluxes. In addition some important conclusions regarding the seriousness of spurious telescope-triggering events are obtained. Inasmuch as the present proton-flux upper limit is substantially lower than values deduced from earlier G-M counter measurements, the proton data are perhaps the most interesting aspect of the experimental results.

† Assisted by the joint program of the U. S. Office of Naval Research and the U. S. Atomic Energy Commission.

[1] S. F. Singer, Phys. Rev. **76**, 701 (1949).
[2] M. A. Pomerantz and F. L. Hereford, Phys. Rev. **76**, 997 (1949).
[3] S. F. Singer, Phys. Rev. **80**, 47 (1950).
[4] Goldfarb, Bradt, and Peters, Phys. Rev. **77**, 751 (1950).
[5] B. Peters, *Progress in Cosmic Ray Physics* (North Holland Publishing Company, Amsterdam, 1952), Vol. 1, Chap. IV.
[6] E. P. Ney and D. M. Thon, Phys. Rev. **81**, 1069 (1951).
[7] Perlow, Davis, Kissinger, and Shipman, Phys. Rev. **88**, 321 (1952).
[8] Davis, Caulk, and Johnson, Phys. Rev. **91**, 431 (1953).
[9] J. R. Winckler and K. Anderson, Phys. Rev. **93**, 596 (1954).
[10] J. Lindsley, Phys. Rev. **93**, 899 (1954).
[11] M. A. Pomerantz, J. Franklin Inst. (to be published).

II. DESCRIPTION OF THE APPARATUS

A diagram of the counter telescope is shown in Fig. 1. The four counters C_1, C_2, C_3, and C_4 (glass walls, Aquadag cathodes, effective dimensions 17.8 cm×3 cm) define the acceptance solid-angle of the instrument. The basic requirement for an event to be recorded is that these counters be discharged in coincidence. The tray S serves as a shower detector and functions as such whenever two or more of the seven counters it contains are discharged in coincidence with $C_1C_2C_3C_4$. Owing to the thickness of the counter envelopes, adjacent counters of tray S have spaces of approximately 1.6 mm between their internal "active" volumes. All counters contain a mixture composed of 86 percent argon and 14 percent butane at a total pressure of 100 mm Hg.

The ionization chamber is of the fast, electron-collection variety, filled with 99.9 percent pure argon at a pressure of 300 psi. Internal constructional details are the same as those of an earlier design described elsewhere.[12] Pulses from a calibration Po-α source built into the ion chamber wall (operative only during ground tests) reach voltage saturation at a cathode potential of 800 volts. A single 1000-volt battery operates the ion chamber in the region of pulse-height saturation and supplies the proper operating potential for the G-M counters.

The general arrangement of the electronics is indicated in the block diagram, Fig. 2. Each quadruple coincidence $C_1C_2C_3C_4$ (10-μsec resolving time) intensifies for 50 μsec the "spot" on the screen of a 3-inch cathode-ray tube, (C.R.T.), and triggers simultaneously a sweep circuit which generates a linear "sawtooth" wave form. The amplified ionization chamber pulse causes a vertical deflection of the C.R.T. spot proportional to the ionization of the particle initiating the main fourfold coincidence. When no shower is detected, the sweep sawtooth is allowed to pass the clamping circuit and a voltage *vs* time oscilloscope presentation of the ion-chamber pulse results. When two or more counters of tray S are discharged simultaneously with $C_1C_2C_3C_4$, indicating a multiple-particle or "shower" event, the clamping circuit prevents the sawtooth pulse from reaching the horizontal deflection plates and the ion-chamber pulse appears on the C.R.T. as a vertical "spike" with no horizontal extension. Thus, events accompanied by showers are clearly distinguished from those in which no shower is detected. All pulses appearing on the C.R.T. screen are recorded on a continuously moving 16-mm photographic film.

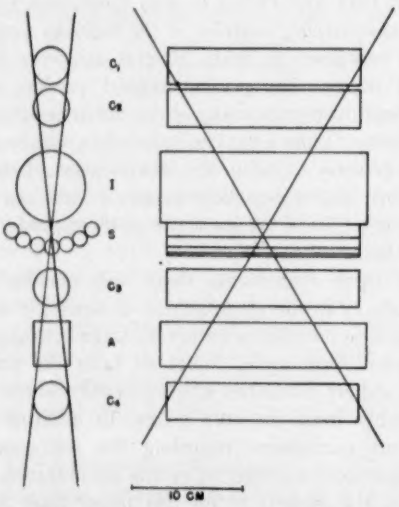

FIG. 1. Diagram of counter telescope. C_1, C_2, C_3, C_4—G-M counters. S-shower tray containing seven G-M counters. I-electron collection ionization chamber. A—4 cm Pb absorber.

The ion-chamber linear amplifier comprises three stages with 0.025 percent inverse feedback and has an over-all gain of 4000. The frequency band width of the amplifier is adjusted to provide the best signal to noise ratio consistent with the accurate preservation of the ion-chamber pulse shape. The rise time of the chamber pulses as viewed at the amplifier output is 10 μsec and the decay time about 100 μsec. Through selection of the (6AK5) amplifier input tube it was possible to attain an amplifier noise level less than one-tenth the average amplitude of the pulses produced by sea-level mesons.

The output pulses from the linear amplifier are fed into a push-pull output stage which provides additional amplification required to drive the oscilloscope. The 10-μsec delay-line between the linear amplifier and scope amplifier allows the horizontal sweep and intensifier circuits to start before the ion-chamber pulse arrives at the vertical deflection plates. This delay provides a clearly-defined base line for each pulse, eliminating any difficulty that might arise from low-frequency amplifier microphonics or gradual drift of the quiescent position of the oscilloscope spot. In a shower event, where the horizontal sweep does not operate, the base of the ion-chamber pulse is marked by a bright spot where the intensified oscilloscope beam rests for several μsec prior to the onset of the pulse.

The set of instruments surrounding the screen of the C.R.T. includes a thermometer, a clock, and a mercury manometer. The manometer indicates atmospheric pressure to within ±0.5 mm in the range 0–70 mm Hg. Readings of these instruments are recorded on the film by momentary scale illumination at 5-minute time intervals. One-minute time markers also appear on the film record. An aneroid barometric switch attached to the outside of the flight gondola operates a light near the oscilloscope, marking the film at predetermined pressure-intervals in the range of altitudes below the operating threshold of the 70-mm manometer. In this

[12] M. A. Pomerantz and G. W. McClure, Phys. Rev. 86, 536 (1952).

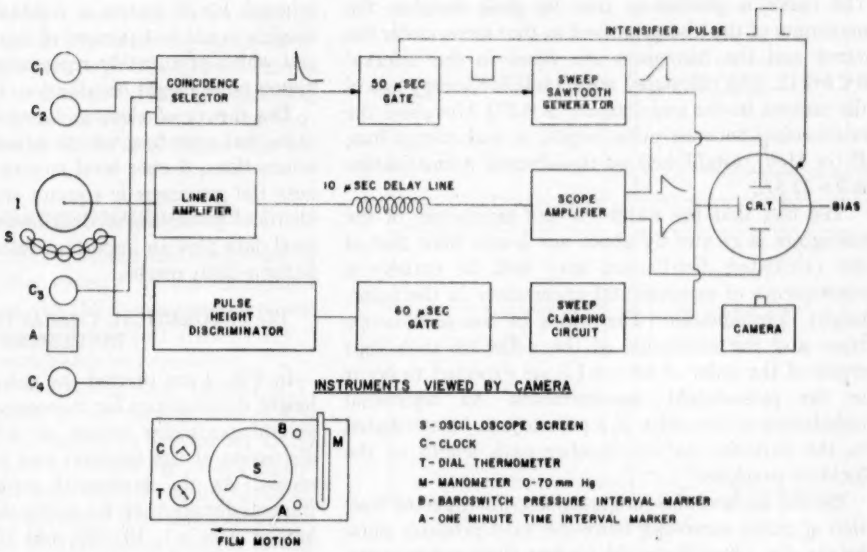

FIG. 2. Circuit block-diagram and arrangement of instruments viewed by camera.

manner, a complete time-altitude record directly correlated with the cosmic-ray pulses is obtained at all altitudes.

The 4-cm Pb absorber interposed in the telescope at position A is intended to prevent the triggering of the instrument by slow protons whose specific ionization is such as to cause confusion with relativistic α-particle events.

The entire apparatus including the oscilloscope and camera recorder is contained in a 24-in. diameter aluminum sphere sealed at 1 atmosphere in order to eliminate high voltage corona troubles, and to preserve the film record in cases where the instrument might land on water. In flight the gondola is wrapped in three loosely-fitting pliofilm bags to provide warmth by the "greenhouse" effect.

III. SEA-LEVEL TESTS

A preliminary account of sea-level results obtained with the present type of ion chamber mounted in a modified form of G-M counter train has been published previously.[13] Results obtained with the actual balloon-borne apparatus at $\lambda = 52°$ are shown in Fig. 3. In order to simulate actual flight conditions as nearly as possible, a battery pack identical to that used in flight was employed in the ground tests. The shapes and heights of the pulses were ascertained by projection of the film record on the screen of a 16-mm film editor. Within statistical uncertainties, the pulse-height distributions obtained in the first and final halves of the 445-min. run analyzed in Fig. 3 were identical. The excellent stability of the instrument against battery strength depletion is indicated by the fact that the average pulse height during the two time intervals differed by less than 2 percent.

[13] G. W. McClure, Phys. Rev. **87**, 680 (1952).

The pulse height $h = 6.1$ in the scale of Fig. 3 and all subsequent data presentations corresponds approximately to the most probable ionization of the cosmic rays at sea level. The distribution of pulse heights above and below the peak is attributable to: (1) statistical fluctuations in gas ionization arising from the finite number and large energy spread of the primary knock-on electrons;[14,15] (2) inhomogeneity of energy and particle composition of the incident radiation; (3) variation in path length of particles traversing the ion chamber; and (4) experimental uncertainties in the measurement of pulse height.

Neglecting (3) and (4), which have a minor broadening effect, we have calculated the shape of the pulse height distribution to be expected on the basis of the Symon theory of energy-loss fluctuations[15] and the sea-level meson spectrum of Wilson.[16] The smooth curve in Fig. 3 represents the calculated distribution.

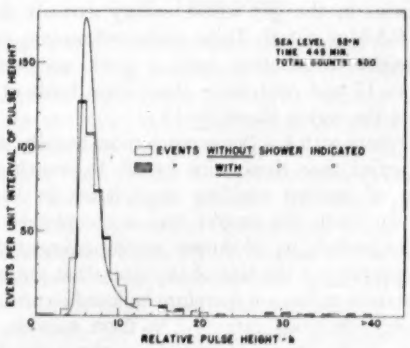

FIG. 3. Sea level differential pulse-height distribution ($\lambda = 52°$ N).

[14] L. Landau, J. Phys. (U.S.S.R.) **8**, 201 (1944).
[15] K. R. Symon, thesis, Harvard University, 1948 (unpublished).
[16] J. G. Wilson, Nature **158**, 414 (1946).

The curve is plotted so that its peak matches the maximum of the histogram and so that areas under the curve and the histogram are equal in the interval $0<h<12$. The calculated most probable energy loss of the mesons in the ion chamber is 0.272 Mev, and the relationship between pulse height, h, and energy loss, E (in Mev), established by the abscissa normalization is $h=22.5E$.

The fact that the width (at half-maximum) of the histogram is greater by about one h-unit than that of the calculated distribution may well be entirely a consequence of experimental uncertainty in the pulse-height determination. The width of the oscilloscope trace and the amplitude of the noise are such that errors of the order of $\Delta h=\pm 1.0$ are expected to occur in the pulse-height measurements. An additional broadening of the order of 5 percent can be attributed to the variation in ion-chamber path length of the incident particles.

On the basis of the computations, the expected fraction of pulses exceeding twice the most probable pulse height (i.e., $h=12$) should be less than one percent. The number of events with $h>12$ actually observed is 11 percent of the total. Of these, about one-third (mostly shower-accompanied) are larger than $h=20$. The larger size of the histogram "tail" can neither be attributed to errors in pulse-height measurement, nor to geometrical effects, and is believed to arise in part from electrons knocked out of the chamber walls by the incoming mesons—roughly 9 percent of the mesons should be accompanied by such knock-ons[17,18]—and partly from approximations made in our selection of fluctuation-function parameters. (We assumed that the maximum energy transferred to a secondary electron in the gas is equal to the value 0.3 Mev, for which the electron range in the argon equals the radius of the chamber. In so doing we attempted to compensate roughly for the energy "lost" by long range secondaries which are produced in the gas and stop in the chamber walls. According to the knock-on theory,[19] about 5 percent of the sea-level mesons produce one or more secondaries in the gas whose energy exceeds the assumed 0.3-Mev cutoff. These neglected mesons yield a pulse-height distribution with a peak occurring at about $h=12$ and contribute about two-thirds of their pulses to the region above $h=12$.)

The events with $h>20$ are much more heavily shower accompanied than those with $h<20$. Inasmuch as the fraction of mesons yielding secondaries in the gas which can reach the shower tray is completely negligible, the probability of shower accompaniment should be independent of the size of the ionization pulse. The larger shower pulses are therefore believed to arise from cosmic-ray electrons rather than from mesons. Subtraction of the shower events from the pulse height interval $h>20$ leaves a residual tail whose area is roughly equal to 1 percent of the total histogram area, and which presumably represents the high end of the meson pulse-height distribution.

The theory of electron knock-on production[19] indicates that aside from effects introduced by local nuclear interactions, the sea-level mesons and primary protons near the geomagnetic equator should yield practically identical pulse-height distributions. Hence, the sea-level data play an important role in the analysis of the balloon-flight results.

IV. THEORETICAL CHARACTERISTICS OF THE INSTRUMENT

In Fig. 4 are plotted the calculated integral pulse-height distributions for monoenergetic particles having several particular values of p/mc pertinent to the discussion of the sea-level and high-altitude measurements. As the horizontal separations between the integral distributions for singly-charged particles ($z=1$) having $p/mc=1$, 10, 100, and 1000 are comparable to the experimental pulse-height resolution, the instrument cannot be expected to yield detailed information on energy spectra of relativistic particles.

The manner in which the tail of the theoretical distribution for monoenergetic particles with $p/mc\approx 10$ must be modified in accordance with the sea-level observations is indicated by the dot-dash curve. (The sea-level momentum spectrum is peaked at $p/mc\simeq 18$ and all but a few percent of the mesons belong to the interval $2<p/mc<200$.) Also shown is the calculated distribution for primary alpha particles having momenta equal to the geomagnetic cutoff in the vertical direction at $\lambda=10°$ ($p/mc\simeq 7$). It is evident from inspection of these curves that relativistic protons and π mesons which traverse the ion chamber unaccompanied by secondaries from nuclear events contribute practically no pulses above the pulse-height threshold for relativistic α particles.

The curves labeled P and P' are the integral pulse-height distributions for the lowest energy protons (208 Mev) which can penetrate the telescope material. The former is the limiting curve for protons which enter from above the telescope moving downward, and the latter for those which enter from below proceeding

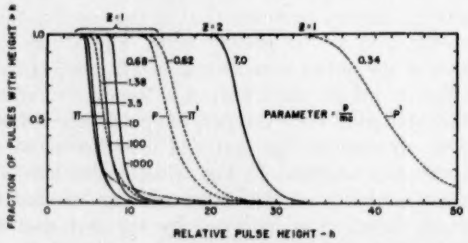

FIG. 4. Calculated integral pulse-height distributions for singly-charged ($Z=1$) and doubly-charged ($Z=2$) particles having various values of parameter p/mc.

[17] Brown, McKay, and Palmatier, Phys. Rev. 76, 506 (1949).
[18] F. L. Hereford, J. Franklin Inst. 249, 449 (1950).
[19] H. J. Bhabha, Proc. Roy. Soc. (London) 164, 257 (1938).

upward. The corresponding curves for the lowest energy π mesons (107 Mev) capable of penetrating the absorber are labeled π and π' respectively. The primed curves P' and π' are displaced to the right of the corresponding unprimed curves, owing to the asymmetrical distribution of stopping material above and below the ion chamber.

V. BALLOON-FLIGHT OBSERVATIONS

Two instruments of the type described were flown in September, 1953 in the vicinity of the Galapagos Islands as one phase of the ONR-sponsored Skyhook balloon expedition designated "Project CHURCHY." Only one of the two instruments was recovered.

The successful flight was launched at 1430 G.M.T. on September 6, ascended at an average rate of 720 ft/min until 1635 G.M.T. and then leveled off at an atmospheric depth of 12.5 to 13 mm Hg for 4.2 hours. The gondola drifted due west while at ceiling altitude, and descended at a point about 400 miles from the launching-site. The time *vs* atmospheric pressure record of the flight obtained independently by General Mills, Inc., agreed within ± 0.5 mm with pressure readings on the film record.

The temperature inside the gondola was 19°C at the beginning of level-off, slowly decreased to a minimum of 4°C after 3 hrs. at altitude and then gradually increased, reaching 8°C at the time of descent. Data recorded during the first and last halves of the period of level flight agreed within statistical uncertainties, giving no indication of adverse effects associated with the temperature variations.

Preflight calibration of the instrument in the field with Po-α particles and sea-level mesons verified that the relationship between pulse height and energy loss was the same as in the sea-level tests described above.

The differential pulse-height distribution recorded during the 255-min level-off period at 12.5–13.0 mm Hg

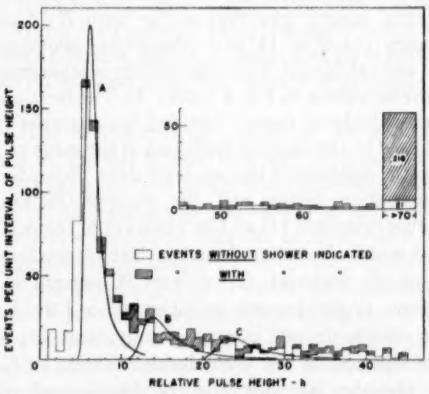

FIG. 5. Differential pulse-height distribution recorded at 12.5–13 mm Hg, $\lambda = 10°$ N (histogram). Curves *A*, *B*, and *C* are calculated pulse-height distribution for primary protons, 208-Mev protons and He nuclei (of geomagnetic cutoff energy) respectively.

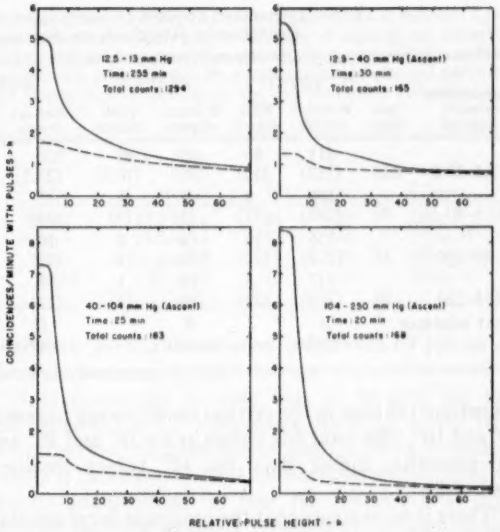
12.5 - 13 mm Hg
Time : 255 min
Total counts : 1294
12.9 - 40 mm Hg (Ascent)
Time : 30 min
Total counts : 165
40 - 104 mm Hg (Ascent)
Time : 25 min
Total counts : 183
104 - 250 mm Hg (Ascent)
Time : 20 min
Total counts : 159
COINCIDENCES/MINUTE WITH PULSES > h
RELATIVE PULSE HEIGHT - h

FIG. 6. Integral pulse-height distributions recorded at various altitudes. Smooth curves = total counting rate. Dashed curves = shower counting rate.

is shown in Fig. 5, and integral distributions corresponding to this and three lower altitude intervals traversed during the ascent are plotted in Fig. 6. Numerical data used in the analysis are given in Table I.

Many pulses which saturated the amplifier were recorded. The tops of the saturation pulses appeared below the upper edge of the oscilloscope screen and are clearly visible on the film record, so that few events, if any, could have been overlooked in scanning the film. All pulses are counted in calculating the apparent total flux discussed in the next section, but only those in the range $0 < h < 70$, which are undistorted by the amplifier, are considered in the detailed analysis.

VI. ANALYSIS OF BALLOON-FLIGHT RESULTS

A. Total Flux

Figures 5 and 6 and the last two columns of Table I indicate that a large percentage of the recorded events high altitudes are multiple-particle or "shower" events. It will be shown at the conclusion of the analysis that not all of the showers which occur near the "top of the atmosphere" are caused by local nuclear events produced in the telescope material by single particles incident within the counter-defined solid angle. Nevertheless it is of some interest to compare the "apparent" total intensity—computed with the usual assumption that all counts result from telescope-oriented incident particles—with the results of other investigations in equatorial regions. The pertinent total flux measurements are listed in Table II. The present results for $\lambda = 10°$ agree very closely with prior measurements at $\lambda = 0°$ and 3° as is to be expected from the small

TABLE I. Observed numbers of events in various pulse-height categories *vs* atmospheric pressure. Quantities in parenthesis are corresponding flux values; units sterad^{-1} m^{-2} sec^{-1}.

Atmospheric pressure interval	Time (min)	$0<h<12$ Without shower	$0<h<12$ With shower	$12<h<20$ Without shower	$12<h<20$ With shower	$20<h<48$ Without shower	$20<h<48$ With shower	$48<h<70$ Without shower	$48<h<70$ With shower	$h>70$ Without shower	$h>70$ With shower	Totals Without shower	Totals With shower	With and without
12.5–13.0	255	611 (132)	56 (12)	95 (21)	49 (10.6)	118 (25.5)	81 (17.5)	14 (13)	40 (18.7)	21 (4.5)	209 (45)	859 (186)	435 (94)	1294 (280)
12.5–40	30	104 (190)	9 (17)	5 (9)	5 (9)	13 (24)	5 (9)	0 (0)	1 (2)	2 (4)	21 (39)	124 (228)	41 (75)	165 (303)
40–104	25	126 (278)	10 (22)	14 (31)	2 (4)	10 (22)	8 (18)	0 (0)	3 (7)	1 (2)	9 (20)	151 (332)	32 (71)	183 (403)
104–250	20	127 (350)	8 (22)	14 (39)	1 (3)	8 (22)	3 (8)	1 (3)	2 (6)	1 (3)	3 (8)	151 (415)	17 (47)	168 (462)
Text reference		*A* events		*B* events		*C* events								

(5 percent) change in the vertical cutoff energy between 0° and 10°. The total flux values at $\lambda=18°$ and 20° are all somewhat higher than the 10° values obtained herewith.

There is no evidence that the unusually large amount of material placed near the slides of the counter telescope in the present experiment (70 lb of batteries, electronics, etc.) had an effect upon the telescope counting rate.

B. Relativistic Singly-Charged Particles

By comparing a measured pulse-height distribution with the calculated distribution for a group of incident particles having a pre-determined or assumed energy spectrum, it is possible to deduce an upper limit for the flux of particles in question. In performing such deductions, allowance must be made not only for ionization fluctuations but also for the possibility that the incident particles may undergo nuclear interactions in the telescope material thereby creating events of substantially larger ionization that would otherwise occur. (While the sea-level μ mesons do not give rise to such interactions, the protons, π mesons and α particles present in the high-altitude radiation probably give rise to a large number of locally-produced bursts.)

TABLE II. Total flux values near the equator.

Geomagnetic latitude	Flux of particles sterad^{-1} m^{-2} sec^{-1}	Absorber	Atmospheric depth	Author
0°	270±10	3 cm Pb	15 g/cm²	a
0°	310±10	No Pb	15 g/cm²	a
0°	280±40	No Pb	Rocket	b
3°	300±20	4 cm Pb	10 mm Hg	c
3°	240±10	4 cm Pb	Top extrapolated	c
3°	280±20	7.5 cm Pb	10 mm Hg	c
3°	230±10	7.5 cm Pb	Top extrapolated	c
10°	280±8	4 cm Pb	13 mm Hg	d
10°	260±8	4 cm Pb	Top extrapolated	d
18°	390±20	4 cm Pb	10 mm Hg	c
18°	350±10	4 cm Pb	Top extrapolated	c
18°	360±20	7.5 cm Pb	20 mm Hg	c
18°	330±10	7.5 cm Pb	Top extrapolated	c
20°	310±10	3.0 cm Pb	15 g/cm²	a

[a] Winckler, Stix, Dwight, and Sabin, Phys. Rev. **79**, 656 (1950).
[b] J. A. Van Allen and S. F. Singer, Phys. Rev. **78**, 819 (1950).
[c] M. A. Pomerantz, Phys. Rev. **95**, 531 (1954).
[d] Present work.

To derive flux-values for the various components, the recorded pulses are broken down into three main groups as follows: (1) Pulses in the interval $0<h<12$ most of which are produced by relativistic singly-charged particles ($E/mc^2>1.0$), (2) Pulses in the interval $12<h<20$ from which an upper limit can be established on the intensity of slow particles likely to interfere with the He flux determination, (3) Pulses in the interval $20<h<48$ from which will be derived an upper limit for the flux of relativistic He nuclei.

The letters *A*, *B*, and *C* denote events in categories (1), (2) and (3) respectively which are *unaccompanied by shower indications*. (Analysis of the shower events on the basis of this particular division of the data is not especially significant because the number of particles which traverse the chamber in any such event is unknown.) The symbols I_A, I_B, and I_C represent the fluxes of particles yielding events of types *A*, *B*, and *C* respectively. Numerical values of these fluxes are listed in Table III.

Using the Symon theory of energy loss fluctuations,[15] the pulse-height distribution of primary protons with an integral energy spectrum of the form $E^{-1.6}$ and a low-energy cutoff of 14 Bev (theoretical geomagnetic cutoff) was calculated. This distribution is superimposed upon the histogram in Fig. 5 (curve *A*). The relationship between calculated energy loss and ion-chamber pulse height used in the abscissa matching is the same as that used in the analysis of the sea-level data. According to the fluctuation theory and the sea-level calibration the *A* events include (1) all but 9 percent of the primary protons which do not undergo nuclear interactions in the telescope material, (2) at least 90 percent of the secondary singly-charged particles with $1.0<E/mc^2<14.0$, which do not interact locally, and (3) some smaller fraction of the secondaries with $0.22<E/mc^2<1.0$. (In the last instance the fraction of pulses contributed to the interval $0<h<12$ is strongly energy-dependent.)

Because of the limited resolution of the instrument

TABLE III. Fluxes I_A, I_B, I_C of particles yielding events of types A, B, and C respectively, and derived flux values as follows: I_A'—intensity of particles with $Z=1$ and $E_{kin}/mc^2>1.0$ corrected for ionization fluctuation only; I_A''—intensity of same group corrected for maximum effect of local nuclear interactions (upper limit); I_B'—intensity of slow particles—principally protons incident from below with $235<E_{kin}<348$ (see text); I_C'—intensity of He nuclei corrected only for ionization fluctuation of singly-charged particles. I_C'' intensity of He nuclei corrected for maximum effect of local nuclear interactions (upper limit). See text for further considerations regarding He intensity. Units—sterad^{-1} m^{-2} sec^{-1}.

Atmospheric pressure interval (mm Hg)	I_A	I_A'	I_A''	I_B	I_B'	I_C	I_C'	I_C''	I_{total}
12.5–13.0	132±5	145	210	20.6±2	10±2	25.5±2.5	24	39	280±8
12.5–40	190±19	209	304	9±4	−7±5	24.0±6.7	22	36	303±24
40–104	278±25	306	445	31±8	7±8	22.0±7.0	19	31	403±30
104–250	350±31	385	560	39±10	9±10	22±8.0	18	29	462±36

it is not possible to separate the primaries from either the relativistic or the slow secondaries in the categories (2) and (3). One can, however, derive an upper limit for the flux of particles with $E/mc^2>1.0$ which do not undergo local nuclear interactions by simply attributing all events in the interval $0<h<12$ to particles in categories (1) and (2) and making the indicated (9 percent) allowance for ionization fluctuations. When this correction is applied to the recorded A events one obtains the flux values I_A' listed in Table III. With a further correction for the maximum loss of pulses from the A group which could occur through the production of local nuclear interactions, the flux values I_A'' are obtained.

In calculating I_A'' we assume that every particle which passes within the "geometrical" radius of a nucleus anywhere in the telescope gives rise to a pulse not included in the A group, i.e., either a shower event or an ionization burst with $h>12$. To obtain the "geometrical" collision probabilities, we have used here and elsewhere in this paper cross sections given by the formula

$$\sigma=\pi r_0^2(A_1^{\frac{1}{3}}+A_2^{\frac{1}{3}}-1)^2, \quad r_0=1.38\times10^{-13}\text{ cm}, \quad (1)$$

where A_1 and A_2 are the atomic weights of the incident and target nuclei, respectively. Mean free paths calculated from this expression agree well with the data of Kaplon *et al.*[20] on α-particle and heavy-nucleus collisions in glass and brass, and the formula also gives reasonable values for collision mean free paths of single high-energy nucleons.

In view of the extreme nature of the applied correction for nuclear interactions and the possibility that the A events include some non-relativistic particles, I_A'' must be regarded as a conservative upper limit on the relativistic-particle flux in each altitude range. Comparison of the values I_A'' and I_{total} (plotted as a function of altitude in Fig. 7) yields the conclusion that *at most 75 percent of the telescope counting rate at 12 mm Hg can be attributed to relativistic singly-charged particles, including albedo, incident within the counter-defined solid angle. Extrapolation of the I_A'' and I_{total} curves to zero pressure indicates that at the "top of the atmosphere" the relativistic particle contribution is less than 60 percent of the telescope counting rate.*

It is interesting to note that at 50 mm Hg the calculated curve I_A'' rises above the I_{total} curve. This indicates that the correction of flux I_A' for local nuclear events is excessive, at least for particles encountered at depths greater than 50 mm Hg. Inasmuch as I_A'' exceeds I_{total} by a nearly constant percentage in the two lower altitude intervals, it would appear that the correction referred to above might be in error by approximately the same amount, percentagewise, over the entire range of altitude investigated, including the 12.5–13 mm Hg interval. If this were actually the case, the extrapolated flux of relativistic singly-charged particles at zero pressure would be <120 sterad^{-1} m^{-2} sec^{-1}, or less than half the extrapolated value of I_{total}.

We have attempted to estimate from photographic emulsion data on stars produced by high-energy protons the approximate fraction of proton traversals of the telescope which should give rise to nuclear interactions of the type that yield either a shower indication or an ionization pulse outside of the A interval. Such attempts

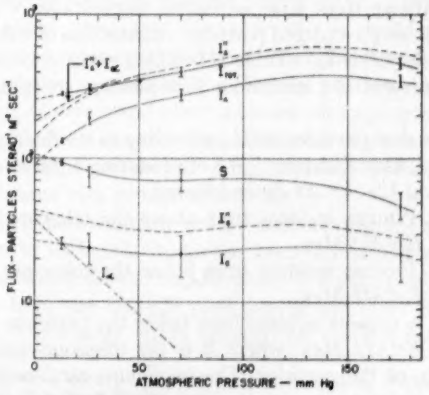

FIG. 7. Altitude variation of several measured and derived particle fluxes. I_A, I_B, I_C=fluxes of particles yielding events of types A, B and C respectively. I_A''=maximum flux of relativistic singly-charged particles (derived from curve I_A by applying corrections for large ionization fluctuations and removal of events from A group by nuclear interactions); I_C''=maximum flux of He nuclei derived from curve I_C; I_{He}=maximum flux of He nuclei to a more refined approximation (see text); S=effective flux of shower associated particles.

[20] Kaplon, Peters, Reynolds, and Ritson, Phys. Rev. **85**, 295 (1952).

are considered to be of somewhat dubious value since most of the emulsion stars for which the primary-particle energy has been established result from C, N, Ag, and Br collisions, whereas nearly all of the proton interactions in the counter telescope occur in the Pb absorber. The manner in which the multiplicity, energy distribution, and angular distribution of secondaries varies with the atomic weight of the struck nucleus, is as yet not completely known.

Finally it should be emphasized that the instrument is incapable of distinguishing between particles incident from the 0° and 180° zenith angles, so that the relativistic particle flux may include a substantial albedo contribution. The measurements of Anderson and Winckler[21] at $\lambda=10°$N (Čerenkov detector) indicate that the flux of relativistic singly-charged albedo amounts to approximately 15 percent of the total intensity. This would imply an albedo flux of approximately 40 sterad^{-1} m^{-2} sec^{-1} and would reduce our estimate of the primary proton flux to <100 sterad^{-1} m^{-2} sec^{-1}.

C. Slow Protons and π Mesons

In this section we attempt to estimate the flux of slow singly-charged particles capable of yielding ionization pulses of the same size as those produced by primary He nuclei. To obtain such an estimate we examine the slow-particle contribution to the recorded B events, i.e., events unaccompanied by shower indications with pulse-heights in the interval $12<h<20$. (The total flux of particles yielding this type of event is designated I_B, and is given for each altitude interval in Table III.) The minimum contribution to the flux I_B from particles whose most-probable pulse height is less than $h=12$ is $0.08\,I_A'$; this is simply the contribution arising from large ionization fluctuations of relativistic singly-charged particles. Subtraction of $0.08\,I_A'$ from I_B yields I_B' (Table III) which we shall consider to represent the maximum slow-particle contribution to I_B.

The slow particles which, according to the fluctuation theory, have a chance ≥ 0.5 of producing a pulse in the interval $12<h<20$ are as follows:

(1) Protons incident from above the telescope with $208<E<253$ Mev.

(2) Protons incident from below the telescope with $235<E<348$ Mev.

(3) π mesons incident from below the telescope with $107<E<113$ Mev, where E is the telescope-entrance energy of the particles. The maximum combined flux of particles in these categories, given by $2\,I_B'$, is less than 8 percent of the total intensity in each altitude interval.

The slow singly-charged particles most likely to yield pulses in the relativistic α-particle range ($h>20$) are protons incident from below the telescope with energies in the region $208<E<235$ Mev. Inasmuch as this range is only $\frac{1}{4}$ as wide as the adjacent energy interval listed under item (2) above, it appears that the flux of slow protons yielding pulses which might be confused with α-particle pulses is less than 2 percent of I_{total}. This is quite small compared to the intensity of particles producing "α-candidate" pulses (C events); consequently, the slow protons will be left out of the consideration in the following section.

D. Relativistic α Particles

The calculated integral and differential pulse-height distributions for α particles of the geomagnetic cutoff energy (7 Bev per nucleon) are shown in Figs. 4 and 5, respectively. The ionization fluctuations of relativistic α particles are such that, with any reasonable assumption regarding the primary energy spectrum, less than 1 percent of those α particles which do not undergo local nuclear collisions should yield pulses with $h>48$. Thus, the events in the interval $20<h<48$ which are not shower-accompanied (C events) will be assumed to include all of the α particles which traversed the telescope without undergoing nuclear collisions. Subtraction from the C events of the expected contribution from large ionization fluctuations of relativistic singly-charged particles yields the flux values I_C' listed in Table III. Correction of the fluxes I_C' for the maximum percentage (38 percent) of α-particle pulses which could have occurred outside the C-interval by virtue of local nuclear interactions yields the α-particle flux upper limits I_C''. The probability of α-particle interaction in the telescope material was calculated with the aid of the cross section formula given in Sec. VI, B.

Curves representing the altitude variation of intensities I_C and I_C'' are plotted in Fig. 7. Inspection of the form of curve I_C'' indicates that the lower-altitude values must be far in excess of the actual α-particle flux. If the flux at 12 mm Hg were equal to the calculated upper limit, 39 sterad^{-1} m^{-2} sec^{-1}, and if the atmospheric absorbtion occurs as expected from the collision cross-section formula, the α-flux should be less than 1.0 sterad^{-1} m^{-2} sec^{-1} in the lowest altitude interval, as compared with the calculated upper limit 29 sterad^{-1} m^{-2} sec^{-1}.

If we assume that the spurious C events (i.e., those produced by particles other than α particles) are in equilibrium with the vertical flux of relativistic singly-charged particles in the interval 0–180 mm Hg—as is suggested by the approximate constancy of the ratio I_C/I_A in the interval 40 to 250 mm Hg—we obtain a revised α-flux value of 26 sterad^{-1} m^{-1} sec^{-1} at 12 mm Hg. The curve I_α in Fig. 7 is normalized to this value and is drawn with a slope corresponding to the expected atmospheric absorbtion of primary α particles (mean free path 44 g/cm^2). The zero-pressure intercept of curve I_α, 38 sterad^{-1} m^{-2} sec^{-1}, is believed a conservative upper limit for the primary α-particle flux at $\lambda=10°$.

[21] K. Anderson and J. R. Winckler (private communication).

It is interesting to note that if one computes from curve I_α the expected flux of proton fragments arising from the break up of vertically directed α particles, the computed flux accounts almost completely for the apparent transition (rapid change of slope) of the curve I_A in the top 50 g/cm² of the atmosphere. Proton fragments of heavier nuclei may also contribute to the indicated transition, but, according to existing data on the heavy primary flux and atomic weight distribution, fragments of these alone could not account for more than a small fraction of the effect noted.

Addition of the fluxes I_A'' and I_α yields the curve $(I_A''+I_\alpha)$ shown in Fig. 7. Comparison of this curve with I_{total} indicates that at 12 mm Hg at most 80 percent of the telescope counting rate can be attributed to vertically-incident relativistic protons and α particles. (The corresponding fraction at zero pressure, assuming the curves I_α and I_A'' to be extrapolated correctly, is 70 percent.) This gives a very strong indication that the telescope is triggered often at the "top of the atmosphere" by external showers or by particles incident from outside the telescope solid angle. It is interesting to note in this connection that the shower frequency (curve S, Fig. 7) has a very different altitude variation from the curve $(I_\alpha+I_A'')$ in the top 50 g/cm² of the atmosphere, and that the frequency of showers in this region is in excess of the maximum frequency of multiple-particle events that can arise from local nuclear interactions of telescope-oriented protons and α particles. This constitutes additional evidence of the presence of spurious telescope-triggering events and indicates that great care must be exercised in the interpretation of primary flux data obtained by means of telescopes having no shower protection.

VII. THE PROTON AND α-PARTICLE ENERGY SPECTRA

In Fig. 8 we have plotted the results of most of the existing α-particle flux measurements (see Introduction for methods and references) as a function of the theoretical geomagnetic cutoff energy at the location of each of the respective measurements.[22] The smooth curve A represents an integral energy spectrum of the form

$$N(\epsilon)=K/(1+\epsilon)^{\gamma} \qquad (2)$$

where ϵ is the primary-particle kinetic energy in Bev per nucleon and K and γ are assigned the values 420 sterad^{-1} m^{-2} sec^{-1} and 1.35 respectively. This spectrum agrees satisfactorily with the indicated He flux measurements and has the same form, except for the value of K, as the analytical expression chosen by Kaplon *et al.*[20] to represent the energy distribution of the primary nuclei with $Z \geqslant 10$.

[22] The upper and lower limits of experimental uncertainty on the author's point plotted in Fig. 8 are obtained, respectively, on the assumptions that *all* or *none* of the α particles which suffered nuclear collisions in the telescope gave rise to events other than those designated by C in the analysis.

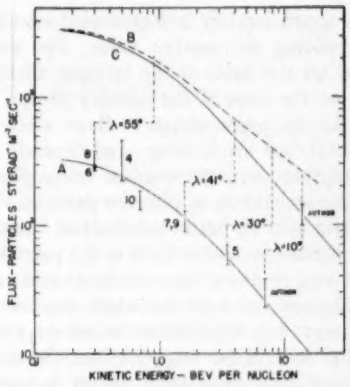

FIG. 8. Integral number-energy spectra of primary protons and α particles. The experimental data with the numerical indices (referring to footnote references) represent He flux measurements of other investigators. Curve A is a plot of the integral spectrum $N(\epsilon)=420(1+\epsilon)^{-1.35}$, where ϵ = primary energy in Bev/nucleon. Curve B is the "apparent" proton spectrum obtained by subtracting the α flux (curve A) from counter-telescope total-flux data. Curve C represents a spectrum of the form $N(\epsilon)=K(1+\epsilon)^{-1.35}$ fitted to the author's $\lambda=10°$ proton flux value.

The upper curve, B, in Fig. 8 represents an approximation to the primary proton energy spectrum deduced by subtraction of the estimated α-particle flux (curve A) from total flux values measured at various latitudes with G-M counter telescopes.[23] While the present total-flux measurement, corrected in a similar manner for the α-particle contribution, agrees precisely with curve B, the proton flux upper limit obtained from the pulse-height analysis (145 sterad^{-1} m^{-2} sec^{-1}) falls far below the curve.[24] The curve C shown in Fig. 8 represents a spectrum of the form of Eq. (2) with $\gamma=1.35$ and K adjusted to bring the curve into agreement with the present proton-flux estimate. Since curve C does not rise above curve A at low values of ϵ, it would appear that the proton spectrum could have the same form as that chosen to represent the He data, provided that the effects (showers and other spurious telescope-triggering events) which cause a departure between curve B and the present proton-flux value gradually become less important with increasing latitude.

The total cosmic-ray energy incident upon the atmosphere at various latitudes has been estimated from the ionization *vs* depth measurements of Bowen *et al.*[25] and also from the latitude variation of the total particle flux. The energy fluxes deduced by the two methods

[23] From a data compilation by Winckler, Stix, Dwight, and Sabin, Phys. Rev. **79**, 656 (1950).

[24] The upper and lower limits on the $\lambda=10°$ proton-flux value plotted in Fig. 8 are obtained by zero-pressure extrapolations of fluxes I_A'' and I_A' (Table III). The two limits correspond, respectively, to the assumptions that *all* or *none* of the protons which undergo interaction in the telescope give rise to events outside the A pulse-height interval.

[25] Bowen, Millikan, and Neher, Phys. Rev. **53**, 856 (1938) see interpretation presented by D. J. X. Montgomery, *Cosmic Ray Physics* (Princeton University Press, Princeton, 1949), p. 146.

differ by approximately a factor of 2, the ionization method yielding the smaller value. The energy flux calculated on the basis of the latitude effect depends critically on the form of the primary proton spectrum assumed for the region above 14 Bev—where accurate experimental data are lacking—and depends also upon the assumption that the counter telescopes measure directly the actual flux of primary particles. While the present data give no better information than has been available heretofore on the form of the particle spectra, there is strong evidence that the equatorial proton flux is approximately one-half that which has been assumed in the energy flux calculations based on the latitude effect. This observation suggests that the discrepancy noted above may arise from errors in particle flux measurements rather than from any serious oversight in the interpretation of the ionization *vs* depth data.

ACKNOWLEDGMENTS

The author wishes to thank Dr. W. F. G. Swann, Director of the Bartol Research Foundation, for his support and encouragement during all phases of this work. Among those who participated in the organization and execution of the balloon-flight operation, Project CHURCHY, were Lieutenant Commander Malcolm D. Ross of the Office of Naval Research, C. F. Merill of General Mills, Inc., and the officers and men of the U. S. Navy Ships Currituck, Rodman, and Ellison. The assistance of R. C. Pfeiffer and W. C. Porter, of the Bartol Research Foundation, is greatly appreciated.

PHYSICAL REVIEW VOLUME 96, NUMBER 5 DECEMBER 1, 1954

Production Spectra of Cosmic-Ray Mesons in the Atmosphere*

STANISLAW OLBERT
Massachusetts Institute of Technology, Laboratory for Nuclear Science, Cambridge, Massachusetts
(Received August 9, 1954)

Recent experimental data on the differential vertical intensities of μ mesons in the atmosphere make it possible not only to improve the original Sands' production spectrum of μ mesons but also to study its dependence on the geomagnetic latitude. It is shown that, for the residual ranges, R', between 100 g cm^{-2} and 6000 g cm^{-2}, the production spectrum may be approximated by an empirical formula of the type: $C(a+R')^{-\gamma}$ where C and γ are numerical constants practically independent of the geomagnetic latitude. The latitude dependence of the production spectrum is thus expressed through the parameter a which displays a monotonic decrease with increasing latitude. With numerical values of a, C, and γ, compatible with experimental data, the production spectrum of μ mesons is then used as a basis for the derivation of the differential and integral energy spectra of charged π mesons. The latitude dependence of the π-meson spectrum is linked to the geomagnetic cut-off of the primary cosmic radiation, which leads to some crude conclusions on the average multiplicity of π mesons produced in proton collisions with air nuclei. In particular, the dependence of the multiplicity on the primary energies between 2 and 13 Bev is studied in detail and compared with Fermi's statistical theory of π-meson production.

I. INTRODUCTION

THE original idea of M. Sands to introduce an empirical μ-meson spectrum at production[1] has been proven to be very useful in dealing with many problems concerning the mesonic components of cosmic rays in the atmosphere. The knowledge of this empirical production spectrum makes possible not only the computation of the vertical intensities of μ mesons at any desired altitude, but it also offers a basis for testing various theories of π-meson production in nucleonic collisions. The latter aspect is demonstrated, for example, by P. Budini and G. Molière in their review article in Heisenberg's *Kosmische Strahlung*[2] where the authors test Heisenberg's theory of multiple meson production.

Sands derived his production spectrum from early experimental data (partly his own, partly those of others) taken in the proximity of 45° geomagnetic latitude. Unfortunately, these data were then rather imcomplete and not quite suitable for Sands' task. Moreover, the values of the physical constants (like the rest mass or the lifetime of the μ meson) employed in Sands' calculations were, at the time, burdened by large experimental errors.

The purpose of this paper is, therefore, twofold: (a) to bring Sands' spectrum more up-to-date (Sec. II), (b) to extend its applicability to various geomagnetic latitudes (Sec. III). In addition, in Sec. IV we shall utilize the obtained latitude dependence of the μ-meson spectrum at production to study the relationship between the geomagnetic cut-off of the primary radiation and the integral energy spectrum of π mesons at production.

* Supported in part by the joint program of the U. S. Office of Naval Research and the U. S. Atomic Energy Commission.

[1] M. Sands, Technical Report No. 28, Laboratory for Nuclear Science, Massachusetts Institute of Technology, 1949 (unpublished); Phys. Rev. 77, 180 (1950).

[2] *Kosmische Strahlung*, edited by W. Heisenberg (Springer-Verlag, Berlin-Göttingen-Heidelberg, 1953), second edition, p. 391 ff.

The latter discussion will lead us to some crude conclusions concerning the problem of multiple meson production in air nuclei for energies ranging from about 2 to 13 Bev.

II. SANDS' SPECTRUM AT 50°N

(a) Unidimensional Equation of the Vertical μ-Meson Intensity

Consider the number of μ mesons produced per cm²-sec-sterad in an infinitesimal horizontal layer dx at the atmospheric depth x, which have residual ranges between R' and $R'+dR'$ and move toward the earth along the vertical. This number will then, in general, depend on three parameters: the atmospheric depth x, the residual range R', and the geomagnetic latitude λ, so that it may be denoted by $H(x,R';\lambda)dxdR'$. Following Sands, let us assume that $H(x,R';\lambda)$ may be represented by the following product:

$$H(x,R';\lambda)=G(R';\lambda)\exp(-x/L), \qquad (1)$$

where L is a constant. Equation (1) is equivalent to the assumption that the meson-producing component is absorbed exponentially throughout the atmosphere with an effective attenuation mean free path L. This assumption is justified experimentally[3] for all atmospheric depths larger than about 250 g cm^{-2}. At higher altitudes it is subject to some uncertainty. However, one should expect a sizeable deviation from the exponential law only at atmospheric depths smaller than 100 g cm^{-2}, a region which contributes relatively little to the μ-meson intensities in the lower parts of the atmosphere (provided that the μ-meson energies are not exceedingly high). In what follows, we shall use for L Tinlot's numerical value of 120 g cm^{-2}.[3]

It is worth noting that the assumption on an exponential attenuation of the N-component does not necessarily imply that the theoretical absorption mean free path $L_a(x)$ remains constant throughout the atmosphere. For instance, the altitude dependence of $L_a(x)$ describable by a formula: $L_a(x)=L_0x/(b+x)$, where L_0 and b are free parameters, still leads to an exponential absorption of the N-component, since $\exp[-x/L_a(x)]=\exp(-b/L_0)\times\exp(-x/L_0)$. Note that, even if the parameter b should vary with the geomagnetic latitude, Eq. (1) still retains its original form.

Following Sands we shall refer to the quantity $G(R';\lambda)$ defined by Eq. (1) as the "production spectrum of μ mesons." However, we shall bear in mind that its physical significance is not so direct as the term might suggest. It is sometimes well to remember that it is the quantity $H(x,R';\lambda)$, rather than the quantity $G(R';\lambda)$, which has an unambiguous physical meaning.

Having accepted Eq. (1) as a sufficient approximation to reality, one can express the differential vertical intensity of μ mesons, observed at the atmospheric depth s, by the following equation:

$$i_v(R,s;\lambda)=\int_0^s G(R+s-x;\lambda)\times\exp(-x/L)w(x,s,R)dx, \qquad (2)$$

where $R=R'+x-s$ is the residual range of the μ meson at the depth s, and $w(x,s,R)$ is the survival probability of the μ meson produced at x and arriving at s with the residual range R.[4] It is evident from the form of Eq. (2) that it contains the following simplifying assumptions: (a) the air layer traversed by π mesons before their decay into μ mesons is negligible; (b) the production and propagation of π and μ mesons is restricted to a narrow cone about the vertical (unidimensional model). It is readily seen that the above assumptions place an upper and lower limit on the validity of Eq. (2). However, we shall show in the Appendix that Eq. (2) represents a satisfactory approximation to reality, when one restricts oneself to the interval of residual ranges between $R=100$ g cm^{-2} and $R=6{,}000$ g cm^{-2}. It is fortunate that the preponderant part of the mesonic component is contained within this interval.

(b) Production Spectrum for Large Residual Ranges of μ Mesons

Consider the differential vertical intensity of μ mesons at sea level ($s=x_0$) for relatively large residual ranges, say 2000 g cm$^{-2}<R<6000$ g cm^{-2}. In this case one can solve Eq. (2) analytically with respect to the production spectrum $G(R';\lambda)$, i.e., one can express $G(R';\lambda)$ explicitly in terms of i_v and w. This is possible because, at large R, the argument of $G(R';\lambda)$, $R'=R+x_0-x$, does not change its relative value by a large amount within the interval of integration $0\leqslant x\leqslant x_0$. Consequently, $G(R';\lambda)$ may be considered in this interval as a slowly varying function of x, and one may apply the mean-value theorem of integral calculus to the right-hand side of Eq. (2), *viz.*,

$$i_v(R,x_0;\lambda)=G(R+x_0-x_m;\lambda)\times\int_0^{x_0}\exp(-x/L)w(x,x_0,R)dx. \qquad (3)$$

One can estimate the value of the (unknown) quantity x_m ($0<x_m<x_0$) by expanding $G(R+x_0-x;\lambda)$ in Eq. (2) into the Taylor's series at $x=x_m$; neglecting higher derivatives of G, one then finds:

$$x_m=\int_0^{x_0} x\exp(-x/L)w(x,x_0,R)dx \Big/ \times\int_0^{x_0}\exp(-x/L)w(x,x_0,R)dx. \qquad (4)$$

[3] See, e.g., J. H. Tinlot, Phys. Rev. **73**, 1476 (1948); **74**, 1197 (1948).

[4] For a detailed discussion on the survival probability the reader is referred to S. Olbert, Phys. Rev. **92**, 454 (1953).

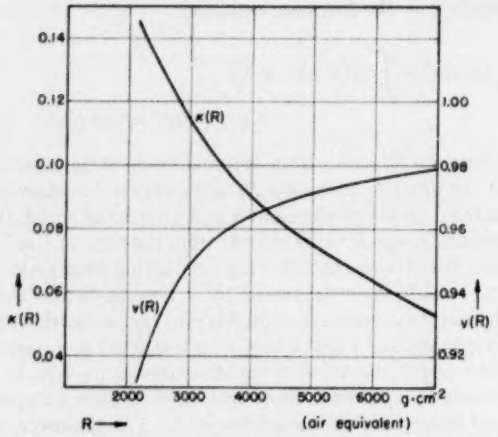

FIG. 1. The empirical functions $v(R)$ and $\kappa(R)$ describing the survival probability, w, of μ mesons produced at x and arriving at sea level with residual ranges $R>2{,}000$ g cm^{-2}, *viz.*: $w=v(R)\times(x/x_0)^{\kappa(R)}$. The functions $v(R)$ and $\kappa(R)$ correspond to the annual mean of the vertical temperature distribution at 40° geographic latitude (see reference 4).

The above estimate of x_m is quite accurate due to the additional fact that the integrand $\exp(-x/L)w(x,x_0,R)$ displays a single, sharp maximum in the vicinity of $x=L$. For the evaluation of the integrals occurring on the right-hand side of Eqs. (3) and (4), it is convenient to make use of the following empirical representation of the survival probability:

$$w(x,x_0,R)=v(R)(x/x_0)^{\kappa(R)}, \tag{5}$$

where the quantities $v(R)$ and $\kappa(R)$ depend only on the residual ranges at sea level and can be computed numerically for any given geographic location (see Fig. 1). Equation (5) reproduces the actual values of the survival probability accurately for all production levels $x<500$ g cm^{-2}. At the production levels closer to the ground [contributing very little to the values of $i_\nu(R,x_0;\lambda)$], the empirical formula (5) introduces errors amounting only to a few percent. Substituting Eq. (5) into Eqs. (3) and (4), one finds:

$$G(R+x_0-x_m;\lambda)=\frac{i_\nu(R,x_0;\lambda)}{Lw(L,x_0,R)\Gamma(1+\kappa)} \tag{6}$$

with:

$$x_m=(1+\kappa)L. \tag{7}$$

Here we made use of the fact that $x_0/L\gg1$, i.e., we extended the integrals appearing in Eqs. (3) and (4) up to infinity. Equation (6) represents the required solution of Eq. (2) with respect to the production spectrum of μ mesons for large residual ranges.

In order to study the explicit behavior of G with respect to R' we have chosen the experimental data of Caro, Parry, and Rathgeber[5] on the distribution-in-momentum of μ mesons at sea level (geomagnetic latitude $\lambda\approx50$°S) as the most reliable source of information on $i_\nu(R,x_0;\lambda)$. The results of the numerical evaluation of the right-hand side expression of Eq. (6) show then that the production spectrum $G(R';50°)$, may be represented by an empirical formula of the type:

$$G(R';50°)=C/(a+R')^\gamma, \tag{8}$$

where C, a, and γ are positive constants. Unfortunately, the range interval for which Eq. (6) is valid (see below) is not sufficient to yield an unambiguous set of unique numerical values of these constants. Explicit calculations show that one can reproduce $G(R';50°)$ for 2000 g cm$^{-2}<R'<6000$ g cm^{-2} with *equal* accuracy by assuming for the parameter a any arbitrary value between 200 and 700 g cm^{-2}, provided one adjusts correspondingly the two remaining constants, C and γ. In order to eliminate this ambiguity, one must turn to experimental data which are more sensitive to the assumed values of the parameter a. This will be done in the next section where we shall make use of the observations on the altitude dependence of the differential intensity of μ mesons with small residual ranges.

The degree of accuracy that one may claim for the solution (6) can be estimated from the relative error made in our derivation of $G(R';50°)$. This error is given by:

$$\tfrac{1}{2}(1+\kappa)L^2\left[\frac{1}{G}\frac{\partial^2 G}{\partial R'^2}\right]_{R'=R+x_0-x_m}=\tfrac{1}{2}\gamma(1+\gamma)(1+\kappa)\left[\frac{L}{a+R+x_0-x_m}\right]^2.$$

With proper choice of γ and a, one finds that, for $R>2000$ g cm^{-2}, this error is smaller than 1.2 percent. Hence, for large residual ranges, the production spectrum of μ mesons is known almost as well as the intensity at sea level itself.

(c) Production Spectrum for Small Residual Ranges of μ Mesons

One of the experiments which can yield a sufficiently accurate information on the behavior of the production spectrum at small residual ranges is that dealing with the altitude dependence of differential intensities of relatively slow μ mesons. We have chosen the measurements of M. Conversi[6] as most suitable for the purpose of our analysis. Combining the techniques of delayed coincidences and anticoincidences Conversi was able to determine the absolute number of μ mesons (per g-sec-sterad), stopped in 10 cm of graphite after traversing 15.2 cm of lead, as a function of the atmospheric depth, s. The data were taken at 50°N geomagnetic latitude. The vertical allowed cone was relatively narrow and the statistical accuracy of the data exceeded that of earlier

[5] Caro, Parry, and Rathgeber, Australian J. Sci. Research **A4**, 16 (1950).

[6] M. Conversi, Phys. Rev. **79**, 750 (1950).

measurements of this kind[7] considerably. Thus, according to Eq. (2), one may express Conversi's "altitude curve" by the following equation:

$$i_v(R_0,s;\lambda)=\int_0^s G(R_0+s-x;\lambda)\times\exp(-x/L)w(x,s,R_0)dx, \quad (9)$$

where $R_0=100$ g cm^{-2} (air equivalent) and $\lambda=50°$N are now fixed parameters so that the intensity, i_v, is a function of the atmospheric depth s, only.

Equation (9) represents a linear integral equation for the unknown function $G(R_0+s-x;\lambda)$. Due to the complicated character of the kernel function $e^{-x/L}w(x,s,R_0)$ and the limited knowledge of $i_v(R_0,s;\lambda)$, it is practically impossible to apply successfully the ordinary methods of solving an equation of this type. We have attempted to solve Eq. (9) by assuming: (a) that the dependence of G on $R'=R_0+s-x$ may be expressed by a formula of the type of Eq. (8); (b) that there exists a unique set of values for the parameters C, a, and γ, which not only solves Eq. (9) but also reproduces solution (6) at large R'.

Using thus as a guide the solution at large residual ranges, we have chosen several tentative sets for the numerical values of these three parameters and then, for each of these sets, we have computed the right-hand side of Eq. (9).[8] By this procedure we could find a final set of constants, C, a, and γ, which yielded an $i_v(R_0,s;\lambda)$-curve compatible with the experimental data of Conversi, and which was consistent with Eq. (6). This set is the following:

$$C=7.3\times10^4[\text{g}^{-2+\gamma}\,\text{cm}^{2-2\gamma}\,\text{sec}^{-1}\,\text{sterad}^{-1}],$$
$$a=520\text{ g cm}^{-2}\text{ (air equivalent)}, \quad (10)$$
$$\gamma=3.58.$$

Conversi's experimental points covered the atmospheric depths from sea level up to about $s=230$ g cm^{-2}. Unfortunately, the data show a gap at atmospheric depths in the proximity of 700 g cm^{-2}. To complete Conversi's curve in this region we made use of the measurements of Kraushaar,[9] which give the differential vertical intensity of μ mesons as a function of residual ranges at Echo Lake, Colorado (see Fig. 2). The experimental points and the curve computed on the basis of Eqs. (9) and (10) are shown in Fig. 2. One sees that the agreement is practically complete except for one point at the depth of 230 g cm^{-2} where Conversi's point falls above the calculated curve. We believe, however, that this point is to be corrected for the μ mesons stemming from the π mesons locally produced in the lead absorber

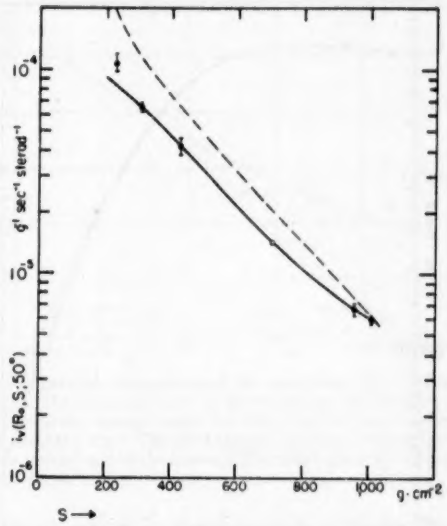

FIG. 2. Differential vertical intensity of μ mesons with residual ranges $R_0=100$ g cm^{-2} (air equivalent) as a function of the atmospheric depth, s, at 50°N geomagnetic latitude. The full circles, with corresponding errors, indicate the measurements of Conversi (see reference 6); the open circle represents one of Kraushaar's measurements (see reference 9) at Echo Lake, Colorado. The dashed line represents Sands' measurements (see reference 1) on μ mesons with residual ranges between 5 and 83 g cm^{-2}. The solid line was computed by means of Eqs. (9) and (11).

by the nucleons (and π mesons) which are still abundant at this high altitude.[10] Corrections of this kind may be expected to be of the order of 20 percent, so that we do not consider this single discrepancy as crucial.

To summarize, we conclude that, at the geomagnetic latitude of 50°N, the production spectrum of μ mesons can be expressed by the following formula:

$$G(R';50°)=\frac{7.3\times10^4}{(520+R')^{3.58}}[\text{g}^{-2}\,\text{cm}^2\,\text{sec}^{-1}\,\text{sterad}^{-1}]. \quad (11)$$

According to Eq. (9) and the above requirement (b), Eq. (11) is valid for the residual ranges between $R'=100$ g cm^{-2} and $R'=6000$ g cm^{-2} (air equivalent). In order to check the validity of Eq. (11) in this interval, we have computed the vertical differention intensity of μ mesons at sea level for various residual ranges from $R=100$ g cm^{-2} up to $R=5000$ g cm^{-2}. The results obtained are indicated in Fig. 3 by open circles. The solid line represents the experimental curve deduced from the data of Caro *et al.*;[5] the dashed line represents Rossi's curve.[11] Note a significant discrepancy between these two curves at $R>2000$ g cm^{-2}.

Figure 4 shows a comparison between the original Sands' spectrum (dashed line) and the production spectrum given by Eq. (11)—(solid line). One notices that the two spectra are similar except for the Sands'

[7] Rossi, Sands, and Sard, Phys. Rev. **72**, 120 (1947); see also reference 1.

[8] For detailed curves of the survival probability used in these calculations, the reader is referred to S. Olbert, Technical Report No. 61, Laboratory for Nuclear Science, Massachusetts Institute of Technology, 1954 (unpublished).

[9] W. L. Kraushaar, Phys. Rev. **76**, 1045 (1949).

[10] For remarks on this problem, see also reference 6.

[11] B. Rossi, Revs. Modern Phys. **20**, 537 (1948).

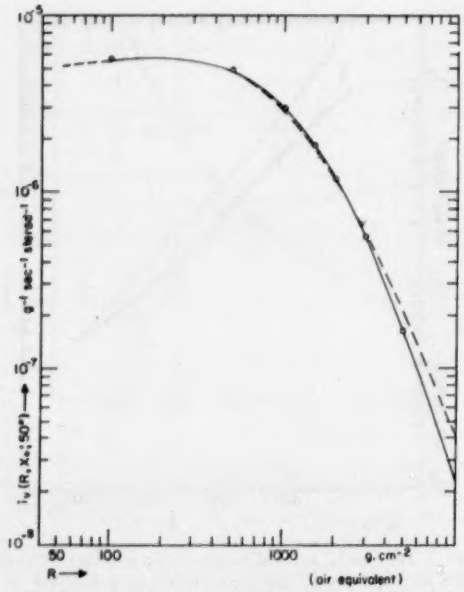

FIG. 3. Differential vertical intensity of μ mesons at sea level, x_0, as a function of the residual range R ($\lambda \approx 50°$S). The solid line corresponds to the measurements of Caro *et al.*;[5] the dashed line represents Rossi's curve.[11] The open circles represent the intensity computed by means of Eqs. (2) and (11).

"dip" at $R' = 100$ g cm^{-2}. We cannot make any definite statement about the behavior of our spectrum at this point since our solution is valid only for $R' > 100$ g cm^{-2}. At any rate, according to the investigations of Ascoli,[12] the dip obtained by Sands is too pronounced to correspond to a real phenomenon.

III. THE LATITUDE DEPENDENCE OF THE PRODUCTION SPECTRUM OF μ MESONS

Thus far we have considered the production spectrum of μ mesons only in the proximity of 50° geomagnetic latitude. We now turn to the discussion concerning the latitude dependence of $G(R';\lambda)$.

In contrast to the abundance of the experimental material concerning the latitude dependence of the *total* cosmic radiation, the information on the latitude dependence of the differential μ-meson intensity itself is incomplete. This is especially true for the high-altitude measurements. To our knowledge, there exists, at present, only one experiment of this type, namely, that of Conversi.[6] Conversi's data were taken at a constant altitude of 30 000 feet for several latitudes ranging from the geomagnetic equator up to 70°N. The measurements were made with the apparatus and technique discussed in the foregoing section, so that the data can be interpreted as a direct measure of the latitude dependence of $i_v(R_0,s_0;\lambda)$ for $R_0 = 100$ g cm^{-2} and $s_0 = 307$ g cm^{-2}. The statistical accuracy achieved in this series of measurements was, unfortunately, smaller than that at 50°N; thus, one cannot give too much weight to the "latitude curve" chosen by Conversi as the best fit (see reference 6).

One is offered primarily two advantages by studying the latitude dependence of differential intensities of slow mesons at *high* altitudes: (1) the effect is large compared with that at low altitudes, (2) the atmospheric latitude effect is practically negligible.

The latter effect stems from the fact that, in general, the survival probability of μ mesons varies with the (geographic) latitude due to the different air-mass distribution at different latitudes. According to meteorological observations, one finds an increase in the annual mean of the atmospheric temperature when one moves southward along any given isobar *below* the tropopause and, inversely, a decrease when one moves southward *above* the tropopause. This implies that the existing temperature gradients can reduce or enhance the μ-meson intensity depending on whether one makes the measurements below or above a certain atmospheric depth. One can show[8] that this atmospheric latitude effect practically disappears for a layer between 250 and 300 millibars.

It follows from the above remarks that the observed latitude variation of $i_v(R_0,s_0;\lambda)$ originates almost exclusively from the geomagnetic effect on the production spectrum of μ mesons. We may, therefore, use Conversi's latitude curve as a direct index of the latitude dependence of this quantity. For the purpose of the derivation of this dependence, let us assume that the production spectrum $G(R';\lambda)$ can be expressed at all latitudes, λ, by an empirical formula of the type given by Eq. (8). If this is so, then, among the three parameters C, γ, and a, only the latter may vary with the geomagnetic latitude. The following argument shows that the

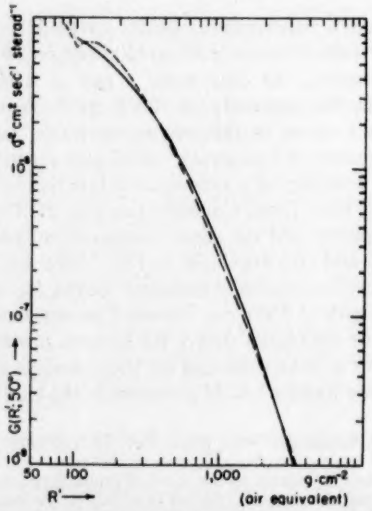

FIG. 4. Comparison of Sands' production spectrum (dashed line) with that computed by means of Eq. (11) (solid line).

[12] G. Ascoli, Phys. Rev. **79**, 812 (1950).

parameters C and γ ought to be practically independent of λ:

A μ meson with a residual range larger than, say, 3000 g cm^{-2} has for its parent a π meson of kinetic energy of not less than 8 Bev; a π meson of that energy can be produced by the primary particle only if the kinetic energy of the latter exceeds 12 Bev.[13] Thus, most of the μ mesons with residual ranges above 3000 g cm^{-2} are originated by the primaries which are sufficiently energetic to overcome the magnetic field of the earth at all latitudes. This implies that the production spectrum of μ mesons with $R'>3000$ g cm^{-2} should be practically the same for all geomagnetic latitudes. Since a noticeable latitude variation of the characteristic constants C and γ would violate this conclusion, we see that the latitude dependence of $G(R';\lambda)$ must be expressed through the parameter a, the only parameter with respect to which $G(R';\lambda)$ is insensitive at large residual ranges R'. Using the numerical values for C and γ determined at $\lambda=50°$, we may, thus, write for the production spectrum of μ mesons at any given latitude:

$$G(R';\lambda)=\frac{7.3\times10^4}{\lfloor a(\lambda)+R'\rfloor^{3.58}}[\text{g}^{-2}\text{ cm}^2\text{ sec}^{-1}\text{ sterad}^{-1}]. \quad (12)$$

Inserting Eq. (12) into Eq. (2) with constant $R=R_0=100$ g cm^{-2} and constant $s=s_0=300$ g cm^{-2}, one obtains a unique functional relation between $a(\lambda)$ and $i_\nu(R_0,s_0;\lambda)$ (the other quantities occurring on the right-hand side of Eq. (2) are, in the present case, practically independent of λ). Figure 5 shows the parameter $a(\lambda)$ as a function of $i_\nu(R_0,s_0;\lambda)$. On the abscissa of Fig. 5 we have also indicated the geomagnetic latitudes corresponding to the values of $i_\nu(R_0,s_0;\lambda)$ observed by Conversi.[6] One sees that $a(\lambda)$ decreases monotonically from 646 g cm^{-2} at the geomagnetic equator to 513 g cm^{-2} at $\lambda=60°$N (see also Table II). Of course, among these values of $a(\lambda)$, the value of 520 g cm^{-2} at 50° geomagnetic latitude is to be considered as most reliable. This value has been derived in the preceding section where we had at our disposal a more accurate and rather complete set of experimental data.

IV. PRODUCTION SPECTRUM AND THE AVERAGE MULTIPLICITY OF CHARGED π MESONS

The above empirical production spectrum of μ mesons may be used as a basis for the derivation of the differential energy spectrum $S(E_\pi;\lambda)$ of charged π mesons at production. The functional relationship between $S(E_\pi;\lambda)$ and $G(R';\lambda)$ is well defined, if one assumes that *all* μ mesons stem from the decay of charged π mesons. In view of the recent discovery of K mesons decaying into μ mesons,[14] this assumption may now be considered only as an approximation to reality. However, the relative abundance of K mesons is probably too small to affect significantly our results.

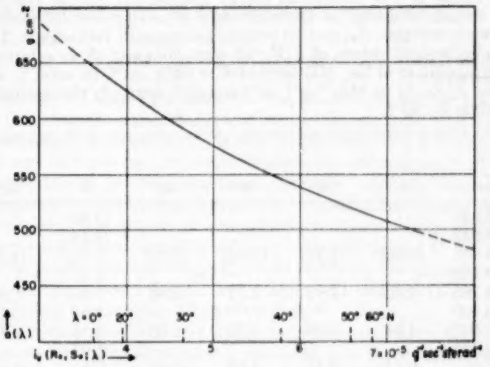

FIG. 5. Latitude dependence of the parameter $a(\lambda)$ defined by Eq. (12). The parameter $a(\lambda)$ is plotted *versus* the intensity of μ mesons with the residual range $R_0=100$ g cm^{-2} at the atmospheric depth $s_0=300$ g cm^{-2}. The geomagnetic latitudes indicated on the abscissa correspond to the μ-meson intensities given by Conversi's latitude curve.[6]

The numerical evaluation of $S(E_\pi;\lambda)$ is simplified further by the fact that, in the energy interval of interest, the energy spectrum of π mesons at decay is practically identical to that at production (see Appendix). Following Ascoli,[12] we find that $G(R';\lambda)$ is related to $S(E_\pi;\lambda)$ by the equation:

$$G(R';\lambda)dR'=\frac{m_\pi^2}{m_\pi^2-m_\mu^2}dE_\mu \times\int_{E_{\min}}^{E_{\max}}\frac{S(E_\pi;\lambda)}{(E_\pi^2+2m_\pi c^2E_\pi)^{\frac{1}{2}}}dE_\pi, \quad (13)$$

where m_μ, E_μ and m_π, E_π are the rest mass and the kinetic energy of μ and charged π mesons respectively, and $E_{\min}$ and $E_{\max}$ are the lower and upper limits of the energies of π mesons that can give rise to a μ meson of energy E_μ.

The solution of Eq. (13) with respect to $S(E_\pi;\lambda)$ can be obtained by means of the method developed by Ascoli.[12] Table I shows the results for various energies, E_π, and various geomagnetic latitudes, λ. Again, among these energy spectra, $S(E_\pi;\lambda)$ at $\lambda=50°$N is to be looked upon as most accurate. It is interesting to note that this energy spectrum behaves in a manner similar to that observed at high altitudes in photographic emulsions.[15] The numerical values of $S(E_\pi;\lambda)$ at lower energies, occurring in parenthesis of Table I, were obtained by an arbitrary extrapolation of Eq. (12) beyond $R'=100$ g cm^{-2}.

With the aid of Table I we can estimate the number (per cm^2-sec-sterad) of charged π mesons produced

[13] One obtains the value of 12 Bev as a lower limit for the primary energy by assuming that the inelastic nucleon-nucleon collision gives rise to only one π meson of 8 Bev produced in forward cone.

[14] M. G. K. Menon and C. O'Ceallaigh, Proc. Roy. Soc. (London) **221**, 292 (1954).

[15] Camerini, Fowler, Lock, and Muirhead, Phil. Mag. **41**, 413 (1950).

TABLE I. The differential energy spectra, $S(E_\pi;\lambda)$, of charged π mesons at decay (or approximately at production) for various kinetic energies, E_π, and for various geomagnetic latitudes, λ. The parenthesized values of $S(E_\pi;\lambda)$ were obtained by an arbitrary extrapolation of Eq. (12) beyond $R'=100$ g cm^{-2}. In order to obtain $S(E_\pi;\lambda)$ in Mev^{-1} g^{-1} sec^{-1} sterad^{-1}, multiply the tabulated values by 10^{-6}.

E_π Bev \ λ	0°	20°	30°	40°	50°	60°
0.030					(2.61)	
0.065					(4.16)	
0.108	(2.09)	(2.32)	(2.84)	(3.73)	(4.41)	(4.60)
0.186					4.16	
0.266	1.76	1.93	2.32	2.96	3.44	3.58
0.409					2.43	
0.547	1.01	1.09	1.28	1.56	1.78	1.84
0.840					1.07	
1.06	0.44	0.47	0.53	0.62	0.69	0.71
1.51					0.36	
1.96	0.14	0.15	0.17	0.19	0.20	0.20
3.53	0.039	0.040	0.043	0.046	0.049	0.049
6.32	0.009	0.009	0.009	0.009	0.010	0.010
11.3					0.002	

throughout the atmosphere and moving *downward* with kinetic energies greater than E_π. Denoting this number by $\Pi(E_\pi;\lambda)$, we have, according to the definition of $S(E_\pi;\lambda)$ and Eq. (1),

$$\Pi(E_\pi;\lambda)=L\int_{E_\pi}^{\infty}S(E_\pi';\lambda)dE_\pi'. \tag{14}$$

Since we do not know the behavior of $S(E_\pi;\lambda)$ below a certain energy, $E_\pi<E_0$, we cannot determine the total number of π mesons of all energies, i.e., the quantity $\Pi(0;\lambda)$. In what follows, we shall limit ourselves to $\Pi(E_0;\lambda)$ with $E_0\approx 260$ Mev. For this fixed value of the kinetic energy of π mesons, the quantity $\Pi(E_0;\lambda)$ is a function of the geomagnetic latitude only. Qualitatively, it is evident that the latitude dependence of Π is a direct consequence of the geomagnetic cut-off imposed upon the flux of the primary radiation. Assuming that the primary differential energy spectrum displays a sharp cut-off at E_p (E_p being well-defined by λ) we can consider $\Pi(E_0;\lambda)$ also as a function of the cut-off energy, E_p (see Table II).

TABLE II. Geomagnetic data pertinent to the primary radiation and the μ- and π-meson components. The symbols below have the following meaning: λ is the geomagnetic latitude; E_p is the kinetic cut-off energy of vertical primary protons [from M. S. Vallarta, Phys. Rev. 74, 1837 (1948)]; J is the integral intensity of the primary radiation;[16] the parameter a is defined by Eq. (12); $\Pi(E_0;\lambda)$ represents the number of charged π mesons with energies greater than $E_0=260$ Mev produced throughout the atmosphere in the forward cone.

λ	E_p (Bev)	J cm^{-2} sec^{-1} sterad^{-1}	a g cm^{-2}	Π cm^{-2} sec^{-1} sterad^{-1}
0°	14.2	~0.026	646	0.135
10°	13.7	~0.027	642	0.137
20°	12.0	~0.031	627	0.145
30°	8.4	~0.046	591	0.165
40°	4.2	~0.080	546	0.197
50°	1.6	~0.18	520	0.217
60°	0.43	~0.29	513	0.225

The functional relationship between $\Pi(E_0;\lambda)$ and E_p enables one to draw some crude conclusions with respect to the effective multiplicity of charged π mesons produced by primary particles with energies between 2 and 13 Bev. For this purpose consider the following quantity

$$\bar{n}(E_0;E_p)=-\frac{d\Pi}{dE_p}\Big/\frac{dJ}{dE_p}, \tag{15}$$

where $J(E_p)$ is the integral energy spectrum of the N-component of cosmic rays averaged over the whole atmospheric depty. According to the definition of $\Pi(E_0;\lambda)$, $\bar{n}(E_0,E_p)$ represents approximately the average number of charged π mesons with energies greater than E_0, produced in the foreward cone by a particle with energy E_p.

One can get a rough idea about the dependence of $\bar{n}$ on E_p by substituting the energy spectrum of the *primary* cosmic rays[16] for the quantity $J(E_p)$ in Eq. (15). This procedure, although very crude, should yield the values of $\bar{n}$ which are correct within a factor of two. It is probably not worthwhile to use a more elaborate expression for $J(E_p)$ because the present data on the absolute values of primary intensities are rather uncertain and may be in error by about the same factor (*albido* effect, etc.). The results of our estimate are indicated by the solid line in Fig. 6. One sees that $\bar{n}$ increases with increasing E_p much more rapidly at lower than at higher energies. The flattening-off begins at about 6 Bev.

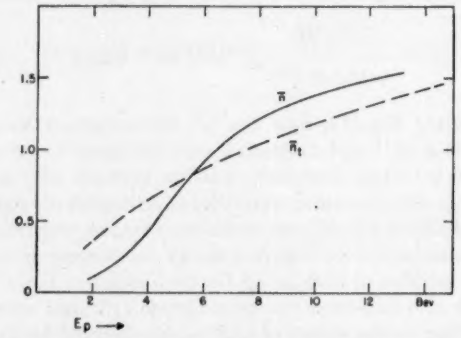

FIG. 6. Multiplicities of charged π mesons produced in the foreward cone by the primary particle with the kinetic energy E_p. $\bar{n}$ is the empirical multiplicity estimated by means of Eq. (15); $\bar{n}_t$ is the theoretical multiplicity predicted by Fermi's statistical model of nucleon-nucleon collisions.

It is interesting to compare the above results with those predicted by Fermi's statistical theory of meson production in nucleon-nucleon collisions.[17] According to this theory, the probability of observing n π mesons

[16] We made use of the data compiled by G. Puppi and N. Dallaporta in *Progress in Cosmic Ray Physics* (North-Holland Publishing Company, Amsterdam, 1952), p. 320.

[17] E. Fermi, Progr. Theoret. Phys. (Japan) 5, 570 (1950).

(both charged and neutral) produced in a nucleon-nucleon collision is approximately given by:

$$f_n(w)=\frac{A}{(3n+\frac{1}{2})!}\left[\frac{250(w-2)^3}{w}\right]^n, \tag{16}$$

where $wMc^2=(4M^2c^4+2Mc^2E_p)^{\frac{1}{2}}$ is the total energy carried by both nucleons before the collision in the center-of-mass system, and A is normalization constant, given by:

$$A^{-1}=\sum_{n=0}^{\infty}\frac{1}{(3n+\frac{1}{2})!}\left[\frac{250(w-2)^3}{w}\right]^n. \tag{17}$$

By means of Eqs. (16) and (17), one then can compute the expected mean number of charged π mesons produced in the foreward cone in a nucleon-nucleon collision, *viz.*,

$$\bar{n}_t\simeq\tfrac{1}{3}\sum_{n=1}^{\infty}nf_n(w). \tag{18}$$

The factor $\frac{1}{3}$ in Eq. (18) arises from the fact that, on the average, among the produced mesons only $\frac{2}{3}$ are charged, and among them only $\frac{1}{2}$ are emitted in the foreward cone The energy dependence of $\bar{n}_t$ is indicated in Fig. 6 by a dashed line. Note that the discrepancy between $\bar{n}$ and $\bar{n}_t$ is more pronounced at lower than at higher energies. The theoretical multiplicity, $\bar{n}_t$, decreases less rapidly with decreasing E_p than the empirical multiplicity, $\bar{n}$.

In view of the crudeness with which both multiplicities, $\bar{n}$ and $\bar{n}_t$, are derived, it is difficult to draw any definite conclusion with regard to the found discrepancy at lower energies. This difficulty is enhanced by the lack of a theory which would enable us to properly correct $\bar{n}_t$ for the plural processes inside the air nucleus. The simple models of the air nucleus considered recently by Haber-Schaim[18] and Amaldi *et al.*[19] are not applicable to the energies of several Bev.

The author is greatly indebted to Professor Bruno Rossi for his interest and assistance in the preparation of this paper.

APPENDIX

The assumption (*a*) in Sec. II(a) represents a good approximation if the momenta of π mesons are not exceedingly high. The mean free path, L_d, of the π meson before decay is given by:

$$L_d=\tau_\pi\frac{p_\pi}{m_\pi}\rho(x)\simeq 10^{-3}\frac{p_\pi}{m_\pi c}x\ [\text{g cm}^{-2}], \tag{A-1}$$

where τ_π, p_π, m_π are the mean life, the momentum, and the mass of the π meson, respectively, and $\rho(x)$ is the air density in the (isothermal) atmosphere. L_d is only of the order of a few grams per cm^2 for the π mesons produced above the 100-millibar level if $p_\pi<14$ Bev/c. For momenta larger than this value, L_d becomes comparable with the mean free path for nuclear collisions, and the assumption that almost *all* π mesons decay into μ mesons before interacting with air nuclei is no longer valid. By taking 14 Bev/c as the largest possible value of p_π still justifying the assumption (*a*), we thus restrict Eq. (2) to μ mesons with residual ranges at production smaller than about 6000 g cm^{-2}.

The assumption (*b*) in Sec. II(a) places a lower limit on Eq. (2) The unidimensional treatment is justifiable only if the production and the decay of π mesons as well as the propagation of μ mesons are collimated along the vertical.

The experimental observations in photographic emulsions at high altitudes[20] indicate that most of the π mesons with momenta larger than about 300 Mev/c (minimum ionizing secondary tracks) are omitted in the laboratory system at angles smaller than 15° with respect to the direction of the primary particle.

Secondly, the maximum angle of emission of a μ meson in the decay process of a π meson is given by:

$$\sin\vartheta_{\max}=\tfrac{1}{2}\left(\frac{m_\pi}{m_\mu}-\frac{m_\mu}{m_\pi}\right)\frac{m_\pi c}{p_\pi}, \tag{A-2}$$

i.e., $\vartheta_{\max}<8°$ if $p_\pi>300$ Mev/c.

Finally, the mean-square angle of multiple scattering of μ mesons in the atmosphere is given by:

$$\langle\theta^2\rangle_{Av}=\frac{E_s^2}{\mathbf{X}_0}\int_{\pi_\mu(x_2)}^{\pi_\mu(x_1)}\frac{d\pi_\mu}{\pi_\mu^2[-d\pi_\mu/dx]}, \tag{A-3}$$

where $E_s\approx 21$ Mev, $\mathbf{X}_0=38$ g cm^{-2} (the radiation length of air), π_μ is the product of the velocity times the momentum of the μ meson, and x_1, x_2 are the levels of production and observation, respectively. The ionization loss of π_μ, $-d\pi_\mu/dx$, is practically constant for all π_μ's larger than 200 Mev (its numerical value for air is 2.0 Mev g^{-1} cm^2) so that one has

$$\langle\theta^2\rangle_{Av}=\frac{E_s^2}{[-d\pi_\mu/dx]\mathbf{X}_0}\left[\frac{1}{\pi_\mu(x_2)}-\frac{1}{\pi_\mu(x_1)}\right]. \tag{A-4}$$

Equation (A-4) implies, for example, that a μ meson produced at the 100-millibar level and arriving at sea level with a momentum of about 300 Mev/c (corresponding residual range about 100 g cm^{-2}) will have a rms angle of scattering of about 7°.

Combining the above three angular spreads, we see that, if we exclude μ mesons with residual ranges smaller than 100 g cm^{-2}, we may expect the local μ-meson intensity, produced by the vertical N-component, to be contained within a cone of about 30° zenith angle. The unidimensional treatment of the μ-meson component can be considered valid within these limits.

[18] U. Haber-Schaim, Phys. Rev. **84**, 1199 (1951).

[19] Amaldi, Mezzetti, and Stoppini, Nuovo cimento **10**, 803 (1953).

[20] Brown, Camerini, Fowler, Heitler, King, and Powell, Phil. Mag. **40**, 862 (1949).

Abundance of Lithium, Beryllium, and Boron in the Primary Cosmic Radiation*

M. F. KAPLON, J. H. NOON, AND G. W. RACETTE
University of Rochester, Rochester, New York

(Received July 27, 1954)

The flux of nuclei of charge greater than two of the primary cosmic radiation has been measured at 41° and 55° geomagnetic latitudes with photographic emulsions flown in "Sky Hook" balloons. The technique used at the lower latitude is similar in principle to that employed originally by Bradt and Peters, while that used at the higher latitude is the method of Dainton, Fowler, and Kent. The different experimental methods are discussed and the latter is found more satisfactory for the light-element problem. Primary flux values are reported for the medium nuclei ($6 \leqslant Z \leqslant 10$) and the heavy nuclei ($Z > 10$) at the two latitudes. It is concluded that there exists a finite primary flux of the light nuclei ($3 \leqslant Z \leqslant 5$) and the most reliable value from these experiments of the ratio of the primary light-nuclei flux N_L^0 to the primary medium-nuclei flux N_M^0 at the top of the atmosphere is found to be 0.46 ± 0.15.

INTRODUCTION

ONE of the important problems in the study of the cosmic radiation today is that of determining the charge and energy spectrum of the primary beam. After the existence of multiply charged nuclei in the primary radiation was established,[1] the results of many different laboratories on experiments carried out at varying geomagnetic latitudes were in essential agreement on the magnitude of the incoming flux of nuclei with $Z \geqslant 6$, and established in first order the shape of their energy spectrum.[2] Because of the lack of agreement of subsequent experiments[3,4] designed to investigate in greater detail the chemical composition of the nuclei with $Z \geqslant 3$, and since a detailed knowledge of the chemical composition, especially the existence or nonexistence of the light nuclei, is of great importance in assessing the role of collisions of the heavy nuclear component with interstellar matter and its subsequent implications with respect to theories of the origin of cosmic radiation,[3] we have undertaken to repeat and evaluate the two experimental methods[3,4] which gave such markedly different results. To accomplish this purpose, two separate experiments, employing a different technique in each case have been carried out. The first experiment[5] was done with an emulsion stack flown at high altitude at 41° geomagnetic latitude and employed a technique similar to that used by Bradt and Peters.[3] The second was carried out with a stripped emulsion stack flown at 55° geomagnetic latitude and used the technique of Dainton, Fowler, and Kent.[4] We shall consider in order the two different experiments after a short discussion on the general problems involved in measurements on heavy nuclei in photographic emulsion.

DETECTION OF HEAVY NUCLEI IN EMULSION

In any experiment in photographic emulsion in which a systematic selection of a certain type of event is undertaken two general features always present themselves. The first involves the scanning of the emulsion and requires the fixing of some set of criteria so that the experimenter is assured that the particular class of events one is looking for is a subclass of that fixed by the scanning criteria; this is merely a reflection of setting the criteria loosely enough so that there exists a very high efficiency (which we will call scanning efficiency) for the inclusion of all events of the type sought. The second general feature that presents itself is that of selecting from all the events found in the scan those of the particular type sought; we shall call the efficiency with which this is done the decision efficiency.

The most general basis for selecting heavy nuclei in emulsion is that in which some measure of ionization is used, since for any given nuclear charge Z, the ionization at any arbitrary velocity less than c is greater than that at velocity c. Thus if it is desired to select all nuclei of $Z \geqslant 3$, which would be characterized by having $I/I_{\min} \geqslant 9$, one need only set the scanning criteria at some value sufficiently less than 9 so that a very high efficiency for the selection of all tracks having $I/I_{\min} \geqslant 9$ is realized. This scanning basis (along with some others) is the one adopted in the following experiments and a very high scanning efficiency is attained. It is in realization of the second feature (selection of class of events sought from those obtained in the scan) that the two experiments to be described here differ and indeed it is this feature which seems to be the root of discrepancies.

The necessity of setting the scanning criteria for ionization low enough so that a high scanning efficiency is attained has the consequence of introducing a large background of undesired events into the experiment

* This research was supported in part by the United States Air Force through the Office of Scientific Research, Air Research and Development Command.

[1] P. Freier *et al.*, Phys. Rev. **74**, 213 (1948).

[2] For a review of the situation as of 1951 see the article by B. Peters in *Progress in Cosmic Ray Physics* (North-Holland Publishing Company, Amsterdam, 1952), Vol. I. A survey covering the results as of the Fall of 1953 is given by E. P. Ney in the Report of the Duke Conference on Cosmic Radiation (unpublished).

[3] H. L. Bradt and B. Peters, Phys. Rev. **80**, 943 (1950). They find $N_L^0/N_M^0 < 0.1$ at $\lambda = 30°$.

[4] Dainton, Fowler, and Kent, Phil. Mag. **43**, 729 (1952). They find $N_L^0/N_M^0 \approx 1$ at $\lambda = 55°$.

[5] First reported by Racette, Kaplon, and Ritson, and Kaplon, Racette, and Ritson, Phys. Rev. **93**, 914(A) (1954).

and the decision efficiency attained while working in this background is quite crucial to the success of the experiment. Since it is desired to select nuclei of charge $Z \geqslant 3$ this requires the measurement of some property of the track that is a function of the mass of the particle giving rise to it, since the measurement of ionization for a given charge is a measure only of velocity. There are two readily measurable properties in emulsion which serve this purpose; the first is the range which is a function of the mass, charge, and velocity, and the second is multiple Coulomb scattering which is a different function of the same parameters. The combination of either of these two measurements with ionization will serve to select multiply charged particles from the background of slow singly charged particles observed in the scan.

In the first experiment to be described nuclei of charge greater than two are selected by the combined measurements of ionization and range; this method is in principle simple to implement and results from the fact that for a particle with an ionization $\geqslant 9I_{\min}$ to be at least triply charged it must have a certain minimum range in which the ionization remains constant. In the second experiment the nuclei are selected by combining the measurements of ionization and multiple Coulomb scattering. While in principle each of these techniques is straightforward it will be seen that there is basis for criticism of the results obtained in employing them.

EXPERIMENT I

Experimental Arrangement

In this experiment twenty-four 4 in.×6 in.×250μ Ilford emulsions mounted on 1.4-mm glass were arranged in 8 triads of G-5, C-2, and D-1, emulsions, each plate separated from its neighbor by thin paper. The stack was flown with the 6 in.×250μ emulsion edge vertical for approximately 8 hours at White Sands, New Mexico (41° geomagnetic latitude); the flight curve is shown in Fig. 1 (an additional 4 g/cm^2 of effective residual atmosphere must be added to account for the packing and the stack material above the survey plate). The emulsions were processed by the usual methods of temperature development and after completion each plate was cut into four 2-in.×3-in. sections for microscopic observation. The relative alignment of the cut plates was determined by using very heavy nuclei ($Z>10$) as markers and a coordinate transformation scheme was derived to facilitate the tracing of tracks from plate to plate. The thickness of the emulsion at the time of exposure was determined by measurements on heavy nuclei which traversed the entire stack.

Scanning Criteria and Charge Calibration

The scanning for heavy nuclei was carried out under low magnification (diameter of field of view = 720μ) on the top sections of the 5th and 7th G-5 emulsions. Only those tracks were selected which had a projected length $L_p \geqslant 720\mu$ and a grain density $g > 100/75\mu$. The length criterion was adopted to reduce background and ensure more efficient tracing; the ionization criterion insured the inclusion of all nuclei with $Z \geqslant 3$, while excluding fast α particles since this grain density corresponded to $I/I_{\min} > 5.1$.

Charge calibration was obtained in the following way. The value of minimum ionization for singly charged particles is easily obtained from observations on the decay electrons from μ mesons, and, from this, the value for fast α particles is predicted. From observations on the breakup of fast heavy nuclei fast α particles are selected and from these we determine in G-5 emulsion the values of grain density per 75μ (g), δ-ray density per 100μ (n_δ), and the gap density (G) and the corresponding values in C-2 emulsion for grain density (g') and gap density (G'), thus establishing the values of these quantities for $I/I_{\min} = 4$.

To extend the calibration, gap-density measurements were made on stopping μ mesons in the G-5 emulsion, and it was found that μ mesons of residual range $R = 1900\mu$ had the same ionization as the fast α particles; in addition the gap-density of μ mesons of 290μ residual range was the same as that of particles tentatively identified as fast Li nuclei (on the basis of δ-ray and grain density) in the collision fragments of heavy nuclei. Since the ratio of specific ionization for a μ meson of 290μ residual range to that of one with 1900μ residual range is $\approx 2.2 = 9/4$, the identification of fast Li nuclei ($I/I_{\min} = 9$) is established. The grain and gap density of these particles was then determined in the C-2 emulsion.

Since the δ-ray density for fast α particles and Li nuclei was known, the δ-ray density for fast particles of arbitrary Z could be predicted. From $n_\delta(2)$ and $n_\delta(3)$ we obtain $n_\delta'(1)$, the true δ-ray density for a fast singly charged particle and the background contribution b by using the relation $n_\delta(Z) = Z^2 n_\delta'(1) + b$. For these emulsions and our counting criterion (4 grain convention) we determined $n_\delta'(1) = 0.09$ per 100μ and $b = 0.24$ per

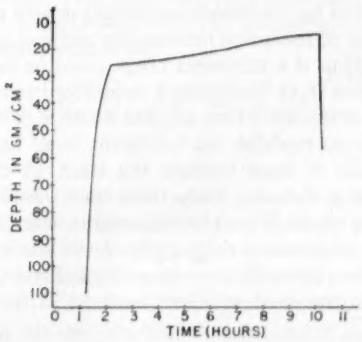

FIG. 1. Flight curve of balloon carrying plates used in experiment I.

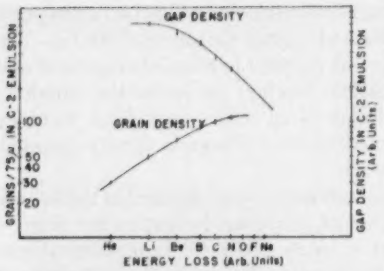

FIG. 2. Grain-density and gap-density calibration curves for C-2 emulsions of experiment I.

100μ. This calibration was further checked by studying an interaction in emulsion which could be interpreted only as the breakup of a fast N nucleus. (Two doubly charged and one triply charged particles emitted.) The observed $n_\delta(7)$ agreed very well with the predicted value; the grain density in C-2 emulsion for this particle was then determined enabling a calibration curve for this emulsion extending from $I/I_{\min}=4$ to 49 to be constructed (Fig. 2). Since the high sensitivity of our C-2 emulsion, compared to that of normal C-2 emulsion, did not allow accurate charge resolution for fast nuclei of $Z>7$[6] (but did allow excellent discrimination between B and C) the gap density of identified nuclei with $Z\leqslant 7$ was determined in C-2 emulsion to establish a calibration curve which was extrapolated to higher Z (Fig. 2).

Scanning and Decision Efficiency-Observed Fluxes

The minimum grain density $g>100$ used in the selection of tracks in the scan corresponded to $I/I_{\min}>5.1$. Since this ionization acceptance is quite conservative it ensures the inclusion of all nuclei of $Z\geqslant 3$ (as will be demonstrated shortly) in the scan. To establish which of the tracks accepted in the scan were indeed heavy nuclei of $Z\geqslant 3$, it was necessary to establish a minimum range. At the geomagnetic latitude of this flight the cut-off kinetic energy per nucleon $\epsilon=1.58$ Bev. At this energy all nuclei with $3\leqslant Z\leqslant 10$ are sufficiently relativistic at flight altitude so that their ionization (n_δ, g or G) is a direct measure of their charge; the distinction is not valid for the heavier nuclei but is such that there is no lack of resolution between the medium and heavy group. Thus if a minimum range could be established for a given track its charge is established as being $\geqslant 3$, and its ionization is then a direct measure of its charge. In order to establish the minimum range an attempt was made to trace through the stack all the tracks obtained in the scan. Only those tracks were accepted as heavy nuclei ($Z\geqslant 3$) which could be traced either to a point of entrance at the top of the stack or to an interaction above the survey plate, and which in addition had traversed sufficient material in the stack to ensure that they were not slow α particles. Since an α particle of the same ionization as a fast Be nucleus has a range <7.2 g/cm^2 this discrimination could be made positively for all nuclei with $Z\geqslant 4$; an α particle of the same ionization as a fast Li nucleus has a residual range of 36 g/cm^2 so that a track must be traced for at least 12 g/cm^2 with no change in ionization (an α particle would change its ionization by more than 15 percent) to be accepted as Li. In two cases (due to geometrical restrictions) it was not possible to distinguish with certainty between a slow α and a Li nucleus; these two cases are accepted in the analysis as Li nuclei.

The observed charge spectrum on the survey plates resulting from the decisions made in the tracing (this is the weighted result as determined by δ-ray, grain, and gap density) is shown in Fig. 3 and corresponds to:

$$L \text{ nuclei } (3\leqslant Z\leqslant 5): \quad 20/15.6 \text{ cm}^2;$$
$$M \text{ nuclei } (6\leqslant Z\leqslant 10): \quad 31/15.6 \text{ cm}^2;$$
$$H \text{ nuclei } (Z>10): \quad 8/15.6 \text{ cm}^2.$$

The plates were scanned and the tracks followed by two independent observers. Their results are given in Table I. In addition 0.8 cm^2 of the same emulsion was scanned by both observers. In this scan, observer A found 6 tracks missed by B; of these, 3 had g so close to 100 as to represent fluctuations in grain counting, and the other three had $g\leqslant 110$ corresponding to $I/I_{\min}\leqslant 6$. It thus seems highly probable that the scanning efficiency for tracks with $I/I_{\min}\geqslant 9$ is 100 percent. In tracing, observer A traced one track not successfully traced by B due to an error in sign in determining the coordinate transformation; however in this aspect of tracing the sign convention was always independently checked so this could not be a contribution to decision inefficiency. Two other tracks were traced by both observers, but the remainder of the tracks found in this area could not be traced by either observer.

In an experiment of the type under discussion here it is quite important to realize 100 percent decision efficiency; since the observed signal-to-noise ratio (see Table I) is ≈ 0.05, it is seen that a decision inefficiency of only 2 percent would imply that ~ 1.6 tracks/cm^2 were not traced and included as heavy nuclei when they should have been, and this would correspond to

TABLE I. Results obtained in scanning and tracing in Experiment I.

Observer	A	B
Total area scanned	10.03 cm^2	5.57 cm^2
Tracks/cm^2 with $g>100$	73.5±8.6	89.6 ±9.5
Tracks traced/cm^2 (total)	4.1±0.64	3.24±0.76
$Z>10$	0.5±0.22	0.54±0.32
$6\leqslant Z\leqslant 10$	2.2±0.46[a]	1.62±0.54[a]
$3\leqslant Z\leqslant 5$	1.4±0.37[a]	1.08±0.45[a]

[6] Though it was originally hoped to use the D-1 emulsions to obtain a higher degree of charge resolution for the heavier nuclei this was not possible due to the existence of a high fog background in these emulsions.

[a] One of the total number traced of these particles was found to arise from an interaction above the survey plate.

losing approximately $\frac{1}{3}$ to $\frac{1}{2}$ of the signal. It is quite difficult to estimate in a reliable way the decision efficiency attained, but one estimate can be made as follows. Because of the stack arrangement each track selected in the scan in the G-5 emulsion had to pass through a C-2 emulsion before passing through another G-5 emulsion, so that in tracing an attempt was first made to locate a track in the nearest C-2 emulsion (since the distance involved was least). In a separate survey covering 4.25 cm² on plate 14 (a C-2 emulsion) which accepted tracks with $L_p \geq 432\mu$ and $g' \geq 45$, 7 tracks were found which were followed to the survey area of plate 13 (a G-5 emulsion) and which met the acceptance criteria for that plate; all of these had been previously found and successfully traced from the G-5 plate. We find then from the scan and tracing from the C-2 emulsion the selection of $7/4.25 = 1.65 \pm 0.6$ tracks per cm² as nuclei with $Z \geq 3$. This figure is the order of $\frac{1}{2}$ the number of tracks selected per cm² from the G-5 emulsion as being L nuclei or heavier and indicates certainly that the product of scanning efficiency and decision inefficiency in the insensitive emulsion is about twice that in the G-5; in addition, it certainly seems reasonable and is borne out by subsequent observations that the L nuclei are the ones most strongly affected. This feature (lack of 100 percent efficiency for detecting a particle known to be in the insensitive emulsion) was recognized in the course of the experiment and to remedy this the tracing was attempted directly to the nearest G-5 emulsion if a null result was obtained on the tracing attempt to the nearest C-2 emulsion. This increase of distance over which the tracing must be done, especially for the light nuclei, would tend to reduce the decision efficiency for this class. A crude estimate of the decision inefficiency may be obtained by saying that it is equal to 100η (tracks traced/cm² from G-5 − tracks traced/cm² from C-2)/(tracks accepted/cm² in G-5), where $0 \leq \eta \leq 1$; for $\eta \sim \frac{1}{2}$ the decision inefficiency is ~1.4 percent.

An additional check on the decision efficiency is obtained by an examination of the interactions undergone in glass by those nuclei successfully traced below the survey plate. We find for the interaction mean free paths in g/cm² of glass the values $\lambda_H = 19.4 \pm 9$, $\lambda_M = 38.5 \pm 12$, and $\lambda_L = 26 \pm 12$. The values obtained for the heavy and medium nuclei are in excellent agreement with those expected[7] (and support the contention that the decision and tracing efficiency for these nuclei is 100 percent), but the value for the eight nuclei is considerably less than the expected value of 42 g/cm². Since a particle is said to have interacted if (*a*) interaction products can be seen or (*b*) if it cannot be traced further, a possible contribution to the measurement of a too short mean free path could be due to a tracing inefficiency giving rise to pseudointeractions. If the discrepancy in the measured value of λ_L is ascribed to tracing inefficiency we find this implies that an additional 10 L nuclei which should have been detected and successfully traced from the scanning area were missed. This leads to an estimate of decision inefficiency of 100 (true tracks not traced from survey area/cm²)/(tracks accepted/cm²) ≈ 0.8 percent. The approximate agreement between these two different estimates of the decision inefficiency suggests that there exists a systematic error arising from this which affects the L nuclei predominantly; the magnitude of this effect being a loss of ~0.65 to 1.2 L nuclei per cm². It is thus possible that if the above estimates are meaningful that at least 10 to 18 L nuclei which existed in the area scanned on the survey plates were not properly classified due to a small departure from 100 percent decision efficiency so that the true light nucleus flux per 15.6 cm² could be as high as 30 to 38.

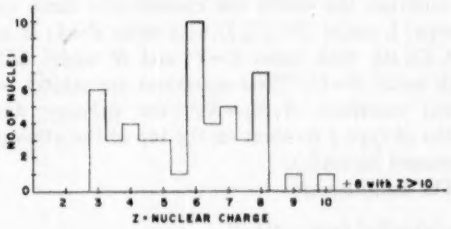

FIG. 3. Charge spectrum observed at flight altitude in Experiment I.

Primary Flux Values

In order to obtain the true flux values of the various components of the heavy nuclei at the top of the atmosphere it is necessary to extrapolate the values observed at flight altitude back through the residual atmosphere to the top. Since it is known that in the interactions of these nuclei, nuclei of lower Z are emitted as fragmentation products with appreciable probabilities (especially the light nuclei),[8] a straight exponential type of extrapolation is not appropriate and one should consider the diffusion equations for the heavy nuclei. With the neglect of ionization loss and the assumption of energy independence for the parameters λ_I, $P_{I'I}$ (defined below) these are

$$dN_I(x)/dx = -N_I(x)/\lambda_I + \sum_{I' \geq I} P_{I'I} N_{I'}(x)/\lambda_{I'} \qquad I = H, M, L$$

$$H > M > L,$$

where λ_I is the mean free path in g/cm² of atmosphere for the Ith component of the heavy element flux, $P_{I'I}$ is the probability that in an interaction of a nucleus of type I' a nucleus of type I (of assumed comparable momentum per nucleon) is emitted, $x = h/\cos\theta$ is the amount of atmosphere traversed, h the vertical depth below the top of the atmosphere and θ the zenith angle;

[7] M. F. Kaplon *et al.*, Phys. Rev. **85**, 295 (1952).

[8] J. H. Noon and M. F. Kaplon (to be published).

in addition the nuclei are classed into three charge groups: L nuclei ($3 \leqslant Z \leqslant 5$) with mean $Z=4$; M nuclei ($6 \leqslant Z \leqslant 10$) with mean $Z=7$; and H nuclei ($Z>10$) with mean $Z=15$. These equations are subject to the initial condition $N_I(0)=N_I^0=$ the primary flux of nuclei of type I incident on the top of the atmosphere (assumed isotropic).

The solutions are:

$$N_H(x)=N_H^0 \exp(-x/\lambda_H'),$$

$$N_M(x)=N_M^0 \exp(-x/\lambda_M')+(\alpha_{HM}P_{HM}/\lambda_H) \times[N_H^0 \exp(-x/\lambda_M')-N_H(x)],$$

$$N_L(x)=N_L^0 \exp(-x/\lambda_L')+(\alpha_{ML}P_{ML}/\lambda_M) \times[N_M^0 \exp(-x/\lambda_L')-N_M(x)] +(\alpha_{HL}/\lambda_H)(P_{HL}+P_{HM}P_{ML}\alpha_{ML}/\lambda_M) \times[N_H^0 \exp(-x/\lambda_L')-N_H(x)],$$

where $\lambda_I'=\lambda_I/(1-P_{II})$, $\alpha_{IJ}=\lambda_J'\lambda_J'/(\lambda_J'-\lambda_I')>0$; $\lambda_J'>\lambda_I'$. In the above the first term on the right-hand side represents the absorption of the incident flux of type I, and the other terms represent contributions to this flux at depth x due to interactions of heavier nuclei.

For this experiment the detection efficiency of the plates for their geometry at exposure (a function of zenith angle θ) and the time variation of the flight curve must be taken into account. The detection efficiency factor $F(\theta)$ for vertically oriented plates is given in Sec. IV of a paper by Bradt and Peters.[9] In this experiment the altitude variation can be well represented by $h(t)=h_0-(\Delta h)t$. The solutions of the equations given above are then multiplied by $F(\theta)d\theta dt$ and integrated. The following values of the parameters were used:[8] $\lambda_L=31.5$ g/cm^2, $\lambda_M=26.5$ g/cm^2, $\lambda_H=18$ g/cm^2, $P_{LL}=P_{MM}=0.13$, $P_{HH}=0.25$, $P_{HM}=0.27$, $P_{ML}=0.42$, and $P_{HL}=0.48$. The results obtained are given below where $N_I(F)$ means the number of nuclei of type I observed at flight altitude

$$N_H^0=2.6\pm0.9 \text{ particles/meter}^2 \text{ sec steradian.}$$

$$N_M^0=7.1\pm1.3 \text{ particles/meter}^2 \text{ sec steradian.}$$

$$N_L(F)=0.76N_M(F)+(N_L^0/N_M^0)(32.3\pm6).$$

The flux values obtained for the medium and heavy nuclei agree with values previously reported.[7] Due to fragmentation into L nuclei of M and H nuclei in the residual atmosphere we see that 23.5 ± 4.3 of the L nuclei observed must be due to these processes and are not of a primary nature. Thus we find that $N_L^0/N_M^0=0$, if no correction for decision efficiency is made in obtaining the light element flux at flight altitude. On the other hand, since the estimate of decision efficiency would predict a value of $N_L(F)$ as high as 38, an upper limit can be set at $N_L^0/N_M^0 \leqslant 0.55$. It is thus readily apparent that the value of the light element flux at the top of the atmosphere is extremely sensitive to the decision efficiency attained in this type of experiment.

[9] H. L. Bradt and B. Peters, Phys. Rev. 77, 54 (1949).

EXPERIMENT II

Experimental Arrangement

A stack of twenty-four 4-in.×6-in.×400μ G-5 stripped emulsions (in direct contact with each other) was flown with vertical geometry for 8.2 hours at 102 000 ft at 55° geomagnetic latitude; the flight curve is given[10] in Fig. 4 (an additional 2 g/cm^2 must be added to account for the packing material). The stripped emulsions were mounted on glass before development and then processed by the usual temperature methods. After completion of the processing each plate was cut into four 3-in.×2-in. sections which were then mounted and consecutively aligned on Lucite frames using very heavy nuclei as markers.[11] The degree of alignment attained was such that minimum ionizing tracks could be unambiguously traced through the stack. The emulsion thickness at the time of exposure was determined by measurements on long tracks traversing the stack.

Scanning Criteria and Charge Calibration

The survey plates were scanned for tracks satisfying the following four criteria: (1) projected length in emulsion $L_p>3$ mm; (2) zenith angle $\theta<45°$; (3) so located geometrically that each track had a possible range in the stack $R \geqslant 20$ g/cm^2 of emulsion; (4) $I/I_{\min} \geqslant 6.2$ on the basis of grain density. Criteria (1) and (3) were adopted to ensure sufficient track length so that scattering and δ-ray measurements could be done with sufficient statistical accuracy; criterion (2) was adopted in order to reduce the uncertainties involved in the extrapolation of the observed fluxes to the top of the atmosphere (all particles accepted in the scan had traversed <25.4 g/cm^2 of atmosphere, including the atmospheric equivalent of the packing material); and criterion (4) was adopted to ensure the inclusion in the scan of all tracks with $I/I_{\min} \geqslant 9$.

The basic charge calibration for fast nuclei was established in the G-5 emulsion used in this experiment in an identical manner to that described in Experiment I. For these emulsions, using a 4 grain convention in δ-ray counting, we obtained $n_8'(1)=0.097$ and a background contribution $b=0.1$. The grain density g corresponding to the acceptance criterion (4) was $g=125$. In addition to the measurements made above to establish the calibration for fast nuclei, an extensive check was possible in this experiment by studying a number of interactions in emulsion of fast heavy nuclei (a measure of the energy per nucleon can be obtained from the degree of collimation of the fragments) in which charge balance between the incoming nucleus and its fragmentation products was obtained;[8] the results obtained in this study were in excellent agree-

[10] We are indebted to Professor E. P. Ney for a discussion of the characteristics of this balloon flight and its latitude trajectory. He informs us that a more realistic figure for the ceiling attained is 92 000 ft instead of the 102 000 ft shown in the curve of Fig. 4.

[11] J. Crussard *et al.*, Phys. Rev. 93, 253 (1954).

ment with those obtained by the method of Experiment I.

In an experiment of this type charge identification is made by the simultaneous measurement of momentum (by multiple Coulomb scattering) and velocity (by δ-ray density). This requires knowledge of the dependence of δ-ray density on velocity. No systematic attempt was made in this experiment to verify the relationship between velocity and δ-ray density obtained by the Bristol group.[4] Verification of their relation on both a theoretical and experimental basis has recently been obtained by Tidman, George, and Herz.[12] The results obtained in this experiment in the low momentum region[13] also support the validity of that relationship. Measurements on several stopping nuclei supply an independent verification of this relationship; the observed variation of δ-ray density with range for these nuclei is in agreement with that derived from the Bristol results giving the velocity dependence of δ-ray density. We have adopted this calibration for charge identification of non-relativistic nuclei.

Scanning and Decision Efficiency-Observed Fluxes

The scanning was done on the top sections of 7 emulsions using the criteria given previously. A total area of 210 cm² was scanned by two observers independently, and an area of 30 cm² included in the above was scanned by a third. In the total area observer A found 680 tracks satisfying the scanning criteria, B found 708, and no additional tracks were found by observer C in scanning the area of 30 cm². The over-all scanning efficiency is thus ~96 percent for the inclusion of tracks with $I/I_{\min}>6.2$. In the tracks selected in the scan there is a considerable background of slow singly charged particles as well as nonrelativistic α particles. The slow singly charged particles are easily discriminated against in tracing through the stripped emulsion since they have a residual range <7.2 g/cm² (1.8 cm) and exhibit a striking change in grain density over this region. By this procedure most singly charged particles were rejected leaving a total of 136 (by observer A) and 142 (by observer B) tracks retained for measurement of δ-ray density and multiple scattering. The results of these measurements showed that the 6 additional tracks found by B were α particles; since the ionization criterion was set sufficiently low we believe that no tracks with $I/I_{\min}>7.5$ were missed in the scan, and thus a scanning efficiency of 100 percent was attained for the inclusion of nuclei with $Z\geqslant 3$. Since the tracing in the stripped emulsion serves to eliminate the background of singly charged particles and some few doubly charged particles and the charge of the remaining tracks are all determined by the same method of scattering and δ-ray density, then, with the assumption that this method is not subject to systematic errors the decision efficiency for nuclei with $Z\geqslant 3$ is 100 percent.

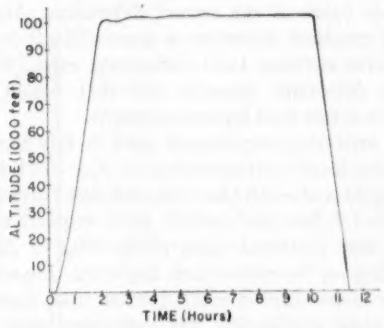

FIG. 4. Flight curve of balloon carrying emulsions used in Experiment II. (See reference 10.)

The scattering measurements were made using the coordinate method.[14] In this method the scattering in degrees/100μ is given by

$$\bar{\alpha}_{100}=KZ/(A\,p\beta c)=0.573\bar{D}_t/(t/100)^{\frac{1}{2}},$$

where K is a constant slightly dependent on the cell size t used.[15] A is the mass number of the nucleus with charge Z, βc its velocity, p the momentum per nucleon, and $\bar{D}_t$ is the average of the absolute value of the second differences obtained by the coordinate method. In the measurement of $p\beta c$ by multiple scattering any sources of error are usually of such a nature as to increase the measured scattering angle and therefore lead to an underestimate of the true momentum. The systematic errors inherent in the measurement of scattering are of two different types: (1) statistical and (2) nonstatistical. Errors of the first type arise from uncertainties involved in setting the hairline due to finite track thickness and also from the pseudoscattering arising from stage noise; the setting error is relatively unimportant except for the very thickest tracks. With the assumption that these errors are independent of cell size and are distributed Gaussianly we may consider them together as a statistical noise. It is then possible to correct for these errors in the measurement by the method of noise elimination between different cell sizes[16] or by the use of the third differences obtained in the coordinate method.[17] The most important error of a nonstatistical nature arises from emulsion distortion. If the emulsion distortion is of the normal C-shaped type it may be corrected for by subtracting from each second difference the average of the

[12] Tidman, George, and Herz, Proc. Phys. Soc. (London) **A66**, 1019 (1953).

[13] It is in the low momentum region that the greatest deviation of the Bristol results from that of the so-called Rutherford formula for δ-ray density occurs. The verification obtained from our results is most reliable in this region since any systematic sources of error, such as stage noise or emulsion distortion, will have the least effect for particles of low momentum.

[14] P. H. Fowler, Phil. Mag. **41**, 169 (1950).

[15] L. Voyvodic and E. Pickup, Phys. Rev. **85**, 91 (1952).

[16] M. G. K. Menon *et al.*, Phil. Mag. **42**, 932 (1951).

[17] J. E. Moyal, Phil. Mag. **41**, 1058 (1950).

algebraic value of the second differences. Any other type of emulsion distortion is more difficult to correct for; where extreme local distortions exist, these are usually detectable visually and that region of the emulsion is not used for measurement.

The scattering microscopes used in this experiment had noise levels corresponding to $\bar{\alpha}_{100}\sim 0.01$ for 500μ cell lengths and ~ 0.02 for 250μ cell sizes corresponding to $p\beta c\sim 1.3$ Bev and ~ 0.65 Bev, respectively. The tracks were scattered using either 500μ or 250μ cells depending on the momentum. Since the true scattering for low momentum is much greater than that due to noise, noise elimination was performed only on the faster tracks. In addition the correction referred to in the previous paragraph for distortion was applied to all measurements.

The results obtained by the measurement of multiple scattering and δ-ray density are shown in Fig. 5 (the crosses refer to stopping tracks). We have plotted δ-day density normalized to that of a fast α particle *versus* the scattering angle $\bar{\alpha}_{100}$. The solid curves drawn represent lines of constant charge derived from the Bristol calibration. The charge spectrum at flight altitude derived from this figure is given in Fig. 6 and corresponds to 30 light, 28 medium, and 5 heavy nuclei.

Discussion of Data

An inspection of Fig. 5 shows that there are only 8 nuclei with $Z\geqslant 3$ having a kinetic energy per nucleon $\epsilon>850$ Mev, corresponding to $\epsilon>1$ Bev at the top of the atmosphere. An integral energy spectrum of the form[7] $1/(1+\epsilon)^{1.85\pm 0.1}$ would predict that the ratio of the number of nuclei with $\epsilon>1$ Bev to those with $\epsilon<1$ Bev at this latitude should be ~ 0.9 in contrast to the observed ratio of ~ 0.15 (the observed ratio for those nuclei with $Z\geqslant 6$ is ~ 0.22). It is difficult to see how the predictions of the above spectrum could be in serious error for these energy ranges since it is derived from the results of flux measurements of heavy nuclei at different latitudes. (This spectrum is consistent with the flux values observed at the two different latitudes reported in this paper.) This discrepancy strongly suggests the existence of a systematic error in the estimation of the momentum by the scattering method, resulting in an underestimation of the true momentum. This does not affect charge determination for $\bar{\alpha}_{100}\leqslant 0.01 (p\beta c\geqslant 1.3$ Bev) because the δ-ray density for a given nucleus of $\beta=1$ differs from that of a nucleus of this momentum by less than 10 percent. However for $\bar{\alpha}_{100}\gtrsim 0.01$ this error can result in underestimation of charge by one unit and a resultant distortion of the charge spectrum for this momentum region.

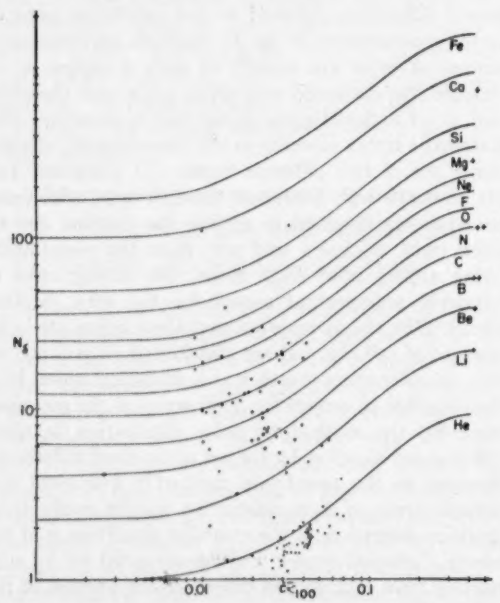

FIG. 5. Plot of δ-ray density (normalized to that of relativistic α particles) *vs* scattering angle $\bar{\alpha}_{100}$ (degrees/100μ) for tracks observed in Experiment II. The curves represent lines of constant charge.

An inspection of Fig. 5 shows that with the exception of one nucleus at $\bar{\alpha}_{100}=0.0025$ (which value was derived by using the relative scattering method[18] and for which a value of ~ 0.01 was obtained using the conventional method), that the maximum detectable value of $p\beta c$ in this experiment is ~ 1.3 Bev. The discrepancy previously mentioned may therefore be due to limitations imposed by instrumental or emulsion characteristics. The minimum value of the scattering detected in this experiment implies the existence of some systematic error of $\sim 0.01°$ in the scattering measurements which may exist for all the tracks. This error may be of a statistical nature arising from microscope noise which was not constant with cell size or it may be of a nonstatistical nature, possibly due to some anomalous emulsion distortion, in which case it would contribute arithmetically. If it is of a statistical nature (assumed Gaussian for purposes of estimation) it will appreciably affect only those values of $\bar{\alpha}_{100}\lesssim 0.02$. A correction of this nature does not alter the charge spectrum but does have the consequence of making the ratio of nuclei with $\epsilon>1$ Bev to those with $\epsilon<1$ Bev of the order of 0.5. An error of a nonstatistical nature which would contribute arithmetically to the observed scattering would affect those values of $\bar{\alpha}_{100}\lesssim 0.06$. This results in a considerable distortion of the charge spectrum but only a minor change in the total number of nuclei in the light and medium groups; we obtain a reclassification corresponding to 27 light nuclei, 32 medium nuclei and 5 heavy nuclei as contrasted with 30, 28, and 5 respectively (this involves the reclassification of one α-particle); the breakdown into component elements corresponds to 10 Li, 7 Be, 10 B, 10 C, 12 N, 5 O, 2 F, and 3 Ne as contrasted with 10 Li, 13 Be, 7 B, 12 C, 9 N,

[18] Noon, Kaplon, and Crussard, Phys. Rev. 95, 1103 (1954).

3 O, 3 F, and 1 Ne in the uncorrected charge distribution shown in Fig. 6. The ratio of nuclei above and below $\epsilon=1$ Bev now becomes ~ 0.71. Since an arithmetical correction is the most extreme method of correcting a scattering measurement the results given above represent the maximum of charge spectrum distortion in this experiment.

Due to the uncertainties involved in the correction of the charge spectrum we adopt the following median values of the two limiting spectra at flight altitude for the analysis; 28.5 light nuclei, 30 medium nuclei, and 5 heavy nuclei.

Primary Flux Values

The tracks selected in this experiment have all traversed between 18 and 25.4 g/cm² of atmosphere (including packing material)[10] before reaching our emulsion stack. For the track length criterion adopted in this experiment the geometrical detection factor becomes independent of zenith angle, and at the depth of this exposure it is sufficiently accurate to consider all these nuclei as having traversed this depth at a mean zenith angle of 30° corresponding to a mean path in atmosphere of 20.7 g/cm².

TABLE II. Extrapolated primary flux values observed at 41° and 55° geomagnetic latitudes.

	Primary flux values (particles/meter² sec steradian)		
Geomagnetic latitude	$M(6\leqslant Z\leqslant 10)$	$H(Z>10)$	$N_L^0/N_M^0(3\leqslant Z\leqslant 5)$
41°	7.1±1.3	2.6±0.9	$\leqslant 0.55$
55°	11.5±1.7	3.0±1.2	0.46±0.15

The observed fluxes at flight altitude are then extrapolated to the top of the atmosphere by means of the diffusion equations whose solutions were given previously under Experiment I; the same values of the parameters are used here. The following flux values were obtained after making a correction for ionization loss in the residual atmosphere.

$$N_H^0=3.0\pm 1.2 \text{ particles/meter}^2 \text{ sec steradian},$$

$$N_M^0=11.5\pm 1.7 \text{ particles/meter}^2 \text{ sec steradian},$$

$$N_L^0/N_M^0=0.40\pm 0.12.$$

The values for the medium and heavy nuclei fluxes are in substantial agreement with those obtained elsewhere.[2,4] If the flight did indeed obtain the altitude of 102 000 ft we find then $N_L^0/N_M^0=0.52\pm 0.15$ for the same ratio of light to medium nuclei at flight depth. The extreme limits for this ratio taking into account the uncertainty in depth and the effect of charge distortion are 0.35 and 0.65. We feel the most reliable value is 0.46±0.15.

An independent estimate of the contribution of interactions to the observed flux of light nuclei at flight altitude is obtained by an examination of those light nuclei whose measured energy when extrapolated to the top of the atmosphere is below the geomagnetic cut-off value for the latitude of the flight; four of the light nuclei are in this category and certainly must come from interactions of slow heavier nuclei. The maximum energy of heavy nuclei at the top of the atmosphere which could produce these secondaries is ~ 0.56 Bev/nucleon (we assume the velocity per nucleon is invariant in these interactions). If we assume energy independence for the production probabilities we then calculate, using the energy spectrum of Kaplon *et al.*[7] that the number of light secondaries produced by heavier nuclei with $\epsilon\geqslant 0.56$ Bev is $\geqslant 11$. This corresponds to a secondary light nuclei flux of $\geqslant 15$ in approximate agreement with the predictions obtained using the diffusion equations.

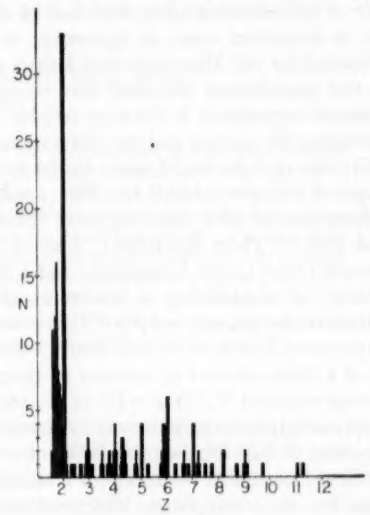

FIG. 6. Charge spectrum observed at flight altitude in Experiment II (not corrected for charge distortion).

DISCUSSION AND CONCLUSIONS

The results obtained for the primary flux values at the top of the atmosphere in this experiment are given in Table II. Within the limited statistics of these experiments, the relative fluxes for nuclei of $Z\geqslant 6$ at these two latitudes are consistent with the published spectra for heavy nuclei[7] and are in agreement with the flux values obtained at other laboratories.[1,2,4,7,19] Because of the limited statistics available it is impossible to say anything definitive about the charge spectrum for those nuclei with $Z>10$. We find the medium element group is predominantly composed of C, N, and O, the elements F and Ne comprising <10 percent of this charge group; of the elements C, N, and O we find C and N occurring in comparable amounts and the abundance of O< that of N. This result is in disagreement with that of Bradt and Peters who find that the

[19] G. D. Freier *et al.*, Phys. Rev. **84**, 322 (1951).

abundance of N is distinctly less than that of either C or O and is somewhat more in agreement with the results obtained by the Minnesota and Bristol groups.

Of the two experiments described here we conclude that the second experiment is the most reliable in view of the preceding discussions and we therefore conclude that a finite flux of light nuclei exists at the top of the atmosphere, $N_L^0/N_M^0=0.46\pm0.15$. This result is in marked disagreement with that originally obtained by Bradt and Peters.[3] Their experiment, done at $\lambda=30°$, was of a similar type to our Experiment I and involved the necessity of establishing a minimum range to identify their tracks as nuclei of $Z\gtrsim3$. It is possible (as in our Experiment I) that their null result is due to the existence of a finite amount of decision efficiency. The Bristol group reported $N_L^0/N_M^0\approx1.1$ at the top of the atmosphere; this result was obtained by extrapolation using the value of 0.23 for the probability of obtaining a light nucleus from either a medium or a heavy one in an interaction in atmosphere. Observationally our results at a comparable atmospheric depth are quite similar with respect to the ratio of light and medium nuclei. We have applied our extrapolation procedure to their data and find that it is consistent with a value of $N_L^0/N_M^0\approx0.6\pm0.1$. Their experiment is subject to the same criticism as that of our Experiment II. The energy spectrum derived from their data predicts a flux of medium nuclei at $\lambda=41°$ of $\frac{1}{3}$ the actual flux observed at that latitude. This suggests the existence of some systematic error in their scattering measurements such that the momentum is underestimated and could result in a distortion of their charge spectrum, the result of which would be to increase the flux of medium elements at the expense of the light-element group. Hourd, Fleming, and Lord[20] have recently reported their results of an analysis of a stack of emulsion flown at $\lambda=10°$ and obtain (using fragmentation probabilities similar to those used in the analysis here) a value of $N_L^0/N_M^0=0.33\pm0.09$. Further results on this problem have been recently obtained by the Minnesota group[21] using counter techniques in balloons flown at 41° geomagnetic latitude; they report an upper limit of $N_L^0/N_M^0\leqslant0.4$ and find that the best interpretation of their data is consistent with 0.

In view of the fact that substantial evidence has been presented for the existence of a finite ratio of light to medium nuclei at the top of the atmosphere of comparable amounts at both 10° and 55° geomagnetic latitude, the assumed validity of the null results obtained would imply the existence of an extreme time variation for this component. Since such a result would be quite difficult to understand (if at all), and in view of the fact that the experiments (at least in emulsion) giving a null result may be criticized on the basis of decision inefficiency, we conclude that the present evidence supports the existence of a finite flux of light nuclei in the primary radiation incident on the earth's atmosphere and the ratio of this flux to that of the medium-element group as obtained by different laboratories is consistent with 0.46 ± 0.15 and does not seem to be energy-dependent.

The existence of this finite flux of light nuclei in the primary radiation has important consequences for theories of the origin of cosmic radiation. If Li, Be, and B do not exist in significant amounts in the source region (or regions) of cosmic rays[22] which are retained in our galaxy by magnetic fields,[23] then an approximate value of the average lifetime of travel in interstellar matter can be set at $t\sim10^6/\rho$ years, where $\rho=$ No. of H atoms/cm^3. In addition, with these assumptions, the relative magnitude of medium and heavy nuclei injected at the source cannot be significantly different from that observed in the primary radiation incident on the earth's atmosphere. In finite amounts of Li, Be, and B exist in the source region and the above assumption of galactic retention is retained, then $t<10^6/\rho$ years; if the galaxy has no retentive property and extra galactic origin is not considered, then the light elements must exist in the source region. In conclusion, we note that the lifetime $t\sim10^6$ years ($\rho\sim1$) is in agreement with that deduced by Morrison, Olbert, and Rossi[24] from considerations involving the isotropy and composition (other than Li, Be, and B) of the cosmic radiation.

We wish to thank the Aero Medical Field Laboratory of Holloman Air Force Base for supplying the balloon flight for Experiment I and the U. S. Office of Naval Research for sponsoring the balloon flight for Experiment II. We are indebted to Miss Phyllis Hull for her assistance both in scanning and in making scattering measurements and to Miss Barabara Hull for her assistance in some of the scanning.

[20] Hourd, Fleming, and Lord, Phys. Rev. **95**, 647 (1954).
[21] Leland Bohl (private communication).
[22] L. Aller, *Astrophysics*; *The Atmospheres of the Sun and Stars* (Ronald Press, New York, 1953). The astrophysical abundance of the light elements given here is $<10^{-3}$ that of the medium elements.
[23] E. Fermi, Phys. Rev. **75**, 1169 (1949).
[24] Morrison, Olbert, and Rossi, Phys. Rev. **94**, 440 (1954).

Measurement of Coulomb Interference in 113-Mev π^+-p Scattering*

JAY OREAR†
Institute for Nuclear Studies, University of Chicago, Chicago, Illinois
(Received August 6, 1954)

Pion-proton scatterings with a small angle cutoff of 12.5° in the center-of-mass system were detected using the area-scanning, nuclear-emulsion technique. Ilford G5 plates 600 microns thick were exposed to a flux of 4.4×10^6 mesons/cm² in the 122-Mev π^+ beam of the Chicago cyclotron. Various checks indicated a scanning efficiency greater than 90 percent for scatterings on the hydrogen content of the emulsion between 12.5° and 160°. Out of a total 420 hydrogen events only two scatterings were less than 20°. The data when analyzed according to the two possible sets of signs of the phase shifts give a strong preference for destructive interference, i.e., attractive $p_{\frac{3}{2}}$ interaction. In this case the maximum likelihood solution is $\alpha_3=-(10.9\pm2)°$, $\alpha_{33}=(27.0\pm1.5)°$, and $\alpha_{31}=-(3.2\pm1)°$ for the s- and p-wave phase shifts with no definite indication of a d-wave component. The total nuclear cross section is (79±5) millibarns. The mean energy of pions in the emulsion is (113.0±1.6) Mev as determined from 33 events where the proton stops in the emulsion.

I. INTRODUCTION

SINCE the only interaction positive pions of 113 Mev can have with protons is an elastic scattering, the interaction may be described in terms of the partial wave phase shifts. These phase shifts can be obtained from the shape of the angular distribution except for their sign. Knowledge of whether the pion-proton interaction is attractive or repulsive would establish the sign. Since we do have knowledge that part of this interaction (the Coulomb part) is repulsive, we can in principle determine the absolute signs of the phase shifts. The quantitative separation of the scattering into nuclear and Coulomb parts has been discussed by several workers.[1]

The scattering of negative pions by hydrogen may also be described by these phase shifts if the pion-nucleon interaction is charge independent. Allowances can be made for the Coulomb part of the interaction which is, of course, not charge independent.[1] Under these assumptions the signs of the phase shifts may also be found by observing the Coulomb interference effects in π^- scattering. This determination has been made for 65-Mev pions at Columbia.[2] They were able to fit all their data with both sets of signs for the phase shifts. The set with large positive α_{33} (commonly called the Fermi solution) connects smoothly with results at lower and higher energies.[2,3] However, the set with negative α_{33} (commonly called the Steinberger solution) requires such a small $|\alpha_{33}|$ and such a large $|\alpha_3|$ that reasonable assumptions about the energy dependence of the phase shifts would rule out a negative α_{33}.

The present experiment which has the advantage that it requires no assumptions about charge independence also predicts a positive α_{33}. For the case of destructive interference the maximum likelihood solution is $\alpha_3=-10.9\pm2°$, $\alpha_{33}=27.0\pm1.5°$, and $\alpha_{31}=-3.2\pm1°$. This is a much better fit than is obtained in the case of construction interference. Positive α_{33} gives a destructive Coulomb interference in the forward direction because the scattered wave (predominantly $p_{\frac{3}{2}}$) is then from an attractive nuclear force which is partially "neutralized" by the repulsive Coulomb force. Quantitatively the expression for pions of relativistic energies as obtained by Solmitz[1] is [neglecting terms of the order $(v_p/c)^2$]:

$$\frac{d\sigma}{d\omega}=\left|\frac{1}{2ik}(P+Q\cos\chi)+f^{(nf)}(\chi)\right|^2+\left|\frac{1}{2ik}R\sin\chi+f^{(f)}(\chi)\right|^2,$$

$$P=\exp(2i\alpha_3)-1,$$

$$Q=\exp(2i\alpha_{31})+2\exp(2i\alpha_{33})-3, \qquad (1)$$

$$R=\exp(2i\alpha_{33})-\exp(2i\alpha_{31}),$$

$$f^{(nf)}=-\frac{e^2}{2p(v_\pi+v_p)\sin^2\chi/2}\left[1+\frac{v_\pi v_p}{2c^2}(1+\cos\chi)\right],$$

$$f^{(f)}=\frac{e^2}{2p(v_\pi+v_p)\sin^2\chi/2}\frac{\mu_p v_\pi v_p}{2c^2}$$

(all quantities in the center-of-mass system).

This function is plotted in Fig. 1 for the values of α_3, α_{33}, and α_{31} obtained in this experiment assuming both possibilities of sign. The two curves begin to depart significantly below 25°. This interference effect is less noticeable for π^+-p scattering in the energy region 30 to 70 Mev where the repulsive s-wave is the same order of magnitude as the attractive p-wave.[4]

Except for the detection of small-angle scatterings down to 12.5°, the scanning technique is the same as that described by the author.[5] The scanning technique

* Supported in part by the Office of Naval Research and the U. S. Atomic Energy Commission.

† Now at the Department of Physics, Columbia University, New York, New York.

[1] L. van Hove, Phys. Rev. **88**, 1358 (1952); J. Ashkin and L. Smith, Technical Report No. 1, Carnegie Institute of Technology, February 2, 1953 (unpublished); and F. T. Solmitz, Phys. Rev. **94**, 1799 (1954).

[2] Bodansky, Sachs, and Steinberger, Phys. Rev. **93**, 1367 (1954).

[3] J. Orear, Phys. Rev. **96**, 176 (1954).

[4] Orear, Lord, and Weaver, Phys. Rev. **93**, 575 (1954).

[5] J. Orear, Phys. Rev. **92**, 156 (1953).

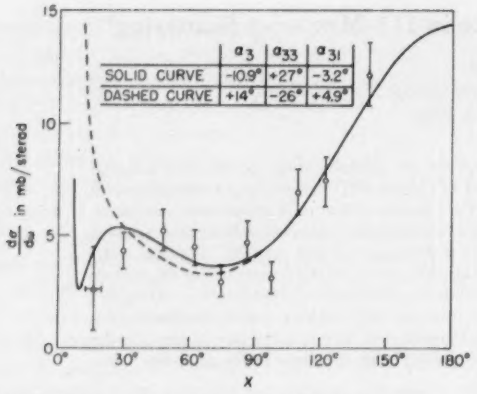

FIG. 1. The average $d\sigma/d\omega$ in mb/sterad corresponding to dividing the data into 9 equal units of solid angle. The two events found in the region $12.5°<\chi<20°$ are represented by the triangle. The solid curve is the best fit assuming positive α_{33}. The dashed curve is the best fit assuming negative α_{33}.

used here along with estimates of scanning efficiency is discussed in Sec. III. The experimental results are displayed and analyzed in Sec. IV. The following section gives details of the geometry and beam used.

II. EXPOSURE

Ilford G5 plates 600 microns thick were exposed in the geometry shown in Fig. 2. One inch of polyethylene was used to filter out the many protons of about the same momentum. This filter reduced the proton-pion ratio at least a factor 10^4. Since the π^+ are taken off the target in the backward direction where the production cross section is low, about 20 hours of exposure time were needed to reach the flux of 4.4×10^5 tracks/cm^2. Range curve analysis in this beam indicates a 7 percent contamination caused by muons of the same momentum.[6] Total pion track length corresponding to the region scanned was determined as described in reference 5 by counting a total of 1235 tracks. The product of the track density so determined by the total area scanned gives $L_\tau=(1.56\pm0.05)\times10^5$ cm.

In 46 of the events the proton stops in the emulsion. The incoming pion energy is then determined by the proton energy and scattering angle. The values of incoming pion energy are used to determine the average beam energy in the plate as (113.0±1.6) Mev. This agrees with the energy loss in the polyethylene and range curve determination of the beam energy. The rms spread of beam energy in the plates is about 7 Mev. The small angle (pion-proton) scatterings are not used in this beam energy determination, because the proton angle cannot be determined accurately. In the case of the small angle scatterings a better value can be obtained for χ, the center-of-mass scattering angle, by using the proton range and assuming a pion energy of 113 Mev to calculate χ. This is done for the 13 events where $\chi<30°$.

III. SCANNING

The scanning technique used here is described in detail in reference 5. The entire volume of emulsion is covered by scanning overlapping strips 115 microns wide defined by a whipple disk reticle. The scanner examines all single proton beginnings for an incoming and scattered pion. All 3-pronged events of this type were recorded. The difficulty in finding small angle scatterings is the short recoil proton (9.2 microns for $\chi=12.5°$). Because of this, the scanners were required to search for and record all short protons longer than 7 microns and perpendicular to the beam direction within 30°. This added condition reduced the scanning rate a factor two. Scanning efficiency for these small angle scatterings can be checked strip by strip since an average of 9 of these short background protons

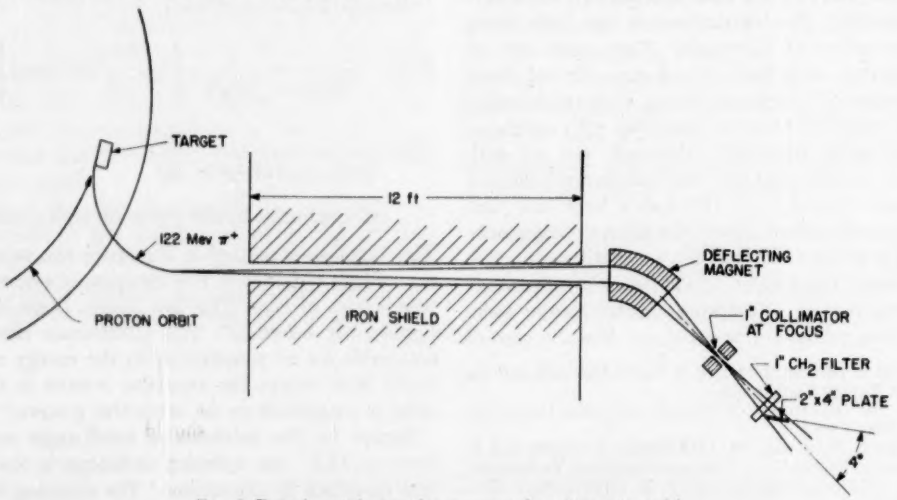

FIG. 2. Experimental setup for exposure (not drawn to scale).

[6] Anderson, Fermi, Martin, and Nagle, Phys. Rev. 91, 155 (1953).

occurred in each strip. Over 3000 were recorded in all. About 50 strips distributed fairly uniformly over the area were spot checked. Consistently no more than 15 percent of the short protons were missed. As an independent check a scanning test was constructed using short protons and scattering events especially selected for being difficult to see. The testee was given a list of toothline coordinates[7] defining the selected strips. He then scanned the selected strips no slower than his usual rate. Scores on this test were 85 percent, 88 percent, and 89 percent. Since a short proton which has two pion tracks leading to it is easier to notice, these scanning efficiency determinations should give a lower limit for scatterings where the recoil proton is greater than 9 microns long in the plane of the emulsion. On the basis of the above evidence it is assumed that the region $12.5°<\chi<15°$ and $\phi<40°$ has been scanned with at least 90 percent efficiency. ϕ is the angle between the plane of the event and the plane of the emulsion. The event with the smallest proton range in the plane of the emulsion (12.5 microns) that was found is shown in Fig. 3. The true proton range is 30 microns corresponding to $\chi=19°$ and $\phi=64°$. The next region where high-scanning efficiency is assumed is $15°<\chi<20°$ and $\phi<65°$. The other regions used are 20° to 130°, no limit on ϕ; and 130° to 160°, $\phi<60°$. These restrictions on large angle scatterings are in a region where the recoil protons are lighter tracks (~60 Mev) and are within 6° of the beam direction. In this case they might tend to be considered as two pion beam tracks which accidentally overlap, and thus not be given proper attention. Events within 15 microns (after shrinkage) of each surface might be missed and are difficult to measure. This region is also excluded. Finally, events are rejected which either are not coplanar within the accuracies of measurement[5] or do not satisfy the angular correlation dictated by energy-momentum conservation. The total number of events surviving all these restrictions is 333. Nonhydrogen collisions which are quasi-elastic and give no other visible prongs contribute about a 4 percent background. The technique of how this background determination is made is discussed in detail in reference 5. In calculating cross sections the scanning efficiency is assumed to be 96±4 percent. This correction is exactly offset by the 4 percent background correction.

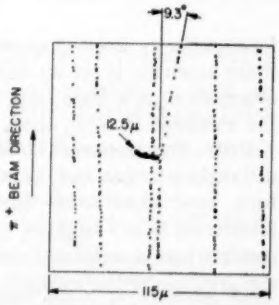

FIG. 3. Small angle (π^+,p) scattering showing other beam tracks in the same field of view. $\chi=19°$. Plane of event is inclined 64° to plane of emulsion.

[7] J. Orear, Rev. Sci. Instr. **25**, 1023 (1954).

TABLE I. Data broken up into 9 equal units of solid angle (1.26 sterad each).

$\Delta\chi$	ΔN	$d\sigma/d\omega$(mb/sterad)
12.5°– 40.2°	28	4.31
40.2°– 55.7°	34	5.24
55.7°– 68.7°	29	4.46
68.7°– 80.6°	19	2.93
80.6°– 92.1°	31	4.77
92.1°–103.7°	20	3.08
103.7°–115.9°	45	6.94
115.9°–129.5°	48	7.4
129.5°–159°	79	12.2

IV. ANALYSIS OF RESULTS

Table I gives a breakdown of the data into 9 equal units of solid angle. The average values of the differential cross section obtained from this data are shown in Fig. 1. Two events were found in the region of the "Coulomb dip" from 12.5° to 20°. This "point" is also represented in Fig. 1.

In calculating the phase shifts and their errors the data were broken into 3° intervals and the maximum likelihood method was used.[4] In this method the probability that the experiment would turn out the way it did is calculated assuming Eq. (1) is the true shape. The phase shifts which maximize this probability are solved for. We obtained the solutions $\alpha_3=-(10.9\pm2)°$, $\alpha_{33}=(27\pm1.5)°$, and $\alpha_{31}=-(3.2\pm1)°$ for the destructive Coulomb interference and $\alpha_3=(14\pm2)°$, $\alpha_{33}=-(26\pm1.5)°$, and $\alpha_{31}=(4.9\pm1)°$ for the constructive. The errors given are the statistical standard deviations assuming there is no d-wave. All possible variations of a, b, and c within their errors allow the destructive phase shifts to fall within the following limits: $\alpha_3=-10.9°\pm3.5°$, $\alpha_{33}=27°\pm2.5°$, and $\alpha_{31}=-3.2°\pm2.8°$. The only other possible phase shift solution is the Yang type which is $\alpha_3=-10.9°$, $\alpha_{33}=7.8°$, and $\alpha_{31}=38°$, for the destructive case. A Steinberger-type solution with positive α_2 large enough to give destructive interference is completely ruled out.

According to the maximum likelihood method the data fit much better in the destructive case than the constructive. The ratio of these two probabilities turned out to be about 4000 to 1 in favor of the destructive interference.

There are other ways of expressing this preference of the data for positive α_{33} which are perhaps easier to visualize. One simple approach is to use only the data in the region where Coulomb effects are negligible ($\chi>40°$) to solve for the phase shifts. Then these phase shifts when used in Eq. (1) will predict the average number of events which should have been found in the region where the Coulomb effects are large ($\chi<25°$). Six events were found in this region. According to the Poisson distribution the ratio of the probability of getting 6 events assuming positive α_{33} to the probability

of getting 6 events assuming negative α_{33} is 340 to 1 in favor of the destructive interference. This same type of calculation when made using the best-fit phase shifts to *all* the data will give artificially suppressed odds. This is because the experimental "low value" of the cross section at small angles will exert a strong effect in pulling the constructive interference curve part way down to it. In this case the ratio is only 11 to 1. We do not consider this experiment by itself as conclusive proof that α_{33} is positive, but when considered along with all the other evidence pointing toward an attractive $p_{\frac{3}{2}}$ interaction, the "odds" in favor of a positive α_{33} become overwhelming.

Some of the other evidence comes from the 65-Mev experiments at Columbia[2] and the 40-Mev experiments at Rochester[8] assuming charge independence. This is because the knowledge that α_{33} must become large as shown by the recent results from the Carnegie Institute of Technology[9] makes the Steinberger solution implausible. Also an attractive $p_{\frac{3}{2}}$ interaction is preferred theoretically in order to explain such large values of α_{33} as found in the 150 to 200-Mev region.[9] The values of the small angle scatterings below 30° are 17.9°, 19, 20, 23.4, 23.5, 23.6, 26.5, 27, 27.6, 28.9, 29.5, 29.6, and 29.7.

The earlier 110-Mev counter results of Anderson *et al.*[6] are fairly consistent with these plate results. Their values of a, b, and c at 110 Mev are 3.6 ± 0.7, -4.8 ± 0.8, and 7.5 ± 1.9 mb per steradian. Our values are 4.0 ± 0.4, -3.5 ± 0.7, and 6.8 ± 1.3. At 120 Mev their phase shifts are $\alpha_3=-15°$, $\alpha_{33}=30°$, and $\alpha_{31}=4°$. Ours are $-10.9°$, 27°, and $-3.2°$ at 113 Mev.

The data shown in Table I gave an M value of 11.8 when analyzed by the least squares method. M is the least squares sum in units of the standard deviations of each point. According to statistics the mean value of M should be 6 in the case of 9 experimental points and 3 parameters.[10] Since M is χ^2 distributed with $N=6$ in this case,[10] the probability that this experiment give $M\geq 11.8$ is 7 percent. Of course a small amount of d-wave might improve this fit, although the odds, 1 in 14, for having a fit as poor as this are not unreasonable. Inspection of Fig. 1 shows that the 9 experimental points alternate above and below the curve. We feel that this large M value is just a statistical oddity. To support this view a second least squares analysis was made. This time the data was divided into 6 equal units of solid angle giving $M=3.2$, which is very close to the expected mean value of 3 (for the case of 6 points and 3 parameters). Statistics would have to be improved in order to be sure of seeing any d-wave.

The author wishes to thank Mr. Paul Taylor, Mrs. Enid Bierman, and Mr. James Ross for their excellent job of scanning. Dr. Frank Solmitz kindly helped with the calculations and statistical problems which arose. In addition the author is grateful to Professor Enrico Fermi for helpful discussions.

[8] J. Tinlot and A. Roberts, Phys. Rev. **95**, 137 (1954).
[9] Blaser, Ashkin, Feiner, Gorman, and Stern, Phys. Rev. **95**, 624 (1954).

[10] H. Cramer, *Mathematical Methods of Statistics* (Princeton University Press, Princeton, 1946), Chap. 37.

PHYSICAL REVIEW VOLUME 96, NUMBER 5 DECEMBER 1, 1954

Method of Transition Probabilities in Quantum Mechanics and Quantum Statistics

P. T. LANDSBERG*
Randal Morgan Laboratory of Physics, University of Pennsylvania, Philadelphia, Pennsylvania
(Received February 23, 1954)

The concepts microscopic reversibility, detailed balancing, equal probabilities, equilibrium, H theorem are often used in (coarse grained) quantum statistics. It is pointed out that each has a (fine grained) quantum-mechanical counterpart. These concepts are formulated, and their interrelations discussed, at an abstract mathematical level. The results are then interpreted by taking first the fine grained and then the coarse grained point of view. A type of transition matrix arises which does not seem to have been investigated so far, and some of its properties are discussed.

1. INTRODUCTION

TWO starting points for quantum statistical mechanics and the statistical foundation of thermodynamics are often used. In the first one appeals at the outset to some principle of equal *a priori* probabilities and random *a priori* phases without making any attempt to establish these from more fundamental considerations. These assumptions make possible the introduction of ensembles into the theory. The microcanonical ensemble enables one to prove an H theorem for a perfectly isolated system in the following sense: if the ensemble is set up in accordance with an initial observation at a time $t=0$, when the value of H for the ensemble is $H(0)$, then, at all later times t, $H(t)\leq H(0)$. The statement "$dH/dt\leq 0$ at all times t" is definitely stronger, and, as far as we know, it has never been established from this kind of argument. By identifying H as a negative multiple of the entropy (S) one has here a restricted quantum statistical proof of the principle of the increase of entropy with time in a perfectly isolated system. The restriction resides in the fact that $S(t)\geq S(0)$ is weaker than $dS/dt\geq 0$. It

* On leave of absence from Department of Natural Philosophy, The University, Aberdeen, Scotland.

should, however, be noted that, by using a canonical ensemble for a system in essential isolation, the second law can be established in the unrestricted form (in Tolman's notation) $\Delta S \geq \int \delta Q/T$. This approach via ensembles is essentially the quantum-mechanical extension of Gibbs's statistical mechanics.[1]

The second approach, which is older, and is falling slowly into disuse, is associated with Boltzmann. Formulated in a modern manner, its object is to justify the use of ensembles. This is done by showing that the quantum-mechanical time average of macroscopically observable quantities in a closed system, and the microcanonical average of these quantities, taken at a fixed time, are almost always equal to each other. This is the quantum-mechanical ergodic theorem.[2] It holds if the number of macroscopically indistinguishable microscopic states is large enough, and if the energy levels of the system satisfy a certain restrictive condition.[3] The same conditions are sufficient (their necessity has not been proved) to establish the H theorem in the following sense: the time average of (a suitably defined) H for a quantum-mechanical system is approximately equal to the microcanonical average. While some of the concepts involved in this approach have been criticized,[4] it is more fundamental than the first approach, since it aims at being based on quantum mechanics, while the statistical assumptions play a subsidiary role. None the less, it is to be emphasized that this method also depends for its success upon an implicit assumption which is similar to that of equal *a priori* probabilities and random *a priori* phases.[5] This assumption occurs when one sets out to calculate the chances of finding conditions which are at variance with thermodynamics.

A third approach, which we shall call the method of transition probabilities, exhibits interesting differences. Its advantages are mathematical simplicity and a somewhat weaker statistical assumption. The method depends on an assumption of random *a priori* phases, but the principle of equal probabilities of accessible quantum states in equilibrium is not assumed, but is deduced by quantum mechanics.[6] The drawback of the method is that, it is valid only for limited time intervals, as will be discussed in Sec. 4. For these time intervals, it leads to the strong form $dH/dt \leq 0$ of the H theorem.

We wish to emphasize that the older assumption of molecular chaos is replaced in all three approaches by an assumption concerning the perfect irregularity of certain phase constants.

The method of transition probabilities has recently been used in an interesting manner for the discussion of basic principles of statistical mechanics and thermodynamics.[7] The reason for taking up this problem again is that it seems desirable to develop the results a little further, and to clarify the foundations of this work with the following points in view. (1) It is essential in this type of discussion to make a clear distinction between coarse grained and fine grained probabilities. One must therefore introduce groups of microscopic states which cannot be distinguished by macroscopic methods. (2) It seems desirable to make explicit, and discuss separately, the assumption that, after a finite time, the probability that a system, chosen at random from the ensemble, is in its ith accessible state, becomes a constant. This would exclude fluctuations in ensemble averages,[8] and it is therefore best not to assume it automatically. (3) The assumption that all states of the systems in the ensemble are interconnected can be dropped altogether, and its effect investigated separately.

We shall set up our problem in abstract mathematical terms in Sec. 2, and offer the solution at the same level in Sec. 3. Thereafter we shall discuss the physical interpretation of the relations obtained, and show that the same mathematical scheme is useful from two entirely different points of view.

2. THE PRINCIPLES

Let W be a finite, positive, and nonzero integer. Let $G_1, \cdots, G_W$ be a set of finite, positive, and nonzero integers. Let $P_1, \cdots, P_W$ be a set of numbers which are continuous functions of the time t, such that $0 \leq P_j \leq 1$, $\sum_1^W P_i = 1$ at all values of t. Lastly, let A_{ij} $(i, j = 1, 2, \cdots, W)$ be a set of W^2 non-negative real numbers. All numbers, other than the P's are independent of t. The principles whose interrelations we wish to investigate are that for all $i, j = 1, 2, \cdots, W$:

$$A_{ij} = A_{ji}, \tag{Q}$$

$$\sum_j A_{ij} G_j = \sum_j A_{ji} G_i, \tag{X}$$

$$P_i A_{ij} G_j = P_j A_{ji} G_i, \tag{D}$$

$$A_{ij} \neq 0 \text{ only if } P_i/G_i = P_j/G_j, \tag{P}$$

$$(P) \text{ holds for a nonzero interval of } t. \tag{P'}$$

$$\dot{P}_i \equiv \frac{dP_i}{dt} \equiv \sum_j (P_j A_{ji} G_i - P_i A_{ij} G_j) = 0, \tag{Eq}$$

$$\dot{H} \equiv \frac{dH}{dt} \equiv \frac{d}{dt}\{\textstyle\sum_i P_i \log(P_i/G_i)\} = 0, \tag{H'}$$

$$\dot{H} \leq 0. \tag{H}$$

[1] R. C. Tolman, *Principles of Statistical Mechanics* (Oxford University Press, London, 1938).

[2] J. von Neumann, Z. Physik **57**, 30 (1929); W. Pauli and M. Fierz, Z. Physik **106**, 572 (1937); W. Pauli, Suppl. Nuovo cimento **6**, 166 (1949).

[3] If E_j be the exact energy levels of the system, we must have

$$E_j \neq E_k, \quad E_j - E_l \neq E_k - E_m \quad \text{for } j \neq k, \quad l \neq m.$$

[4] E. C. Kemble, Phys. Rev. **56**, 1146 (1939).

[5] The author is indebted to Professor von Neumann for an opportunity to discuss this point with him.

[6] W. Pauli, *Probleme der modernen Physik*, edited by P. Debye (Hirzel, Leipzig, 1928), p. 30. See also T. Sakai, J. Phys. Soc. Japan **19**, 172 (1937); O. Halpern and F. W. Doerman, Phys. Rev. **55**, 1077 (1939); J. Davydov, J. Phys. (U.S.S.R.) **11**, 33 (1947).

[7] J. S. Thomsen, Phys. Rev. **91**, 1263 (1953).

[8] In finite ensembles fluctuations may have to be considered.

Unless stated otherwise, each principle is assumed to hold only at a certain value of t, so that our inferences will be of the form if (A) is valid at t, then (B) is valid at t. However, in the case of the first two principles it is clear that if they hold at a certain value of t, then they hold at all values of t. We shall write $(A)\rightarrow(B)$ for (A) implies (B), but (B) does not imply (A); and $(A)\rightleftarrows(B)$ for (A) implies (B), and (B) implies (A). $(A)+(B)\rightleftarrows(C)+(D)$ shall mean that if one assumes both (A) and (B), one can deduce both (C) and (D), and conversely. It is assumed that $A_{ii}=0$ for all i.

The question as to the extent to which any one of these principles, or some combination of these principles, implies others, presents clearly a problem in pure mathematics, and is fully defined by the above information. Its solution is attempted in the next section.

3. THE THEOREMS

Lemma 1.—If the quantities P_i are arbitrary (except for the condition $\sum P_i=1$), then in order that $\dot{H}$ be an extremum with respect to P_r, when all other P's are kept fixed, P_r must satisfy

$$\mu=F_r-\sum_{j=1}^{W}\left\{\frac{G_r}{P_r}A_{jr}(P_jG_r-P_rG_j)+A_{rj}G_j\log\frac{P_jG_r}{P_rG_j}\right\},$$

where μ is a constant which does not depend on r, and

$$F_r\equiv\sum_{i=1}^{W}(A_{ri}-A_{jr})G_j.$$

The proof depends on the use of a Lagrangian multiplier μ to ensure that the P's are normalized.

Lemma 2.—If the conditions of Lemma 1 are fulfilled for every $r=1, 2, \cdots, W$, and if $F_r=0$ for every r, then condition (P) holds. $\dot{P}_1, \dot{P}_2\cdots, \dot{P}_W$, and $\dot{H}$ all vanish as a consequence.

Proof.—Consider a pair of suffixes with the properties $A_{st}\neq0$, $P_s/G_s>P_t/G_t$, and another pair with the properties $A_{uv}\neq0$, $P_u/G_u<P_v/G_v$. We must consider four possibilities. (α) A pair of suffixes of both types exists. (β) A pair of suffixes like (s, t) exists, but no pair exists with the properties of the pair (u, v). (γ) A pair of suffixes with the properties of the pair (u, v) exists, but no pair exists with the properties of the pair (s, t). (δ) No pair of suffixes exists which has either property. Situation (α) can be ruled out as follows. Of all suffixes s, t; u, v consider one of those for which P_j/G_j has its largest value, and let this suffix be $j=a$. Consider also one of those suffixes s, t; u, v for which P_j/G_j has its smallest value, and let this suffix be $j=b$. On choosing $r=a$ in Lemma 1, one finds $\mu>0$. On choosing $r=b$ in Lemma 1, one finds $\mu<0$, and this is a contradiction. Situations (β) and (γ) can be eliminated without reference to Lemma 1.[9] Since

$$\dot{P}_i=\sum_j G_iG_j\left(\frac{P_j}{G_j}-\frac{P_i}{G_i}\right)A_{ji}-P_iF_i,$$

and $F_i=0$, $A_{ji}\geq0$, it follows that $\dot{P}_i\geq0$ for all i. Now $\dot{P}_t>0$, so that $\sum_i\dot{P}_i>0$. This contradicts the normalization conditions, and situation (β) must therefore be ruled out. A similar argument eliminates (γ), since one would find $\sum_i\dot{P}_i<0$. This leaves only situation (δ) which implies that if $A_{ij}\neq0$, then $P_i/G_i=P_j/G_j$. Hence $\dot{P}_i=0$ for all i. Therefore,

$$\dot{H}=\sum_i\dot{P}_i\log(P_i/G_i)=0.$$

Interpretation of Condition (P). Our W suffixes can be subdivided into groups according to the following rule. For any pair of suffixes x, y within the same group it must be possible to form a nonzero product of A's of the form:

$$\text{either } A_{x\alpha}A_{\alpha\beta}\cdots A_{\rho\theta}A_{\theta y} \text{ or } A_{y\alpha}A_{\alpha\beta}\cdots A_{\rho\theta}A_{\theta x}.$$

Let the smallest number of groups of suffixes obtainable in this manner be v, and let the αth group contain w_α suffixes. It follows that

$$\sum_1^v w_\alpha=W, \quad A_{ij}=0 \text{ if } i, j \text{ belong to different groups.}$$

If i and j be in the same group, A_{ij} *can* be zero, but it *need not* be zero. Again in some cases one may have some w_α's which are unity; in others no subdivision of suffixes into groups may be possible, so that $v=1$. This subdivision of the suffixes into groups is independent of the value of t, since it depends only on the properties of the A's.

If now (P) holds at a certain value of t, we find simply that for all i within a group of suffixes the value of P_i/G_i is independent of i, and depends only on α. Suppose that for all i within the αth group $P_i/G_i=K_\alpha$ $(\alpha=1, 2, \cdots, v)$. One can then arrange the v groups of suffixes according to the size of K_α, e.g., so that

$$K_1\leq K_2\leq\cdots\leq K_v,$$

and this will be assumed whenever (P) holds. If (P) holds and $v=1$, then $K_1=1/W$ in virtue of the normalization condition.

As a simple application of these ideas, we note from the result,

$$\dot{H}=\sum_{i,j}(P_jA_{ji}G_i-P_iA_{ij}G_j)\log(P_i/G_i),$$

that each group of suffixes contributes to $\dot{H}$ a value which is independent of the other groups. Thus the total value of $\dot{H}$ is simply a sum of the contributions to $\dot{H}$ which arise from each group of suffixes. Our next lemma deals with a typical contribution to $\dot{H}$ when condition (P) holds very nearly.

Lemma 3.—If for all i in the αth group of suffixes $P_i=K_\alpha G_i(1+\Delta_i)$, $|\Delta_i|\ll1$, where K_α is a non-negative constant, then the contribution to $\dot{H}$ from the αth group of suffixes is given by

$$2\dot{H}=-K_\alpha\sum_{i,j}G_jA_{ji}G_i(\Delta_j-\Delta_i)^2-K_\alpha\sum_i G_iF_i\Delta_i(1+\Delta_i).$$

[9] Alternatively, the argument used for case (α) may also be applied in these cases.

The proof depends only on some algebraic manipulations.

Theorem 1.—$(Q)+(D) \rightarrow (P)+(D) \rightarrow (D) \rightarrow (Eq) \rightarrow (H') \rightarrow H$.

$(Q)+(D)$ implies $P_iA_{ij}G_j=P_jA_{ij}G_i$. If $A_{ij}\neq 0$, $P_iG_j=P_jG_i$ follows. Thus $(Q)+(D)$ implies (P), so that $(Q)+(D)$ implies $(P)+(D)$. On the other hand if

(i) $\qquad A_{ij}=0, \quad A_{ji}\neq 0, \quad P_i=P_j=0,$

then (P) and (D) are both satisfied, but (Q) is violated. This shows that $(P)+(D)$ does not imply (Q). Again, $(P)+(D)$ obviously implies (D), but (D) does not imply (P), as shown by the following example:

(ii) $W=2$; $G_1=G_2=1$; $P_1=\frac{1}{3}$, $P_2=\frac{2}{3}$; $A_{ij}=\begin{pmatrix}0 & 2\\ 1 & 0\end{pmatrix}$.

This satisfies (D), but violates (P). Again (D) implies (Eq), as follows immediately from the definition of $\dot{P}_i$. That (Eq) does not imply (D) is proved by the following example:

(iii) $W=3$; $G_1=G_2=G_3=1$;

$$P_1=\tfrac{1}{6}, \quad P_2=\tfrac{1}{3}, \quad P_3=\tfrac{1}{2}; \quad A_{ij}=\begin{bmatrix}0 & 6 & 12\\ 6 & 0 & 3\\ 2 & 4 & 0\end{bmatrix}.$$

This leads to (Eq) and to

$$P_1A_{12}=P_2A_{23}=P_3A_{31}=1, \quad P_2A_{21}=P_3A_{32}=P_1A_{13}=2,$$

so that it contradicts (D). Since

$$\dot{H}=\textstyle\sum_i \dot{P}_i \log(P_i/G_i),$$

(Eq) implies (H'). The converse does not hold, as shown by example (IV).

(iv) $W=3$; $G_1=G_2=G_3=1$;

$$P_1=P_2=P_3=\tfrac{1}{3}; \quad A_{ij}=\begin{bmatrix}0 & 1 & 1\\ 1 & 0 & 0\\ 2 & 0 & 0\end{bmatrix}.$$

By the definition of $\dot{P}_i$ this leads to

$$\dot{P}_1=\tfrac{1}{3}, \quad \dot{P}_2=0, \quad \dot{P}_3=-\tfrac{1}{3},$$

thus satisfying (H'), but violating (Eq). The result $(H') \rightarrow (H)$ is obvious.

Theorem 1a.—If $v=1$, then $(P)+(D)$ implies (Q).

If there is only one group of suffixes and (P) holds, then $P_i=G_i/W>0$ for all i, so that $(P)+(D)$ implies $G_iA_{ij}G_j/W=G_jA_{ji}G_i/W$ (all i, j), and this leads to (Q).

Theorem 2.—$(Q)+(D) \rightarrow (Q) \rightarrow (X) \rightarrow (H)$.

Obviously $(Q)+(D)$ implies (Q). The converse is untrue, as proved by Example (v).

(v) $W=2$; $G_1=G_2=1$; $P_1=\frac{1}{3}$, $P_2=\frac{2}{3}$; $A_{ij}=\begin{pmatrix}0 & 1\\ 1 & 0\end{pmatrix}$.

This satisfies (Q), but contradicts (D). The result $(Q) \rightarrow (X)$ is obvious from the definitions. Now (X) implies $F_i=0$ for all i, and imposes no restriction on the P's, so that Lemmas 1 and 2 apply. Hence $\dot{H}$ attains its extreme value with respect to each P_r if (P) holds, so that, as a consequence, $\dot{H}=0$. On the other hand, if (X) holds but $\dot{H}$ does not attain its extreme value, then $\dot{H}<0$ by Lemma 3. Hence (X) implies $\dot{H}\leq 0$, and this is (H). The converse is disproved by Example (iv). This implies $\dot{H}=0$, so that (H) holds, but it contradicts (X).

Theorem 3.—$(Q)+(D) \rightleftharpoons (Q)+(Eq) \rightleftharpoons (Q)+(P)$.

Since $(Q) \rightarrow (X)$ (Theorem 2), and (X) implies $F_r=0$ for all r, one can use Lemmas 1 to 3. Since $(D) \rightarrow (Eq)$ (Theorem 1), therefore $(Q)+(D)$ implies $(Q)+(Eq)$. Since $(Eq) \rightarrow (H')$ (Theorem 1), the maximum value of $\dot{H}$, whose existence is implied by (Q), is actually attained, so that (P) holds by Lemma 2. Thus $(Q)+(Eq)$ implies $(Q)+(P)$. Lastly, it is clear that (Q) implies (D) if A_{ij} or A_{ji} are known to vanish. If neither vanishes, however, $(Q)+(P)$ implies $A_{ij}(P_i/G_i)=A_{ji}(P_j/G_j)$, and this is again (D). Thus $(Q)+(P)$ implies $(Q)+(D)$, and this establishes the complete equivalence of the above three propositions (from each one the other two can be deduced).

Theorem 4.—$(P)+(D) \rightarrow (P)+(Eq) \rightleftharpoons (X)+(Eq) \rightleftharpoons (X)+(H') \rightleftharpoons (P') \rightarrow (X)$.

Since $(D) \rightarrow (Eq)$ (Theorem 1), therefore $(P)+(D)$ imply $(P)+(Eq)$. The converse is disproved by the following example:

(vi) $W=3$; $G_1=G_2=G_3=1$;

$$P_1=P_2=P_3=\tfrac{1}{3}; \quad A_{ij}=\begin{bmatrix}0 & 1 & 2\\ 2 & 0 & 0\\ 1 & 1 & 0\end{bmatrix}.$$

This satisfies (P) and (Eq), but contradicts (D). Again, $(P)+(Eq)$ implies that

$$\dot{P}_i=\sum_j G_iG_j\left(\frac{P_j}{G_j}A_{ji}-\frac{P_i}{G_i}A_{ij}\right)=\sum_j G_iG_j\frac{P_i}{G_i}(A_{ji}-A_{ij})=0.$$

Hence $\sum_j G_j(A_{ji}-A_{ij})=0$ (all i), and this is (X). Since, in addition, $(Eq) \rightarrow (H')$ (Theorem 1), it follows that $(X)+(Eq)$ implies $(X)+(H')$. Again, if $(X)+(H')$ hold a certain value T of t, then, by Lemmas 2 and 3, at $t=T$, (P) holds, and $\dot{P}_i=0$ for all i. Since we have just shown that $(P)+(Eq)$ implies (X), it follows that (X) must hold at $t=T$, and therefore (X) holds at all values of t. If the first change of a P_i away from its value given by condition (P) occurs at $t=T'$, then we must have $d^nP_i/dt^n=P_i[\sum_j G_j(A_{ji}-A_{ij})]^n\neq 0$ for some positive integer n, and for some i at $t=T'$, and this would imply that (X) fails for some i. This is a contradiction, so that $(X)+(H')$ implies (P'). Again, (P') implies clearly (P) as well as (Eq), since for the nonzero interval of t for which (P) is valid, all P_i are given by equations of the form $P_i=K_\alpha G_i$ (i in group α of suffixes), and are therefore independent of t. This proves the equivalence of the four intermediate propositions of Theorem 4. Lastly, $(X)+(H')$ clearly implies (X). That (X) does not imply either (P) or (Eq) is proved by Example (v).

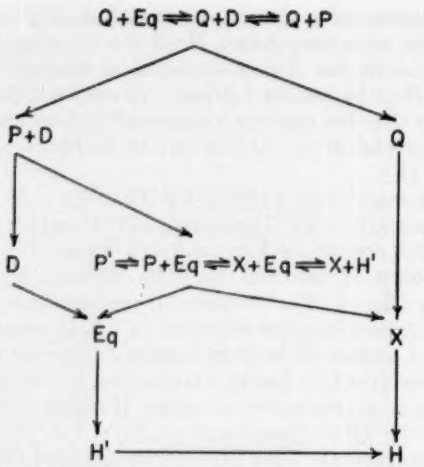

FIG. 1. General scheme of implications. $A \rightarrow B$ means that if (A) is true of the ensemble of duplicates of a certain system at time T, then (B) is also true of this ensemble at that time. The converse, (A) follows from (B), does not hold. $A \rightleftarrows B$ means that both the direct result and its converse apply.

Theorem 5.—$(X)+(Eq) \rightarrow (Eq)$.

It must merely be shown that (Eq) does not imply (X). This is accomplished by Example (iii).

A summary of the relations established is given in Fig. 1. Inspection of the figure raises the question if a relation of implication can be established between a pair of the following three proposition: (Q), (D), $(X)+(Eq)$, or between the following two propositions: (X), (Eq). However, this can be shown to be impossible. Example (v) shows that (Q) does not imply (D) or (Eq). (D) does not imply (Q) or (X) [Example (ii)]. $(X)+(Eq)$ does not imply (Q) or (D) [Example (vi)]. Again, (X) does not imply (Eq) (Theorem 4), nor does (Eq) imply (X) (Theorem 5).

4. THE TWO POSSIBLE INTERPRETATIONS

(A) By way of physical interpretation of the above formalism, we consider an ensemble of identical systems whose energies lie all in the same small energy range $(E, E+\Delta E)$. W is interpreted as the number of different macroscopically distinguishable states $i=1, 2, \cdots, W$ which each system of the ensemble can exhibit. However, each state i may be any one of a group of G_i microscopically distinct states, between which our measurements cannot distinguish. P_i is interpreted as the probability of finding a member of the ensemble in the state i, i.e., in the group of G_i macroscopically indistinguishable states. Alternatively we may say that P_i is the probability, as averaged over a microcanonical ensemble, of finding the system of interest in the state i. P_i is a so-called "coarse grained" probability; the P_i's go over into "fine grained" probabilities as W is increased and the integers G_i decreased until $G_1=G_2=\cdots=G_W=1$. If the P's are coarse grained probabilities, H is then the quantity, characteristic of an ensemble, which occurs in the quantum-mechanical H theorem. From it one can obtain the statistical mechanical analog of the second law of thermodynamics, by noting that the quantity $S=-kH$ has the required properties of the entropy. (Eq) states that, as far as can be ascertained by the macroscopic measurements under consideration, the ensemble averages of the various physical quantities exhibited by the system of interest have constant values. In general, such a situation can arise only if the fluctuations in the ensemble averages can be neglected (e.g., if the macroscopic measurements are sufficiently coarse, and extended over a sufficiently short period). Thus (Eq) postulates ensemble equilibrium (as revealed by the measurements under consideration). The principle (P) is most easily interpreted if it is assumed that the system can reach each of the W macroscopic states from every state i. If this assumption of the interconnection of states is adjoined to (P), then (P) states $P_i=G_i/W$ for all i. This is simply the principle of equal *a priori* probabilities (at equilibrium) of all accessible microscopic states.[10] The statement (P) is just the required generalization of this principle when one does not wish to make an assumption as to the interconnection of states. The A's are transition probabilities per unit time, and (Q) is a statement of a result, concerning transitions and inverse transitions, which depends on the Hermitian character of the perturbation operators, and on an assumption concerning random phases. (Q) is sometimes referred to as the principle of microscopic reversibility. (D), on the other hand, equates the transition rate $i \rightarrow j$ and the transition rate $j \rightarrow i$, so that it may be regarded as a statement of the principle of detailed balancing for transitions between macroscopically distinguishable states.

The time independence of the A's is the basic assumption which underlies our discussion. It applies in fact only to systems whose Hamiltonian can be split into an unperturbed part, for which the Schrödinger equation can be solved, and a sufficiently weak perturbation. Hence, if at least one of the states between which transition is made belongs to a practically continuous spectrum of unperturbed energy levels, one arrives at A's which are independent of the time for certain restricted time intervals.

(B) The mathematical discussion of Sec. 3 admits of an alternative interpretation, which is free of all statistical elements. In this approach the P's are the fine grained probabilities and the G's are all unity. The basic limitation of the discussion resides again in the assumed existence of time-independent transition probabilities A_{ij}, but the assumption of random phases is not now involved, and (Q) is an exact quantum-me-

[10] Our principle (P) is a generalization of the principle (E) of reference 7, which is there called the ergodic hypothesis. We reserve this name here for a hypothesis which relates time averages of probabilities to ensemble averages of probabilities. Jordan calls the principle (E) Liouville's theorem for quantum statistics. We prefer to adopt as the latter one of Tolman's formulations.

chanical result (provided, of course, the perturbation operator and the time satisfy the usual requirements). But there is not now any contact, through the condition (H), with the macroscopic measurements of thermodynamics, even though a theorem corresponding to the H theorem can again be proved, and is not in this case based on an assumption of random *a priori* phases. All the results which one obtains by adopting this fine grained point of view are to be regarded as results in quantum mechanics proper, and not as results in quantum statistical mechanics.

Strictly speaking all principles of Sec. 2, excepting (Q) and (X), are thus seen to be principles which may or may not apply to an ensemble of duplicates of a system of interest. Their truth or falsehood is therefore characteristic of the ensemble rather than of the system itself.

5. DISCUSSION

We first of all adopt interpretation (B), which uses the fine grained probabilities. In this case (Q) may be taken as correct, and hence leads to (H). The proof, freed from the assumption as to the existence of transition probabilities, is due to Klein.[11] But this is a result in quantum mechanics, and therefore not the H theorem proper. To investigate the limiting value which H approaches, we adjoin to (Q) the assumption (Eq), and deduce from Fig. 1 the validity of both (P) and (D). Thus, if the states i and j are connected (directly or via other states), the P_i and P_j tend to become equal. This is the well-known effect of quantum-mechanical "spreading," which has no classical analog. Assuming the interconnection of states, Jordan[12] has already observed that $(Q)+(Eq)$ implies equal probabilities for different states.

In interpretation (A) the proof that the assumption of random phases leads to (Q), and that (Q) in turn implies (H) is due to Pauli.[6]

We wish to emphasize the very limited part which the interconnection of states can play in these considerations. Theorem 1a represents the only example we have found of a relation of implication which holds only if this assumption is made, and Fig. 2 represents the scheme of implications for this case. On the other

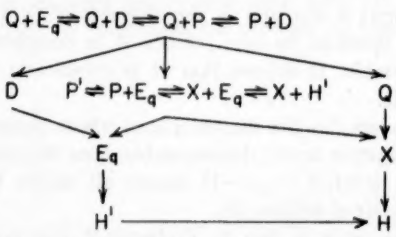

FIG. 2. Scheme of implications, provided the states $i, j, \cdots$ are interconnected. See caption of Fig. 1.

[11] O. Klein, Z. Physik **72**, 767 (1931).

[12] P. Jordan, *Statistische Mechanik auf Quantentheoretischer Grundlage* (Vieweg, Braunschweig, 1933), p. 25.

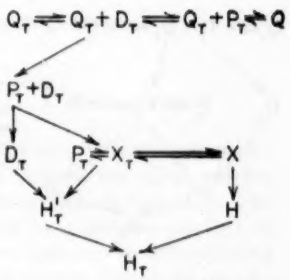

FIG. 3. Scheme of implications, provided the ensemble attains the condition (Eq) at some time (T). See caption of Fig. 1.

hand, the assumption of equilibrium in the stringent form (Eq) is very powerful. Figure 1 shows that if at a certain time (Q) be true and (Eq) be false (e.g., due to fluctuations in ensemble averages about a mean value), then (X) and (H) must also be true, but (P), (P'), (D), and (H') must all be false at that time. Yet, restrictive though the equilibrium assumption (Eq) is, it alone does not enable one to infer the existence of detailed balancing.

It may possibly be of interest to draw attention to the time-independent condition (X) which does not appear to have been noticed before (it is a generalization of Thomsen's λ hypothesis).[7] It is sufficient to deduce the H theorem, and, if (H') be adjoined to it, it implies (P), even (P'), as well as (Eq). The implication in some writings that the validity of (Q) is a necessary condition for the validity of the H theorem, is therefore not correct.

As an example of a series of stipulations in which each is more restrictive than the preceding one, we may note the following: If (P) holds at a time T for a certain system S (more accurately: for the ensemble of duplicates of a certain system S), this does not imply that any of the other statements of Sec. 2 shall be true of S at T or at any other time. If (P) and (Eq) are both true of S at time T, however, (H') must hold at time T, while (X), and therefore (H), must be true of S at time T, and therefore also at all other times. Neither (D) nor (Q) need be true of S at any time in this case. If (P) and (D) are both true of S at time T, this is a more restrictive condition, in that (D) must now definitely be true of S at time T. (Q) need still not be true of S at any time. Lastly, if (P) and (D) be both true of S at time T, and the states are interconnected, then all the other principles of Sec. 2 must be true of S at time T. In particular, (Q), (X), and (H) are then true of S at all times.

As a further example of the use of Figs. 1 and 2, let us consider now a system such that the ensemble of its duplicates attains the condition (Eq) at some time T. Let us denote by (A_T) a principle if it is true of the ensemble at the time T, and let (A) denote the same principle if it is true of the ensemble at all times. The schemes of Figs. 1 and 2, give them rise to those of Figs. 3 and 4, which are self-explanatory.

Figure 4 incorporates all assumptions made by Thomsen,[7] provided our G's are set equal to unity. It

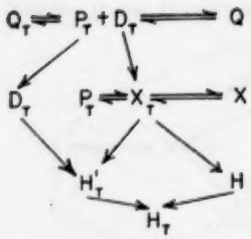

FIG. 4. Scheme of implications, provided the assumptions of both Figs. 2 and 3 are made. See caption of Fig. 1.

should therefore be compared with his results which are summarized in Fig. 5. The only significant difference is seen to reside in the fact that his principle (S) and our principle (H) do not occupy analogous positions, although they are both supposed to represent the statistical counterpart of the second law of thermodynamics. The reason resides in Thomsen's Theorem 3, in which he proves that (S) implies (P_T). In the present treatment it is impossible to prove such a theorem, as evidenced by our example (iii). This shows that (H) may be valid, even for an indefinite period of time, without enabling one to infer (P), (X), or (D): and that this remains true even if the condition (Eq) is adjoined to (H). The H theorem is therefore seen to imply only comparatively weak restrictions on the parameters of the theory. This is also clear on the general grounds that (H') and (H) each represent just one restrictive equation which is to be imposed on the parameters at any one time, whereas all the other conditions represent several restrictive equations.

6. SIGNIFICANCE OF THE CONDITION (X): COARSE GRAINED TRANSITION MATRICES

In this section, we wish to consider briefly the properties of those transition matrices A which satisfy the condition (X). Such considerations belong properly to the theory of matrices whose elements are real and non-negative. This was initiated by Frobenius,[13] and has been developed more recently by other authors.[14,15] Such matrices are also of importance in the theory of probability,[16,17] and, in particular, in connection with Markov processes.[18] In these theories one often studies stochastic matrices, i.e., matrices whose elements are real and non-negative, and whose row sums are unity. Occasionally doubly stochastic matrices are also studied. In such matrices the elements in any one row and in any one column add up to unity. If we agree to take any one row sum in an order defined by the requirement that the column suffix shall increase, and any one column sum in the order indicated by an increasing row suffix, and if we also agree to give the jth term in any one such sum the finite and nonzero weight G_j, we shall speak of the "weighted" row sum and of the "weighted" column sum. A matrix which satisfies condition (X) is clearly not a stochastic, or a doubly stochastic, matrix; it is a matrix whose jth weighted row sum is equal to its jth weighted column sum for all $j=1, 2, \cdots W$. A matrix satisfying this requirement for some set of weights G_j, and having all its elements non-negative, will be said to be a "coarse grained" transition matrix. We shall establish some of its properties.

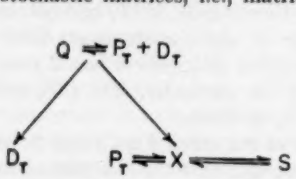

FIG. 5. Scheme of implications deduced by Thomsen (see reference 7). The symbols Q, D_T, P_T, X correspond to Thomsen's symbols M, D, E, L, respectively.

Let $B(p,q)$ be a matrix of p rows and q columns. Let O denote a matrix whose elements are all zero. Frobenius[13] defined a matrix B as *decomposable* if it could be expressed in terms of submatrices according to the scheme

$$B(n,n)=\begin{pmatrix} P(a,a) & Q(a,n-a) \\ O(n-a,a) & R(n-a,n-a) \end{pmatrix}, \qquad 1\leq a\leq n-1, \quad (1)$$

by applying a permutation to the row suffixes, and the same permutation to the column suffixes. If Q is also a zero matrix, B is said to be *completely decomposable.*

Theorem 6.—If a coarse-grained transition matrix is decomposable, then it is completely decomposable.

Proof.—Let $A(n,n)$ be the matrix under consideration, and let the weighting factors be $G_1, \cdots G_W$. Let G be a diagonal matrix whose (j,j) element is G_j, and let a matrix B be defined by $B\equiv GAG$. The sum of the jth row of B is then equal to the sum of the jth column of B [by condition (X)]. B can be decomposed as in (1), since A is decomposable; also the elements of the matrices P, Q, R are all non-negative. Now the sum of the first a rows of B must be equal to the sum of the first a columns of B. But the difference between these two sums is the sum of the elements of Q, and this must therefore be zero. Hence B is completely decomposable. It follows that A is completely decomposable.

Theorem 7.—If a matrix $A(n,n)$ whose elements are non-negative is not decomposable, then the quantities $(A^r)_{jk}$ $(r=1, 2, \cdots, n-1)$ cannot all vanish for any given pair of suffixes j,k.

This result is due to Frobenius.[19] The quantities $(A^r)_{jk}$ are just the products which we introduced in Sec. 2.

[13] G. Frobenius, Sitzber. Kgl. preuss. Akad. Wiss. Berlin, p. 456 (1912).
[14] H. Wielandt, Math. Ann. **52**, 642 (1950).
[15] Y. K. Wong, Proc. Natl. Acad. Sci. **40**, 121 (1954).
[16] M. Fréchet, in *Traité du calcul des probabilités et ses applications*, edited by E. Borel (Gauthiers-Villars, Paris, 1938), Vol. I, Part III, Book 2.
[17] W. Feller, *An Introduction to Probability Theory and its Applications* (John Wiley and Sons, Inc., New York, 1950).
[18] V. Romanovsky, Acta Math. **66**, 137 (1935).
[19] See reference 13, p. 461.

Theorem 8.—By applying the same permutation to the rows and columns of a coarse grained transition matrix the latter may be completely decomposed into indecomposable parts, or it is itself indecomposable.

This result follows from the last two theorems. As a special case, we note that "fine grained" transition matrices, for which $G_1=G_2=\cdots G_W=1$, and doubly stochastic matrices, are all completely decomposable.

By Theorem 8 condition (X) ensures that the W macroscopically distinguishable states can be subdivided into groups of states such that no transitions are possible between groups, while transitions *in either direction* are always possible between any two states which belong to the same group. Thus, whatever the values of the weighting factors G_j, condition (X) ensures that if transitions are possible from a state j to a state k (possibly via other states), then converse transitions are also possible.

The author is indebted to Dr. J. S. Thomsen for a careful reading of the manuscript, and a resulting helpful discussion.

APPENDIX

In this appendix we shall derive two additional results, which, while not essential to the main arguments of the text, will serve to clarify the relations obtained.

In Lemma 3 we have neglected terms of order Δ_j^3, and this will now be justified by showing that the terms in Δ_j^2 must in all important cases make some contribution.

Lemma 4.—If condition (P) can hold for a system, then, when it holds very nearly and at least one Δ_j of Lemma 3 is nonzero, we must have

$$\sum_{i,j} G_j A_{ji} G_i (\Delta_j-\Delta_i)^2>0$$

(i, j in αth group of suffixes; valid for all α).

Proof.—When condition (P) holds, the probability of finding one of the suffixes i is

$$\sum_{i=1}^{w_\alpha} P_i = K_\alpha \sum_{i=1}^{w_\alpha} G_i.$$

This equation must remain valid even when (P) does not hold, as no transitions are possible between different groups of states. Hence

$$\sum_{j=1}^{w_\alpha} \Delta_j = 0.$$

Thus, if one Δ_j, Δ_k say, is nonzero, we must have $w_\alpha>1$ and, also, there must exist at least one other nonzero Δ_j, Δ_l say, which has a sign opposite to that of Δ_k. The states k and l can be joined by a nonzero product of the A's, and, by definition, this can be formed using only suffixes from the αth group. Let it be $A_{ka}A_{ab}\cdots A_{pq}A_{ql}$. We can now show that, if Lemma 4 were not true, one could arrive at a contradiction.

Suppose, then, $\Delta_k\neq 0$, $\sum_{i,j} G_j A_{ji} G_i (\Delta_j-\Delta_i)^2=0$. Then each term in this sum must vanish separately. Consider those terms of this sum which are specified by the pairs of suffixes: $(i,j)=(k,a)$, (a,b), $\cdots$ (p,q), (q,l). Since the A's are nonzero for these terms, they will vanish separately only if $\Delta_k=\Delta_a=\Delta_b\cdots\Delta_p=\Delta_q=\Delta_l$. Since Δ_k, Δ_l are of opposite sign and nonzero, this is a contradiction. Hence Lemma 4 holds.

It follows from this lemma that in the neighborhood of $\dot{H}=0$, for which $\ddot{H}\neq 0$, $\ddot{H}$ is in fact negative, provided $F_r=0$ for all r. Under these conditions $\dot{H}$ must attain a maximum value when $\dot{H}=0$. This result is used in Theorem 3.

Theorem 1b.—If $(P)+(D)$ holds (so that $P_i/G_i=K_\alpha$ for all v groups $\alpha=1, 2, \cdots, v$ of suffixes), and if $K_\alpha>0$ for all α, then (Q) holds.

Consider the αth group of suffixes. Suppose $P_i/G_i \neq P_j/G_j$, then $A_{ij}=A_{ji}$ by (P), so that (Q) holds in this case for the αth group of suffixes, there being no need to appeal to (D). Suppose next $P_iG_j=P_jG_i$. By (D) $P_iA_{ij}G_j=P_jA_{ji}G_i$, and these two results enable one to deduce (Q) for the αth group of suffixes also in this case, provided $P_i>0$. But, by hypothesis, $K_\alpha=P_i/G_i>0$, so that (Q) is established for the αth group of suffixes in both cases. Repeating the argument for the other groups of suffixes, the proposition is finally proved.

If the states are interconnected, $v=1$ and $K_1=1/W>0$, so that the conditions of Theorem 1b are fulfilled. Hence,

Theorem 1a.—If the states are interconnected, then $(P)+(D)$ implies (Q).

It is therefore clear that Theorem 1b is somewhat stronger than Theorem 1a of the main text.

Scattering of Light of Very Low Frequency by Systems of Spin $\frac{1}{2}$*

F. E. Low
Department of Physics, University of Illinois, Urbana, Illinois
(Received August 13, 1954)

It is shown that the first two terms in the expansion of the scattering amplitude of light by a system of spin $\frac{1}{2}$ in powers of the frequency can be simply expressed in terms of the macroscopic properties of the system. The first term is the well known Thomson amplitude, and depends only on the total charge and mass. The second term is found to depend only on the charge, mass, and magnetic moment of the system.

I. INTRODUCTION

IT is well known that the scattering of zero-energy photons by a charged system is given by the Thomson formula and hence is independent of the structure of the system. In this paper it will be shown that not only the zero-frequency limit of the scattering amplitude but also its first derivative with respect to the photon frequency is determined by the static properties of the system (charge, mass, and magnetic moment), at least for a system of spin $\frac{1}{2}$. Unlike the Thomson limit, which appears as a consequence of gauge invariance in the usual theoretical formulation, the new limit appears to be a consequence of gauge and relativistic invariance.

The derivatation to be given here applies to systems consisting of spin-$\frac{1}{2}$ fermions locally coupled to spin-zero bosons, but could presumably be generalized, if necessary, to almost any gauge and Lorentz invariant system. The proof applies formally to all orders in $e^2/\hbar c$ (as well as to all orders in the meson-nucleon coupling) provided the virtual photons are given a fictitious rest mass λ; it may or may not be correct in the limit $\lambda \to 0$, depending on whether or not the derivative in question exists. Failure of the derivative to exist would, of course, appear as an infrared divergence. In our derivation such an infrared divergence would be due to the existence of too great a density of excited states of the scattering system whose energy was infinitesimally close to that of the ground state. We shall have to assume the scatterer (proton, neutron, electron, etc.) to have a minimum excitation energy with respect to which the photon frequency can be measured. For protons and neutrons this energy is of course $\mu_\pi c^2$, where μ_π is the π-meson rest mass; the corresponding length with respect to which the photon wavelength must be large is $\hbar/\mu_\pi c$.

Our method consists in showing that if the scattering amplitude be expanded in powers of k (for $\hbar ck \ll \mu_\pi c^2$) the first two terms in the expansion can essentially be expressed in terms of matrix elements of the charge density, $\rho(x)$, rather than in terms of the current density, $\mathbf{j}(x)$. Since $\int \rho(x) d\mathbf{x} = e$, the total charge, whereas $\int \mathbf{j}(x) d\mathbf{x}$ has large off-diagonal components, considerable simplification is achieved: no excited states need be included in the sum over states which determines the scattering amplitude to this order in k. The diagonal elements of ρ, as is well known, can be simply expressed in terms of e, m and μ (the static magnetic moment of the system) for small momentum transfer. The first term in the expansion, of course, turns out to be the Thomson term; the second, which is linear in the spin vector of the system, is somewhat more complicated, except in the forward direction, where it must be a multiple of $i\boldsymbol{\sigma}\cdot(\mathbf{e}'\times\mathbf{e})k$; the multiple turns out to be $2\lambda^2$,[1] where λ is the anomalous part of the magnetic moment.

The total scattering amplitude, correct to order k, is

$$H' = (e^2/m)\mathbf{e}\cdot\mathbf{e}' - (ie/m)(2\mu - e/m)k\boldsymbol{\sigma}\cdot(\mathbf{e}'\times\mathbf{e}) - 2\mu^2 i\boldsymbol{\sigma}\cdot[(\mathbf{e}\times\mathbf{k})\times(\mathbf{e}'\times\mathbf{k})]/k - i(e/m) \times\mu[(\mathbf{e}\cdot\mathbf{k}')\mathbf{e}'\cdot(\boldsymbol{\sigma}\times\mathbf{k}')/k - (\mathbf{e}'\cdot\mathbf{k})\mathbf{e}\cdot(\boldsymbol{\sigma}\times\mathbf{k})/k].^2 \quad (1.1)$$

Here $\mathbf{e}$ and $\mathbf{e}'$ are the initial and final polarization vectors of the scattered photon.

II. CALCULATION: GAUGE INVARIANCE

We shall work within the framework of a specific theory: we calculate the scattering of light by a spin-$\frac{1}{2}$ system locally coupled to a scalar (or pseudoscalar) meson field. The method of calculation will make it clear that the result has a much wider range of validity.

The S matrix for scattering of a light quantum from a state $(\mathbf{k},\omega,\mathbf{e})$ to a state $(\mathbf{k}',\omega',\mathbf{e}')$, where $|\mathbf{k}| = \omega$, $|\mathbf{k}'| = \omega'$, $\mathbf{e}\cdot\mathbf{k} = \mathbf{e}'\cdot\mathbf{k}' = 0$, is given by

$$S = -[2i/(4\omega\omega')^{\frac{1}{2}}]\int \epsilon^2\phi^*(x)\phi(x)e^{i(k-k')x}dx(\mathbf{e}\cdot\mathbf{e}') - [1/(4\omega\omega')^{\frac{1}{2}}]\int P[\mathbf{j}(x)\cdot\mathbf{e}, \mathbf{j}(y)\cdot\mathbf{e}'] \times e^{ik'y}e^{-ikx}dxdy, \quad (2.1)$$

where all integrations and coordinates are four dimensional, $\phi(x)$ is the charged meson field operator, P is

* Work supported in part by the joint program of the Office of Naval Research and the U. S. Atomic Energy Commission.

[1] We use units in which $\hbar = c = 1$, $e^2/4\pi = 1/137$.

[2] The author has been informed that a result essentially equivalent to Eq. (1.1) has been independently obtained by M. Gell-Mann and M. Goldberger using a different method of proof. See M. Gell-Mann and M. Goldberger, Proceedings of the Glasgow Conference on Nuclear Physics, 1954 (unpublished); and Phys. Rev., following paper [Phys. Rev. **96**, 1433 (1954)]. The author would like to thank Dr. Gell-Mann for communicating this result to him.

Dyson's time-ordering operator, and $\mathbf{j}(x)$ is the current-density operator. In our example

$$j_\mu(x)=\begin{cases}\rho(x)=\epsilon[\phi_1(x)\pi_2(x)-\phi_2(x)\pi_1(x)]\\ \qquad +\epsilon\bar{\psi}(x)\gamma_4\tfrac{1}{2}(1+\tau_3)\psi(x),\\ \mathbf{j}(x)=\epsilon[\nabla\phi_1(x)\phi_2(x)-\nabla\phi_2(x)\phi_1(x)]\\ \qquad +i\epsilon\bar{\psi}(x)\boldsymbol{\gamma}\tfrac{1}{2}(1+\tau_3)\psi(x),\end{cases} \tag{2.2}$$

and

$$\phi=(\phi_1+i\phi_2)/\sqrt{2},\quad \phi^*=(\phi_1-i\phi_2)/\sqrt{2}. \tag{2.3}$$

ϵ is the electronic charge, $\epsilon^2/4\pi=1/137$. The time dependence of all operators is given by the Heisenberg equations of motion for the scattering system. We may rewrite Eq. (2.1) as follows:

$$S=-\epsilon_i'\epsilon_j g_{ij}(4\omega\omega')^{-\frac{1}{2}}, \tag{2.4}$$

where

$$g_{ij}=2i\epsilon^2\int\phi^*(x)\phi(x)e^{i(k-k')x}dx\delta_{ij}+\int P[j_i(x),j_j(y)]e^{iky}e^{-ik'x}dxdy. \tag{2.5}$$

For purposes of orientation we give g_{ij} for Thomson scattering:

$$g_{ij}(\tau)=\delta_{ij}(2\pi)^4i\delta(\Delta k_\mu+\Delta p_\mu)e^2/m, \tag{2.6}$$

where e and m are the total charge and mass of the scatterer. Δp_μ is the 4-momentum transfer to the scatterer.

The theorem which makes our calculation possible is the following:

$$k_i'g_{ij}k_j=\omega'\omega\int P[\rho(x),\rho(y)]e^{iky}e^{-ik'x}dxdy. \tag{2.7}$$

Equation (2.7) is obviously a consequence of the gauge invariance of the theory. It is valid for any gauge-invariant theory in which the system interacts with a scalar potential $V(x)$ through an interaction Hamiltonian $H_v=\int\rho(x)V(x)d\mathbf{x}$. This can be shown quite simply and generally by considering the scattering of the system by an arbitrary external electromagnetic field and requiring the S matrix to be invariant under a gauge transformation of the external field.

To prove (2.7) for our special example, we operate on (2.5) with k_i'. Thus:

$$k_i'g_{ij}=2ik_j'\epsilon^2\int\phi^*(x)\phi(x)e^{i(k-k')x}dx+\frac{1}{i}\int P[\partial j_i(x)/\partial x_i,j_j(y)]e^{iky}e^{-ik'x}dxdy. \tag{2.8}$$

The second term on the right may be transformed by using the equation of continuity,

$$\partial j_i(x)/\partial x_i=-\partial\rho(x)/\partial x_0, \tag{2.9}$$

and the relation

$$P\left[\frac{\partial\rho(x)}{\partial x_0},j_j(y)\right]=\frac{\partial}{\partial x_0}P[\rho(x),j_j(y)]-\delta(x_0-y_0)[\rho(x),j_j(y)]. \tag{2.10}$$

We find, after an integration by parts,

$$k_i'g_{ij}=2i\epsilon^2k_j'\int\phi^*(x)\phi(x)e^{i(k-k')x}dx+\frac{1}{i}\int dxdye^{-ik'x}e^{iky}\delta(x_0-y_0)[\rho(x),j_j(y)]+\omega'\int dxdye^{-ik'x}e^{iky}P[\rho(x),j_j(y)]. \tag{2.11}$$

The first two terms on the right of Eq. (2.11) cancel exactly as a consequence of the definitions (2.2) and (2.3) and the canonical commutation relations. We now multiply the remaining terms in (2.11) by k_j and find easily that

$$\begin{aligned}k_i'g_{ij}k_j&=\omega'\int dxdye^{-ik'x}e^{iky}P\left[\rho(x),-\frac{1}{i}\frac{\partial j_j(y)}{\partial y_j}\right]\\&=\frac{\omega'}{i}\int dxdye^{-ik'x}e^{iky}P\left[\rho(x),\frac{\partial\rho(y)}{\partial y_0}\right]\\&=-\frac{\omega'}{i}\int dxdye^{-ik'x}\left[\frac{\partial e^{iky}}{\partial y_0}\right]P[\rho(x),\rho(y)]\\&=\omega'\omega\int dxdye^{-ik'x}e^{iky}P[\rho(x),\rho(y)],\end{aligned} \tag{2.12}$$

where we have made use of the fact that $\rho(x)$ and $\rho(y)$ commute for $x_0=y_0$.

It follows from (2.12) that if we can obtain enough information about the tensorial character of g_{ij} from other sources, we can use (2.12) to calculate g_{ij} itself. Let us look at the defining equation for g_{ij}, Eq. (2.5).

The first term in (2.5) is a multiple of δ_{ij}, and, since $\phi^*\phi$ is a scalar, must be independent of the spin to order k^2. The second term can be rewritten in terms of a sum over intermediate states with appropriate energy denominators. The contribution $g_{ij}^{(0)}$ to the sum arising from unexcited intermediate states can be explicitly calculated to the required order in k. We shall perform this calculation in Sec. IV. It turns out that $k_i'g_{ij}^{(0)}k_j=0$ so that $g_{ij}^{(0)}$ will give no contribution to (2.12).

In the sum over excited states, $g_{ij}^{(e)}$, there can be no singularities as $\{k,\omega\}\to 0$, because of the minimum excitation energy μ_π. The only tensors that can enter $g_{ij}^{(e)}$ to order k are thus δ_{ij} and σ_{ij}, where $\sigma_{12}=\sigma_3$, etc.

We may therefore write

$$g_{ij}=g_{ij}^{(0)}+A\delta_{ij}+B\sigma_{ij}. \tag{2.13}$$

Substituting (2.13) into (2.12), we find

$$\mathbf{k}'\cdot\mathbf{k}A+\boldsymbol{\sigma}\cdot(\mathbf{k}'\times\mathbf{k})B=\omega'\omega C,$$

where

$$C=\int dxdye^{-ik'x}e^{iky}P[\rho(x),\rho(y)]. \tag{2.14}$$

We may now think of (2.14) expanded into a sum over states. Those terms arising from excited states will contribute at most of order k^2, since $\int\rho(x)d\mathbf{x}$ is a c-number, the total charge. Thus to our order we may calculate (2.14) using only *unexcited* intermediate states.

We proceed to rewrite Eq. (2.14) as a sum over states (suppressing all excited states):

$$\langle\mathbf{p}_f|P[\rho(x),\rho(y)]|\mathbf{p}_i\rangle$$
$$=e^{iE_fx_0}e^{-iE_iy_0}\langle\mathbf{p}_f|\rho(\mathbf{x})e^{-iH(x_0-y_0)}\rho(\mathbf{y})|\mathbf{p}_i\rangle \quad (x_0>y_0)$$
$$=e^{iE_fy_0}e^{-iE_ix_0}\langle\mathbf{p}_f|\rho(\mathbf{y})e^{-iH(y_0-x_0)}\rho(\mathbf{x})|\mathbf{p}_i\rangle \quad (x_0<y_0),$$

so that

$$C=\int_{-\infty}^{\infty}dx_0e^{i(\omega'+E_f)x_0}\left\langle\mathbf{p}_f\left|\int\rho(\mathbf{x})e^{-i\mathbf{k}'\cdot\mathbf{x}}d\mathbf{x}e^{-iHx_0}\right.\right.$$
$$=\int_{-\infty}^{x_0}dy_0e^{i(H-E_i-\omega)y_0}\int\rho(\mathbf{y})e^{i\mathbf{k}\cdot\mathbf{y}}d\mathbf{y}\left|\mathbf{p}\right\rangle$$
$$=\int_{-\infty}^{\infty}dy_0e^{i(E_f-\omega)y_0}\left\langle\mathbf{p}_f\left|\int\rho(\mathbf{y})e^{i\mathbf{k}\cdot\mathbf{y}}d\mathbf{y}e^{-iHy_0}\right.\right.$$
$$\times\int_{-\infty}^{y_0}dx_0e^{i(H-E_i+\omega')x_0}\int\rho(\mathbf{x})e^{-i\mathbf{k}'\cdot\mathbf{x}}d\mathbf{x}\left|\mathbf{p}_i\right\rangle$$
$$=\frac{2\pi}{i}\delta(\omega'+E_f-\omega-E_i)\left[\left\langle\mathbf{p}_f\left|\int\rho(\mathbf{x})e^{-i\mathbf{k}'\cdot\mathbf{x}}d\mathbf{x}\right.\right.\right.$$
$$\times\frac{1}{H-E_i-\omega}\int\rho(\mathbf{y})e^{i\mathbf{k}\cdot\mathbf{y}}d\mathbf{y}\left|\mathbf{p}_i\right\rangle+\left\langle\mathbf{p}_f\left|\int\rho(\mathbf{y})\right.\right.$$
$$\left.\left.\left.\times e^{i\mathbf{k}\cdot\mathbf{y}}d\mathbf{y}\frac{1}{H-E_i+\omega'}\int\rho(\mathbf{x})e^{-i\mathbf{k}'\cdot\mathbf{x}}d\mathbf{x}\right|\mathbf{p}_i\right\rangle\right]$$
$$=\frac{(2\pi)^4}{i}\delta(\Delta p_\mu+\Delta k_\mu)\sum_{\boldsymbol{\sigma}}\left[\frac{\langle\mathbf{k}-\mathbf{k}'|\rho|\mathbf{k},\boldsymbol{\sigma}\rangle\langle\mathbf{k},\boldsymbol{\sigma}|\rho|0\rangle}{E(k)-E(0)-\omega}\right.$$
$$\left.+\frac{\langle\mathbf{k}-\mathbf{k}'|\rho|-\mathbf{k}',\boldsymbol{\sigma}\rangle\langle-\mathbf{k}',\boldsymbol{\sigma}|\rho|0\rangle}{E(k')-E(0)+\omega'}\right], \tag{2.15}$$

where we have made use of momentum conservation and set $\mathbf{p}_i=0$ in arriving at (2.15).

We may now find immediately the Thomson limit from (2.15). Since $\int\rho(x)d\mathbf{x}=e$, $\langle\mathbf{k}|\rho|0\rangle\approx\langle0|\rho|0\rangle=e$ $+\sim k^2$, so that as $k\to0$ we have for the bracketed quantity

$$e^2\left[\frac{1}{E(k)-E(0)-\omega}+\frac{1}{E(k')-E(0)+\omega'}\right]$$
$$=e^2[E(k')-E(0)+\omega'+E(k)\cdot E(0)-\omega]$$
$$\times[E(k)-E(0)-\omega]^{-1}[E(k')-E(0)+\omega]^{-1}$$
$$\approx-\frac{e^2}{\omega\omega'}[E(k')-E(0)+E(k)-E(0)+E(0)-E(k'-k)]$$
$$\cong-\frac{e^2}{\omega\omega'}\left[\frac{k'^2}{2m}+\frac{k^2}{2m}-\frac{(\mathbf{k}-\mathbf{k}')^2}{2m}\right]=-\frac{e^2}{m}\frac{\mathbf{k}\cdot\mathbf{k}'}{\omega\omega'}, \tag{2.16}$$

whence the constant A in (2.14) is given by $A=-(2\pi)^4$ $i\delta(k_\mu'-k_\mu+\Delta p_\mu)e^2/m$ which leads trivially to the Thomson formula (2.6).

III. RELATIVISTIC INVARIANCE

We return now to Eq. (2.15), and investigate the properties of $\langle\mathbf{p}_2|\rho|\mathbf{p}_1\rangle$.

The four vector $\langle\mathbf{p}_2|j_\mu|\mathbf{p}_1\rangle$ must have the general form, for a spin-$\frac{1}{2}$ particle,

$$\langle\mathbf{p}_2|j_\mu|\mathbf{p}_1\rangle=i\bar{u}(\mathbf{p}_2)[e\gamma_\mu f((\Delta p_\lambda)^2)$$
$$-\sigma_{\mu\nu}\Delta p_\nu g((\Delta p_\lambda)^2)]u(\mathbf{p}_1), \tag{3.1}$$

where u and $\bar{u}$ are the Dirac spinors for the momentum states $\mathbf{p}_2$ and $\mathbf{p}_1$ and the γ's and σ's are the well-known Dirac matrices. Here f and g are functions of $(\Delta p_\lambda)^2$ only, and $f(0)=1$, $g(0)=\lambda$, the anomalous magnetic moment of the particle.

Using (3.1), we find

$$\langle\mathbf{p}_2|\rho|\mathbf{p}_1\rangle=(1/i)\langle\mathbf{p}_2|j_4|\mathbf{p}_1\rangle$$
$$=\bar{u}(\mathbf{p}_2)[\beta ef-\sigma_{4i}\Delta p_ig]u(\mathbf{p}_1)$$
$$=efu^*(\mathbf{p}_2)u(\mathbf{p}_1)+gu^*(\mathbf{p}_2)\beta\boldsymbol{\alpha}\cdot\Delta\mathbf{p}u(\mathbf{p}_1). \tag{3.2}$$

Let us call the bracketed quantity in Eq. (2.15) Q:

$$Q=\sum_{\boldsymbol{\sigma}}\left[\frac{\langle\mathbf{k}-\mathbf{k}'|\rho|\mathbf{k},\boldsymbol{\sigma}\rangle\langle\mathbf{k},\boldsymbol{\sigma}|\rho|0\rangle}{E(k)-E(0)-\omega}\right.$$
$$\left.+\frac{\langle\mathbf{k}-\mathbf{k}'|\rho|-\mathbf{k}',\boldsymbol{\sigma}\rangle\langle-\mathbf{k}',\boldsymbol{\sigma}|\rho|0\rangle}{E(k')-E(0)+\omega'}\right] \tag{3.3}$$

We wish to evaluate Q only to order k. Thus, the numerator in (3.3) need be accurate only to order k^2. Since $(\Delta E)^2\approx k^4$, we may set $(\Delta p_\lambda)^2=(\Delta\mathbf{p})^2$, and since the $(\Delta\mathbf{p})^2$ are the same in both terms of (3.3) (although in opposite order), the f and g functions will be common factors to both terms. Their $\Delta\mathbf{p}$ dependence may therefore be neglected in our limit, which considerably simplifies the remaining calculation. We thus set $f=1$,

$g=g(0)=\lambda$, the anomalous part of the magnetic moment. Equation (3.3) for Q becomes, if we insert projection operators for the spin sums over intermediate states:

$$Q=u^*(\mathbf{k}-\mathbf{k}')\Big[\frac{[e+\lambda\beta\boldsymbol{\alpha}\cdot(-\mathbf{k}')]}{[E(k)-E(0)-\omega]}\frac{[\boldsymbol{\alpha}\cdot\mathbf{k}+\beta m+E(k)]}{2E(k)}\times(e+\lambda\beta\boldsymbol{\alpha}\cdot\mathbf{k})+\frac{(e+\lambda\beta\boldsymbol{\alpha}\cdot\mathbf{k})}{[E(k')-E(0)+\omega']}\times\frac{[-\boldsymbol{\alpha}\cdot\mathbf{k}'+\beta m+E(k')]}{2E(k')}[e+\lambda\beta\boldsymbol{\alpha}\cdot(-\mathbf{k}')]\Big]u(0). \quad (3.4)$$

All the terms of the form $\beta\boldsymbol{\alpha}\cdot\mathbf{k}$ or $\boldsymbol{\alpha}\cdot\mathbf{k}$ in (3.4) will be of order k^2/ω, so that they may be evaluated to their lowest nonvanishing order. The only term we have to watch is the one with every $\boldsymbol{\alpha}\cdot\mathbf{k}$ left out. Since $\beta u(0)=u(0)$, and since $k'^2-k^2\approx k^3/m$, this term is

$$(u^*(\mathbf{k}-\mathbf{k}'),u(0))e^2\frac{[m+E(k)]}{2E(k)}\Big[\frac{1}{E(k)-E(0)+\omega}+\frac{1}{E(k')-E(0)+\omega'}\Big]=-\frac{e^2}{m}\frac{\mathbf{k}\cdot\mathbf{k}'}{\omega\omega'[1+\sim k^2]}\cong-\frac{e^2}{m}\frac{\mathbf{k}\cdot\mathbf{k}'}{\omega'\omega}.$$

In evaluating the remaining terms in (3.4) we may set $E(k')=E(k)=m$, $\omega'=\omega$ everywhere. Since $u(p)\cong(1+\boldsymbol{\alpha}\cdot\mathbf{p}/2m)u(0)$, we have

$$\begin{aligned}Q&=-\frac{e^2}{m}\Big(\frac{\mathbf{k}'\cdot\mathbf{k}}{\omega'\omega}\Big)+\frac{1}{\omega}u_f^*(0)\Big(1+\frac{\boldsymbol{\alpha}\cdot(\mathbf{k}-\mathbf{k}')}{2m}\Big)\\&\times\Big[(e+\beta\boldsymbol{\alpha}\cdot\mathbf{k})\Big(\frac{-\boldsymbol{\alpha}\cdot\mathbf{k}'+m+\beta m}{2m}\Big)(e-\lambda\beta\boldsymbol{\alpha}\cdot\mathbf{k}')\\&-(e-\lambda\beta\boldsymbol{\alpha}\cdot\mathbf{k}')\Big(\frac{\boldsymbol{\alpha}\cdot\mathbf{k}+m+\beta m}{2m}\Big)(e+\lambda\beta\boldsymbol{\alpha}\cdot\mathbf{k})\Big]u_i(0)\\&=-\frac{e^2}{m}\Big(\frac{\mathbf{k}\cdot\mathbf{k}'}{\omega'\omega}\Big)+i\Big(\frac{\boldsymbol{\sigma}\cdot(\mathbf{k}'\times\mathbf{k})}{\omega}\Big)\Big(\frac{e^2}{2m^2}+\frac{2\lambda e}{m}\Big)\\&=-\frac{e^2}{m}\Big(\frac{\mathbf{k}\cdot\mathbf{k}'}{\omega'\omega}\Big)+i\Big(\frac{\boldsymbol{\sigma}\cdot(\mathbf{k}'\times\mathbf{k})}{\omega}\Big)\frac{e}{m}\Big(2\mu-\frac{e}{2m}\Big). \quad (3.5)\end{aligned}$$

Here μ is the total magnetic moment. Equation (2.45) now becomes

$$C=\frac{(2\pi)^4}{i}\delta(\Delta p_\mu+\Delta k_\mu)\times\Big[-\frac{e^2}{m}\frac{\mathbf{k}\cdot\mathbf{k}'}{\omega\omega'}+i\boldsymbol{\sigma}\cdot(\mathbf{k}'\times\mathbf{k})\frac{e}{m\omega}\Big(2\mu-\frac{e}{2m}\Big)\Big], \quad (3.6)$$

and (2.14) informs us that

$$A=-\frac{(2\pi)^4}{i}\delta(\Delta p_\mu+\Delta k_\mu)\frac{e^2}{m}, \quad (3.7)$$

and

$$B=\frac{(2\pi)^4}{i}\delta(\Delta p_\mu+\Delta k_\mu)i\frac{\omega e}{m}\Big(2\mu-\frac{e}{2m}\Big). \quad (3.8)$$

The off-diagonal contribution to the scattering is thus given, correct to order (k,ω), by

$$g_{ij}-g_{ij}^{(0)}=\frac{(2\pi)^4}{i}\delta(\Delta p_\mu+\Delta k_\mu)\times\Big[-\frac{e^2}{m}\delta_{ij}+i\omega\frac{e}{m}\Big(2\mu-\frac{e}{2m}\Big)\sigma_{ij}\Big]. \quad (3.9)$$

Note that this term is exactly zero for a neutron.

In the next section we shall calculate $g_{ij}^{(0)}$.

IV. DIAGONAL MAGNETIC SCATTERING

In complete analogy with the derivativation of Eq. (2.15) for the quantity C defined by Eq. (2.14), we may derive an expression for $g_{ij}^{(0)}$ directly from the defining Eq. (2.5). We find

$$g_{ij}^{(0)}=\frac{(2\pi)^4}{i}\delta(\Delta p_\mu+\Delta k_\mu)\sum_{\boldsymbol{\sigma}}\Big[\frac{\langle\mathbf{k}-\mathbf{k}'|j_i|\mathbf{k}\rangle\langle\mathbf{k}|j_j|0\rangle}{E(k)-E(0)-\omega}+\frac{\langle\mathbf{k}-\mathbf{k}'|j_j|-\mathbf{k}'\rangle\langle-k'|j_i|0\rangle}{E(k')-E(0)+\omega'}\Big], \quad (4.1)$$

with

$$\langle\mathbf{p}_2|j_i|\mathbf{p}_1\rangle=i\bar{u}(\mathbf{p}_2)[e\gamma_i f((\Delta p_\lambda)^2)-\sigma_{i\nu}\Delta p_\nu g((\Delta p_\lambda)^2)]u(\mathbf{p}_1). \quad (4.2)$$

Since γ_i and $\sigma_{ij}\Delta p_j$ vanish with k, we may disregard $\sigma_{i4}\Delta E$ and set $f((\Delta p_\lambda)^2)=1$, $g((\Delta p_\lambda)^2)=\lambda$. With these approximations

$$\begin{aligned}\langle\mathbf{p}_2|\mathbf{j}|\mathbf{p}_1\rangle&=u^*(\mathbf{p}_2)[e\boldsymbol{\alpha}-i\lambda\Delta\mathbf{p}\times\boldsymbol{\sigma}]u(\mathbf{p}_1)\\&\cong(e/2m)(\mathbf{p}_2+\mathbf{p}_1)+i(e/2m+\lambda)\boldsymbol{\sigma}\times\boldsymbol{\Delta}\mathbf{p}\\&=(e/2m)(\mathbf{p}_2+\mathbf{p}_1)+i\mu\boldsymbol{\sigma}\times\Delta\mathbf{p}, \quad (4.3)\end{aligned}$$

which is, of course, the current of a nonrelativistic particle interacting with a magnetic field according to the Hamiltonian

$$H_{\text{N.R.}}'=-(e/2m)(\mathbf{p}\cdot\mathbf{A}+\mathbf{A}\cdot\mathbf{p})-\mu\boldsymbol{\sigma}\cdot\mathbf{H}. \quad (4.4)$$

We may now verify the statement made in Sec. II that $k_i'g_{ij}^{(0)}k_j=0$. This is obvious for all those terms involving the spin, since $\Delta\mathbf{p}$ is in each case the $\mathbf{k}$ with which an inner product is being taken. For the spin-

independent terms, we have

$$g_{ij}^{(0)}|_{\text{no spin}}=\frac{(2\pi)^4}{i}\delta(\Delta p_\mu+\Delta k_\mu)\left(\frac{e}{2m}\right)^2\frac{2}{\omega}\times(k_i'k_j'-k_ik_j), \quad (4.5)$$

which is manifestly orthogonal to $k_i'k_j$. Furthermore, since $\mathbf{e}\cdot\mathbf{k}=\mathbf{e}'\cdot\mathbf{k}'=0$, the spin-independent terms make no contribution to the scattering matrix.

The contribution to the scattering matrix of $g_{ij}^{(0)}$ is thus

$$\begin{aligned}S^{(0)}&=-\frac{1}{(4\omega'\omega)^{\frac{1}{2}}}\frac{(2\pi)^4}{i}\delta(\Delta p_\mu+\Delta k_\mu)\\&=\left[\left\{\frac{e}{m}\mathbf{e}'\cdot\mathbf{k}+i\mathbf{e}'\cdot[\boldsymbol{\sigma}\times(-\mathbf{k}')]\mu\right\}\frac{i\mathbf{e}\cdot(\boldsymbol{\sigma}\times\mathbf{k})\mu}{-\omega}\right.\\&\left.+\left\{-\frac{e}{m}\mathbf{e}\cdot\mathbf{k}'+i\mathbf{e}\cdot(\boldsymbol{\sigma}\times\mathbf{k})\mu\right\}\frac{i\mathbf{e}'\cdot[\boldsymbol{\sigma}\times(-\mathbf{k}')\mu]}{\omega}\right]\\&=-\frac{1}{(4\omega'\omega)^{\frac{1}{2}}}\frac{(2\pi)^4}{i}\delta(\Delta p_\mu+\Delta k_\mu)\\&\times\left\{\frac{2i\mu^2}{\omega}\boldsymbol{\sigma}\cdot[(\mathbf{e}\times\mathbf{k})\times(\mathbf{e}'\times\mathbf{k}')]+\frac{ie\mu}{m\omega}\right.\\&\left.\times[(\mathbf{e}\cdot\mathbf{k}')\mathbf{e}'\cdot(\boldsymbol{\sigma}\times\mathbf{k})-(\mathbf{e}'\cdot\mathbf{k})\mathbf{e}\cdot(\boldsymbol{\sigma}\times\mathbf{k})]\right\}. \quad (4.6)\end{aligned}$$

The contribution to the scattering matrix of $g_{ij}-g_{ij}^{(0)}$ is

$$S-S^{(0)}=-\frac{e_i'e_j}{(4\omega'\omega)^{\frac{1}{2}}}\frac{(2\pi)^4}{i}\delta(\Delta p_\mu+\Delta k_\mu)\times\left[-\frac{e^2}{m}\delta_{ij}+i\sigma_{ij}\omega\frac{e}{m}\left(2\mu-\frac{e}{2m}\right)\right],$$

so that in all

$$\begin{aligned}S=&\frac{(2\pi)^4}{i}\frac{1}{(4\omega'\omega)^{\frac{1}{2}}}\delta(\Delta p_\mu+\Delta k_\mu)\\&\times\left[\frac{e^2}{m}\mathbf{e}\cdot\mathbf{e}'-i\frac{e}{m}\omega\boldsymbol{\sigma}\cdot(\mathbf{e}'\times\mathbf{e})\left(2\mu-\frac{e}{2m}\right)\right.\\&-\frac{2i\mu^2}{\omega}\boldsymbol{\sigma}\cdot(\mathbf{e}\times\mathbf{k})\times(\mathbf{e}'\times\mathbf{k}')-\frac{e\mu i}{m\omega}\\&\left.\times[(\mathbf{e}\cdot\mathbf{k}')\mathbf{e}\cdot(\boldsymbol{\sigma}\times\mathbf{k}')-\mathbf{e}'\cdot\mathbf{k}\mathbf{e}\cdot(\boldsymbol{\sigma}\times\mathbf{k})]+\sim k^2\right]. \quad (4.7)\end{aligned}$$

The bracketed term is what we have called the scattering amplitude, H', in the introduction.

In the forward direction $\mathbf{k}=\mathbf{k}'$, and (4.7) simplifies considerably. We find for this case:

$$\begin{aligned}H'&=(\mathbf{e}\cdot\mathbf{e}')\frac{e^2}{m}-\frac{ie}{m}\left(2\mu-\frac{e}{2m}\right)\omega\boldsymbol{\sigma}\cdot(\mathbf{e}'\times\mathbf{e})\\&\quad+2\mu^2i(\mathbf{e}\times\mathbf{k})\cdot\mathbf{e}'(\mathbf{k}\cdot\boldsymbol{\sigma})\\&=\frac{e^2}{m}\mathbf{e}\cdot\mathbf{e}'+i\omega\boldsymbol{\sigma}\cdot(\mathbf{e}'\times\mathbf{e})\left[2\mu^2-\frac{e}{m}\left(2\mu-\frac{e}{2m}\right)\right]\\&=(e^2/m)\mathbf{e}\cdot\mathbf{e}'+i\omega\boldsymbol{\sigma}\cdot(\mathbf{e}'\times\mathbf{e})2(\mu-e/2m)^2\\&=(e^2/m)\mathbf{e}\cdot\mathbf{e}'+i\omega\lambda^2\boldsymbol{\sigma}\cdot(\mathbf{e}'\times\mathbf{e}), \quad (4.8)\end{aligned}$$

where λ is the anomalous part of the magnetic moment.

In conclusion, we may make a few general remarks. Our results depend primarily on gauge and relativistic invariance, so that they should not be difficult to generalize to cases of higher spin. They are valid for atoms, nuclei, and elementary particles. Unfortunately, experimental verification seems almost out of the question since in every case the coefficient of k (which we have calculated) is anomalously small compared to the coefficient of k^2 (Rayleigh scattering) which is known to be structure-dependent in a nontrivial way.

Scattering of Low-Energy Photons by Particles of Spin $\frac{1}{2}$*†‡

M. GELL-MANN AND M. L. GOLDBERGER§
Institute for Nuclear Studies and Department of Physics, University of Chicago, Chicago, Illinois
(Received September 3, 1954)

The first two terms in a frequency expansion of the photon scattering amplitude are considered in the case where the scatterer is a particle of spin $\frac{1}{2}$. It is shown that an exact calculation in quantum field theory gives results identical with those obtained by classical methods or else by use of the Dirac equation with an anomalous Pauli moment. The results depend only on the charge, mass, and magnetic moment of the scatterer. In the case of the proton, the second term, arising from scattering by the magnetic moment, appears to be negligible in comparison with effects due to Thomson and Rayleigh scattering.

I. INTRODUCTION

IT has long been known that the scattering of photons in the limit of zero frequency is described correctly by the classical Thomson amplitude, which depends, of course, only on the charge and mass of the scattering particle. The result is surely independent of the spin of the particle. In the case where the spin is $\frac{1}{2}$, however, explicit proofs have been given that the result of the classical calculation is reproduced in quantum mechanics: for a normal Dirac particle, in the lowest order of perturbation theory, the proof is contained in the famous calculation of Klein and Nishina;[1] it has since been shown by Thirring[2] and by Kroll and Ruderman[3] that the Thomson formula is *exactly* correct in any local, renormalizable field theory, including, for example, electromagnetic and mesonic radiative corrections.

In general, the amplitude for the scattering of photons by a particle of spin $\frac{1}{2}$ may be expanded in a power series in the frequency of the photon. The Thomson amplitude is the zeroth term in such an expansion. It is the next term, linear in frequency, that we shall consider here. We shall calculate the linear term in three different ways: (1) Classically, using Kramer's classical description[4] of a Dirac particle; besides the Dirac magnetic moment considered by Kramers, a classical anomalous moment is added. (2) In quantum mechanics, for a Dirac particle with a Pauli anomalous magnetic moment, in the lowest order of perturbation theory. (3) *Exactly* in quantum field theory, for a Dirac particle interacting with arbitrary local and renormalizable fields, for example photons and mesons.

The results of the three calculations are identical and show that the linear term depends only on the charge, mass, and static magnetic moment of the scattering particle.

II. CLASSICAL CALCULATION

Let us consider an incoming plane light wave with the electric field $\mathbf{E}_0$ given by[5]

$$\mathbf{E}_0=\mathbf{e}\exp(i\mathbf{q}\cdot\mathbf{r}-iqt). \tag{2.1}$$

The scatterer is taken to be at rest at the origin initially ($t=0$). After a long time and at great distance, a scattered wave appears with the asymptotic electric field given (to first order in the incoming field strength) by

$$\mathbf{E}_{sc}=\mathbf{G}(\mathbf{n}',\mathbf{n})\cdot\mathbf{e}r^{-1}\exp[iq(r-t)], \tag{2.2}$$

where $\mathbf{G}(\mathbf{n}',\mathbf{n})$ is a dyadic describing the scattering from the incident direction along the unit vector $\mathbf{n}\equiv\mathbf{q}/q$ to the final direction along the unit vector $\mathbf{n}'\equiv\mathbf{q}'/q'$. The scattering amplitude[6] f is now defined by the equation,

$$f=\mathbf{e}'\cdot\mathbf{G}(\mathbf{n}',\mathbf{n})\cdot\mathbf{e}, \tag{2.3}$$

in terms of a final polarization vector $\mathbf{e}'$ orthogonal to $\mathbf{n}'$.

The scattering particle, with charge e and mass M, is characterized by its position vector $\mathbf{R}(t)$ and a spin angular momentum $\mathbf{S}(t)$ that is constant in magnitude but free to rotate. The magnetic moment $\boldsymbol{\mu}(t)$ is taken to be proportional to $\mathbf{S}(t)$; the gyromagnetic ratio g will be written as the sum of the "normal" Dirac value e/M and an "anomalous" part g_A. Of course the Dirac g-factor is often thought to be anomalous from the classical point of view. However Kramers has presented a

* Some of the work presented here was reported at the Glasgow International Nuclear Physics Conference, 1954, and is summarized in the Conference Proceedings.

† Supported by grants from the U. S. Atomic Energy Commission.

‡ The authors are indebted to Dr. Francis E. Low for sending them a copy of his paper on the same subject before publication. His results and ours are in complete agreement although obtained by different methods.

§ Visiting Scientist at Brookhaven National Laboratory while part of this work was carried out.

[1] O. Klein and Y. Nishina, Z. Physik **52**, 853, 869 (1929).

[2] W. Thirring, Phil. Mag. **41**, 1193 (1950).

[3] N. Kroll and M. Ruderman, Phys. Rev. **93**, 233 (1954).

[4] H. A. Kramers, *Grundlagen der Quantentheorie* (Edwards Brothers, Ann Arbor, 1944), p. 227 ff.

[5] We have set $c=1$; we will further put $\hbar=1$, and use units in which $e^2/\hbar c=1/137$.

[6] Strictly speaking, there is a frequency dependent correction factor by which Eq. (2.3) must be multiplied in order that it be the exact scattering amplitude in the laboratory system. This factor arises classically from the Doppler shift of the radiation emitted by the particle which is set into motion by the incident wave. In quantum theory the factor is precisely q'/q where the frequency ratio is computed from the Compton law. We shall continue to employ the same quantity, f, in quantum theory, where it is equal to the correct scattering amplitude in the center-of-mass system, and also to the Feynman matrix element in either system.

classical theory[4] in which the Dirac g-factor appears naturally. In describing the interaction of the scattering particle with the electromagnetic field, we shall make use of Kramers' formulation of the problem.

Kramer's equations of motion for a classical Dirac particle may be derived from the following Lagrangian (accurate to order V/c):

$$L_K=\tfrac{1}{2}M\mathbf{V}^2+\tfrac{1}{8}\pi\int(\mathbf{E}^2-\mathbf{H}^2)d^3r+e\mathbf{V}\cdot\mathbf{A}(\mathbf{R})+\frac{e}{M}\mathbf{S}\cdot[\mathbf{H}(\mathbf{R})-\tfrac{1}{2}\mathbf{V}\times\mathbf{E}(\mathbf{R})], \quad (2.4)$$

where $\mathbf{V}=\partial\mathbf{R}/\partial t$, $\mathbf{A}$ is the transverse vector potential, and $\mathbf{E}$ and $\mathbf{H}$ are given, of course, by the equations

$$\mathbf{E}=-\partial\mathbf{A}/\partial t, \quad \mathbf{H}=\nabla\times\mathbf{A}. \quad (2.5)$$

In Eq. (2.4), the scalar potential has been ignored since it does not contribute to the scattering of light waves. The factor of $\frac{1}{2}$ in the last term is the celebrated Thomas factor.

In order to include the effects of the anomalous magnetic moment, we add to the Lagrangian of Kramers the additional quantity

$$L_A=g_A\mathbf{S}\cdot[\mathbf{H}(\mathbf{R})-\mathbf{V}\times\mathbf{E}(\mathbf{R})]. \quad (2.6)$$

The absence of the Thomas factor in the case of the anomalous moment is familiar. From the total Lagrangian L_K+L_A we obtain the following equations of motion for field and particle:

$$\nabla\times\mathbf{E}+\partial\mathbf{H}/\partial t=0, \quad (2.7)$$

$$\nabla\times\mathbf{H}-\partial\mathbf{E}/\partial t=4\pi\mathbf{J}=4\pi e\mathbf{V}\delta(\mathbf{r}-\mathbf{R})+4\pi\nabla\times[g\mathbf{S}\delta(\mathbf{r}-\mathbf{R})]+4\pi\frac{d}{dt}\left[\left(\frac{e}{2M}+g_A\right)\mathbf{V}\times\mathbf{S}\delta(\mathbf{r}-\mathbf{R})\right], \quad (2.8)$$

$$M\partial^2\mathbf{R}/\partial t^2=e\mathbf{E}(\mathbf{R})+g_A(\mathbf{S}\cdot\nabla)\mathbf{H}+\frac{e}{M}\frac{(\mathbf{S}\cdot\nabla)\mathbf{H}+\nabla(\mathbf{S}\cdot\mathbf{H})}{2}, \quad (2.9)$$

$$\partial\mathbf{S}/\partial t=g\mathbf{S}\times\mathbf{H}. \quad (2.10)$$

In Eqs. (2.7) and (2.8) we have simply two of Maxwell's equations. The current in Eq. (2.8) comprises three terms: the ordinary translational current; the curl of the density of magnetization; and a displacement current which arises from the fact that a moving magnetized medium acquires an effective electric polarization. Only the last term is affected by the Thomas factor. In Eq. (2.9), the forces acting on the particle are exhibited. We have omitted the self-force and also other terms, such as the Lorentz force, which depend on the field-induced velocity and angular acceleration of the particle and are therefore effectively quadratic in the field strengths. We have left only the electric force and the interaction of the magnetic moment with the gradient of the magnetic field. The Dirac moment, affected by the Thomas factor, behaves as if half of it were due to a genuine magnetic dipole and half to a current loop; the anomalous moment behaves entirely as a point dipole. Equation (2.10) is merely the usual formula for the torque on a magnetic dipole; again terms effectively quadratic in the field strengths have been dropped.

The asymptotic electric field may now be computed from the relation

$$\mathbf{E}\to\mathbf{E}_0(\mathbf{r},t)+\mathbf{E}_{sc}(\mathbf{r},t)=\mathbf{E}_0-r^{-1}\int d^3r'\int_{-\infty}^{\infty}dt'(\partial/\partial t)\mathbf{J}_\perp(\mathbf{r}',t')\times\delta(t'-t+r-r^{-1}\mathbf{r}\cdot\mathbf{r}'), \quad (2.11)$$

in which $\mathbf{J}_\perp$ is the part of the current that is perpendicular to $\mathbf{r}$, i.e., to the direction of observation. In substituting into Eq. (2.11) the formula (2.8) for the current, we may simplify the result by omitting higher order terms in the field strengths. (It must be borne in mind that $\mathbf{R}$, $\partial\mathbf{R}/\partial t$, $\partial^2\mathbf{R}/\partial t^2$, $\partial\mathbf{S}/\partial t$, and $\partial^2\mathbf{S}/\partial t^2$ would all be zero in the absence of the incident field.) We find

$$\mathbf{E}_{sc}(\mathbf{r},t)=-r^{-1}\mathbf{Z}_\perp(t-r), \quad (2.12)$$

where

$$\mathbf{Z}=e\frac{\partial^2\mathbf{R}}{\partial t^2}-gr^{-1}\left(\mathbf{r}\times\frac{\partial^2\mathbf{S}}{\partial t^2}\right)-gr^{-2}\left(\mathbf{r}\cdot\frac{\partial^3\mathbf{R}}{\partial t^3}\right)(\mathbf{r}\times\mathbf{S})-\left(\frac{e}{2M}+g_A\right)\left(\mathbf{S}\times\frac{\partial^3\mathbf{R}}{\partial t^3}\right). \quad (2.13)$$

Finally, we must substitute into Eq. (2.13) the equations of motion of Eqs. (2.9) and (2.10), simplifying as before. We obtain, up to terms linear in the frequency, the expression

$$\mathbf{Z}=\left\{\frac{e^2}{M}\mathbf{e}+ig^2q\mathbf{n}'\times[\mathbf{S}\times(\mathbf{n}\times\mathbf{e})]+\frac{ieg}{M}q[(\mathbf{n}\cdot\mathbf{S})(\mathbf{n}\times\mathbf{e})+(\mathbf{n}'\cdot\mathbf{e})(\mathbf{n}'\times\mathbf{S})]+\frac{ie}{M}\left(\frac{e}{2M}+g_A\right)q(\mathbf{S}\times\mathbf{e})\right\}\exp[iq(r-t)], \quad (2.14)$$

so that the scattering amplitude defined by Eq. (2.3) is given by the equation

$$f=-\frac{e^2}{M}(\mathbf{e}'\cdot\mathbf{e})-ig^2q\mathbf{S}\cdot[(\mathbf{n}'\times\mathbf{e}')\times(\mathbf{n}\times\mathbf{e})]-\frac{ieg}{M}q\left[\mathbf{S}\cdot\left\{\frac{\mathbf{n}(\mathbf{n}\times\mathbf{e})+(\mathbf{n}\times\mathbf{e})\mathbf{n}}{2}\right\}\cdot\mathbf{e}'-\mathbf{S}\cdot\left\{\frac{\mathbf{n}'(\mathbf{n}'\times\mathbf{e}')+(\mathbf{n}'\times\mathbf{e}')\mathbf{n}'}{2}\right\}\cdot\mathbf{e}'\right]+\frac{ieg_A}{M}q\mathbf{S}\cdot(\mathbf{e}'\times\mathbf{e}). \quad (2.15)$$

Here **S** is the initial value of the spin angular momentum.

It is not difficult to trace through Eqs. (2.13)–(2.15) the meaning of the various terms in the scattering amplitude. The first term is, of course, the Thomson amplitude. The second represents magnetic dipole scattering; the magnetic moment absorbs $M1$ radiation, precesses, and re-emits $M1$ radiation. The first half of the third term represents the absorption of $M2$ radiation (through the interaction of the magnetic moment of the particle with the gradient of the magnetic field of the incident wave) followed by the emission of $E1$ radiation because of the resulting acceleration. The second half of the third term describes the reverse process; the particle absorbs $E1$ radiation and is accelerated, emitting $M2$ radiation by virtue of the magnetic moment coupling. Now the translational force on the particle due to the *anomalous* part of the magnetic moment is not of pure $M2$ origin, as can be seen from Eq. (2.9); there is an $E1$ part as well. Hence the fourth term in the scattering amplitude, representing $E1$ scattering.

III. QUANTUM-MECHANICAL CALCULATIONS

The scattering of photons by a Dirac particle with a Pauli anomalous magnetic moment, without radiative corrections, has been discussed by Powell.[7] The wave function of the scatterer obeys the equation

$$\{\gamma_\mu(\partial/\partial x_\mu - ieA_\mu)+M-\tfrac{1}{2}\mu_A\sigma_{\mu\nu}F_{\mu\nu}\}\psi=0. \quad (3.1)$$

The quantum-mechanical scattering amplitude is most easily calculated as the sum of the two Feynman matrix elements corresponding to absorption followed by emission and vice versa. The result is, up to terms linear in the frequency,

$$f=-\frac{e^2}{M}(\mathbf{e}'\cdot\mathbf{e})-2i\mu^2 q\boldsymbol{\sigma}\cdot[(\mathbf{n}'\times\mathbf{e}')\times(\mathbf{n}\times\mathbf{e})]$$
$$-\frac{ie\mu}{M}q\left[\boldsymbol{\sigma}\cdot\left\{\frac{\mathbf{n}(\mathbf{n}\times\mathbf{e})+(\mathbf{n}\times\mathbf{e})\mathbf{n}}{2}\right\}\cdot\mathbf{e}'\right.$$
$$\left.-\boldsymbol{\sigma}\cdot\left\{\frac{\mathbf{n}'(\mathbf{n}'\times\mathbf{e}')+(\mathbf{n}'\times\mathbf{e}')\mathbf{n}'}{2}\right\}\cdot\mathbf{e}\right]$$
$$+\frac{ie\mu_A}{M}q\boldsymbol{\sigma}\cdot(\mathbf{e}'\times\mathbf{e}). \quad (3.2)$$

The correspondence with the classical formula (2.15) is perfect; we must of course identify **S** with $\boldsymbol{\sigma}/2$, g with 2μ, and g_A with $2\mu_A$.

We must now demonstrate that Eq. (3.2) is rigorously correct in quantum field theory (except, of course, for higher terms in the frequency). We abandon the phenomenological Pauli moment; instead we suppose that the scatterer is a normal Dirac particle, coupled to fields describing photons, mesons, etc. The anomalous moment is attributed to the effects of these couplings. In what follows, the interaction with photons must have conventional local, gauge-invariant character and all interactions must be renormalizable; otherwise we need not specify the nature of the fields and interactions in detail. We shall employ the language of Feynman diagrams, but it should be emphasized that no use is made of perturbation theory.

Let us refer to the scatterer as a nucleon, for definiteness. We may picture the entire sequence of Feynman diagrams in the following way: The nucleon line proceeds from the beginning to the end of the diagram, emitting and absorbing, in between, various virtual quanta that belong to its self-field. The initial and final real photon lines terminate on charge-bearing lines, which may correspond to the nucleon itself or to virtual mesons or members of pairs, etc. We may divide all the diagrams into two classes, A and B.[8] In Class A we include all the diagrams in which those parts that include the terminations of the two real photon lines are separated by a strength of bare nucleon line, i.e., nucleon line free of virtual quanta. Class B comprises all other diagrams, those in which there is no stretch of bare nucleon line between the absorption and the emission of the real photons.

For the sum of all diagrams of Class A, we can write a simple closed expression. Let q and q' be the initial and final four-momenta of the photon,[9] and $p=(0,0,0,iM)$ be the initial four-momentum of the nucleon. The indices μ and ν will denote the initial and final direction of polarization. Then the contribution of diagrams of class A to the scattering amplitude is

$$T_{\nu\mu}{}^{(A)}(q',q)=t_{\nu\mu}(q',q)+t_{\mu\nu}(-q,-q'), \quad (3.3)$$

where

$$t_{\nu\mu}(q',q)=-e^2\bar{\psi}_f(p+q-q')\Gamma_\nu(p+q-q',p+q)$$
$$\times S(p+q)\Gamma_\mu(p+q,p)\psi_i(p). \quad (3.4)$$

Here $\psi_i(p)$ is the initial Dirac spinor; $\Gamma_\mu(p+q,p)$ is the exact renormalized vertex operator corresponding to the absorption of the initial photon; $S(p+q)$ is the exact renormalized propagation function for the virtual state of the nucleon with momentum $p+q$; $\Gamma_\nu(p+q-q',p+q)$ is the vertex operator for the emission of the final photon; and $\bar{\psi}_f(p+q-q')$ is the final Dirac spinor. The second term in Eq. (3.3) describes the "crossed diagrams" in which emission of the final photon precedes absorption of the initial one.

It is evident from Eq. (3.3) that the partial scattering amplitude $T^{(A)}$ obeys a symmetry relation; this relation actually holds for the total scattering amplitude T and

[7] J. L. Powell, Phys. Rev. **75**, 32 (1949).

[8] For a discussion of a similar calculation, see Appendix of paper by Deser, Thirring, and Goldberger, Phys. Rev. **94**, 711 (1954).

[9] In the remainder of this section, q stands for the four-vector momentum of the incident photon. The photon frequency, which is denoted elsewhere by q, is here called q_0.

is given by the equation

$$T_{\nu\mu}(q',q)=T_{\mu\nu}(-q,-q'). \tag{3.5}$$

This symmetry condition depends only on the fact that for every "crossed" diagram there is a corresponding "uncrossed" one and vice versa.

To proceed further with the evaluation of $T^{(A)}$ up to terms linear in frequency, we must exhibit expansions of Γ, S, and ψ_f in powers of q and q'. We write the propagation function in the form

$$S(p+q)=\{i\gamma\cdot(p+q)G[(p+q)^2]+MF[(p+q)^2]\}^{-1}, \tag{3.6}$$

and, expanding, we find[10]

$$\begin{aligned}S(p+q)\simeq\frac{1}{2p\cdot qF}\Big[&(-i\gamma\cdot p+M)F-i\gamma\cdot qF\\&+2p\cdot q(-i\gamma\cdot pG'+MF')-i\gamma\cdot q(2p\cdot q)G'\\&+2(p\cdot q)^2(-i\gamma\cdot pG''+MF'')\\&-2p\cdot q\left\{2G'+M^2\left(F''-G''+\frac{F'^2-G'^2}{F}\right)\right\}\\&\times\{2p\cdot q(-i\gamma\cdot pG'+MF')-Fi\gamma\cdot q\}\Big].\end{aligned} \tag{3.7}$$

The functions F, F', etc. are evaluated at $p^2=-M^2$. It should be noted that not all terms linear in q have been retained, but only those that contribute to (3.4) in the required order. The form of the vertex operator, like that of the propagation function, can be specified on general grounds of invariance; one finds, to first order in the frequency,

$$\begin{aligned}&\Gamma_\mu(p+q,q)\\&=\Gamma_\mu(p,p)+\frac{1}{2}q_\lambda\frac{\partial}{\partial p_\lambda}\Gamma_\mu(p,p)+\frac{p\cdot q}{M^2}\sigma_{\mu\lambda}p_\lambda F_1(p^2)\\&\quad+\frac{1}{2M}\sigma_{\mu\lambda}q_\lambda F_2(p^2)+\frac{q_\lambda\sigma_{\lambda\rho}p_\rho p_\mu}{M^2}F_3(p^2);\end{aligned} \tag{3.8}$$

$$\begin{aligned}&\Gamma_\nu(p+q-q',p+q)\\&=\Gamma_\nu(p,p)+\frac{1}{2}(2q_\lambda-q_\lambda')\frac{\partial}{\partial p_\lambda}\Gamma_\nu(p,p)\\&\quad-\frac{p\cdot q'}{M^2}\sigma_{\nu\lambda}p_\lambda F_1(p^2)-\frac{1}{2M}\sigma_{\nu\lambda}q_\lambda' F_2(p^2)\\&\quad-\frac{q_\lambda'\sigma_{\lambda\rho}p_\rho p_\nu}{M^2}F_3(p^2).\end{aligned} \tag{3.9}$$

Among the symmetry principles useful in deriving (3.8) and (3.9) are those related to charge conjugation and space-time inversion:

$$\begin{aligned}C^{-1}\Gamma_\mu(p_1,p_2)C&=-\Gamma_\mu{}^T(-p_2,-p_1),\\\gamma_5\Gamma_\mu(p_1,p_2)\gamma_5&=-\Gamma_\mu(-p_1,-p_2),\end{aligned} \tag{3.10}$$

where C is the charge-conjugation matrix. The vertex operator for equal arguments is connected with the propagation function through Ward's identity:

$$\begin{aligned}\Gamma_\mu(p,p)=\frac{1}{i}\frac{\partial}{\partial p_\mu}S^{-1}(p)&=\gamma_\mu G(p^2)\\&\quad-2ip_\mu\{i\gamma\cdot pG'(p^2)+MF'(p^2)\}.\end{aligned} \tag{3.11}$$

Furthermore, we may make use of the fact that for small values of $i\gamma\cdot p+M$, the reciprocal of the propagation function has the form

$$S^{-1}(p)=i\gamma\cdot p+M+\sigma(i\gamma\cdot p+M)^2;$$

we then obtain the identities

$$\begin{aligned}F&=G,\\F+2M^2(F'-G')&=1,\end{aligned} \tag{3.12}$$

where the quantities are evaluated at $p^2=-M^2$. Finally we must expand the spinors $\psi_i(p)$ and $\bar\psi_f(p+q-q')$ in powers of the frequency:[11]

$$\begin{aligned}\psi_i(p)&=\begin{pmatrix}u\\0\end{pmatrix},\\\bar\psi_f(p+q-\zeta')&=(v,-\boldsymbol{\sigma}\cdot(\mathbf{q}-\mathbf{q}')v/2M).\end{aligned} \tag{3.13}$$

The evaluation of $T^{(A)}$ is completely straightforward in terms of the quantities introduced above; we shall simply give the result. To facilitate comparison with previous formulae, we write $e_\nu'T_{\nu\mu}{}^{(A)}e_\mu=v^*f^{(A)}u$, with

$$\begin{aligned}f^{(A)}=&-\frac{e^2}{M}\mathbf{e}'\cdot\mathbf{e}F-2i\frac{e^2}{4M^2}(F-F_2)^2q_0\boldsymbol{\sigma}\cdot(\mathbf{n}'\times\mathbf{e}')\times(\mathbf{n}\times\mathbf{e})\\&-\frac{ie}{M}\frac{e}{2M}(F-F_2)q_0[\boldsymbol{\sigma}\cdot\{\mathbf{nn}\times\mathbf{e}+\mathbf{n}\times\mathbf{en}\}\cdot\mathbf{e}'\\&-\boldsymbol{\sigma}\cdot\{\mathbf{n}'\mathbf{n}'\times\mathbf{e}'+\mathbf{n}'\times\mathbf{e}'\mathbf{n}'\}\cdot\mathbf{e}]\\&+\frac{ie}{M}\frac{e}{2M}(F-F_2-1+4F_1)q_0\boldsymbol{\sigma}\cdot\mathbf{e}'\times\mathbf{e}.\end{aligned} \tag{3.14}$$

We must still evaluate the sum of the contributions from all diagrams of class B. It may be expressed concisely as follows, to first order in the frequency:

$$\begin{aligned}T_{\nu\mu}{}^{(B)}(q',q)=&-ie^2\bar\psi_f(p+q-q')\\&\times\left\{\frac{\partial}{\partial p_\nu}\Gamma_\mu(p,p)+\frac{\partial}{\partial p_\nu}q_\lambda\frac{\partial}{\partial p_\lambda'}\Gamma_\mu(p',p)\right.\\&\left.-\frac{\partial}{\partial p_\mu}q_\lambda'\frac{\partial}{\partial p_\lambda'}\Gamma_\nu(p',p)\right\}_{p'=p}\psi_i(p).\end{aligned} \tag{3.15}$$

[10] Primes attached to F and G indicate differentiation with respect to p^2.

[11] u and v are two-component Pauli spinors describing the initial and final states.

Using the expansions and relations given above, we obtain from (3.15) the simple result

$$f^{(B)}=-\frac{e^2}{M}\mathbf{e}'\cdot\mathbf{e}(1-F)-\frac{ie}{M}\frac{eq_0}{2M}4F_1\boldsymbol{\sigma}\cdot(\mathbf{e}'\times\mathbf{e}). \quad (3.16)$$

Adding $f^{(B)}$ to $f^{(A)}$ as given in (3.14), we see that we have exactly the formula (3.2) for the total scattering amplitude, provided we can set

$$\mu_A=(e/2M)(F-F_2-1). \quad (3.17)$$

In order to prove Eq. (3.17), we consider the scattering of a nucleon by an external electromagnetic potential that transfers four-momentum q to the nucleon. The transition matrix element R is

$$R=-\bar{\psi}(p+q)ie\Gamma_\mu(p+q,\,p)A_\mu(q)\psi(p). \quad (3.18)$$

If we choose A to correspond to a uniform magnetic field and p to a nucleon at rest, we may compute the term in R proportional to q, using (3.8) and (3.13):

$$R\simeq-\bar{\psi}(p)(e/2M)(F-F_2)\tfrac{1}{2}\sigma_{\mu\nu}F_{\mu\nu}\psi(0). \quad (3.19)$$

We may also compute R on the basis of Eq. (3.1) for a Dirac particle with a Pauli moment:

$$R\simeq-\bar{\psi}(p)(e/2M+\mu_A)\tfrac{1}{2}\sigma_{\mu\nu}F_{\mu\nu}\psi(p). \quad (3.20)$$

We conclude that Eq. (3.17) is correct.

IV. DISCUSSION

We have derived an expression for the scattering amplitude up to terms linear in the photon frequency, and the expression is valid for any known theory. It is in order to discuss what predictions, if any, can be made of quantities that are likely to be measured experimentally. Let us first see what information we have about cross sections on the basis of our formula for the scattering amplitude.

For a neutral particle, we simply put $e=0$ and $\mu=\mu_A$ in Eq. (3.2). If we square the amplitude and sum and average over spins and polarizations, we obtain the leading term in an expansion of the cross section in powers of the frequency:

$$d\sigma/d\Omega\simeq 4q^2\mu^4(1+\tfrac{1}{2}\sin^2\vartheta). \quad (3.21)$$

For a charged particle, the leading term is of course the Thomson cross section. The next term, quadratic in frequency, is composed of two contributions, only one of which we can calculate by squaring the linear term in the scattering amplitude (3.2). The other contribution is made by the interference of the Thomson amplitude and the quadratic term in the scattering amplitude, which should come largely from Rayleigh scattering and which we have not hitherto discussed. If we denote the second contribution by $q^2I(\vartheta)$, then we have

$$\frac{d\sigma}{d\Omega}=\frac{e^4}{M^2}\frac{(1+\cos^2\vartheta)}{2}+q^2\Big[I(\vartheta)+\Big\{6\mu^4+\frac{e^2\mu^2}{M^2}-\frac{e^3}{M^3}\mu+\frac{3}{8}\frac{e^4}{M^4}\Big\}+\cos\vartheta\Big\{-\frac{8e\mu^3}{M}+\frac{2e^2\mu^2}{M^2}\Big\}+\cos^2\vartheta\Big\{-2\mu^4+\frac{3e^2\mu^2}{M^2}-\frac{e^3\mu}{M^3}-\frac{e^4}{8M^4}\Big\}\Big]+\cdots. \quad (3.22)$$

In general there is no way to compute $I(\vartheta)$ without a detailed study of the mechanism of Rayleigh scattering for the particular case in question; in the forward direction, however, there is a useful general formula[12] for I:

$$I(0)=-\frac{e^2}{M\pi^2}\int_0^\infty\frac{\sigma_T(q')}{q'^2}, \quad (3.23)$$

where $\sigma_T(q')$ is the total cross section in the laboratory system for light of frequency q' incident on the scatterer. Equation (3.23) may be deduced from the Thomson formula and the principle that a light signal cannot be transmitted with velocity greater than c. Using Eqs. (3.22) and (3.23), we have for the forward direction:

$$\left(\frac{d\sigma}{d\Omega}\right)_{0^\circ}=\frac{e^4}{M^2}+q^2\Big\{-\frac{e^2}{M\pi^2}\int_0^\infty\frac{\sigma_T(q')}{q'^2}dq'+4\mu_A{}^4\Big\}+\cdots. \quad (3.24)$$

Perhaps the most interesting application of these formulas is to the proton. If we take Eqs. (3.23) and (3.24) literally, we must in that case include in σ_T the cross section for electron pair production in the Coulomb field of the proton as well as the cross section for such processes as photomeson production. However, at energies above a few Mev, but still small compared to the meson rest energy, the Delbrück scattering arising from real and virtual pair production has an angular distribution sharply peaked in the forward direction; on the other hand the Thomson and Rayleigh scattering and the scattering from the magnetic moment should have rather slowly varying angular distributions at these energies. We may therefore omit the Delbrück scattering, but leave Eq. (3.24) otherwise unchanged, if we evaluate $d\sigma/d\Omega$ at an angle near 0° but far enough away so that the Delbrück scattering is small. In that case the principal contribution to σ_T is the cross section σ_P for the photopion effect. Empirical data on this process indicate the relation[12]

$$\frac{1}{2\pi^2}\int_{m_\pi}^\infty\frac{\sigma_P(q')}{q'^2}dq'\simeq\frac{e^2}{3m_\pi{}^2M}. \quad (3.25)$$

[12] Gell-Mann, Goldberger, and Thirring, Phys. Rev. 95, 1612 (1954).

Thus we find

$$\left(\frac{d\sigma}{d\Omega}\right)_{\text{near }0^\circ} \simeq \frac{e^4}{M^2}+\frac{2q^2e^4}{3M^2}\frac{1}{m_\pi{}^2}\left\{-1+\frac{3m_\pi{}^2\beta_A{}^4}{8M^2}\right\}+\cdots, \tag{3.26}$$

where β_A is the anaomalous magnetic moment in nuclear Bohr magnetons. Since $3m_\pi{}^2\beta_A{}^4/8M^2\simeq 0.08$, we see that near the forward direction the scattering by the magnetic moment is greatly overcompensated by the interference of Thomson and Rayleigh scattering. We cannot say with certainty, of course, that this situation persists at most angles, but it seems likely.

So far we have treated the scatterer as a "particle," but it seems reasonable that Eq. (3.2) should be valid for any system of spin $\frac{1}{2}$, whether elementary or complex, and that the expansion in frequency should be possible when the photon energy is small compared to the energy of the first excited state of the system. Thus complex nuclei of spin $\frac{1}{2}$ may be treated, as well as the proton.

The generalization of the result to other spins is an interesting problem. For spin zero, the term in the scattering amplitude linear in frequency must *vanish* in order that the symmetry condition (3.5) be satisfied. For spins higher than $\frac{1}{2}$, we conjecture that it is still possible to express the linear term in terms of static properties of the system.

We acknowledge with thanks conversations with Professors G. Wentzel and V. L. Telegdi concerning classical methods of calculation.

PHYSICAL REVIEW VOLUME 96, NUMBER 5 DECEMBER 1, 1954

Calculation of Potentials from the New Tamm-Dancoff Equation

J. C. TAYLOR
Peterhouse, Cambridge, England
(Received July 26, 1954)

This note is about the construction of energy-independent potentials from the Tamm-Dancoff equations, by a systematic method of Klein's. It is shown that, when the method is applied to the new Tamm-Dancoff equation of Dyson, the difficulty of the spurious singularities can be overcome. It is proved further that the old and new Tamm-Dancoff methods give the same potential in the adiabatic limit.

INTRODUCTION

IN this note, we are concerned with the use of the Tamm-Dancoff methods[1] to derive, for the two-nucleon system, a single integral equation like that used, for instance, by Lévy.[2] The old Tamm-Dancoff method (O.T.D.), which has been used in the past, suffers from infinite vacuum-to-vacuum terms. These do not occur in the new Tamm-Dancoff method (N.T.D.) of Dyson.[3] N.T.D. has also the advantage of being generally closer than O.T.D. to the covariant, renormalizable theories.

The kernel of the N.T.D. integral equation contains "spurious" poles,[4] which are not at the threshold for any real physical process. We thus have the problem of imposing boundary conditions on the amplitude which satisfies the integral equation, so that it should have no singularities arising from the spurious poles. This problem, which amounts to the definition of the vacuum state in the Dyson amplitudes, has not yet been solved.

The purpose of this note is to examine what form the problem of the spurious singularities takes when the kernel of the N.T.D. integral equation is considered as a generalized potential. The kernel is dependent upon the total energy, and so does not give a straightforward eigenvalue equation for bound states. We adopt a systematic method of eliminating the energy dependence, which has been proposed by Klein.[5] Klein's actual suggestion was for the adiabatic limit; but in Sec. 1 we give a natural generalization of his method, which, while it would probably be useful only near the adiabatic limit, enables one to obtain some general properties of the energy-independent potential.

In Sec. 1, we also give a method of generating energy-independent potentials, using the four-dimensional formalism of N.T.D. of Mathews and Salam.[6] This method, which agrees with Klein's except for a few special terms, is the basis of our general results.

In Sec. 2, we show that, for the energy-independent potential, the problem of the spurious singularities reduces to the simpler question of how to define the poles in a certain integral. It is no longer a boundary condition problem. The essential step in this demonstration is a generalization of a result already given by Klein[7] for the fourth order. This states that, if the total energy is replaced by the kinetic energy, the kernel is free of spurious poles on a suitable rearrangement of terms.

[1] S. M. Dancoff, Phys. Rev. **78**, 382 (1950).
[2] M. M. Lévy, Phys. Rev. **88**, 72 (1952).
[3] F. J. Dyson, Phys. Rev. **90**, 994 (1953).
[4] F. J. Dyson, Phys. Rev. **91**, 1543 (1953).
[5] A. Klein, Phys. Rev. **94**, 195 (1954).
[6] Quoted by the present author in reference 9.
[7] A. Klein, Phys. Rev. **95**, 1653 (1954).

In Sec. 3, we prove that, in the adiabatic limit, O.T.D. and N.T.D. are identical. This result has been found by Kurşunoğlu[8] for the fourth order.

1. THE POTENTIAL

In three-dimensional momentum-space, the two-nucleon integral equation derived from O.T.D. or N.T.D. has the general form

$$\{W-H(p)-H(q)\}\chi(p,q) = \sum_n \int V_n(W;\, p,q,k)\chi(p+k,\, q-k)dk, \quad (1)$$

where W is the total energy, $H(p)=\alpha\cdot p+\beta M$, M is the nucleon mass, and V_n is of the nth order in the coupling constant. In O.T.D., or in N.T.D., if the negative energy components have been eliminated, $H(p)$ should be replaced by $E(p)=(p^2+M^2)^{\frac{1}{2}}$, etc. But we can leave this open by supposing χ to contain positive-energy projection operators if necessary.

We write (1) shortly as

$$(W-T)\chi=\sum V_n(W)\chi. \quad (2)$$

Then our generalization of Klein's[5] equation with the energy-independent potential U is given by the successive approximations:

$$\begin{aligned}(W-T)\chi&=V_1(T)\chi=U_1\chi,\\ (W-T)\chi&=\{V_1(T)+V_2(T)+V_1'(T)(W-T)\}\chi \quad (3)\\ &\simeq\{V_1(T)+V_2(T)+V_1'(T)V_1(T)\}\chi\\ &=(U_1+U_2)\chi, \quad \text{etc.}\end{aligned}$$

In the right hand side of Eq. (3), the operator T takes the value $T(k)=H(p+k)+H(p-k)$. (In the adiabatic limit actually considered by Klein, $T=2M$ everywhere.)

V contains poles for values of the energy and momenta at the thresholds for the creation of new particles. Klein's method is only applicable for values of W well away from these poles, i.e., for bound states and low energy scattering. In N.T.D., spurious poles occur in V for all values of W.

We now translate the above procedure for generating U into the four-dimensional form of N.T.D. of Matthews and Salam.[9] The starting point is Eq. **A**(7). When the approximation which gives an integral equation is made, **A**(7) becomes, with the use of **A**(15),

$$\exp(-iWt)\chi(p,q)=(i)^n\int_{-\infty}^{t} dt_1\cdots\int_{-\infty}^{t_{n-1}} dt_n\int dk \times F(t;\, t_1,\cdots t_n;\, p,q,k) \times\exp\{-it_n[W-T(k)]\}\chi(p+k,\, q-k). \quad (4)$$

In Eq. (4) we have transformed to momentum-space in the spatial components, but preserved the form of the time integrations. F, which is independent of W, is an integral over the internal momenta of a sum of exponentials, each of which, when $t_1=t_2=\cdots=t_n$, is proportional to

$$\exp[-it_1\{T(k)-T(0)\}-itT(0)]. \quad (5)$$

Integrating by parts in (4) successively over the t_n, t_{n-1}, $\cdots t_2$-integrations,[10] we get

$$\begin{aligned}&\exp(-iWt)\chi(p,q)\\ &=(i)^n\int_{-\infty}^{t} dt_1\exp[-it_1\{W-T(k)\}]\\ &\quad\times\int_{-\infty}^{t_1} dt_2\cdots\int_{-\infty}^{t_{n-1}} dt_n\int dk\\ &\quad\times F(t;\, t_1,\cdots t_n;\, p,q,k)\chi(p+k,\, q-k)-R, \quad (6)\end{aligned}$$

where the remainder term R has $(n+1)$ time integrations, and contains the factor $\{W-T(k)\}\chi(p+k,\, q+k)$. It follows from (5) that, when the time integrations are done in (6), the resulting equation has the form

$$(W-T)\chi=V_n(T)\chi+V_n{}^{\dagger}(W)(W-T)\chi, \quad (7)$$

where $V_n{}^{\dagger}$ comes from R. Repeating the integration by parts in R, $R_n{}^{\dagger}(W)$ gives $V_n'(T)$ together with higher order terms. Thus the general equivalence of the two methods is clear on comparing (7) with (3).

However, there are certain exceptional terms for which the four-dimensional formalism gives different results from Klein's procedure. These are terms arising from the elimination of an amplitude which contains the destruction operators for the initial nucleons in their initial state, and also both the creation and destruction operators for the same particle with the same momentum. A typical energy denominator corresponding to such an intermediate state is

$$\{W-T(k)-E(p+k+k')+E(p+k+k')\}^{-1}. \quad (8)$$

For the one-nucleon equation, an example of such a term is Eq. (14) of reference 7.

We cannot immediately put $W=T$ in expression (8), but terms of this type always appear in pairs whose sum is nonsingular at $W=T$. Graphically, the relation of such a pair is shown by Figs. 1(c) and (d) of reference 7. In Klein's procedure, then, these pairs must be combined before we put $W=T$.

In the four-dimensional formalism, such terms show themselves up after the integration by parts as the time integral of a constant. This would be infinite if it were not for the factor

$$\exp\{\epsilon(t_1+t_2+\cdots t_n)\},$$

[8] B. Kurşunoğlu, Phys. Rev. (to be published).

[9] J. C. Taylor, Phys. Rev. **95**, 1313 (1954). Hereafter referred to as **A**.

[10] This device is due to M. Cini and S. Fubini, Nuovo cimento **10**, 1695 (1953).

which must always be inserted in (4) to insure convergence (ϵ is a small positive number). Again, such terms appear in pairs which, after combination and integration, are finite as $\epsilon \to 0$.

For these terms, Klein's procedure gives just twice the result of the four-dimensional formalism. This discrepancy arises because the limits $\epsilon \to 0$ and $W \to T$ are taken in different orders in the two cases. We shall adopt the four-dimensional method, because it enables us to deduce general results. However, the whole matter is somewhat academic, because the terms concerned are all infinite nucleon self-energy terms with which it is not known how to deal at present.

Finally we remark that in the Matthews-Salam form of the Tamm-Dancoff equations all the terms in the kernel are of the same order in the coupling constant; so that some are reducible and may be regarded as iterations of a lower-order kernel. In the usual, and more useful, form of the equation these do appear as lower-order kernels. It is always possible formally to pass from one equation to the other by iteration or the reverse process.

2. SPURIOUS POLES

We begin this section by proving that $V(T)$ is free from spurious poles. From the relation established in the last section between (3) and (6), we have, using (5),

$$V_n(T)=\{T(k)-T(0)\}\exp\{itT(k)\}(i)^n \times\int_{-\infty}^{t} dt_1\cdots\int_{-\infty}^{t_{n-1}} dt_n F(t;t_1\cdots t_n;p,q,k). \quad (9)$$

The integral on the right hand side of (9) is the same as the integral in (4), except that the exponential in the latter is replaced by unity. From the derivation of (4) from **A**(7), one sees that the dependence of the intergal in **A**(7) upon the state vectors $|t_n\rangle$ and ${}_0\langle t_n|$ of **A** has dropped out in (9). It follows that $V_n(T)$ is proportional to the momentum-space form of the right hand side of **A**(21).

Now consider Eq. **A**(22). The four-dimensional momentum-space form of this contains only Feynman functions S_F and Δ_F. The integrations over the fourth-components of the internal energy-momenta may be performed, so as to obtain a three-dimensional form. Because of the definition of the Feynman functions, the only combinations of internal energies that can result are sums, for differences would have ambiguous poles. Thus, in the three-dimensional momentum-space form of **A**(22) there are no spurious poles.

A(21) is obtained from **A**(22) by a Dyson[11] Heisenberg-operator analytical continuation process. This changes only the way the integration is done round the poles and leaves their position unchanged. Therefore, **A**(21), and so also $V(T)$, are free of spurious poles.

This is the result obtained by Klein[7] in the fourth order. He finds additional terms which happen also, in this case, to be without spurious poles. As explained in Sec. 1, the extra terms are due to a slightly different way of defining $V(T)$.

Thus the spurious poles are connected with the W dependence of V. We will now show that Klein's method for expressing the W dependence allows us to apply the boundary conditions immediately, and obtain a potential free from spurious singularities.

To see this, note that all terms in the potential, U, defined by Eqs. (3), are of the form

$$U(p,q;k)=\int dk' V(p,q;k')V(p,q;k,k'), \quad (10)$$

where V is free of spurious poles. Thus the k' integration may be done, giving a potential U free of spurious poles. It is still necessary to define the path of the integration round the spurious poles in Y. Following Dyson,[4] we suggest that the vacuum state is correctly defined in this case if the spurious poles are taken as principal values.

3. ADIABATIC LIMIT

The results of the previous sections hold, in particular, for the adiabatic limit. We now prove more strongly that N.T.D. yields the same potential, $V(W)$, as O.T.D., in the adiabatic limit; so that $V(W)$ itself is free from spurious poles.

Suppose that we know that the wave function is small except for values of the momenta of the order of magnitude of μ, the meson mass. Then, by the adiabatic limit, we mean here that we work to the zeroth order in μ/M.

V, defined by Eq. (2), contains energy denominators of two kinds, typified by

$$\{W-E(p)-E(q-k)-\omega(k)\}^{-1} \quad (11)$$

and

$$\{W-E(p)-E(q)-E(q-k)-E(q-k-k')-\omega(k')\}^{-1}, \quad (12)$$

where $\omega(k)=(k^2+\mu^2)^{\frac{1}{2}}$. In the adiabatic limit, these become, respectively,

$$\{\mathcal{E}-\omega(k)\}^{-1} \quad (13)$$

and

$$(-2M)^{-1}, \quad (14)$$

where $\mathcal{E}=W-2M$ is the binding energy. Whereas the $\mathcal{E}$ dependence of (13) must be retained, the neglect of $\mathcal{E}$ in (14) means the neglect of a term of relative order μ/M, and is consistent with the adiabatic approximation.

Our proof is based upon the relation between the Tamm-Dancoff equations and a three-dimensional approximation (L.K.), given by Lévy[2] and Klein,[12] to the

[11] F. J. Dyson, Phys. Rev. **92**, 428 (1951).

[12] A. Klein, Phys. Rev. **90**, 1101 (1953).

Bethe-Salpeter equation. This relation has been investigated in **A**. There, use was made of the four-dimensional formalism, which, as explained in Sec. 1, gives in a few cases results different from the three-dimensional formalism. This discrepancy is unimportant here, since the relevant terms are all neglected in the adiabatic limit.

Consider first O.T.D. It differs from L.K. by changes in the energy denominators described by a rule of Klein's.[12] According to this rule, denominators of the type of (11) are unchanged, whereas (12) becomes

$$\{-E(q-k)-E(q-k-k')-\omega(k')\}^{-1}. \tag{15}$$

(15) has the same adiabatic limit, (14), as (12); and it is true generally that O.T.D. and L.K. agree in the adiabatic limit.

For N.T.D. there is a corresponding L.K. equation, given in **A**, to be called N.L.K. An argument similar to the above shows that N.T.D. and N.L.K. agree in the adiabatic limit. Thus the problem is now reduced to the relation between L.K. and N.L.K.

According to Klein,[12] the L.K. kernel is given by

$$\int dp_0[\{\tfrac{1}{2}W+p_0-E(p+k)+i\epsilon\}^{-1} +\{\tfrac{1}{2}W-p_0-E(q-k)+i\epsilon\}^{-1}]K(p,q,k;\,p_0), \tag{16}$$

where K is the corresponding kernel of the Bethe-Salpeter equation, and p_0 is a relative energy. Correspondingly, the N.L.K. kernel is given by (16) with K replaced by K'; where K' is an analytic continuation of K of the sort introduced by Dyson[11] for Heisenberg-operators. We are assuming that the negative energy components in N.T.D. have been eliminated.

In general, K is given as an integral over a number of internal energy-momenta. With the aid of the Feynman prescription for the poles, we may integrate over the internal energy-components. In the resultant expression, p_0 occurs in denominators of two kinds, typified by

$$\{\tfrac{1}{2}W-p_0-E(p+k')-\omega(k')+i\epsilon\}^{-1} \tag{17}$$

and

$$\{\tfrac{1}{2}W-p_0+E(q)+\omega(k)+\omega(k')-i\epsilon\}^{-1}; \tag{18}$$

the point being that (17) contains only positive energies and (18) only negative energies. No term can contain both because of the Feynman prescription. K' is identical with K, except that $-i\epsilon$ is replaced by $i\epsilon$ in terms of the type (18).

When the p_0-integration is done in (16), terms arise from each pair of coincident poles chosen from among the denominators like (17) and (18) and those shown explicitly in (16). The only terms that can come from a pair containing a term of type (18) are of type (12).

The pairs of coincident poles that are affected by the change from K to K' are the pairs containing just one factor of type (18). If for K the other factor is one of the terms shown explicitly in (16), say the second, then for K' it is replaced by the first. However, in the adiabatic limit, the contribution to (16) is in either case the same, $(2M)^{-1}$.

There remains the case in which the pair of poles contains one of type (17) and one of type (18). For any term from such a pair of poles, there is always a term arising from the pole of type (17) and one of the poles shown in (16). The contribution from the former pair is of order μ/M times the contribution from the latter pair, and so is consistently neglected in the adiabatic limit.

This completes the proof that the contribution to (16) is the same when K is replaced by K'. It follows that L.K. and N.L.K., and therefore O.T.D. and N.T.D., agree in the adiabatic limit.

Finally, the remark at the end of Sec. 1 is relevant here. In particular, it is because we are using the "iterated" form of the Tamm-Dancoff equations, that we need consider only the positive energy components of Dyson's amplitude in the N.T.D. equation; in the "iterated" form, terms appear automatically that otherwise would have to be found by eliminating negative-energy matrix elements of the lower order parts of the kernel.

The author is indebted to Dr. A. Klein and Dr. B. Kurşunoğlu for the opportunity of seeing their unpublished manuscripts,[7,8] to Professor F. J. Dyson and Dr. A. Klein for written advice, and to Dr. A. Salam for many discussions.

Letters to the Editor

PUBLICATION of brief reports of important discoveries in physics may be secured by addressing them to this department. The closing date for this department is five weeks prior to the date of issue. No proof will be sent to the authors. The Board of Editors does not hold itself responsible for the opinions expressed by the correspondents. Communications should not exceed 600 words in length and should be submitted in duplicate.

Theory of Superconductivity

M. R. SCHAFROTH

The F. B. S. Falkiner Nuclear Research and Adolph Basser Computing Laboratories, School of Physics, The University of Sydney, Sydney, New South Wales, Australia*

(Received October 4, 1954)

IN a previous note,[1] it was pointed out that a charged boson gas below its condensation point is a superconductor. This shows that a theory of superconductivity is established if it can be shown that in a metal at low temperatures charge-carrying bosons occur which condense at a critical temperature T_C. The purpose of this note is to point out that if the total interaction between electrons (Coulomb-interaction, interaction by lattice vibrations[2] and other effects) is such that it produces resonant states of electron pairs, then one should expect the onset of superconductivity.

In a rough way one might try to describe a resonant state as a bound state of two electrons with negative binding energy, i.e., ignore the width. Assuming such a state at an energy $\zeta_0(1-\delta)$ per electron (ζ_0 being the Fermi energy of the free electron gas at absolute zero) the theory of chemical equilibrium applied to the equilibrium between electrons and these "bosons" yields qualitatively all the essential equilibrium features of superconductivity. At a critical temperature T_C given by

$$\delta=6.54(kT_C/\zeta_0)^{\frac{1}{2}}+0.824(kT_C/\zeta_0)^2+O((kT_C/\zeta_0)^4), \quad (1)$$

a transition of the second kind occurs with a discontinuity in the specific heat. Below T_C, the Meissner-Ochsenfeldt effect is exhibited; the number of superconducting (i.e., condensed) bosons at absolute zero is

$$n_{s0}=N\cdot\tfrac{3}{4}\delta. \quad (2)$$

(The penetration depth is determined by inserting (2) into London's theory[3]); the contribution of the noncondensed bosons can be neglected.

Quantitative agreement can, however, not be reached by this simple approach. The discontinuity in the specific heat is $\gamma\delta^2$; the difference in free energy between the normal and the superconducting state is of order $\zeta_0\delta^2$. If δ is computed from formula (1) by using the experimental T_C, both these quantities turn out to be much too small. Moreover, the trend of the specific heat curve below T_C is still essentially linear with almost the same slope as for the normal state.

Thus the description of the resonant state in terms of a single parameter δ is sufficient to give the qualitative features of superconductivity, but insufficient for quantitative purposes. In a quantitative treatment, the width of the resonance must play a crucial role. Furthermore, the problem has to be looked upon as a self-consistent one: the form of the resonance depends critically on the occupation of the electron states, and only in the vicinity of the Fermi surface can such resonances occur at all. At higher energies they will be too wide to have any effect; at low energies where all electron states are occupied, the resonances will be quenched by the Pauli principle. Qualitative considerations seem to indicate that the trend of these effects is indeed in the right direction for improving the agreement between theory and experiment.

The author is deeply indebted to Dr. J. M. Blatt and Dr. S. T. Butler for many stimulating discussions which greatly clarified essential points of this note.

* Also supported by the Nuclear Research Foundation within the University of Sydney.

[1] M. R. Schafroth, Phys. Rev. **96**, 1141 (1954).
[2] H. Fröhlich, Phys. Rev. **79**, 845 (1950).
[3] F. London, *Superfluids* I, (J. Wiley and Sons, Inc., New York, 1950).

Exponential Temperature Dependence of the Electronic Specific Heat of Superconducting Vanadium

W. S. CORAK, B. B. GOODMAN, C. B. SATTERTHWAITE, AND A. WEXLER

Westinghouse Research Laboratories, East Pittsburgh, Pennsylvania

(Received September 20, 1954)

THE specific heat of a specimen of vanadium has been measured in the superconducting state from its transition temperature, 5.05°K, down to 1.2°K. Vanadium lends itself well to the study of the electronic specific heat of a superconductor because, in this metal, quite low values of T/T_c are easily attainable and the lattice contribution to the specific heat is small compared with the electronic contribution.

The specimen, a cylinder of mass 85 g, was prepared by arc-melting crystals of vanadium which had been made by the van Arkel iodide process. The specimen was annealed in vacuo ($p<3\times10^{-6}$ mm) for 3 hours at 850°C and then cooled slowly at about 50°C per hour. No quantitative estimates of the purity of the specimen have been obtained yet, but for the purpose of comparing the present results with previous work[1] its hardness (121±11, diamond pyramid hardness) and its residual

resistivity (0.08 of its ice-point resistivity) are of interest. The breadth of the superconducting transition, shown by the present calorimetric measurements to be 0.10°K, is somewhat less than the value 0.15°K found by Worley, Zemansky, and Boorse[2] for each of two separate vanadium specimens.

The specific heat determinations were carried out in the conventional manner; in detail the experimental technique was identical with that to be described in a forthcoming paper on the specific heats of the noble metals.[3] The uncertainties in the results for the specific heat of vanadium were largely attributable to the 1948 temperature scale in which, it was thought, the values of dT/dp might be in error by as much as 3 percent below 4.2°K and by a larger amount above 4.2°K.[3-5] In the discussion of the present measurements the usual assumption is made that the electronic and lattice contributions to the specific heat are additive, with the latter taking the same values as in the normal state. In the absence, so far, of measurements on the present specimen in the normal state a value of the Debye θ of 298°K, the mean of the values for the two separate vanadium specimens measured by Worley, Zemansky, and Boorse,[6] was assumed. The contribution of the lattice to the total specific heat ranged from 5 percent to 15 percent. Taking all the probable sources of error into consideration, including the probable error of 10 percent in the Debye θ, the probable error in the results for the electronic specific heat of vanadium is about 5 percent over the whole temperature range. The coefficient of the normal electronic specific heat, γ, was deduced from the entropy of the present specimen at 5.2°K, obtained from the present measurements, and from the above value of θ, by the application of the third law of thermodynamics. The resulting value, $\gamma=21.5\times10^{-3}$ cal mole^{-1} deg^{-2}, is in close agreement with the values 21.9, 21.4, and 21.1×10^{-3} cal mole^{-1} deg^{-2} given by Worley, Zemansky, and Boorse.[6]

In Fig. 1 a representative selection of the present values of the reduced electronic specific heat, $C_{es}/\gamma T_c$, is plotted (open circles) logarithmically against the reciprocal, T_c/T, of the reduced temperature; the significance of plotting the results in this way will become clear later. In most previous calorimetric measurements on superconductors the results could be expressed in terms of an electronic specific heat given by

$$C_{es}/\gamma T_c=3(T/T_c)^3, \tag{1}$$

the continuous curve in Fig. 1. It is clear that the present results show a marked departure from this equation, especially at the lowest temperatures. Agreement with the rather complicated expression for $C_{es}/\gamma T_c$ given by Koppe[7] is somewhat better. However, it may be seen from Fig. 1 that the relation between $\log(C_{es}/\gamma T_c)$ and T_c/T for the present results is closely linear, suggesting an empirical equation of the form

$$C_{es}/\gamma T_c=ae^{-bT_c/T}. \tag{2}$$

The broken straight line in Fig. 1 represents this equation with $a=10.0$ and $b=1.52$ and, except for $T_c/T<1.1$, it fits the experimental points to within the probable error of 5 percent over a temperature range in which C_{es} varies by a factor of more than 100. A detailed investigation of Koppe's expression for $C_{es}/\gamma T_c$ reveals that in this also the dominant term is of the form $\exp(-bT_c/T)$, where b is a constant of the order of unity. In vanadium the percentage correction to be applied to the total specific heat for the lattice contribution is smaller than in any other superconductor so far measured. It is therefore especially suited for investigating C_{es}. Moreover, the present measurements have been carried to larger values of T_c/T than any previous calorimetric measurements on a superconductor. The results suggest, for the first time, that the temperature

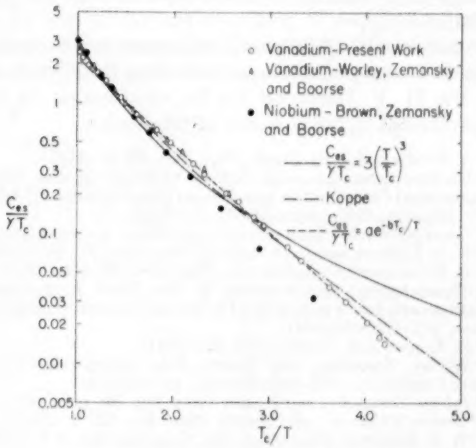

FIG. 1. Temperature dependence of the electronic specific heat of a superconductor.

dependence of C_{es} may be exponential, of the type represented by Eq. (2). It may be seen from Fig. 1 that the present results are in agreement in the limited overlapping temperature range with those obtained by Worley, Zemansky, and Boorse[8] (open triangles) for a vanadium specimen with $T_c=4.68$°K.

Previously, the measurements of Brown, Zemansky, and Boorse[9,10] on the electronic specific heat of superconducting niobium had been the first to suggest that there might be departures from Eq. (1). A selection of their smoothed values of $C_{es}/\gamma T_c$ has been plotted in Fig. 1 (solid circles). The differences between the result for niobium and those for vanadium may either be attributable to differences in experimental conditions or they may be genuine, representing a departure from a law of corresponding states among superconductors. Nevertheless, the results for niobium also can now be seen from Fig. 1 to be not inconsistent with an exponential temperature dependence of the type represented by Eq. (2). More indirect evidence for this type of temper-

ature dependence of C_{es} has been obtained from measurements by Goodman[11] on the thermal conductivity of superconducting tin below 1°K, which extended to values of T_c/T as large as 8. Here the electronic contribution to the thermal conductivity of the superconductor, which would be expected to be related to its electronic specific heat, also varied, over a wide range of temperature, in the exponential manner represented by Eq. (2).

On any single-electron model of a superconductor with a gap ϵ in the energy level spectrum, the expression for the specific heat would be expected to be dominated, at sufficiently low temperatures, by the term $\exp(-\epsilon/kT)$. The experimental evidence for vanadium, niobium, and tin discussed above supports the concept of such an energy gap; the magnitude of this energy gap, deduced from the experiments, is of the order of kT_c.

A full account of this work will appear in due course. The authors would like to acknowledge their gratitude to Dr. M. P. Garfunkel for his contribution to the experimental techniques used in this work.

[1] A. Wexler and W. S. Corak, Phys. Rev. **85**, 85 (1952).
[2] Worley, Zemansky, and Boorse, Abstracts of the Third International Conference on Low Temperature Physics and Chemistry, Houston, 1953 (unpublished), pp. 57–58.
[3] Corak, Garfunkel, Satterthwaite, and Wexler (to be published)
[4] R. A. Erickson and L. D. Roberts, Phys. Rev. **93**, 957 (1954).
[5] R. Berman and C. A. Swenson, Phys. Rev. **95**, 311 (1954).
[6] These results were reported at the Third International Conference on Low Temperature Physics and Chemistry, Houston Texas, 1953 (unpublished).
[7] H. Koppe, Ann. Physik (6) **1**, 405 (1947).
[8] Worley, Zemansky, and Boorse, Proc. Schenectady Cryogenics Conference, 1952 (unpublished), pp. 128–130.
[9] Brown, Zemansky, and Boorse, Phys. Rev. **86**, 134 (1952).
[10] Brown, Zemansky, and Boorse, Phys. Rev. **92**, 52 (1953).
[11] B. B. Goodman, Proc. Phys. Soc. (London) **A61**, 217 (1953).

X-Ray Diffraction Patterns from Liquid Helium*

W. L. Gordon, C. H. Shaw, and J. G. Daunt
Department of Physics, Ohio State University, Columbus, Ohio
(Received September 20, 1954)

INTENSITY as a function of scattering angle for copper $K\alpha$ x-rays has been determined for liquid helium (mass 4) at temperatures above and below its lambda point. Proportional counter registration of the scattered x-ray intensity was used together with a Ross differential x-ray filter and a differential pulse height analyzer for monochromatization and for spurious background reduction. Scattering angles from 1.5° to 90° were covered. The helium sample was contained in a one quarter inch diameter, thin-walled beryllium tube in good thermal contact with, but separate from, a temperature regulating helium bath. The sample temperature was determined from its vapor pressure.

The collimating and observation slit systems both permitted a maximum horizontal crossfire of ½ degree. The vertical divergence for each slit system for scattering angles >5° was about 7° and was decreased to about 2° for smaller angles. The scattering curves at 1.4°K and 4.2°K were repeated many times with a final estimated observational error in the curves of approximately ±0.7 percent near the peak, ±1 percent at 10° increasing to ±4 percent at 1.5° and ±1.5 percent at large angles. Only a small amount of data was taken at 2.2°K.

The resulting curves shown in Fig. 1 have been corrected for polarization, absorption in the helium, and for change of scattering volume with angle. The 1.4°K and 2.2°K data have been corrected to correspond to the number density at 4.2°K. These data are apparently in general agreement with the results of Keesom and Taconis[1] and of Reekie and co-workers[2] who state that there is little difference in diffraction patterns above and below the lambda point for scattering angle >12°. The diffraction peak at 1.4°K is shifted approximately 0.7° toward larger angles as might be expected for a density increase of 15 percent.

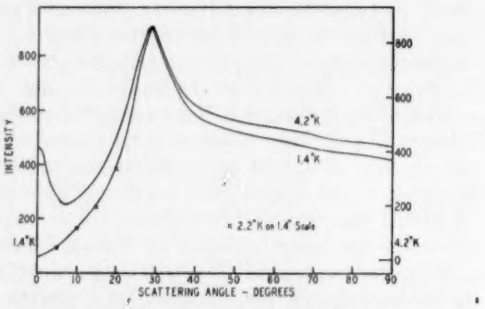

FIG. 1. Reduced scattering curves for liquid helium. The 1.4°K curve and the 2.2°K points follow the intensity scale, in arbitrary units, on the left while the scale on the right applies to the 4.2°K curve.

Two methods are available for reducing these corrected intensities to the liquid structure factors, $\mathfrak{L}(\lambda,\theta,T)$ at each temperature. The conventional approach[3] is that of determining the proportionality constant relating scattered intensities to the atomic scattering cross sections by assuming that at large scattering angles each atom scatters independently. Thus, the incoherently scattered portion can be subtracted using the computed incoherent cross section and the remaining coherently scattered intensity compared to the atomic structure factor. Because of the undulations observed near 90° this method is not entirely satisfactory here. Tweet[4] has suggested an alternative method using a comparison to the scattering from a gas whose scattering cross section must also be known. Argon gas was used in the present experiment and by requiring analytically that both methods give identical results for $\mathfrak{L}$ it was possible to determine the above proportionality constant

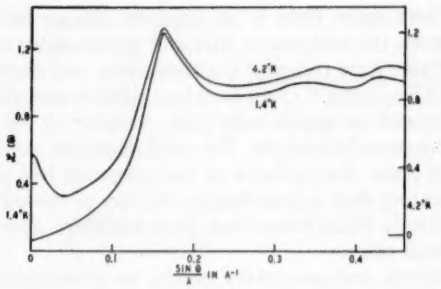

FIG. 2. Liquid structure factors for helium at 1.4° and 4.2°K. The ordinate scale on the left applies to the 1.4°K curve; that on the right to the 4.2°K curve.

unambiguously without consideration of the incoherent contribution.

Figure 2 shows the liquid structure factor curve at 4.2 and 1.4°K. In order that $\mathfrak{L}$ approach unity at 90° it was necessary to reduce the calculated incoherent scattering cross section of helium[5] by 10 percent. An overall increase of the calculated argon coherent scattering cross section by 10 percent would produce the same effect by reducing the proportionality constant for helium scattering, although of course the form of $\mathfrak{L}(\lambda,\theta,T)$ would be altered somewhat.

The liquid structure factor should approach zero scattering angle parabolically[6] with its limiting value given by $\mathfrak{L}(0°,T)=nkT\chi_T$, where n is the number density, k is the Boltzmann constant, T the absolute temperature, and χ_T the isothermal compressibility. Such a parabolic extrapolation for the experimental data in Fig. 2 yields a value for $\mathfrak{L}(0°,T)$ of 0.475 at 4.2°K and 0.065 at 1.4°K with a probable error of ±7 percent as compared to 0.45 and 0.055 predicted by Goldstein in a private communication and approximately 0.6 at 4.2°K according to Tweet.[4]

Details of the experiment will be published shortly.

* This work was supported by a grant from the Research Corporation of New York.

[1] W. H. Keesom and K. W. Taconis, Physica **5**, 270 (1938).
[2] Hutchison, Beaumont, and Reekie, Proc. Phys. Soc. (London) **A66**, 409 (1953).
[3] N. S. Gingrich, Revs. Modern Phys. **15**, 90 (1943).
[4] A. G. Tweet, Phys. Rev. **93**, 15 (1954).
[5] A. H. Compton and S. K. Allison, *X-Rays in Theory and Experiment* (D. Van Nostrand Co., Inc., New York, 1935), p. 782.
[6] L. Goldstein, Phys. Rev. **84**, 466 (1951).

Electrical Resistivity Minimum and Structural Defects in Copper

R. W. SCHMITT AND M. D. FISKE

General Electric Research Laboratory, Schenectady, New York

(Received October 4, 1954)

BLEWITT, Coltman, and Redman[1] have reported that a resistance minimum was observed in pure copper upon introducing grain boundaries by straining a single crystal and subsequently annealing it. The original single crystal as well as the strained, unrecrystallized sample, however, did not show a minimum. The authors therefore proposed that the minimum in electrical resistivity may arise as a result of scattering or trapping at grain boundaries.

If this proposal were true, one might expect alterations in the grain structure of copper to produce changes in any resistivity minimum observed. Experiments done at this Laboratory indicate that no such effect occurs. These experiments consist of measuring the small minimum occurring in cold-drawn copper wires and in the same samples after they are subjected to annealing treatments. The copper is American Smelting and Refining Company high-purity copper,[2] samples $0-A$ having been prepared by swaging and cold drawing the original stock into wires, sample $0-B$ by chopping the stock into pieces and remelting in evacuated quartz tubes prior to swaging and drawing. The results are illustrated in Fig. 1, where $\rho_{\text{anom}}\equiv\rho_T-\rho_{4.2°K}$ *vs* temperature is plotted for the liquid helium temperature region. Earlier measurements on $0-A$ show no signs of a resistance minimum, whereas recent, more precise measurements show a slight minimum of the order of or less than that observed by MacDonald[3] in his pure copper (the quantity δ indicated in the figure represents approximately MacDonald's value of $\rho_{4.2°K}-\rho_{\min}$). The pertinent observation on this sample is that after being

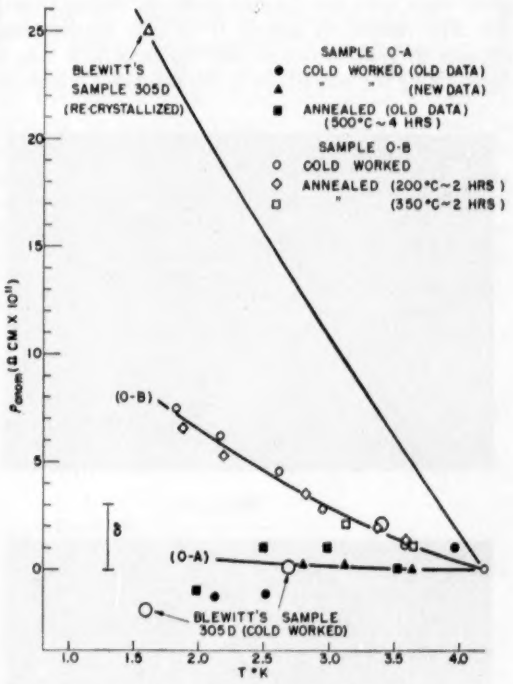

FIG. 1. $\rho_{\text{anom}}\equiv\rho_T-\rho_{4.2°K}$ *vs* temperature for copper samples.

TABLE I. Resistivities, electronic mean free paths (l), and grain diameter (d).

Sample	Temp. of anneal, °C	4.2°K Ωcm ×10⁹	l cm ×10⁵	d cm ×10⁵
	Present data			
0−A	C.W.[a](new)	4.88	0.13	...
	C.W.(old)	4.18	0.16	...
	~500(old)	0.34	1.9	0.9
0−B	C.W.	5.09	0.13	...
	~200	1.18	0.55	...
	~350	0.81	0.81	0.9
	Blewitt *et al.*			
305D	C.W.	1.31	0.50	...
	~1000	0.91	0.72	10²

[a] C.W. = cold-worked.

annealed in high vacuum at approximately 500°K it does not show a larger ρ_{anom} than do the highly cold-worked samples. Figure 2 shows the microstructure of the sample in the highly cold-worked and annealed states. It is clear that the number and arrangement of grain boundaries has changed markedly during annealing. The results on sample 0−B also confirm that changes in grain structure play no detectable role in determining the magnitude of the resistance minimum,

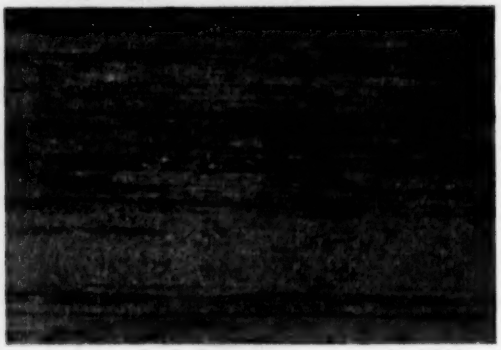

(a)

(b)

FIG. 2. Microstructure of cold-worked and annealed samples 0−A. ×500. (a) Cold-worked; (b) annealed.

for here again there is no apparent change in ρ_{anom} between the cold-drawn wire and the annealed wires. In Table I are compiled the resistivities and electronic mean free paths, l, of our samples at helium temperature along with an approximate grain diameter, d, for some of the annealed samples. The grain diameters are of the same order of magnitude as the computed free paths, indicating that a considerable fraction of the residual resistivity likely arises from grain-boundary scattering in these cases.

Blewitt and co-workers' results on a worked single crystal and on the same sample after recrystallization are given in Fig. 1 and Table I. The mean free path in Blewitt's recrystallized samples is a small fraction of the grain size[4] of these samples.[5] Thus, grain-boundary scattering must contribute very little to the total residual resistivity of these samples—in contrast with the case of our recrystallized samples. It is possible, then, that the resistance minimum observed by Blewitt may arise from additional scattering centers present within the grains of his samples.

Koehler[4] points out that using the grain size of Blewitt's samples as a mean free path gives a computed resistivity roughly equal to only ρ_{anom} extrapolated to 0°K. This correspondence he takes as confirmation of the hypothesis that the resistance minimum may be the result of grain-boundary scattering. However, a similar argument with respect to our samples would lead one to expect ρ_{anom} in the annealed samples at 0°K to be of the same order of magnitude as the residual resistivity itself. This result is incorrect by about two orders of magnitude.

[1] Blewitt, Coltman, and Redman, Phys. Rev. **93**, 891 (1954).
[2] Smith, Smart, and Phillips, Trans. Am. Soc. Mech. Engrs. **143**, 272 (1941).
[3] D. K. C. MacDonald, Proceedings of the Schenectady Cryogenics Conference, October, 1952, p. 154.
[4] J. S. Koehler, Phys. Rev. **94**, 1071 (1954).
[5] M. H. Cohen and C. S. Barrett, Phys. Rev. **95**, 1094 (1954).

Electrical Resistivity Minimum Reported in Copper-Zinc Alloys

R. W. SCHMITT

General Electric Research Laboratory, Schenectady, New York

(Received October 4, 1954)

GERRITSEN and Linde[1] report that the addition of small amounts of zinc to copper gives rise to a resistance minimum. Experiments done at this Laboratory do not confirm this result, and we have found no resistance minimum in these low-percentage alloys that can be ascribed to the zinc. Our results are illustrated and compared with those of Gerritsen and Linde in Fig. 1, where $\rho_{anom} \equiv \rho_T - \rho_{4.2°K}$ is plotted *vs* temperature in the liquid helium temperature region. The curves attributed to Gerritsen and Linde are computations

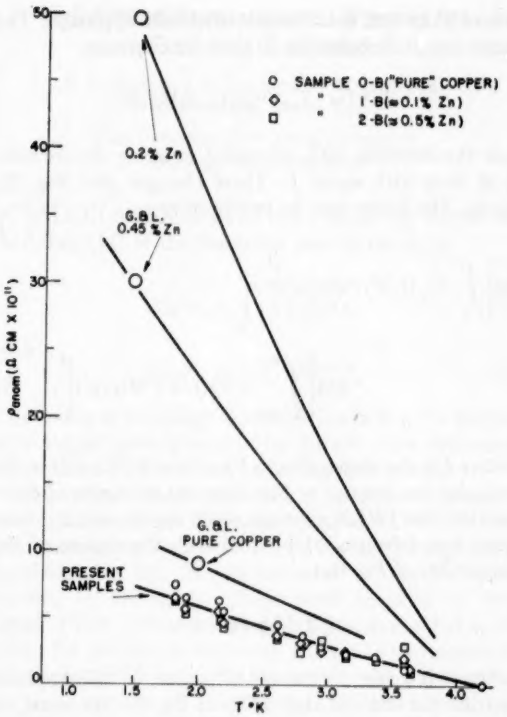

FIG. 1. $\rho_{\text{anom}} \equiv \rho_T - \rho_{4.2°K}$ *vs* temperature for copper-zinc alloys.

from their smoothed curves of resistance ratio *vs* temperature for their alloys. Our samples, which were prepared by melting the components in sealed-off, evacuated quartz tubes, show a smaller ρ_{anom} than do their samples. Moreover, the magnitude of the anomalous resistance does not vary as a function of either the zinc content or the state of anneal. Thus, no distinction is made in the figure between the data taken on a particular sample in its various stages of anneal (cold worked; 200°C for about two hours; 350° for about two hours). Distinction is made, however between the different samples consisting of pure copper (American Smelting and Refining Company high-purity—nominal 99.999 percent—copper stock[2] treated and prepared in the same manner as the alloys), of ~0.1 atomic percent zinc, and of ~0.5 atomic percent zinc in American Smelting and Refining copper. Figure 1 clearly shows that ρ_{anom} *vs* temperature is the same for all samples. There is thus no evidence allowing one to ascribe the observed anamolous temperature-dependent resistivity to zinc in either of the alloys.

The anomalous temperature-dependent resistivity observed in the particular sample of "pure" copper used in these experiments is larger than any we have observed in other samples of pure American Smelting and Refining copper[3] even though it is somewhat less than that reported by Gerritsen and Linde for their copper. The indication is, then, that our method of preparing the alloys, to which the pure copper is also subjected, may result in picking up very small amounts of minimum-producing impurities.

A more detailed report of these measurements, along with measurements in the hydrogen temperature range and on higher percentage zinc alloys, will be given soon.

[1] A. N. Gerritsen and J. O. Linde, Physica **18**, 877 (1952).
[2] Smith, Smart, and Phillips, Trans. Am. Soc. Mech. Engrs. **143**, 272 (1941).
[3] R. W. Schmitt and M. D. Fiske, Phys. Rev. **96**, 1445 (1954).

Correspondence between Semiclassical and Quantum Treatments of Coulomb Excitation*

G. BREIT AND P. B. DAITCH
Yale University, New Haven, Connecticut
(Received October 4, 1954)

FROM the experimental evidence[1] regarding correctness of the dependence of the cross section on incident energy, it is not possible to conclude directly that the absolute value of the cross section is correctly given by the usual semiclassical treatment, referred to as SCT. In this and the following notes only the simple case of one nuclear proton, initially in an *s* state, being responsible for the interaction, is considered, the generalization to several nuclear protons being irrelevant to the question of accuracy of the SCT. The first order Born approximation with the nuclear quadrupole interaction as the small quantity is taken to be adequate.

The collision cross section for the reaction can be represented as

$$\sigma = (4/25)(mk_f/v_i\hbar^3)Z_1^2e^2B(2)\mathfrak{A}, \tag{1}$$

$$\mathfrak{A} = \Sigma \mathfrak{A}_L, \tag{2}$$

$$\mathfrak{A}_L = 16\pi^2 k_i^{-2}k_f^{-2}\left\{\frac{3L(L+1)}{2(2L+1)}\right.$$
$$\times\left[\left|\int F_{L-1}(k_i r)F_{L+1}(k_f r)r^{-3}dr\right|^2\right.$$
$$\left.\left.+\left|\int F_{L+1}(k_i r)F_{L-1}(k_f r)r^{-3}dr\right|^2\right]\right.$$
$$\left.+\frac{L(L+1)(2L+1)}{(2L-1)(2L+3)}\left|\int F_L(k_i r)F_L(k_f r)r^{-3}dr\right|^2\right\}$$
$$= 16\pi^2\mathfrak{C}_L. \tag{2'}$$

$$B(2) = 5e^2\left|\int_0^\infty r_p^4 R_i(r_p)R_f(r_p)dr_p\right|^2, \tag{3}$$

with the normalization $\int_0^\infty R^2 r^2 dr = 1$. Here i,f refer to initial and final states, $k/(2\pi)$ is the wave number of the incident particle, r is the distance of the projectile from the target, Z_1 is the charge of the projectile, r_p is the distance of the nuclear proton from the nuclear center, the R's are radial functions, F_L is the Coulomb function in the notation of Yost *et al.*[2] In Eq. (2′), the limits of integration are understood to be 0 and ∞. The effect of the proton and nuclear spin results in a factor common to both treatments and is therefore left out of account. The corresponding expression on the SCT is

$$\sigma_{cl} = (2\pi^2/25)[k^2/(Z_2^2 e^2)]B(2)g_2(\xi), \tag{4}$$

according to Ter-Martirosyan[3] in the notation of Bohr and Mottelson[4] which is followed below except where symbols are otherwise defined. Agreement of the two imples

$$(\pi^2/2)g_2(\xi) \cong \eta_{cl}^2 (k_f/k_i)\mathfrak{A}, \tag{5}$$

where

$$\eta_{cl} = Z_1 Z_2 e^2/(\hbar v_{cl}) \tag{5′}$$

is the value of the Coulomb parameter η corresponding to the value of the classical velocity, v_{cl} used in the SCT. Since the dependence of σ on $\xi = \Delta E t/\hbar$ is established experimentally, the approximate correctness of σ_{cl} as an approximation to σ for $\xi = 0$ may be considered as a partial argument for the validity of σ_{cl} also if $\xi \neq 0$. For $\xi = 0$ the comparison may be carried out by attributing an SCT contribution of an interval $\delta\epsilon$ with the contribution to $\mathfrak{A}$ caused by a given L to $\mathfrak{A}$ in Eq. (2). The connection of ϵ with L is given by

$$\epsilon^2 = 1 + L^2/\eta^2. \tag{6}$$

The correspondence between the quantum and SCT results postulated to apply for corresponding ranges of angular momenta gives

$$(\pi^2/2)\int_1 \sum_\mu |S_\mu^{(2)}|^2 \epsilon d\epsilon \cong \eta_{cl}^2 (k_f/k_i)\mathfrak{A}_L, \tag{7}$$

where $\int_1$ indicates integration over a range of L of width 1 with a mean L approximately that of $\mathfrak{A}_L$. In Eq. (2′), integrals with the same average of the L values of the F's are grouped together. Correspondence to the SCT is not sensitive to the type of grouping.

A qualitative argument for the validity of Eq. (7) can be made by means of the JWKB approximation. For small L/η the quantity $\epsilon^2 - 1$ is small, and hence for $\xi = 0$

$$|S_2^{(2)}| = |S_{-2}^{(2)}| \cong (3/2)^{\frac{1}{2}} |S_0^{(2)}|.$$

The three integrals entering $\mathfrak{A}_L$ are approximately equal in this case and hence Eq. (7) yields

$$64\left|\int F_L^2 (r/a')^{-3} d(r/a')\right|^2 \cong \sum_\mu |S_\mu^{(2)}|^2 \cong 4|S_0^{(2)}|^2, \tag{8}$$

where a' is half the distance of closest approach. The same condition holds for $L/\eta \gg 1$. In this case,

$$|S_2^{(2)}| = |S_{-2}^{(2)}| \cong (1/6)^{\frac{1}{2}} |S_0^{(2)}|,$$

and the integrals with unequal L entering $\mathfrak{A}_L$ are each $\frac{1}{3}$ of that with equal L. These changes give Eq. (8) again. The latter may be rewritten as

$$16\left|\int_0^\infty F_L (r/a')^{-3} d(r/a')\right|^2 \cong 4\left|\int_{r_{\min}}^\infty (v/\dot{r})(r/a')^{-3} d(r/a')\right|^2, \tag{9}$$

where $\dot{r}$ is the classical velocity of the SCT and v is the velocity for infinite r. For short wavelengths of the r motion, the JWKB approximation applies and F_L^2 may then also be replaced by $\frac{1}{2}$ of A_L^2, the square of the amplitude of F_L. But

$$[A_L^2]_{\text{JWKB}} = v/\dot{r}, \tag{10}$$

where $\dot{r}$ is again the "classical" value. In this approximation the left and right sides of Eq. (9) are equal, as expected from the general connection of classical mechanics and geometrical optics.

For large η and moderate L, the JWKB method gives errors of the order of 5 percent in the value of the amplitude A_L at the first maximum and is qualitatively wrong at the classical turning point. The replacement of F_L^2 by $\frac{1}{2}A_L^2$ together with the omission of the region from $\rho = 0$ to the turning point have no obvious justification except for large L. On the other hand the contributions to the integrals from the turning point to the first node are of the order of 60 percent of the whole. For these reasons Eq. (7) has been investigated numerically for $\xi = 0$ with results described in the following note. In this case, Eq. (7) becomes

$$32\eta^2 \mathfrak{C}_L \cong \int_1 \sum |S_\mu^{(2)}|^2 L dL/\eta^2. \tag{11}$$

The authors have been kindly informed by Dr. A. Bohr that Dr. Alder and Dr. Winther have made considerations by means of the JWKB approximation related to those presented here.

* This research was supported by the Office of Ordnance Research, U. S. Army.

[1] T. Huus and Č. Zupančič, Kgl. Danske Videnskab. Selskab, Mat.-fys. Medd. **28**, No. 1 (1953); G. M. Temmer and N. P. Heydenburg, Phys. Rev. **94**, 1399 (1954).
[2] Yost, Wheeler, and Breit, Phys. Rev. **49**, 174 (1936).
[3] K. A. Ter-Martirosyan, J. Exptl. Theoret. Phys. (U. S. S. R.) **22**, 284 (1952).
[4] A. Bohr and B. Mottelson, Kgl. Danske Videnskab. Selskab, Mat.-fys. Medd. **27**, No. 16 (1953).

Validity of Semiclassical Treatment of Coulomb Excitation*

P. B. Daitch, J. P. Lazarus, M. H. Hull, Jr., F. D. Benedict, and G. Breit
Yale University, New Haven, Connecticut
(Received October 4, 1954)

CALCULATIONS have been made by means of Eq. (11) of the preceding note in the form

$$32\eta^2\mathcal{C}_L=\int_L^{L+1} b(L)dL, \tag{1}$$

with

$$b(L)=L\eta^{-2}\sum|S_\mu^{(2)}|^2. \tag{2}$$

The choice of the range of integration in Eq. (1) is such as to obtain good agreement for the two sides. Here and below the notation of the preceding note is used.

The value $\eta=8.156$ was used so as to correspond to the experiment of Huus and Zupančič[1] for 2-Mev protons bombarding tantalum. Values of F_b were kindly furnished by Dr. M. Abramowitz of the National Bureau of Standards. These were checked by the series of Eqs. (13) and (14) of Biedenharn *et al.*[2] at ρ_L to about 0.1 percent, in the range $10<\rho<18$ by numerical integration (NI) for nearly the same η with a correction for the difference of ~0.0003 in η, in the range $18<\rho<35$ by computing F'' by differences from F and hence $Q^2=-F''/F$. At $\rho=50$, the NI of the continuation was checked against asymptotic series, and a NI was used as a consistency check in $6<\rho<10$. The values of F_b were used for the calculation of F_L for $L\leqslant10$ in the range $0<\rho<35$. For $L=20$, 30, 50 the values at the classical turning point, ρ_L, have been computed by Eqs. (13) and (14) of reference 2 and continued by NI in steps of 0.50 in ρ to larger and smaller distances. The integrals in Eq. (2′) will be referred to as the (L,L) and $(L+1, L-1)$ integrals. They were calculated by evaluating the contributions from two ranges of ρ, the small ρ range and the tail range, the former furnishing the main contribution. For $0\leqslant L\leqslant10$ the tail ranges began at the highest zero of F_L for $\rho<35$; for $L=20$ at $\rho\cong47.3$, the third node of F above $\rho=0$; for $L=30$ at $\rho\cong86.5$; for $L=50$ at $\rho\cong101$. Different procedures were employed in the evaluation of contributions from the small ρ range and the tail. The work for the small range will be described first. For $L\leqslant10$ Simpson's rule at intervals of 0.50 in ρ with checks by the Newton-Cotes fourth degree fit rule was used. The calculation of both types of integrals took place by direct evaluation of the integrand. For $L=20$, 30, 50 the (L,L) integral for the small ρ range was handled as for $L\leqslant10$. The $(L+1, L-1)$ integrals were first transformed by means of recurrence relations and partial integrations to a form involving integrands of the type

$$(A/\rho^3+B/\rho^4+C/\rho^5)F_L^2. \tag{3}$$

The calculation then proceeded as for the (L,L) integrals.

The evaluation of the tail contributions for $(L+1, L-1)$ integrals was carried out by reducing them to the type of Eq. (3). These as well as the (L,L) forms are conveniently calculated by means of the phase amplitude quantities which yield

$$F_L^2=(A_L^2/2)-(A_L^2/2)\cos(2\varphi_L). \tag{4}$$

The second part oscillates with a high frequency so that its contribution is much smaller than that of the first, low frequency part. The first part has been obtained by means of a series[3] for A_L in descending powers of ρ. The last term of the series for A_L was 3 percent or less of the contribution of the tail, this relatively high fractional error occurring however for a tail contribution of about 10 percent of the desired integral. The error caused by breaking off the series for A_L is thus of the order of 0.3 percent or less in the value of the integral and this error was not exceeded in other cases. The high frequency part is of the order of the error caused by omission of the last term in the series for A_L. It has been evaluated by successive partial integrations giving terms in descending powers of ρ. The second term is of the order 0.001 of the first. The procedure has been checked by the consideration of the curvature of the factor multiplying $\cos2\varphi$. The accuracy of the results for the integrals is thus believed to be generally 0.3 percent or better, corresponding to 0.6 percent in the value of contributions to $b(L)$. The results of the comparisons of contributions to $10^6\mathcal{C}_L$ and the corresponding SCT quantity are shown in Table I. The integral

$$(10^6/32\eta^2)\int_0^\infty b(L)dL=532.8$$

and the contribution to it from the region $L>50$ is ~12 percent of the whole. Assuming the last column to give about the same fractional difference for the remaining relevant region as for the last three entries the

Table I. Comparison of quantum and classical contributions to $(25/64\pi^2)[vh^3/(Z_1^2e^2mkB(2))]\sigma\times10^6$ with σ = total cross section.

L	Quantum quantity $10^6\mathcal{C}_L$	Classical quantity $10^6b(L)/(32\eta^2)$	Excess of quantum over classical in percent
0	0	6.21	
1	18.98	17.63	7.1
2	26.91	26.57	1.2
3	32.45	32.32	0.4
4	35.10	35.00	0.3
5	35.42	35.26	0.5
6	33.95	33.89	0.2
7	31.63	31.58	0.2
8	28.84	28.84	0.0
9	26.04	26.00	0.1
10	23.27	23.27	0.0
20	7.54	7.62	−1.1
30	3.10	3.14	−1.1
50	0.896	0.909	−1.5

excess of the quantum cross section over the SCT cross section is 0.1 percent of the whole. The numbers recorded in the table are not as accurate as the number of significant figures would suggest. The intended accuracy was about one percent but internal consistency indicates that it may be better. The second column minus the third when summed over different L contributes to the excess of $10^6 \sum \mathcal{C}_L$ over the SCT approximation the amounts -6.2, $+2.2$, -1.3, and -0.6 from the L ranges 0, 1–10, 11–50, 51—∞ respectively. The total difference is -5.9, about -1 percent of the total. At the end of the work a slight error was found in the quantum values for $L=20$, 30, 50. A crude correction replaces the -1.1, -1.1, -1.5 percent entries by roughly $+3$ percent to 1.7 percent, replacing the total quantum-classical difference by ~ 1.0, *i.e.*, ~ 0.2 percent of total. With either interpretation the difference is one percent or less of the total cross section.

* This research was supported by the Office of Ordnance Research, U. S. Army.

[1] T. Huus and Č. Zupančič, Kgl. Danske Videnskab. Selskab, Mat.-fys. Medd. **28**, No. 1 (1953).

[2] Biedenharn, Gluckstern, Hull, and Breit, Phys. Rev. (to be published).

[3] Bloch, Hull, Broyles, Bouricius, Freeman, and Breit, Phys. Rev. **80**, 553 (1950); B. E. Freeman, Dissertation, Yale University, 1950 (unpublished).

Spin, Magnetic Moment, and Hyperfine Structure of Rb^{81}*

J. P. Hobson,† J. C. Hubbs,‡ W. A. Nierenberg, and H. B. Silsbee

University of California, Berkeley, California

(Received October 11, 1954)

THE spin, hyperfine splitting, and nuclear moment of Rb^{81} (4.7 hr) have been measured. They are 3/2, 5000±125 Mc/sec, and 2.00±0.06 nuclear magnetons respectively. The zero-moment method of atomic beams was used. Figure 1 shows the zero-moment curve

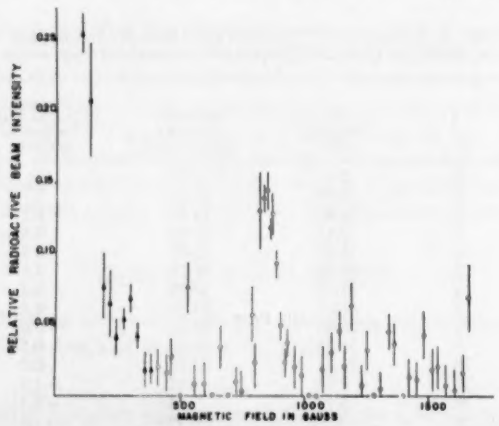

FIG. 1. Rb^{81} zero-moment curve.

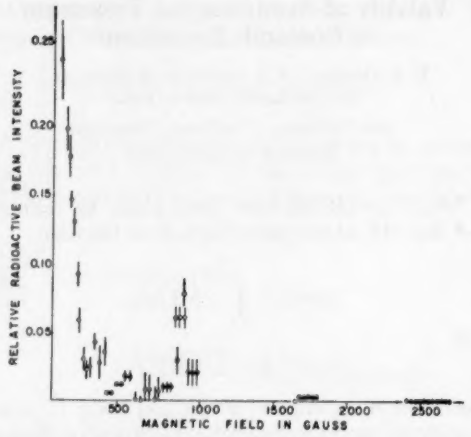

FIG. 2. Rb^{81} zero-moment pattern.

(beam intensity *vs* magnet current) for Rb^{81}. A peak appears at approximately 850 gauss. The run did not remove the possibility of spin 5/2 or 7/2. Figure 2 is another run which shows the 850-gauss peak but shows no peaks at 1700 or 2550 gauss, thus establishing the spin as 3/2. Calibration of the fields with natural Rb established the hyperfine splitting, and the ratio of radio-rubidium to natural rubidium hyperfine splittings determined the magnetic moment.

The detection was accomplished by collection of the neutral beam on sulfur buttons and counting the K x-rays. The sulfur surface collection was one of many methods tried and it apparently gave nearly full efficiency. The K x-rays were absorbed in a 1 mm×½ in. ×½ in. NaI(Tl) crystal which gave nearly 50 percent efficiency with a minimum counting background.

The isotope was produced by α bombardment and therefore had carrier added to optimize the beam. It was identified by the chemistry, its decay curve, and the behavior of the sample as a function of α energy.

There is a suggestion of a peak at 290 gauss in Fig. 1, possibly due to Rb^{85}. Further runs are being made to improve the statistics in this region and at multiples of this field.

* This research has been supported by the U. S. Office of Naval Research.

† Now at the National Research Council of Canada, Ottawa, Canada.

‡ Now at Columbia University, New York, New York.

*E*3 Isomer in Ir^{191}*

J. W. Mihelich,† M. McKeown, and M. Goldhaber

Brookhaven National Laboratory, Upton, New York

(Received October 15, 1954)

IT has been established[1] that Os^{191} (16 day) decays via a β transition to an excited level in Ir^{191}, followed by two γ-ray transitions in cascade (42 and 129 kev).

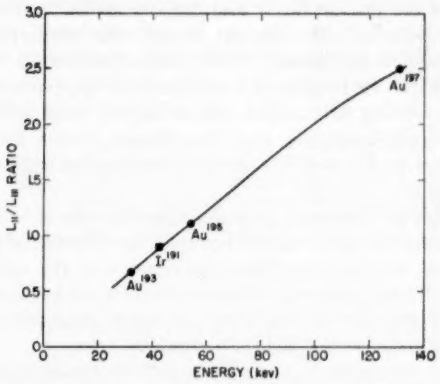

FIG. 1. Experimental L_{II}/L_{III} ratios for $E3$ transitions as a function of energy for transitions in elements of $Z=79$ and $Z=77$.

Kondaiah[2] had reported the existence of $\beta-\gamma$ coincidences. Since the L conversion pattern for the 42-kev transition ($L_I:L_{II}:L_{III}=<0.1:0.8:1.0$) indicated either an $E2$ or $E3$ transition, Swan and Hill[3] concluded that the multipolarity was $E2$. Since then, however, McGowan[4] has found that no $\beta-\gamma$ coincidences could be observed. Hence, the existence of an isomer of $\Delta I=3$ is indicated.

Accordingly, we have searched for a measurable half-life by irradiating separated Ir isotopes (shielded by boron) with fast pile neutrons and observing the decay rate of the 129-kev γ-ray. The technique used was that of Scharff-Goldhaber and McKeown[5] as employed in their search for isomers with half-lives of the order of seconds. We have found a photopeak of 129 kev connected with Ir^{191} and decaying with a half-life of 6.8 ± 1.0 sec. Naumann and Gerhart have subsequently obtained a more accurate value of this half-life ($T_{\frac{1}{2}}=5.6\pm0.4$ sec).[6] Hence, we must conclude that either the 42-kev transition or an as yet unobserved transition is responsible for the 5.6-sec half-life. It has been shown previously that the 129-kev γ-ray is in prompt coincidence with preceding γ-rays in the K-capture decay of Pt^{191}.[7]

It is of interest to note that Butement and Poe[8] have assigned a 7.3-second isomer to Ir^{194m}, because they produced such an activity with fast neutrons on Ir and Pt. They observe a γ-ray of 125 kev (with an x_K/γ ratio of 1.5, as compared to the value of 2.0 for the 129-kev transition in Ir^{191}) and a γ-ray of 5.6 Mev, both decaying with the 7.3-second half-life. We should like to suggest tentatively that they were exciting the isomeric level in Ir^{191}, and that the 5.6-Mev peak may correspond to the 6.1-Mev transition (full energy less 0.51 Mev) in N^{16} (7.3 sec) produced by the $O^{16}(n,p)N^{16}$ reaction on oxygen present as an impurity in the Ir and Pt samples. We have, however, not pursued this point further.

In the series of $E3$ isomers[9] found in the odd-A isotopes of Au, L ratios were obtained for several transition energies. Figure 1 is a plot of these ratios ($Z=79$) as a function of energy. The point for Ir($Z=77$) is indicated. Hence, on the basis of these empirical data

TABLE I. Dependence of L_{II}/L_{III} ratio on Z.

Z	Energy kev	L_{II}/L_{III}	Ref.
85	100	2.9	a
79	100	1.9	b
66	109	1.4	c
47	93	1.1	d

[a] From tables of reference 10.
[b] Interpolated value from data on Au isomers. See reference 9.
[c] Jordan, Cork, and Burson, Phys. Rev. 91, 497 (1953).
[d] F. A. Johnson, Can. J. Phys. 31, 1136 (1953).

it is not unreasonable to assume that the 42-kev transition in Ir^{191} be of $E3$ character.

The tables of Rose, Goertzel, and Swift[10] do not, so far, include values of L_{III} conversion coefficients for atomic numbers other than $Z=85$. For this atomic number and an $E3$ transition of 42 kev, the value of L_{II}/L_{III} would be 2.34. The measured value for Ir^{191} is ~0.8.[3,11] However, apparently this ratio is a rapidly varying function of Z between $79\leq Z\leq85$. This is shown in Table I which lists L_{II}/L_{III} ratios for several $E3$ transitions of approximately 100 kev and various values of the atomic number.

Ir^{191} has a ground state characterized by the assignment $d_{3/2}$.[12] Since the successively higher levels are depopulated by $M1+E2$[13] and $E3$ transitions, respectively, the indicated level assignment for the excited states on the unified model[14] are $d_{5/2}$ and $h_{11/2}$, in strong analogy with the odd-A isomers of Au.[9] Figure 2

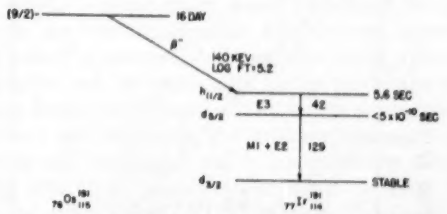

FIG. 2. Levels of Ir^{191} populated by β decay of Os^{191}.

presents a decay scheme which is consistent with the experimental data and with theoretical expectations.

The separated Ir isotopes were obtained from the Stable Isotope Division, Oak Ridge.

* Under the auspices of the U. S. Atomic Energy Commission.
† Now at University of Notre Dame, Notre Dame, Indiana.
[1] *Nuclear Data*, National Bureau of Standards Circular No. 400 (U. S. Government Printing Office, Washington, D. C., 1950); Hollander, Perlman, and Seaborg, Revs. Modern Phys. 25, 469 (1953).
[2] E. Kondaiah, Arkiv Fysik 3, 47 (1951).
[3] J. B. Swan and R. D. Hill, Phys. Rev. 88, 831 (1952).
[4] F. K. McGowan, Phys. Rev. 93, 163 (1954).
[5] G. Scharff-Goldhaber and M. McKeown, Phys. Rev. 95, 613(A) (1954).
[6] R. A. Naumann and J. B. Gerhart, following letter [Phys. Rev. 96, 1452 (1954)].
[7] Tomlinson, Naumann, and Mihelich, Phys. Rev. 94, 794 (1954).

[8] F. D. S. Butement and A. J. Poe, Phil. Mag. **45**, 31 (1954). [*Note added in proof.*—See also the subsequent communication by these authors, Phil. Mag. **45**, 1090 (1954).]
[9] Gillon, Krishnan, de Shalit, and Mihelich, Phys. Rev. **93**, 124 (1954).
[10] Rose, Goertzel, and Swift, "L-Shell Conversion Coefficients" (privately circulated).
[11] J. W. Mihelich, Phys. Rev. **87**, 646 (1952).
[12] Brix, Kopferman, and Siemans, Naturwiss. **37**, 397 (1950).
[13] An upper limit of 5×10^{-10} sec for the half-life of this transition has been found by A. W. Sunyar (private communication).
[14] M. G. Mayer, Phys. Rev. **78**, 16, 22 (1950); Haxel, Jensen, and Seuss, Z. Physik **128**, 301 (1950); A. Bohr and B. Mottelson, Kgl. Danske Videnskab. Selskab, Mat.-fys. Medd., **27** (1953).

5.6-Second Ir^{191m} Following Os^{191} Decay*

R. A. Naumann and J. B. Gerhart
Palmer Physical Laboratory, Princeton University, and Frick Chemical Laboratory, Princeton University, Princeton, New Jersey
(Received October 15, 1954)

An isomeric transition in Ir^{191} has been found by direct isolation of the short-lived iridium activity from Os^{191}. This activity has previously been identified by Mihelich, McKeown, and Goldhaber by inelastic neutron excitation of iridium.[1] The osmium activity was prepared by a two-day neutron irradiation of natural osmium in the Brookhaven National Laboratory reactor.

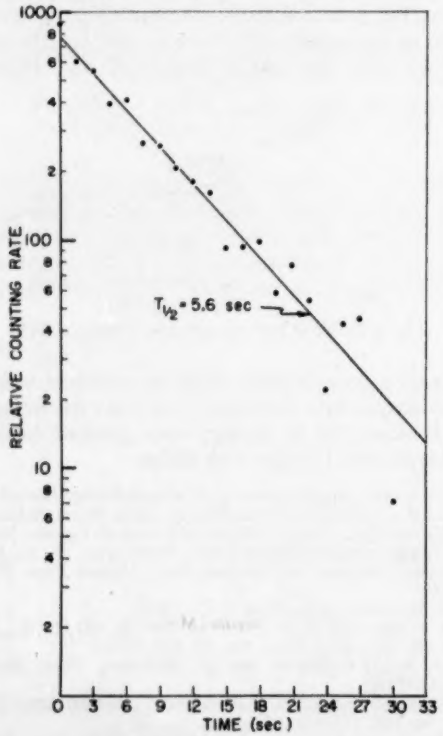

FIG. 1. Decay curve of Ir^{191m}.

After the 14-hour Os^{191m} and the 31-hour Os^{193} activities had decayed, the osmium target was converted to ammonium perosmiate, $(NH_4)_2OsO_5$, dissolved in dilute NH_4OH. To prepare the iridium activity, portions of this solution with added iridium carrier were dried on 1-mil platinum foils and then flamed over a Bunsen burner to drive off the osmium, leaving the iridium on the foil.

The Ir^{191m} sources were investigated with a NaI(Tl) scintillation spectrometer equipped for differential pulse height analysis. Positive identification of the activity as Ir^{191m} was made by observation of the 64-kev iridium x-ray and the 129-kev γ ray previously reported in the Pt^{191} decay,[2,3] and the Os^{191} decay.[4]

To determine the half-life of Ir^{191m} a constant-amplitude output signal from a differential discriminator set to accept pulses in the photopeak of either the iridium x-ray or the 129-kev γ ray was displayed on a 20-channel pulse height analyzer whose base line was varied at a uniform rate by a synchronous motor drive. In this manner the usual pulse height scale of the analyser was converted to a time scale, the channels registering counts occurring in consecutive 1.50-second periods. The half-lives obtained for the x-radiation and the 129-kev γ ray were identical. The average of several measurements, corrected for background, yielded a half-life for the Ir^{191m} activity of 5.6 ± 0.4 seconds. Figure 1 shows the decay curve obtained.

Os^{191} decays to an excited state of Ir^{191} which then emits γ rays of 129 and 42 kev.[5] On the basis of the conversion ratios $K:L_I:L_{II}:L_{III}$ the 129-kev transition has been identified as a mixed $M1+E2$ transition,[2] and consequently is expected to have a lifetime of the order of 10^{-10} seconds. Because the 129-kev transition in Ir^{191m} was observed to decay with a 5.6-second half-life, it must be concluded that the 129-kev γ ray follows the 42-kev γ ray, which experimentally confirms the level order previously surmised from the Pt^{191} data.[2]

Using Weisskopf's formulas for the lifetimes of radiative transitions[6] and the tables of conversion coefficients of Rose *et al.*,[7] the expected lifetimes of various 42-kev transitions in Ir^{191} have been calculated and are given in Table I. The entries in this table are the radiative lifetime divided by the sum of conversion coefficients $1+\alpha_{LI}+\alpha_{LII}+\alpha_{LIII}$ (K-shell conversion is prevented by the low γ-ray energy). It is evident that the measured

TABLE I. Calculated lifetimes of 42-kev transitions in Ir^{191} for various multipole orders.

Multipole order	Electric transition sec	Magnetic transition sec
1	$2(-15)^a$	$3(-11)$
2	$1(-5)$	$1(-7)$
3	$9(-1)$	$7(0)$
4	$5(5)$	$6(6)$
5	$4(14)$	$3(11)$

[a] $a(b)=a\times10^b$.

lifetime is consistent only with the identification of the 42-kev transition as $E3$ or $M3$ since Weisskopf's formulas appear to be valid within a factor of 10^4. It is not possible to choose between $E3$ and $M3$ on the basis of the lifetime measured here.

* This work was supported by the U. S. Atomic Energy Commission and the Higgins Scientific Trust Fund.

[1] Mihelich, McKeown, and Goldhaber, preceding letter [Phys. Rev. **97**, 1450 (1954)]. The authors are indebted to Dr. Mihelich for allowing them to make use of these data before publication.

[2] Tomlinson, Naumann, and Mihelich, Phys. Rev. **94**, 794 (1954).

[3] Swan, Portnoy, and Hill, Phys. Rev. **90**, 257 (1953).

[4] J. B. Swan and R. D. Hill, Phys. Rev. **88**, 831 (1952); E. Kondaiah, Arkiv. Fysik **3**, 47 (1951); Bunker, Canada, and Mitchell, Phys. Rev. **79**, 610 (1950); D. Saxon, Phys. Rev. **74**, 1264 (1948); Cork, Schreffler, and Fowler, Phys. Rev. **72**, 1209 (1947).

[5] See reference 1 for decay scheme.

[6] J. M. Blatt and V. F. Weisskopf, *Theoretical Nuclear Physics*, (John Wiley and Sons, Inc., New York 1952), p. 627.

[7] Rose, Goertzel, and Swift, "L-Shell Internal Conversion Coefficients" (privately circulated).

Multiple Photon Production in Electron-Positron Annihilation

SURAJ N. GUPTA

Department of Physics, Purdue University, Lafayette, Indiana

(Received October 18, 1954)

DUE to the small value of the fine structure constant, multiple processes in quantum electrodynamics have not received much attention. In fact, it is usually believed[1,2] that the cross section for a process involving multiple production of photons is always much smaller than the cross section for a similar process involving the production of a lesser number of photons.

In order to see whether the above belief is justified even at very high energies, we have investigated the multiple production of photons due to the annihilation of an electron-positron pair. It is found that in the extreme relativistic case the cross section for the production of three photons in the electron-positron annihilation is

$$\sigma_3=\alpha^3\frac{c^2\hbar^2}{\mu E}\left(\log\frac{2E}{\mu}\right)^3, \tag{1}$$

where α is the fine structure constant, μ is the rest energy of the electron or the positron, E is the energy of the incident positron, and we have assumed that the electron is at rest. Further, an estimate of the cross section for the production of n photons in the electron-positron annihilation shows that

$$\sigma_n\approx\pi^{3-n}\alpha^n\frac{c^2\hbar^2}{\mu E}\left(\log\frac{2E}{\mu}\right)^{2n-3}. \tag{2}$$

We can now compare the cross sections (1) and (2) with the cross section for the production of two photons in the electron-positron annihilation, which in the extreme relativistic case is given by[1]

$$\sigma_2=\pi\alpha^2\frac{c^2\hbar^2}{\mu E}\log\frac{2E}{\mu}. \tag{3}$$

It is then evident that σ_n is of the same order as σ_2 when

$$\frac{\alpha}{\pi}\left(\log\frac{2E}{\mu}\right)^2\approx 1. \tag{4}$$

Thus, in spite of the smallness of the fine structure constant, the role of multiple processes in quantum electrodynamics is not negligible at very high energies.

Recently Schein and co-workers[3] have observed a very unusual shower of about 20 photons, which are unaccompanied by charged particles and are contained in a very narrow cone. Due to the absence of charged particles in the photon shower, it seems that these photons were produced by the annihilation of a charged particle and its antiparticle. Moreover, in order to account for the narrow width of the photon shower, Schein[4] has estimated that the energy of the incident particle is about 10^3 times its rest energy. Now, when $E\approx 10^3\mu$, we find that $(\alpha/\pi)[\log(2E/\mu)]^2\approx 1$, and therefore in such a case multiple production of photons can easily take place. This shows that Schein's photon shower could have been produced by the annihilation of an electron-positron pair, the energy of the incident positron being about $10^3\mu$ or about 0.5×10^{14} ev.

It should be noted that it would be rather difficult to provide any other explanation for the event observed by Schein. For instance, in the annihilation of a proton-antiproton pair the probability for the production of π mesons far exceeds the probability for the production of photons,[5] and therefore the proton-antiproton annihilation can hardly give rise to a pure photon shower.

The present investigation also serves to show that more attention should be paid to the study of multiple photon production in various elementary processes in quantum electrodynamics. Multiple processes may provide us with a test of the validity of the present quantum electrodynamics at exceedingly high energies.

A detailed account of this work will be published shortly.

I would like to express my sincerest thanks to Professor K. Lark-Horovitz and Professor M. Schein for several interesting discussions.

[1] W. Heitler, *Quantum Theory of Radiation* (Clarendon Press, Oxford, 1954).

[2] R. E. Marshak, *Meson Physics* (McGraw-Hill Book Company, Inc., New York, 1952).

[3] Schein, Haskin, and Glasser, Phys. Rev. **95**, 855 (1954).

[4] M. Schein (private communication).

[5] Ashkin, Auerback, and Marshak, Phys. Rev. **79**, 266 (1951).

Proceedings of the American Physical Society

Minutes of the 1954 Fall Meeting of the Ohio Section of The American Physical Society at University of Toledo, Toledo, Ohio, October 8–9, 1954

THE regular fall meeting of the Ohio Section of The American Physical Society was held at the University of Toledo, Toledo, Ohio, on Friday and Saturday, October 8 and 9, 1954. Invited papers included: "An Introduction to Concepts of Modern Computing Devices," by Dr. Edward S. Foster, University of Toledo; "Analog Computers," by Dr. Reinhart Rosenberg, University of Toledo; "Digital Computers," by Mr. Jack Belzer, Battelle Memorial Institute, Columbus, Ohio; and a brief outline of the program in engineering physics being developed at University of Toledo by Dr. John J. Turin, who is in charge of the Department of Physics, University of Toledo. On Saturday morning, there was presented an invited paper on "Thermal Emissivity of Refractories and its Importance for Glass Furnace Operation," by Dr. Wilhelm Eitel of the Institute of Silicate Research, University of Toledo. Five contributed papers were presented, the abstracts of which follow. At the end of these contributed papers, the Section heard a report by Dr. Arthur Lutz, Wittenberg College, concerning the work of the seminar on the teaching of the natural sciences in relation to religious concepts, which was held during the summer at the Pennsylvania State University.

Leon E. Smith, *Secretary*
The Ohio Section
American Physical Society
Granville, Ohio

1. A Study of Moisture Condensation Patterns on Glass and Crystalline Surfaces. W. C. Levengood, *Libbey-Owens-Ford Glass Company.*—A method was devised whereby moisture condensation patterns on glass and crystalline surfaces can be examined under the microscope and photographed. The technique was applied in a detailed study of minute surface fracture patterns or Griffith flaws. Experiments were made showing the type of fracture patterns produced on glass by various mechanical means Variations in the surface structure produced by etching, polishing, and chemical treatments were also studied by this method.

2. Beta Spectrum of Bismuth-210 Using a Diffusion Cloud Chamber.[1] A. A. Silvidi and J. G. Maxwell, *Kent State University.*—Using a diffusion type cloud chamber built at this laboratory 430 pictures were taken of a Pb-210 sample. 326 pictures had 510 measurable tracks. A beta spectrum was constructed. Using standard methods,[2] the end point energy was determined by two different ways A plot of $(N/\eta^2)^{\frac{1}{2}}$ *versus* ϵ gave an error of less than 10 percent but a Fermi-Kurie plot did not produce a straight line. Possible reasons for such deviation and ways to improve the accuracy will be discussed.

[1] Supported by the National Science Foundation.
[2] Natl. Bur. Standards (U. S.) Applied Mathematics Series 13, "Tables for Analysis of Beta Spectra."

3. A New Method for High Precision Studies of Rate Processes. W. Haller and G. L. Calcamuggio, *University of Toledo, Institute of Silicate Research.*—A method for the measurement of extremely small forces, acting upon an immersed sample, has been developed using a pressure-controlled hydraulic balance of the "Cartesian Diver" type. The position of a pressure-sensitive glass float, carrying the sample, is observed, while the pressure on the float is adjusted until equilibrium of the forces is reached and movement ceases. Changes in weight or volume of the sample or in density of the liquid result in forces compensated for by a corresponding pressure adjustment. The pressure response of the float has been determined by calibration and, therefore, the magnitude of the forces can be calculated from the pressure readings. The method promises to be useful for the study of rate processes, density-temperature, and density-concentration relations. Applied to rate processes, it was possible to measure continuously the weight loss of silicate glasses due to corrosion by water with an accuracy of 3×10^{-6} of 3 grams, which was the normal total sample weight. The accuracy attained depends upon the design of the compressible float and of a special thermostatic system controlling the temperature of the immersion liquid within ±0.001°C.

4. The Final-State Interaction in the Multiple Production of Mesons in Nucleon-Nucleon Collisions. Julius S. Kovacs, *University of Toledo.*—The Fermi statistical model for the multiple production of mesons[1–3] in high energy nucleon-nucleon collisions enables one to predict the relative probability for the production of the various multiplicities of mesons as a function of the incident energy. In recent Brookhaven experiments[4] collisions leading to single and double meson production were observed between cosmotron-produced neutrons and protons in a hydrogen-filled diffusion cloud chamber. The results of these observations give a ratio of double to single meson production which is about twenty times higher than that predicted by the statistical model. A possible modification of the statistical model in which the effect of the final state interactions (which are neglected from the point of view of purely statistical considerations) were taken into account will be discussed. These final state interactions (nucleon-nucleon, meson-nucleon, etc.) which enhance the cross section for all types of production could presumably account for the discrepancy occurring between the experimental results and the predictions of the statistical model.

[1] E. Fermi, Progr. Theoret. Phys. (Japan) **5**, 570 (1950).
[2] E. Fermi, Phys. Rev. **92**, 452 (1953).
[3] E. Fermi, Phys. Rev. **93**, 1434 (1954).
[4] Fowler, Shutt, Thorndike, and Whittemore, Phys. Rev. **95**, 1026 (1954).

5. Time of Flight Mass Spectrometer. Earl E. Hays, *University of Toledo.*—A time of flight mass spectrometer of the Goudsmit type[1] has been constructed at the University of Toledo. Details of construction of the spectrometer and the electron multiplier used as the detector will be given. The instrument has been built to use in research and instruction of undergraduate students.

[1] S. A. Goudsmit, Phys. Rev. **74**, 1537 (1948).

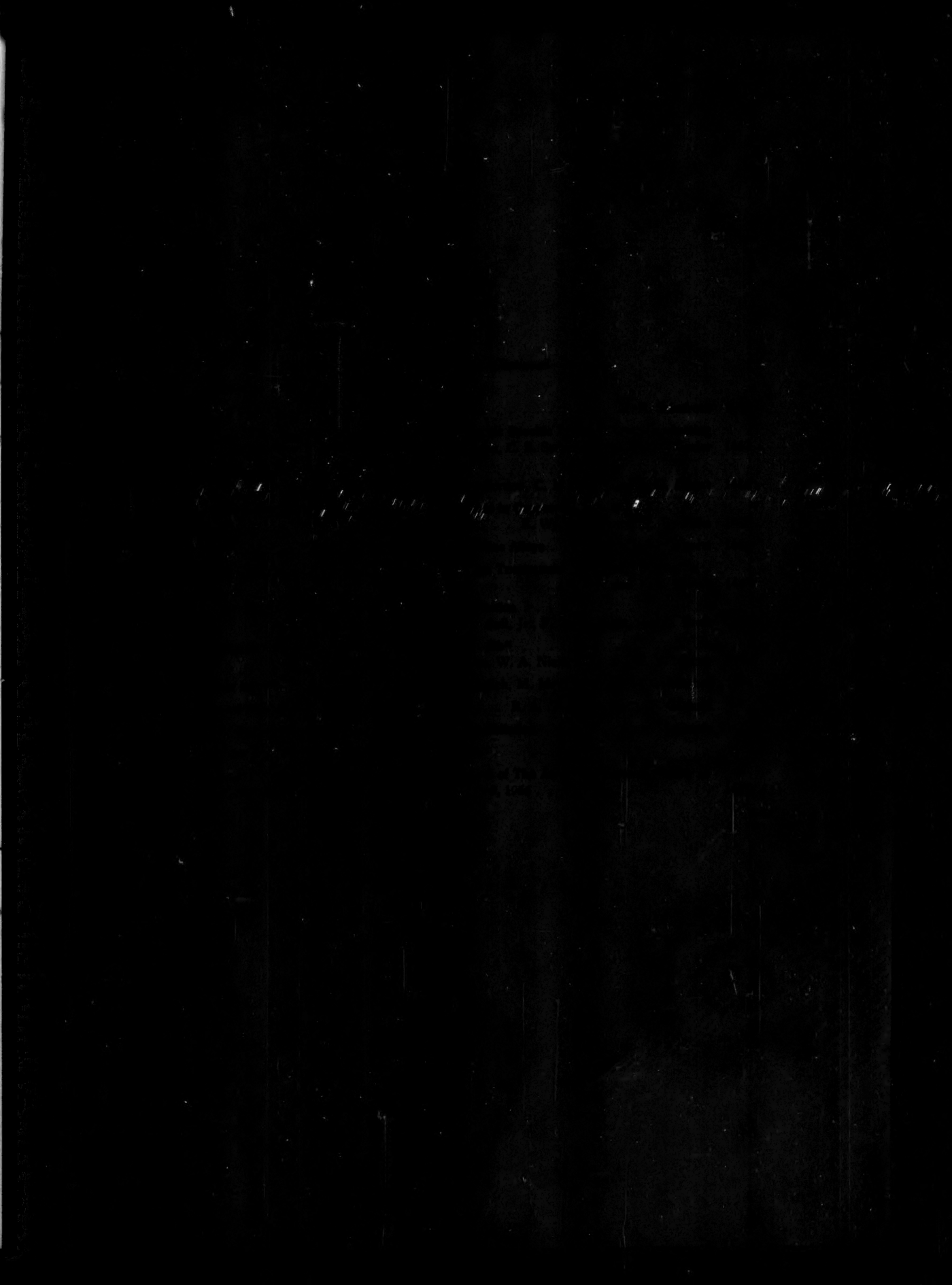

CONTENTS

THE PHYSICAL REVIEW SECOND SERIES, VOLUME 96, NO. 5 DECEMBER 1, 1954

Theory of the Thermoelectric Power of Semiconductors . . . Conyers Herring 1163

Optical Studies of Injected Carriers. II. Spontaneous Recombination and Absorption in Germanium at Low Temperatures . . . Roger Newman 1188

Antiferromagnetic Cobaltous Telluride . . . Dietrich A. Jenny and Richard H. Bube 1190

Magnetic Anisotropy at 0°K . . . Jack R. Tessman 1192

Electron Density in Crystalline Potassium . . . David Fox and O. Schnepp 1196

High-Frequency Resistance of Tin and Indium in the Normal and Superconducting State . . . C. J. Grebenkemper 1197

Evaporation of Isotopic Boron-Ionization Produced by Electron Bombardment . . . R. A. Sharpe, J. F. Marshall, and M. A. Pomerantz 1199

Hall Effect in Bismuth at Low Temperatures . . . J. M. [illegible], R. W. Hemstreet, T. E. Leinhardt, and D. D. Trimble 1203

Simplified Impurity Calculations . . . G. F. Koster and J. C. Slater 1208

Hall-Diffusion in Copper . . . [illegible] C. Lotsy, Jr., L. Slifkin, E. Sonder, and C. T. Tomizuka 1224

Resistivity and Hall Effect of Germanium at Low Temperatures . . . C. S. Hung and J. R. Gliessman 1226

Absorption of Microwaves by Copper in the Millimeter Wavelength Region . . . J. O. Artman and J. P. Gordon 1237

Diffusion Measurements of Thermal Neutrons in Water . . . G. von Dardel and N. G. Sjöstrand 1245

Fluorine-Light-Proton Reactions . . . R. W. Peterson, W. A. Fowler, and C. C. Lauritsen 1250

Coulomb Excitation of F^{19} by Alpha Particles . . . R. Sherr, C. W. Li, and R. F. Christy 1258

Elastic Scattering of 9.7-Mev Protons by Oxygen . . . Bruce Cork and Walter Hartsough 1267

Scattering of 9.5-Mev Protons by Elements . . . R. G. Fussmantle, D. J. Prowse, and J. Rotblat 1268

Scattering of 9.5-Mev Protons by Nickel and Argon . . . R. G. Fussmantle, D. J. Prowse, A. Hossain, and J. Rotblat 1270

Excitation Curves for $C^{12}(d,p)C^{13}$ and Properties of C^{13} . . . James A. Harvey, Bennett L. Hudspeth, and William W. Claudson 1272

Gamma Radiation from Co^{60} and Fe^{59} . . . W. E. Kreger and C. Sharp Cook 1276

Nuclear Quadrupole Spectra in Solids . . . M. H. Cohen 1278

Nuclear Resonance of Nb^{93} in $KNbO_3$ . . . R. M. Cotts and W. D. Knight 1283

Upper Limit on the Neutrino Magnetic Moment . . . C. L. Cowan, Jr., F. Reines, and F. B. Harrison 1294

Energies of the Radiations from Co^{60} and Fe^{59} . . . J. M. Cork, M. K. Brice, and L. C. Schmid 1295

Slow Neutron Cross Sections of Gold, Silver, Antimony, Mercury, and Nickel Oxide . . . R. G. Allen, T. E. Stephenson, C. P. Stanford, and Seymour Bernstein 1297

Photodisintegration of Helium . . . Everett G. Fuller 1306

Neutron-Proton Scattering at 90 Mev . . . R. H. Stahl and N. F. Ramsey 1310

(d,p) Reactions from Carbon, Nitrogen, and Oxygen . . . A. Sperduto, W. W. Buechner, C. K. Bockelman, and C. P. Browne 1316

Proton-Proton Scattering at 5.77 Mev . . . E. J. Zimmerman, Jr., G. Freier, Sidney Singer, F. Gerald Krieger, and W. Jentschke 1323

Determination of Alpha-Alpha Scattering Phase Shifts . . . James N. Snyder 1333

Classical Theory of the Temperature Dependence of Magnetic Anisotropy Energy . . . C. Zener 1335

Angular Distribution of 12- and 16-Mev Gamma Rays from the Proton Bombardment of a Thin Boron Target . . . H. H. Gleis, G. K. Farney, T. M. Hahn, and B. D. Kern 1337

Disintegration of Cs^{137} . . . Charles H. Pruett and Roger G. Wilkinson 1340

Thick-Target Bremsstrahlung Spectra for 1.65-, 1.85-, and 1.95-Mev Electrons . . . William Miller, J. W. Motz, and Carmen Cialella 1344

Orbital Electron Capture in the Neutron Deficient . . . R. W. Hoff and S. G. Thompson 1350

Energy Levels of Be^{10} . . . J. J. Jung and C. K. Bockelman 1353

Angular Distribution of Protons from (d,p) Reactions on Be^9, F^{19}, and Zn^{67} . . . P. S. Eby 1355

Charged Particles from the Bombardment of Li by He^3 . . . C. D. Moak, W. M. Good, and W. E. Kunz 1363

Fine Structure in the Velocity Distribution of Slowed Fission Fragments . . . R. B. Leachman and H. W. Schmitt 1366

Radiation from Ho^{166} . . . Hugh N. Brown and Robert A. Becker 1372

Interaction of Heavy Primary Cosmic Rays in Lead . . . Y. Eisenberg 1378

Interaction of a Negative Heavy Meson . . . J. E. Nafe, E. P. Ney, P. S. Freier, and W. B. Cheston 1383

Search for the Production of π^0-Mesons [illegible] in a 340-Mev Synchrotron Beam . . . H. [illegible], A. C. Odian, L. S. Osborne, and A. Wattenberg 1386

Composition of the Primary Cosmic Radiation at $\lambda = -107°$ . . . G. W. McClure 1391

Production Spectra of Cosmic-Ray Mesons in the Atmosphere . . . Seiandaw Olbert 1400

Abundance of Lithium, Beryllium, and Boron in the Primary Cosmic Radiation . . . M. F. Kaplon, J. H. Noon, and G. W. Ruscetta 1408

Measurement of Coulomb Interference in Low-Energy π^+-p Scattering . . . Jay Orear 1417

Method of Transition Probabilities in Classical Mechanics and Quantum Statistics . . . P. T. Landsberg 1420

Scattering of Light at Very Low Frequency by Systems of Spin $\frac{1}{2}$ . . . F. E. Low 1428

Scattering of Low-Energy Photons by Systems of Spin $\frac{1}{2}$ . . . M. Gell-Mann and M. L. Goldberger 1433

Calculation of Potentials from the Kerr Nonrelativistic Equation . . . J. C. Taylor 1438

(Continued on other side)

LANCASTER PRESS, INC., LANCASTER, PA.